Development of a structural, petrophysical and mechanical model of faults in porous sandstone environment : implications for the migration and trapping of fluids

Sven Philit

THÈSE POUR OBTENIR LE GRADE DE DOCTEUR DE L'UNIVERSITÉ DE MONTPELLIER

En Géosciences

École doctorale GAIA

Unité de recherche GEOSCIENCES MONTPELLIER

ELABORATION D'UN MODELE STRUCTURAL, PETROPHYSIQUE ET MECANIQUE DE FAILLES DANS LES GRES POREUX ; IMPLICATION POUR LA MIGRATION ET LE PIEGEAGE DES FLUIDES

Présentée par Sven PHILIT
Le 13 novembre 2017

Sous la direction de Roger SOLIVA et Alexandre CHEMENDA

Devant le jury composé de

Olivier LACOMBE, Professeur, ISTeP – Université Pierre et Marie Curie – Paris VI	Rapporteur
Pierre BESUELLE, Docteur, 3SR – Grenoble	Rapporteur
Hervé JOURDE, Professeur, Hydrosciences Montpellier – Université de Montpellier	Examinateur & Président
Christopher WIBBERLEY, Docteur, Total S.A.	Examinateur
Roger SOLIVA, Maître de Conference, Géosciences Montpellier – Université de Montpellier	Directeur de thèse
Alexandre CHEMENDA, Professeur, Géoazur – Université de Nice-Sophia Antipolis	Co-directeur de thèse
Claude GOUT, Docteur, Total S.A.	Invité

UNIVERSITÉ DE MONTPELLIER

THESIS FOR THE DEGREE OF DOCTOR OF PHILOSOPHY (PH.D.)
UNIVERSITY OF MONTPELLIER

In Geosciences

Doctoral School of GAIA

Scientific laboratory of GEOSCIENCES MONTPELLIER

ELABORATION OF A STRUCTURAL, PETROPHYSICAL AND MECHANICAL MODEL OF FAULTS IN POROUS SANDSTONES; IMPLICATION FOR MIGRATION AND FLUID ENTRAPMENT

Defended by Sven PHILIT
The 13th November 2017

Under the supervision of Roger SOLIVA
and Alexandre CHEMENDA

In front of the thesis jury composed of

Olivier LACOMBE, Professor, ISTeP – Université Pierre et Marie Curie – Paris VI	Reviewer
Pierre BESUELLE, Ph.D., 3SG – Grenoble	Reviewer
Hervé JOURDE, Professor, Hydrosciences Montpellier – Université de Montpellier	Examiner
Christopher WIBBERLEY, Ph.D., Total S.A.	Examiner
Roger SOLIVA, Senior lecturer, Géosciences Montpellier – Université de Montpellier	Supervisor
Alexandre CHEMENDA, Professor, Géoazur – Université de Nice-Sophia Antipolis	Co-supervisor
Claude GOUT, Ph.D., Total S.A.	Guest

Laboratoire Géosciences Montpellier – UMR 5243 – Université de Montpellier – 2 place Eugène Bataillon – 34095 Montpellier Cedex 5 – FRANCE

Summary

Deformation through cataclasis, which corresponds to grain crushing, is an effective process of porosity and permeability reduction in porous sandstones, classical aquifers and hydrocarbon reservoirs at depth. A major stake concerning the deformation in sandstone is to understand what processes govern the growth of the cataclastic structures and to recognize what parameters influence the expression of the deformation at microscopic scale and at basin scale.

In this study, we focus on the analysis of cataclastic deformation band clusters in order to consider a significantly concentrated deformation regarding the potential of fluid flow baffling. We select seven study sites presenting clusters formed in extensional and contractional tectonics, under different Andersonian regimes, at various burial depths and in sandstones of varying lithologies. To complement the structural analysis, we use an analytical approach to estimate the stress-state evolution of the sandstones leading to deformation. Numerical modeling allows the analysis of the influence of physical parameters on the structuring of the deformation.

We show that the position of failure along the failure envelope of the sandstone (which depends on its lithology) seems to determine the morphology of deformation. On the other hand, normal, strike-slip and thrust Andersonian regime clusters respectively seem to form frequently on the same part of the envelope.

Normal regime clusters (favorably formed in extensional tectonics) have thin to medium thickness, with high band density and form, with other clusters, networks of km-scale length - often localized near a major fault. They are likely to baffle fluid flow. Strike-slip regime clusters (favorably formed in contractional tectonics) have medium thickness with medium band densities. Due to their sparseness, they seem unlikely to form a baffle for fluids. Thrust regime clusters (favorably formed in contractional tectonics) have medium thickness and medium band density if failure is attained on the brittle part of the envelope. They seem potentially thicker, with low band density and tend to form arrays of deformation bands if failure is attained on the cap of the envelope. Because they are short and sparse, they do not represent an effective baffle for fluid flow.

We relate the process of cluster growth and their resulting morphology to the microscopic arrangement of the clasts in the deformed material. The minor compaction in the deformed material of normal and strike-slip regime clusters seems to be at the origin of the dense localization of the bands through the presence of weaker planes in the deformed material. For the same degree of deformation, the more compacted material in thrust regime clusters would favor the distribution of the bands.

Faulting of normal regime clusters is enhanced by the presence of layers including weak minerals between the sandstones. These weak layers are responsible for the initiation and propagation of major slip-surfaces in the adjacent sandstone from small displacements. The initiation of major slip-surfaces is also favored when porous sandstone is juxtaposed with a hard lithology.

We find that the quartz cementation of the most deformed parts of the clusters is common, even in clusters that were never buried below 800 m. This cementation is promoted by an intense degree of cataclasis, seems to form by “self-healing”, and may reduce the petrophysical properties of clusters.

Key-Words

Deformation band clusters; porous sandstone; cataclasis; faults, tectonic loading, Andersonian regime; mechanics

Amas de bande de déformation ; grès poreux ; cataclase ; failles ; chargement tectonique ; régime Andersonien ; mécanique

Foreword

This Ph.D. thesis was possible through the partnership of the laboratory of Géosciences Montpellier and the company TOTAL S.A. whose main interest in the case of this work relates to the exploitation of oil and gas reservoirs. We remind that this thesis was funded equally by the Doctoral School Gaïa (Université de Montpellier) and by TOTAL S.A.

The work undertaken in this thesis, dealing with the deformation in sandstone, represents the continuation of an important project involving many actors. Previous works include the Ph.D. thesis of E. Saillet until 2009 under the supervision of C. Wibberley at the Université de Nice-Sophia Antipolis, two Master's degree internships by T. Cavailhes in 2009 and G. Ballas in 2010 under the supervision of R. Soliva at the Université de Montpellier and in collaboration with A. Benedicto (from the company AREVA), the Ph.D. thesis of G. Ballas until 2013 under the supervision of R. Soliva at the Université de Montpellier and in partnership with AREVA, and eventually, a Master's degree internship by S. Philit in 2014 under the supervision of R. Soliva at the Université de Montpellier and in partnership with TOTAL S.A.

In this thesis, we teamed up with Alexandre Chemenda (Université de Nice-Sophia Antipolis) to complement the structural study undertaken with geomechanical analysis undertaken through numerical modeling. We also had the opportunity to collaborate with G. Ballas and H. Fossen for some discussions of the structural aspects of this work. In particular, this collaboration gave birth to an article published in Geology that we attach to the thesis in Appendix A.

We note that this thesis was initially designed to be based on scientific articles. The writing of the manuscript is therefore built on one published article and two articles in the process of revision. We added complementary observations and results attached to the articles that we thought deserved further insights. The part dealing with the numerical modelling is presented in a convention-free manner as an individual chapter of the thesis and its content could later be reshaped to satisfy the classical format of an article for publication. The reader can distinguish the parts relative to (future) articles with the different font style we used. Note that the figures linked to the articles are numbered independently from the general numbering of the thesis.

For convenience, we provide a glossary summarizing all the symbols used in the thesis.

Acknowledgments

I would like to pay great thanks to Roger Soliva for his guidance and support over the past few years, and for giving me the opportunity to develop this project. I am very grateful to the time he invested in me, as he contributed to build the person that I am now. I thank Alexandre Chemenda for his support on geomechanics, his education on the subject and his patience in answering my many and often clumsy questions. Gregory Ballas is thanked for making himself available and providing useful advice on a topic he masters perfectly.

Many thanks are due to Raymi Castilla who read my reports for Total S.A., and who willingly came to me in Montpellier and even in the field. The time we spent together was appreciated and gave rise to useful and thoughtful discussions. I am also thankful to Claude Gout from Total S.A. who made the birth of this project possible several years ago and followed its development behind the scenes until its achievement.

I am in debt to Doriane Delmas and Chrisophe Nevado for their precious help on the preparation of the thin-sections that constituted the grounding of the microstructural analysis, a significant part of my work. The time they gave to the understanding of my needs and their skillful work were invaluable.

I thank Laurent Dezileau for his sympathy and for the convenient access to the Laser granulometer that he made possible.

I must pay a specific thanks to Sablex, GEA Materiaux and Sibelco who readily opened the gates of their quarries.

Thanks to the members of my committee, Olivier Lacombe, Pierre Bésuelle, Hervé Jourde and Christopher Wibberley, who were willing to dedicate a “bit” of their time on my work and made constructive comments on my manuscript and defense.

I am immensely grateful to Audrey Taillefer who was my office mate for several years, and also a valued peer on the many field trips she accompanied me. A large amount of measurements necessary for my work would not have been possible without her. I thank Séverine Furst and Samuel Doucet for their support, their patience and their kindness during the years I shared the room with them. Their good mood was essential to a peaceful work environment. I must thank all my friends at Geoscience Montpellier, Ph.D. students or not: Lise, Benjamin, Anita, Alizia, Oswald, Robin, Carlotta, Sarah, Olivier, Cyprien, the two Maximes, Sophia, Manon, Anaïs, Laure, Enora, Justine, Alexandre, Toogii, Romain, Manar, Manuel, Badr: you made my time at GM enjoyable. I do not forget all the nice people I met in the lab, in particular, the G2R team headed by Jean-Jacques Cornée, the members of the technical staff who make our life easier on a daily basis, and the people of the management department, Céline Romestant, Amélie Armanet and Renaud Trinquier, who bailed me out more than once.

I am very grateful to David Kerr-Munslow who generously accepted the task of checking and correcting the English in key parts of this manuscript.

Much gratitude goes to « My Miss », Anne-Elizabeth, who constantly supported me in all situations, when I was away enjoying the exercise of geology abroad as well as when my mind was in distress near the end of the journey. Eventually, I pay thanks to my parents who, from afar, always conveyed their moral support.

Glossary of definitions and symbols

Definitions relative to this work

Cataclasis: mechanism consisting in the grain crushing, in particular via fracturing at the Hertzian contacts, leading to the size reduction (comminution) of the particles and particle size distribution.

Deformation band: (in porous sandstones) discrete tabular structure where the deformation is localized. In our study, most of the deformation bands are formed by cataclasis and may be referred to as "*cataclastic deformation bands*" (*CDB*).

Cluster: grouping of several deformation bands, accounting for at least 10% of band thickness. Clusters may or may not include slip-surface. In this study, the considered clusters generally display least widths of 10 cm.

Degree of cataclasis: (in this study) percentage volume of clast material whose Feret diameter is lower or equal to 1/10th of the modal host rock grain diameter D_{mod} (designed to describe the microscopic amount of deformation of the cluster). Because the degree of cataclasis is an equivalent of the matrix percentage, this definition can be used to classify the deformed material according the classification of Sibson (1977), for instance.

Band density: cumulated band thickness divided by the cluster thickness (designed to describe the macroscopic amount of deformation of the cluster).

DSB: Dilatant Shear Band

SSB: Simple Shear Band

CSB: Compactional Shear Band

SECB: Shear-Enhanced Compaction Band

PCB: Pure Compaction Band

Stress-path: evolution of the stress state of a formation, depending on σ_1, σ_2 and σ_3, with $\sigma_1 \geq \sigma_2 \geq \sigma_3$, from the deposition of the sandstone, to its failure.

Symbols for petrophysical properties and shape descriptors

ϕ : porosity (%)

k: permeability (mD)

R: radius of the grains (µm or mm)

D_{mod}: modal host rock grain diameter (µm or mm)

s: sorting according the formula proposed by Folk and Ward (1957):

$$s = \frac{\frac{\log(d_{84})}{\log(2)} - \frac{\log(d_{16})}{\log(2)}}{4} + \frac{\frac{\log(d_{95})}{\log(2)} - \frac{\log(d_5)}{\log(2)}}{6.6}$$

where d_5, d_{16}, d_{84} and d_{95} are the diameters of the largest particles from the cumulative particle population occupying 5, 16, 80 and 95% of the cumulative sample area, respectively.

Round: Roundness shape descriptor estimating the elongation of the particle (roughness) [0 – 1]:

$$Round = 4 \times \frac{Area}{\pi \times [Major\ axis]^2}$$

Circ: Circularity shape descriptor estimating the elongation and irregularity of the particle (roughness) [0 – 1]:

$$Circ = 4\pi \times \frac{Area}{Perimeter^2}$$

Solid: Solidity shape descriptor estimating how "ruffled" the grain surface is [0 – 1]:

$$Solid = \frac{Area}{Convex\ area}$$

Symbols for mechanics

$\boldsymbol{g}$: Earth gravity (m s^{-2})

$\boldsymbol{\sigma_1}$: Maximum principal stress (Pa or MPa)

$\boldsymbol{\sigma_2}$: Intermediate principal stress (Pa or MPa)

$\boldsymbol{\sigma_3}$: Minimum principal stress (Pa or MPa)

$\boldsymbol{\sigma_v}$: Vertical stress (Pa or MPa)

$\boldsymbol{\sigma_H}$: Major horizontal stress (Pa or MPa)

$\boldsymbol{\sigma_h}$: Minor horizontal stress (Pa or MPa)

$\boldsymbol{K_0}$: Coefficient of Earth's pressure at rest in the absence of tectonic stresses

$\boldsymbol{P}$ or $\boldsymbol{\sigma_m}$: Effective mean stress (Pa or MPa):

$$P = \frac{\sigma_1 + \sigma_2 + \sigma_3}{3} - Pf$$

where Pf is the fluid pressure exerted by a free water column (Pa or MPa)

P*: Hydrostatic critical state (Pa or MPa):

$$P^* \sim (\phi R)^n$$

where the exponent n = -3/2.

C': Plastic softening critical stress state (Pa or MPa)

C*: Plastic hardening critical stress state (Pa or MPa)

$\boldsymbol{Q}$: Differential/Deviatoric stress (Pa or MPa):

$$Q = \sigma_1 - \sigma_3$$

$\boldsymbol{Q_{lin}}$ **E**quation of the critical state line (used as a simplification for the brittle part of the failure envelope) in the Q-P diagram (Pa or MPa):

$$Q_{lin} = M\ P$$

with M the slope of the critical state line:

$$M = \frac{6 \sin \varphi}{3 - \sin \varphi}$$

$\boldsymbol{Q_{cap}}$: Simplified equation of the ductile part of the failure envelope, describing an ellipse in the Q-P diagram (Pa or MPa):

$$Q_{cap}^2 = \left(\frac{6\sin\varphi}{3-\sin\varphi}\right)^2 P(P^* - P)$$

$\boldsymbol{P_{bur}}$: Effective mean stress at deformation burial

$\boldsymbol{Q_{bur}}$: Differential stress at deformation burial

$\Delta\boldsymbol{\sigma_{ext}}$: Stress deficit along the horizontal axis submitted to extension

$\Delta\boldsymbol{\sigma_{con}}$: Stress excess along the horizontal axis submitted to contraction

$\boldsymbol{\eta_{ext}}$: Fraction of stress deficit along the horizontal axis perpendicular to the axis submitted to extension [0 – 1]

$\boldsymbol{\eta_{con}}$: Fraction of stress excess along the horizontal axis perpendicular to the axis submitted to contraction [0 – 1]

$\boldsymbol{\bar{\tau}}$: Von Mises stress (Pa or MPa):

$$\bar{\tau} = \frac{1}{\sqrt{6}}\sqrt{(\sigma_1-\sigma_2)^2 + (\sigma_2-\sigma_3)^2 + (\sigma_3-\sigma_1)^2}$$

$\boldsymbol{N}$: Lode parameter :

$$N = -\frac{(\sigma_2 - \sigma_m)}{\bar{\tau}}$$

$\boldsymbol{\theta}$: Cosine Lode angle [0 – 60 °], with the relation to N:

$$N = \frac{2}{\sqrt{3}}\cos\left(\frac{2\pi}{3} - \theta\right)$$

$\boldsymbol{\bar{\gamma}^p}$: Inelastic shear strain

$\boldsymbol{\varepsilon^p}$**:** Inelastic volume strain

$\boldsymbol{\varphi}$: Friction angle of the host rock

$\boldsymbol{\alpha}$: Internal friction coefficient:

$$\alpha = \left(\frac{\partial f(\sigma_m, \bar{\gamma}^p)}{\partial \sigma_m}\right)_{\bar{\gamma}^p}$$

$\boldsymbol{\beta}$: Dilatancy factor:

$$\beta = \left(\frac{\partial \varepsilon^p(\sigma_m, \bar{\gamma}^p)}{\partial \bar{\gamma}^p}\right)_{\sigma_m}$$

$\boldsymbol{E}$: Young modulus

$\boldsymbol{G}$: Shear modulus

$\boldsymbol{\nu}$: Poisson's ratio

$\boldsymbol{\kappa}$: Cohesion (Pa or MPa)

$\boldsymbol{h}$: hardening modulus:

$$h = \frac{1}{G}\left(\frac{\partial \bar{\tau}(\sigma_m, \bar{\gamma}^p)}{\partial \bar{\gamma}^p}\right)_{\sigma_m} = \frac{1}{G}\left(\frac{\partial \kappa}{\partial \bar{\gamma}^p}\right)_{\sigma_m}$$

Table of Content

Introduction

Introduction

For decades, a substantial part of our resources in water, oil, gas and some ore deposits have been extracted from porous geological reservoir. A major part of these porous reservoirs consists of porous sandstone formations, which are also considered as conventional reservoirs in the hydrocarbon exploitation domain. These sandstones reservoirs all have different histories in terms of time and environment of deposition, burial, and deformation in response to tectonic loading. It is therefore important to determine the quality of the sandstone reservoirs as a function of these parameters. In particular, the deformation of sandstones leads to structural and petrophysical alteration of the formation (e.g. folding, faulting, jointing) likely to modify the trapping potential and the fluid flow behavior (e.g. Faulkner et al., 2010 and references inside – see also Figure), and consequently likely to affect the production of the resource. Face to the rarefying conventional reservoirs and the costly development of the unconventional reservoirs (e.g. oil in fractured carbonates, shale gas, gas hydrates), and since porous reservoirs constitute a fair solution for future CO_2 storage, the industry must constantly enhance the recovery and better predict the fluid flow in sandstone reservoirs. Therefore, it is essential to improve our knowledge of the evolution of deformation processes in sandstone.

Figure 1. Picture illustrating the impact of deformation in sandstone on potential resource compartmentalization (credit to Fossen). On this example a thin cluster of deformation bands baffles the migration of oil from the hanging wall to the footwall of the sandstone reservoir, Pismo Basin (California). Note the person with the blue shirt for the scale.

In porous sandstones, incipient fault stage corresponds to cataclastic deformation zone described as deformation bands. The deformation bands are typically millimeter to centimeter thick and have a lateral and vertical extent of a few tens of meters (Aydin, 1978; Aydin et Johnson 1978; Antonellini and Aydin, 1995; Shipton and Cowie, 2003; Wibberley et al., 2007; Ballas et al., 2013). These bands are formed by the microprocess of cataclasis, involving grain crushing, spalling and

rearrangement, thus modifying the original grain structure of the host rock (Fowles and Burley, 1994; Antonellini et al., 1994; Gibson, 1998; Ogilvie and Glover, 2001; Fossen et al., 2007). Although of subseismic scale, this deformation results in an alteration of the petrophysical properties of these bands (porosity and permeability) compared to the host rock and will influence the petrophysical quality of the reservoir (Antonellini and Aydin, 1994; Fisher and Knipe, 2001; Fossen and Bale, 2007; Saillet and Wibberley, 2013). It is known that deformation bands and potential subsequent faults play a role on fluid circulation in a reservoir. More specifically, bands and faults tend to baffle or impede fluid flow across the structures and that faults sometimes enhance fluid flow along them (Jourde et al., 2002; Sidga and Wilson, 2003; Tueckmantel et al., 2012; Farrell et al., 2014; Ballas et al., 2015) (Figure). Deformation bands have diverse shear-to-compaction ratios and display different modes of localization as a function of the tectonic loading (Bésuelle, 2001; Schultz and Siddharthan, 2005; Ballas et al., 2014; Fossen et al., 2017). Contractional tectonic events seem to favor the deformation under the form of distributed network of deformation band whereas extensional tectonic events seem to favor the localization of deformation under the form of multiple deformation bands gathered side by side, forming clusters of deformation bands (Ballas et al., 2015; Soliva et al., 2016). Yet, other parameters can influence the process of deformation, its resulting structure, distribution and the petrophysical properties of the cataclastic deformation. In particular, the influence of the burial (Fisher and Knipe, 2001; Soliva et al., 2013), the shape of the grains (Mair et al., 2002; Anthony and Marone, 2005; Karner et al., 2005; Guo and Morgan, 2006; Cho et al., 2006), or the mineralogy and diagenetic state of the rock (Logan and Rauenzahn, 1987; Milliken et al., 2005; Lommatzsch et al., 2015) on the formation of clusters are poorly constrained. The processes, the cause of band clustering and the organization of the clusters have long been debated and remain poorly understood (Aydin and Johnson, 1978; Shipton and Cowie, 2001; Wibberley et al., 2007; Nicol et al., 2013; Soliva et al., 2013).

Aims of the study and study areas

In this thesis, we aim at clarifying and constraining the ideal conditions for cluster formation as a function of diverse parameters, and describing their morphology and dimension relative to these parameters. We also aim at expressing the processes governing the evolution of a cataclastic deformation band to a cluster of cataclastic bands, and of a cluster to a fault with the development of a major slip-surface. This study should allow us to precise the model established by Ballas (2013) concerning the deformation of porous sandstone.

To do so, we propose to perform an integrated field analysis, studying seven sites located in the Southeast basin of Provence (France), on the Moray Coast (Scotland), on the eastern border of the Harz Mountain (Germany), and in the San Rafael desert (Utah). The sites are selected for the diversity of their settings (lithology of the host rock, burial, tectonic regime of deformation), each of those constrained in the literature. Our analysis ranges from microscopic scale to characterize precisely the cataclastic and diagenetic processes in stake, to pluri-kilometer scale to better account for the extent of the structures relative to reservoir exploitation at basin scale. We will also use numerical modeling based on explicit finite difference to give a mechanical insight of the process of deformation involved in the cluster development.

Thesis contents

To address the aims of this thesis, we organize our work as follows:

- In Chapter I, we will review the current knowledge on the subject of porous sandstone deformation, including the structural and petrophysical characteristics of cataclastic deformation, its distribution in the formation and its impact on fluid flow. This state of the art will be drawn from field studies, experimental analyses and numerical modeling. In particular, we will expose the existing models proposing explanations for the evolution of clusters and indicate what, in our opinion, lacks of precision or fails to be consistent with field observations. As an attempt to fill these gaps, we will expose the questions that we will try to answer in this work.

- In Chapter II, we will present the results of our field investigation concerning cataclastic deformation in porous sandstones. We will firstly introduce the geological settings of the studied sites and explain our choices relative to the aim of the study. Secondly, in order to frame the process of cataclastic deformation compared to other processes of deformation, we will study the interplay between different deformation mechanisms linked to lithological variations in sandstone-dominated formations. We will show that different mechanisms of deformation can overprint over each other through time and space, leading to contrasting fluid flow behaviors in a reservoir. In particular, we will expose that the lithological contrasts in sandstone-dominated formation are likely to initiate faults subsequently propagating in the clusters. Thirdly, to better understand the influence of the tectonic loading and sandstone lithology on the morphology of clusters and its influence on fluid flow, we will analyze the structuring of the clusters as a function of these two parameters based on qualitative and quantitative analysis of the deformation at the scale of the exposure. We will show that in some cases, the cluster can represent efficient baffle to fluid flow. A microscopic analysis of the intracluster deformation helps characterizing the processes of cluster growth; we will give our interpretation of the processes involved in the evolution of a cataclastic deformation band to a cluster as a function of the granular properties of the deformed rock. We will present the analytical tool developed for the interpretation of stress-state evolution until failure for each of our study sites as a function of the estimated failure envelope of the rock and type of deformation undergone by the rock. Eventually, to better grasp the possible evolution of the clusters and their potential influence on fluid flow, we will study the influence of cataclasis on cementation based on field observation and microscopic analysis. We will thereby show that cementation is not restricted to deeply buried sandstone formation and that it can have a dramatic impact on the petrophysical properties of cataclastic structures in terms of porosity, permeability and hardening.

- In Chapter III, we will present the results of the numerical modeling used to test the influence of several physical parameters on the geometry of clusters, confront them with the field observations and discuss their mechanical implications for the understanding of the processes of development of cataclastic band clusters.

- In Chapter VII, we will summarize and discuss the main results of this work combined together and establish a model for the development of clusters in sandstones as a function of the several parameters controlling their growth. We will also draw up a qualitative assessment of the implications for reservoir exploitation before bringing some general conclusions.

Chapter I

1. State of the art and issues

In this chapter, we summarize the knowledge of cataclastic deformation acquired by previous works including field studies, experimental analysis, mechanical and numerical modeling. We also give a reminder of some definition pertaining to the deformation in sandstones. Our review encompasses the following topics: the processes of deformation; the localization of deformation in porous sandstones; the mechanics of porous granular media; the impact of cataclastic deformation on fluid flow; the scaling to reservoir exploitation. We put a specific emphasis on the few preexisting models of cluster evolution, underlining their shortcomings in the light of the current knowledge from field observations. Eventually, we will expose our problem in relation of the gaps of the previous works.

1.1. Sandstone deformation

1.1.1. Deformation mechanisms

As observed in the field, the deformation localizes in porous sandstones under the form of bands of variable aspects that depend on their mechanism of deformation. Although our study mainly focuses on cataclastic deformation, we review here the most frequent mechanisms of deformation and distinguish them, as each mechanism implies contrasted evolution of the petrophysical properties.

Cataclastic bands (CDB) are formed by cataclasis. The mechanism of cataclasis consists in the grain crushing following several mechanisms of deformation, leading to the size reduction (comminution) of the particles and particle size distribution (Sammis et al. 1987; Rawling and Goodwin, 2003) (Figure 2a). The loading of sandstone leads to a stress accumulation along force chains and grain contacts (Figure b), oriented parallel to the maximum principal stress (Gallagher et al., 1974; Anthony and Marone, 2005; Taboada et al., 2005). The loading of the force chains provokes the fracturing of the grains between the Hertzian contacts (Hertzian fracturing) (Figure 2b&c); the fracturing can affect an entire force chain (Gallahager et al., 1974). A significant component of shear also involves spalling and flaking by shearing and rolling. The degree of cataclasis, which is the percentage of deformed material relative to the whole volume of rock (equivalent to the matrix volume percentage), allows classifying the cataclastic deformation structures as crush-microbreccia, protocataclasite, cataclasite and ultracataclasite (Figure 3 - Sibson 1977; Scholz, 2002). The degree of cataclasis is considered as a function of the displacement (e.g. Engelder, 1974; Ballas, 2012). The process of cataclasis occurs in clean, poorly lithified sandstones, with porosity generally higher than 15% (Aydin, 1978; Aydin and Johnson, 1978; Pittman, 1981; Antonellini and Aydin, 1994; Antonellini et al., 1994; Cashman and Cashman, 2000; Davatzes et al., 2003; Myers and Aydin, 2004; Wong et Baud, 2012; Ballas, 2014). The cataclasis mostly induces a porosity decrease and seems to generally enhance the cohesion of the deformed rock compared to the host rock. We note that the origin of this cohesion is poorly defined in the literature. As a consequence of this favored cohesion of the cataclastic material, cataclastic deformation bands (CDB) (Figure 4a) generally exhibit a slight relief compared to the surrounding host rock (Aydin 1978; Antonellini et Aydin, 1994, 1995; Cashman et Cashman, 2000; Du Bernard, 2002a; Fossen et al., 2007; Wibberley et al., 2007; Saillet et Wibberley, 2010). Remark that, in deformed zones, even the apparent pristine rock record a minor degree of cataclasis (Lanatà, 2014).

Disaggregation Bands (Figure 4b) are formed by the rearranging of the granular structure through rotation, dilation and slipping of the grains, without significant grain crushing. They are formed in sands or poorly lithified sandstones (Du Bernard et al., 2002b; Fossen, 2010; Kristensen et al., 2013; Schultz et al., 2013).

Pyllosilicate Bands (Figure 4c) are formed by smearing of phyllosilicates between the grains along the bands, favoring the shear deformation of the material (Gibson, 1998). These bands occur in sandstones with phyllosilicate content higher than 10 – 15% (Leveille et al., 1997).

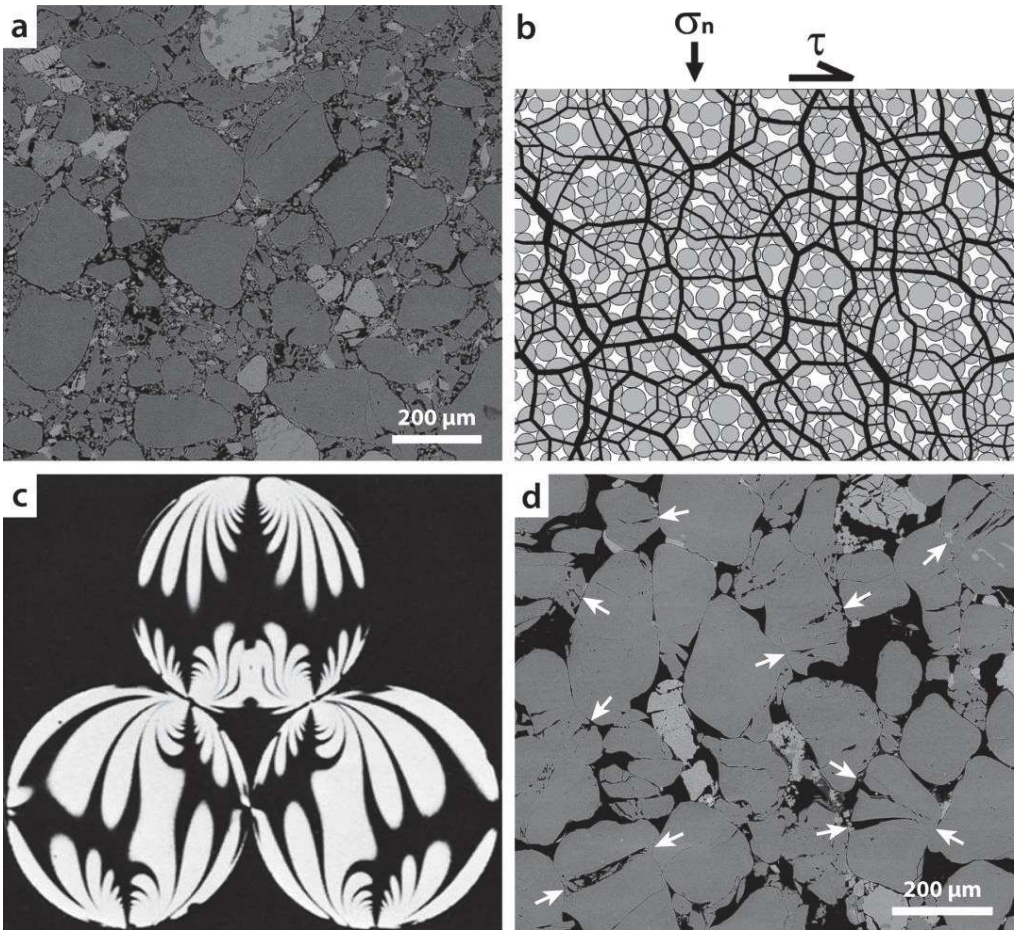

Figure 2. (a) Quartz-rich sandstone deformed by cataclasis as imaged via Scanning Electron Microscopy (SEM) in Backscattered Electrons (BSE). The grain size population is generally dispersed and, although a few initial grains remain undeformed, the average grain size is lowered. (b) Force chains between the grains induced by stress loading, as modeled by Aharonov and Sparks (2002). (c) Intragranular elastic stress loading of glass beads during photoelastic analysis as imaged by Gallagher et al. (1974). The stress was applied vertically on the beads that were laterally confined. The transition between black and white areas reflects iso-stress lines. Major stresses locate at the grain-grain contacts, which are named the Hertzian contacts. (d) Intragranular microfractures developed between the Hertzian contacts (arrows) in a quartz-rich sandstone (SEM-BSE imaging).

1.1.2. Kinematic-types of deformation

Depending on the amount of shear and compaction recorded by a band, several types of deformation band are distinguished. The quantification of the shear by marker analysis and compaction by porosity variation analysis (Soliva et al., 2013) allows a relevant kinematic classification of the bands comprised between three poles which are Pure Dilation Bands, Simple Shear Bands and Pure compaction bands (Fossen et al., 2017).

Pure Dilation bands (PDB) (Figure 5a&b) are characterized by an increase of porosity in the band relative to the porosity of the host rock, without shear component along the band surface. The geometry of these bands can be slightly irregular but remains rather tabular. This type of band is deformed by disaggregation and therefore involves no cataclasis. PDB were first described by Du Bernard (2002b) and would have a similar stress state origin than joints and Mode I fractures in general (Chemenda et al., 2011).

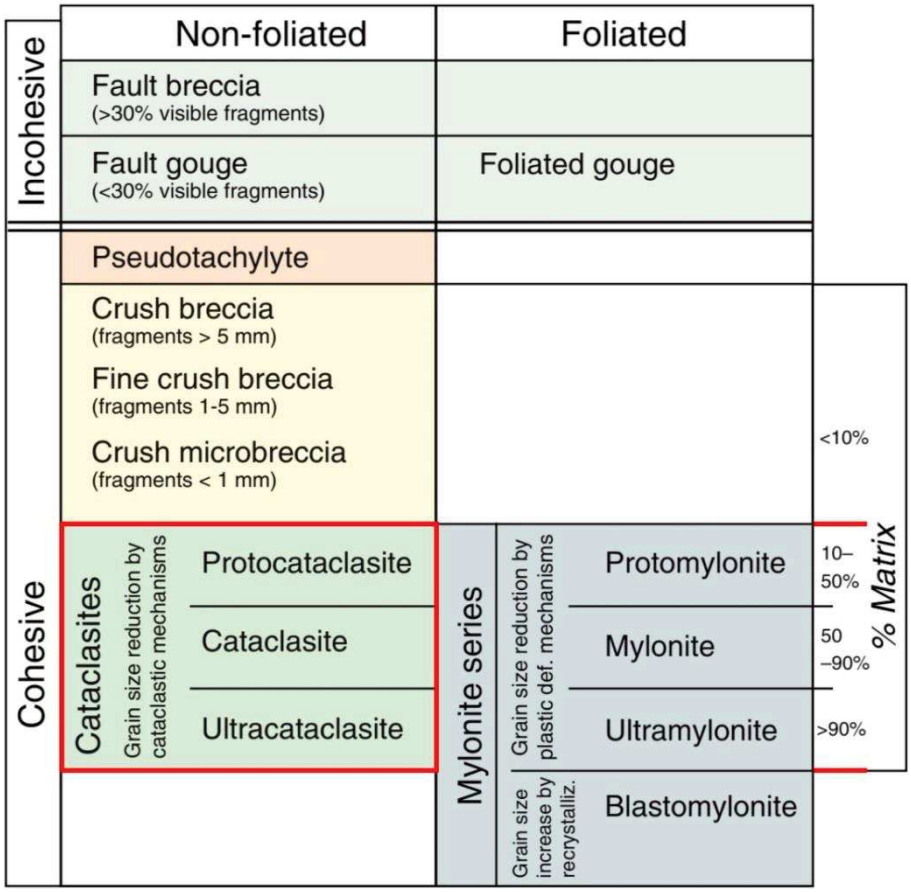

Figure 3. Fault rock classification of Sibson (1977), revised by Fossen (2016). The matrix volume percentage corresponds to the degree of cataclasis of the deformation material and allows classifying the different types of cataclastic structures (red frame).

Simple Shear bands (SSB) (Figure 5a&c) are characterized by a near-isochoric deformation, accompanied by a shear displacement of a few millimeters to a few centimeters maximum near the center of the structure (Fossen and Hesthammer, 1997; Aydin et al., 2003). The geometry of these bands is tabular. If the bands are slightly dilatant, then the disaggregation mechanism of deformation will be favored (Antonellini et Aydin, 1995; Fossen et Hesthammer, 1997; Cashman et Cashman, 2000). If the band is slightly compactant, cataclasis will be favored (Fossen et al., 2007; Rotevatn et al., 2008; Tueckmantel et al., 2010; Saillet et Wibberley, 2010).

Pure Compaction bands (PCB) (Figure 5a&d) are characterized by a porosity reduction of the band without shear component (Aydin et al., 2006). These bands are rather wriggly and shorter than the other bands (Sternlof et al., 2005). Although these bands do not record significant grain size reduction, their deformation is governed by cataclasis (Mollema et Antonellini, 1996; Sternlof et al., 2006; Eichhubl et al., 2010; Schultz et al., 2010; Fossen et al., 2011; Deng et Aydin, 2012).

Shear-Enhanced Dilation bands (SEDB) and **Dilational Shear bands** (DSB) are the kinematic intermediary between the PDB and the SSB. The deformation of these types of bands is controlled by disaggregation. Macroscopically, these bands present a small negative relief.

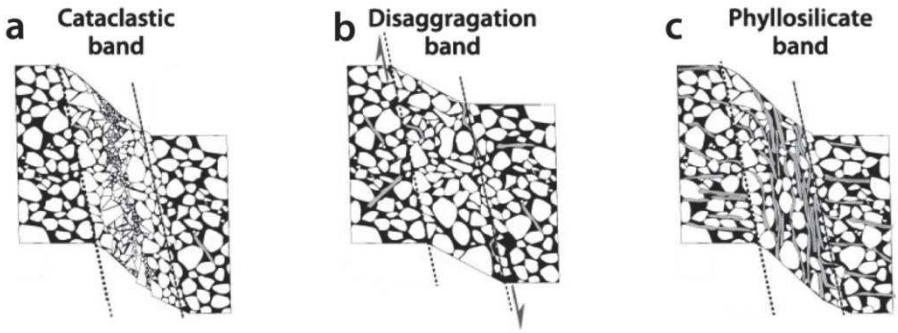

Figure 4. Summary of the different processes of deformation in sandstones (modified from Fossen et al., 2007). (a) Catacclastic deformation. (b) Disaggregation. (c) Phyllosilicate-induced deformation.

Compactional Shear bands (CSB) and **Shear-Enhanced Compaction bands** (SECB) are the kinematic intermediary between the SSB and the PCB. The deformation of these types of bands is controlled by cataclasis.

Fault surfaces are singular structures in the fact that their edges are made of deformed material resembling to shear bands (Figure e and f). The slip-surface marking the fault may accommodate displacements of up to several meters.

The deformation structures covered by this study are cataclastic, involving both shear and compaction, encompassing CSB and SECB. We will henceforth refer to this group of bands as cataclastic deformation bands (CDB).

1.1.3. Dimensions and localization

CDB measure from a few tens of centimeters to a few tens of meters in lateral extent, and account for similar extent vertically, within the limit of the sandstone formation (Fossen and Hesthammer, 1997; Schultz and Fossen, 2002). CDB accommodate displacement lower than one millimeter to about one centimeter (Figure 6a). Depending on multiple parameters such as the tectonic regime, the lithology of the sandstone or the burial, the CDB are observed with variable degrees of distribution. The cataclastic deformation can localize as single deformation band as described before. Several bands can also gather to form “multi-strand band”, including 2 to 5 bands (Figure 7a), which have an extent of a few meters to several tens of meters and a width of a few centimeters (Wibberley et al., 2007; Eichhubl et al., 2010; Ballas et al., 2012). Their displacement is proportional to the number of individual band they include, ranging from several millimeters to several centimeters (Fossen and Hesthammer, 1997).We note that the expression “multi-strand band” is ambiguous as under the name of “band” it actually refers to several bands/”strands”.

Further band gathering (up to several tens of bands) are defined as “clusters of deformation bands” (or “cluster”). The clusters are the core interest of our study. According to the previous definitions and descriptions of the clusters in the literature, the clusters are defined as the grouping of two or more bands (Fossen et al., 2017), accounting for at least 10% of band thickness (based on a usual frequency of 20 - 30 bands per meter reported by Johansen and Fossen, 2008 and a typical band thickness of about 4 mm as shown in Wibberley et al., 2007). Clusters usually form relief at the outcrop (Figure 7b). They commonly display a continuous extent of ten to a few tens of meters in

length and a width of few centimeters to a meter, accommodating displacement of tens of centimeters to a meter (Figure 6b) (Antonellini and Aydin, 1994; Shipton and Cowie, 2001; Fossen and Bale, 2007; Wibberley et al., 2007; Rotevatn et al., 2008; Saillet and Wibberley, 2010; Nicol et al., 2013; Klimczak and Schultz, 2013; Ballas et al., 2015). We note that clusters sometimes form networks whose morphology, geometry and spatial distribution are not well understood.

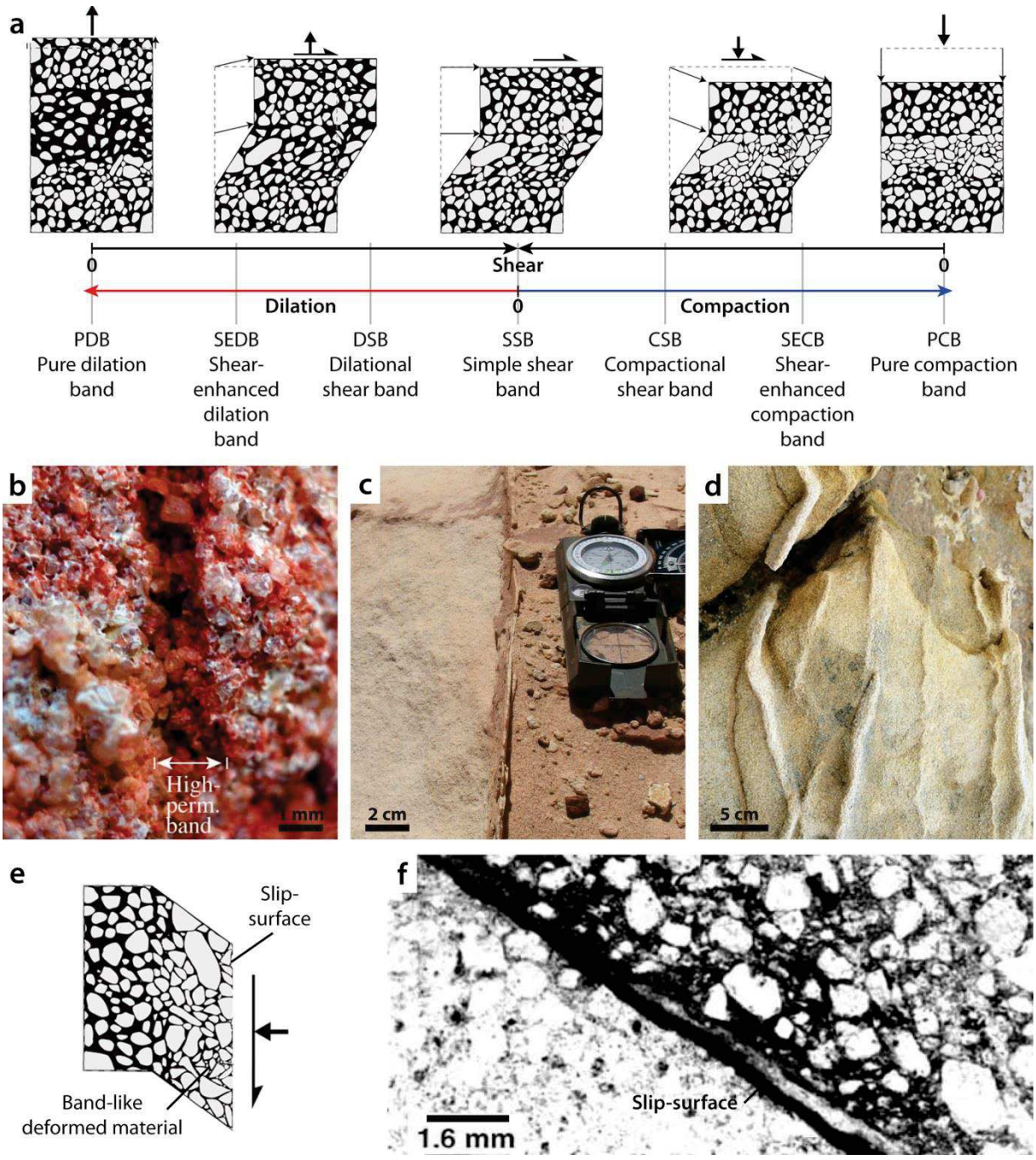

Figure 5. (a) Summary of the different kinematic-types of deformation bands in porous sandstones, classified between three poles: pure dilatancy, simple shear and pure compaction (modified after Fossen et al., 2007 and 2017). (b) Macrostructural aspect of the Dilation band (from Fossen et al., 2007). (c) Macrostructural aspect of the Shear band. (d) Macrostructural aspect of the Compaction bands (Fossen et al., 2015). (e) The fault slip-surface edged by deformed material; the shear component is very important. (f) Example of a slip-surface seen in thin section (from Shipton et al., 2002).

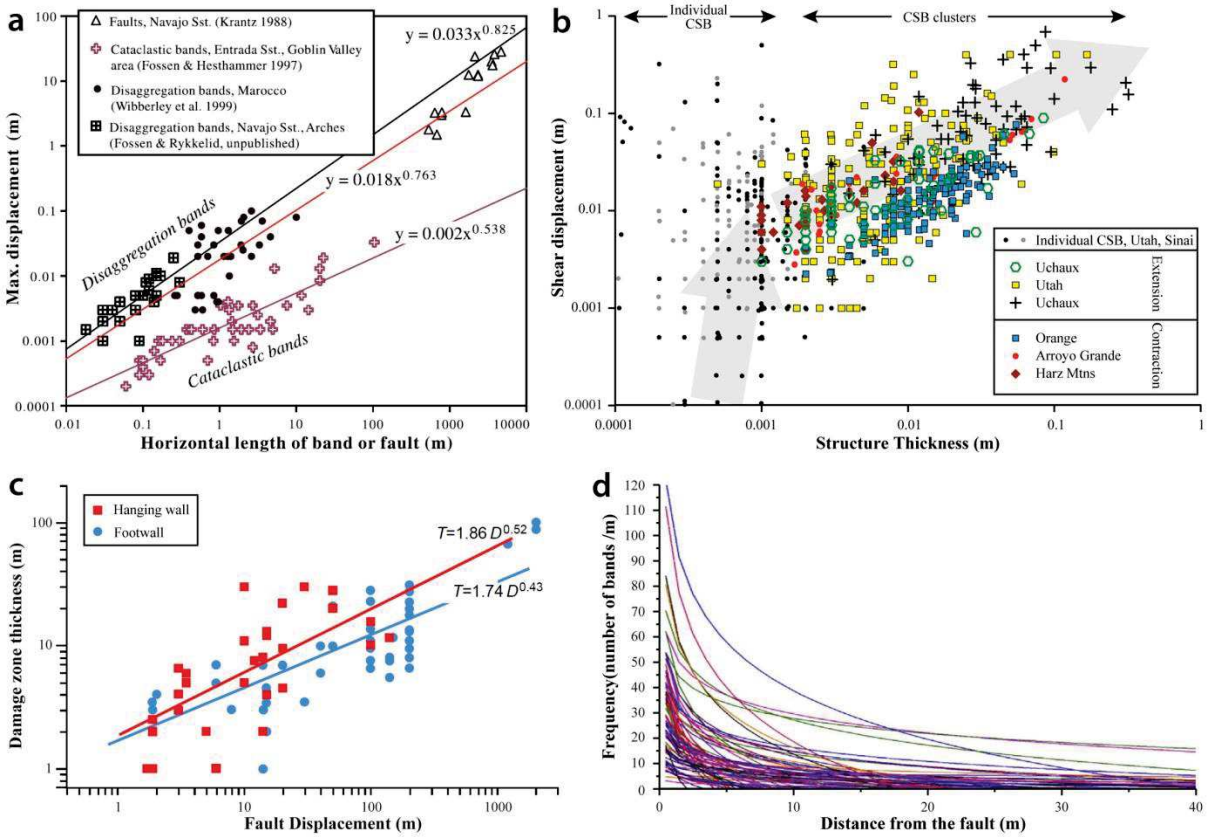

Figure 6. (a) Graph showing the relationship between the displacement and the length of disaggregation and cataclastic bands, and faults in porous sandstones (modified from Fossen et al., 2007). (b) Graph showing the relationship between the displacement and the thickness of the cataclastic deformation structures, including individual bands and clusters (modified from Fossen et al., 2017). (c) Examples of logarithm fits of the decreasing cataclastic structures with increasing distance from the fault (from Schueller et al., 2013). (d) Damage zone widths as a function of fault throws display power-law relationships, with slightly more important thickness in the hanging wall (modified from Fossen et al., 2017, from Schueller et al., 2013). The limit of the damage zone is defined by the distance at which the band frequency gets lower than 5 bands per meter.

In some cases, the clusters can become faults, including a through-going slip-surface (Figure 7c&d). When concerning cataclastic deformation band clusters, fault lengths are poorly reported and are potentially of similar dimension as clusters, displaying subseismic to seismic displacements similarly to classical faults (Figure 6c) (e.g. Schultz and Fossen, 2002; Schueller et al., 2012).

Measurements of the spatial distribution of band sets around the faults have been performed (Edwards et al., 1993; Du Bernard et al., 2002a; Harris et al., 2003; Johansen and Fossen, 2008; Solum et al., 2010; Ballas, 2013; Schueller et al., 2013; Fossen et al., 2017), and a logarithmic decrease of the band frequency with an increasing distance from the fault is generally observed (Figure 6d). Accounting for a damage zone width as defined by Schueller et al. (2013) (limiting the width at the distance where the band frequency is lower than 5 bands per meter), the width of the fault damage zone relative to the displacement seems to behave as a power-law with an exponent close to 0.5 (Figure 6c) and is statistically wider in the hanging wall than in the footwall.

1.1.4. Parameters controlling the structuring of the deformation process

Many studies have been realized to understand the processes of initiation, localization and development of cataclastic deformation in porous sandstones (Aydin, 1978; Aydin et Johnson, 1978,

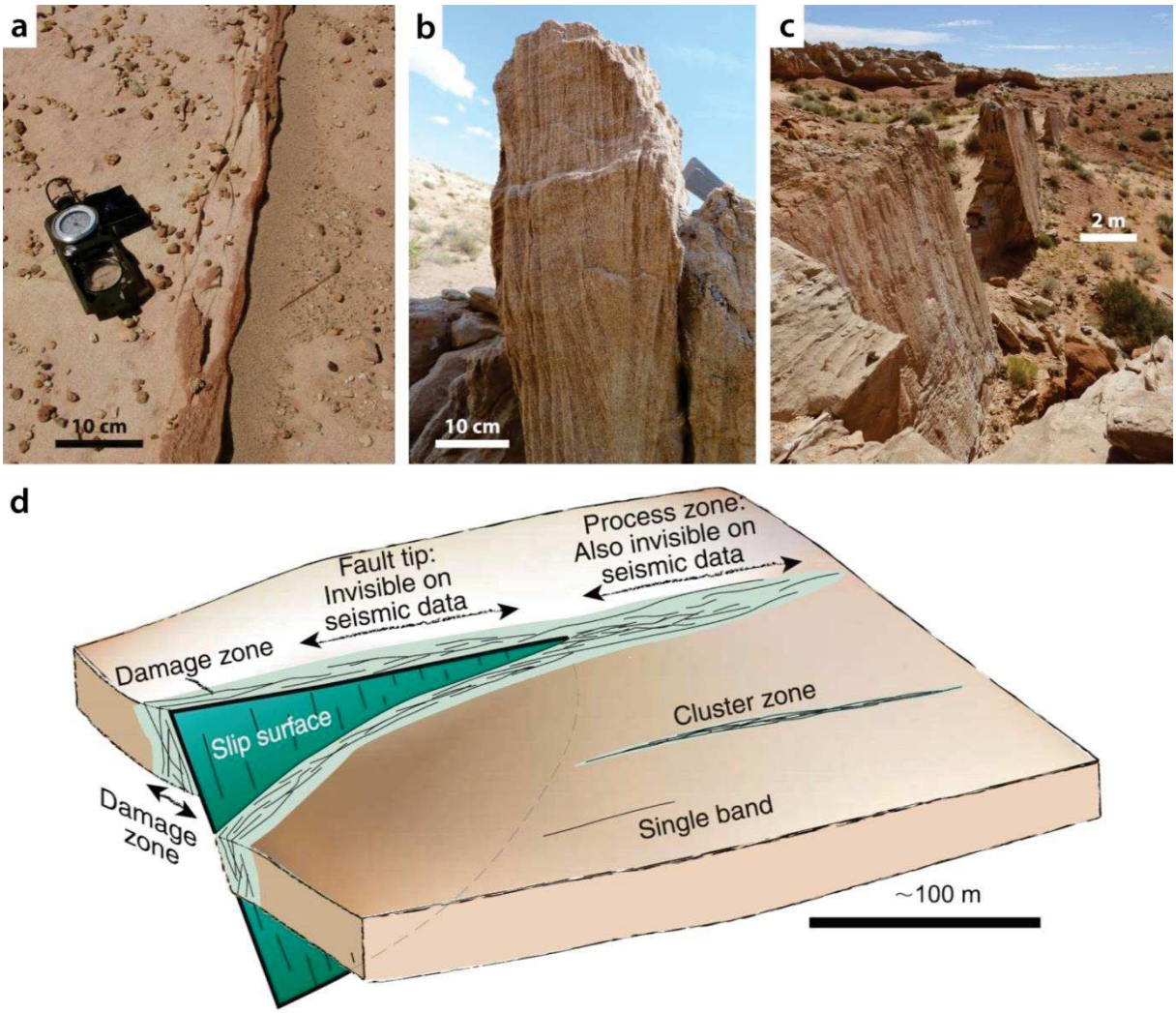

Figure 7. Increasing thickness of a deformation structure by increasing number of bands. (a) Multi-strand band. (b) Cluster. (c) Faulted cluster (includes a through-going slip-surface). (d) Bloc diagram displaying fault architecture in porous sandstones (Fossen et al., 2007).

1983; Antonellini et Aydin, 1995; Myers et Aydin, 2004; Wibberley et al., 2000, 2007; Hesthammer et Fossen, 2001; Davatzes et al., 2003, 2005; Shipton et Cowie, 2001, 2003; De Joussineau et Aydin, 2007; Saillet et Wibberley, 2010; Nicol et al., 2013; Soliva et al., 2013). A successive band addition during the evolution of the deformation is commonly advocated for the difference in morphology of these cataclastic structures, from the single band until faulting (Figure 8a), where strain hardening is often inferred as responsible for the band accumulation (e.g. Aydin and Johnson, 1978). Shipton and Cowie (2003) proposed a model where the clusters grow as an accumulation of small slip patches (Figure 8b) corresponding to the deformation bands, where the thickest part of the cluster near the center of the structure testifies to the most important displacement (Figure 8c). The clusters would laterally develop from its tips where the stress would be enhanced. The fault would be the most developed stage of deformation, marking a strain softening of the deformation.

Few models have been proposed to explain this addition of successive bands and the reason for the occurrence of a though-going slip-surface corresponding to faulting. In particular, Nicol et al. (2013) use a geometrical analysis of the bands to interpret the band accumulation as formed as a

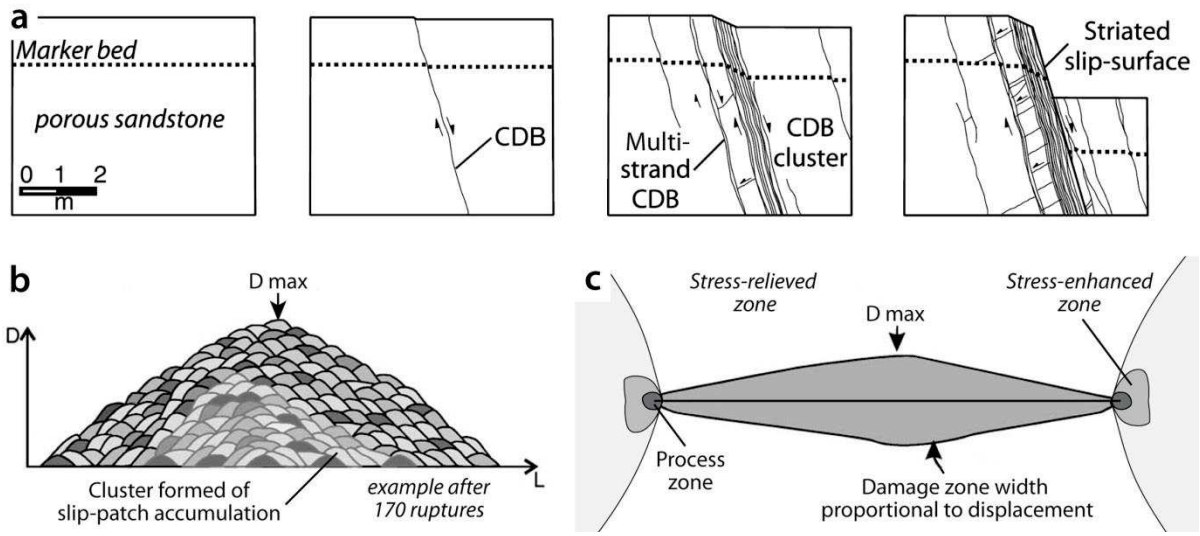

Figure 8. (a) Schematic hypothesis for the evolution of the cataclastic deformation in porous sandstone from the single deformation band to the fault (modified from Aydin and Johnson, 1978; Antonellini and Aydin, 1995; Davatzes et al., 2002. (b) and (c) Conceptual model of cluster development proposed by Shipton and Cowie (2003).

side effect of the presence of preexisting fault (in the sense where major through-going surfaces are present). In this case, the authors suggest that the clusters of deformation bands are formed at a fault irregularities such as relay zones between fault segments and that the band develop sequentially, locally accommodating the strain and coalescing with each other during each step of the fault development. The authors also use these interpretations to refute the band accumulation as being due to strain hardening. On the basis of further literature inspection, we do not agree on these arguments; for a matter of convenience, we explain why in section 1.4 where the issue of our work is exposed.

In the detail, different parameters inherent to the host rock control and alter the cataclastic process of deformation in sandstones, thus modifying the structural organization (geometry, distribution) of the deformation and its petrophysical properties (porosity and permeability). These parameters can be classified under two categories: the internal characteristics, inherent to the host rock (e.g. porosity, grain size, grain size distribution, mineralogy, inclusion of weak minerals, cementation); the external parameters applied on the formation during its evolution (burial, tectonics).

1.1.4a. Internal host rock characteristics

The porosity is the main factor controlling the process of deformation in sandstones (Flodin et al., 2003). High porosity favors the formation of cataclastic deformation bands whereas low porosity favors the formation of fractures (e.g. Scott and Nielsen, 1991; Du Bernard et al., 2002a; Davatzes et al., 2003; Aydin et al., 2006). A high porosity can also favor the formation of disaggregation bands over cataclastic deformation bands (Schultz et al., 2010).

The cementation of a formation generally evolves with burial (increasing diagenesis) (Renard et al., 1997). Quartz cementation is frequently reported in quartz-rich sandstones through the process of pressure-solution and quartz precipitation. Quartz cementation could potentially happen at depths as low as 2 km (Milliken et al., 2005) and for temperatures down to 40°C (Pollington et al.,

2011). At significant burial (from depths of 3km and temperatures higher than 90°C - e.g. Walderhaug, 1994; Renard, 1997, Bjørkum et al., 1998; Walderhaug, 2000), the important increase of lithostatic pressure and temperature considerably favors the process of pressure-solution of the quartz-rick host rock (Figure 9a). This process participates to the filling of the porosity by quartz cement growth from the detrital grain surfaces (Figure 9b). In particular, it is known that the quartz cement precipitation is favored in cataclastic material because the fresh reactional surfaces where the cement nucleation is favored are numerous (Fowles and Burley, 1994; Fisher and Knipe, 1998, Ngwenya et al., 2000; Fisher and Knipe, 2001; Lander et al., 2008; Williams et al., 2015). This cementation reduces the permeability of the sandstone and drastically increases the cohesion (e.g. Walderhaug, 1994; Wangen, 1999; Worden and Morad, 2000; Molenaar et al., 2007; Pollington et al., 2011; Saïag et al., 2016). If the cementation is low (therefore preserving the porosity), the grain rearrangement is prevented and the cataclasis possible (Johansen et al., 2005). Further cementation (significantly reducing the porosity) prevents grain slip and rotation hence inhibiting cataclasis (Labaume and Moretti, 2001) whereas intergranular fracturing and jointing are enhanced. Note that weak minerals such as iron oxides may favor slip by friction decrease between grain contacts (Friedman et al., 1974; Underhill and Woodcock, 1987).

Field studies seem to show that the grain size mainly affects the expression of compaction bands, with a preferential localization of the bands by cataclasis in coarse sandstones (Chuhan et al., 2002; Aydin and Ahmadov, 2009; Shultz et al., 2010; Deng and Aydin, 2012). Ballas et al. (2013, 2015) showed that, in contractional tectonics, coarse grain sandstone favors the formation of PCB and SECB whereas fine sandstone favors SECB and CSB.

Grain size distribution (also sorting) influences the localization and the type of mechanism of deformation. Disaggregation and compaction bands are only observed in sandstones with narrow grain size distribution (good sorting) (Antonellini and Pollard, 1995; Mair et al., 2002; Eichhubl et al., 2010; Schultz et al., 2010). Cataclastic deformation bands (including CSB, and SECB) are observed in sandstones with narrow and moderate grain size distribution (moderate sorting). A large grain size distribution (poor sorting) corresponds to a decreased porosity (Rogers and Head, 1961; Marone and Scholz, 1989) and consequently inhibits the cataclasis since the large number of particle contacts strengthens the material (Arzt, 1982; Morgan, 1999; Mavko et al. 2009; Estrada and Taboada 2013) (Figure 10a). Instead, grain slip occurs and leads to the formation of fractures as mentioned earlier.

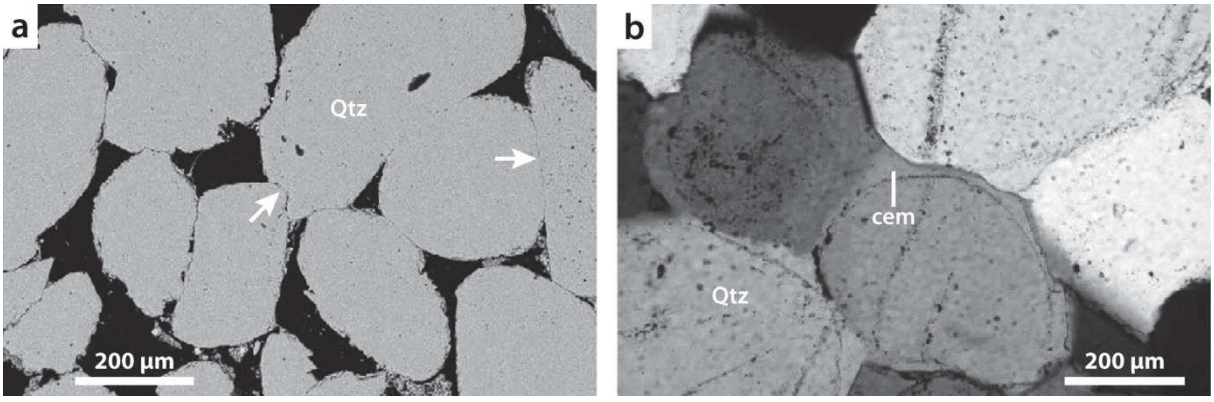

Figure 9. Influence of the burial (external parameter of the sandstone host rock sandstone evolution. Increasing burial at depth allowing significantly high temperatures (ca. 80°C) induces (a): pressure solution at grain contact (arrows on the top image in SEM-BSE) and (b): cement precipitation in the porosity (bottom image in cross-polarized microscopy) (from Molenaar et al., 2007).

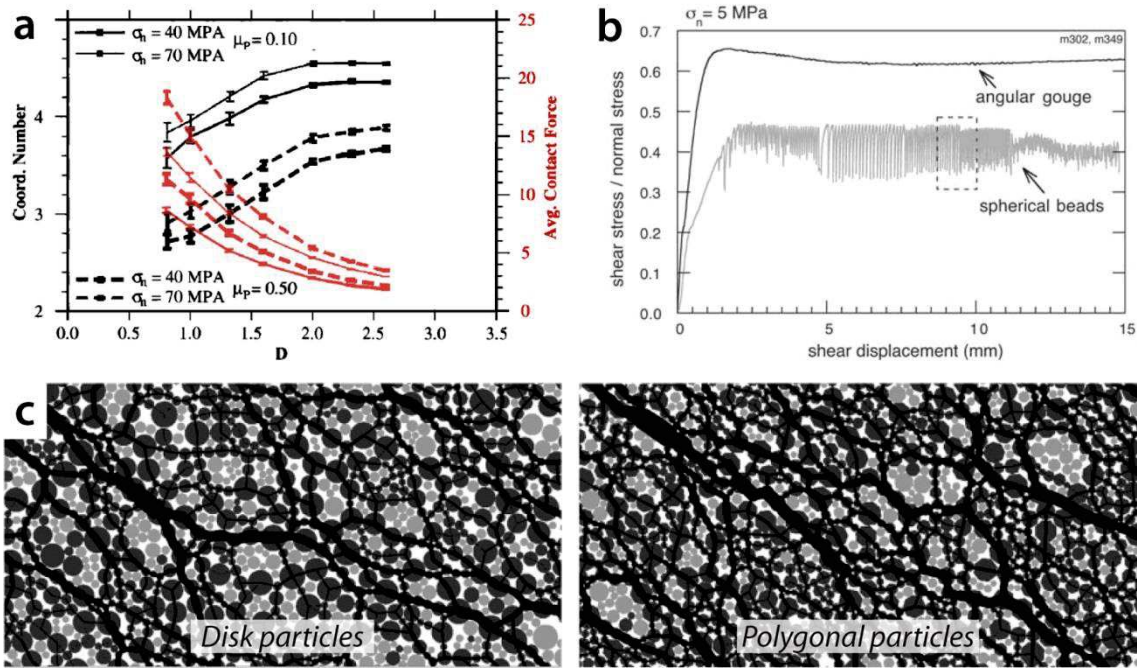

Figure 10. (a) Graph showing the influence of the grain size distribution (expressed through the D exponent) on the number of particle contacts and the resulting force at the contacts (modified from Morgan, 1999). (b) Graph showing the friction induced by the shear of angular and rounded particles with near isochoric deformation (from Mair et al., 2002). (c) Modeling of contact behavior in disk particle (left) and polygonal particles (right) moderately sorted materials showing the influence of particle shape on the force chains distribution and rotational behavior (from Estrada et al., 2011).

Grain shape influences the friction of the material, and therefore the strength of the rock and the mechanism of deformation. Angular-grained host rock display a higher friction than well-rounded sandstones (Mair et al., 2002; Anthony and Marone, 2005; Cho et al., 2006) (Figure 10b). For a similar sorting, the angularity prevents particle rotation and makes the particles less resistant to crushing, hence favoring cataclasis (Cho et al., 2006; Guo and Morgan, 2006; Mesri and Vardhanabuti, 2009; Estrada et al., 2011; Azéma et al, 2012) (Figure 10c). Rounded sandstones seem to favor the cataclasis disaggregation (grain rearranging).

We note that the size and distribution of the grains also affect the deformation mechanism. Indeed, the cataclasis induces a grain size reduction and increases the distribution of the clasts that become potentially more angular (Engelder, 1974; Sammis et al. 1987; Blenkinsop, 1991; Mair et al., 2002; Rawling and Goodwin, 2003 2006; Hadizadeh et al., 2010; Kaproth, 2010). Added to the porosity reduction induced by grain rearrangement (which is valid for CSB and SECB, but no for isochoric SSB – Rotevatn et al., 2008; Wong and Baud, 2012), these variations of internal parameters may explain the strengthening of the material with further deformation (e.g. Underhill and Woodcock, 1987; Mair et al., 2002; Anthony and Marone, 2005). This material strengthening (relative to the stress loading) corresponds to the process of “strain hardening” and would partially explain the evolution of cataclastic deformation to faults in porous sandstones as described by Aydin and Johnson (1978).

The composition of the sandstone can influence the initiation of the deformation in porous sandstone. Sandstones including between 5 and 15% of clay content or weak minerals will induce some slipping at grain contacts and will favor disaggregation bands (Figure 11a and b) (Gibson, 1998;

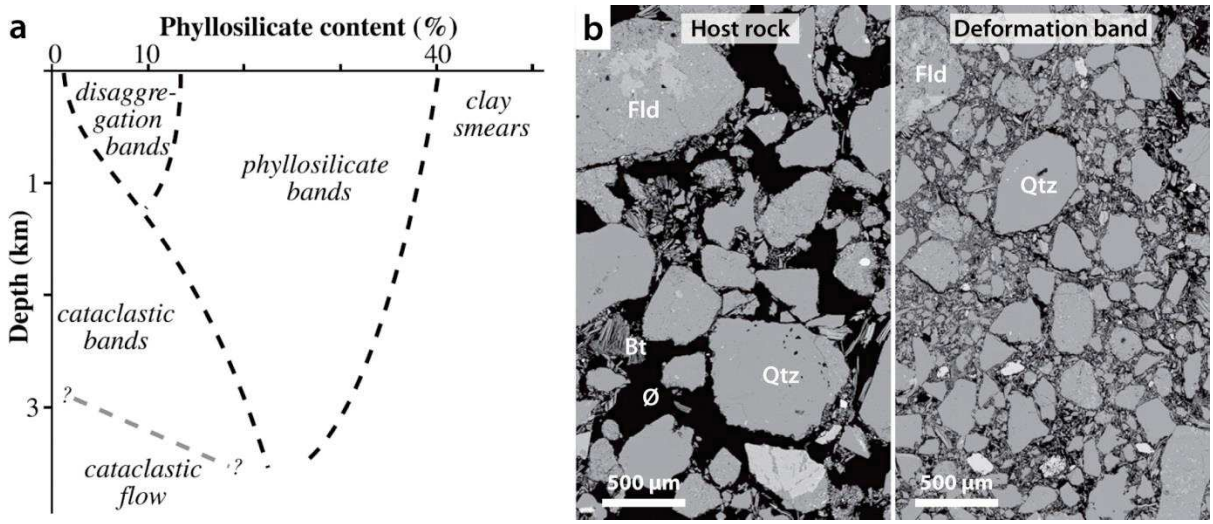

Figure 11. (a) Schematic synthesis of the inferred domains of the different deformation mechanisms as functions of the phyllosilicate content and depth (from Fossen et al., 2007). (b) Images in scanning electron microscopy in backscattered electron (SEM-BSE) illustrating the influence of the presence of weak minerals (e.g. Feldspars or Biotite) in the enhancement of the cataclasis (from Exner et Tschegg, 2012).

Fisher and Knipe, 2001). Sandstones including between 15 and 40% of clay drastically enhance slipping at grain contacts and favor the formation of phyllosilicate bands (Antonellini et al., 1994). More than 40% of clay induces clay smearing (Fisher and Knipe, 2001; Hesthammer and Fossen, 2001; Ketterman, 2016). The presence of weak minerals in the mineralogical composition of sandstone also affects the mechanism of deformation. For instance, the presence of a significant proportion of feldspars minerals (weaker than quartz) enhances the inception and the degree of cataclasis compared to quartzarenites (Antonellini et al., 1994; Wong et al., 1997). The diagenetic decay of feldspars into phyllosilicates (Solum et al., 2010b; Exner and Tschegg, 2012; Cavailhes et al., 2013) could also favor disaggregation or phyllosilicate bands (depending on the degree of clay authigenesis) instead of cataclasis.

1.1.4b. External stress loading

The external stress loading results from the motion of the tectonic plates, applying forces on the lithosphere at the regional scale (Zoback et al., 1989). The stress state applied on an increment on rock can be decomposed in three principal stresses oriented normally to each other. The principal stresses induced by the tectonic are assumed to be horizontal; the third principal stresses is generally vertical and corresponds to the weight of the sedimentary column induced by burial (Anderson, 1905). We note that the burial is indirectly linked to the tectonic loading because the tectonic loading is at the origin of the subsidence and uplift, thereby modifying the base level controlling the zones of erosion and sediment deposition.

In porous sandstones, the burial represents an external parameter influencing the deformation mechanisms in two different manners: (1) through the increase of the confining pressure (mean stress), and (2) through the compaction of the granular material and the activation of pressure-solution. The increase of burial corresponds to increase of lithostatic pressure and causes the compaction of poorly lithified sandstones. The absence of cementation allows a pervasive rearrangement of the granular material. As expressed before, the burial increase is also responsible

for the processes of pressure-solution and cementation, modifying the petrophysical properties of the sandstone.

Accounting for the burial-induced processes introduced before, the formation of the following types of bands as a function of the burial depth are reported (Figure 12). Disaggregation bands are preferentially formed at burial depth of up to 1 – 1.5 km, where the grain contacts are sufficiently weak to be slipped and rolled (Karner et al., 2005; Mesri and Vardhanabhuti, 2009; Fossen, 2010). We note that at this depth, unlithified sands can hold fluids in the porosity, likely to promote localized fracturing (Baud et al., 2000; Sulem and Ouffroukh, 2006). For a similar range of depth, the presence of slight cementation strengthens these contacts and prevent particle rotation, therefore promoting cataclasis as the grain contacts of the force chains are not yet numerous enough to support important stress (Estrada et al., 2008). This could explain the presence of cataclastic deformation bands at depths lower than 300 m reported by Cashman and Cashman (2000), Kaproth et al. (2010) or Ballas (2013) for instance. Cataclastic deformation bands are thought to be mainly formed at greater depths (Blenkinsop, 1991; Antonellini et al., 1994; Hesthammer and Fossen, 2001; Fisher and Knipe, 2001; Fossen, 2010; Kristensen et al., 2013) because compaction prevents grain rearrangement (Hadizadeh and Johnson, 2003).

Recent works show that the localization of the deformation and the type of band formed during sandstone deformation are mostly controlled by the tectonic regime (e.g Soliva et al, 2016, see appendix A – Figure 13a). Deformation bands and fractures, as well as cataclastic, disaggregation and phyllosilicate bands are observed in both extensional and contractional tectonics, potentially corresponding to either normal, thrust or strike-slip Andersonian stress regime (Aydin et al., 2006). Numerous authors report from the field that pure dilation bands are only observed in extensional tectonics; that pure compaction bands are only observed in contractional regime (e.g. Mollema and Atonellini, 1996; Saillet; 2009; Eichhubl et al., 2010). Normal Andersonian stress regime seems to favor the localization of clusters of SSB (including compaction), CSB and SECB, sometimes faulted,

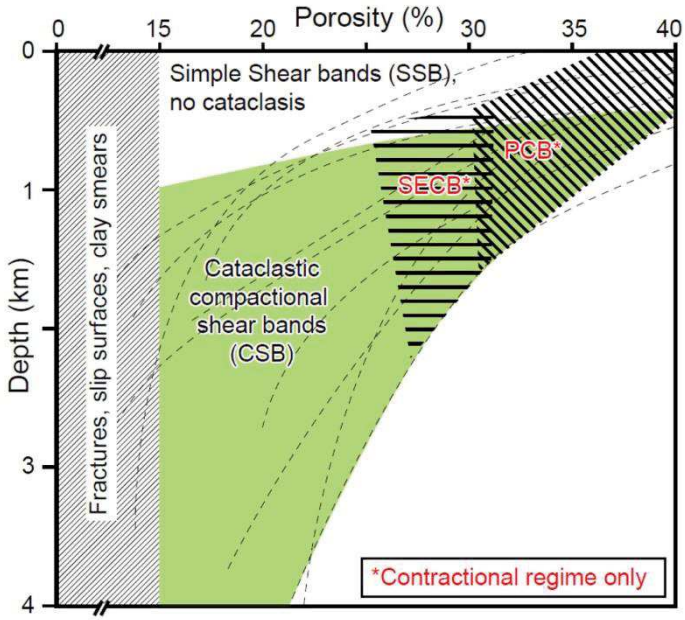

Figure 12. Influence of the burial and porosity of the type of bands generated by the deformation (from Fossen et al., 2017).

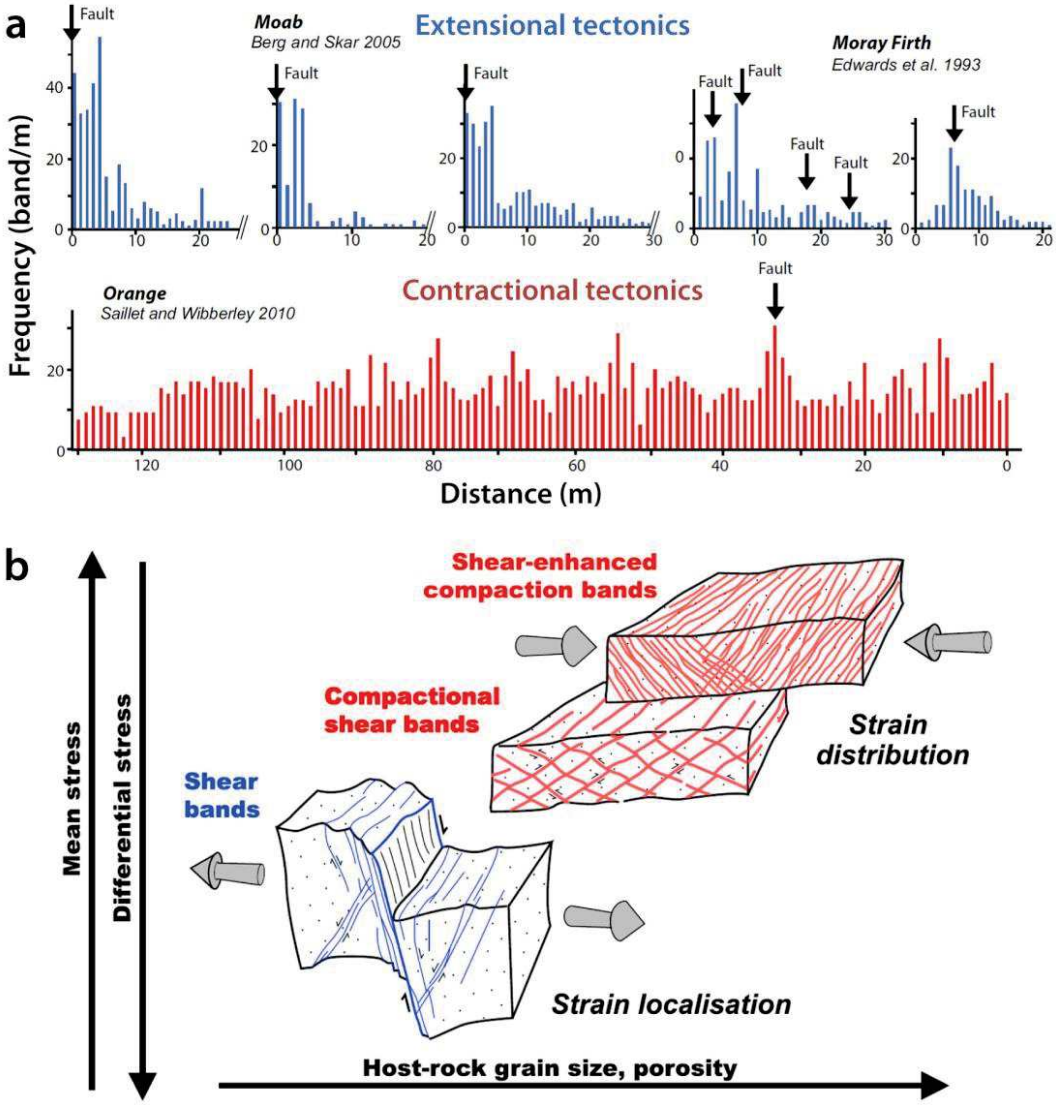

Figure 13. (a) Example of typical distribution of the deformation as measured at the outcrop in extensional tectonics (top) and contractional tectonics (bottom) (modified from Soliva et al., 2016 – see appendix A). (b) Synthetic scheme showing the influence of the parameters controlling the localization of the cataclastic deformation in porous sandstones (simplified from Soliva et al., 2013). The tectonic regime mostly controls the localization of the deformation.

whereas thrust Andersonian regime seems to promote conjugate networks of distributed PCB, SECB to CSB (Figure 13a and b) (Du Bernard et al., 2002a; Johansen and Fossen, 2008; Solum et al., 2010a; Schueller et al., 2013; Soliva et al., 2013; Ballas et al., 2015; Soliva et al., 2016). Although these observations constrain the loading conditions for the distribution or localization of the deformation, they do not explain the process of band accumulation leading to clusters and faulting. Moreover, the link between the tectonic loading and the Andersonian stress regimes relative to the type of deformation is not well established.

Eventually, to qualify the general orientation of the principal stresses introduced at the beginning of this section, we must remark that specific structural boundary conditions (e.g. presence of an evaporite layer, a fault propagating below the sandstone, a local fold) can modify the local stress field, and locally alter the general observations enounced above (Figure). The interpretation of the organization of the deformation structures therefore becomes more complex in some cases.

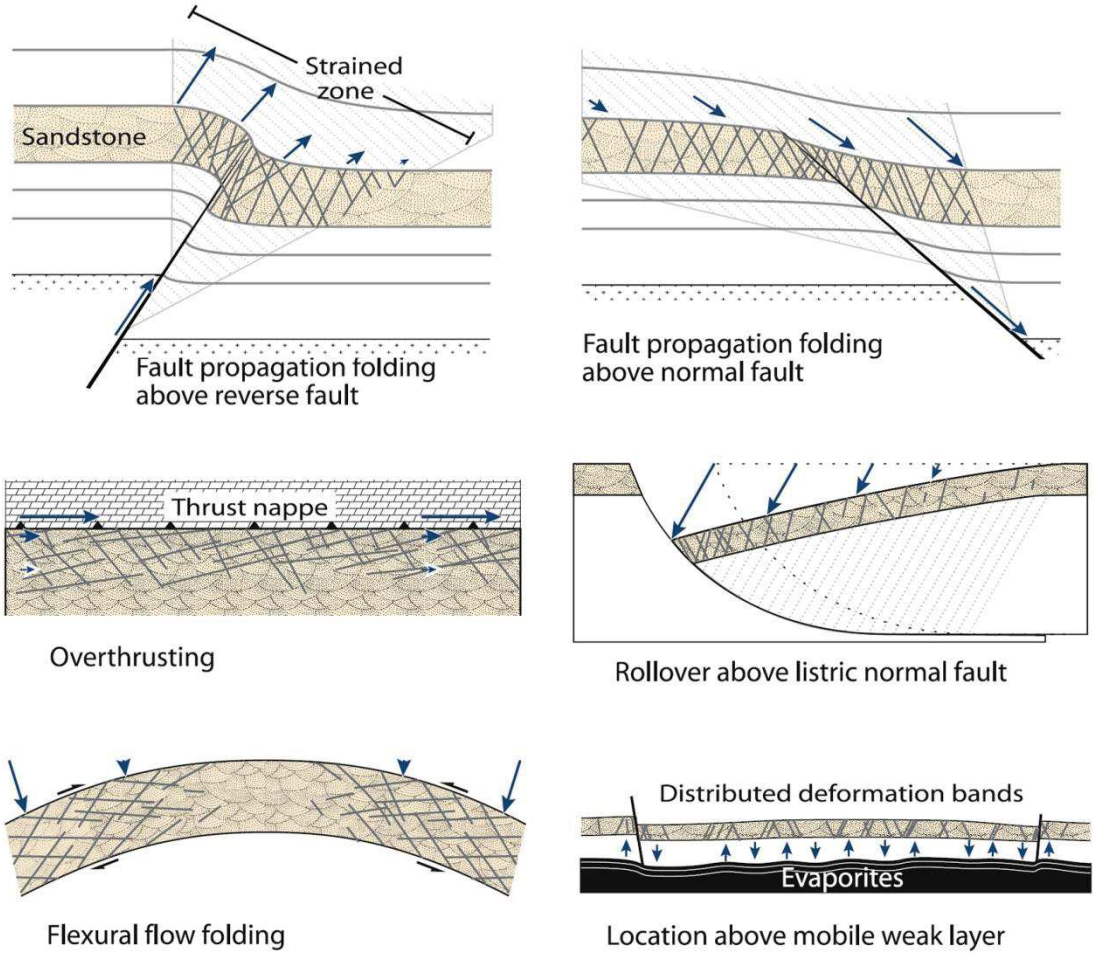

Figure 14. Examples of locally altered stress field due to specific structural contexts (modified from Fossen and Rotevatn, 2012).

1.2. Impact of the deformation on fluid flow

The petrophysical properties of the different types of deformation bands and faults in porous sandstones were measured and analyzed in many studies (Pittman, 1981; Jamison and Stearns, 1982; Harper and Moftah, 1985; Fowles and Burley, 1994; Antonellini and Aydin, 1994; Gibson, 1994, 1998; Crawford, 1998; Fisher and Knipe, 1998, 2001; Taylor and Pollard, 2000; Ogilvie et al., 2001; Ogilvie and Glover, 2001; Jourde et al., 2002; Lothe et al., 2002; Shipton et al., 2002; Flodin et al., 2003; Fisher et al., 2003; Flodin et al. 2005; Fossen and Bale, 2007; Rotevatn et al., 2008; Torabi et al., 2008; Al-Hinai et al., 2008; Torabi and Fossen, 2009; Aydin and Ahmadov, 2009; Solum et al., 2010a; Medeiros et al., 2010; Tueckmantel et al., 2010; Fossen et al., 2011; Sun et al., 2011; Balsamo et al., 2013; Saillet and Wibberley, 2013; Torabi et al., 2013; Ballas et al., 2015). These studies evidence a large variability of the petrophysical properties of these deformation bands, between the bands from different categories (Figure 15a) and between bands from the same category, with permeability generally decreasing with increased burial depth experienced (Figure 15b).

1.2.1. Petrophysical properties of non-cataclastic deformation bands

Dilation bands display a porosity increase of up to 8% (absolute) compared to the host rock (Antonellini et al., 1994; Du Bernard et al., 2002b). Their permeability can increase of more than one order of magnitude (Fossen and Bale, 2007). We note that these bands can also be clogged or cemented and hence become almost non-porous and impermeable (Ogilvie and Glover, 2001; Brandes and Tanner, 2012). **Shear bands** have a very diverse range of petrophysical properties, depending on the active micromechanisms. Dilation bands and, sometimes, shear bands deformation bands seem to enhance the oil and gas migration (Sample et al., 2006). Outcrops showing oxidation are used to testify to the effect of deformation bands on meteoric paleo-fluid flow in vadose zones or aquifers (Taylor and Pollard, 2000; Sigda and Wilson, 2003; Eichhubl et al., 2004; Parry et al., 2004;

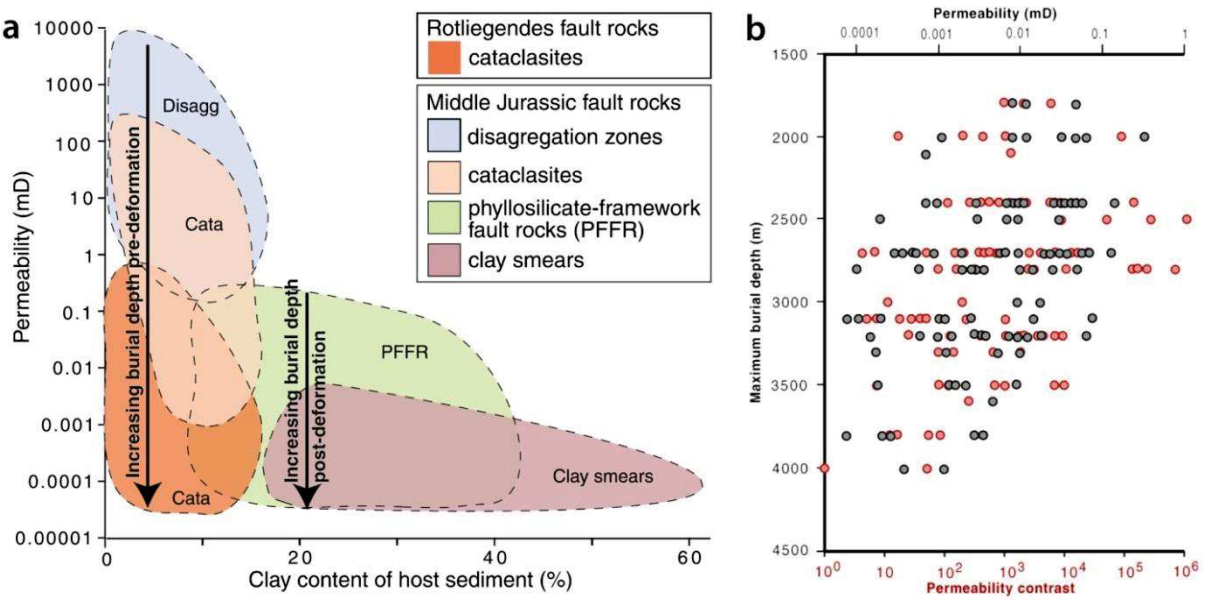

Figure 15. Graph showing the commonly observed ranges of permeability of the different types of deformation bands as a function of the clay content (from Fisher and Knipe, 2001). (b) Graph showing the decreasing permeability of cataclastic deformation bands with increasing depth (modified from Fisher and Knipe, 2001). We note that this permeability decrease is relative because the permeability contrast with the host rock also decreases with burial depth.

Wibberley et al., 2007; Exner and Tschegg, 2012; Balsamo et al., 2013). These studied show that the dilation bands generally have no apparent effect on the fluid circulation, leaving a homogeneously oxidized formation. Some bands seem to act as drains, provoking the leaching of the oxides in an around the bands (Figure 16a).

Disaggregation bands do not significantly alter the petrophysical properties of the host rock (Antonellini and Aydin, 1994; Fisher and Knipe, 1998; Fossen and Bale, 2007; Fossen, 2010). **Phyllosilicate bands** can induce permeability reductions of up to three orders of magnitude compared to the host rock (Pittman, 1981; Torabi and Fossen, 2009). Nevertheless, low permeability contrasts are generally measured between these bands and the initially low-permeable host rock (Fisher and Knipe, 1998; Ogilvie and Glover, 2001).

1.2.2. Petrophysical properties of cataclastic deformation bands, clusters and faults

Cataclastic bands (CDB), encompassing SSB, CSB, SECB and PCB, display porosity reduction of up to 30% (absolute), and permeability reduction of up to six orders of magnitude compared to the host sandstone (Figure 17a) (Fowles and Burley, 1994; Fisher and Knipe, 1998; Ogilvie et al., 2001; Fossen and Bale, 2007; Solum et al., 2010a; Ballas et al., 2015). The drastic permeability decrease of the cataclastic bands is due to the process of cataclasis itself, providing a large range of particle distribution and allowing efficient pore filling in the bands (Crawford, 1998). CDB able to influence reservoir fluid flow have been reported by several studies (e.g. Lewis and Couples, 1993; Antonellini et al., 1999; Al-Hinai et al., 2008). Reservoir analyses reveal that sealing CDB forming entrapment for hydrocarbons exist (Parnell et al., 2004). Oxidation studies demonstrate that some bands baffle the fluids, thus favoring oxide deposition on one side of the band (Figure 16b). On the other hand, in some cases of reservoir productions, the presence of deformation bands have no influence on fluid migration (e.g. Hesthammer and Fossen, 2001; Fossen and Bale, 2007). For instance, the cataclasis in **PCB** is low, displaying porosity reductions of up to 15% (absolute) and permeability reductions up to one orders of magnitude compared to the host rock (Aydin and Ahmadov, 2009; Sun et al., 2011).

The distribution of CDB in the reservoir also have a main impact on the permeability, and consequently on the fluid flow (e.g. Sternlof et al., 2006). Indeed, isolated bands are generally more

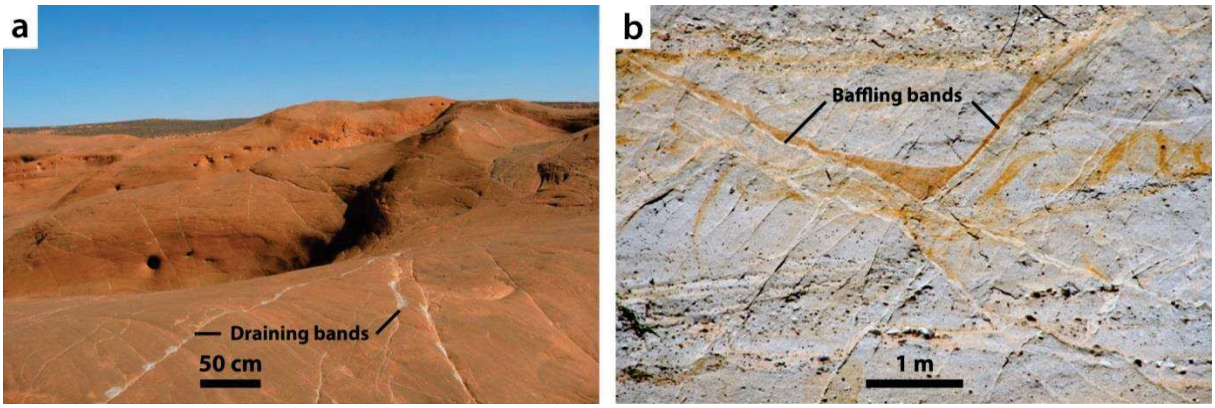

Figure 16. Illustration of oxides used as markers of the meteoric paleo-fluid flow. (a) The iron oxide deposits on one side of the bands testify of the baffling effect of the bands (from Parry et al., 2004). (b) Iron oxides leached out of the bands testify of the draining effect of the bands on the flow (from Exner and Tschegg, 2012).

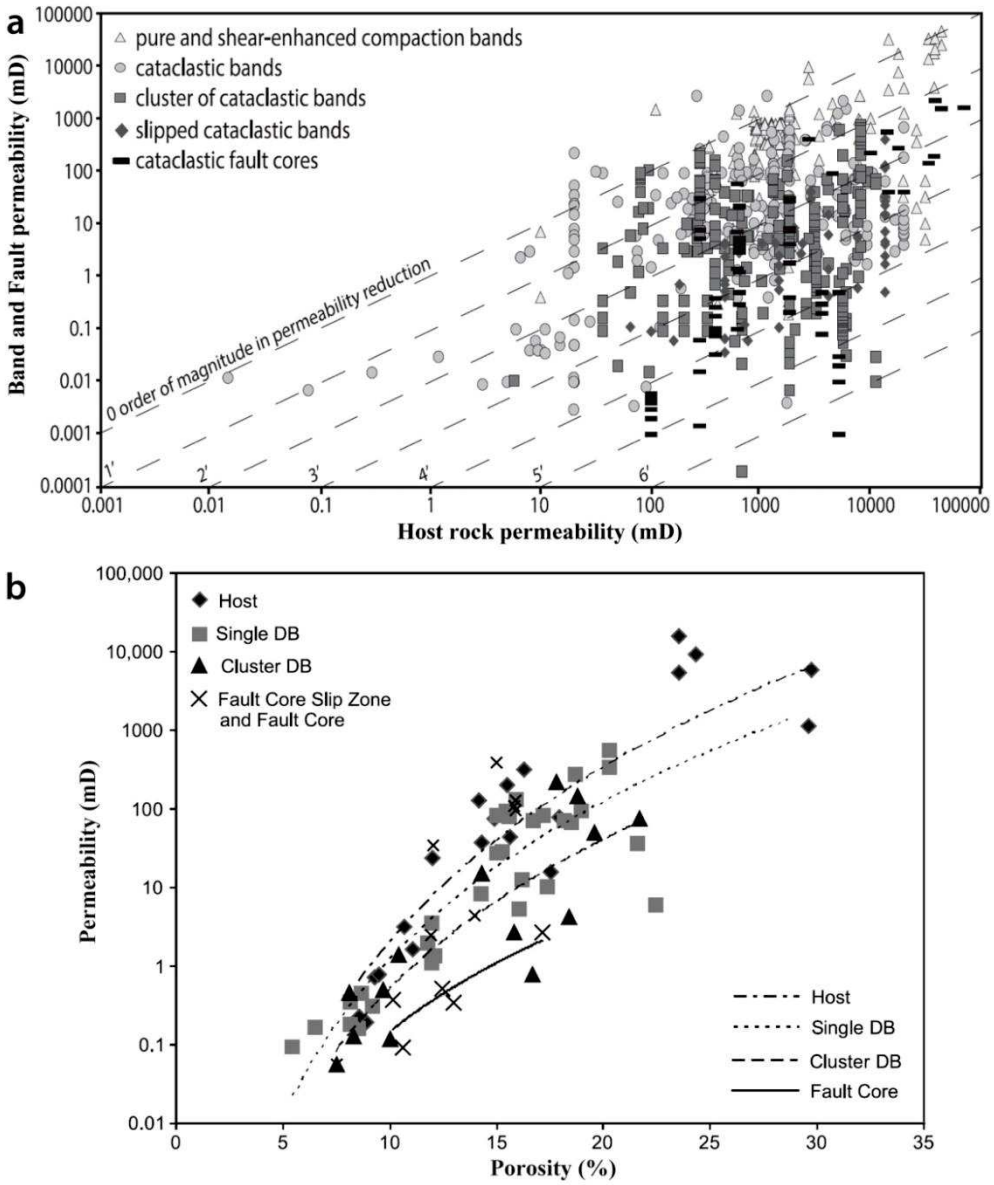

Figure 17. (a) Graph showing the permeability of various types of cataclastic deformation bands as a function of the permeability of the host rock (from Ballas et al., 2015). (b) Graph showing the relationship between the permeability and porosity of various stages of evolution of cataclastic structures (modified from Torabi et al., 2013).

permeable than the clusters of cataclastic bands (Figure 16a and b) (Gibson, 1998 ; Lothe et al., 2002 ; Fossen et Bale, 2007 ; Tueckmantel, 2010 ; Saillet et Wibberley, 2013). The slip-surface of the faults are generally less permeable than the clusters (Fowles and Burley, 1994; Shipton et al., 2002). Thus, the bands with the most reduced permeability and with the densest distribution (clusters) are likely to affect the reservoir permeability, and affect the fluid flow behavior during reservoir exploitation (e.g. Solum et al., 2010; Brandenburg et al., 2012). Some authors, assuming that the band clustering corresponds to the evolution of deformation, suggest that the petrophysical properties of CDB are mainly controlled by their stage of evolution towards faulting (Figure 17b) (e.g. Pittman, 1981; Torabi et al., 2013). On the other hand, Ballas et al. (2014) showed that the type of band formed in extensional tectonics and the corresponding localization of deformation under the form of clusters is

likely to compartmentalize a reservoir, whereas the deformation in contractional tectonics would have no or only weak baffling effect on a sandstone reservoir (Figure 18).

As explicated in section 1.1.4, the processes of pressure-solution and cementation are likely to further affect the porosity and permeability of the bands (Pittman, 1981; Renard et al., 1997; Ogilvie and Glover, 2001; Fisher and Knipe, 2001; Hesthammer and Fossen, 2001; Lothe et al., 2002; Al-Hinai et al., 2008).

Numerical modeling have been performed to analyze the influence of CDB arrays and faults in sandstone on fluid flow behavior at the basin scale (Jourde et al., 2002; Sternlof et al., 2005, 2006; Rotevatn et al., 2009; Tueckmantel et al., 2012; Rotevatn et al., 2013; Zuluaga et al., 2016; Rotevatn et al., 2017). These studies highlight that the presence of bands may induce a channelization of the flow and retard the flow perpendicular to the band array (Sternol et al., 2006; Rotevatn et al., 2009) (Figure 19a). Because they constitute high dimension and low permeability structures (Figure b), faults are probably the most important barriers for reservoir fluid flow (Tueckmantel et al., 2012).

We see that despite all this knowledge, the impact of the clusters on fluid flow at basin scale is still not well understood, as the above studies do not account for the general dimension and geometry of these structures. For instance, the variability of thickness (Fossen and Bale, 2007; Rotevatn et al., 2013), permeability (Jourde et al., 2002; Torabi and Fossen, 2009), the presence of joints cross-cutting the structures (Tindall, 2006) or relay zones (Figure 19b) are as many potential sources of fluid leakage in the deformation bands and faults. In opposition to band arrays, no model exists simulating the influence of a network of cluster (if existing), accounting for the presence of a through-going slip-surface in the cluster, or a potential connection between the structures.

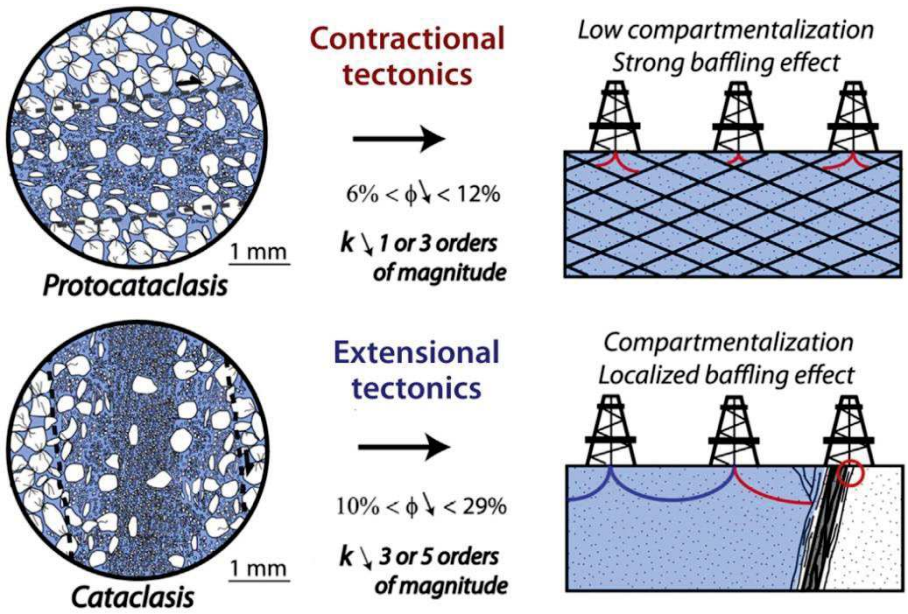

Figure 18. Synthetic diagram showing the influence of the distribution and the type of band on the permeability of the system (modified from Ballas et al., 2014). The low-permeability and distributed cataclastic bands generated in contractional tectonics only baffles the reservoir fluid flow (top) whereas the cataclastic bands generated in extensional tectonics have low permeabilities and are more likely to compartmentalize the reservoir (bottom).

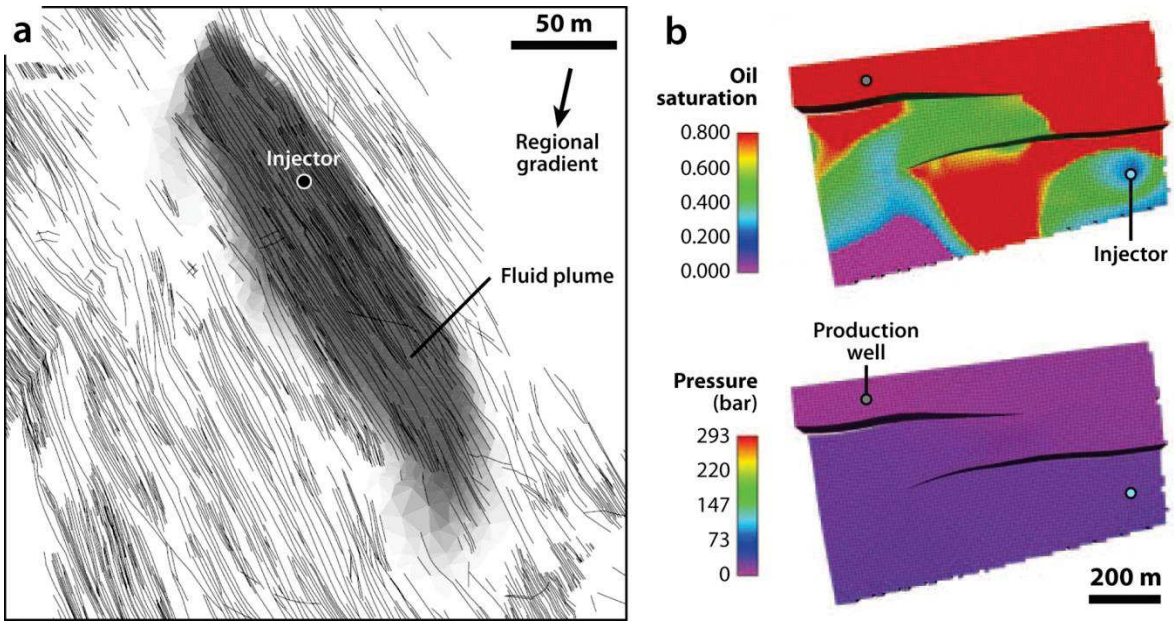

Figure 19. Examples of numerical modeling of fluid flow through deformed porous sandstone. (a) Test of the influence of the presence of an array of low-permeability compaction bands (thin black lines) during a fluid injection. The network of bands induces the channelization of the fluid plume (from Sternlof et al., 2006). (b) Test of the influence of the presence of a fault relay ramp during an injection-production test on the oil saturation of the system (from Rotevatn et al., 2009).

1.3. Mechanics of porous granular medium

As presented in sections 1.1 and 1.2, the cataclastic deformation takes on a diversity of characteristics, in terms of mechanisms of formation, distribution, and resulting petrophysical properties influencing the fluid circulation. The study of the mechanics of a granular media is an essential tool to better understand reservoir deformation. Indeed, several parameters were constrained through mechanical analyses of the deformation of granular material at the laboratory. A specific effort has been made to anticipate the failure mode of the sandstone when plastic deformation occurs.

1.3.1. Tri-axial tests

The most convenient way to understand the occurrence of deformation draws from rock mechanics applied to porous rock deformation (e.g. Rudnicki and Rice, 1975; Bésuelle and Rudnicki, 2004). Different sorts of triaxial tests can be performed on sandstone samples (see example on Figure 20a) to reproduce the evolution of the stress and strain state in the sandstone during tectonic loading and burial/exhumation (Scott, 2007). The stress-paths are monitored and reported on graphs; the mechanical behavior of the sample is reported as a function of the type of loading (Wong et al., 1997). One of the most common approach consists in imposing a stress-paths evolution which can be described as a function of the deviatoric stress Q, expressed as the difference between the maximum and the minimum principal stresses ($Q = \sigma_3 - \sigma_1$), and of the effective mean stress $P = \frac{\sigma_1 + \sigma_2 + \sigma_3}{3} - Pf$ (Figure 20b), where Pf is the pore pressure.

Different loading configurations are used. Hydrostatic loading corresponds to an equal loading of all principal stresses ($\sigma_1 = \sigma_2 = \sigma_3$, with the confining pressure equals the axial loading). Axial loading (e.g. Zhang et al., 1990; Wong et al., 1997; Bésuelle et al., 2000; Fortin et al., 2005; Baud et al., 2006) corresponds to a maximum stress along the axis of the triaxial cell ($\sigma_1 \geq \sigma_2 = \sigma_3$). True-triaxial loading (e.g. Bésuelle and Hall, 2011; Ingraham, 2013; Ma and Haimson, 2013) correspond to three different principal stresses possible ($\sigma_1 \geq \sigma_2 \geq \sigma_3$).

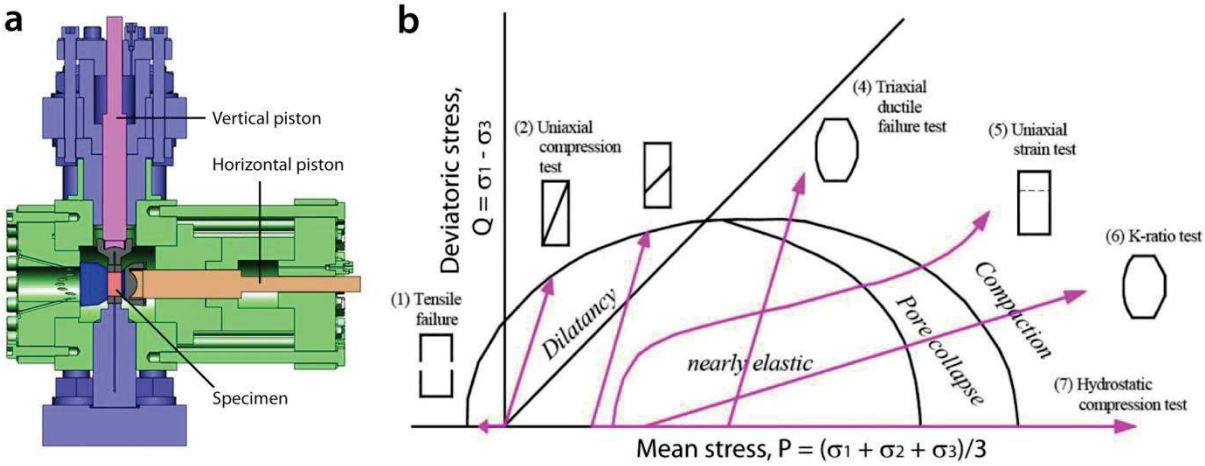

Figure 20. (a) Example of a true-triaxial apparatus (modified from Lanatà, 2016). (b) Q-P diagram within which the different tested stress paths are represented until failure (plastic deformation) (from Scott, 2007).

1.3.2. Analysis of the elastic domain and failure envelope

1.2.2a. Failure modes

The sample loading results in porosity decrease (relative to the volumetric strain) (Figure 6a). Hence, the porosity evolution was often used as a proxy describing the state of deformation as a function of the mean stress (e.g. Wong et al., 1997; Baud et al., 2004; Karner et al., 2005; Nguyen et al., 2011; Wong and Baud, 2012). The graphs displaying these parameters allow determining the changes in behavior of the deformation, from elastic deformation (reversible) to plastic deformation (irreversible) (Schultz and Siddharthan, 2005). On the Mean stress – Porosity change curve, the change of behavior between the two deformation modes is observed by an inflexion of the slope and corresponds to the "critical state" from which the plastic deformation occurs. This stress state is noted C', C^* or P^* depending on the type of loading and/or failure occurring. The measurement of this stress state for different loading conditions permits determining the "failure envelope" (or "yield surface") of the rock.

The $\boldsymbol{C'}$ stress state corresponds to a softening (or negative hardening) of the deformation revealed by a sudden porosity increase and mean stress drop (Figure 21a). This type of failure generally occurs under axial loading at low confining pressure (Baud et al., 2000; Bésuelle, 2001a; Ingraham et al., 2013). The deformation associated with this failure is defined as "brittle", generally localized under the form of shear fracture, displaying a rather low angle with the major principal stress (Figure 22) (Scott and Nielsen, 1991; Fortin et al., 2005). Grain rearrangement and sometimes cataclasis can precede fracturing (Menéndez et al., 1996; El Bied et al., 2002). The increase of fluid pressure in the rock can enhance the occurrence of this fracturing (Sulem and Ouffroukh, 2006).

The $\boldsymbol{C^*}$ stress state corresponds to a strain hardening, revealed by a sudden porosity drop without mean stress drop (Figure 21a). This type of failure occurs at high confining pressure

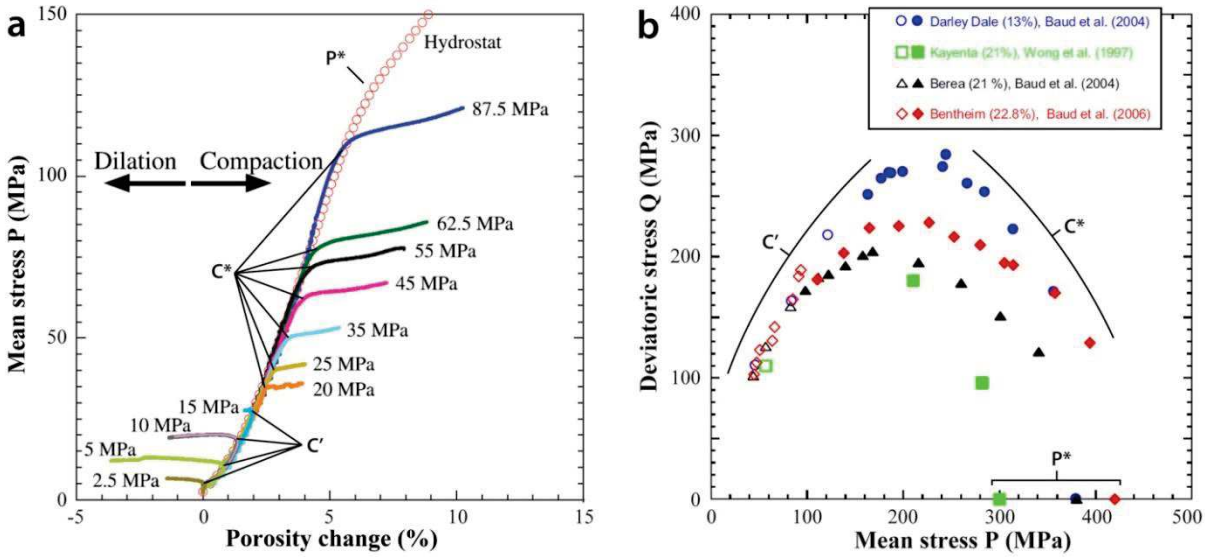

Figure 21. (a) Graph showing the relation between the mean stress (P) and the porosity change during a triaxial test (modified from Karner et al., 2005). The different types of inflexion in the slope indicate that the critical state is reached (failure) and that the sample is further deformed plastically. (b) Q-P diagram showing the failure envelope, imaged by the the plots of several critical stress states for different stress loadings (modified from Wong and Baud, 2012). The critical states drawing a positive correlation between Q and P correspond to brittle failure (dilatant softening); the critical states drawing a negative correlation between Q and P correspond to cataclastic flow (compactant hardening).

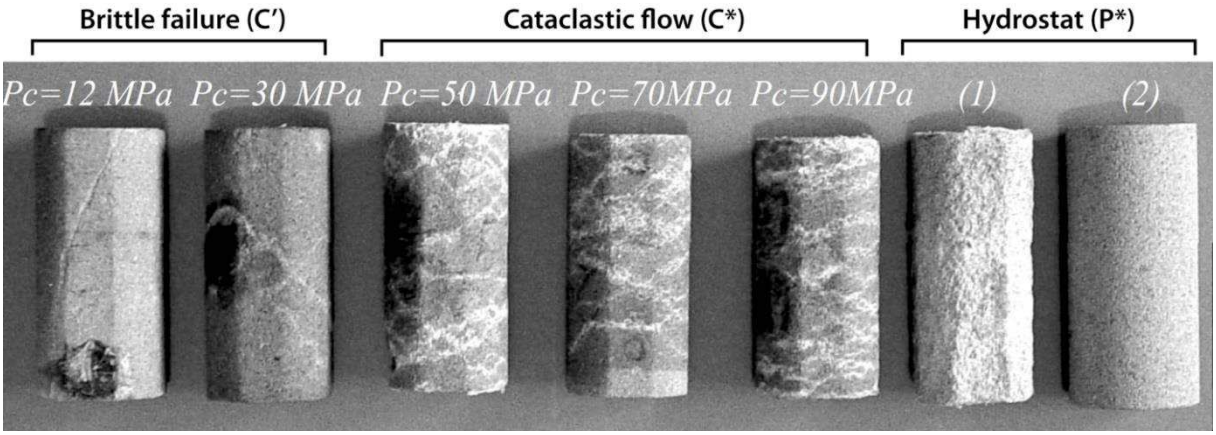

Figure 22. Photograph of specimen that underwent triaxial tests until failure. The geometry and localization of the plastic deformation depends on the type of failure (from Guéguen and Fortin, 2005).

(Bésuelle, 2001) during axial loading, corresponding to important mean and deviatoric stresses. The associated deformation is defined as a "cataclastic flow", materialized by distributed compactional shear bands (CSB) and shear-enhanced compaction bands (SECB), displaying a high angle with the maximum principal stress (Figure) (Scott and Nielsen, 1991; Bésuelle et al., 2000; Fortin et al., 2005). Acoustic Emission (AE) analyses reveal the initiation of cataclasis by fracturing involving an intense acoustic activity (Menéndez et al., 1996; Wong et al., 1997; Baud et al., 2006; Zhu et al., 2007; Fortin et al., 2009; Charalampidou et al., 2011), leading to localized cataclastic bands (Baud et al., 2004; Fortin et al., 2009; Stanchits et al., 2009; Charalampidou et al., 2014).

P^* is the grain crushing pressure at the hydrostatic loading (Figure 21b) (Zhang et al., 1990; Fortin et al., 2005). This failure is indicated by a slight inflexion on the slope of the evolution of the porosity (Figure 21a) and is associated with "cataclastic flow" and grain rearrangement with a pervasive pore collapse (Figure 22) (Scott and Nielsen, 1991; Fortin et al., 2005).

As indicated in Figure 21b, the plot of the different critical stress states under different loading conditions describes the failure envelope of the rock. As shown in (Figure 23), this failure envelope is described by two distinct parts (Wong et al., 1997; Cuss et al., 2003; Schultz et Siddharthan, 2005), corresponding to the brittle deformation (for low to intermediate mean stress P on the left), and cataclastic flow (for intermediate to high P on the right). The line linking the origin of the failure envelope and the limit between the brittle and cataclastic flow (/ductile) parts of the failure envelop is referred to as the "*critical state line*" (CSL). Failure on the CSL is isochoric. Rutter and Glover (2012) proposed the following equation to describe the critical state line:

$$M = \frac{6 \sin \varphi}{3 - sin\, \varphi} \quad (1)$$

where the friction coefficient estimated as μ = tan φ, φ being the internal friction angle of the material. Rutter and Glover (2012) report from the compilation of several failure tests on several sandstones critical state line slopes close to 1.2 (Figure 24). These authors show that the critical state line has to be distinguished from the friction slope.

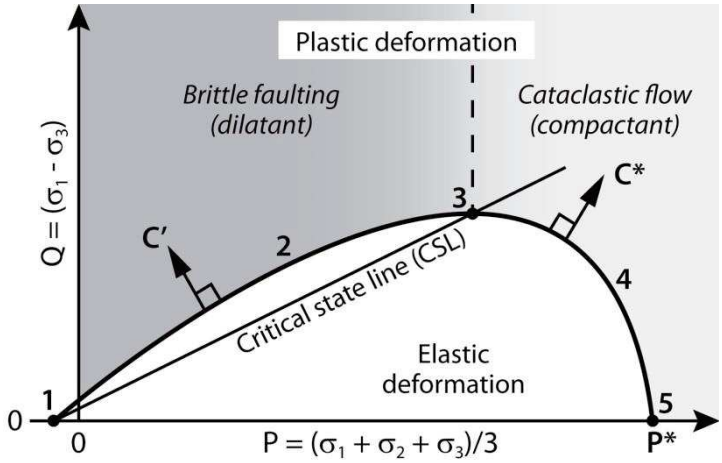

Figure 23. Theoretical failure envelope of a porous sandstone (modified from Schultz and Siddharthan, 2005). The numbers correspond to the types of band induced by deformation. 1: Dilation bands; 2: Dilational shear bands; 3: Simple shear bands; 4: Compactional shear bands; 5: Hydrostatic pervasive pore collapse.

1.2.2b The failure envelope for brittle deformation regime

The failure envelope of the brittle deformation (C') corresponds to low confining pressures and displays a slightly parabolic trend with a positive correlation between Q and P (e.g. Wong et al., 1997, Cuss et al., 2003; Schultz et Siddharthan, 2005; Schultz et al., 2010; Rutter et Glover, 2012).

The deformation on the failure envelope of the brittle deformation is described as localizing under the form of dilatant shear bands or fractures (Wong et al., 1997; Bésuelle, 2000; El Bied et al., 2002; Baud et al., 2004; Sulem and Ouffroukh, 2006).

1.2.2c. The cataclastic flow failure envelope

The failure envelope of the cataclastic flow (ductile deformation) corresponds to high confining pressure and displays an elliptical function, with a negative relation between Q and P (Zhu and Wong, 1997; Baud et al., 2000; Fortin et al., 2005; Baud et al., 2006; Rutter and Glover, 2012;

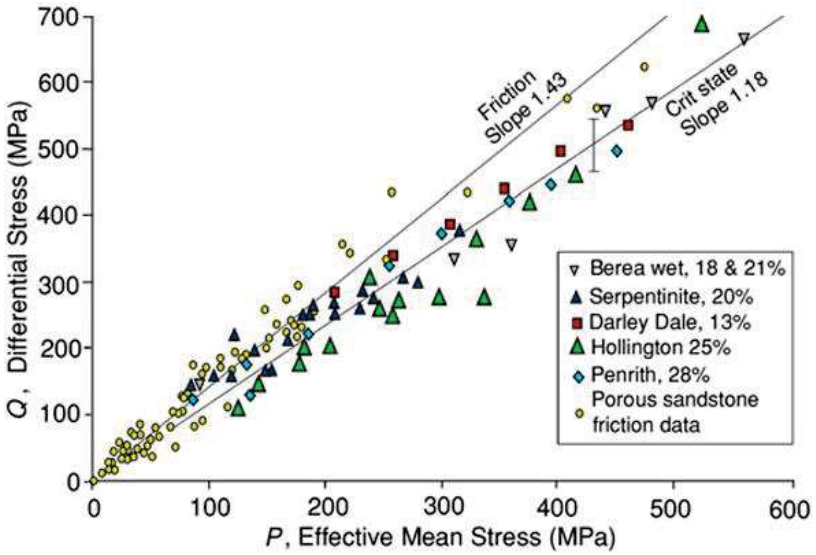

Figure 24. Plot of the critical stress states in brittle softening failure and plot of the friction slope of porous sandstones. The critical state line and the friction slopes are to be distinguished (from Rutter and Glover, 2012).

Wong and Baud, 2012). This part of the failure envelope is referred to as the “cap”.

The position of the cap ellipse depends on several parameters. In particular, Zhang et al. (1990), Wong et al. (1997), Karner et al. (2005) stated that the P* position on the P axis depends on the porosity and grain size of the sandstone. Their triaxial tests reveal that the porous material undergoes hydrostatic failure (pervasive pore collapse) at lower confining pressure threshold when the initial porosity of the sandstone is more important (Figure 25a). The failure envelope is shrunk towards the left of the Q-P diagram when the host rock porosity is least; conversely, the failure envelope is stretched towards the right for more porous host rocks. Zhang et al. (1990), Wong et al. (1997) show by their comparative analysis of previous works that the influence of the porosity is coupled with the sandstone grain size according to a negative correlation between the porosity, multiplied by the mean grain size and P^* (Figure 25b), following the relation:

$$\boldsymbol{P^* = (\phi R)^n} \quad (2)$$

where ϕ is the porosity, R the mean radius of the host rock grain size, and n is approximately -3/2.

Hence, the grain size and the porosity influence the initiation of inelastic deformation.

Furthermore, as the cataclasis induced by the cataclastic flow and hydrostatic failure participates to the particle size reduction of the granular material (section 1.1.1), Schultz and Siddharthan (2005), Rutter and Glover (2012) suggest that the cap part of the failure envelope may subsequently be shifted to the right (Figure 26). The mechanical framework proposed by the authors therefore suggests that the CDB accumulation (eventually forming a cluster) leads to faulting once the strain hardening of the structures have increased the cap part of the envelope until intersecting the frictional strength surface. We think this explanation is not satisfactory to explain the formation of clusters and faults since there is no reason for the localization of faulting in the strain-hardened clusters while the pristine sandstone around the cluster is not hardened and can therefore accumulate further deformation. Although it is true that the rock undergoes pervasive slight deformation at the onset of the cataclastic flow (and brittle failure) (Lanatà, 2014), this increase of

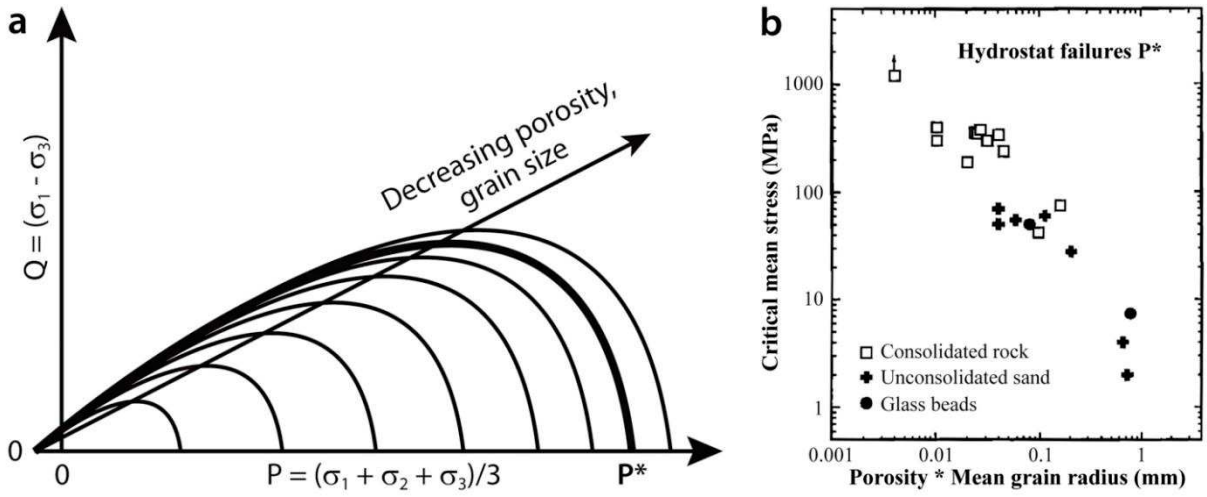

Figure 25. (a) Q-P diagram showing an increasing failure envelope as the porosity and mean grain size decrease (from Schultz and Siddharthan, 2005). (b) Graph showing the relationship between the critical mean stress at the onset of hydrostat failure as a function of the porosity and mean grain radius of the host rock (from Wong et al., 1997).

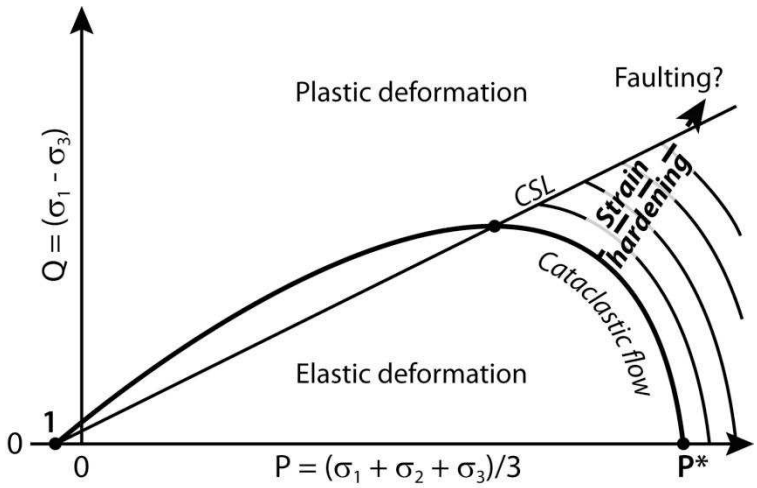

Figure 26. Q-P diagram showing the evolution of the cap part of the failure envelope as strain hardening increases in the deformed structures due to a local grain thinning and porosity reduction (modified from Schultz and Siddharthan, 2005).

the cap to the right described by Schultz and Siddharthan would rather correspond to the local increase of strain in the formed band itself. In contrast, unless completely deformed, one could expect that the failure envelope of the host rock would conserve a failure envelope almost similar to the envelope before the formation of a band.

1.3.3. Influence of the loading type on the deformation

1.2.3a. Influence on the geometry

As evoked before, the type of loading controls the geometry and distribution of the deformation when the stress-path reaches the failure envelope. Bésuelle (2001a) and Tembe et al. (2006) show from triaxial experiments that the angle ψ between the shear bands and the maximum principal stress increases with increasing confining pressure (Figure 27a). Shear bands are generally observed when the differential stress is higher than the mean stress. Compaction bands are more distributed and display variable diffuse or discrete structures under high mean stress (Mair et al., 2002a; Baud et al., 2004, 2006; Fortin et al., 2005; Tembe et al., 2008). Although higher mean stress appears to be necessary in the laboratory to form deformation bands (Tembe et al., 2008), and although the bands formed in triaxial tests are generally thinner and more cataclased (Baud et al., 2004), laboratory experiments are consistent with the field studies realized by Saillet and Wibberley (2010), Ballas (2013) and Soliva et al. (2013, 2016) (Figure 27b). As mentioned on section 1.1.4, they reveal that the localized deformation structures rather occurs in extensional tectonics under the form of cataclastic band clusters and faulted clusters. On the other hand, the distributed deformation forms in contractional tectonics setting, under the form of conjugate network of distributed deformation bands. Similarly, the angular variations of ψ as a function of the confining pressure are consistent with those found in laboratory tests. In their work, Saillet and Wibberley (2010), Ballas (2013) and Soliva et al. (2013) reconstruct the stress-path via the knowledge of the burial depth of the formation at the time of deformation (sedimentary column) and the deduction of the Andersonian regime (kinematics and the geometry of the deformation structures). The type of failure is worked out at the intersection of the stress-path with the failure envelope, which can be estimated with the equation (2).

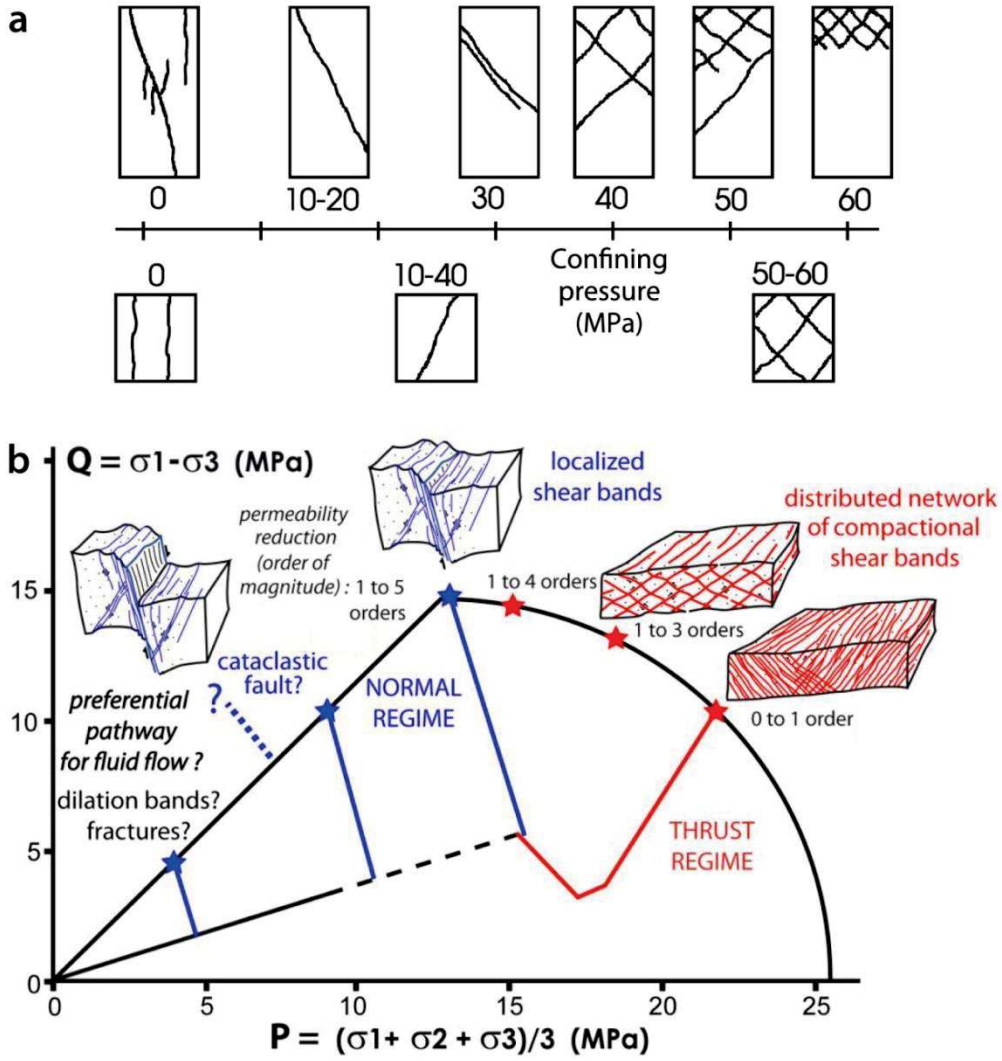

Figure 27. (a) Representation of the geometrical evolution of deformation as a function of the confining pressure (from Bésuelle, 1999). (b) Q-P diagram showing the analogy of the geometry and distribution of the deformation as worked out from field analysis and reconstruction of the stress-path and yield envelope (modified from Ballas, 2013).

1.2.3b. Influence on the petrophysical properties

The evolution of permeability relative to the formation of a cataclastic band with varying degree of dilatancy/compaction and shear was studied. On the cap part of the envelope (C^*), corresponding to high confining pressure, the porosity and permeability tend to decrease (Figure 28a) (Zhu and Wong., 1996; Lothe et al., 2002; Ngwenya et al., 2003; Zhu et al., 2007; Dautriat et al., 2009; Baud et al., 2012). The porosity and permeability reduction are even more important at high differential stress (Zhu and Wong, 1996). The experiments of Baud et al. (2012) suggest that high differential stress does not necessarily requires high confining pressure to yield low-porosity and low-permeability structures. Indeed, they do not measure significant difference in permeability contrast between structures formed at confining pressures of 40 and 150 MPa (Figure 28b).

1.3.4. Mechanical modeling of deformation

The mechanical modeling of band formation in porous sandstones is based on the bifurcation theory. This theory assumes that the localization of the bands results from a constitutive instability of

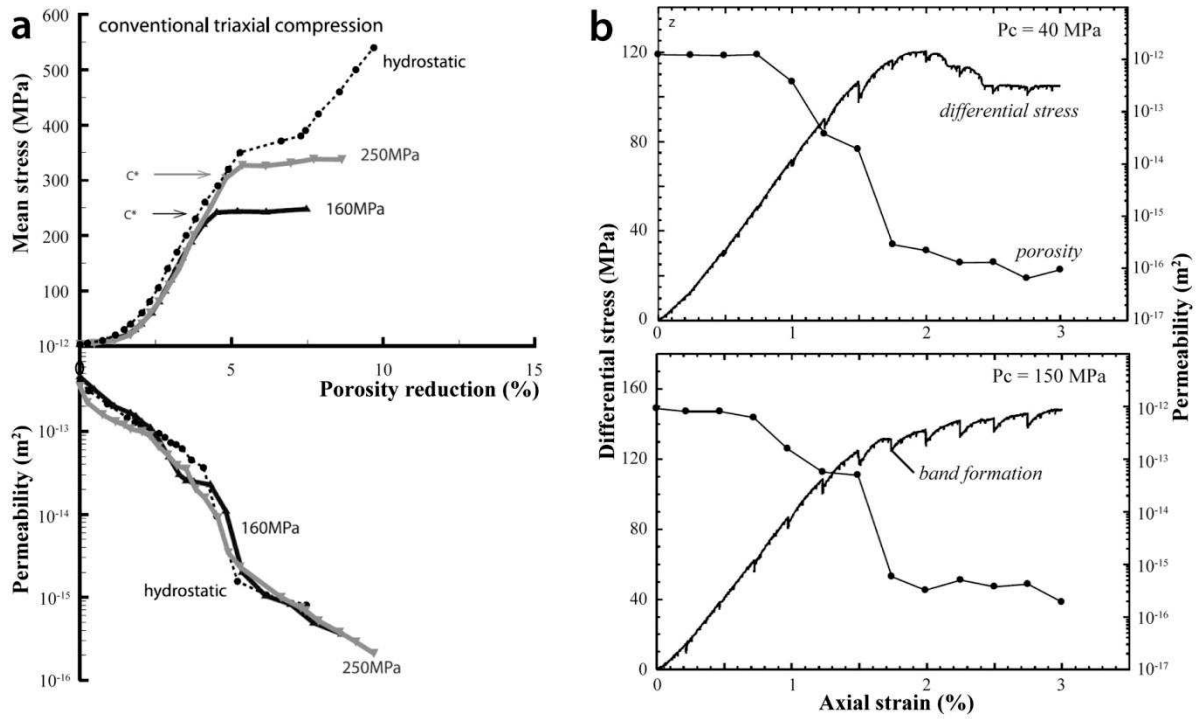

Figure 28. (a) Mean stress and permeability as a function of the porosity reduction for different confining pressures (modified from Zhu et al., 2007). (b) Differential stress and permeability as a function of the axial strain for triaxial tests realized with a confining pressure of 40 MPa and 150 MPa (modified from Baud et al., 2012).

the material (c.f. Rudnicki and Rice, 1975 and references in it; Bésuelle, 2001b; Bésuelle and Rudnicki, 2004; Chemenda, 2007). The initially homogeneous material is assumed to deform elasto-plastically and homogeneously until bifurcation occurs, from which a non-uniform inelastic deformation is localized along a narrow band. The localization is predicted from the material properties and the loading conditions. The failure envelope can be represented as a function of the Von Mises equivalent stress $\bar{\tau}$, which is a proxy of the maximum shear stress ($[\sigma_1 - \sigma_3]/3$), and the mean normal stress σ_m (= P) (Rudnicki and Rice, 1975; Olsson, 1999; Mas and Chemenda, 2015) (Figure 29a). To each point of the envelope corresponds an internal friction coefficient α (slope of the envelope – Figure a), and a dilatancy factor β, defined as follows.

The internal friction coefficient is:

$$\boldsymbol{\alpha} = \left(\frac{\partial \bar{\tau}}{\partial \sigma_m}\right)_{\bar{\gamma}^p} \tag{3}$$

where $\bar{\gamma}^p$ is the inelastic shear strain. In porous granular material, α is then positive in the shear and brittle part of the envelope and negative in the cap part.

Large data sets of triaxial deformation on natural and synthetic granular material allowed evidencing the influence of the accumulated inelastic strain $\bar{\gamma}^p$ on the modification of the failure envelope. Mas and Chemenda (2015) distinguish the “yield surface” from the “failure envelope” in that the yield surface (Figure 29b) accounts for the evolution of $\bar{\gamma}^p$

Accounting for the influence of $\bar{\gamma}^p$, the dilatancy factor β is defined as follows (Figure 29c):

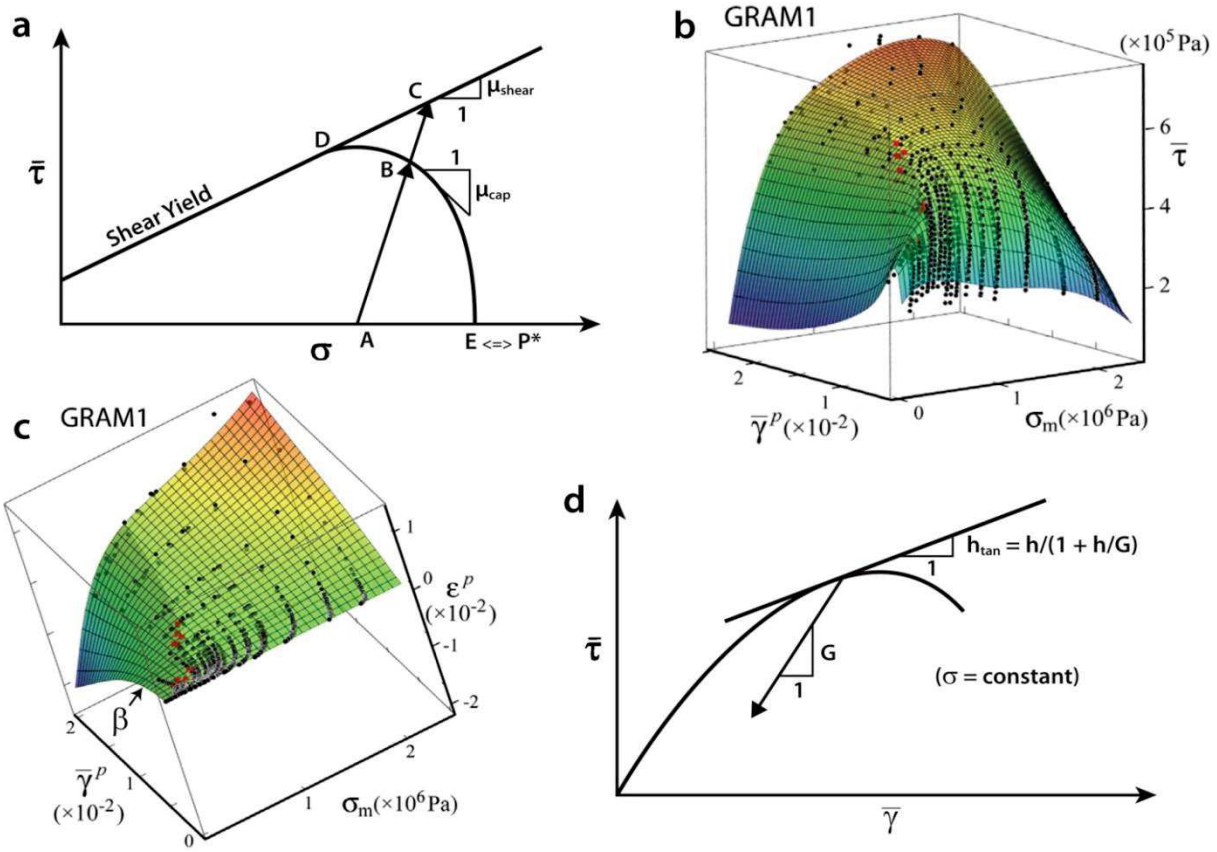

Figure 29. (a) The internal friction coefficient μ is obtained as the slope of the failure envelope in the $\bar{\tau}$-$\sigma_m$space (from Olsson, 1999). μ is positive in the critical state line part ("Shear yield"), and negative on the cap part of the envelope. (b) Results from multiple triaxial tests on synthetic GRAM material (from Mas and Chemenda, 2015). The consideration of the accumulated inelastic strain permits evidencing its role of failure, which is then described in the $\bar{\tau}$-$\bar{\gamma}^p$-σ_m space as a "yield surface" from which the "real internal friction coefficient" α can be obtained. (c) The dilatancy factor β is calculated from the ε-$\bar{\gamma}^p$ space at σ_m = constant (from Mas and Chemenda, 2015). (d) The hardening modulus h is obtained from the slope of the yield surface in the $\bar{\tau}$-$\bar{\gamma}^p$ space, at σ_m constant (from Rudnicki and Rice, 1975). h is supposed to be dependant on several parameters such as the elastic shear modulus G.

$$\boldsymbol{\beta} = \left(\frac{\partial \boldsymbol{\varepsilon}^{\boldsymbol{p}}(\boldsymbol{\sigma_m}, \bar{\boldsymbol{\gamma}}^{\boldsymbol{p}})}{\partial \bar{\boldsymbol{\gamma}}^{\boldsymbol{p}}}\right)_{\boldsymbol{\sigma_m}} \tag{4}$$

where ε^p is the inelastic volume strain. β is positive in the brittle part of the envelope and negative (compaction) in the cap part.

The strain hardening controlling the onset of deformation localization is defined as:

$$\boldsymbol{h} = \frac{\boldsymbol{1}}{\boldsymbol{G}}\left(\frac{\partial \bar{\boldsymbol{\tau}}(\boldsymbol{\sigma_m}, \bar{\boldsymbol{\gamma}}^{\boldsymbol{p}})}{\partial \bar{\boldsymbol{\gamma}}^{\boldsymbol{p}}}\right)_{\boldsymbol{\sigma_m}} \tag{5}$$

A theoretically predicted constitutive instability (deformation bifurcation) has been obtained in numerical models (e.g., Poliakov and Herrmann., 1994; de Borst and Pamin, 1996; Stefanov et al., 2011) and allowed reproducing conjugate networks of deformation bands (e.g. Figure 30 a and b). These models reveal the relation between the hardening modulus h and the thickness/spacing ratio of the bands (Chemenda, 2007, 2009), the influence of compaction bands on the propagation of others (Chemenda, 2011), the influence of multi-layers systems and α and β parameters on the evolution of network structuring (Chemenda et al., 2012, 2014).

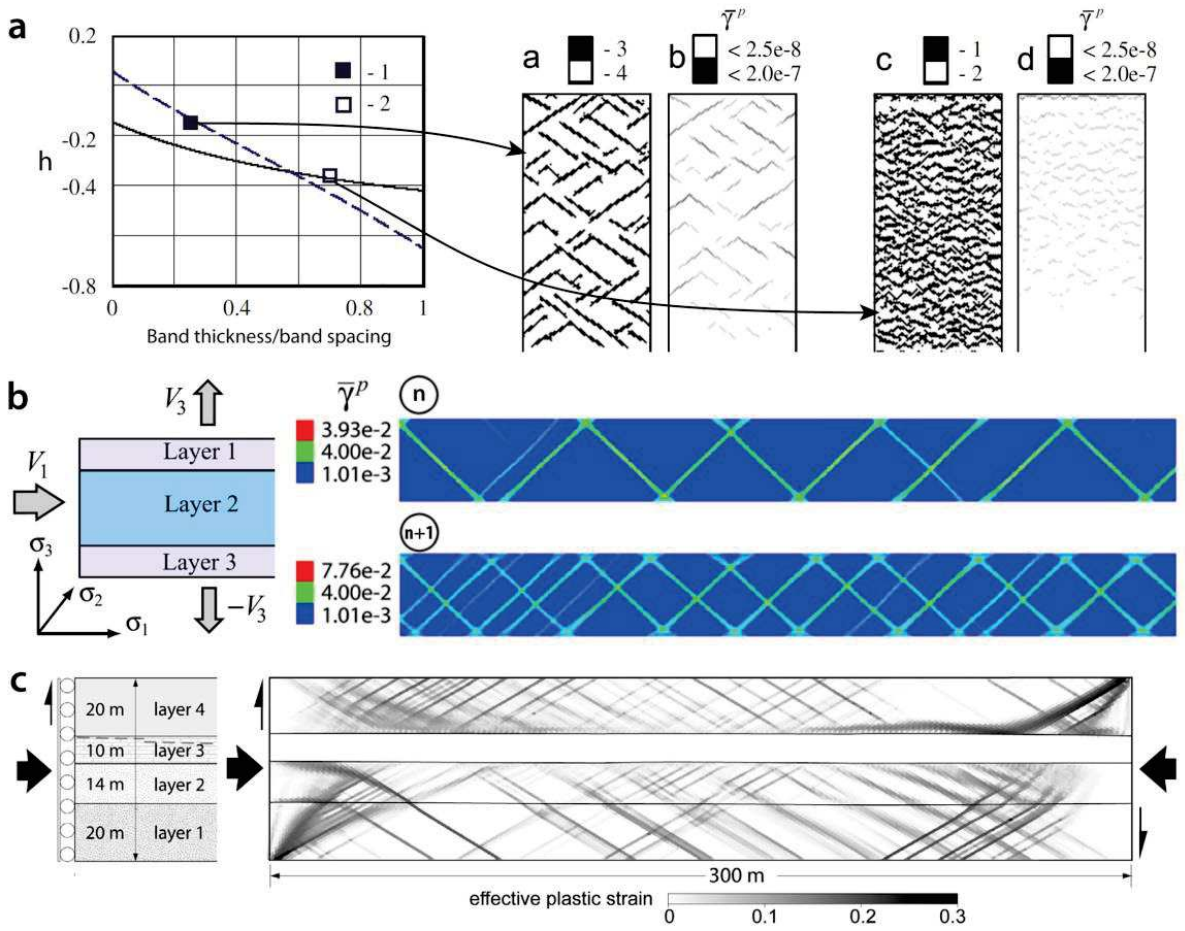

Figure 30. Examples of finite-difference numerical modeling of deformation in porous sandstone using Drucker-Prager constitutive models. (a) Compaction banding (from Chemenda, 2009). (b) Band networks in contraction in a multi-layer system (from Chemenda et al., 2014). (c) Deformation band network in contraction in a multi-layer system (from Klimczak et al., 2011).

Other models based on finite element system and different constitutive models exist (e.g. Klimczak et al., 2011). They also successively reproduce in different layers deformation structures of geometry close the band organization observed in the field, respective to the tectonic loading imposed (Figure 30 c).

Nevertheless, the Q-P or $\bar{\tau}$-σ diagrams remain convenient tools to anticipate the first stages of deformation. In particular, Issen and Rudnicki (2000), Bésuelle (2001b) and Issen (2002) observed a link between the friction coefficient μ, the dilatancy factor β, the angle ψ and the type of band formed. The authors show that a threshold of equation $\beta = -\mu - \sqrt{3}$ separates a domain of compaction band formation (Figure 31a – below and to the left of the line) and a domain of shear band formation (above and to the right of the line). The trend is verified by triaxial tests (e.g. Olsson, 1999; Baud et al., 2006) (Figure 31b).

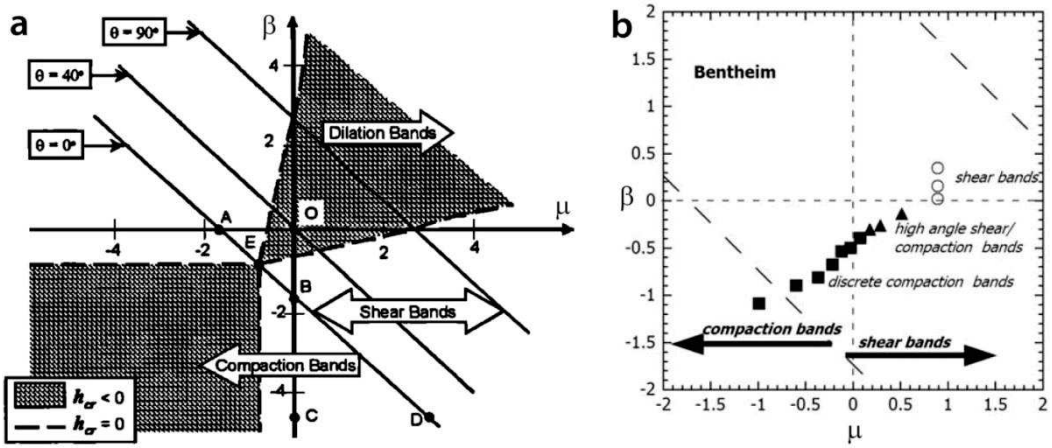

Figure 31. (a) Predicted band orientation as a function of the internal friction coefficient μ and the dilatancy factor β (from Issen and Rudnicki, 2000). (b) Results of the types of deformation bands formed from triaxial tests plotted as a function of μ and β (from Baud et al., 2006).

1.4. Issues and presentation of the work undertaken

1.4.1. Limits of previous works

As presented in this chapter, numerous characteristics of the deformation in porous sandstone were already evidenced. We saw that several parameters control the inception, the type, the distribution and the petrophysical properties of deformation in sandstones. In particular, clusters, because of their important size and because they are potentially faulted with low permeability, are likely to influence fluid migration during reservoir exploitation at basin scale. However, despite the many field analyses, experimental tests and numerical modeling (both granular and finite-elements) (sections 0 and 1.3.4), we note that, linked to cataclasis, the process leading to band accumulation responsible for the formation of clusters is poorly understood (e.g. Kaproth et al., 2010; Nicol et al., 2013; Fossen et al., 2017). The evolution from cluster to fault (with the inception of a major through-going slip-surface) is not constrained either. The resulting cluster morphology and dimensions is not well understood. Finally, little is known of the diagenetic evolution of clusters at shallow burial. We will recall here why the previously proposed models for clustering are not satisfying.

As seen in section 1.1.1, the cataclastic deformation and the formation of cluster is possible in clean sandstones. Yet, at basin scale, the sandstone-dominated reservoirs generally comprise lithological heterogeneities. The many deformation mechanisms are individually well understood and well constrained (e.g. Allan, 1989; Knipe, 1997). Nevertheless, the interplay between the cataclasis and other mechanisms through time and space is rarely analyzed (e.g. Davatzes et al., 2003, 2005), we do not know if the interplay between the cataclasis and other mechanisms is common, and we do not know the influence of such potential interplays of the created fault rocks and their impact on fluid flow.

We saw that, in relation to the first assumption of Aydin proposing strain hardening as being involved in the CDB clustering, models explaining the evolution of clusters by localized band accumulation have been attempted, in particular on the basis of geometrical analysis and under the form of mechanical framework. As introduced in section 1.1.4 Nicol et al. (2013) suggest that the deformation band clusters are formed at a fault irregularities (e.g. relay zones between fault segments) and that the band develop sequentially, locally accommodating the strain and coalescing with each other during each step of the fault development. The authors also refute the band accumulation as being due to strain hardening. We think this model is not satisfying because (i) many clusters are observed with a significant extent along the shear plane (by opposition to a supposedly local strain accommodation) (e.g. Johansen and Fossen, 2008), and (ii) because numerous clusters are observed free and away from faults (i.e. not including a though-going slip-surface) (e.g. Edwards, 1993; Ballas et al., 2014). On the other hand, as presented in section 1.3.2, the mechanical approach of Schultz and Siddharthan (2001) proposing that faulting occurred after that the failure envelope cap reached the friction line due to strain hardening by successive band addition also has, in our opinion, shortcomings. In this model, we do not understand why the localization of a fault would occur in the cluster thickness (or at the edge of the cluster) while the cap part of the failure envelope of the little deformed host rock around the cluster would remain close to the original. We would rather expect that successive band would indefinitely form in the host rock, where the failure envelope is weaker than the envelope of the deformed material.

The recent work of Ballas (2013) and Soliva et al. (2016) tend to showed that the clusters are favored in extensional tectonics compared to contractional regime where the deformation tends to distribute. In particular, Ballas et al., (2014) showed that the clusters locally form networks associated with map-scale faults. Yet, we remark that the morphology and the dimensions of the clusters are poorly reported, and that the interaction between these dimensions, the tectonic loading and the Andersonian stress regimes are not well established.

The diagenetic and cementation processes of the host rock at depth of more than 2 kilometers are well known and the diagenetic state of the bands below this limit is often reported as being preferentially cemented due to cataclasis. However, we note that the potential cementation of the cataclastic deformation structures at shallow burial (<2 km) suffers a lack of information (e.g. Milliken et al., 2005), both in terms of process and result on the petrophysical properties. In particular, we wonder if cementation could explain why cataclastic deformation band cluster are often more competent than the surrounding host rock, presenting positive reliefs at the outcrop. Information on this topic could yield interesting implication for the early diagenetic evolution of clusters and potentially on the deformation mechanisms leading to strain localization.

1.4.2. Questions

Relative to this state of knowledge, and in a concern of addressing the gaps in the literature, our study aims at answering the following questions concerning the cataclastic deformation. In the goal of answering a potential issue of fluid-flow in the context of reservoir production, our study focuses on the cataclastic deformations band clusters:

- **What processes/mechanisms govern the evolution of clusters by band accumulation?**
- **Does a critical condition exist to explain the faulting of a cluster?**
- **How do the cataclastic clusters interact with different lithologies and fault rock mechanisms?**
- **To what extent does tectonic loading control the dimension, geometry and distribution of the clusters?**
- **What other internal parameters significantly influencing their morphology?**
- **What is the role of cataclasis on cementation at shallow depth (<2 km)?**

1.4.3. Organization of this study

In order to address these questions, we chose to undertake an integrated study of the evolution of cataclastic deformation band clusters through the analysis of porous sandstones at seven sites in the world, representing a variety of reservoir analogs. The aim of the integrated study is to analyze the influence of several parameters on the occurrence of the cataclastic deformation, its evolution to cluster and then to fault. Agreeing with the definition of cluster proposed in section 1.1.3, we will in this study consider clusters of 10 cm wide or more. This choice is made to study structures likely to represent a potential baffle for fluid flow. Still, the clusters we study may become narrower than 10 cm and still be considered as part of a cluster if the narrowing is local and linked to structures 10 cm wide or more laterally.

In **Chapter II**, we present the results of the whole field study performed in this work. We will firstly present the geological settings of the sites selected for the study, providing information on the sedimentary and structural context of the studied sandstones as well as the several parameters compared regarding their influence on the clusters. These parameters encompass the tectonic loading, the burial and the lithology of the sandstones. In order to set a framework to the importance of the process of cataclasis amongst other processes of deformation, we will inform the reader on the different deformation mechanisms frequently encountered in sandstone-dominated formations and on the possible interplays between these mechanisms. The relevance of this study is motivated by the fact that aquifers, oil and gas reservoirs do not exclusively consist of pure clean sandstones. Then, to relate the dimensions and geometry of the clusters with the tectonic loading and the Andersonian stress regimes, and to provide information for reservoir scaling, we will analyze the structuring of the clusters through qualitative and quantitative analyses of the intra-cluster deformation as well as macro- and micro-structural analyses. An analytical study of the evolution of stress-path until failure will be presented to better understand the relation between the tectonic loading, the stress-state at failure and the type of deformation induced. The microstructural analysis, with the contribution of the literature of granular materials, allows an interpretation of the potential reasons for the phenomenon of band accumulation participating to the cluster development in extensional tectonics. Finally, to fill the gap of information concerning the early diagenesis of clusters, we provide an analysis of the potential diagenetic evolution of the cataclastic deformation structures at shallow burial.

In **Chapter III**, we present the results of our work concerning the mechanical analysis of the formation of cataclastic deformation band clusters. Because no numerical modeling simulates the formation of clusters until now, we propose numerical models based on the distinct element method to analyze the evolution of clusters formed in normal stress regime as a function of several physical parameters. These parameters comprise the inelastic shear strain, the Von Mises equivalent stress, the internal friction coefficient and the dilatancy factor. These parameters are set based on mechanical processes described in the field and in laboratory experimental tests.

In **Chapter VII**, we eventually deliver a general synthesis of our work dealing with the cataclastic deformation band clusters. We combine our field observations and the results from the mechanical numerical modeling to propose a model for the process of clustering and the necessary conditions to form such structures. We also remind the potential implications of the presence of cataclastic band clusters in sandstones formation for reservoir fluid flow.

Chapter II

2. Field analysis of cataclastic deformation and cataclastic deformation band clusters

In this chapter, we present the base of our work, namely the field study. The chapter is composed of four parts, in which we firstly present the studied field sites, the different mechanisms observed in the sandstone-dominated formations, the clusters and the mechanisms of cluster formation, and finally, the potential diagenetic evolution of the cataclastic deformation structures at shallow depth. In the first section, we will present the geological settings, explaining the choice of the study sites in regard with the framework of our study, and provide a presentation of the structural context of the area and sedimentology of the formation localizing the deformation. In the second section, we will show that the interplay in time and space between different mechanisms of deformation in sandstone-dominated formation yield juxtaposed fault cores of contrasted behaviors regarding fluid flows. In a third section, to better understand the influence of the tectonic loading and sandstone lithology on the morphology of clusters and its influence on fluid flow, we will analyze the structuration of the clusters as a function of these three parameters based on qualitative and quantitative analysis of the deformation at the scale of the exposure. We show that the cataclastic deformation band clusters involve different morphologies and degrees of deformation, depending on both the tectonic loading and the Andersonian stress regime. The microstructural analysis of the cataclastic material allows understanding of the process of band gathering responsible for the cluster development. The diagenetic evolution of the cataclastic deformation is undertaken in a fourth section that is under the form of a published paper. We show in this paper that increasing degree of cataclasis in the deformation material positively influences their quartz cementation. The observation on this phenomenon at the 5 sites whose maximum burial was no deeper than 800m evidences that the cementation is common in the clusters at shallow depth. The early diagenesis of the cluster could be synchronous of the deformation and could therefore directly affct the process of cluster growth.

2.1. Geological settings of the studied sites

We chose to work on seven different sites in order to undertake an integrated study of several parameters constraining the evolution of the clusters of cataclastic deformation bands. We recall that these parameters are:

- The tectonic loading (extensional or contractional)
- The burial depth at deformation
- The presence of an underlying map-scale fault propagating in the overlying sandstones.
- The Andersonian stress regime (normal, strike-slip or thrust)
- The sandstone lithology (mineralogy, porosity, cementation, modal grain size, sorting)

The different parameters aforementioned are obtained either through the literature concerning the tectonic loading and the burial depth, or by direct field analysis concerning the Andersonian stress regime (orientation and kinematics of the structures). We detail here the methodology used to get the lithological parameters of the host rocks.

The mineralogy, porosity and cementation of the host rock were obtained by the examination of thin sections of host rock samples collected in the field. The mineralogy and porosity were qualified by their nature and volume from microscope analysis in plane polarized light and in SEM backscattered electrons. The quantification of the mineralogy and porosity was worked out by image processing through the ImageJ-Fidji software. The cementation was qualified and estimated from cold cathodoluminescence microscope analysis. The modal grain size and sorting (equivalent to the particle size distribution – PSD) were obtained via laser diffraction measurements on selected samples using a Coulter LS 13320 instrument.

For convenience, we summarize the parameters pertaining to the different host rock sandstones studied at each site (presented here individually) at the end of the section in Table 1.

2.1.1. Boncavaï

The site of Boncavaï locates in the South-East Basin, in Provence (France), ten kilometers to the North of the town of Orange (Figure 32a). The region was affected by three main tectonic episodes (Arthaud and Séguret, 1981; Roure et al., 1992; Séranne et al., 1995; Champion et al., 2000): the SSW-NNE Pyrenean compression from Paleocene to Oligocene, the NW-SE Golfe du Lion extension from the Oligocene to early Miocene (rifting), and the SW-NE Alpine compression from Miocene to Quaternary. At the regional scale, the Pyrenean compression is responsible for the contractional wedge at the South of the basin, limited by the SW-NE sinistral strike-slip Nîmes Fault to the Northwest (Figure 32a and b) and the N-S dextral Salon-Cavaillon Fault to the East. The Pyrenean contraction is also accommodated by the E-W North-verging Roquemaure Thrust. The E-W Ventoux-Lure Thrust was also probably initiated during this contractional episode. The thrust faults root in the evaporate-rich Triassic series. The Golfe du Lion rifting provoked the normal reactivation of the Nîmes and Salon-Cavaillon faults. Finally, the Alpine compression participated to the deformation of the Diois-Baronnies to the Northeast; the contraction was also absorbed by the Ventoux-Lure Thrust.

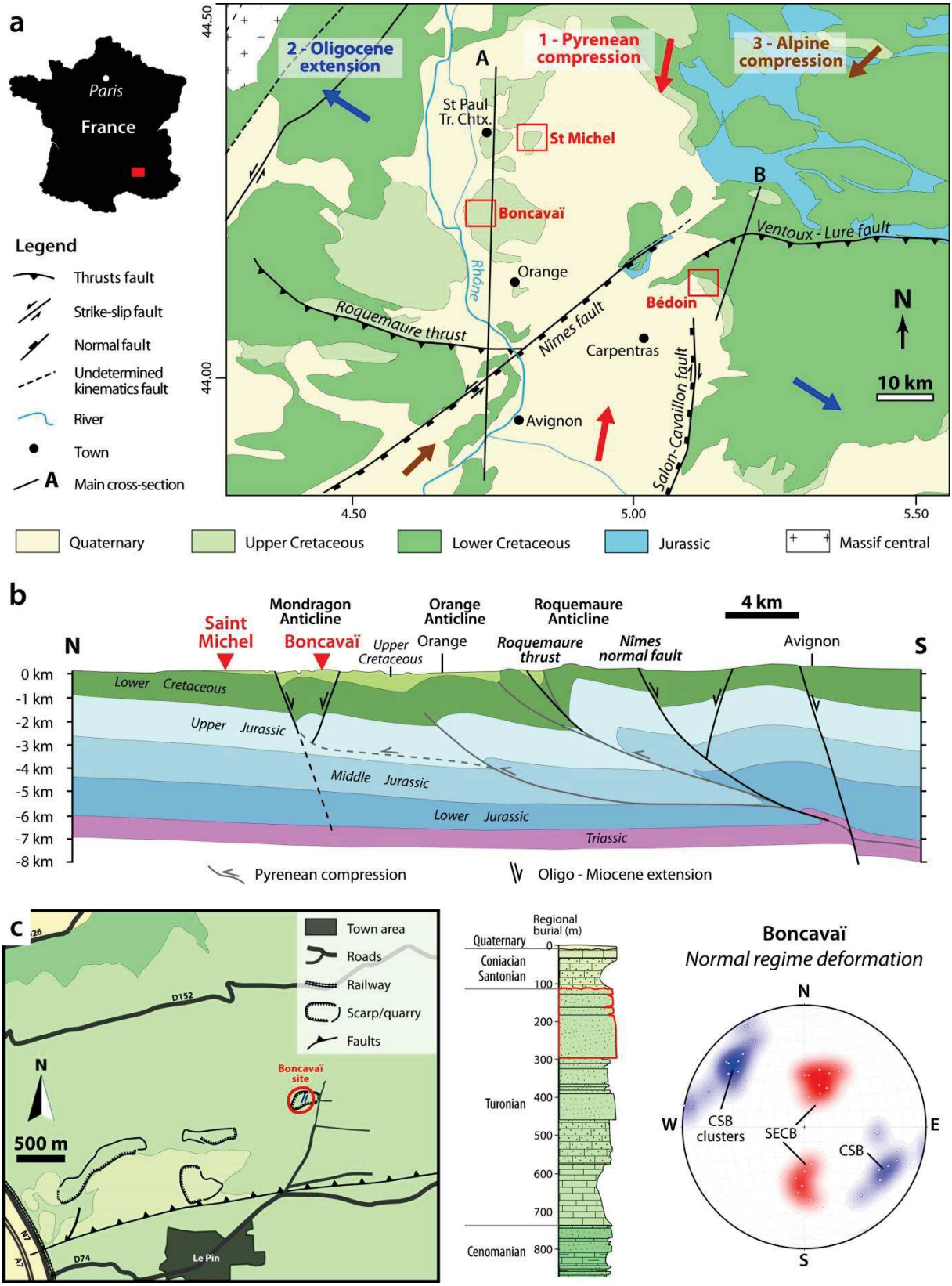

Figure 32. (a) Structural map of the SE Basin region (France), displaying the major faults, the orientation of the main tectonic episodes. The two straight lines correspond to the regional cross section intercepting the sites of Boncavaï and St Michel (A), and Bédoin (B). (b) Regional cross section intercepting the sites of Boncavaï and St Michel, showing the major faults (modified from Soliva et al., 2013). (c) Localization of the study site (quarry) of Boncavaï, localization of the sandstone formation at the outcrop in the sedimentary column (red contour), and pole projection of the normal and thrust kinematics deformation structures in the quarry in a lower hemisphere equal area stereographic diagram.

The site of Boncavaï consists of a quarry located in Turonian sand (low-cohesion sandstone), which can range from 10 to 200 m in thickness (Figure 32c) and is situated in the Mondragon Anticline (Figure 32b). A North-verging E-W normal fault marks the edge of the anticline 1 km South of the quarry, a South-verging E-W normal fault marks the northern edge of the anticline about 3 km to the North.

The Turonian sands at the Boncavaï quarry are of deltaic to aeolian origin, with laminated fine to coarse modal and bimodal grain population (Figure 33a and b). The host rock sands are not cemented. They are composed of 88 to 92% of quartz, the rest being feldspar. Their porosities range from 30 to 43%. The bedding at the site is about N075 18°S. The deformation is essentially of normal regime, linked to the Oligocene-Miocene extension. At the site, two clusters are observed among which one consists of a 3.2 m displacement fault juxtaposing sands-sands formations including a clay layer of 10 – 20 cm in thickness. This cluster is 10 – 50 cm thick and directly juxtaposes sands (Figure 33c); it forms a small clay smear juxtaposed with a thin cluster where the thin clay layer is intercepted (Figure 33d). A second cluster, 10 – 30 cm thick, is also observed with a similar kinematics and strike; the lack of marker prevents its displacement assessment. Both clusters measure at least 85 and 70 m in length, respectively. Both clusters are oriented about N040 65°SE. Besides the clusters, we note the presence of pervasive and distributed individual CSB and SECB in the quarry faces. The clusters (mostly composed of CSB) and the individual CSB parallel to the clusters were formed during the Golfe du Lion extension; the N100 individual SECB were formed during the Pyrenean contraction. The clusters that we study at the sites are formed at a depth comprised between 100 and 300 m, which seems to correspond to their maximum burial (Ferry, 1997; Saillet, 2009; Ballas et al., 2013).

The site of Boncavaï was chosen because it offers a suitable example of deformation localization under the form of a normal regime cluster in a shallowly buried sandstone. Besides, in

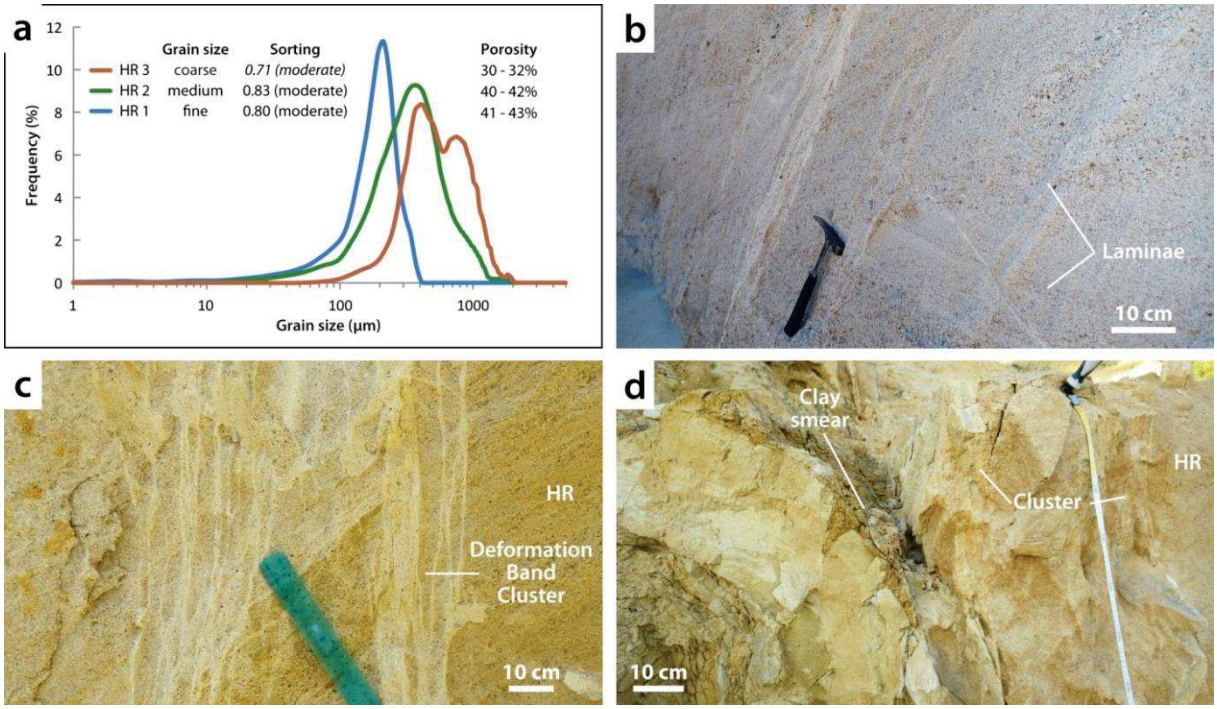

Figure 33. (a) Presentation of the variable grain populations in the various host rocks at the Boncavaï quarry. (b) Example of laminated deltaic host rock sands at the quarry face. (c) Deformation band cluster between juxtaposing sandstones. (d) Clay smear and cluster between a thin clay layer and sand juxtaposition.

this case, in the presence of a specific marker, a displacement can be measured (displacements around clusters are often invisible at the outcrop).

2.1.2. St Michel

The site of St Michel locates 5 km East of the town of Saint-Paul-Trois-Chateaux, in the South East basin, in Provence (France) (Figure 32a and b). The site is poorly studied in the literature and probably underwent similar tectonic history as explained in the previous section. The structural geology around the site reveals a group of N-S strike-slip faults a few kilometers to the West and to the East (Figure 34).

The site consists of a 5 m high scarp made of Turonian sands (low-cohesion sandstones) of deltaic to aeolian origin that can be 10 – 200 m in thickness (Figure 34). Miocene carbonaceous gravels unconformably overlie the Turonian sand formation at the top of the outcrop. The bedding at the site is nearly horizontal. The host rock comprises medium and coarse sands (Figure 35a) and includes no cement. They are composed of 78 to 84% of quartz, the remaining rock volume being feldspar. Their porosities are important, ranging from 35 to 43%. Its partial oxidation in some places testifies to paleo-fluid flow in the formation. The site comprises strike-slip kinematics and thrust kinematics deformations (Figure 34). The studied cluster (Figure 35b) is thought to be mostly composed of CSB and is part of the strike-slip deformation structures (oriented N150 85°NE) whereas the thrust kinematics deformation structures consist of conjugated individual deformation bands (Figure 35c). Both types of deformation structures disappear in the overlying carbonaceous gravels. The Turonian sands at St Michel were deformed during the Pyrenean contraction at a depth of 0 to 200 m (Ferry, 1997). Locally, the Turonian sands may have been buried at a maximum depth of 500 m. Due to the out of shear observation plane, it is not possible to estimate the displacement of the cluster.

2.1.3. Bédoin

The site of Bédoin locates at the East of the SE Basin (Figure 32a), on the southern flank of the Mt Ventoux (Figure 36a). The site is underwent the similar tectonic history explained in the

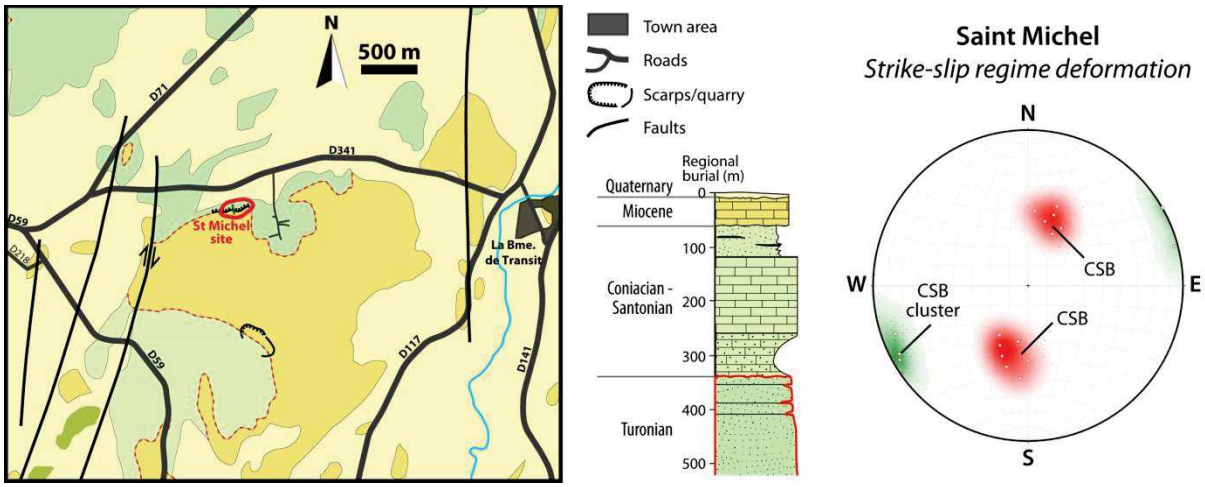

Figure 34. Localization of the study site (scarp) of St Michel, localization of the sandstone formation at the outcrop in the sedimentary column, and pole projection of the strike-slip and thrust kinematics deformation structures at the outcrop in a lower hemisphere equal area stereographic diagram.

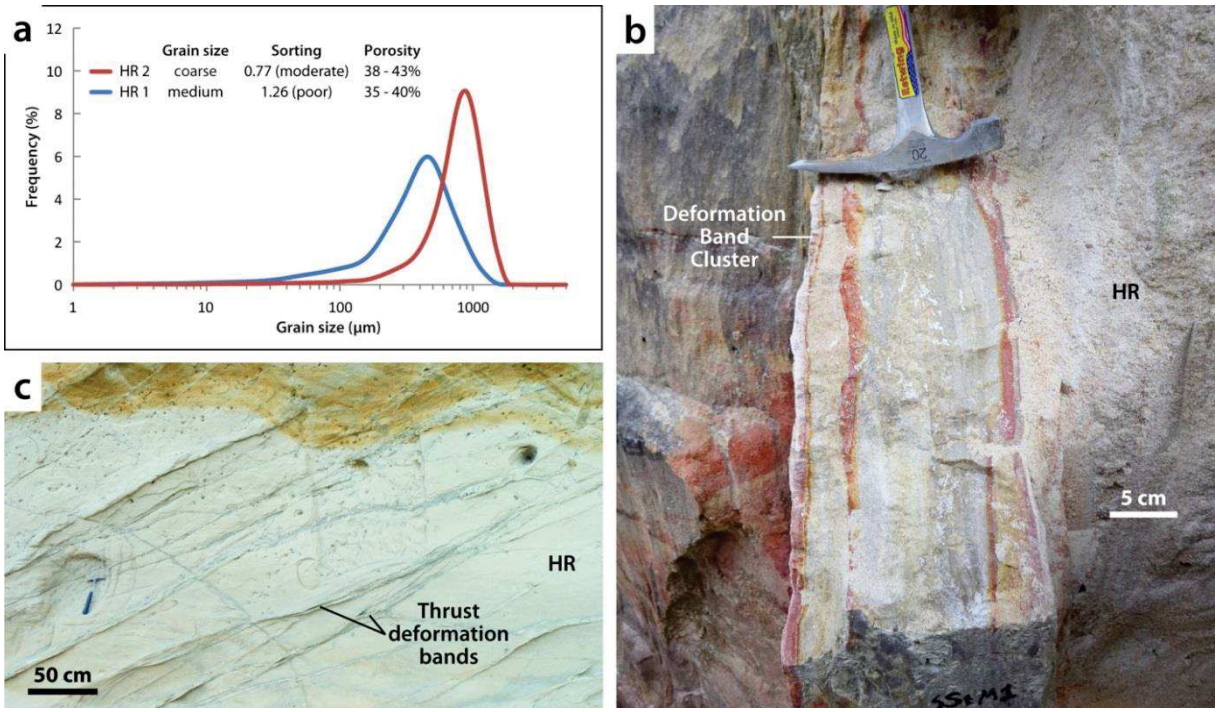

Figure 35. (a) Presentation of the two host rocks grain populations at the St Michel scarp. (b) Section of the strike-slip kinematics cluster of deformation band. We note the presence of oxides in the host rock and in the cluster. (c) The thrust regime deformation materializes under the form of conjugate individual deformation bands in some parts of the formation. Oxides are visible at the top of the formation.

previous sections; the tip of the normal/strike-slip Salon-Cavaillon Fault is estimated to be at a few kilometers at the South of the site.

The Bédoin site locates in the inactive De Cros quarry, 1.5 km to the Northeast of the village of Bédoin (Figure 36b). The quarry is dug in the Cenomanian deltaic sands (low-cohesion sandstones), which can be up to one hundred meters thick. The host rock consists of a rather constant grain size medium sand (Figure 37a). They are composed at 99% of quartz, including almost no feldspar and sometimes comprising a small amount of oxides. Their porosity is important with values of about 35 - 40%. The bedding at the site is about N150 15°SW. The sands comprise several tabular oxidized intervals (Figure 37b) and can be locally tightly cemented, forming tens of centimeter thick tabular structures recognized as silcretes (Figure 37c). Several kinematics of deformation are recognized at the site (Figure 36b): N110 75°N and N150 80°NE and N010 90° strike-slip deformation structures, N070-080 70°N and S normal conjugate deformation structures and N080-090 30°S thrust deformation structures. The clusters (Figure 37d) formed in strike-slip kinematics and are oriented N110 75°N, the rest of the deformation structures are individual deformation bands (mostly CSB). The strike-slip and thrust kinematics deformation of the Cenomanian sands at the Bédoin site were formed during the Pyrenean contraction at a depth of 0 to 200 m (Ferry, 1997; Saillet, 2009). Their maximum burial depth is poorly constrained and could attain 800 m (Delfaud and Dubois, 1984) although it is locally probably shallower.

The sites of St Michel and Bédoin are chosen for the study because they display clusters formed in strike-slip Andersonian stress regimes. To our knowledge, clusters formed in strike-slip regime are rarely (if ever) reported. While the site of St Michel displays a cluster out of the shear plane, the clusters at Bédoin are visible in the plane of shear. Hence, although their respective

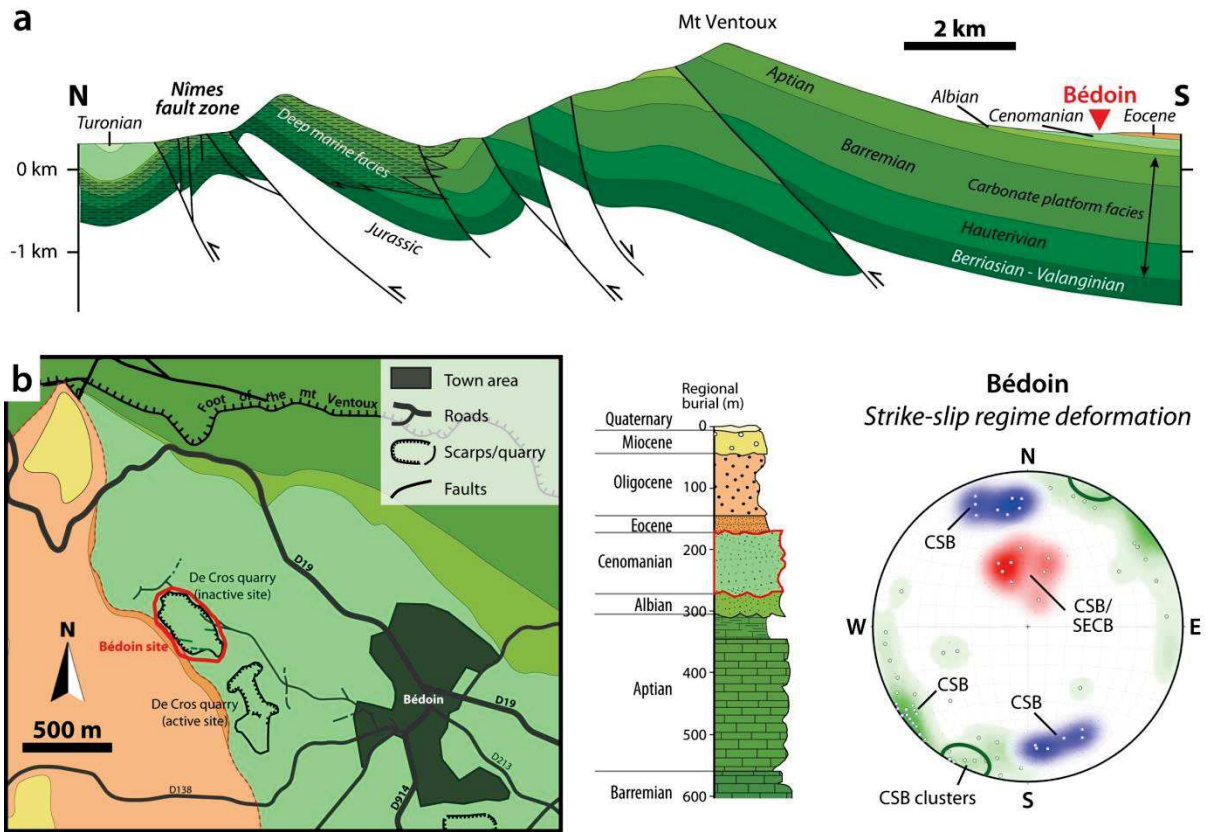

Figure 36. (a) Regional cross section intercepting the site of Bédoin, as positioned in Figure 32a (modified from Ford and Stahel, 1995). (b) . Localization of the study site of Bédoin (De Cros quarry), localization of the sandstone formation at the outcrop in the sedimentary column (red contour), and pole projection of the strike-slip, thrust and normal kinematics deformation structures at the outcrop in a lower hemisphere stereographic diagram.

lithology are somewhat different, the two sites combined form an interesting complement for the study given that they were deformed in the same range of shallow burial depth.

2.1.4. Blankenburg

The Blankenburg site is located in Germany, to the East of the Harz (/Hartz) Mountains, to the southwestern border of the Halbertstadt and Blankenburg Basins (Figure 38a), at the limit of the thrusting Harz Mountains. A regional episode of SW-NE contractional tectonics during Coniacian to early Campanian is responsible for the formation of the Halbertstadt and Blankenburg Basins, and the uplift of the Carboniferous to Devonian basement of the Harz Mountains (Figure 38b) (Voigt et al., 2004; Fischer et al., 2013). The Harz Mountains display a thrusting contact over the Blankenburg Basin, against which the basin sediments from Permian to Cretaceous were significantly folded, showing near vertical dips. A SW verging NW-SE thrust fault is also observed at the contact of the Halbertstadt Basin against the Blankenburg Basin.

The study site is situated at the southeastern edge of the town of Blankenburg and consists of the partially cemented Heidelberg sandstone of Santonian age, measuring from 400 to 600 m in thickness (Figure 38c) (Voigt et al., 2004; French et al., 2012; Klimczack and Schultz, 2013). The host rock consists of homogeneous medium sandstone (Figure 39a), composed of 93% of quartz and 7% of feldspar. Due to the partial cementation, they have a residual porosity of 22 to 28%. The bedding

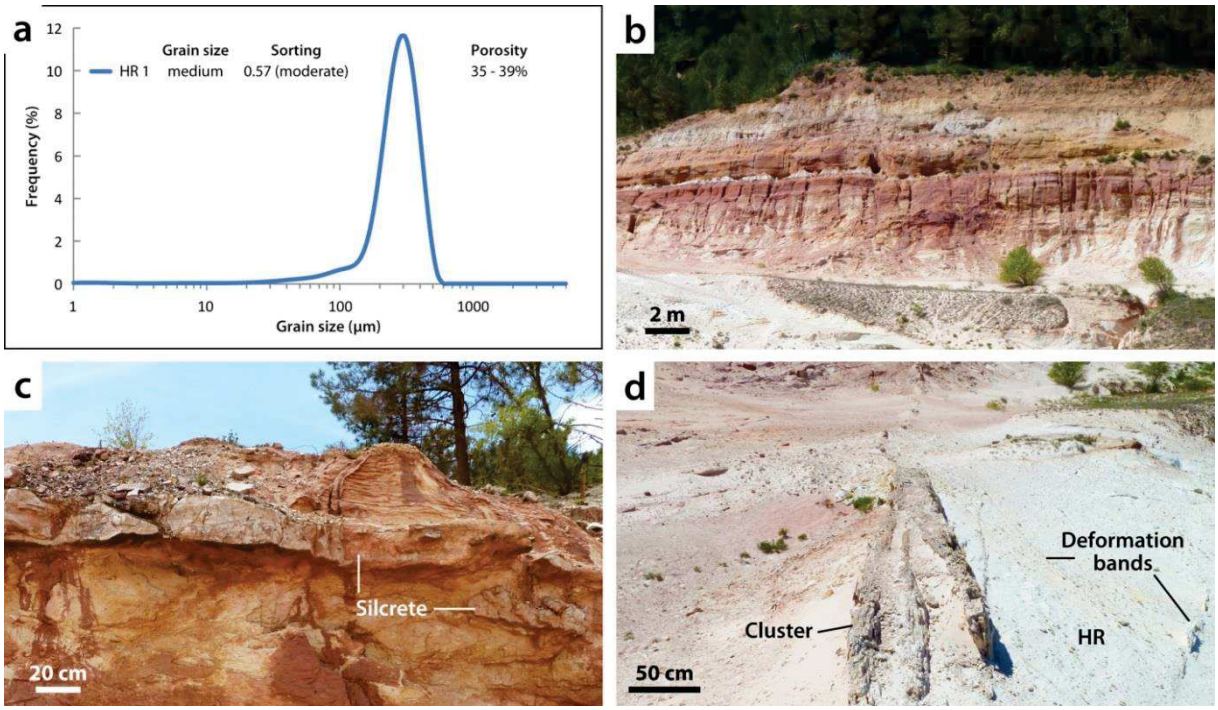

Figure 37. (a) Presentation of the host rock grain population in the De Cros quarry (Bédoin site). (b) Tabular oxidation profile of the De Cros quarry faces. (c) Tabular tightly cemented bodies (silcrete). (d) The main strike-slip cluster at the Bédoin site. Individual deformation bands are also observed in the Cenomanian sands of the site.

is difficult to assess due to the homogeneity of the formation, nevertheless the stratigraphic organization in the zone suggests a N130 orientation with a near-vertical dip (Figure 39a and b). This vertical setting combined with the relative cementation of the grains favors the resistance to the erosion and leaves remarkable linear reliefs in the scenery of the region, also referred to as the Teufelsmauer ("Devil's wall"). At the site, the deformation consists of several thrust regime clusters of 15 to 50 cm in thickness (Figure 39b), locally gathered into one single main cluster measuring up to 110 cm in thickness (Figure 39c). The bands are mostly CSB. The orientation of the clusters is on average N115 70°NE (Figure 38c). Deformation bands aligned with the clusters are also observed. Individual deformation bands oriented N110-120 25°SW are pervasively present between the different branches of cluster and form ladder structures (Figure 39d). The deformation occurred between 0 and 800 m of burial. 800 m also correspond to the maximum burial depth of the formation.

This site represents an interesting field of investigation because the deformation is associated with a major underlying thrust fault. Indeed, the work of Ballas (2013) suggested that the propagation of an underlying fault in the sandstone could condition a specific organization of the cataclastic structures; we would like to study the morphology of the clusters created in such a setting.

2.1.5. Cummingston

The site of Cummingston locates on the Moray coast, which is at the South of the Moray Firth, 10 km to the Northwest of the town of Elgin, in Scotland (UK) (Figure 40a). The site locates on a passive margin of a rifted region. The center of the rift corresponds to the center of the Moray Firth.

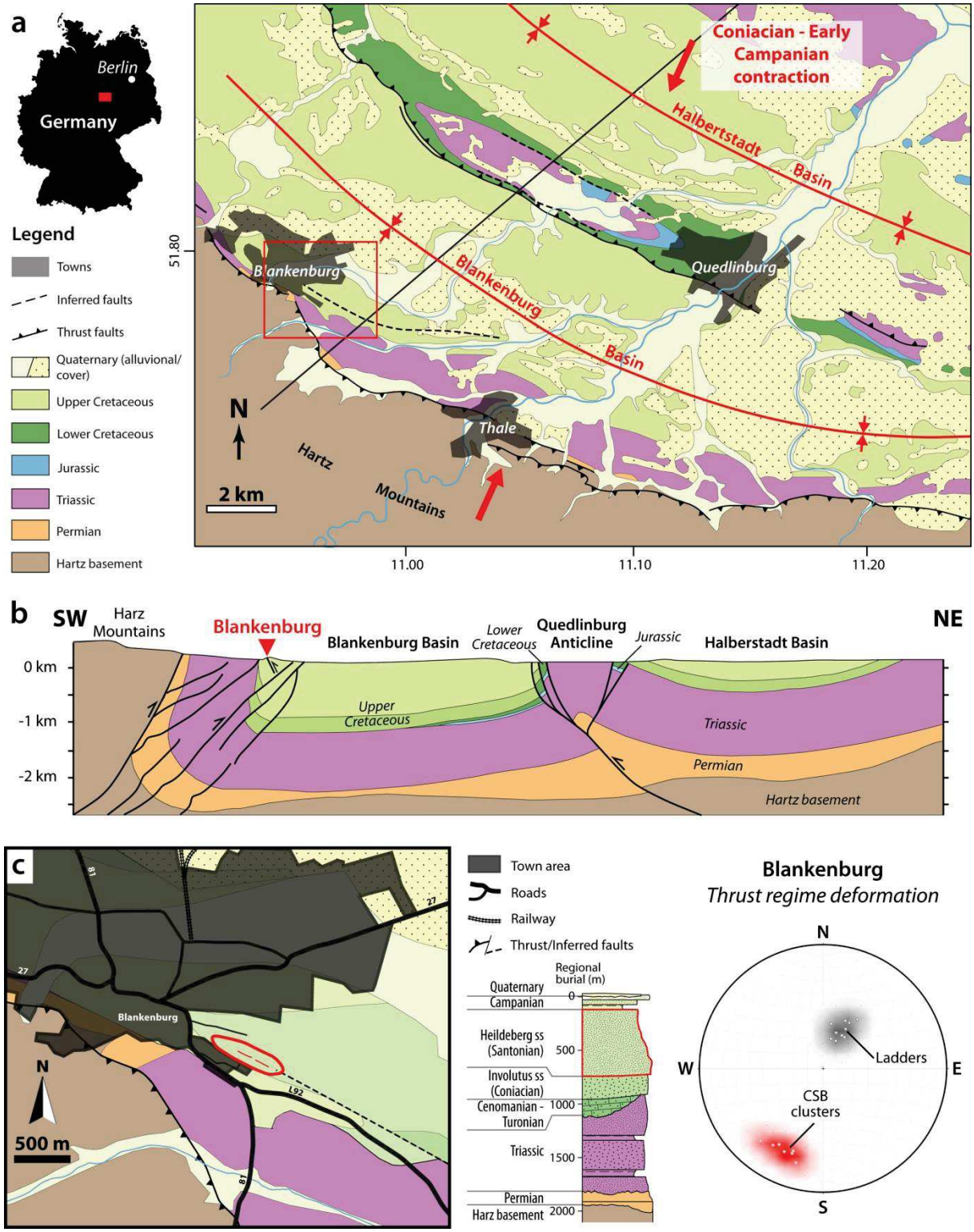

Figure 38. (a) Structural map of the Blankenburg region (Germany) (modified from Klimczak and Schultz, 2013), displaying the major faults and the orientation of the main tectonic episode. The straight line corresponds to the regional cross section intercepting the neighborhood of Blankenburg. (b) Regional cross section intercepting the neighborhood of Blankenburg (modified from Klimczak and Schultz, 2013). (c) Localization of the study site (outcrop) of Blankenburg, localization of the sandstone formation at the outcrop in the sedimentary column (red contour), and pole projection of the thrust kinematics deformation structures at the outcrop in a lower hemisphere equal area stereographic diagram.

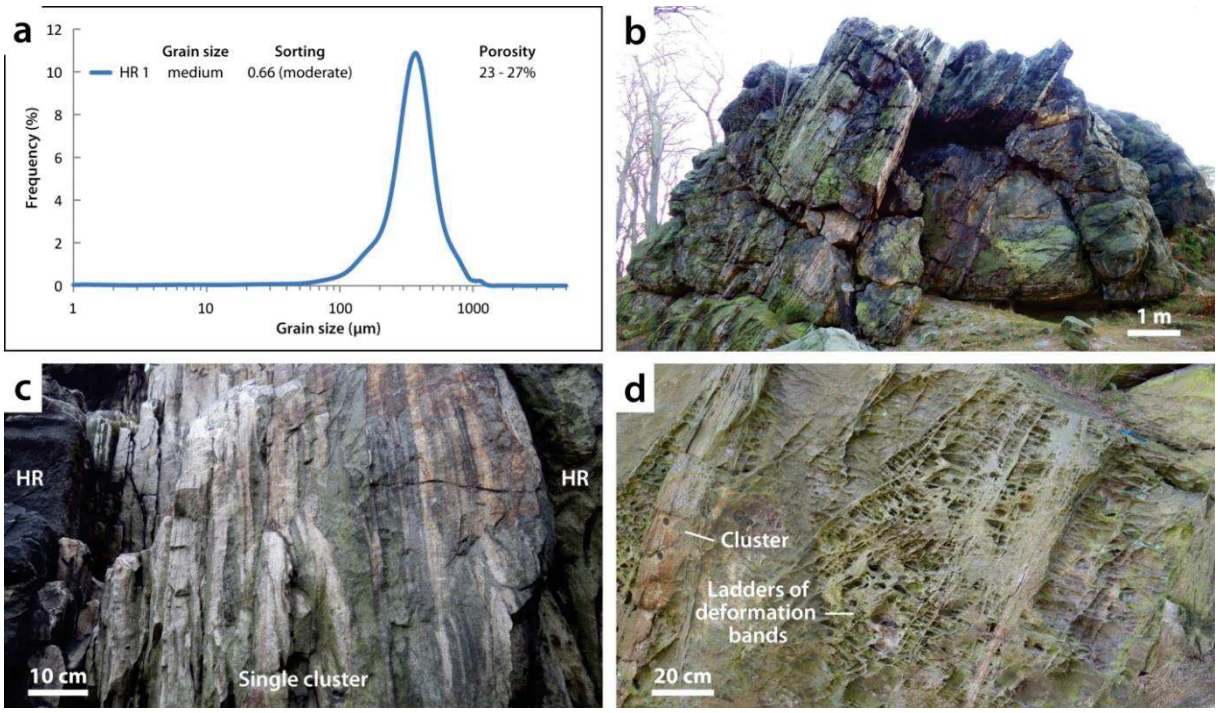

Figure 39. (a) Presentation of the host rock grain population in the De Cros quarry (Bédoin site). (b)The multi-cluster deformation at the Blankenburg site seen in the plane of shear . (c) Morphology of a single cluster, when all clusters are gathered. (d) Pervasive deformation bands between the clusters display ladder geometries.

The rift in the Moray Firth is an arm of the major North Sea rift system, open in two phases, during Triassic and Late Jurassic NNW-SSE extensions. It was reactivated with a transtensive component, potentially in Paleocene Eocene linked to the NE Atlantic rifting (Frostick, 1988; Roberts et al., 1990; Underhill, 1991; Edwards, 1993). The system of horst and graben induced by this rifting (represented in Figure 40b) is clearly imaged by the many seismic studies in the Firth because of petroleum prospects.

The study site outcrop is situated on the foreshore between the villages of Burghead and Cummingston, and spreads on a strip of barren rock nearly 1 km long and about 50 m in width. The outcrop is made of the Permo-Triassic Hopeman aeolian sandstone. The sandstone sequence is locally about 60 m thick (Glennie and Buller, 1983; Quinn, 2005). The host rock is made of a medium sandstone (Figure 41a) made of 92% of quartz and 8% of feldspar; little cementation is present around the quartz grains and at the grain contacts. The residual porosity ranges from 22 to 26%. The local bedding is difficult to assess due to the lack of marker but we estimated it dipping between 5 and 15° towards the North. The major Lossiemouth fault marks out the western limit of the study site and runs along about a few tens of meters to the South of the outcrop. The deformation at the outcrop exclusively consists of a conjugate set of normal kinematics clusters composed of CSB (Figure 41b), oriented N080-100 60° S and N and sometimes branching into several smaller clusters (Figure 41c). Individual CSB of similar orientation are also present. In the absence of marker, the displacements are rarely observable but one major cluster display a displacement of nearly 3 m (Figure 41b). The cataclastic deformation occurred when the Hopeman formation was buried at a depth of 500 m (Roberts et al., 1990; Underhill, 1991; Edwards, 1993; Quinn, 2005; Al-Hinai et al., 2008). The maximum burial depth of the Hopman Sandstone is estimated between 1.5 and 2.4 km.

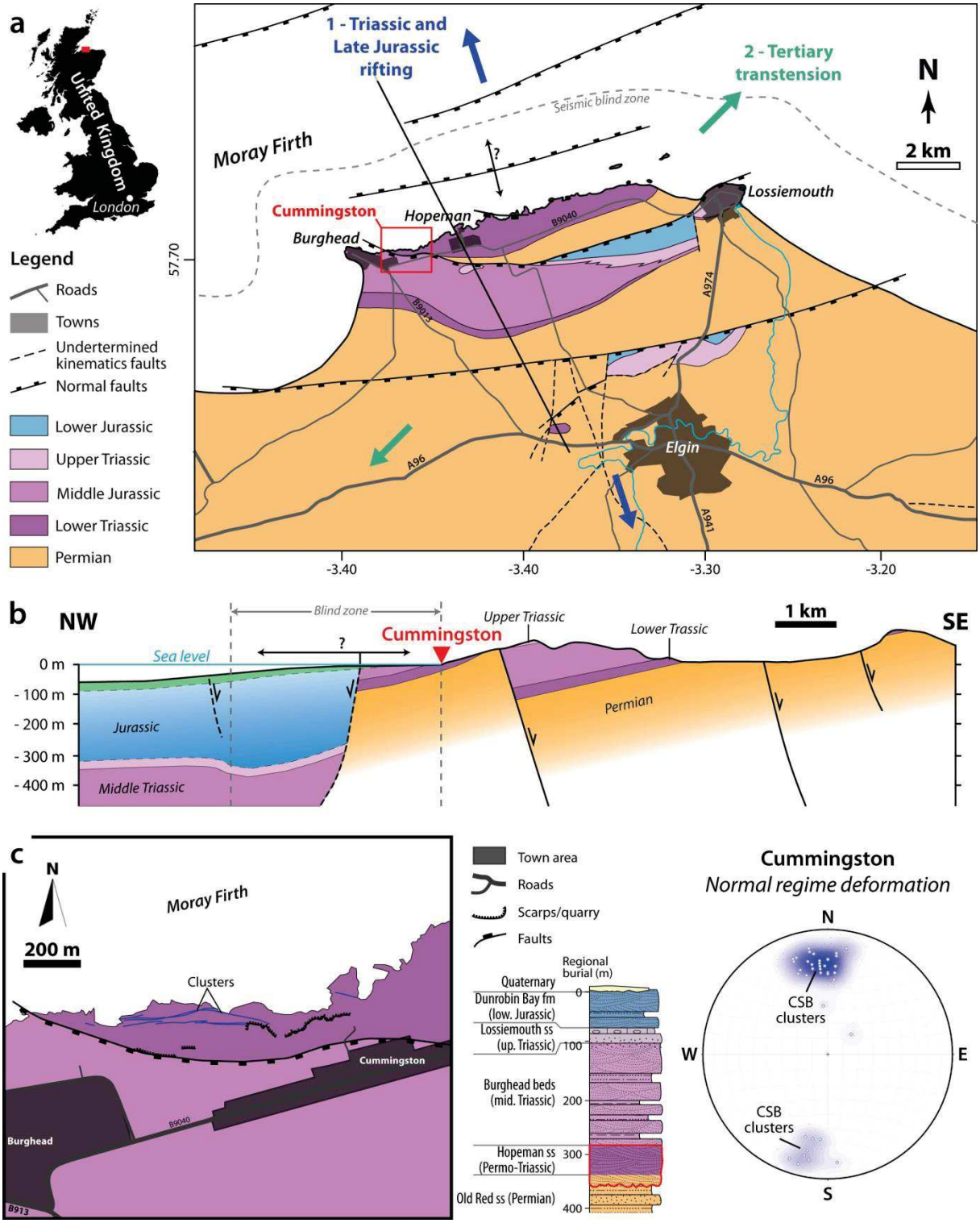

Figure 40. (a) Structural map of the Cummingston site region (UK) (modified from Berridge et al., 1969), displaying the major faults and the orientation of the main tectonic episode. The straight line corresponds to the regional cross section intercepting the neighborhood of the site. (b) Regional estimated cross section intercepting the neighborhood of the study site (modified from Quinn, 2005). (c) Localization of the study site (outcrop) of Cummingston, localization of the sandstone formation at the outcrop in the sedimentary column (red contour), and pole projection of the normal kinematics deformation structures at the outcrop in a lower hemisphere equal area stereographic diagram.

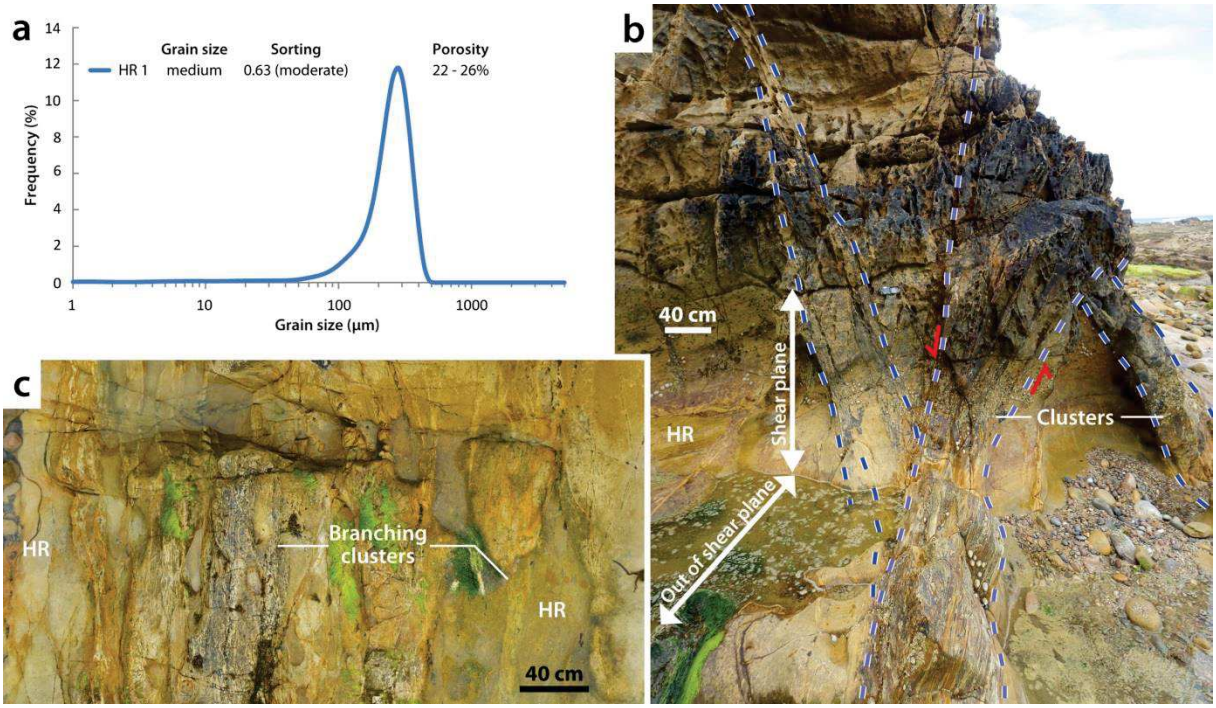

Figure 41. (a) Presentation of the host rock grain population at the outcrop of Cummingston. (b) Typical set of conjugate deformation band clusters at the site. Here the latest cluster cross-cuts the older cluster with a displacement of nearly 3 m. (c) Example of branching clusters seen out of the shear plane.

As in the case of Boncavaï, the site of Cummingston represents another suitable example with clusters formed in normal Andersonian regime at a relative shallow burial depth. In the case of Cummingston, the large outcrop allows observing a network of clusters over nearly 1 km in length and 60 in width. Besides, the displacement of one of the cluster is measurable.

2.1.6. Goblin Valley

The site of Goblin Valley locates in the San Rafael Desert, South of the San Rafael Swell, about 20 km North of the town of Hanksville in Utah (USA) (Figure 42a). The region was affected by two main tectonic events (Figure 42a and b): the NW-SE Laramide Orogeny from the End of the Cretaceous to early Eocene at the origin of the San Rafael Swell, and a SW-NE Oligocene extension associated with the Basin and Range tectonics (Rigby and Beus, 1987; Schultz and Fossen, 2002; Johansen and Fossen, 2008; Doelling et al., 2015).

The study site spreads out over a four-kilometer square area at the North of the Goblin Valley state park and exposes middle Jurassic entrada formation of total thickness ranging from 60 to 140 m (Figure 42c). The Entrada formation is made of aeolian and foreshore very fine to medium sandstones, oxidized silts (Figure 43a) and also includes thin layers of clays. The sandstones are uncemented. They are composed of 62 to 81% of quartz, 8 to 14% of feldspar, 4 to 25% of oxide-bearing oolites, and up to 1% of pure oxide. Their residual porosities range from 6% where the oolites are the most abundant, to 33 % where the oolites are least. The bedding of the formation dips about 5° towards the SE. At the site, the deformation is exclusively of normal kinematics (Figure 42c), with conjugate individual CSB and CSB clusters (Figure 43b) oriented N110-130 75°SW and NE. We note that the clusters are sometimes faulted, which implies that one or several through-going slip-

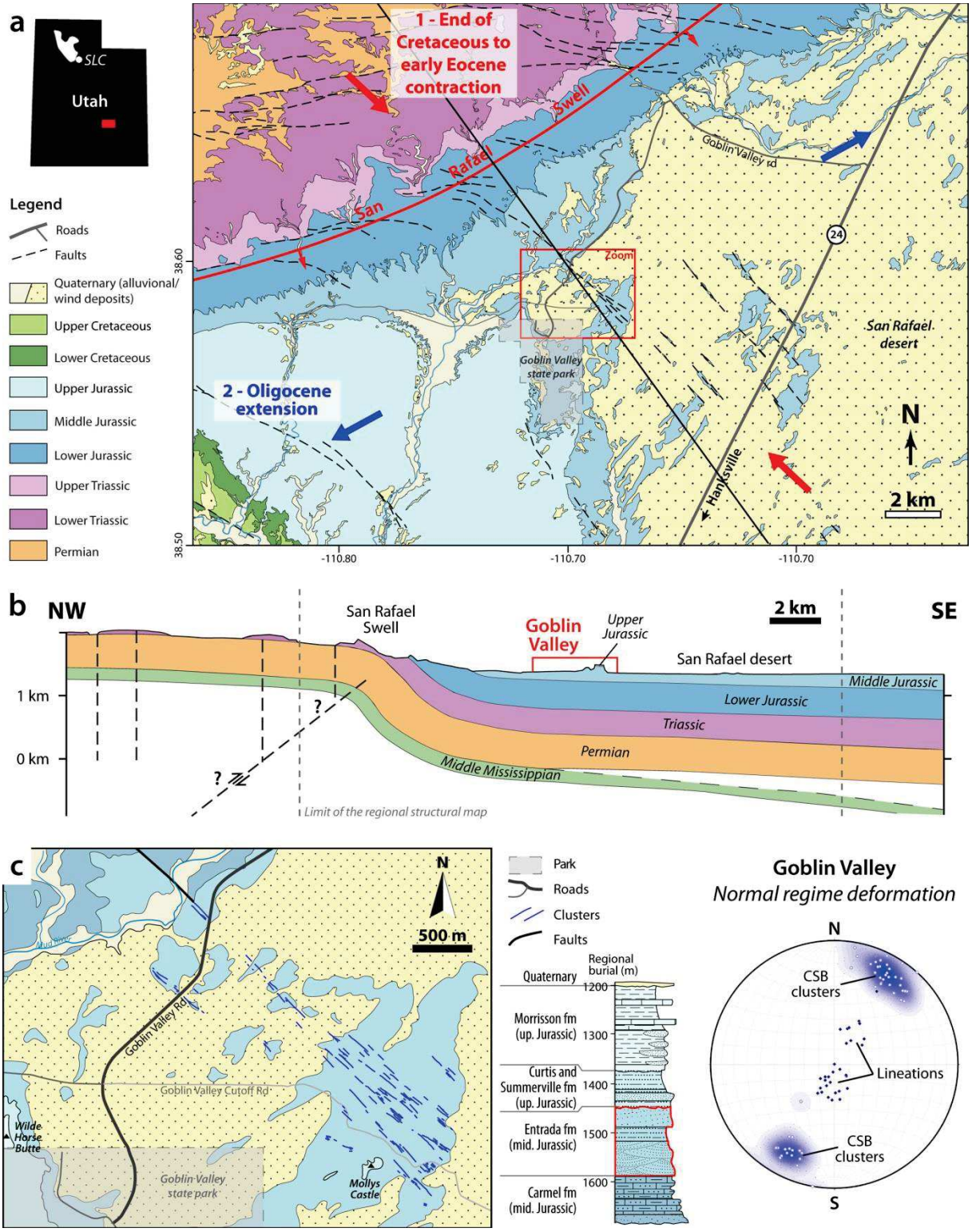

Figure 42. (a) Structural map of the Goblin Valley region (Utah) (modified from Doelling et al., 2015), displaying the major faults and the orientation of the main tectonic events. The straight line corresponds to the regional cross section intercepting the study site. (b) Regional cross section intercepting the site of Goblin Valley (modified from Doelling et al., 2015). (c) Localization of the study site of Goblin Valley, localization of the sandstone formation at the outcrop in the sedimentary column (red contour), and pole projection of the normal kinematics deformation structures at the outcrop in a lower hemisphere equal area stereographic diagram.

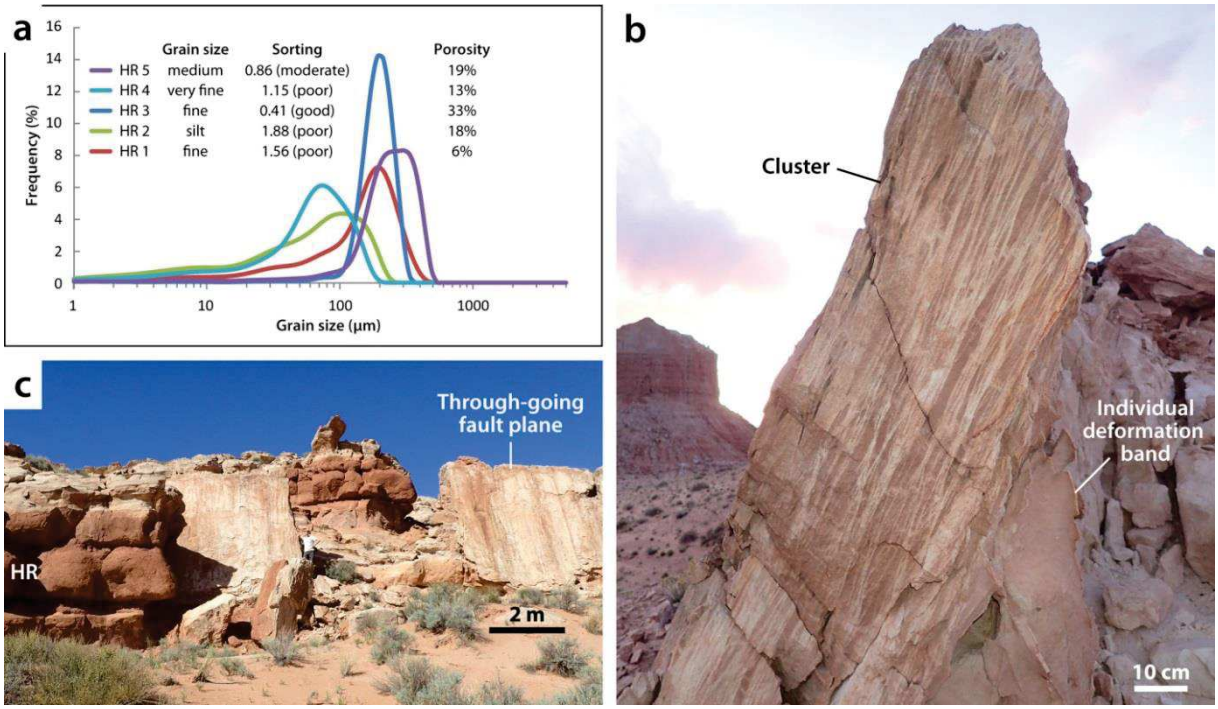

Figure 43. (a) Presentation of the host rock grain populations at the exposures of Goblin Valley. (b) Typical deformation band cluster at the site. A few individual deformation bands are visible on the right. (c) Faulted cluster (comprising a though-going slip-surface). In this case, suitable markers allow assessing a displacement of 7 m on this faulted cluster.

surface(s) developed in their thickness (Figure 43c). The deformation occurred when the Entrada formation was buried between 1100 to 2000 m deep (Johansen and Fossen, 2008; Doelling, 2015)

The choice of the site of Goblin Valley was obvious in that it offers a cropping out area of several hundreds of m^2 and displays a variety of sandstones with diverse lithologies, in terms of mineralogy, grain size, porosity (cf.Table 1). Hence, it was very convenient to follow the vertical (in plane) evolution of the cluster morphology as a function of the lithology. Goblin Valley is a fair example where an extended network of clusters formed in normal stress regime, at a burial depth equal or higher than 900 m. Besides, the displacements of faulted clusters are visible in several occasions.

2.1.7. Buckskin Gulch

The site of Buckskin Gulch locates at the southern border of Utah (USA), 50 kilometers East of Kanab, on the eastern limb of the NNE-SSW Kaibab anticline (namely, the Eastern Kaibab monocline) (Figure 44a). The region was affected by a Pre-Cambrian extension responsible for the probable formation of a NNE-SSW normal fault. This fault would then have been reactivated in transpression with a thrust and, in some parts, a dextral strike-slip component during the late Cretaceous Laramid Orogeny (Mollema and Antonellini, 1996; Tindall and Davis, 1999; Schultz, 2011; Brandenburg et al., 2012). This later tectonic event is at the origin of the Kaibab anticline (Figure 44b).

The study site is situated to the East of this major fault, in the Lower Jurassic Navajo sandstones of thickness ranging from 250 to 500 m (Fossen et al., 2011; Doelling and Willis, 2006; Doelling, 2008). The Navajo sandstone, in the studied interval, consists of fine (bimodal) laminated

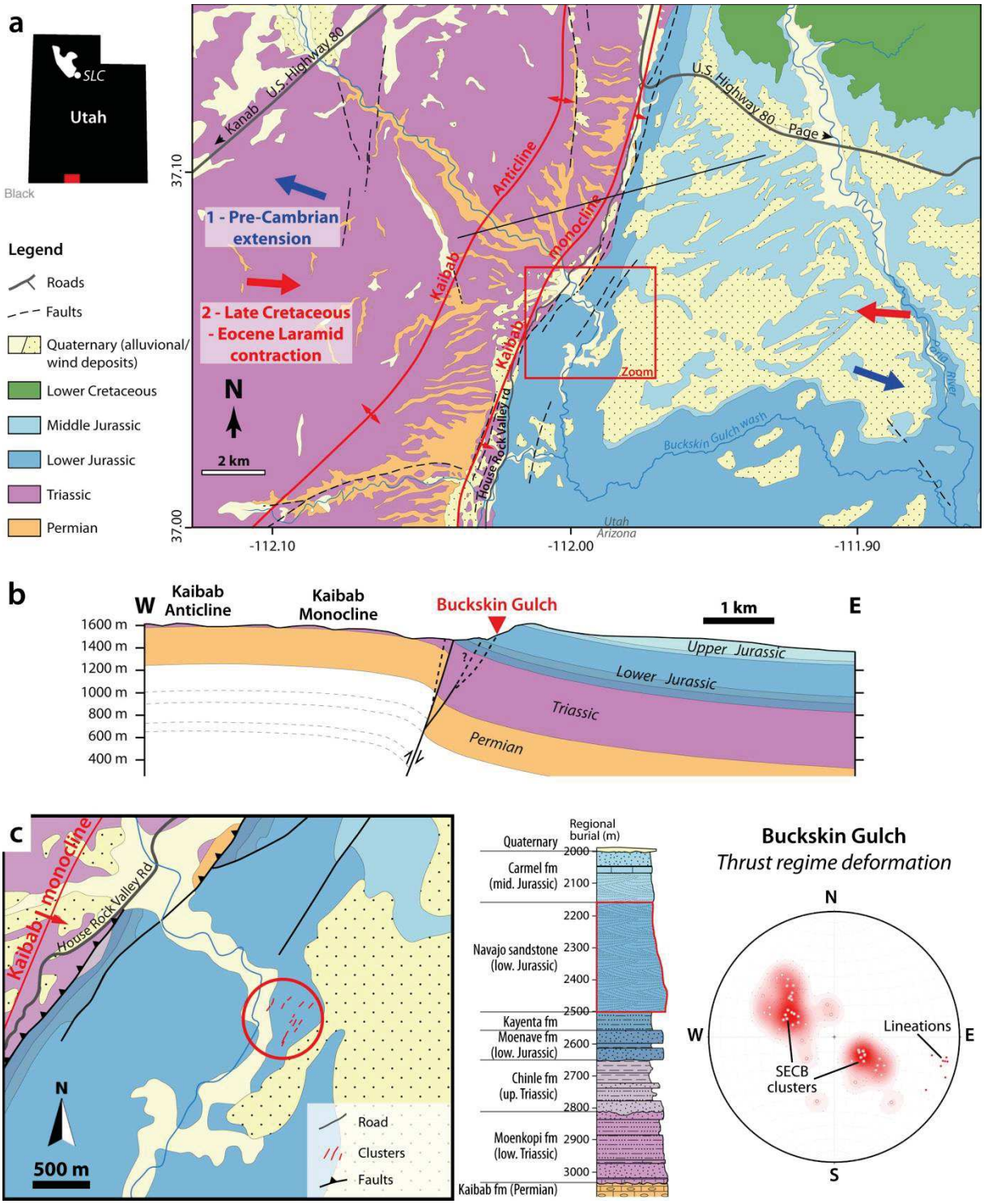

Figure 44. (a) Structural map of the Buckskin Gulch region (Utah) (modified from Doelling and Willis, 2006; Doelling, 2008), displaying the major faults and the orientation of the main tectonic events. The straight line corresponds to the regional cross section intercepting the study site. (b) Regional cross section intercepting the site of Buckskin Gulch (combined and modified from Doelling and Willis, 2006; Doelling, 2008). (c) Localization of the study site of Buckskin Gulch, localization of the sandstone formation at the outcrop in the sedimentary column (red contour), and pole projection of the normal kinematics deformation structures at the outcrop in a lower hemisphere equal area stereographic diagram.

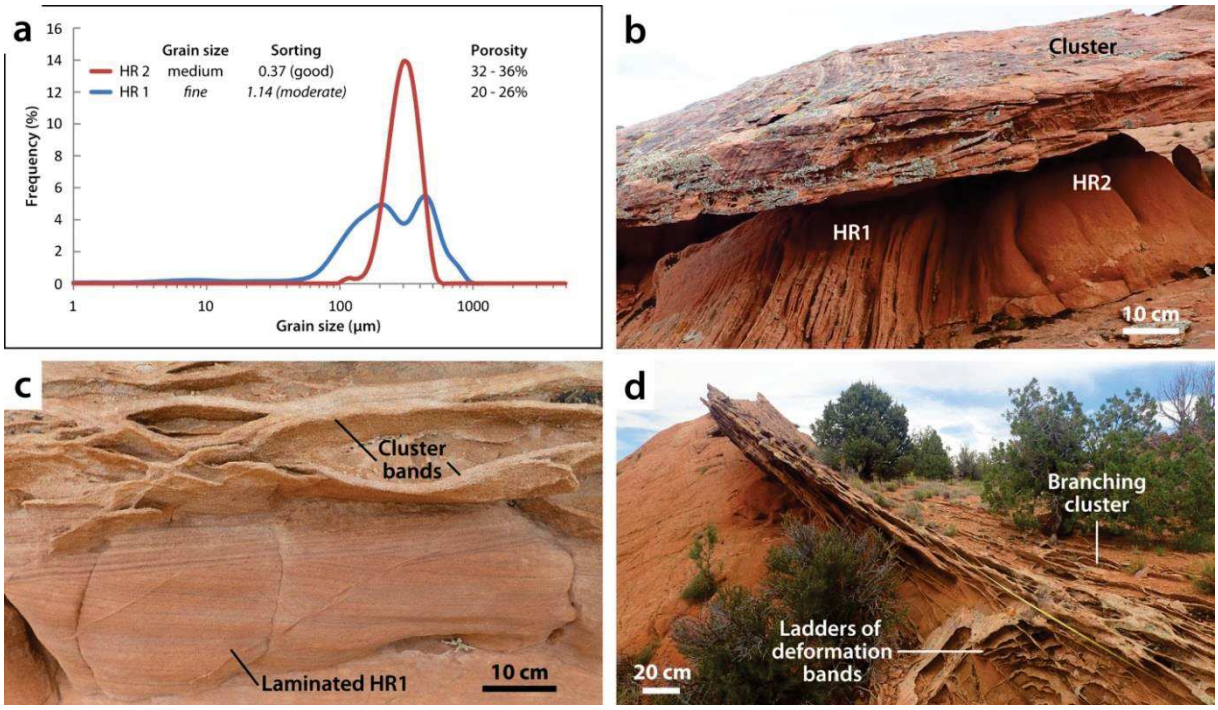

Figure 45. (a) Presentation of the host rock grain populations at the Buckskin Gulch outcrop. (b) The two laminated and homogenous host rocks topped by a cluster. The laminae are visible in the cluster thickness and form suitable markers to assess the small displacement induced by each deformation band. (c) The laminated host rock at the edge of a cluster formed in the homogeneous medium sandstone host rock. (d) Cluster branching off in several individual deformation bands. Conjugate deformation bands forms ladder geometry.

sandstones (Figure 45a, b and c) and medium homogenous sandstone (Figure 45a and b). The sandstone is made of 87 to 91% of quartz, 9 to 12% of feldspars and includes a fraction of oxides. The

porosity ranges from 20 to 36%. No significant cementation is observed. The bedding of the formation at the site is about N170 15°E. The deformation at Buckskin Gulch is exclusively of thrust kinematics. All the clusters (Figure 45b and d) and most of the individual deformation bands form conjugate sets oriented N020-030 25° SE and NW (Figure 44c), and consist of SECB. Some individual bands are oriented N100 90° (not reported of the stereogram of Figure 44c). The burial depth at the time of deformation at Buckskin Gulch is poorly constrained; based on a stratigraphic analysis from the combined geological maps of Doelling and Willis (2006) and Doelling, (2008) it could range from 900 and 2600 m.

The choice of the site was made because Buckskin Gulch is the only site we know deformed in contractional tectonic, not directly above a map-scale fault and where the cataclastic deformation forms clusters. Furthermore, the site seems appropriate for a precise study since the area comprising the deformation crops out over several hundreds of meters square.

Table 1. Summary of the geological and structural context of deposition and deformation of the sandstone formations at the studied sites. We also provide the lithological properties of the different host rocks (HR) studied.

Sites		Boncavaï (Provence)	St Michel (Provence)	Bédoin (Provence)	Blankenburg (Germany)	Cummingston (Scotland)	Goblin Valley (Utah)	Buckskin Gulch (Utah)
Formation name		/	/	/	Heidelberg sandstone	Hopemann sandstone	Entrada formation	Navajo formation
Time of deposition		Turonian	Turonian	Cenomanian	Cretaceous: Coniacian - Santonian	Permo-Triassic	Middle Jurassic	Lower Jurassic
Depositional environment		Deltaic bars	Deltaic	Deltaic and Aeolian	Deltaic (shallow marine)	Aeolian with some fluvial horizons	Interlayered shoreface, tidal & aeolian	Aeolian
Pattern		Low angle cross-laminated (severeal-cm- to m-thick)	Homogeneous	Homogeneous	Homogeneous, well sorted	Large-scale perturbated cross-laminations	Homogeneous & cross-laminated	Homogeneous & cross-laminated
Thickness (m)		>10 Max 150	>6 Max 150	>30	400-600	200-400	63-135	250-500
Max. burial depth (m)		100-300	500	800	800	?	2000	2600
Diagenesis in the formation host rocks		No cements & no pressure-solution	No cements & no pressure-solution	No cements & no pressure-solution	Pressure-solution; synchronous with post-deformation cementation	Post-deformation cements	No cements; no pressure-solution; where a significant amount of oolites are present, they are compacted	Low pressure-solution; little cements
Additional Comments				Ground water environment (silcretes, levels of goethite/hematite oxidation)			Thin bedding of oxidized siltstone to very fine sandstone at the bottom of the formation	Homogeneous sandstone and thin laminations tend to be the more oxidized
Mineralogy ±5 (%)	HR1	Qtz: 92 Fld: 8 Clay : <1	Qtz: 78 Fld: 22	Qtz: 99 Fld: <1	Qtz: 93 Fld: 7	Qtz: 92 Fld: 8	Qtz: 62 Fld: 13 Oolite: 25 Ox: 1	Qtz: 88 Fld: 12 Ox: <1
	HR2	Qtz: 91 Fld: 9	Qtz: 84 Fld: 16				Qtz: 80 Fld: 11 Ox: <1 others: <9	Qtz: 91 Fld: 9 Ox: <1
	HR3	Qtz: 88 Fld: 12					Qtz: 81 Fld: 14 Oolite: 4	
	HR4						Qtz: 74 Fld: 20 Ox: 1.5 others: <5	
	HR5						Qtz: 66 Fld: 8 Oolite: 24 Ox: 1	
Pre-deformation porosity ±4 (%)	HR1	42	37	37	25	24	6	23
	HR2	41	40				18	34
	HR3	31					33	
	HR4						13	
	HR5						19	
Modal grain size (µm)	HR1	200	420	300	370	290	200	200, 450
	HR2	380	920				100	300
	HR3	400, 750					200	
	HR4						70	
	HR5						220-300	
Sorting 0-0.35: very good 0.35-0.5: good 0.5-1.0: moderate 1.0-2.0: poor 2.0-4.0: very poor	HR1	0.80	1.26	0.57	0.66	0.63	1.56	*1.14*
	HR2	0.83	0.77				1.88	0.37
	HR3	*0.71*					0.41	
	HR4						1.15	
	HR5						0.86	
Time of deformation of the studied clusters		Middle Oligocene to Early Miocene	Paleocene to Early Oligocene	Paleocene to Early Oligocene	Coniacian to Early Campanian	Triassic to Late Jurassic	Oligocene	Late Cretaceous
Tectonic loading		Extensional	Contractional	Contractional	Contractional	Extensional	Extensional	Contractional
Andersonian stress regime		Normal	Strike-slip	Strike-slip	Thrust	Normal	Normal	Thrust
Burial at deformation (m)		100-300	0-200	0-200	0-800	100-400	1100-2000	900-2600

2.2. Analysis of the juxtaposition of the mechanical processes of deformation in sandstone-dominated formations.

As introduced, sandstones are classical reservoirs for aquifer, oil and gas resources. These reservoirs are rarely constituted of pure sandstone and commonly include other materials in the sedimentary column, such as silts, clays or less porous and more cohesive materials such as limestone or cemented siliciclastic sediments. Hence, because of these lithological variations, we consider the potential reservoirs as sandstone-dominated formations. In this context, it is essential to differentiate the diversity of mechanical processes in stake in the deformation of sandstone-dominated formation. In particular, we hypothesize that the lithological contrasts could play a role in the process of faulting in sandstone. We thereby set a global framework to the study of clusters, which are deformed by cataclasis, in comparison of other mechanisms.

In this section, after a brief summary of the most common mechanisms of deformation observed in sandstone-dominated formation, including the cataclastic deformation, we study the problematic of the interaction and juxtaposition of different mechanical processes through time and space. Our study based on field analysis of three different faulted exposures and their fault core at two sites allows observing specific cases where the cataclastic deformation such as clusters can evolve to faulting. The studied examples evidence that the interactions between the different mechanisms of deformation are likely to influence fluid flow.

This section is in revision for a resubmission to the AAPG Bulletin for publication. The content presented in this section was subjected to a poster presentation entitled "*Juxtaposition of different fault rocks into fault cores in sandstone-dominated formations*" at the EGU conference (Vienna, 2017).

Juxtaposing multiple fault rocks into fault core

Sven Philit[1], Roger Soliva[2], Gregory Ballas[3], Alexandre Chemenda[4], Raymi Castilla[5]

[1] Géosciences Montpellier, UMR 5243, Université de Montpellier-CNRS, Place Eugène Bataillon, 34095 Montpellier Cedex 5, France, sven.philit@gm.univ-montp2.fr

[2] Géosciences Montpellier, UMR 5243, Université de Montpellier-CNRS, Place Eugène Bataillon, 34095 Montpellier Cedex 5, France, roger.soliva@gm.univ-montp2.fr

[3] Géosciences Marines, Institut Français de Recherche pour l'Exploitation de la Mer, Pointe du Diable, 29280 Plouzané, gregory.ballas@yahoo.fr

[4] Géoazur, Université Côte d'Azur, CNRS, OCA, IRD, Géoazur, 250 rue Albert Einstein, SophiaAntipolis, 06560 Valbonne, France, chem@geoazur.unice.fr

[5] R&D Frontier Exploration, TOTAL S.A., raymi.castilla@total.com

AKNOWLEDGMENTS

We wish to thank the Laboratory of Geosciences Montpellier, the Institut Universitaire de France and TOTAL E&P for their support in this work. We are also grateful to Doriane Delmas and Christophe Nevado for the laborious work they did by providing the numerous and quality thin sections necessary to this work. We thank Jean-Jacques Cornée for the detailed insight he gave us about the depositional environment of some studied rocks. Eventually we thank Randy Williams, John Solum and Sarah Eliott for their helpful advices in the building of the manuscript.

ABSTRACT

Due to their petrophysical implication for reservoir exploitation, many deformation mechanisms in sandstones are individually well known in the literature. Yet, the interplay between these mechanisms and the resulting complex fault core organization (juxtaposition of several fault rocks through time and space) is poorly described. Our field study examines two sites displaying a combination of three deformation mechanisms along normal faults in sandstone–dominated formations. At the first site, we show that a cluster of cataclastic deformation bands made in an initially poorly consolidated sandstone localize overprinting brecciation during a subsequent tectonic episode, after a significant diagenesis of the formation induced by burial. Hence, because the permeability of the clusters ranges between 6 x 10^0 and <5 x 10^{-1} mD and that the breccia is highly dilatant, we evidence that the fault behaved as a baffle for cross-fault fluid flow at early age of the formation, and as a drain after significant diagenetic evolution. At the second site, we show that the presence of clay and clay-rich silt layers as thin as 80 cm (31 in.) are responsible for the initiation of a major slip-surface (fault) in the underlying and overlying sandstone when the sandstone-dominated formation accommodates a displacement as small as 2 meters (7 ft.). The propagation of the fault prevents further cataclastic deformation and cluster development in these sandstones. This displacement juxtaposes clusters of cataclastic deformation bands and clay-rich gouges. Because

both fault rocks have low permeability, their spatial juxtaposition provides a continuous baffle for cross-fault fluid flow.

INTRODUCTION

Faults constitute the economic core of structural geology as they can constitute drains of barrier for fluids in the context of resource exploitation or storage, and because the diversity of their morphology and the petrophysical properties of the fault rocks are complex. Faults generally include one or multiple core zones composed of fault rocks including breccias, cataclasites or gouges (generally clays) as well as discrete slip-surface(s), accommodating most of shear displacement (Sibson, 1977; Caine et al., 1996). Fault cores are surrounded by damage zones containing fractures or deformation bands (e.g. Shultz and Fossen, 2008; Faulkner et al., 2010). In particular, sandstone-dominated formations, which are classical fluid reservoirs, comprise a variety of lithologies, each involving different mechanical processes of deformation and leading to a diversity of fault rocks (e.g. Knipe, 1997). These processes as a function of the lithology are individually well known and we recall here the most commons.

In porous sandstone units (Fig. 1a-c), the deformation materialize as cataclasis (also referred to as "cataclastic flow"). This process is characterized by an important decrease in grain size when grains are rearranged by rolling and splitting due to stress concentrations at the grain-grain contacts (Gallagher Jr et al., 1974; Aydin, 1978). In porous sandstones, the cataclastic deformation localizes as discrete bands within which, at the grain scale, fault rocks correspond to crush microbreccias and cataclasites (e.g. Aydin, 1978; Blenkinsop, 1991; Fossen et al, 2007). With evolving deformation and depending on several parameters such as the tectonic regime, bands can evolve to clusters of bands to fault, when a major slip-surface is formed (e.g. Aydin and Johnson, 1978; Ballas et al., 2014; Soliva et al., 2016). Most of the cataclastic structures have reduced porosity, with a permeability that can be reduced up to 6 orders of magnitude from that of the host rock in the most severe cases (Antonellini and Aydin, 1994; Fossen and Bale., 2007; Ballas et al., 2015).

Deformation of brittle low-porosity rocks (Fig.1d-f) generally leads to brittle dilatant fracturing, producing breccias, and subsequent protocataclasite and cataclasite as rock comminution evolves with the increasing shear strain (e.g. Engelder et al., 1975; Sibson, 1977; Jébrak, 1997; Agosta et al. 2007; Olierook et al., 2014). In low-porosity sandstone (e.g. tightly cemented), brecciation with inhibited shear localization and associated with dilatancy is also possible (e.g. Zhu and Wong, 1997; Woodcock and Mort, 2008). We remark that although Zhu and Wong (1997) qualify of low-porosity sandstone the formations where the porosity is roughly below 5%, no clear study evidence a porosity threshold controlling the localization of deformation bands by cataclasis of the brecciation of the rock. The impact of brecciation on fluid flow is highly variable. Whereas the fractures in adjacent damage zones are dominantly described as increasing the permeability, the fault rocks can be permeable due to inter-clast connected porosity, or impermeable because of the presence of fine matrix depending on the degree of rock comminution (e.g. Agosta et al., 2007). Note that brecciation can be combined with physico-chemical processes such as pressure-solution and cementation (e.g. Jébrak, 1997; Gratier et al., 2011).

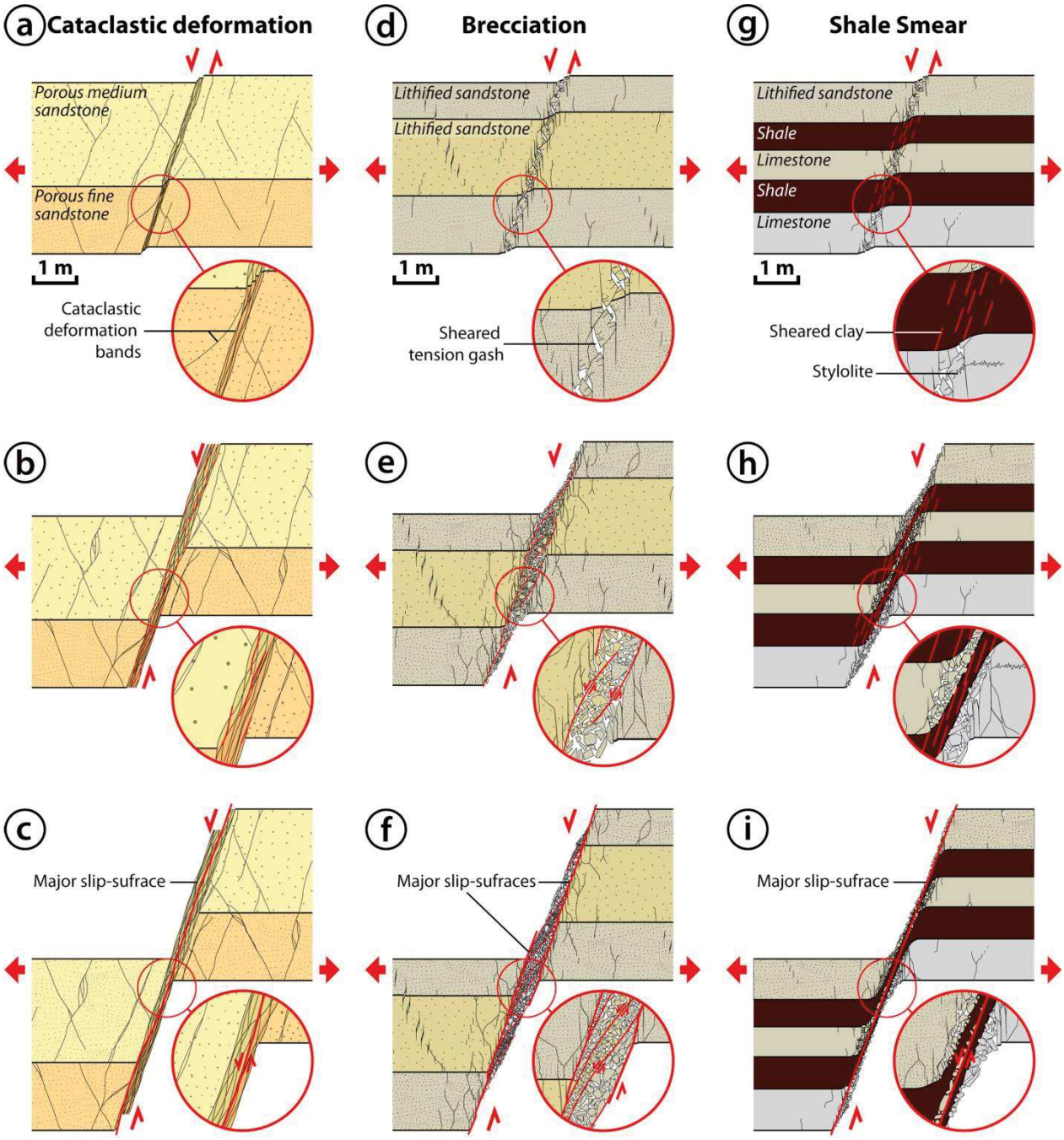

Figure 1. Synthetic schemes of the evolution of extensional deformation to faulting in different materials: (a)-(c) Cataclastic deformation in porous sandstone units; (d)-(f) Brecciation in lithified (e.g. compacted, cemented) sandstone units; (g)-(i) Shale smear in alternating shale and multiple lithified rock units..

Formations bearing poorly consolidated clay silt units (Fig. 1g-i) are likely to deform by smearing (Lindsay et al., 1993; Aydin and Eyal, 2002). The resulting fault rock consists of a "shale gouge". During smearing, the fault core deforms in a ductile manner and grows by entrainment from the footwall and hanging wall. Clay can also be formed within fault cores (authigenesis) by mineral reaction and microfabric changes during faulting (e.g. Vrolijk and van der Plujim, 1999; Solum et al., 2005, 2010; Hadizadeh et al., 2012). The efficiency of the process of smearing is governed by parameters such as the displacement, clay content, clay-layer thickness and spacing, clay composition, pressure (mean stress), consolidation and water saturation (e.g. Clausen and Gabrielsen,

2002; Schmatz et al., 2010). Fault cores composed of clays can be efficient transverse capillary seals when clay-rich cores are continuous and thick (e.g. Fulljames et al., 1997; Yielding et al., 1997; Rawling and Goodwin 2006; Childs et al., 2007).

To our knowledge, the influence of the overprinting of these different processes on the development of a single fault core in sandstone-dominated formations has rarely been described (e.g. Foxford et al., 1998; Davatzes and Aydin, 2005; Rawling and Goodwin, 2006). Yet, the study of this influence is essential to understand the complex fault core organizations resulting from the deformation and the contrasting petrophysical properties induced by the juxtaposed fault rocks.

In this study, we focus on two sites in sandstone-dominated formations of varying lithologies (variable porosity and cementation degree, presence of interbedded clays) and displaying different juxtaposed fault rocks: cluster of cataclastic deformation bands, breccia and clay-rich gouge. These formations and fault rocks are characterized based on macro- and microstructural observations, petrophysical analysis, and quantification of the deformation. The objectives of this work are to: (1) give new insight and characterize the spatio-temporal interplay between the diverse mechanical processes of deformation in sandstone-dominated formations, and (2) evaluate the influence of the juxtaposing fault rocks resulting from these processes on fluid flow during the evolution of the fault.

GEOLOGICAL SETTINGS

The Clashach Cove site is located Northeast of the town of Hopeman, between the towns of Cummingston (to the West) and Lossiemouth (to the East) on the Moray coast in Scotland (Fig. 2a, b). The outcrop exposes quartz-rich sandstones from the Hopeman formation of Permo-Triassic age, buried up to 1.2 to 2.4 km (0.7 to 1.5 mi.) (Quinn, 2005; Al-Hinai et al., 2008). The Hopeman sandstones are of aeolian origin (Shotton, 1956; Glennie and Buller, 1983); the dune foresets are clearly visible in the hanging wall at the site. The sandstone is cross-cut by a 20 to 50 m (66 to 164 ft.) displacement normal fault (Quinn, 2005) (Fig. 2c). Similarly to the many normal seismic-scale structures (≥20 m displacement) in the Moray Firth, the Clashach fault is believed to have been formed during the pre-Jurassic and Late Jurassic rifting and possibly reactivated with an oblique component during the Paleocene-Eocene Northeast Atlantic rifting (e.g. Roberts et al., 1990; Underhill, 1991; Al-Hinai et al., 2008). The rifting also caused the uplift of the Scottish Highlands. The fault juxtaposes grey cohesive sandstone topped by low-cohesive yellow sandstone in the footwall to the North, and the same yellow sandstone in the hanging wall to the South.

The site of Goblin Valley is located in the San Rafael Desert, Northeast of the Goblin Valley State Park, about 20 km (12.4 mi.) North of the town of Hanksville, Utah (Fig. 3a, b). The site displays the Middle Jurassic Entrada formation of total thickness ranging from 76 to 160 m (249 to 525 ft.), buried up to 2.2 km (1.4 mi.) (Rigby and Beus, 1987; Schultz and Fossen, 2002; Johansen and Fossen, 2008). The Entrada formation is made of tabular fine-to-coarse aeolian and foreshore sandstone, including thin layers of silt to clay, 10 to 30 cm (3.9 to 11.8 in.) thick each, at its base. The formation underwent extensional tectonics from the Oligocene linked to the Basin and Range extension. The possible burial at deformation ranges from 1100 to 2000 m (0.7 to 1.2 mi.) (Doelling et al., 2015). At the site of Goblin Valley, the outcrop displays tens of clusters of cataclastic deformation bands oriented NW-SE (Fig. 3c). Even if often hidden by Quaternary wind deposits, these clusters are observed in an area more than 3 km (1.9 mi.) long and 800 m (0.5 mi.) wide (Fig.

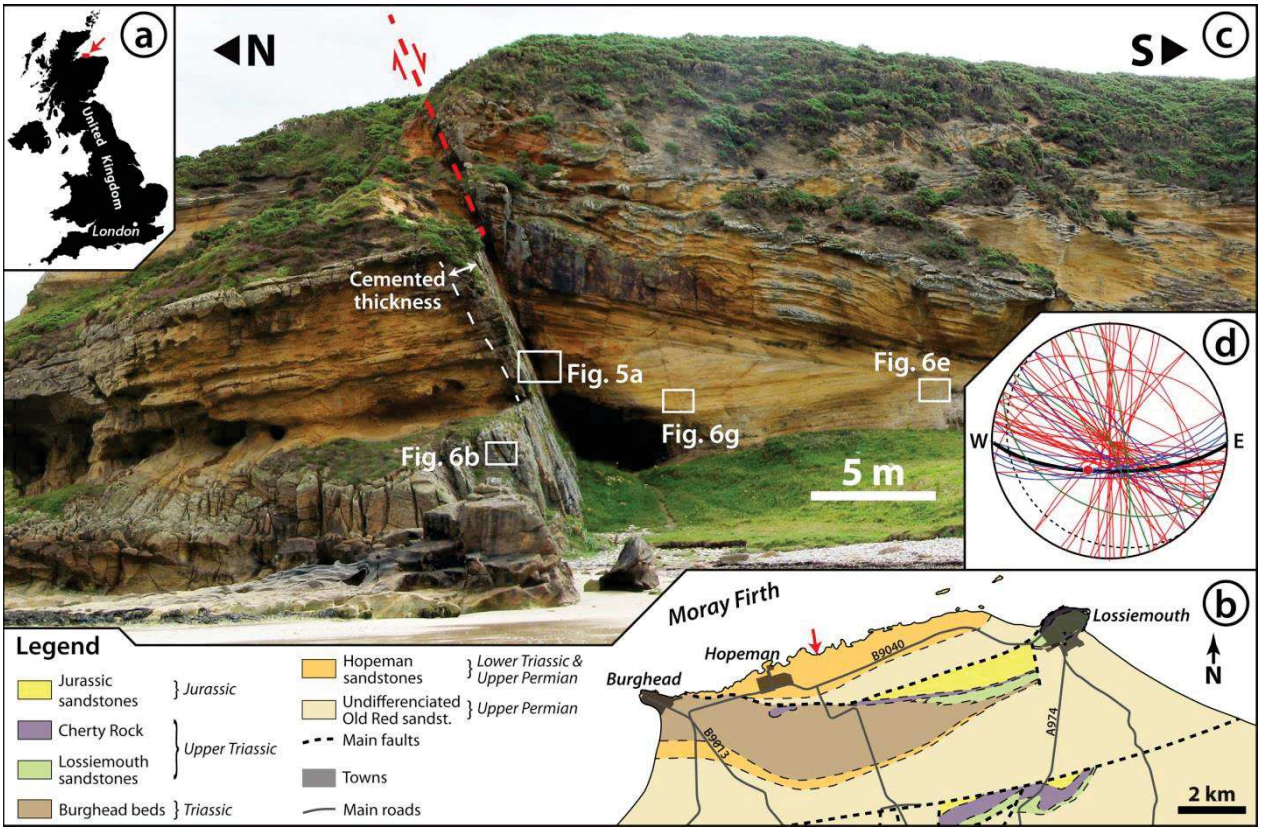

Figure 2. (a) Location of the study site at the scale of the United Kingdom: Moray coast, Scotland. (b) Geological map of the Clashach Cove site (red arrow) in the Lossiemouth-Burghead area, along the Moray coast, modified after Edwards (1993). (c) General view of the faulted Hopeman sandstone at Clashach Cove. (d) Stereographic projection (lower hemisphere) of the deformation structures around the fault at the study site. Blue lines represent the cataclastic structures (CSB and CSB cluster); red lines represent joints; green lines represent dilation bands; the thick black line represents the Clashach fault, with both cataclastic and dilatant compartments; the dashed line represents the average stratigraphy at the site.

3b). We chose two exposures within this area to analyze the cataclastic and smear deformation processes. The first exposure (Fig. 3d) consists of a fault of 6 m (19.7 ft.) displacement into a sandstone-dominated unit including thin layers of silts at the base of the Entrada formation. The second exposure (Fig. 3e) consists of a fault of 2.10 m (6.9 ft.) displacement into a sandstone-dominated formation including a 40 cm (15.7 in.) thick clay layer.

METHODOLOGY

At the Clashach Cove site, to analyze the mechanical processes and to identify the relative chronology of the deformation and characterize its diagenetic setting, we studied the macroscopic deformation and the rock microstructure as well as the properties of the host material (grain size distribution, sorting, porosity and permeability). To do so, microscopic observations using cold Cathodoluminescence (CL) and Scanning Electron Microscopy in Backscattered Electrons (SEM-BSE) were conducted. Because the rock is cemented, the analysis of the grain size distribution was done through CL image measurements using the Fiji software. The sorting (*s*) of the host rocks was obtained from the grain size distribution data, using the formula of the Inclusive Graphic Standard Deviation (Folk and Ward, 1957). Note that spectrums of the grain size distribution and the mineralogical composition of the studied sandstones of the two sites are available in a supplementary

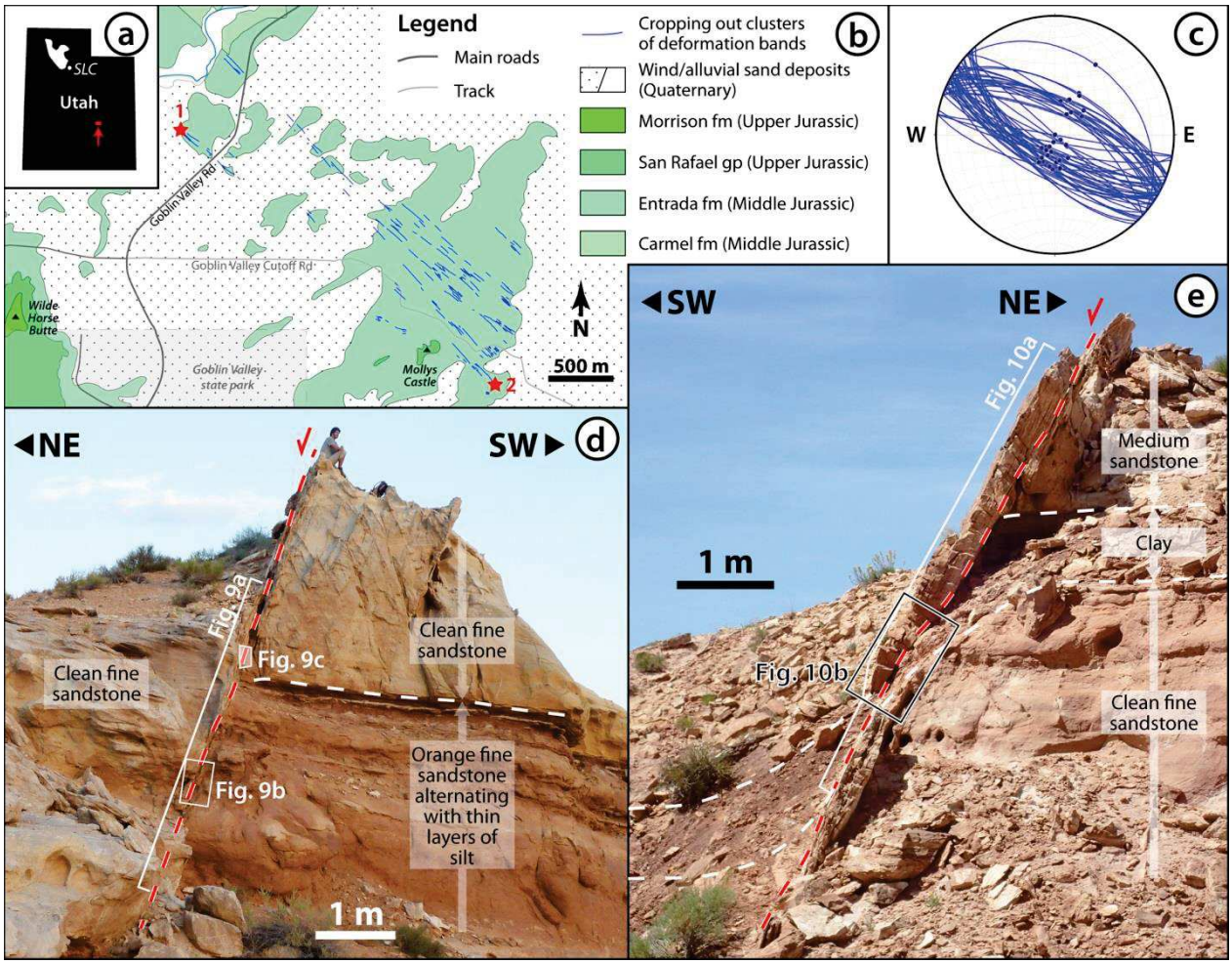

Figure 3. (a) Location of the study site at the scale of Utah (USA): San Rafael desert. (b) Geological map of the site (modified after Doelling et al., 2015) and the two study exposures (red stars), Northeast of the Goblin Valley state park. (c) Stereographic projection (lower hemisphere) of the clusters of deformation bands at the study site. (d) and (e) View of the 6-m fault of exposure 1 and of the 2.1-m fault of exposure 2, respectively.

document. The porosity was obtained from 2D SEM and CL image analysis. The porosity of the host rocks is given as the intergranular volume (*IGV*, see Ehrenberg, 1989) where any potential post-deformation cementation is subtracted; the porosity of the deformation structures is given as residual porosity (ϕ), accounting for potential post-deformation cementation. We measured the permeability (k) at the surface of the host rocks and deformation structures with a portable air-permeameter device (TinyPerm II NER). The resolution of the device does not permit the quantification of permeability higher than 5 x 10^4 mD. For each type of rock surface, the permeability has been measured at least twice for measurements exceeding 10 min, or more for shorter measurements. This time limitation constrains the minimal permeability quantification to approximately 5 x 10^{-1} mD.

At Goblin Valley, we focused on (1) a macroscopic description of the juxtaposition of different types of rocks in the fault cores, (2) a petrophysical and mineralogical analysis of the pristine juxtaposed host rocks and layers properties, (3) a detailed measurement of the amount of cataclastic deformation in the fault cores, and (4) permeability measurements using the similar methodology as described before. The analysis of the grain size distribution was done through Coulter LS 13320 laboratory laser diffraction on selected samples using for four types of host rocks in the Entrada

formation; grain size of other host rocks was estimated in the field using the grain size reference chart of the American Stratigraphic Company. The porosity and permeability were measured with the same methodology as described before. We particularly focused on the analysis of clusters of cataclastic deformation bands. In the absence of accurate definition of "cluster" in the literature, we propose to combine three typical characteristics described in the literature (a minimum band number, a typical frequency and band thickness) to define it. A "*cluster of deformation bands*" (or "*cluster*") corresponds to the grouping of two or more bands (as used in Fossen and Bale, 2007) and accounting for at least 10% of bands thickness (based on a usual frequency of 20-30 bands per meter reported by Johansen and Fossen, 2008 and a typical band thickness of about 4 mm (0.16 in.) as shown in Wibberley et al., 2007). "*Clusters*" may or may not include a slip-surface. Such clusters typically have centimeter to several decimeter- width (e.g. Wibberley et al., 2007) and accommodate centimeter to several decimeter displacements (e.g. Antonellini and Aydin, 1994). From this definition, we introduce the *deformation ratio*, which corresponds to the *cumulated band thickness* divided by the *cluster thickness* to evaluate the deformation within clusters. Although we ignore the inter-band deformation (which is small but not zero - Lanatà, 2014), we believe that the deformation ratio permits a better quantification of deformation than simply counting the number of bands in the deformation structures as it is traditionally done (e.g. Soliva et al., 2016 and references within). The band thickness and the inter-band distance were measured with a ruler (millimeter precision).

OBSERVATIONS

The lithological and petrophysical parameters of the host rocks and the fault rocks presented in this section are summarized in Fig. A1 and Table A1 in the supplementary material; the permeabilities and their error bars are reported in the Fig. 4.

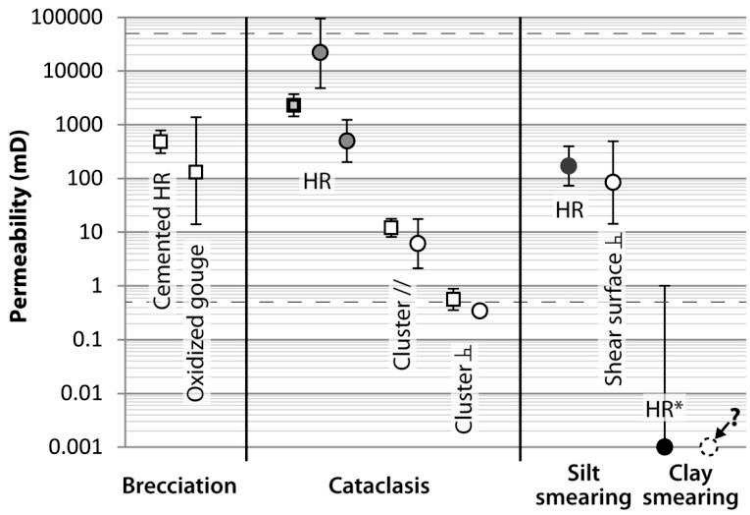

Figure 4. Graph summarizing the permeability of the host rocks and their resulting fault rocks as a function of the deformation mechanisms. The square data concern the measurements at the Clashach Cove site; the circle data concerns the measurements at the Goblin Valley site. The grey scale and thickness of the frame lines reflects the grain-size of the host rocks: light-grey and thick line: medium-grain sandstone; medium-grey and regular line: fine-grain sandstone; dark-grey without line: silt; black: clay.

Cataclastic deformation and breccias at Clashach Cove

Architecture of the Clashach Fault

The fault of 20 to 50 m (66 to 164 ft.) of displacement is oriented N090° 70°S on average (thick black line in Fig. 2d) and has a normal kinematic. The fault zone is made of different materials from the footwall to the hanging wall (Fig. 5a, b). One to two zones of tabular cataclastic deformation showing slickensides are located along the footwall side. An oxide-cemented crush breccia juxtaposes parallel to the cataclastic deformation on the hanging wall side of the fault.

The zones of cataclastic deformation are composed of cataclastic deformation bands forming a 5 to 20 cm (2.0 to 7.9 in.) wide cluster (Fig. 5c, d). CL microscopy reveals that clasts within the cluster are sealed by quartz cements up to 40 µm (15.7 x 10^{-4} in.) in thickness (also see Farrell et al., 2014). The cementation is observed along the cluster and in the host sandstone at its vicinity, even in the yellow generally-porous low-cohesion sandstone unit (grey thickness along the fault plane in upper part of the footwall, Fig. 2c). Although the CL imaging method does not allow measuring precisely the IGV (limit of resolution), we estimate it to range from 5 to 8% in the most cataclased part of the cluster. In-situ TinyPerm permeability along-strike of the cluster plane is 12 mD. The hanging wall edge of the cluster marks the limit with the footwall edge of the breccia compartment and is made of one to two low-permeability slickensides clogged with oxides (Fig. 5c, d).

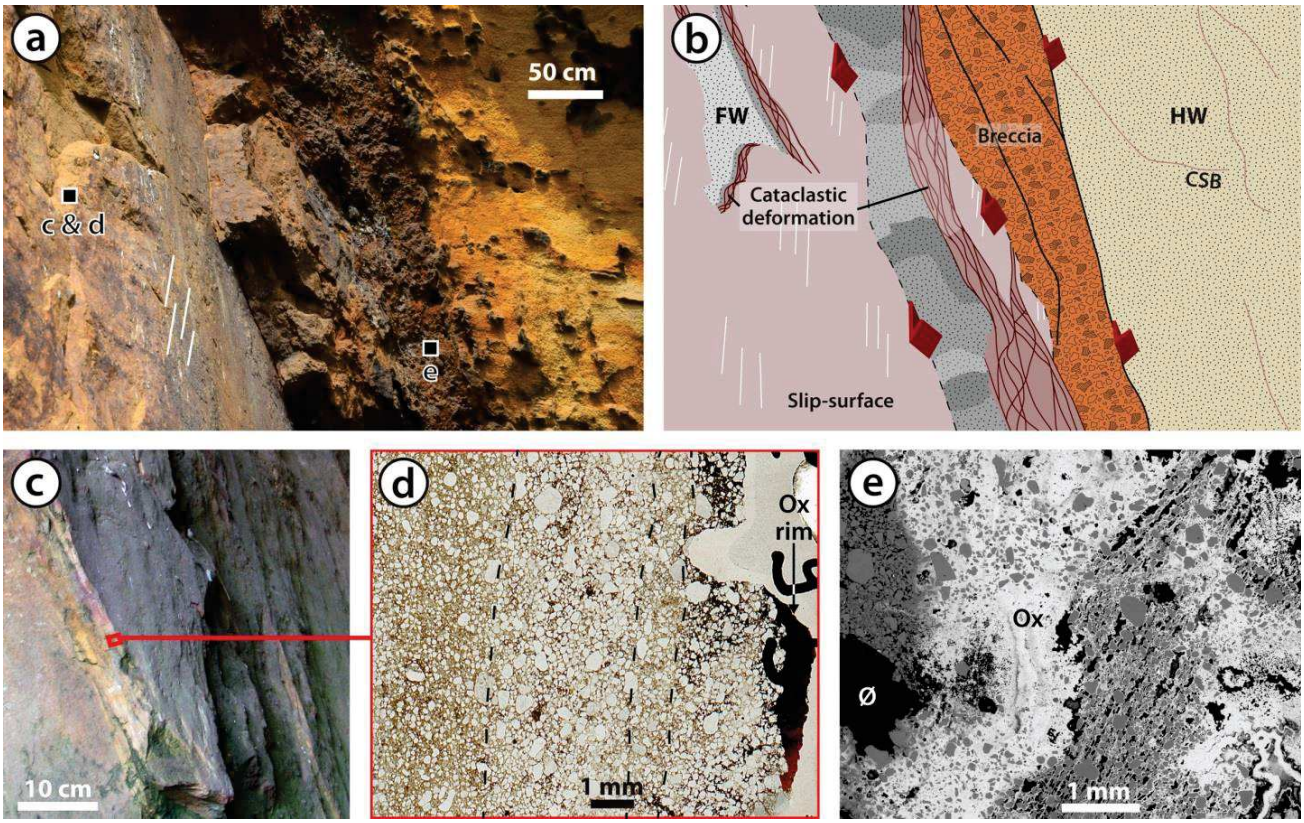

Figure 5. Macro- and microstructural observations at the Clashach Cove site. (a) The Clashach fault zone, with the footwall on the left and the hanging wall on the right. (b) Structural interpretation of (a). (c) Cluster on the footwall edge of the fault; note the slickenside of the fault. (d) Zoom in the cluster section (plane-polarized light); the dashed line indicates the orientation of the deformation bands in the cluster. (e) Oxidized breccia comprising a huge amount of cataclastic material (Scanning Electron Microscope imaged in Backscattered Electron (SEM-BSE); the quartz and feldspar grains appear in grey, the oxides wrapping the grains appear white, the porosity appears black.

Slickenlines are clearly visible and pitch 71°W on average on the fault plane (red spot in Fig. 2d). Permeabilities normal to the slickenside of the fault are as low as 0.56 mD.

The breccia compartment consists of a 50 cm (20 in.) wide crush breccia. The content of the breccia (Fig. 5e) is made of a volume of over 40% of iron oxide coatings, 13% of quartz clasts, 10% of feldspars and other weak minerals overlain by oxide buttering, the rest of the volume being porous (35%). Among the clasts, we recognize in particular fragments of cataclastic sandstone material and loose sand grains. Thin sections SEM analysis shows that porosity ranges between 30 and 40% (also

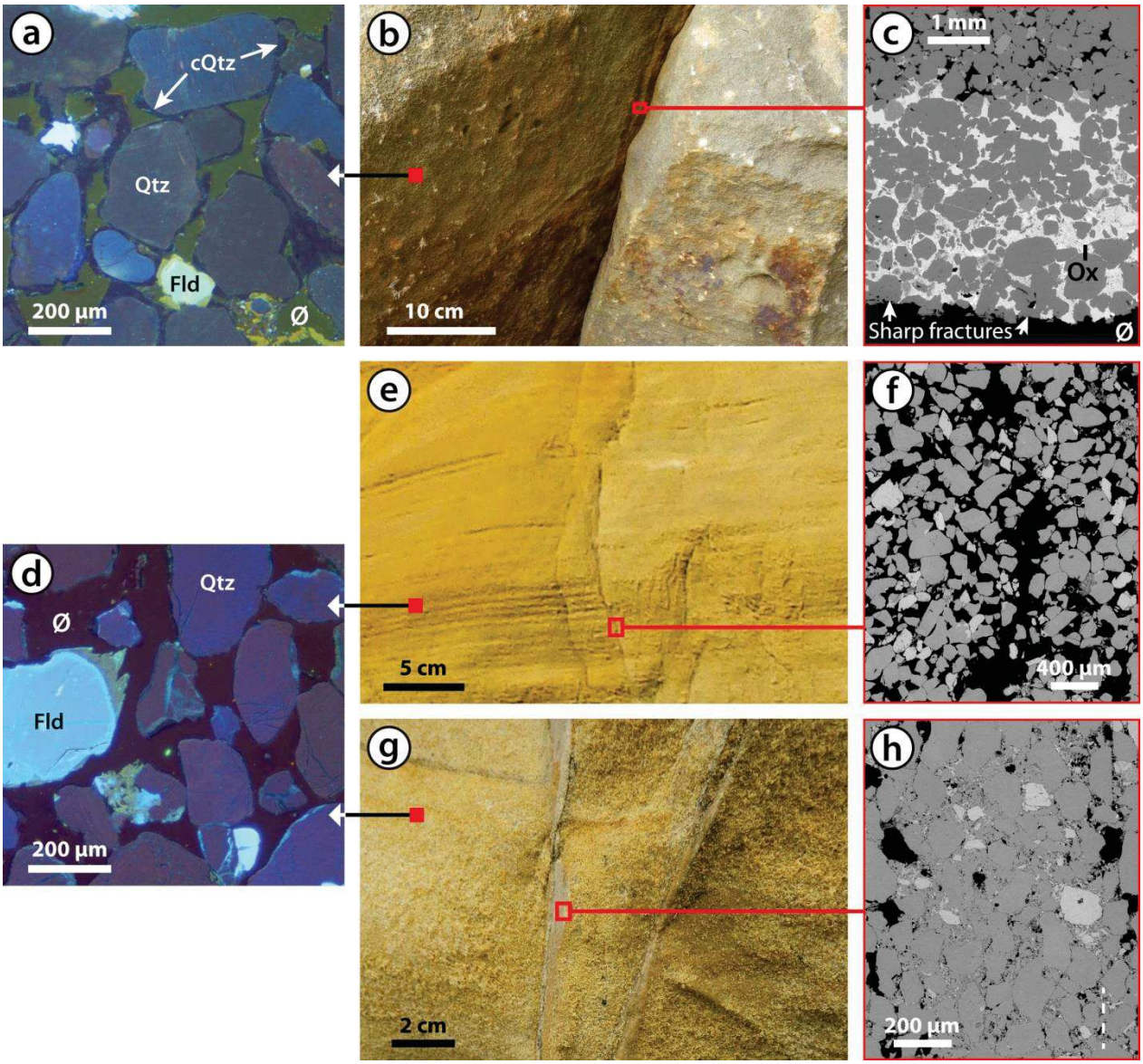

Figure 6. (a) The host rock in the cemented part of the lower footwall (in Cathodoluminescence (CL)). The detrital quartz (Qtz) appear in bluish hues and the quartz cement rims in dark-blue (cQtz - arrows); note the presence of detrital feldspar grains, light-blue (Fld), surrounded by carbonate cement (yellow-green) at the bottom of the image. (b) Oxidized joint in the cemented footwall as visible at the outcrop and (c) as visible in SEM-BSE (the quartz grains appear grey, the feldspar grains appear light grey, the oxides appears light-grey to white and the porosity appears black); arrows point at the sharp limit of the sandstone with the joint. (d) Host rock in the uncemented hanging wall (in CL); (e) Dilation band as visible at the outcrop and (f) as visible in SEM-BSE. (g) Compactional shear bands (CSB) in the hanging wall. (h) Zoom in the CSB section (in SEM-BSE); amongst the cataclastic material, we note the presence of a majority of quartz clasts (gray), a lesser feldspars content (light- grey), and some carbonate cement clasts (also light-grey) amongst the finest cataclastic material; the dashed line at the bottom right corner indicates the orientation of the deformation band.

see Table A1 in the supplementary material). Yet, these values probably overestimate the porosity because some holes visible in Fig.5e were probably quartz grains plucked during the thin section preparation. The plane delimiting the breccia and the yellow sandstone of the hanging wall is sharp but no slickenside is observed.

Deformation structures in the surrounding exposure

The sandstone in the lower part of the footwall (greyish color) consists of a cemented and highly cohesive medium-grain sandstone (moderately sorted, $IGV = 33\%$; $k = 4.8 \times 10^2$ mD; see also Table A1, supplementary material). Microscope observation shows pervasive presence of quartz cement rims around the detrital quartz grains within the formation (Fig. 6a). The quartz cements around detrital quartz grains can reach 20 µm (7.9×10^{-4} in.) in thickness and efficiently bond the grains to each other. The feldspars are often rimed with carbonate cements. A few oxides are also present in minor quantities. The main deformation structures in the cemented part of the footwall are joints (Fig. 6b). Their surfaces are characterized by a sharp fracture of the grains (Fig. 6c) and are clogged with iron oxides penetrating 4 to 5 mm (0.16 to 0.20 in.) into the rock. Permeabilities along-strike of the joints are beyond the device measurement limit, corresponding to permeabilities greater than 5×10^4 mD. Scarce compactional shear bands (CSB) are observed in the cemented sands.

The yellow formation in the hanging wall (and in the upper part of the footwall) is a poorly cemented and very low-cohesive medium-grain sublitharenite sandstone (moderately sorted, $\phi = 31$ %; $k = 2.3 \times 10^3$ mD; see also Table A1, supplementary material). Microscope observations show no or very thin quartz cement rims around the detrital grains (Fig. 6d) and a few carbonate cements around the feldspars grains, but no significant sealing connection is observed between the detrital grains. In some cases, very thin iron coatings are observed in plane polarized light around the detrital grains, giving the sandstone its pervasive yellow color. The deformation structures in the hanging wall of the fault are scarce and include dilation bands and compactional shear bands (CSB). Dilation bands (Fig. 6e) display slightly negative relief at the exposure without visible offset. They are microscopically characterized by irregular 1 to 2 mm (0.04 to 0.08 in.) thick high-porosity (55 ± 2%) tabular zones, where the grains are disaggregated and separated from each other without being significantly fractured (Fig. 6f). CSBs (Fig. 6g) are 5 to 10 mm (0.20 – 0.39 in.) thick with a positive relief and 5 to 20 cm (2.0 to 7.9 in.) of offset. Microscope observations show that these bands are composed of a large amount of cataclastic material (Fig. 6h) with significantly reduced porosity (8 ± 2%). The fraction of carbonate cement is observed completely crushed in the CSB.

The orientation of all the CSBs and dilatant deformation structures (joints and dilation bands) is shown in Fig. 2d. The strike of CSBs (thin blue lines in Fig. 2d) ranges between N075° and N170°, with 47% between N075° and N100°. The majority of them (73%) dips between 60° and 80°. A majority (55%) of the dilatant structures (joints as thin red lines and dilation bands as thin brown lines in Fig. 2d) strikes between N095° and N140° and a second significant proportion (19%) between N170° and N190°. 92% of the dilatant structures dips between 70° and 90°. Although the interactions between these deformation structures are rare, we noted that the dilatant structures cross-cut the CSBs in both the footwall and hanging wall. The distribution profile of the deformation structures is displayed in Fig. 7. The profile shows a trend with increasing intensity of deformation when nearing the fault; that trend is clear in the footwall and more subtle in the hanging wall. The

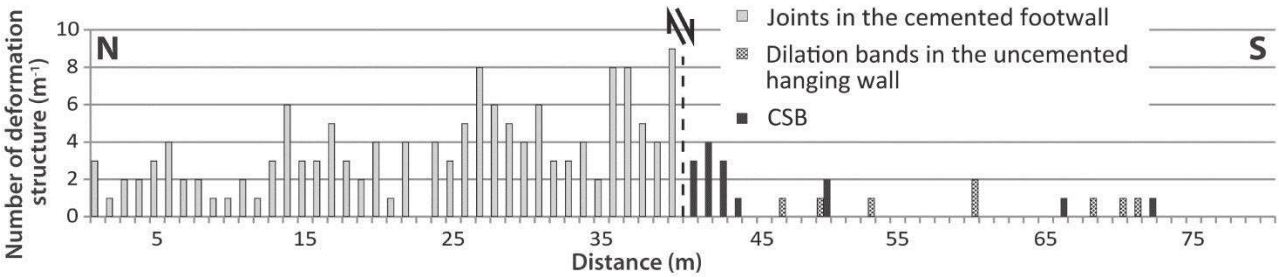

Figure 7. Deformation profile showing the number of deformation structures around the Clashach fault.

frequency of dilatant structures is higher in the footwall where they are in the form of joints in the grey-cemented sandstone layer, often reaching or exceeding six joints per meter when nearing the fault. In the hanging wall, where they are in the form of dilation bands in the yellow incohesive sandstone, they never exceed two dilation bands per meter.

Deformation band clusters and clay smear at Goblin Valley

Two exposures have been studied at Goblin Valley, (1) a normal fault zone juxtaposing porous sandstones and thin silt layers, and (2) a normal fault zone incorporating a clay layer within a porous sandstone formation into the fault core.

Exposure 1: Deformed sandstone including thin silt layers

The first exposure is located at the base of the Entrada group and displays a deformation structure of 6 m (19.7 ft.) displacement (Fig. 3d). At the outcrop, the base of the footwall is made of an orange fine sandstone (poorly sorted, IGV = 6%, k = 5 x 10^2 mD) (Fig. 8a) alternating with 5 to 20 cm (2.0 to 7.9 in.) thick layers of phyllosilicate-bearing silt (poorly sorted, IGV = 18%, k = 1.7 x 10^2 mD) (Fig. 8b). The top of the footwall and the whole hanging wall along the studied thickness of the outcrop is made of massive clean fine sandstone (well-sorted, IGV = 33%, k = 2.2 x 10^4 mD) (Fig. 8c). The reader is addressed to Table A1 in the supplementary material for more detail on the lithological data. The damage zone is about 5 m (16.4 ft.) large on both sides of the fault core. In the damage zone, the deformation is characterized by conjugated deformation bands in the clean sandstones (mean spacing of 11.1 cm – 4.37 in.), by small shear surfaces in the slits (mean spacing of 5.7 cm – 2.24 in.) and in the orange fine sandstone (mean spacing of 10.0 cm – 3.94 in.).

At the macroscopic scale, we observe a cluster of deformation bands where the clean fine sandstones are juxtaposed. The cumulated band thickness reaches 94 mm (3.70 in.) at the topmost end of the cluster (at 6 m, Fig. 9a) where the thickness of the cluster reaches 600 mm (23.6 in.) and forms the total thickness of the fault core. Both the cumulated band thickness and the cluster thickness decrease where the sandstone of the hanging wall juxtaposes against the first layers of silt (at 4.5 m, Fig. 9a) and further downwards. The cumulated band thickness and cluster thickness decreases from 50 mm (2.0 in.) and 320 mm (12.6 in.) respectively at 4.5 m (14.8 ft.), down to 15 mm (0.6 in.) and 50 mm (2.0 in.) respectively at 2.25 m (7.38 ft.). In that interval, a smeared clay-rich silt gouge juxtaposes against the CSB cluster, and both form the fault core material. The footwall side of the fault core includes a small thickness of lenses of deformed orange fine-grained sandstone (Fig. 9b). Downwards (from 2.25 m and lower, Fig. 9a), the cumulated band thickness decreases steadily to 4 mm (0.16 in.) (two bands) at 4 m (13.1 ft.) below the silt juxtaposition (at 0

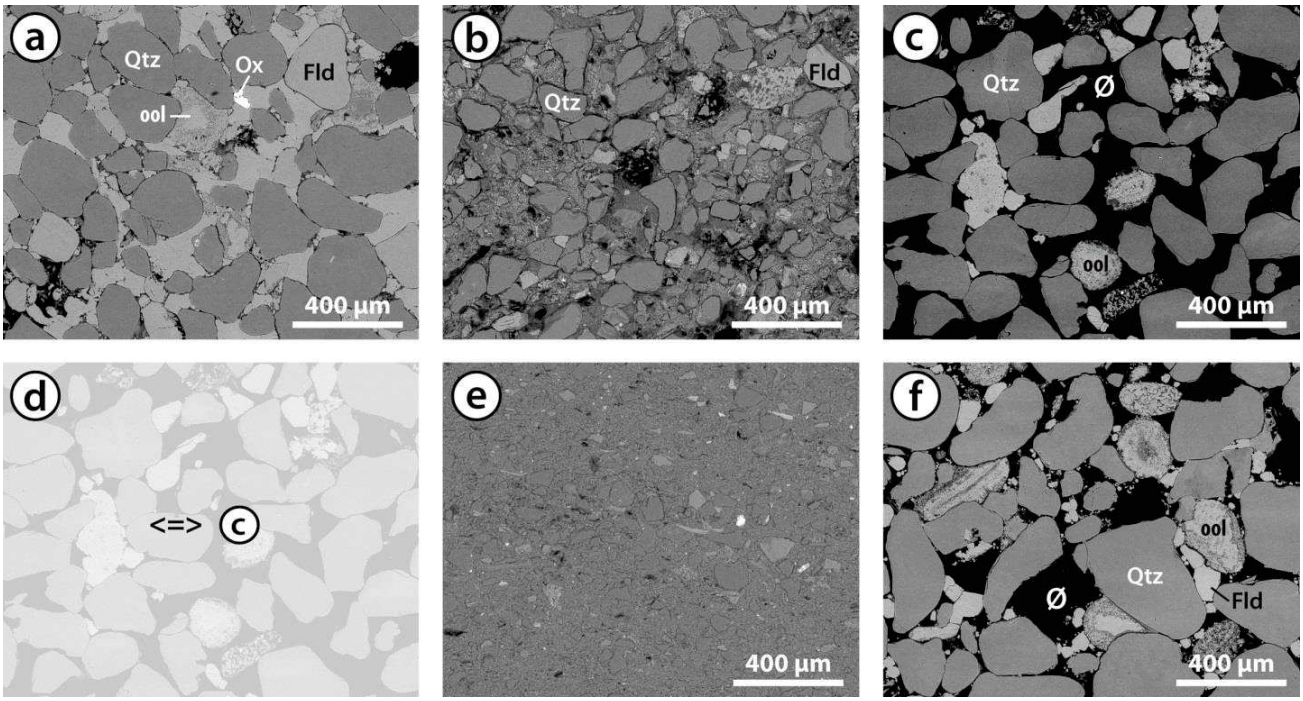

Figure 8. SEM-BSE imaging of the host rocks at Goblin Valley, at the exposure 1 (a)-(c), and at the exposure 2, (d)-(f). (a) Orange fine sandstone host rock. 25% of the rock is made of oxide-bearing oolites crushed between the stronger grains. (b) Silt layer host rock. The matrix is phyllosilicate-rich. (c) Clean fine sandstone host rock. (d) The clean fine sandstone host rock at the second exposure has not been sampled; however due to its similarity in macroscopic aspect, we assume it as equivalent to the clean fine sandstone at the first exposure. (e) Clay layer host rock. (f) Medium sandstone host rock. In each image, Qtz stands for quartz, Fld for feldspar, ool for oolite and Ox for oxide.

m, Fig. 9a); here the smear is almost nonexistent. Hence, the smear forms a fault rock along nearly 4 m (13.1 ft.) below the lowest silt layer, after which the fault core integrally disappears, leaving in contact the hanging wall and footwall along a slip surface. Below along the fault, the slip-surface marks out the footwall edge of the thin cataclastic deformation structure. Note also that from top to bottom of the exposure, a major through-going slip-surface (striated and flat, often smooth – Fig. 9c, d) is observed near the footwall edge of the CSB cluster. No significant mixing between the silt and the cluster is observed in the core zone.

Exposure 2: Deformed sandstone including a clay layer

The second exposure (Fig. 3b) is located in the Entrada group and displays a fault zone of 2.1 m (6.9 ft.) of displacement (Fig. 3e) allowing smearing of clay a in a continuous zone of clay gouge between two parallel and overlapping segments of CSB clusters. The cluster formed in clean fine sandstone at the base of the outcrop (considered as analog to the clean fine-grained sandstone described in the first exposure). The clean fine sandstone is overlain by a 80 cm (31.5 in.) thick clay layer, overlain by a medium sandstone (moderately sorted, ϕ = 19%). All lithological data are summarized in Table A1, in the supplementary material. Again, the damage zone is about 5 m (16.4 ft.) large on both sides of the fault core. In the damage zone, the deformation is characterized by conjugated deformation bands in the sandstones (mean spacing of 13.1 cm – 5.16 in.), by small shear surfaces in the clay (mean spacing of 3.1 cm – 1.22 in.).

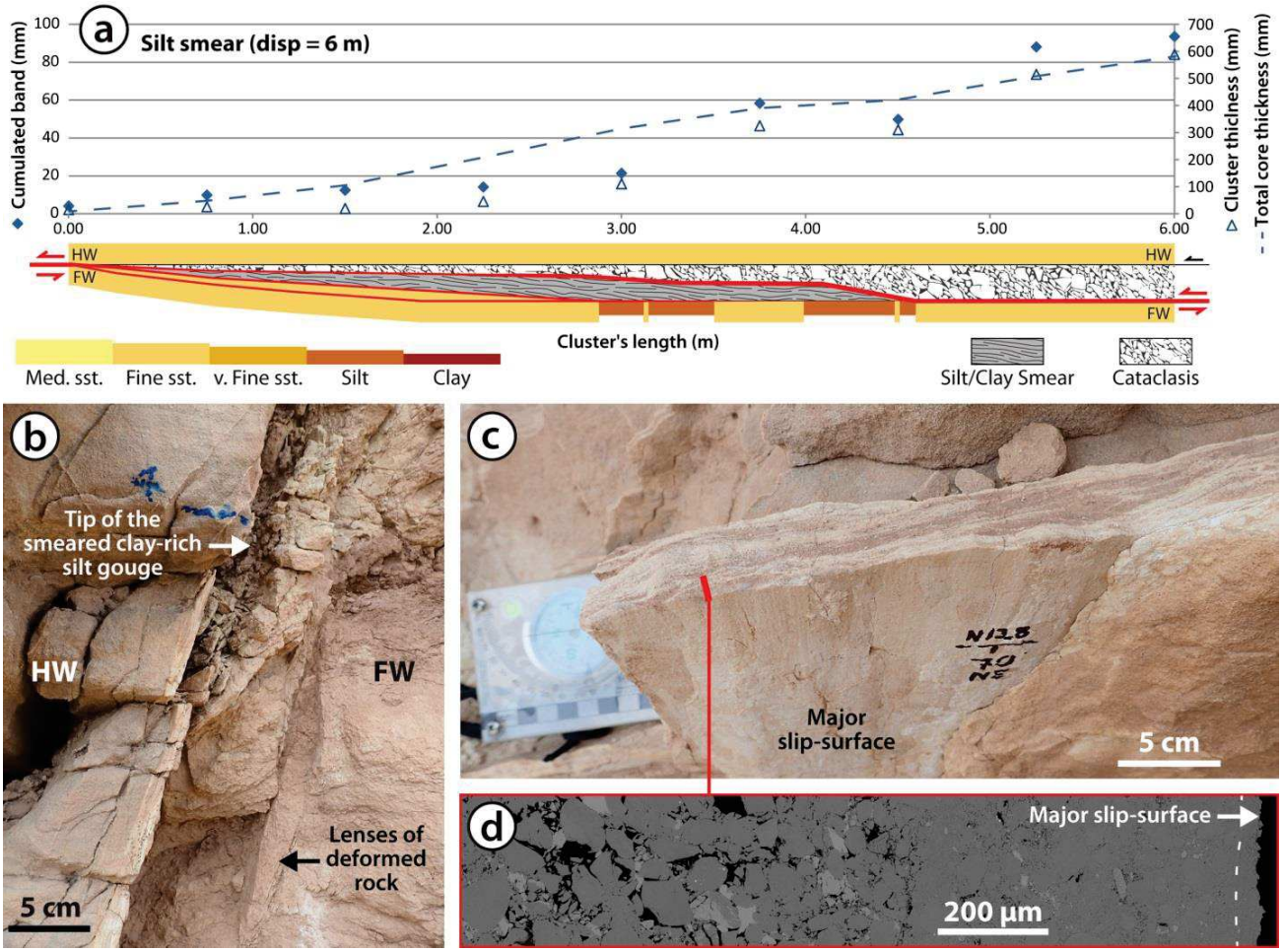

Figure 9. Micro- and macrostructural observations and quantification of the deformation at the first exposure - Goblin Valley. (a) Graph displaying the quantification of the deformation along the length of the cluster of the 6-m fault including alternating thin layers of silt (Fig. 3d). The total core thickness (given as an approximation for reference) accounts for the sum of the cataclastic fault core, the smear and lenses of deformed host rock. The diagram below the graph represents the type of host rock in the hanging wall and footwall, and the type of fault material between (the thickness of the fault material is not to scale). (b) Zoom from Fig. 3d showing the organization of the deformation along the fault plane. (c) Zoom from Fig. 3d showing a branch of the cluster and major slip-surface. (d) SEM-BSE image of major slip-surface at the edge of the cluster (right hand side); the edge of the slip surface (the 20 µm – 4 x 10^{-4} in. thickness to the right of the dashed line) is intensely powdered.

From the top of the outcrop to the limit of the clay layer in the footwall (from 5 to 3.50 m, Fig. 10a) the fault core is exclusively made of a CSB cluster. In this interval, the cumulated band thickness is quite stable, ranging between 122 and 165 mm (4.80 and 6.50 in.); the cluster thickness varies between 290 and 340 mm (11.4 and 13.4 in.). A major slip-surface is located at the footwall side of the cataclastic cluster (red line in Fig. 10a). We note that the position of the slip-surface beyond 5 m (16.4 ft.) (not represented in Fig. 10a) is not clearly identified as it varies within the thickness of the cluster. From 3.50 to 1.30 m (11.5 to 4.3 ft.), the cluster localizes in the hanging wall side of the fault core, against a smeared clay gouge on the footwall side (Fig. 10b). In this interval, the cumulated band thickness drops from 112 to 34 mm (4.41 to 1.34 in.) and the cluster thickness decreases from 350 to 105 mm (13.8 to 4.13 in.). Below that, the cluster thickness on the hanging wall side decreases to 0. The slip-surface marks out the limit with the clay gouge, but whereas it is major at 3.3 m (10.8 ft.) (flat, smooth and striated), it becomes minor at 1.3 m (4.27 ft.) (corrugated and barely striated) and then disappears. No slip-surface is visible at macroscopic scale in the small

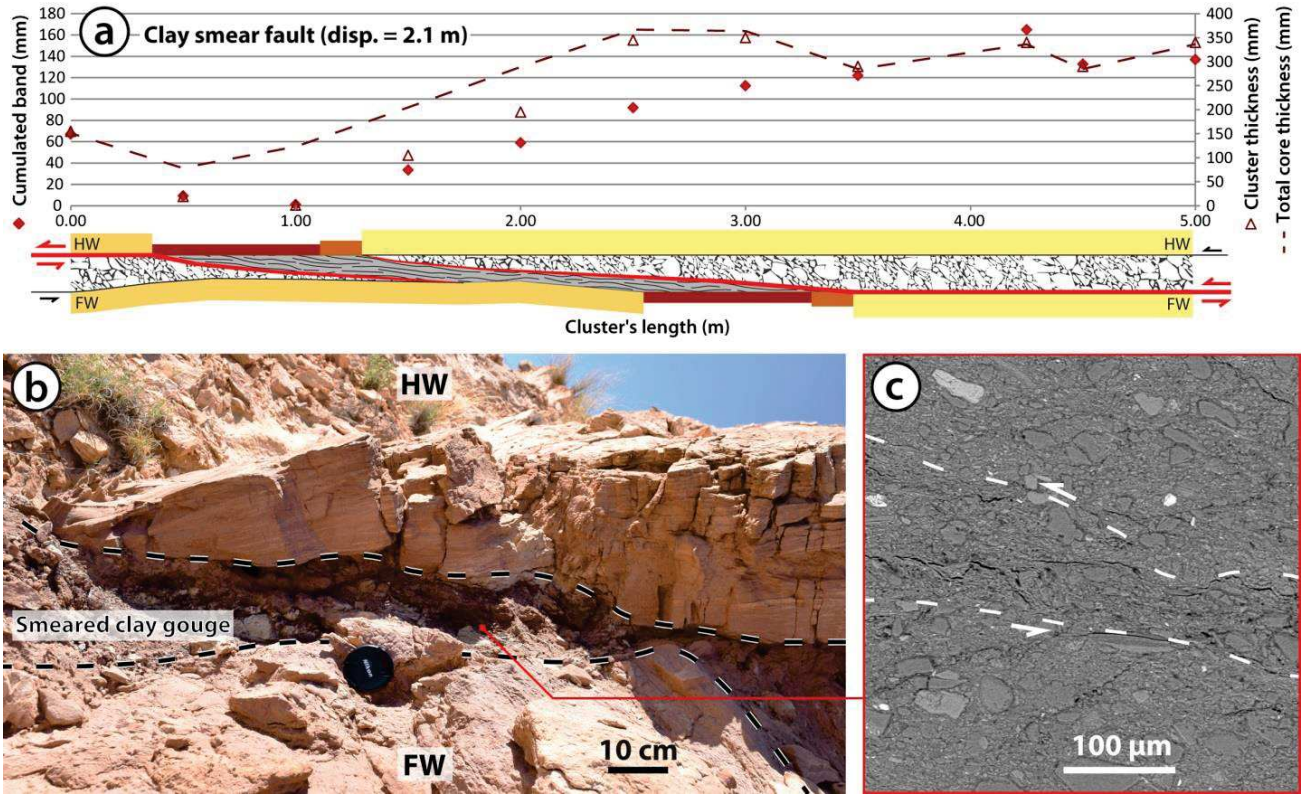

Figure 10. Micro- and macrostructural observations and quantification of the deformation at the second exposure - Goblin Valley (a) Graph displaying the quantification of the deformation along the length of the cluster of the 2.1-m fault including a layer of clay (Fig. 3e). The total core thickness (given as an approximation for reference) accounts for the sum of the cataclastic fault core and the smear. The diagram below the graph represents the type of host rock in the hanging wall and footwall, and the type of fault material between (the thickness of the fault material is not to scale); see Fig. 9a for legend. (b) Zoom from Fig. 3e showing the organization of the deformation along the fault plane around the clay gouge. (c) SEM-BSE image of the deformation in the clays within the clay gouge; the dashed lines encompass a zone where sheared particles are particularly visible.

thickness of the clay gouge. However, microscopic scale imaging allows observation of distributed shear in the clays (Fig. 10c). At 1.50 m (4.9 ft.), a thickness of 1 mm (0.04 in.) of cataclastic deformation band (one band) is measured against the clay gouge on the footwall side of the fault core. From this location down to the bottom of the outcrop (at 0 m), the cumulated band thickness on the footwall increases up to 67 mm (2.64 in.), corresponding to 155 mm (6.10 in.) of cluster thickness. From 1.5 m (4.9 ft.), a minor slip-surface marks out the limit between the cluster in the footwall and the clay gouge. Below that, the clay smear disappears, and the slip-surface is continuous and evolves to a major slip-surface near the bottom of the outcrop. Apart from a few fragments of 1 to 5 cm (0.4 to 2.0 in.) in thickness made of little consolidated cataclastic structures included in the clay smear, no significant mixing between the clay and the cluster is observed in the core zone.

The measured permeability of the different fault rocks in the core zone as well as of the different type of host rocks is reported in Fig. 4 and Table A1 (supplementary material), which also includes the data from the Clashach Cove site for comparison. The host sandstone in Goblin Valley has permeability as high as 2.2×10^4 mD for both the clean fine sandstone at the clay-rich silt gouge exposure and the clean fine sandstone at the clay gouge exposures. We measured a permeability of 5×10^2 mD for the orange fine sandstone of the bottom of the footwall at the clay-rich silt gouge exposure, and down to 1.7×10^2 mD for the silt layers. The permeability of the medium sandstone at the clay gouge exposure was not measured. The permeability of the clay was not measured either

since the clay at the outcrop was highly crumbling; we give instead the range of typical value of clays as reported by Neuzil (1994) as reference, spanning from 1 $x10^{0}$ to 1 $x10^{-8}$ mD. Cataclastic clusters have permeability of 6.1 mD parallel to the fault plane, and lower than 5 x 10^{-1} mD normal to a major slip-surface. The sheared surface of the silt at the first outcrop in Goblin Valley has a permeability of 8.3 x 10^{1} mD. The clay smear permeability in the second outcrop was not measured but is probably comprised in the range for clays mentioned above.

DISCUSSION

Chronology of the deformation and diagenesis at Clashach Cove

The Clashach Cove site records at least two tectonic events, each corresponding to the development of a specific fault rock: 1) an episode of N-S extension characterized by cataclastic deformation and followed by a quartz diagenesis, and 2) a NNE-SSW extensional episode characterized by brecciation followed by an oxide mineralization.

Since joints and dilation bands (dilatant deformation structures) cross-cut the CSB both in the footwall and in the hanging wall, they postdate cataclastic deformation. Given the close orientation of CSBs and the clusters of deformation bands at the edge of the fault zone, we assume that this cataclastic deformation (shear and compactive deformation) occurred during the same extensional tectonic event (Fig. 11a). The N090° strike of the fault and its normal-sense kinematics suggest a N-S extension consistent with the Late Jurassic rifting tectonics of the Moray Firth (Roberts et al. 1990, Underhill, 1991). The N100-120° main orientation of the subsequent dilatant deformation structures and the 71°W pitch of the lineation on the fault slickenside are kinematically consistent and suggest a later extension oriented NNE-SSW, with an oblique reactivation of the fault (Fig. 11b) during which the breccia formed at the hanging wall edge of the cluster. This second extensional episode matches with the oblique extension during the Paleocene-Eocene during the Scottish Highlands uplift as suggested by Roberts et al. (1990). The orientation of the dilatant structures from N140° to N190° could mark a gradual E-W reorientation of this latter extensional episode or potential stress perturbation due to fault interactions (e.g. Kattenhorn et al., 2000).

Both the close orientation and the formation time of dilation bands and joints suggest a genetic similarity of these structures. They form under extensional conditions as a function of the material cohesion. When cohesion is small (no cementation), we observe dilation bands, and when it is higher (cementation), instead of dilation bands we observe joints.

The quartz cementation of the grey sandstone at the lower part of the footwall probably occurred during the burial of the Moray Firth sandstone during Late Jurassic. Underhill (1991) estimates that the Hopeman sandstone near the Moray Coast was buried from a maximum of 1.7 km at the end of Late Jurassic, to a maximum of 1.9 km (1.2 mi.) at the end of Cretaceous. Haszeldine et al. (1984) evidences a quartz overgrowth development in Lower Jurassic clay-poor sandstone from the Beatrice Oilfield (middle Moray Firth) from 68°C (154°F) (no depth mentioned). On the other hand, Pollington et al. (2011) showed that quartz cementation in sandstone can form at temperature as low as 40°C (104°F). Assuming a mean gradient of at least 30°C/km (139°F/mi.) (which is a minimum given the inter-rifting tectonic of the region at the time), this range of temperature seems

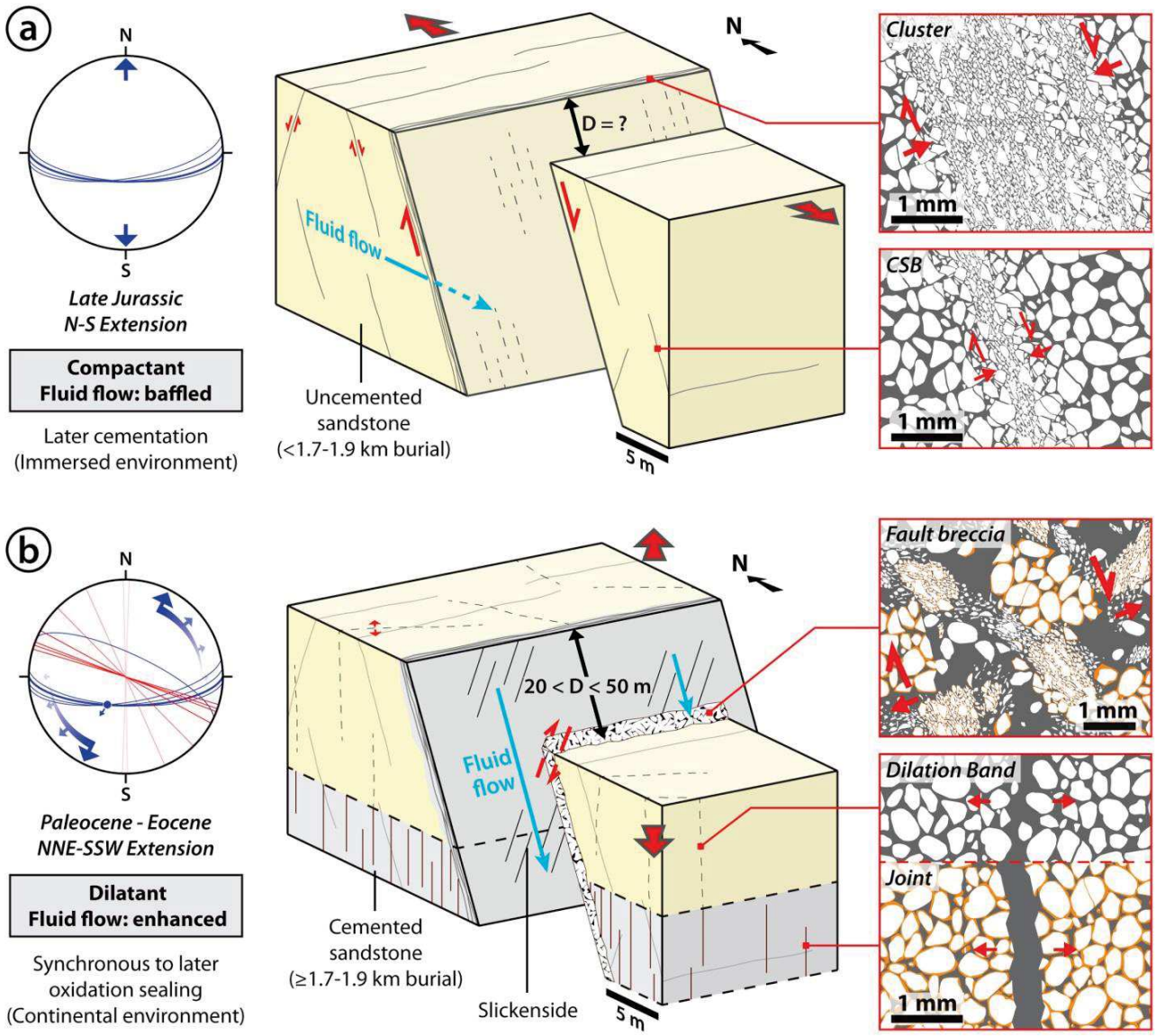

Figure 11. Synthetic diagrams summarizing the chronology of the different tectonic events and the associated fault rock generated at the Clashach Cove site. (a) Late Jurassic extension setting. (b) During the Paleocene-Eocene extension. The orange rims around the white grains in the zooms represent the quartz cements sealing the grains; the dark-grey background represents the porosity.

coherent with the estimated burial depth of the formation. Because the quartz cements along the fault in the cluster are sealing the cataclastic textures of the CSB and are cross-cut by the joints, the quartz diagenesis may therefore be coeval or post-date the cluster and pre-dates the jointing and fault reactivation. Hence this diagenesis could also have happened with the maximum burial of the formation. However, Fisher and Knipe (1998), Lander et al. (2008) and Williams et al. (2015) have documented the enhancement of cementation in cataclastic structures. In particular Milliken et al., (2005) and Philit et al., (2015) have shown that high quartz cementation of cataclastic deformation band clusters is possible even at shallow burial (depth <2 km (<1.2 mi.) and <1 km (<0.6 mi.), respectively). Ngwenya et al. (2000) revealed that this preferential cementation in the cataclastic material can occur through high silica concentration release during cataclastic faulting and subsequent self-sealing. Consequently, and because the sandstone formation in on the footwall edge

of the cluster is not significantly cemented, we think that the quartz cementation in the cluster along the fault plane was rather favored by the presence of cataclasis than by significant burial.

Oxides seal the fault breccia (grain/clast coating) and are clogging the joints. They have precipitated after the reactivation of the fault leading to brecciation during Paleocene-Eocene. We cannot exclude that some oxides may also be contemporaneous with the brecciation. Given that the Paleocene-Eocene rifting caused the uplift of the Scottish highlands (continental conditions), the massive oxide clogging of the breccia and of the surface of the joints most likely originates from meteoric fluid, drained per descensum into the fault core and the joints.

At the Clashach Cove site, we demonstrated that brecciation overprinted the cataclastic cluster. The dilatant characteristic of brecciation is evidenced by the presence of massive iron oxide coatings filling the dilatant fault core. Both the composition of the fault core (i.e. the breccia) and the slickenside lineations indicate that the reactivation of the fault involved hardened and therefore lithified sandstone. The occurrence of the breccia parallel to and against the hardened deformation band cluster (preferentially cemented) indicates that the former mechanical process of cataclastic deformation determined the later localization of faulting (creation of a major through-going slip surface) and brecciation. Joints, which are kinematically consistent with fault reactivation, suggest that the brecciation of the cemented material occured at relatively low effective stress. The example of Clashach shows that juxtaposition of fault rocks can provide very high anisotropy of permeability into fault core. Fluid flow must be inhibited across the cluster after the cataclastic deformation and diagenesis (permeability reduction of about 4 order of magnitude compared to the host rock), whereas it is highly enhanced along dilatant breccia when juxtaposed against the cluster, which allows massive iron oxide deposition. We remark that the permeability increase is transient if we consider that the oxides now seal the breccia. To a lesser extent, a permeability anisotropy of one order of magnitude (higher parallel to fault dip than along-strike) can be obtained in the host rock walls near the fault core because of pervasive micro-scale deformation and grain reorientation (Farrell et al., 2014). Consistently to the results of Williams et al. (2017), for example, we document here that the behavior of a fault through time is highly variable depending on the diagenetic evolution of the hot rock.

Spatial evolution of a layered sandstone/clay formation at Goblin Valley

The Goblin Valley site shows deformation structures formed during the same tectonic episode through a sandstone-dominated formation including layers of silt or clay. Our study evidences the development and juxtaposition of two distinct fault cores made of two fault materials: clusters of cataclastic deformation bands and clay-rich gouges.

Even if the Entrada formation was buried at least at 1100 m (0.68 mi.) at the time of deformation, both exposures record cataclasis as the dominant mechanical process of deformation in the porous sandstone. Although it is true that the thickness of a cluster may considerably vary along its length at the scale of 1 m (Fossen and Bale, 2007), we observed as a general trend that the cumulated band thickness is always maximum between directly juxtaposed sandstones (without clay smear in between) and decreases down to zero where the sandstones are displaced against silts or clays. This observation suggests that clusters grow by an increasing number of cataclastic bands

where the sandstones are still directly in contact (Fig. 12a-b), and could be simply shifted against the smear when displacement increases. In other words, it is highly probable that CSB do not form and add up to the clusters where they juxtapose against the smear. Smearing results in the reduction of the shear stresses since clay (or phyllosilicate-bearing silts) represent weaker material than sandstone or cataclastic structures (Byerlee, 1978; Schmatz et al., 2010, Kettermann et al., 2016). At Goblin Valley, although distributed in the smear thickness (Fig. 10c), we observed that the shear tends to localize as a slip-surface at the cluster contact. Our data also suggest that displacement as small as 2.1 m (6.9 ft.) is sufficient to propagate this slip-surface as a major slip-surface (faulting) in the underlying and overlying sandstones (Fig. 12c), consequently stopping further cluster growth and deformation in the damage zone. This behavior would deserve to be studied in more field examples, and in particular in contractional regime, as this result have major implications concerning the evolution of deformation in sandstones, including the stage of faulting or the extent of growth of the deformation zone (as studied by Harris et al., 2003; Nicol et al., 2013; Schueller, 2013; Ballas et al., 2014; Soliva et al., 2016 for instance). We note that the initiation of clustering may occur simultaneously in both the sandstone units above and below the silt/clay layer since the clusters in the two units are aligned in the same plane at the second exposure. The different thickness of the cataclastic structures on both sides of the smear (hanging vs. footwall) may be related to the fact that the displaced clusters did not form in the same sandstone unit and were therefore generated under different conditions during fault propagation. Also, note that both exposures at Goblin Valley display

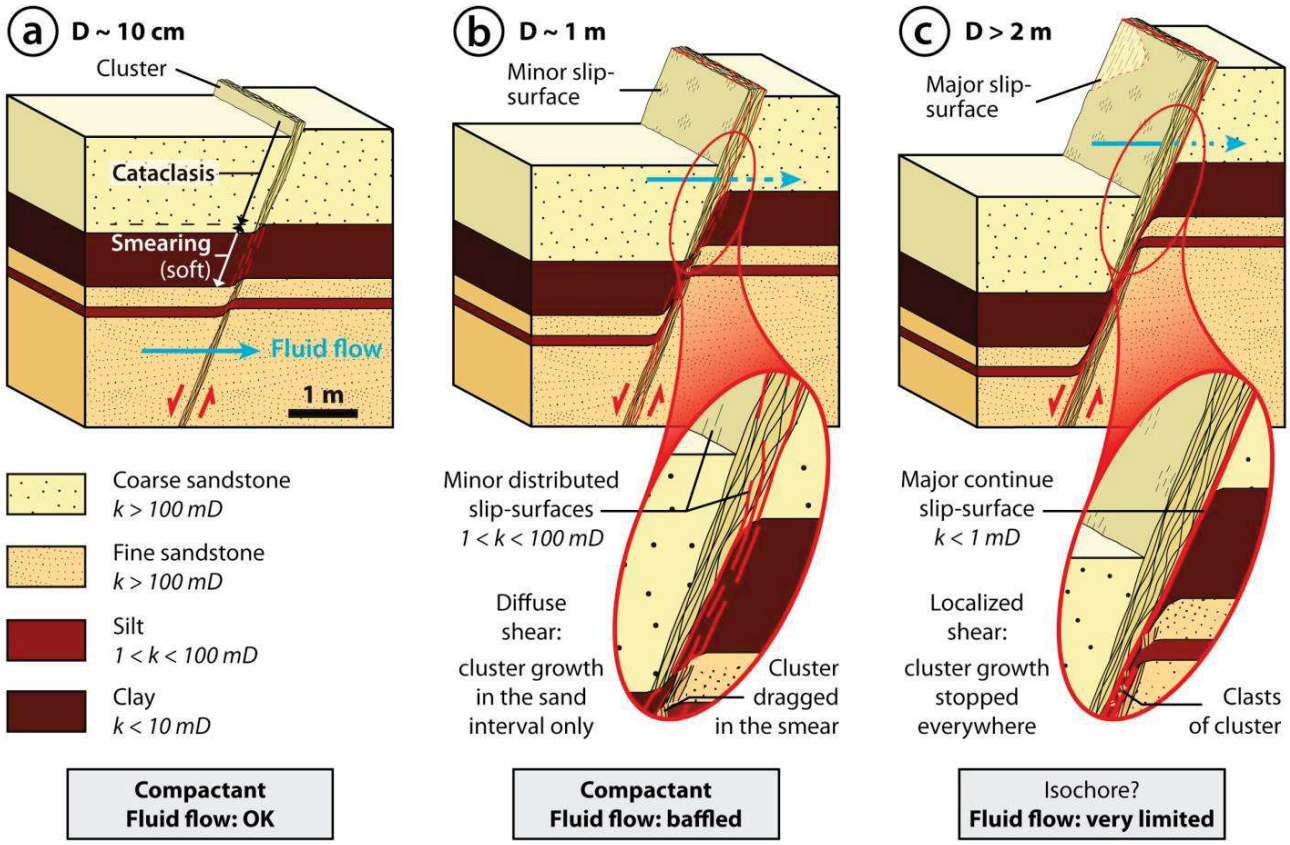

Figure 12. Synthetic diagrams summarizing the evolution of the deformation and its associated processes and the generated fault rocks in the sandstone-dominated formations at Goblin Valley: (a) at the incipient stage of deformation (ca. displacement of 10 cm – 3.9 in.), (b) when both smearing and cataclasis are active (ca. displacement of 1 m – 3.3 ft.), (c) when faulting occurs and cataclasis is inhibited (ca. displacement >2 m >6.6 ft.).

the major slip-surface along the same edge of the cluster, at the interface between the smear and the cluster. Silt/clay layers therefore appear determinant in the initiation and localization of a discrete shear surface in the cluster.

Eventually, we remark that the cataclasis is only possible when the sandstone is porous and clean enough. At Goblin Valley, any sort of sandstone or silt juxtaposed with sandstone of porosity lower than 6% and/or including fragile material such as phyllosilicates or oxide-bearing oolites between the quartz grains don not develop cataclastic deformation. Knipe (1997) suggests that an amount of 10 – 15% of phyllosilicate in siliciclastic material is sufficient to promote grain boundary sliding rather grain fracturing. We assume similar behavior would happen with other weak materials.

This study gives examples of clay and silt smear juxtaposition along cataclastic cluster in porous sandstone units, and shows that smearing prevents the process of cataclasis and leads to slip-surface localization at early stages of displacement (≥2.1 m – ≥6.9 ft.). The example of Goblin Valley shows that highly heterogeneous host rocks can provide a small anisotropy of permeability of fault core. The juxtaposition of cataclastic cluster and smear leads to a localized permeability reduction. Although the case of mixing between sands and clay layers is frequently reported (Gibson, 1998; Rawling et al., 2001, Bense et al., 2003; Ketterman et al. 2016), we note that this process is not observed when the clusters juxtapose against the clay-rich gouges. Yet, in the case of thin alternating sand and clay layers, the latter authors showed that the mixing of the smeared clays and sand grains as displacement increases leads to a sealing material as long as the clay volume exceeds the pore volume of the sand. Linked to the porosity reduction, the permeability reduction of the host rock by cataclasis (at Clashach and Goblin Valley) is comprised between 3 to 4 orders of magnitude in the CSB clusters, and up to 4 to 5 orders of magnitude when a major slip-surface exists. These results are consistent with the measurements of Fossen and Bale, (2007), Ballas et al., (2015), for instance. On the one hand, Eichhubl et al. (2004) and Tueckmantel et al. (2012) report that permeability reduction of two orders of magnitude is enough to baffle meteoric fluids. On the other hand, many studies (e.g., Yielding, 2002; Bretan et al., 2003) have shown that sandstone - sandstone juxtapositions often cannot support significant hydrocarbon column heights where clay-smear is limited. Hence, the juxtaposition of clusters with low permeability of the clay gouge may at least make the whole fault core a transverse fault baffle for fluid flow early in the evolution of the deformation. The baffle effect can be efficient because clusters can be up to hundreds of meters long, and form networks over distances of several km (Fig. 3b).

CONCLUSION

Our field study focuses on the juxtaposition of three fault rocks in normal fault cores during deformation in sandstone-dominated formations at two sites.

Consistently with the previous works related to the influence of the lithology on the mechanical process of deformation, we confirm that, in sandstone-dominated formation, the cataclasis occurs in poorly consolidated sandstone whereas brecciation occurs if the rock is significantly lithified and cohesive. Hence, we evidence at the site of Clashach that the evolution of a sandstone through time can lead to evolving fault behavior. The formation was first deformed while poorly consolidated which led to cataclastic deformation and the formation of a deformation bands cluster. Because of

the permeability reduction in this fault rock, the fluid flow may have been at least baffled across fault. A burial of 1.9 km (1.2 mi.) was sufficient to allow the cementation, hardening and permeability reduction of the formation and the favored cementation of the cluster. We think that the presence of the former hardened cluster provided the necessary lithological condition to localize the major through-going slip-surface and brecciation (reactivation of the structure) during later normal tectonic loading. As a result, the dilatant behavior of this mechanical process of deformation allowed an efficient fluid circulation along the fault, providing an intense oxide clogging of the breccia.

At Goblin Valley, we confirm the smearing of the formation when the sandstone-dominated formation comprises thin layer of clay or clay-rich host rock. We also note that the cataclasis was possible at a burial depth of at least 1.1 km (0.7 mi.). Our study suggests that the mechanical process of smearing inhibits the process of cataclasis and enhance the incipient development and localization of a major slip-surface in the clusters developing in the adjacent sandstone units. Consequently, mixing would not necessarily occur during smearing when clusters are overlapping the clay-rich gouges. Because the permeability of cataclastic fault rocks is 3 - 5 orders of magnitude lower than that of the host rock, and due to the juxtaposition with the low-permeability clay-rich gouge, the clusters of deformation bands are likely to form continuous and efficient barriers to fluid-flow across fault.

As a general conclusion, our contribution shows that the evolution of the deformation in a sandstone-dominated formation through time and space may create strong permeability anisotropy. This will result in contrasted fluid flow behaviors through the reservoir, depending on the lithology of the faulted units, and tectonic history of the formation. For instance, sub-seismic structures (displacement <20 m - <66 ft.) can evolve into seismic-scale faults (displacement ≥20 m ≥66 ft.) with juxtaposing fault rocks and drastically different fluid flow along and across the fault. On the other hand, sub-seismic displacements are sufficient to induce continued low-permeability structures through the juxtaposition of clusters and clay-rich gouge likely to act as barriers for fluid flow. Furthermore, we evidence that the development of a fault in cataclastic deformation band cluster is induced ad propagated from a lithological contrast in the sandstone dominated formation. This contrast can consist of a hardened material against the porous sandstone, or a softer layer in a globally porous sandstone formation.

REFERENCES CITED

Agosta, F., Prasad, M., and Aydin, A., 2007, Physical properties of carbonate fault rocks, fucino basin (Central Italy): implications for fault seal in platform carbonates: Geofluids, v. 7, p. 19–32, doi: 10.1111/j.1468-8123.2006.00158.x.

Al-Hinai, S., Fisher, Q.J., Al-Busafi, B., Guise, P., and Grattoni, C.A., 2008, Laboratory measurements of the relative permeability of cataclastic fault rocks: An important consideration for production simulation modelling: Marine and Petroleum Geology, v. 25, p. 473–485, doi: 10.1016/j.marpetgeo.2007.07.005.

Antonellini, M., and Aydin, A., 1994, Effect of Faulting on Fluid Flow in Porous Sandstones: Petrophysical Properties: AAPG Bulletin, v. 78, p. 355–377.

Aydin, A., 1978, Small faults formed as deformation bands in sandstone: pure and applied geophysics, v. 116, p. 913–930, doi: 10.1007/BF00876546.

Aydin, A., and Eyal, Y., 2002, Anatomy of a normal fault with shale smear: Implications for fault seal: AAPG Bulletin, v. 86, http://archives.datapages.com/data/bulletns/2002/08aug/1367/1367.htm (accessed January 2017).

Aydin, A., and Johnson, A.M., 1978, Development of faults as zones of deformation bands and as slip surfaces in sandstone: pure and applied geophysics, v. 116, p. 931–942, doi: 10.1007/BF00876547.

Ballas, G., Fossen, H., and Soliva, R., 2015, Factors controlling permeability of cataclastic deformation bands and faults in porous sandstone reservoirs: Journal of Structural Geology, v. 76, p. 1–21, doi: 10.1016/j.jsg.2015.03.013.

Ballas, G., Soliva, R., Benedicto, A., and Sizun, J.-P., 2014, Control of tectonic settings and large-scale faults on the basin-scale distribution of deformation bands in porous sandstone (Provence, France): Marine and Petroleum Geology, v. 55, p. 142–159, doi: 10.1016/j.marpetgeo.2013.12.020.

Blenkinsop, T.G., 1991, Cataclasis and processes of particle size reduction: pure and applied geophysics, v. 136, p. 59–86, doi: 10.1007/BF00878888.

Bretan, P., Yielding, G., and Jones, H., 2003, Using calibrated shale gouge ratio to estimate hydrocarbon column heights: AAPG Bulletin, v. 87, p. 397–413, doi: 10.1306/08010201128.

Byerlee, J., 1978, Friction of rocks: pure and applied geophysics, v. 116, p. 615–626, doi: 10.1007/BF00876528.

Caine, J.S., Evans, J.P., and Forster, C.B., 1996, Fault zone architecture and permeability structure: Geology, v. 24, p. 1025–1028, doi: 10.1130/0091-7613(1996)024<1025:FZAAPS>2.3.CO;2.

Childs, C., Walsh, J.J., Manzocchi, T., Strand, J., Nicol, A., Tomasso, M., Schöpfer, M.P.J., and Aplin, A.C., 2007, Definition of a fault permeability predictor from outcrop studies of a faulted turbidite sequence, Taranaki, New Zealand: Geological Society, London, Special Publications, v. 292, p. 235–258, doi: 10.1144/SP292.14.

Clausen, J.A., and Gabrielsen, R.H., 2002, Parameters that control the development of clay smear at low stress states: an experimental study using ring-shear apparatus: Journal of Structural Geology, v. 24, p. 1569–1586, doi: 10.1016/S0191-8141(01)00157-2.

Davatzes, N.C., Eichhubl, P., and Aydin, A., 2005, Structural evolution of fault zones in sandstone by multiple deformation mechanisms: Moab fault, southeast Utah: GSA Bulletin, v. 117, p. 135–148, doi: 10.1130/B25473.1.

Doelling, H.H., Kuehne, P.A., Willis, G.C., and Buck Ehler, J., 2015, Geologic map of the San Rafael Desert 30 x 60-minute quadrangle, Emery and Grand Counties, Utah: Utah Geological Survey.

Ehrenberg, S.N., 1989, Assessing the Relative Importance of Compaction Processes and Cementation to Reduction of Porosity in Sandstones: Discussion; Compaction and Porosity Evolution of Pliocene Sandstones, Ventura Basin, California: DISCUSSION: AAPG Bulletin, v. 73, p. 1274–1276.

Eichhubl, P., Taylor, W.L., Pollard, D.D., and Aydin, A., 2004, Paleo-fluid flow and deformation in the Aztec Sandstone at the Valley of Fire, Nevada—Evidence for the coupling of hydrogeologic, diagenetic, and tectonic processes: Geological Society of America Bulletin, v. 116, p. 1120–1136, doi: 10.1130/B25446.1.

Engelder, J.T., Logan, J.M., and Handin, J., 1975, The sliding characteristics of sandstone on quartz fault-gouge: pure and applied geophysics, v. 113, p. 69–86, doi: 10.1007/BF01592900.

Farrell, N.J.C., Healy, D., and Taylor, C.W., 2014, Anisotropy of permeability in faulted porous sandstones: Journal of Structural Geology, v. 63, p. 50–67, doi: 10.1016/j.jsg.2014.02.008.

Faulkner, D.R., Jackson, C.A.L., Lunn, R.J., Schlische, R.W., Shipton, Z.K., Wibberley, C.A.J., and Withjack, M.O., 2010, A review of recent developments concerning the structure, mechanics and fluid flow properties of fault zones: Journal of Structural Geology, v. 32, p. 1557–1575, doi: 10.1016/j.jsg.2010.06.009.

Fisher, Q.J., and Knipe, R.J., 1998, Fault sealing processes in siliciclastic sediments: Geological Society, London, Special Publications, v. 147, p. 117–134, doi: 10.1144/GSL.SP.1998.147.01.08.

Folk, R.L., and Ward, W.C., 1957, Brazos River Bar: A Study in the Significance of Grain Size Parameters: Journal of Sedimentary Research, v. 27, http://archives.datapages.com/data/sepm/journals/v01-32/data/027/027001/0003.htm (accessed July 2016).

Fossen, H., and Bale, A., 2007, Deformation bands and their influence on fluid flow: AAPG Bulletin, v. 91, p. 1685–1700, doi: 10.1306/07300706146.

Fossen, H., Schultz, R.A., Shipton, Z.K., and Mair, K., 2007, Deformation bands in sandstone: a review: Journal of the Geological Society, v. 164, p. 755–769, doi: 10.1144/0016-76492006-036.

Foxford, K.A., Walsh, J.J., Watterson, J., Garden, I.R., Guscott, S.C., and Burley, S.D., 1998, Structure and content of the Moab Fault Zone, Utah, USA, and its implications for fault seal prediction: Geological Society, London, Special Publications, v. 147, p. 87–103, doi: 10.1144/GSL.SP.1998.147.01.06.

Fulljames, J.R., Zijerveld, L.J.J., and Franssen, R.C.M.W., 1997, Fault seal processes: systematic analysis of fault seals over geological and production time scales, in Koestler, P.M.-P. and A.G. ed., Norwegian Petroleum Society Special Publications, Elsevier, Hydrocarbon SealsImportance for Exploration and Production, v. 7, p. 51–59, http://www.sciencedirect.com/science/article/pii/S0928893797800069 (accessed July 2016).

Gallagher Jr, J.J., Friedman, M., Handin, J., and Sowers, G.M., 1974, Experimental studies relating to microfracture in sandstone: Tectonophysics, v. 21, p. 203–247, doi: 10.1016/0040-1951(74)90053-5.

Gibson, R.G., 1998, Physical character and fluid-flow properties of sandstone-derived fault zones: Geological Society, London, Special Publications, v. 127, p. 83–97, doi: 10.1144/GSL.SP.1998.127.01.07.

Glennie, K.W., and Buller, A.T., 1983, The Permian Weissliegend of NW Europe: The partial deformation of aeolian dune sands caused by the Zechstein transgression: Sedimentary Geology, v. 35, p. 43–81, doi: 10.1016/0037-0738(83)90069-6.

Gratier, J.-P., Richard, J., Renard, F., Mittempergher, S., Doan, M.-L., Toro, G.D., Hadizadeh, J., and Boullier, A.-M., 2011, Aseismic sliding of active faults by pressure solution creep: Evidence from the San Andreas Fault Observatory at Depth: Geology, v. 39, p. 1131–1134, doi: 10.1130/G32073.1.

Hadizadeh, J., Mittempergher, S., Gratier, J.-P., Renard, F., Di Toro, G., Richard, J., and Babaie, H.A., 2012, A microstructural study of fault rocks from the SAFOD: Implications for the deformation mechanisms and strength of the creeping segment of the San Andreas Fault: Journal of Structural Geology, v. 42, p. 246–260, doi: 10.1016/j.jsg.2012.04.011.

Harris, S.D., McAllister, E., Knipe, R.J., and Odling, N.E., 2003, Predicting the three-dimensional population characteristics of fault zones: a study using stochastic models: Journal of Structural Geology, v. 25, p. 1281–1299, doi: 10.1016/S0191-8141(02)00158-X.

Haszeldine, R.S., Samson, I.M., and Cornford, C., 1984, Quartz Diagenesis and Convective Fluid Movement: Beatrice Oilfield,UK North Sea: Clay Minerals, p. 391–402.

Jébrak, M., 1997, Hydrothermal breccias in vein-type ore deposits: A review of mechanisms, morphology and size distribution: Ore Geology Reviews, v. 12, p. 111–134, doi: 10.1016/S0169-1368(97)00009-7.

Johansen, T.E.S., and Fossen, H., 2008, Internal geometry of fault damage zones in interbedded siliciclastic sediments: Geological Society, London, Special Publications, v. 299, p. 35–56, doi: 10.1144/SP299.3.

Kattenhorn, S.A., Aydin, A., and Pollard, D.D., 2000, Joints at high angles to normal fault strike: an explanation using 3-D numerical models of fault-perturbed stress fields: Journal of Structural Geology, v. 22, p. 1–23, doi: 10.1016/S0191-8141(99)00130-3.

Kettermann, M., Thronberens, S., Juarez, O., Lajos Urai, J., Ziegler, M., Asmus, S., and Kruger, U., 2016, Mechanisms of clay smear formation in unconsolidated sediments - insights from 3-D observations of excavated normal faults: Solid Earth, v. 7, p. 789–815, doi: 10.5194/se-7-789-2016.

Knipe, R.J., 1997, Juxtaposition and Seal Diagrams to Help Analyze Fault Seals in Hydrocarbon Reservoirs: AAPG Bulletin, v. 81, p. 187–195.

Lanatà, P., 2014, Full-field experimental characterization of mechanical behaviour and failure in a porous rock in plane strain compression: homogeneous deformation and strain localization [Ph.D. thesis]: Université de Grenoble, 387 p.

Lander, R.H., Larese, R.E., and Bonnell, L.M., 2008, Toward more accurate quartz cement models: The importance of euhedral versus noneuhedral growth rates: AAPG Bulletin, v. 92, p. 1537–1563, doi: 10.1306/07160808037.

Lindsay, N.G., Murphy, F.C., Walsh, J.J., and Waterson, J., 1993, Outcrop studies of shale smear on fault surfaces, in The Geological Modelling of Hydrocarbon Reservoirs and Outcrop Analogues (Special Publication 15 of the IAS), Ian D. Bryant, Association of Sedimentologists Special Publication 15, p. 113–123, https://books.google.fr/books/about/The_Geological_Modelling_of_Hydrocarbon.html?hl=fr&id=DroNmgQVFkYC.

Milliken, K.L., Reed, M.H., and Laubach, S.E., 2005, Quantifying Compaction and Cementation in Deformation Bands in Porous Sandstones, in Sorkhabi, R. and Tsuji, Y. eds., Faults, fluid flow, and petroleum traps, AAPG Memoir 85, p. 237–249, doi: 10.1306/1033726M85252.

Neuzil, C.E., 1994, How permeable are clays and shales? Water Resources Research, v. 30, p. 145–150, doi: 10.1029/93WR02930.

Ngwenya, B.T., Elphick, S.C., Main, I.G., and Shimmield, G.B., 2000, Experimental constraints on the diagenetic self-sealing capacity of faults in high porosity rocks: Earth and Planetary Science Letters, v. 183, p. 187–199, doi: 10.1016/S0012-821X(00)00261-2.

Nicol, A., Childs, C., Walsh, J.J., and Schafer, K.W., 2013, A geometric model for the formation of deformation band clusters: Journal of Structural Geology, v. 55, p. 21–33, doi: 10.1016/j.jsg.2013.07.004.

Olierook, H.K.H., Timms, N.E., and Hamilton, P.J., 2014, Mechanisms for permeability modification in the damage zone of a normal fault, northern Perth Basin, Western Australia: Marine and Petroleum Geology, v. 50, p. 130–147, doi: 10.1016/j.marpetgeo.2013.10.012.

Paxton, S.T., Szabo, J.O., Ajdukiewicz, J.M., and Klimentidis, R.E., 2002, Construction of an Intergranular Volume Compaction Curve for Evaluating and Predicting Compaction and Porosity Loss in Rigid-Grain Sandstone Reservoirs: AAPG Bulletin, v. 86, p. 2047–2067, doi: 10.1306/61EEDDFA-173E-11D7-8645000102C1865D.

Pelto, C.R., 1952, The Mechanical Analysis of Sediments from Thin-Section Data: A Discussion: The Journal of Geology, v. 60, p. 402–406.

Philit, S., Soliva, R., Labaume, P., Gout, C., and Wibberley, C., 2015, Relations between shallow cataclastic faulting and cementation in porous sandstones: First insight from a groundwater environmental context: Journal of Structural Geology, v. 81, p. 89–105, doi: 10.1016/j.jsg.2015.10.001.

Pollington, A.D., Kozdon, R., and Valley, J.W., 2011, Evolution of quartz cementation during burial of the Cambrian Mount Simon Sandstone, Illinois Basin: In situ microanalysis of δ18O: Geology, v. 39, p. 1119–1122, doi: 10.1130/G32195.1.

Quinn, O.F., 2005, Fault controlled fluid flow and quartz cementation in porous sandstones [Ph.D. thesis]: The University of Edinburgh, http://www.era.lib.ed.ac.uk/handle/1842/7103.

Rawling, G.C., and Goodwin, L.B., 2006, Structural record of the mechanical evolution of mixed zones in faulted poorly lithified sediments, Rio Grande rift, New Mexico, USA: Journal of Structural Geology, v. 28, p. 1623–1639, doi: 10.1016/j.jsg.2006.06.008.

Rawling, G.C., Goodwin, L.B., and Wilson, J.L., 2001, Internal architecture, permeability structure, and hydrologic significance of contrasting fault-zone types: Geology, v. 29, p. 43–46, doi: 10.1130/0091-7613(2001)029<0043:IAPSAH>2.0.CO;2.

Rigby, J.K., and Beus, S.S., 1987, Stratigraphy and Structure of the San Rafael Reef, Utah," A Major Monocline of the Colorado Plateau, in Rocky Mountain Section of the Geological Society of America: Decade of North American Geology, Centennial Field Guide Volume 2, Geological Society of America, p. 269–273, https://books.google.fr/books?hl=fr&lr=&id=4n1IAgAAQBAJ&oi=fnd&pg=PA269&dq=Stratigraphy+and+Structure+of+the+San+Rafael+Reef&ots=FZcdEev9ON&sig=o_X-Jn9G52BckhQ1Ul2fSCd4KkM#v=onepage&q&f=false.

Roberts, A.M., Badley, M.E., Price, J.D., and Huck, I.W., 1990, The structural history of a transtensional basin: Inner Moray Firth, NE Scotland: Journal of the Geological Society, v. 147, p. 87–103, doi: 10.1144/gsjgs.147.1.0087.

Schmatz, J., Vrolijk, P.J., and Urai, J.L., 2010, Clay smear in normal fault zones – The effect of multilayers and clay cementation in water-saturated model experiments: Journal of Structural Geology, v. 32, p. 1834–1849, doi: 10.1016/j.jsg.2009.12.006.

Schueller, S., Braathen, A., Fossen, H., and Tveranger, J., 2013, Spatial distribution of deformation bands in damage zones of extensional faults in porous sandstones: Statistical analysis of field data: Journal of Structural Geology, v. 52, p. 148–162, doi: 10.1016/j.jsg.2013.03.013.

Schultz, R.A., and Fossen, H., 2008, Terminology for structural discontinuities: AAPG Bulletin, v. 92, p. 853–867, doi: 10.1306/02200807065.

Shotton, F.W., 1956, Some aspects of the new red desert in britain: Geological Journal, v. 1, p. 450–465, doi: 10.1002/gj.3350010505.

Sibson, R.H., 1977, Fault rocks and fault mechanisms: Journal of the Geological Society, v. 133, p. 191–213, doi: 10.1144/gsjgs.133.3.0191.

Soliva, R., Ballas, G., Fossen, H., and Philit, S., 2016, Tectonic regime controls clustering of deformation bands in porous sandstone: Geology, v. 44, p. 423–426, doi: 10.1130/G37585.1.

Solum, J.G., Davatzes, N.C., and Lockner, D.A., 2010, Fault-related clay authigenesis along the Moab Fault: Implications for calculations of fault rock composition and mechanical and hydrologic fault zone properties: Journal of Structural Geology, v. 32, p. 1899–1911, doi: 10.1016/j.jsg.2010.07.009.

Solum, J.G., van der Pluijm, B.A., and Peacor, D.R., 2005, Neocrystallization, fabrics and age of clay minerals from an exposure of the Moab Fault, Utah: Journal of Structural Geology, v. 27, p. 1563–1576, doi: 10.1016/j.jsg.2005.05.002.

Tueckmantel, C., Fisher, Q.J., Manzocchi, T., Skachkov, S., and Grattoni, C.A., 2012, Two-phase fluid flow properties of cataclastic fault rocks: Implications for CO2 storage in saline aquifers: Geology, v. 40, p. 39–42, doi: 10.1130/G32508.1.

Underhill, J.R., 1991, Implications of Mesozoic—Recent basin development in the western Inner Moray Firth, UK: Marine and Petroleum Geology, v. 8, p. 359–369, doi: 10.1016/0264-8172(91)90089-J.

Vrolijk, P., and van der Pluijm, B.A., 1999, Clay gouge: Journal of Structural Geology, v. 21, p. 1039–1048, doi: 10.1016/S0191-8141(99)00103-0.

Wibberley, C.A.J., Petit, J.-P., and Rives, T., 2007, The mechanics of fault distribution and localization in high-porosity sands, Provence, France: Geological Society, London, Special Publications, v. 289, p. 19–46, doi: 10.1144/SP289.3.

Williams, R.T., Farver, J.R., Onasch, C.M., and Winslow, D.F., 2015, An experimental investigation of the role of microfracture surfaces in controlling quartz precipitation rate: Applications to fault zone diagenesis: Journal of Structural Geology, v. 74, p. 24–30, doi: 10.1016/j.jsg.2015.02.011.

Williams, R.T., Goodwin, L.B., and Mozley, P.S., 2017, Diagenetic controls on the evolution of fault-zone architecture and permeability structure: Implications for episodicity of fault-zone fluid transport in extensional basins: GSA Bulletin, v. 129, p. 464–478, doi: 10.1130/B31443.1.

Woodcock, N.H., and Mort, K., 2008, Classification of fault breccias and related fault rocks: Geological Magazine, v. 145, p. 435–440, doi: 10.1017/S0016756808004883.

Yielding, G., 2002, Shale Gouge Ratio — calibration by geohistory: Norwegian Petroleum Society Special Publications, v. 11, p. 1–15, doi: 10.1016/S0928-8937(02)80003-0.

Yielding, G., Freeman, B., and Needham, D.T., 1997, Quantitative fault seal prediction: AAPG Bulletin, v. 81, p. 897–917.

Zhu, W., and Wong, T., 1997, The transition from brittle faulting to cataclastic flow: Permeability evolution: Journal of Geophysical Research: Solid Earth, v. 102, p. 3027–3041, doi: 10.1029/96JB03282.

APPENDIX

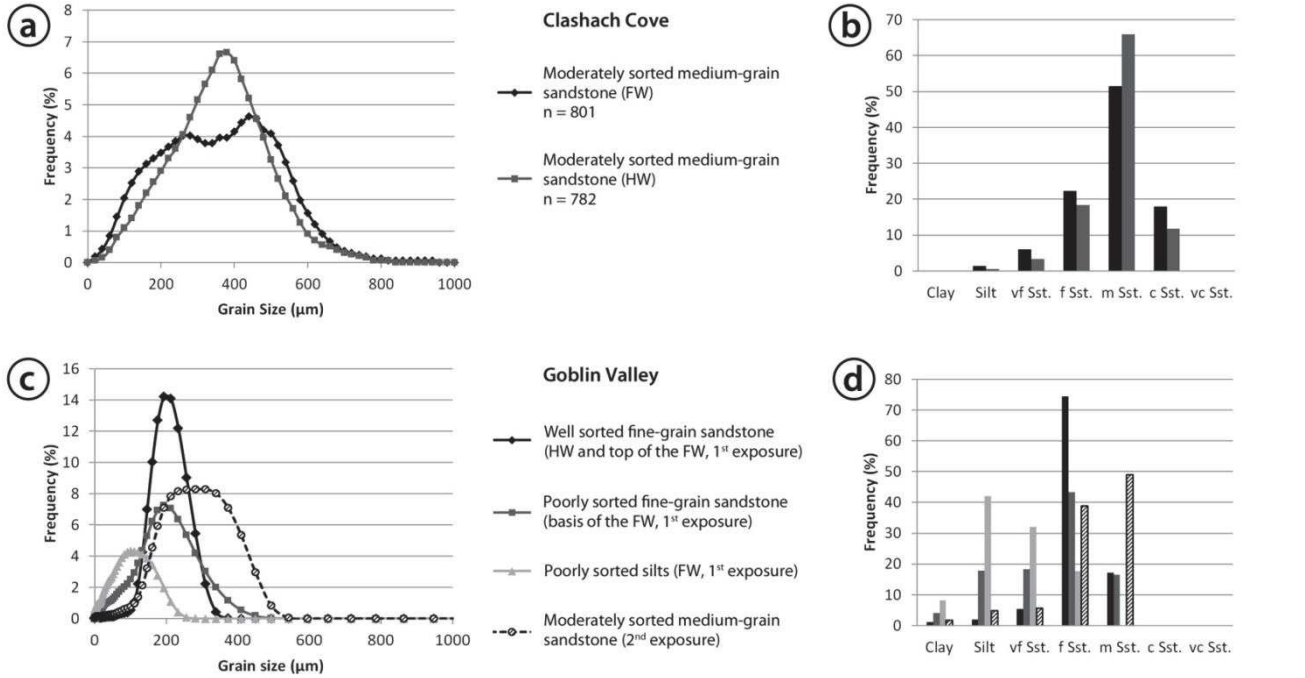

Figure A1. (a) and (b) Grain size distribution of the host rock sandstones at Chashach Cove. The grain populations were obtained by measuring the Feret diameter of a number n of host rock grains in thin section. A statistical factor of $2^{1/2}$ was applied to correct for the underestimation of the diameter in 2D due to truncation effect (sampling effect is neglected), as suggested by Pelto (1952). (c) and (d) Grain size distribution of the host rock sandstones at Goblin Valley. The grain size distribution is obtained through laser diffraction analysis.

TABLE A1. LITHOLOGICAL AND PETROPHYSICAL MEASURMENTS OF THE HOST ROCKS AND FAULT MATERIALS AT THE TWO STUDIED SITES

Unit	Modal size (μm)	Sorting	Mineralogy ±5 (%)	*IGV* ±2 (%)	ϕ	Permeability (mD)
Clashach Cove						
Grey sandstone at the base of the footwall (*host rock*)	Medium [270; 440]	Moderate [0.78]	Qtz: 94%; Fld: 5%	33	17	4.8×10^{2}
Yellow sandstone of the hanging wall (*host rock*)	Medium [370]	Moderate [0.60]	Qtz: 80%; Fld: <20%	31	30	2.3×10^{3}
CSB cluster (cluster-parallel densely spaced CSBs) [†]	N.A.[†]	N.A.[†]	N.A.[†]	N.A.[†]	8	1.2×10^{1}
CSB cluster (cluster-normal slickenside) [†]	N.A.[†]	N.A.[†]	N.A.[†]	N.A.[†]	8	5.6×10^{-1}
Breccia	N.A.[†]	N.A.[†]	Qtz: 13%: Fld and others: 10%; Ox: >40%	N.A.[†]	35	1.3×10^{2}
Joints	N.A.[†]	N.A.[†]	N.A.[†]	N.A.[†]	100	$>5 \times 10^{4}$
Dilation bands	N.A.[†]	N.A.[†]	N.A.[†]	N.A.[†]	55	N.D.[§]
CSBs	N.A.[†]	N.A.[†]	N.A.[†]	N.A.[†]	8	N.D.[§]
Goblin Valley						
Silt smear fault exposure						
Orange sandstone at the base of footwall (*host rock*)	Fine [200]	Poor [1.56]	Qtz: 62%; Fld: 13%; Oolite: 25%; Ox: 1%	6	6	5×10^{2}
Silt on footwall (*host rock*)	Silt [100]	Poor [1.88]	Qtz: 80%; Fld: 11%; Ox: <1%; others: <9%	18	18	1.7×10^{2}
Clean sandstone at the top of footwall and whole hanging wall (*host rock*)	Fine [200]	Good [0.41]	Qtz: 81%; Fld: 14%; Oolite: 4%	33	33	2.2×10^{4}
Clay-rich silt gouge	N.A.[†]	N.A.[†]	N.A.[†]	N.D.[§]	N.D.[§]	8.3×10^{1}
Clay smear fault exposure						
Clean sandstone at the base of the footwall and hanging wall (*host rock*)	*Fine [200]*	*Good [0.41]*	*Qtz: 81%; Fld: 14%; Oolite: 4%*	*33*	*33*	*2.2×10^{4}*
Clay layer (*host rock*) [#]	Clay [N.D.[#]]	N.D.[§]	N.D.[§]	3	3	1×10^{0} - 1×10^{-8}
Sandstone at the top of the footwall and hanging wall (*host rock*)	Medium [280]	Moderate [0.86]	Qtz: 66%; Fld: 8%; Oolite: 24%; Ox: 1%	19	19	N.D.[§]
Clay gouge [#]	N.A.[†]	N.A.[†]	N.A.[†]	3	3	1×10^{0} - 1×10^{-8}
Common						
CSB Cluster (cluster-parallel densely spaced CSBs)	N.A.[†]	N.A.[†]	N.A.[†]	N.A.[†]	13	6.1×10^{0}
CSB cluster (cluster-normal slip-surface)	N.A.[†]	N.A.[†]	N.A.[†]	N.A.[†]	<1	$<5 \times 10^{-1}$

Note: The error bars for permeability measurements are displayed in Fig. 4.

* The permeability values given are representative of the present time and therefore account for the oxide coating of the cataclastic structure.

[†] N.A. = not applicable.

[§] N.D. = no data.

[#] The range of permeability given is from Neuzil (1994) and provided for comparison purpose.

2.3. Integrated study of cataclastic band clusters

This section represents a key part of this thesis as it gathers an integrative field analysis of cataclastic deformation band clusters at seven sites in the world. The selection of this number of site was chosen so as to sample a variety of sandstones involving different intrinsic parameters (presented in section 3.1) such as the tectonic loading, the Andersonian stress regimes, the burial depth at deformation, the host rock lithology. Among these parameters, we pay a specific attention to the tectonic loading and the stress regime of deformation because the tectonic loading was previously mentioned to play a major role on the localization of deformation in porous sandstones (see Soliva et al., 2016 in Appendix A), and because the link with the stress regime is not established. When applicable, the influence of the presence of a map-scale fault underneath the deformed sandstone is accounted for. Indeed, the work of Ballas (2013) suggests that the propagation of an underlying fault in the sandstone could condition a specific organization of the cataclastic structures. The dimension of the clusters is analyzed, the intra-cluster deformation is analyzed macroscopically and microscopically. The microscopic analysis of the deformed material permits, with the contribution of the literature of granular material deformation modeling, to provide and interpretation for the mechanism of band accumulation responsible for the growth of the clusters.

This section is in revision for resubmission to the Journal of Structural Geology. The Microscopic analysis of the deformed cataclastic material was subjected to a poster presentation entitled "*Grain Deformation Processes in Porous Quartz Sandstones - Insights from the Deformation Band Clusters*" at the Powders and Grains conference (Montpellier, 2017).

We add a supplement where we present an analytical method developed to estimate the stress-path evolution of the sandstone, to anticipate the occurrence of the deformation on the failure envelope of the sandstone.

To complement the analysis of the morphology of clusters, we provide at the end of this section an analysis of the geometry of the lenses of deformed material between the bands in the clusters. We think that the quantification and description of the interband geometry informs on the connectivity of the thickness of the cluster and therefore enlightens its characterization.

2.3.1. Clusters of Cataclastic Deformation Bands in porous sandstones – Development and implication for reservoir fluids

Clusters of Cataclastic Deformation Bands in porous sandstones – Development and implication for reservoir fluids

Sven Philit[1], Roger Soliva[2], Raymi Castilla[3], Gregory Ballas[4], Audrey Taillefer[5]

[1] *Géosciences Montpellier, UMR 5243, Université de Montpellier-CNRS, Place Eugène Bataillon, 34095 Montpellier Cedex 5, France, sven.philit@gm.univ-montp2.fr*

[2] *Géosciences Montpellier, UMR 5243, Université de Montpellier-CNRS, Place Eugène Bataillon, 34095 Montpellier Cedex 5, France, soliva@gm.univ-montp2.fr*

[3] *R&D Frontier Exploration, TOTAL S.A., raymi.castilla@total.com*

[4] *pending, gregory.ballas@yahoo.fr*

[5] *Géosciences Montpellier, UMR 5243, Université de Montpellier-CNRS, Place Eugène Bataillon, 34095 Montpellier Cedex 5, France, audrey.taillefer@gm.univ-montp2.fr*

ABSTRACT

Although clusters of cataclastic deformation bands may represent potential barriers or baffles to reservoir fluid flow, their processes of formation remain debated. In this work, we rely on an integrated field study at seven sites to describe the extent of clusters, their morphology and their density of deformation as a function of several parameters: the tectonic loading and the burial depth of deformation, the Andersonian stress regime and the lithology of the sandstone. We perform granular analysis to improve the understanding of microscopic process of cluster development. In agreement with previous works on cataclastic deformation bands, our results reveal that the tectonic loading constrains the extent and the morphology of the clusters. Extensional tectonics favors the formation in normal Andersonian stress regime of series of hundreds of meter long, thin and dense clusters, forming kilometer long networks. Contractional tectonics favors the formation in strike-slip regime of tens of meter long, medium clusters, and more rarely the formation in thrust regime of tens of meter long, low-density, thick clusters. The clusters formed in contractional tectonic settings are sparse. Our analysis of the porosity and shape evolution of the clasts with increasing deformation corroborates the hypothesis of strain hardening of the band by combined increase in particle coordination and roughness of the clasts, and the potential cementation induced by the cataclasis. We hypothesize that this band hardening associated with the variable degree of dilatancy at the band edge controls the development of the cluster and determines the different macroscopic morphologies of clusters depending on their tectonic loading. We find that, in extensional tectonics, the formation of a major slip-surface (faulting) is independent of the cluster thickness and can occur at any stage of thickening. Eventually, since 15% and 79% of the bands/slip-surface of the clusters have permeabilities close to or lower than $1x10^{1}$ mD, we confirm that clusters may be significant baffles, particularly in extensional tectonics, if the vertical continuity of the cluster in the sandstone is important.

INTRODUCTION

Deformation by faulting represents a wide field of study in structural geology due to the academic interest of understanding the involved processes, and linked to resource production since faults can form major drains or barriers for fluids (Caine et al., 1996; Aydin, 2000; Faulkner et al., 2010; Bense et al., 2013). Faults result from a local or regional brittle deformation induced by tectonic stresses at the Earth's crust scale (Scholtz, 2002). They generally include one or multiple core zones, accommodating most of shear displacement and are surrounded by damage zones containing fractures or deformation bands depending on the initial porosity of the rock (Sibson 1977; Caine et al., 1996; Wibberley et al., 2008; Savage and Brodsky, 2001).

Because porous sandstones represent excellent geological reservoirs for water, oil or gas resources, including CO_2 sequestration, numerous studies have been conducted to characterize the properties of faults and faulted rocks in such materials. In porous rocks and sediments, deformation is localized in the form of tabular structures referred to as deformation bands, sometimes densely clustered and displaying a slip surface (e.g. Wibberley et al., 2007; Fossen et al., 2017 and references within). Many of the deformation bands in porous granular materials involve shear and compaction, implying the process of cataclasis, which is characterized by an important decrease in grain size where grains are rearranged by rolling and splitting due to stress concentrations at the grain-grain contacts (Engelder, 1974; Gallagher Jr et al., 1974; Aydin, 1978). Most of the cataclastic bands encompass lower porosity and permeability compared to their host rock (Pittman, 1981; Antonellini and Aydin, 1994; Taylor and Pollard, 2000; Fisher and Knipe, 2001), with a permeability that can be reduced up to 5 orders of magnitude in the most severe cases (Fossen and Bale., 2007; Ballas et al., 2014). The cataclasis tends to localize under the form of clusters of deformation bands in extensional tectonics whereas it tends to distribute under the form of arrays of conjugate sets of individual deformation bands in contractional tectonics (Ballas et al., 2015; Soliva et al., 2016). Despite this broad knowledge of deformation in porous sandstones, the development of clusters of deformation bands and their potential evolution to faults are still poorly understood (Nicol et al., 2013; Fossen et al., 2017).

In our study, we focus on the clusters of deformation bands to describe the parameters constraining their process of formation, their geometry and their microstructure. Our investigation consists of an integrated field study of clusters, combining seven localities where deformation occurred in different tectonic loadings, different depths of deformation and different sandstones. To reach our objectives, we performed quantitative and qualitative macro- and microstructural analysis on several tens of clusters. Petrophysical measurements were performed to illustrate the impact of the complex deformation represented by the clusters on the reservoir fluid flow.

GEOLOGICAL SETTINGS

Given the large number of sites studied in this work, we chose to describe here the succinct geological setting for each site. A more detailed and illustrated version is available in Supplementary document 1[1].

[1] In the thesis manuscript, the "Supplementary material 1" corresponds to section 2.1 (Geological settings)

The sites of Bédoin (quarry), Boncavaï (quarry) and St Michel (outcrop) are all located in the South-East Basin of Provence (France). The site of Bédoin is located 1.5 km Northwest of the village of Bédoin, the site of Boncavaï is located 4 km Northeast of the town of Mornas and the site of St Michel is located 5 km East of the town of St-Paul-Trois-Châteaux. All study sites are located in unlithified quartz-rich sands, deposited in deltaic to aeolian environments; their porosity varies from 36 to 38%. At Bédoin, the Cenomanian sandstone is at least 30 m thick; at Boncavaï and St Michel, the Turonian sandstones are 10 to 150 m thick (Ferry, 1997; Saillet and Wibberley, 2010; Ballas et al., 2012, 2014). The South-East Basin has been affected by three main tectonic episodes (Arthaud and Séguret, 1981; Roure et al., 1992; Séranne et al., 1995; Champion et al., 2000): (1) the N-S Pyrenean-Provencal contraction from middle Eocene to Early Oligocene, (2) a NW-SE extension corresponding to the Gulf of Lion rifting from the middle Oligocene to Early Miocene, and (3) the NE-SW Alpine contraction from the Miocene to Quaternary. At the Boncavaï site, the extensional deformation happened during the Gulf of Lion rifting between 100 and 300 m of burial (Ferry, 1997; Saillet, 2009; Ballas et al., 2013). The studied deformation structures were formed in normal Andersonian stress regime. Most of the bands consist of Compactional Shear Bands (CSB). The study site is located between the Montmout and Bollène normal faults linked to the Gulf of Lion rifting (Saillet, 2009; Schultz and Soliva, 2012). At St Michel, the deformation occurred during the Pyrenean-Provencal contraction at a depth of 0 to 200 m (Ferry, 1997) in a zone where no major fault is known. The studied deformation structures were formed in strike-slip Andersonian stress regime. The bands mostly consist of CSB. At Bédoin, regional and local stratigraphy studies permit constraining the cataclastic deformation as occurring during the Pyrenean-Provencal contraction at a depth estimated between 0 and 200 m (Ferry, 1997; Saillet, 2009; Philit et al., 2015). The studied deformation structures were formed in strike-slip stress Andersonian regime. Almost all the bands are CSB. The study site is located near the junction of three master faults: the sinistral-normal Nîmes Fault 10 km to the West, the dextral-normal Salon-Cavaillon Fault about 10 km to the South, and the major Ventoux-Lure Thrust, located a few km North.

The site of Blankenburg is located Northeast of the Hartz Mountains (Germany), in the southwestern part of the Blankenburg Basin. The study site focuses on a thrusting subvertical intensely cemented sandstone interval, regionally known as the Teufeulsmauer, locally examined in the town of Blankenburg. The outcrop exposes quartz-rich cemented sandstones from the Heidelberg Formation of Coniacian-Santonian age, with a total thickness ranging from 400 to 600 m, consisting of shallow marine deltaic deposits (Voigt et al., 2004; French et al., 2012; Klimczack and Schultz, 2013). The porosity of the formation prior deformation was about 30%. The southwestern part of the Blankenburg Basin was folded during the contraction of the Hartz Basement leading to thrust deformation during Coniancian to Early Campanian, after which cementation occurred (Fischer et al., 2013). The studied deformation structures were formed in thrust Andersonian stress regime. Most of the bands consist of CSB. Deformation occurred between 0 and 800 m burial (from the interpretation of the geological cross-section proposed by Klimczack and Schultz, 2013). The study site is located above a thrust fault propagating from the basement.

The site of Cummingston is located between the towns of Burghead and Cummingston, on the Moray coast, in Scotland. The outcrop exposes quartz-rich sandstones from the Hopeman formation of Permo-Triassic age, with total thickness ranging from 200 to 400 m and consisting of

aeolian deposits (Shotton, 1956; Glennie and Buller, 1983; Roberts et al., 1990; Quinn, 2005; Al-Hinai et al., 2008). The porosity of the formation prior deformation was about 30%. The site is neared by a major normal fault to the South. Similarly to the many normal seismic-scale structures in the Moray Firth, the deformation is believed to have occurred during the pre-Jurassic to Late Jurassic rifting at a depth of about 500 m (Underhill, 1991; Edwards, 1993; Glennie and Underhill, 1998; Quinn, 2005; Al-Hinai et al., 2008). Contrary to other faults in the Moray Firth, the deformation at Cummingston do not display signs of oblique reactivation during Paleocene and Eocene. The studied deformation structures were formed in normal Andersonian stress regime. Most of the bands consist of CSB.

The site of Goblin Valley is located in the San Rafael Desert (Southeast of the San Rafael Swell), Northeast of the Goblin Valley State Park, about 20 km North of the town of Hanksville (Utah). The site exposes the Middle Jurassic Entrada formation of total thickness ranging from 63 to 135 m, made of tabular fine-to-coarse aeolian and foreshore sandstone, often including a up to 20% of oolites (carbonate) (Rigby and Beus, 1987; Schultz and Fossen, 2002; Johansen and Fossen, 2008; Doelling et al., 2015). The porosity of the formation prior deformation was about 26%. The Entrada formation comprises thin layers of silt to clay (10 to 30 cm thick each). Although the region is marked by the Laramid orogeny during the Upper Cretaceous to the Eocene (responsible for the formation of the Sand Rafael Swell a few km to the Northwest of the site), the deformation in the Entrada sandstone was formed during extensional tectonics from the Oligocene linked to the Basin and Range extension. The studied deformation structures were formed in normal Andersonian stress regime. Most of the bands consist of CSB. The possible burial at deformation ranges from 1140 - 2000 m (Doelling et al., 2015).

The site of Buckskin Gulch is located next to the southern border of Utah, midway from the towns of Kanab (Utah) and Page (Arizona), South of the Hwy 89, within the N-S trending East Kaibab Monocline. The site is made of the Lower Jurassic Navajo formation consisting of aeolian sandstones of local total thickness of 250 to 500 m (Fossen et al., 2011; Doelling and Willis, 2006). The porosity of the formation prior deformation was about 34%. The Buckskin Gulch area underwent contractional deformation during the Upper Cretaceous to the Eocene Laramide Orogeny. The studied deformation structures were formed in thrust Andersonian stress regime. Most of the bands consist of Shear-Enhanced Compaction Bands (SECB). Due to the spatial stratigraphic thickness variations (Doelling and Willis, 2006; Doelling, 2008), the deformation depth is poorly constrained and is comprised between 950 and 2600 m. The reactivation of a former normal fault is known farther West (Mollema and Antonellini, 1996; Schultz, 2011; Brandenburg et al., 2012) but does not seem to propagate directly under the study site.

METHODOLOGY

According to previous descriptions in the literature, we propose the following definition for the "*clusters of deformation bands*" or "*clusters*". Strictly speaking, a "*cluster of deformation bands*" (or "*cluster*") corresponds to the grouping of two or more bands (as used in Fossen and Bale, 2007) and accounting for at least 10% of band thickness (based on a usual frequency of 20-30 bands per meter reported by Johansen and Fossen, 2008 and a typical band thickness of about 4 mm as shown

in Wibberley et al., 2007). "*Clusters*" may or may not include a slip-surface. "*Clusters*" are generally distinguished from "*networks of distributed deformation bands*" or "*band arrays*" where the band frequency is lower than 20 bands per meter. They are also distinguished from "*bands in ladder*". In this study, to consider structures that could potentially hinder fluid flow, we consider clusters displaying a thickness of 10 cm (e.g. Fig. 1). In our data, we report values for structures thinner than 10 cm and still consider them as a clusters when the narrowing of the structure is local (the structure thickens again laterally), or when the cluster ends laterally, forming a tip. Individual deformation bands typically accommodate millimeter to a few centimeter displacements (e.g. Wibberley et al., 2007). As introduced by Wibberley et al. (2007), we use the "*band density*" of a cluster, which is the "*total band thickness*" divided by the "*cluster thickness*", to evaluate the deformation within clusters. Although we ignore the interband deformation (which is small but not zero - Lanatà, 2014), we believe that this approach is more accurate than simply counting the number of bands in the deformation structures as it is traditionally done (e.g. Soliva et al., 2016 and references within). "*Clusters thicknesses*" and the "*band thicknesses*" were measured through scanline measurements with millimeter ruler precision. Clusters where recognized in the field and their length was measured through satellite image mapping where the image resolution permitted measurements with an error lower than 5 meters. In the case of the site of Blankenburg, where a part of the cluster is under vegetal cover, the end of the cluster has been reported by a GPS point.

Figure 1. (a), Example of a cataclastic deformation band cluster at Goblin Valley. We see that the length of the cluster can be significant. (b) Example of a cluster section seen in the shear plan at Goblin Valley. On this specific case, the offset of the bands is visible due to the presence of markers in the sandstone formation.

The host rock grain size was measured either visually with the grain size reference chart of the American Stratigraphic Company or through laser diffraction measurements on selected samples using Coulter LS 13320 in laboratory. The host rock grain size at a scanline location is given as the average host rock grain size along the scanline.

Surface permeabilities were obtained through TinyPerm II NER portable air-permeameter device (pressure recovery system) and directly measured in the field on the surface of the bands. The resolution of the device does not permit the quantification of permeability higher than 5×10^4 mD. For each type of rock, the permeability has been measured at least twice for measurements exceeding 10 minutes, or more for shorter measurements. This time limitation constrains the minimal permeability quantification to approximately 5×10^{-1} mD. Note that the absolute values of permeability obtained with this method may be different from values obtained through other permeability assessment method such as Hassel cell gas permeameter for instance (e.g. Ballas et al., 2015). In particular, Fossen et al. (2011) showed that the Tinyperm measurements tend to overestimate the permeability by ~ 1.8 times compared to standard gas plug permeability method. This overestimation is certainly due to slight pressure leakage between the surface of the band and the head of the device where the pressure is applied.

To get an insight of the microscopic localization of deformation, we sampled the host rock and a representative section of cluster at each site. The samples of the representative sections measure between 150 and 400 mm in thickness. The analysis of more than 40 thin-sections of the representative sections and host rocks allowed us to create a microscopic classification, distinguishing seven qualitative categories of deformation for each sites. The category (0) corresponds to the host rock and is sometimes attributed to interband material when no deformation is observed. Categories (1) through (3) correspond to increasing deformation of interband. Category (4) corresponds to diffuse deformation bands. Category (6) corresponds to very discretized bands. Category (5) corresponds to rather discretized bands with a visual aspect comprised between (4) and (6). Based on this classification, we report the different degrees of deformation quantitatively as the degree of cataclasis (indicated as linked to the shear strain by Ballas et al., 2012) and compaction for all the categories of cluster representative section. The compaction was analyzed from scanning electron microscopy (SEM) in backscattered electron (BSE) imaging; the cataclasis imaging was obtained through microscopic cold cathodoluminescence (CL) imaging so as to distinguish the quartz cements when present. In both compaction and cataclasis analysis, the image processing was performed using the Fiji software (gray-scale spectrum analysis in the case of the compaction processing, and manual particle delimitation with the limit of resolution of 20 µm in the case of the cataclasis processing). The compaction was calculated with the intergranular volume (*IGV*, see Ehrenberg, 1989; Paxton et al., 2002) of the deformed rock compared to the host rock, subtracting any potential post-deformation cementation. The cataclastic matrix is considered as the material formed of particles whose Feret diameter is smaller than $1/10^{th}$ of the modal grain diameter D_{mod} measured in the host rock; the degree of cataclasis corresponds to the area percentage occupied by the cataclastic matrix. For a given representative section, the degree of cataclasis of the whole cluster is calculated as the weighted arithmetic mean of the degree of cataclasis of categories (0) through (6); the degree of cataclasis of the bands only is calculated as the weighted arithmetic mean of the degree of cataclasis of categories (4) through (6). The compaction of the whole cluster is calculated

as the sum of compaction of the categories (0) through (6); the compaction of the bands only is calculated as the sum of compaction of categories (4) through (6). Including all sites, the measurements of deformation intensity represents an analysis of a length of 142 cm of representative cluster section, an area of 2300 mm^2 of thin-section for the examination of the porosity, and an area of 208 mm^2 of thin-section for the examination of the degree of cataclasis.

The image analysis of the deformed rocks also allowed us to measure two shape descriptors of the cataclastic particle population (Cox and Budhu, 2008). The Roundness gives an estimate of how elongate the particle is (form) and is expressed as follows:

$$Round = 4 \times \frac{Area}{\pi \times [Major\ axis]^2} \quad (1)$$

The Solidity gives an estimate of how "ruffled" the grain surface is (morphological roughness) and is expressed as follows:

$$Circ = \frac{Area}{Convex\ area} \quad (2)$$

The sorting of the rocks was obtained from the grain size distribution data, either from laser diffraction measurements for the host rock or from CL image measurements for the deformed rocks, using the formula of the Inclusive Graphic Standard Deviation (Folk and Ward, 1957):

$$s = \frac{\frac{\log(d_{84})}{\log(2)} - \frac{\log(d_{16})}{\log(2)}}{4} + \frac{\frac{\log(d_{95})}{\log(2)} - \frac{\log(d_5)}{\log(2)}}{6.6} \quad (3)$$

where d_5, d_{16}, d_{84} and d_{95} are the diameters of the largest particles from the cumulative particle population occupying 5, 16, 80 and 95% of the cumulative sample area., respectively. Note that the sorting is improved with decreasing sorting values and can be qualitatively describes as follows: from 0 to 0.35: very good; 0.35 - 0.5: good; 0.5 - 1 moderate; 1 - 2: poor; 2 - 4: very poor: >4: extremely poor.

OBSERVATIONS

Cluster general characteristics

Field studies of the seven different study sites allow determining the general dimensions of the cluster of deformation bands, in the limit of the truncation effect induces by the sometimes limited extent of the exposures (note that the view showing the mapped clusters at the studied sites is available in the Supplementary material 2[2] through Fig. A1-A6, expect Goblin Valley which is presented directly in the article).

In extensional tectonics (exclusively normal Andersonian stress regimes in our study - Fig. 2a), clusters of deformation bands measure 12 to 270 meters in length. In particular, the two sites of

[2] In the thesis manuscript, the "Supplementary material 2" is available after this section (at the end of this article manuscript).

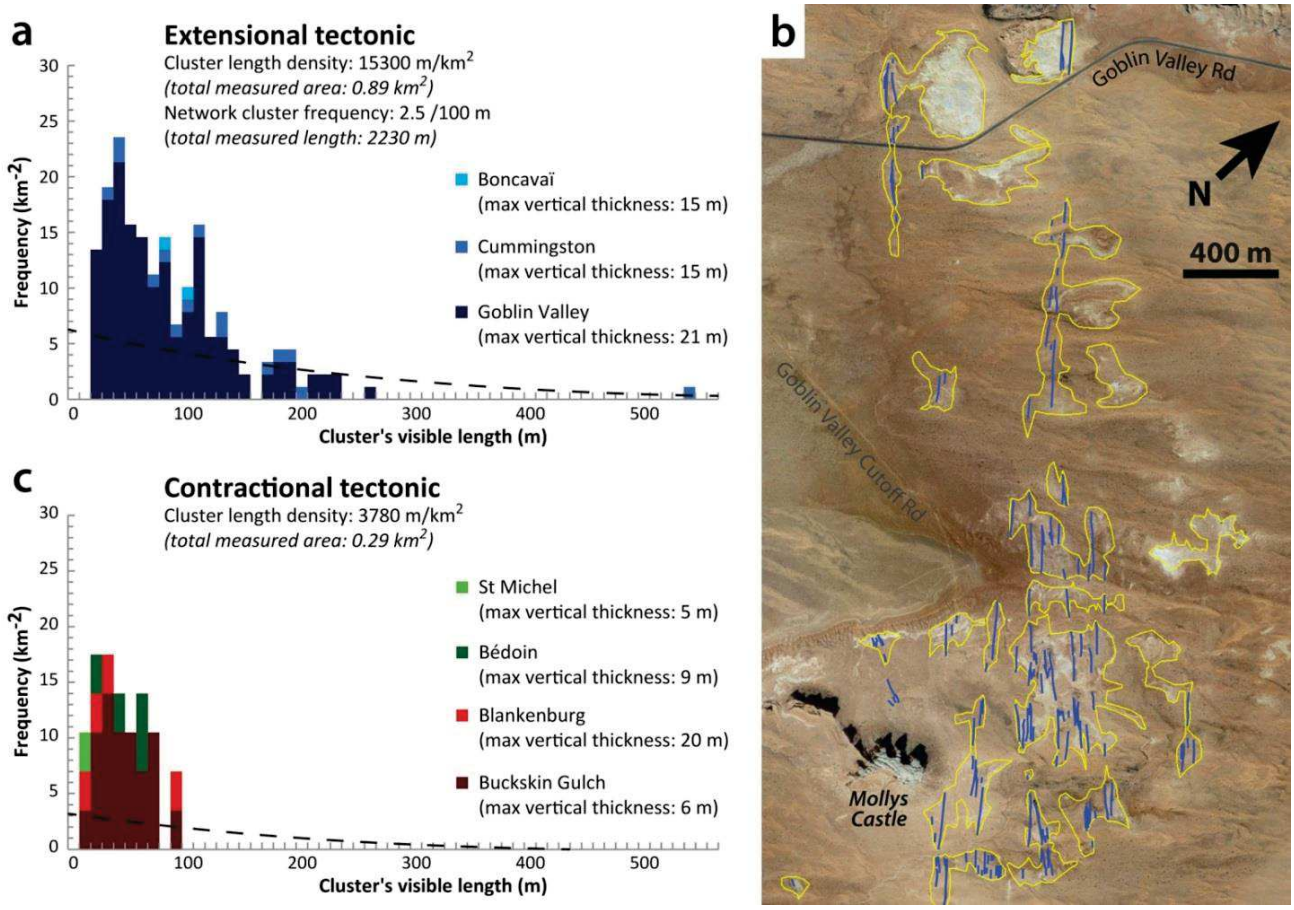

Figure 2. (a) Graph of the cluster frequency in extensional tectonics. The frequency is normalized to the total investigated cropping out areas for all extensional sites together. The cluster density in term of length of cluster per square kilometer is also provided. Note that the cluster length measurements only account for clearly cropping out clusters; the dashed lines are interpretations of the likely presence of actually connected portions of smaller clusters. (b) Example of the large cluster network in the Entrada formation at Goblin Valley (extensional tectonics). The clusters are marked by blue lines; the areas delimited in yellow correspond to the clearly cropping out areas. (c) Graph of the cluster frequency in contractional tectonics. The frequency is normalized to the total investigated cropping out areas for all contractional sites together. The cluster length measurements only account for clearly cropping out clusters; the dashed lines are interpretations of the likely presence of actually connected portions of smaller clusters.

Cummingston and Goblin Valley display connecting networks of conjugate clusters of at least 1 to 3 km in length (e.g. Fig. 2b). These networks are 60 to 800 m wide at least, respectively. A count of the clusters along more than 2.2 km of scanlines perpendicular to the network indicates an average cluster frequency of 2.5 clusters per hundred meters. In extensional tectonics, accounting for all sites (total investigated area of 0.89 km^2), we obtain a total cluster length density of 15300 $m \cdot km^{-2}$.

In contractional tectonics (thrust and strike-slip Andersonian stress regimes in our study - Fig. 2c), where several exposures of tens to a hundred of meter wide are available (i.e., Bédoin and Buckskin Gulch), we note that the apparent clusters tend to be shorter, measuring 5 to 90 meters in length. They are more isolated than in extensional tectonics and do not form networks. In contractional tectonics, accounting for all sites (total investigated area of 0.29 km^2), we obtain a total cluster length density of 3780 $m \cdot km^{-2}$.

The main part of the cluster length is made of a rather continuous body of gathered and connecting deformation bands (Fig. 3a). In extensional tectonics, clusters may laterally (out of the

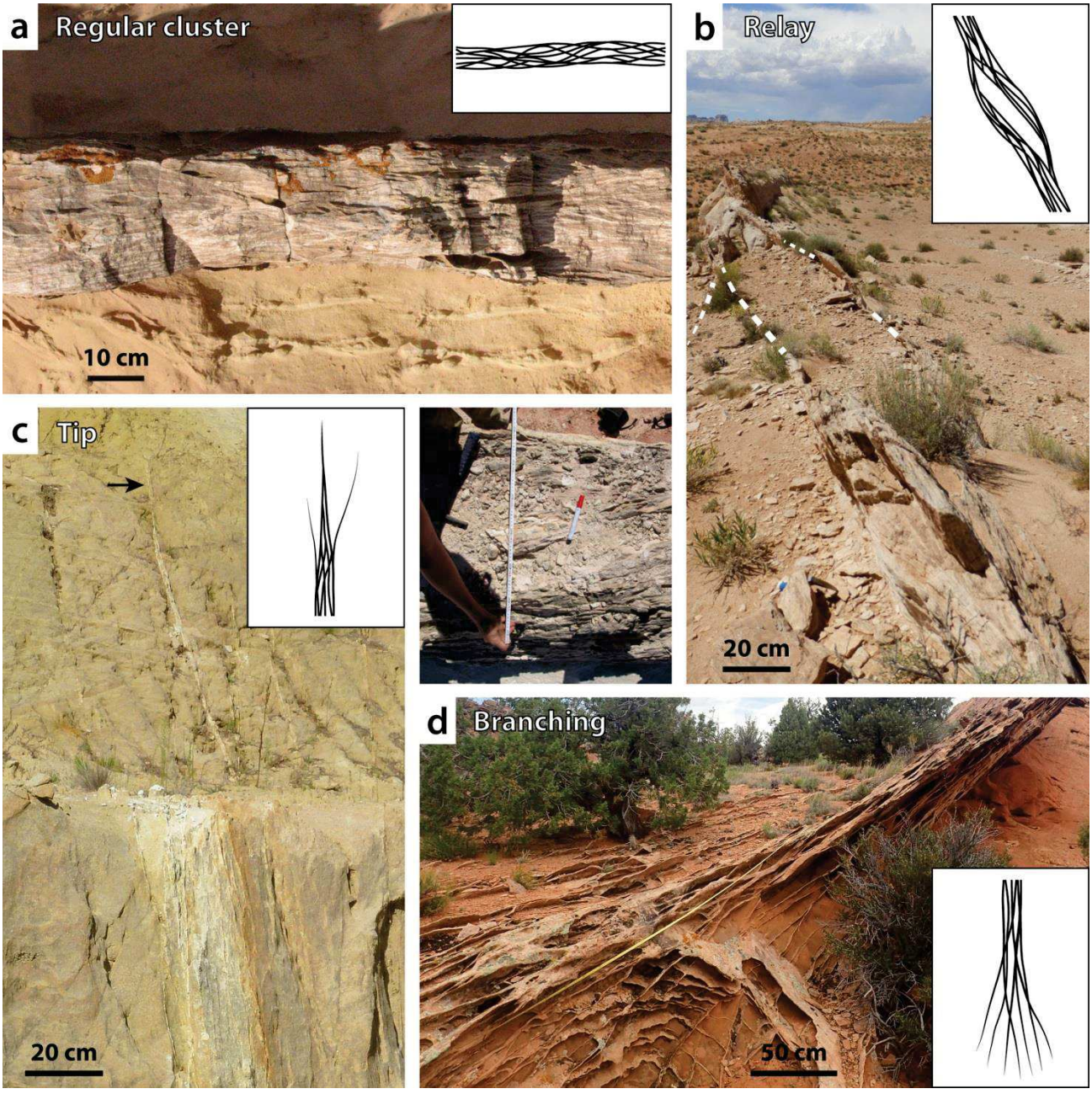

Figure 3. Illustration of the variety of cluster morphologies observed in the field. (a) Regular cluster, consisting of a body of gathered deformation bands (Goblin Valley site). (b) Relay zone, representing a connection between two clusters as frequently observed where the cluster network is well developed (Goblin Valley site). (c) Tip ending, consisting of progressively gathering bands eventually disappearing in the sandstone formation. (d) Branching ending, consisting of dispersing deformation bands within a few tens of meter length (Buckskin Gulch site). In the center image, we are measuring the width of a cluster (Bédoin site).

shear plane) connect to each other through relay zones (Figure 3b). In contractional tectonics, no cluster connection is observed, apart from conjugate sets that connect vertically (in the plane of shear). The clusters endings display two types of geometry: (i) a tip ending (Fig. 3c), where the bands progressively gather into a single band which eventually disappears; (ii) a branching ending (Fig. 3d), where the bands are splitting off over distances of a few tens of meters.

Although the identification of displacements was rare due to the lack of markers in the studied sandstones, we record here the displacement along a 250 m long cluster (Fig. 4),

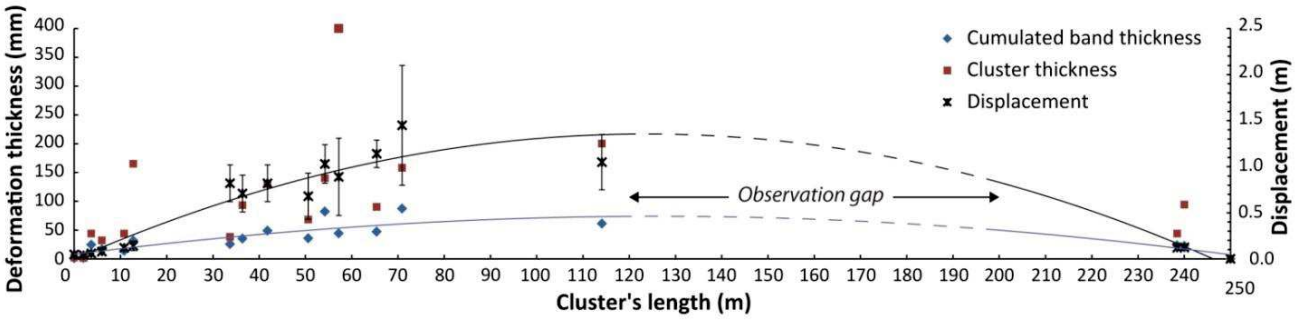

Figure 4. Graph of the geometrical attributes of a typical cluster at Goblin Valley in terms of deformation and displacement. The cluster thickness is represented with red squares; the total band thickness is represented with blue diamonds; the displacement is displayed with its error bar and is represented with black crosses. The trend curves are given as second order polynomial functions for the total band thickness (blue) and the displacement (black).

representative of the typical morphology of cluster at Goblin Valley. The cluster contains no major slip-surface. The cluster displacement increases with the total band thickness from 0 at the tip of the cluster, to a maximum of 1.45 m at 71 m where the total band thickness is 87 cm. The presented cluster includes a gap in observation between 120 m and 200 m that may correspond to a continued cluster or to a relay zone. We observe that the cluster displacement returns to 0 at 250 m as the cluster disappears. Important cluster thickness variations are recorded locally along the length of the cluster. For instance, the cluster thickness varies from 68 mm to 400 mm in less than 6 m from 51.6 to 57.2 m (Fig. 4). On the other hand, the total band thickness in the same interval is locally more constant: it varies between 36 and 82 mm in the same interval.

Inner cluster characteristics

Throughout the seven studied sites, we classify two macroscopic categories of bands entering the cluster composition (which simplifies the microscopic classification). The “diffuse band” (Fig. 5a-b) consists of a deformation discrete enough to be distinguished as a band compared to the interband deformed rock, and whose edges are diffuse (includes the category (4) and half of the category (5) of the microscopic classification). The “discrete band” (Fig. 5c-e), is a discrete deformation whose edges are rather sharp and where incipient striations are identified (its thickness is significantly lighter-colored than the diffuse bands) (includes the category (6) and half of the category (5) of the microscopic classification). We also include in the classification the “slip-surface” (Fig 5f-g), which is smooth and striated and that represents the interface between a band and the surface where a discrete displacement occurred. The “interband” is the interval of deformed rock between the bands in the cluster and is to be differentiated from the “host rock” (theoretically not deformed). The proportion of diffuse bands, discrete bands and slip-surfaces is given respectively for each site in Table 1.

Diffuse and discrete bands have typical lateral and vertical extent of tens of centimeters to a few meters; they end up either connecting with another band or being diffused in the interband thickness. The geometry of a band corresponds to a corrugated surface, with the axis of the corrugation aligned with the shear direction. In section, this result in an undulated geometry out of the shear plane (e.g. Fig. 3a) and is rather straight in the shear plane (e.g. Fig. 3c). A major slip-surface can measure tens to a hundred of meter in lateral and vertical extent, and frequently laterally coalesces in relay with

another slip-surface developed in a different part of the cluster thickness. The major slip-surfaces display relatively flat and straight planes.

Table 1. Summary of the frequency of band type based on the macroscopic classification at the studied localities.

Sites	Tectonic settings	Andersonian stress regime	Cluster band type frequency (%)		
			Diffuse bands	Discrete bands	Slip-surfaces
Boncavaï	Extensional	Normal	100	0	0
Saint Michel	Contractional	Strike-slip	61	39	0
Bédoin	Contractional	Strike-slip	84	16	0
Blankenburg	Contractional	Thrust	31	69	0
Cummingston	Extensional	Normal	85	14	1
Goblin Valley	Extensional	Normal	61	37	1
Buckskin Gulch	Contractional	Thrust	80	20	0

The permeability of the different structures introduced in the classification and the relative errors are presented in Fig. 6. The permeability of the host rocks at the seven sites broadly ranges between $5.0x10^{2}$ and $1.0x10^{5}$ mD. The cluster interbands have permeabilities comprised between $6.2x10^{0}$ mD at Blankenburg and $1.8x10^{3}$ mD at Bédoin (slightly higher than its respective host rock permeability). The diffuse band permeability is comprised between $3.7x10^{1}$ mD at Goblin Valley and $2.7x10^{2}$ mD at Boncavaï (diffuse band at St Michel, Blankenburg and Buckskin Gulch could not be measured). The discrete band permeability is comprised between $1.5x10^{0}$ mD at Blankenburg and $1.3x10^{1}$ mD at St Michel. The only two average permeabilities available for slip-surface are from Goblin Valley with $3.4x10^{-1}$ mD and Cummingston with $5.6x10^{-1}$ mD.

The cluster analysis through all types of sandstones yields information about the influence of the average host rock grain size on the average band thickness (individual strand) of a scanline (Fig. 7a). Accounting for the seven study sites, the average band thickness per scanline for the average host rock grain size of 90-100 µm ranges from 0.5 to 1.5 mm. The average band thickness evolves

positively with increasing average host rock grain size, ranging from 2 to 5 mm for an average host rock grain size of 590-600 µm. The average band thickness shows a similar distribution for an average host rock grain size of 790 µm. The band thicknesses of clusters formed in the three investigated Andersonian stress regimes appear randomly distributed on this plot. The consequence of thickening bands linked to an increase of host rock grain size is an apparent thickening of the cluster itself (Fig. 7b).

Distribution of the cluster deformation

Cluster's band density

Data of cluster thickness and cluster band density from 332 scanline measurements show two different patterns depending on the tectonic loading. In extensional tectonics (Fig. 8a, exclusively normal Andersonian stress regimes in our study), the band density decreases as the clusters thicken, mostly ranging from 0.20 to 0.70 in the thinnest clusters (ca. 5 cm), down to 0.15 to 0.30 for 72 cm

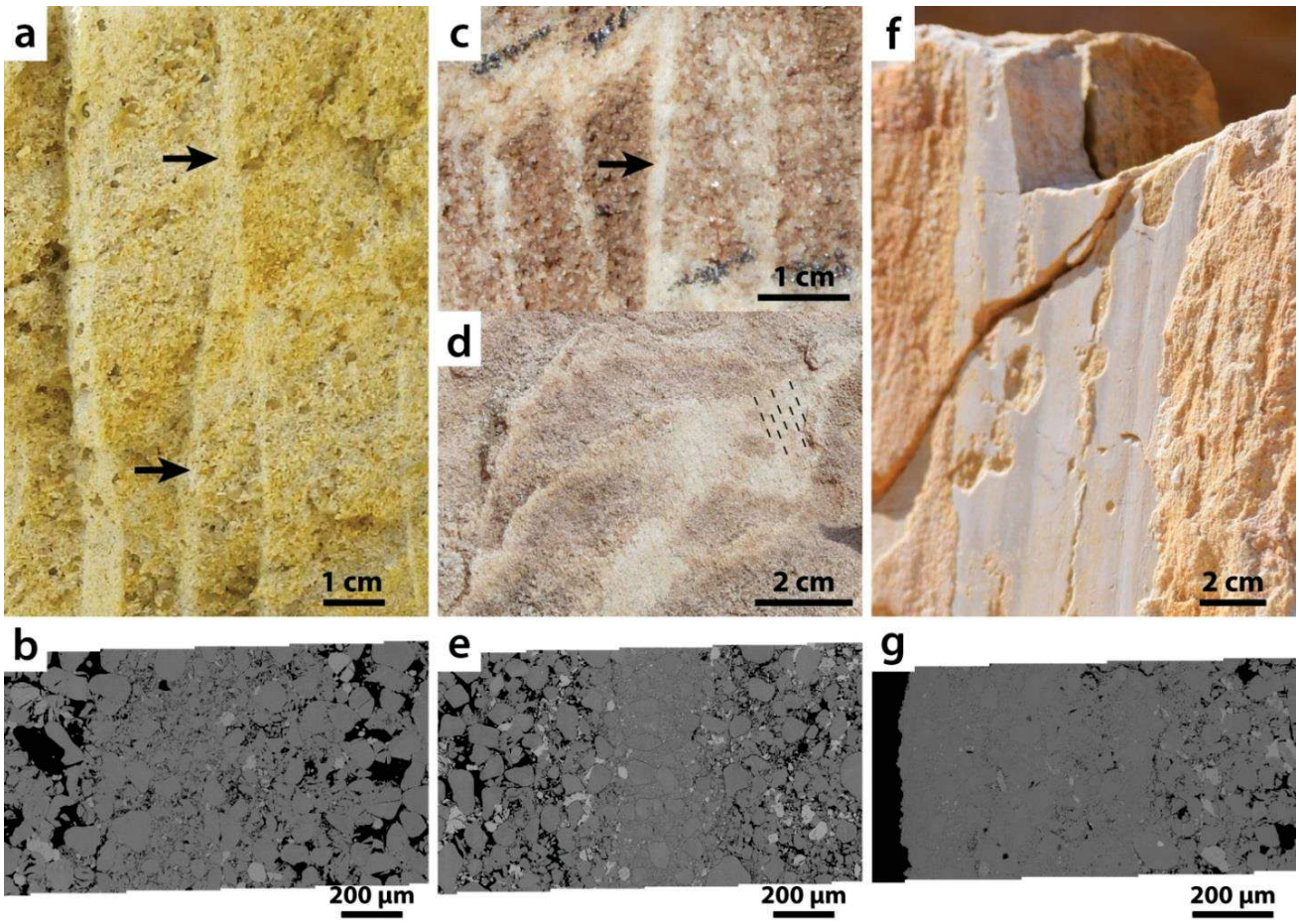

Figure 5. Illustration of the different categories of discretized deformation in the clusters. (a) Diffuse deformation band (arrows) at macroscopic scale and (b) at microscopic scale (scanning electron microscopy in backscattered electron – SEM-BSE). The diffuse deformation band has diffuse edges and commonly display a lesser degree of deformation. (c) and (d) Discrete deformation band (arrow) at macroscopic scale and (e) at microscopic scale (SEM-BSE). The discrete deformation band has rather sharp edges, is generally lighter than the regular deformation band. Often, incipient striation can be observed on its surface. They usually display a high degree of deformation. (f) Slip-surface at macroscopic scale and (g) at microscopic scale (SEM-BSE). Slip-surfaces are smooth, lineated and continuous surfaces accommodating an important displacement. The first millimeter of thickness under a slip-surface is highly deformed.

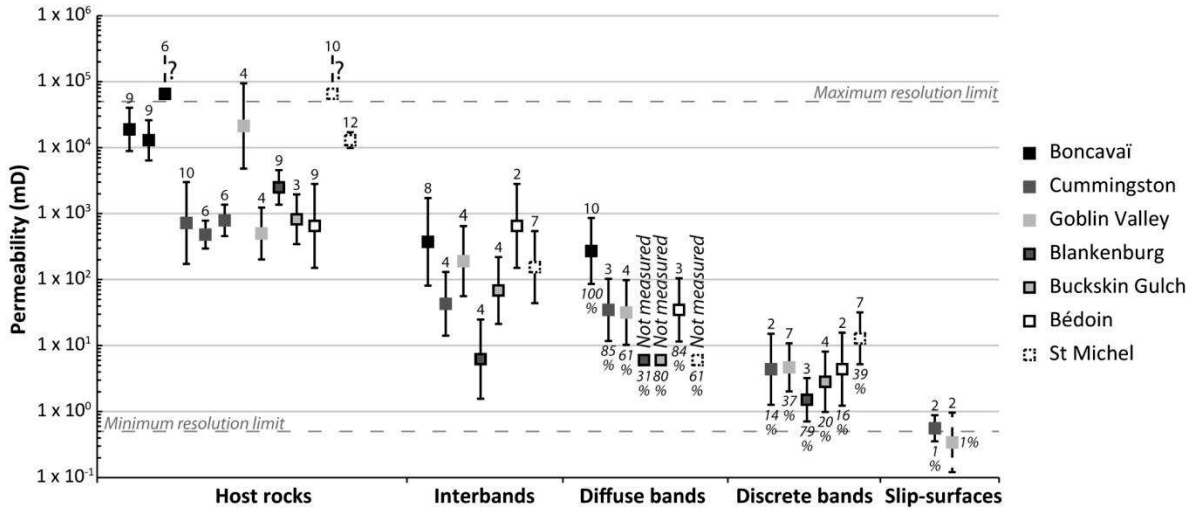

Figure 6. Plot of the Tinyperm permeabilities of the different studied structures at the study sites: The host rocks, the cluster interband intervals, the regular bands, the evolved bands and the slip-surfaces. The number of permeability measurement per type of structure is indicated with regular font above the measures; the percentage of band type per site is indicated in italic below the measures.

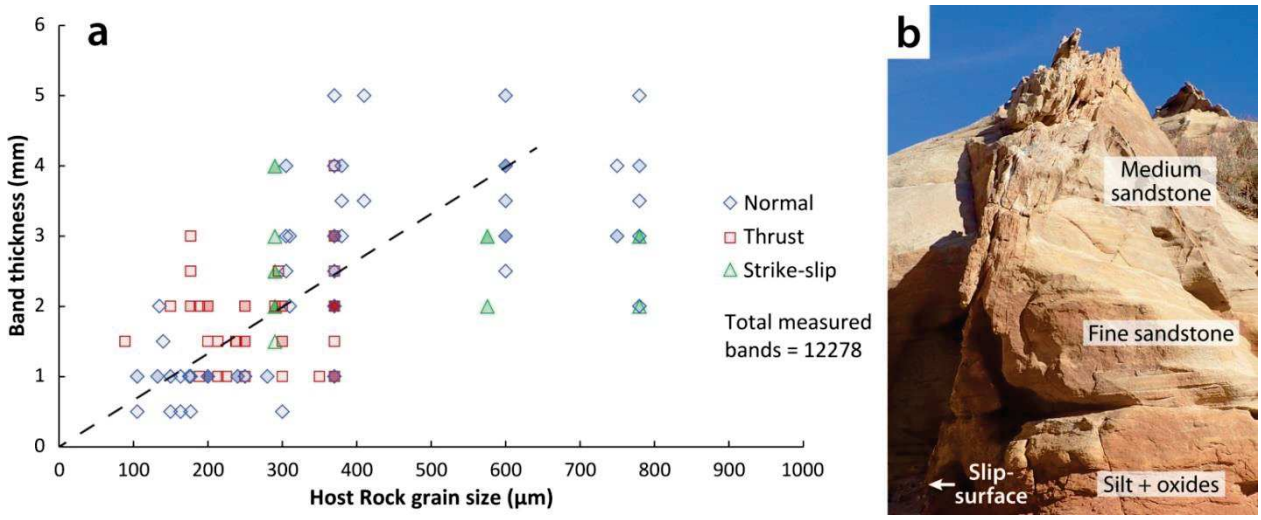

Figure 7. (a) Plot of the average band thickness in a cluster scanline as a function of the host rock grain size (average of the grain size as measured in the footwall and hanging wall for each scanline) for all Andersonian stress regimes and including the seven study sites. Blue-framed diamond markers represent the normal regime, red-framed square markers represent the thrust regime, green-framed triangle markers represent the strike-slip regime. Since data can be superposed, the markers have 10% opacity filling to allow the distinction of up to ten superposing markers. (b) Illustration of the thickening cluster as a function of its thickening bands and coarsening host rock.

thick clusters. The structures with band density lower than 0.10 and/or larger than 90 cm correspond to branching clusters (Fig. 3b). In contractional tectonics (Fig. 8b, strike-slip and thrust Andersonian stress regimes in our study), we observe two types of trends. The two sites deformed in strike-slip regime and the site of Blankenburg deformed in thrust regime display clusters whose thicknesses range from 5 to about 100 cm and whose band density are relatively constant, ranging from 0.18 to 0.55. On a different manner, the site of Buckskin Gulch deformed in thrust regime display clusters whose width ranges from 20 to 180 cm and whose band densities are low, ranging from 0.10 to 0.45. In this latter case, the structures with band density around or lower than 0.10 correspond to branching clusters. In both extensional and contractional tectonics, most of structures thinner than 5 cm correspond to cluster tips; the remaining part of the structures thinner than 5 cm correspond to local thinning of cluster sections. We note that the bands in clusters with band density higher than 0.40 are particularly well connected to each other (e.g. Fig. 3a).

Faulted clusters (including at least one slip-surface) are observed only in extensional tectonics. The representation of five faulted clusters as functions of their thickness, band density and the displacement of the faults is displayed in Fig. 9. We note that faulted cluster have a broad variety of thicknesses, ranging from 2 to 740 mm. Consistently to what we described in the previous paragraph concerning extensional tectonics, the thicker the clusters, the lower the band density of the cluster. We observe no correlation between the displacement, the band density and the thickness of the cluster.

Cluster's deformation degree

Microscopic deformation in the bands and interbands (Fig. 10) yields the following. In extensional tectonics, the representative cluster section from the site of Boncavaï shows a total cluster compaction of 19% and (arithmetic) mean degree of cataclasis in the cluster of 11%. The typical clusters from the site of Cummingston show an average cluster compaction of 12% and mean

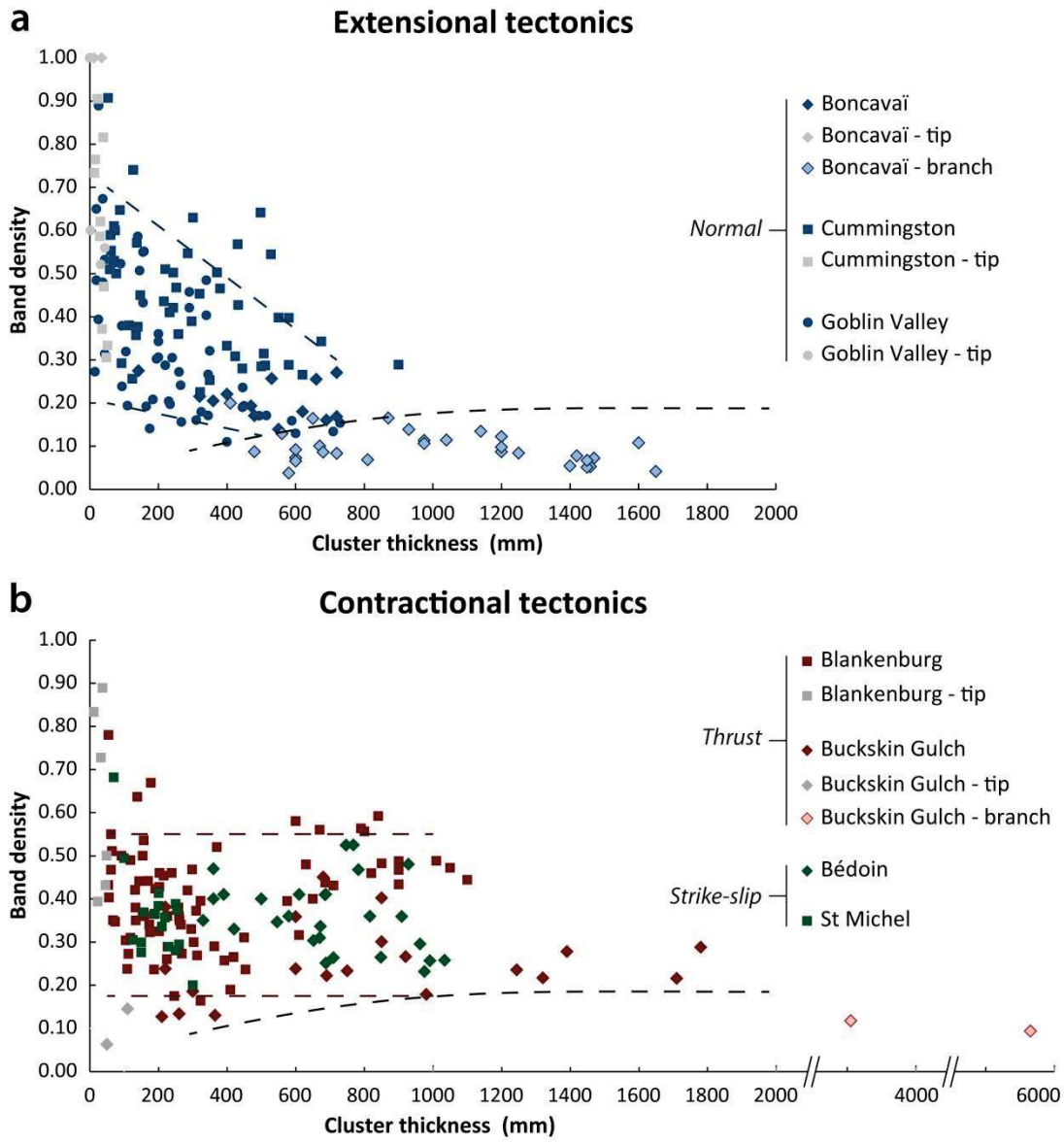

Figure 8. Graphs of the cluster band density as a function of the cluster thickness and the type of geometry of the cluster: tip (gray markers), regular cluster (filled markers) and branching cluster (framed markers). (a) Band density measured at the extensional tectonics sites (Boncavaï, Cummingston and Goblin Valley, all of normal Andersonian stress regimes). (b) Band density measured at the contractional tectonics sites (Blankenburg, Buckskin Gulch, Bédoin and St Michel; sites corresponding to thrust regimes are represented with red markers, sites corresponding to strike-slip regimes are represented with green markers). The black dashed lines marks out the average separation between the regular cluster domain and the branching cluster domain, based on the data observation.

degree of cataclasis in the cluster of 15%. The typical clusters from the site of Goblin Valley show an average cluster compaction of 16% and mean degree of cataclasis in the cluster of 15%. In contractional tectonics, the clusters from the site of Blankenburg show a total cluster compaction of 18% and mean degree of cataclasis in the cluster of 18%. The clusters from the site of Buckskin Gulch show a total cluster compaction of 21% and mean degree of cataclasis in the cluster of 3%. The clusters from the site of Bédoin show a total cluster compaction of 26% and mean degree of cataclasis in the cluster of 19%. The clusters from the site of St Michel show an average cluster compaction of 32% and a mean degree of cataclasis in the cluster of 33%. Relative to the whole

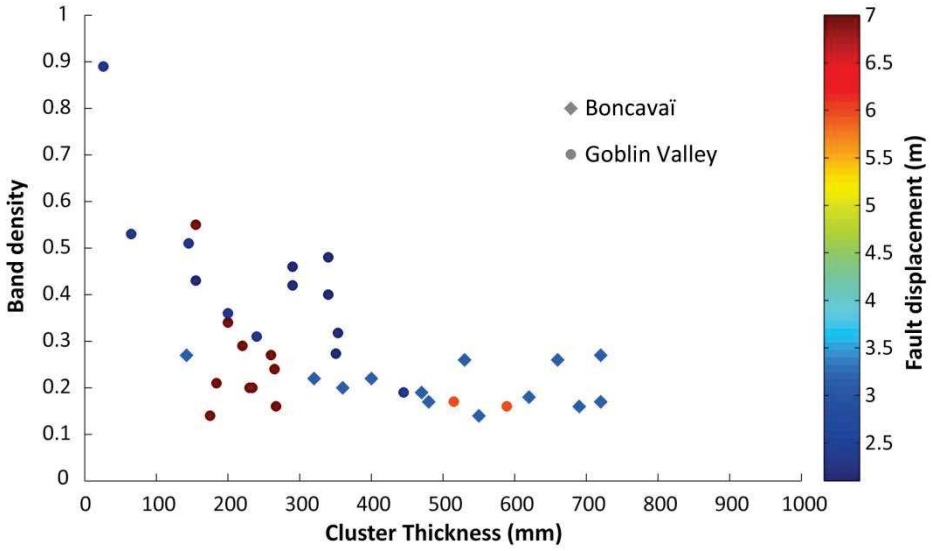

Figure 9. Graphs of the band density of faulted clusters (including at least one main slip-surface) as a function of the cluster thickness and of the displacement. Faults are exclusively observed in extensional tectonics systems, in particular at Boncavaï and Goblin Valley.

clusters, the bands reveal comparable ratios but with higher degrees of cataclasis and compaction, respectively. This indicates that individual bands absorb the majority of deformation.

We also noted that sealing quartz cements are frequently observed in the cataclastic bands and interbands (Fig. 11), with higher cementation as the degree cataclasis increases (see also Philit et al, 2015).

Sorting, porosity and grain shape

We present here the porosity, the sorting and the grain shape of the particles in the deformed material from the sites of Boncavaï, Cummingston, Blankenburg, Buckskin Gulch, Bédoin and St Michel.

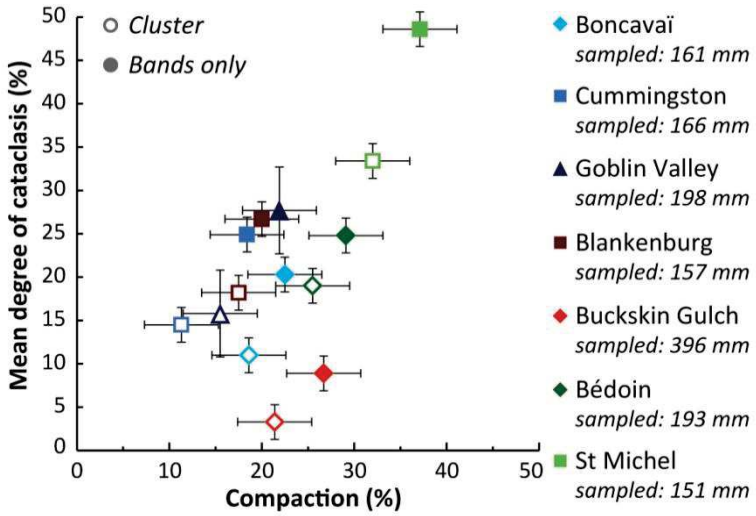

Figure 10. Plot of the arithmetic mean degree of cataclasis and compaction as measured through microscopic analysis along sections of representative clusters for each study sites. Note that we distinguished the degree of cataclasis and compaction in the whole section of the clusters (open markers) and in the bands only (filled markers). The sampled lengths used for the analysis are given of the graph; the corresponding measured surfaces are indicated in the text.

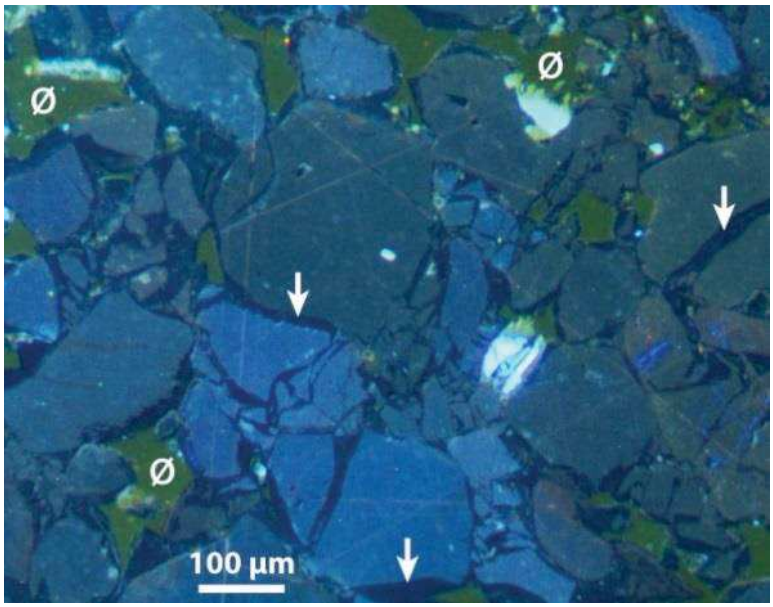

Figure 11. Example of quartz cements sealing a cluster interband at Cummingston in cathodoluminescence (CL).

Figure 12a presents an example of the distribution of the porosity in a cluster section (Goblin Valley, extensional tectonics), depending on the degree of deformation. Generally, we observe that the more deformation, the less porosity, although some interband interval display porosity nearing the host rock porosity (e.g. between 13 and 14 mm). The Fig. 12b presents the porosity of the different categories of deformed materials from the clusters representative sections of each site as a function of the degree of cataclasis. The porosity displays a negative correlation with increasing degree of cataclasis. We note that, for a same degree of cataclasis and until about 20% of cataclasis, the porosity in deformed materials from contractional tectonics sites is slightly lower than for the materials from extensional tectonics sites. The porosity seems to become almost nonexistent around 40% of cataclasis. Also note that, lowering porosity correlates with increasing sorting.

The sorting of the deformed materials of the sites and their host rocks is displayed in Fig. 12c. The grayed zone of the graph encompasses the data for which the sorting calculation is biased because the $d5$ values were lower than the minimum diameter resolution of 20 µm. The unknown $d5$ values were estimated proportionally to the first cumulative area known at the minimum diameter resolution. Concerning the non-biased interval of the plot (until about 20% of cataclasis), the sorting value of all sites describe a linear positive evolution with increasing degree of cataclasis. Except for Buckskin Gulch, all the data within this cataclastic interval represents interband deformation. The data in the biased zone (more than 20% of cataclasis) shows a sorting that keeps increasing with the degree of cataclasis but with an apparent inflexion to an asymptotic behavior towards 3.5 sorting values. Remark that this inflection may not be so pronounced if we consider that the resolution limit prevents from measuring a significant amount of small particles. Indeed, these underestimated small particles are likely contributing to a larger dispersion of the particle size population of the rock and therefore potentially increasing the sorting value. The data higher than 20% of cataclasis almost all correspond to deformation bands.

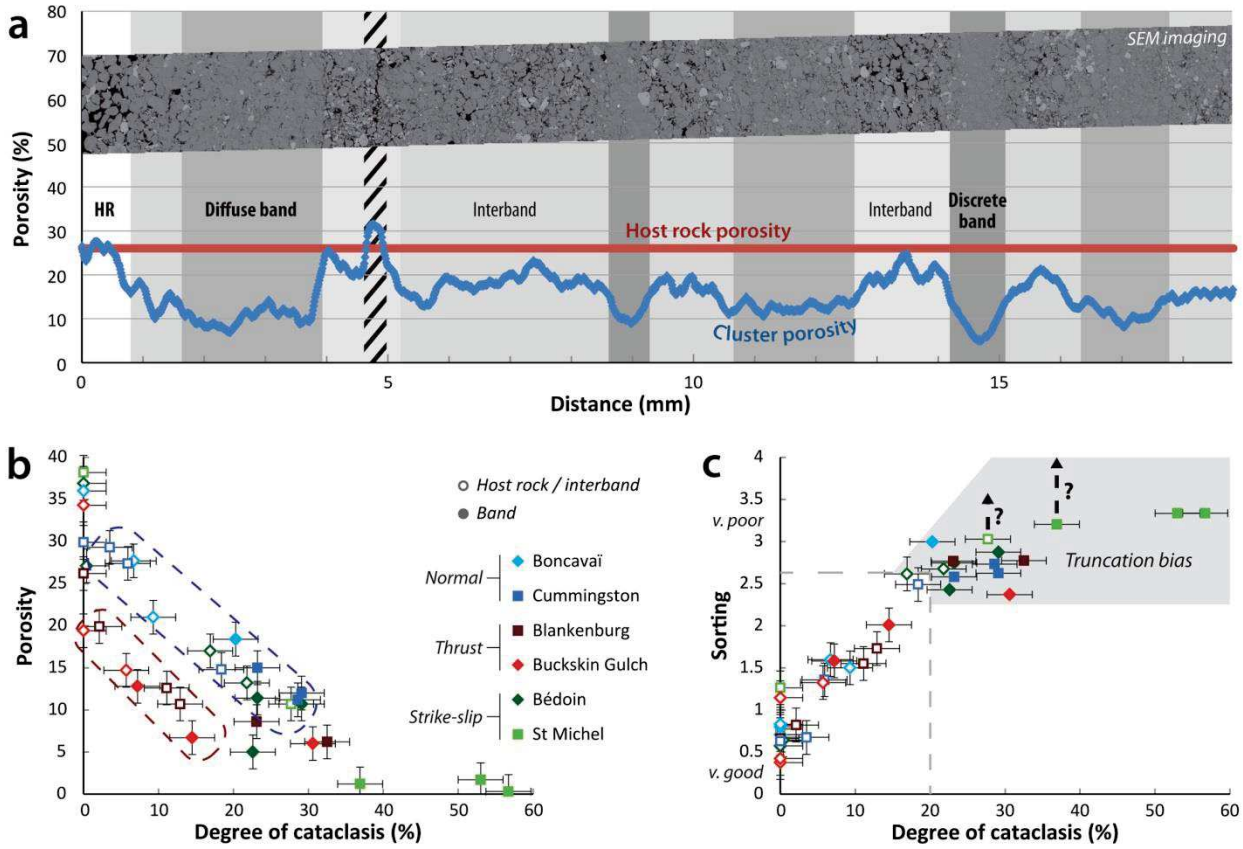

Figure 12. (a) Example of a cluster porosity distribution correlated with the cluster structure in SEM-BSE imaging. The interpretation of the band and interband intervals is indicated on the graph. We note that the porosity in some of the interband intervals is nearing the host rock porosity. The dashed interval corresponds to a zone affected by a fracture linked to the preparation of the thin section. (b) Plot of the porosity subtracted from the post deformation cementation (IGV) as a function of the degree of cataclasis of variably deformed rocks. The porosity of deformed material of all sites decreases with increasing cataclasis. We note that for a same degree of cataclasis (until 20% of cataclasis), the porosity of the deformation structures in contractional tectonics is further reduced. (c) Plot of the sorting of variably deformed rocks (from host rock to bands) as a function of the degree of cataclasis. The lower the sorting value, the better the sorting. The legend is common to (a) and (b).

An example of a typical grain shape evolution with the degree of cataclasis is given in Fig. 13 (site of Cummingston). The mean value of the roundness remains comprised between 0.536 and 0.604 (Fig. 13a through f). In this small range of value, we observe that the roundness firstly decreases from 0.575 to 0.536 during the first stages of cataclasis (from 3.5 to 5.9%). The roundness then increases until 0.604 at 23.2% of cataclasis and stabilizes around 0.603 at a maximum of 29.1% of cataclasis. The mean values of the solidity remain comprised between 0.908 and 0.927 without significant variation with increasing cataclasis. In Fig. 13 g through l, we note that the number of large particles (associated with roundness close to 0.6 – 0.7 and solidities close to 0.95) decreases with increasing degree cataclasis to yield an increasing amount of small particles. This grain shape evolution with deformation is similar at all sites: in all cases the initial roundness and solidity value of the initial grains are both partly increased and partly decreased as the diversity of the formed clasts increases. As a result, for all sites (Fig.14a&b), both the average roundness and the solidity remain comprised within small ranges of values. The roundness decreases during the first stages of deformation (from 0 to 8% of cataclasis) and then slightly increases with the degree of cataclasis until about 40% of cataclasis. The solidity expresses no clear correlation with the degree of cataclasis.

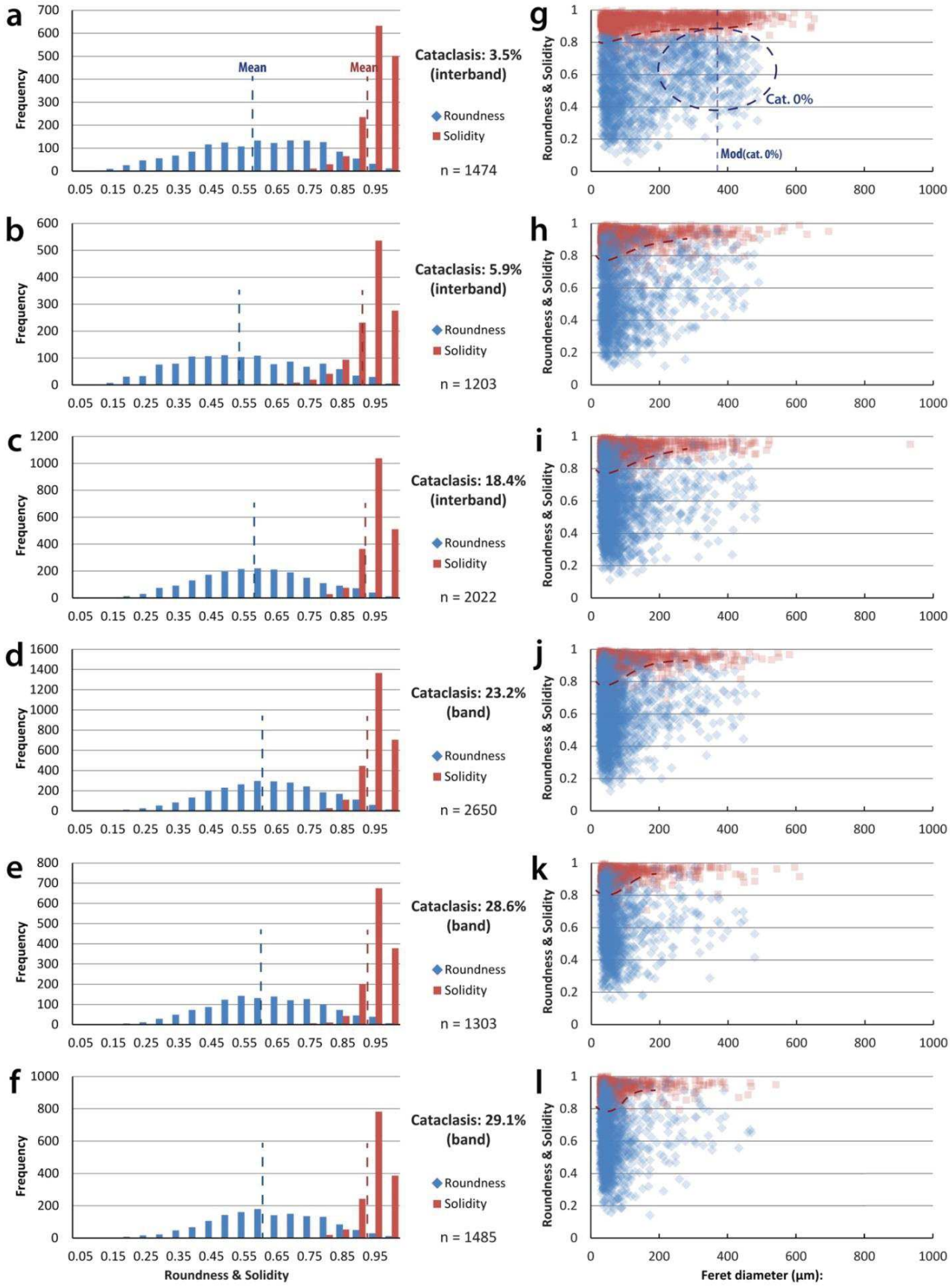
a
b
c
d
e
f
g
h
i
j
k
l
Frequency
Roundness & Solidity
Mean
Mean
Roundness
Solidity
Cataclasis: 3.5% (interband)
n = 1474
Cataclasis: 5.9% (interband)
n = 1203
Cataclasis: 18.4% (interband)
n = 2022
Cataclasis: 23.2% (band)
n = 2650
Cataclasis: 28.6% (band)
n = 1303
Cataclasis: 29.1% (band)
n = 1485
Roundness & Solidity
Cat. 0%
Mod(cat. 0%)
Feret diameter (µm):

Figure 13. Example of a typical evolution of particle shape with increasing degree of cataclasis (example of the site of Cummingston). (a-f) Distribution of the particle roundness and solidity frequencies for increasing degree of cataclasis. For the roundness shape descriptor, the value 1 describes a perfect circle; a roundness approaching from 0 describes an infinitely elongated particle. For the solidity, the value of 1 describes a particle with a totally convex hull; the presence of increasing concave parts in the particle hull lower the solidity. (g-l) Distribution of the particle roundness and solidity as a function of the Feret diameter. Each data point is represented with 20% opacity. The dashed red curve underlines the bottom limit of the zone where more than 4 values of solidity are overlain. In (g), the dashed ellipse (in blue) represents the estimated distribution of the pristine grains (cataclasis = 0%) centered on the modal grain size value of the host rock (dashed vertical blue line).

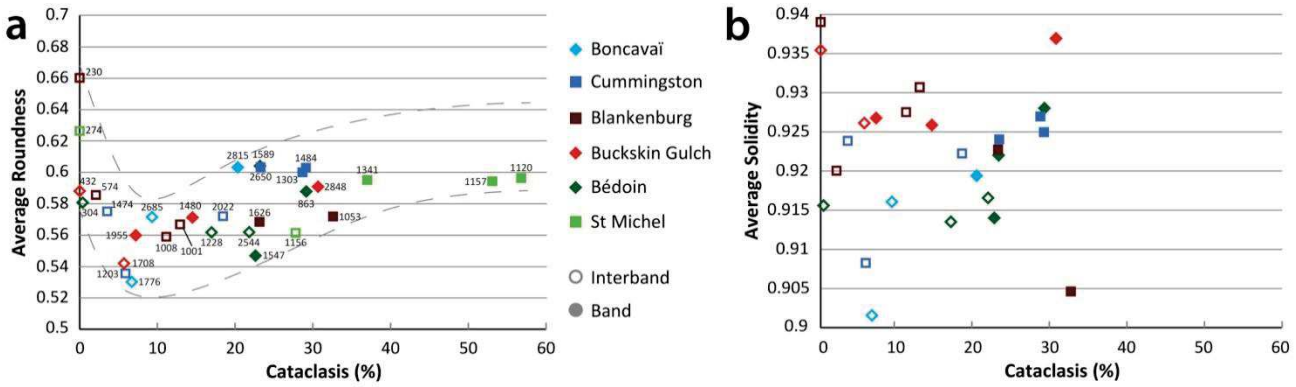

Figure 14. (a) Evolution of the average particle roundness as a function of the degree of cataclasis at each study site. The number associated to each data point corresponds to the number of measured particles comprised on the average calculation. (b) Evolution of the average particle solidity as a function of the degree of cataclasis at the study sites. The number of measured particles comprised on the average calculation for each data point is the same as indicated for the roundness data, respective to the same degree of cataclasis and study site. The legend is common to (a) and (b).

DISCUSSION

Deformation process

Influence of lithology on the formation of the clusters of cataclastic deformation bands

One general observation from this integrated field study is that all the studied clusters localize in unconsolidated or poorly consolidated sandstones with initial porosities ranging from 26 to 38% (no significant compaction, pressure-solution or cementation prior to deformation). This simple analysis confirms the observations of many studies concerning cataclastic deformation (e.g. Pittman, 1981; Aydin and Johnson, 1978; Antonellini et al., 1994; Cashman and Cashman, 2000; Wong et Baud, 2012; Ballas et al., 2014) and implies that clusters of cataclastic deformation bands can form in any clean quartz sandstone, as long as the sandstone is not extensively consolidated. Our study indicates that these conditions can be verified for burials ranging from 0 to at least 1 km in the case of Goblin Valley or Buckskin Gulch (cf. Geological Settings of the article).

At macroscopic scale, we show that the band thickness clearly increases with the average host rock grain size, independently of the Andersonian stress regime. This result from the clusters of deformation bands confirms the observations of Fossen et al. (2017) for single deformation bands. We remark that Tran (2016) also evidence millimeter wide clusters in well-sorted 0.3 µm-diameter particle material (GRAM1 rock analog) deformed through axi-symmetric compressional tests. This

suggests that the thickness of a deformation band would be constrained by a fractal relationship with the host rock grain size, provided that the porosity of the rock remains similar.

Influence of the tectonic loading on cluster morphology

The study of the cluster band density and the cluster thickness (macroscopic analysis) as a function of the tectonic loading and of the Andersonian stress regime reveals distinct morphologies for three types of Andersonian stress regimes. Because the deformation of sandstone is often described as a function of failure envelope and stress-path (e.g. Soliva et al., 2013), we thought relevant to link our findings to the Q-P diagram (Fig. 15), which is the representation of the stress state in the space of the effective mean stress (P) and deviatoric stress (Q). We address the reader to

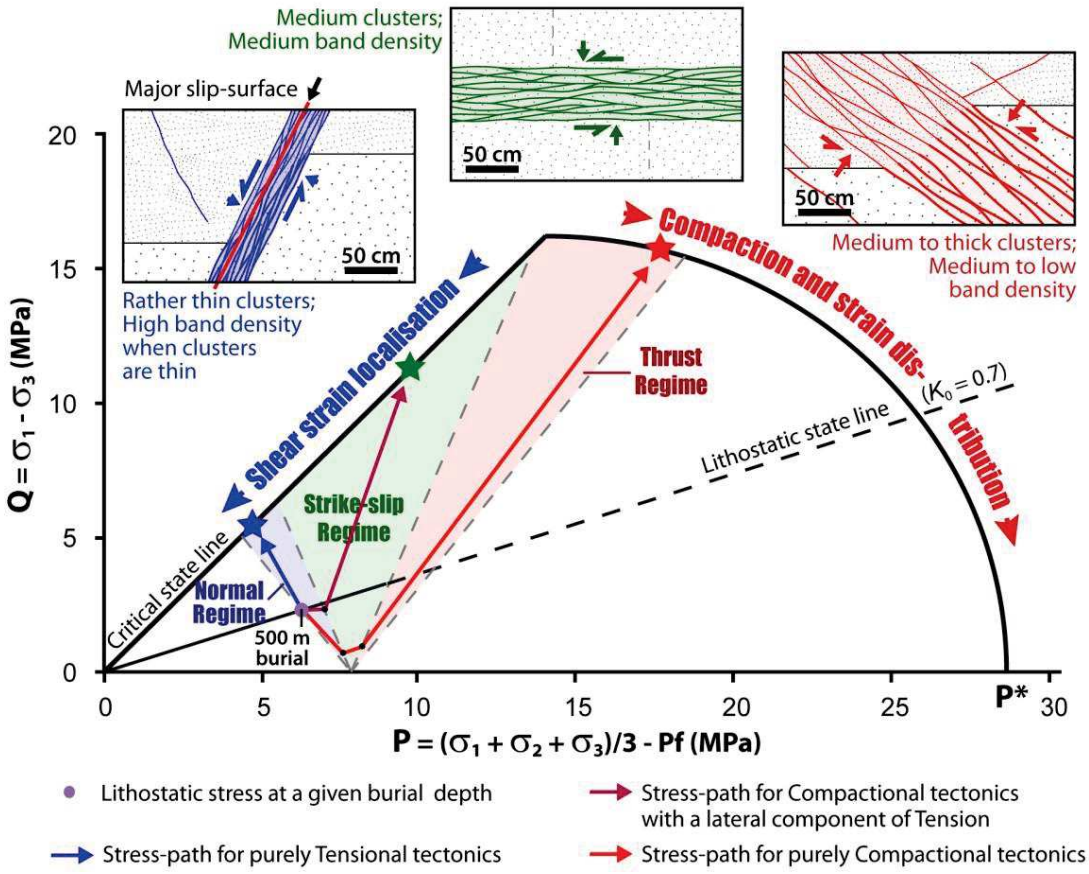

Figure 15. Synthetic diagram showing the expected morphology of clusters of deformation bands as a function of the host rock stress-path and rupture mode in the Q-P space (modified after Soliva et al., 2013); P is the mean effective stress (with σ1, σ2 and σ3 the principal stresses and Pf is the pore pressure) and Q is the deviatoric stress. Depending on the stress-path evolution (function of the burial and the tectonic loading) and the failure envelope of a rock (mainly depending on the porosity and modal grain size of the rock – see Zhang et al., 1990; Rutter and Glover, 2012; Wong and Baud, 2012), we can anticipate the type of cluster formed. The size of the failure envelope and the stress-path at the burial depth of deformation was chosen to be representative of the deformation setting at our study sites. Thin clusters with high band densities that may include a major slip-surface are formed if the stress-path hits the lower part of the brittle part of the failure envelope (simplified here by the Critical state line), which mostly occurs in normal Andersonian stress regime, implying tensional tectonics. Medium clusters with medium band densities are favored for failure along the upper part of the brittle part of the envelope and near the top of the elliptical part of the envelope; this failure is frequent in strike-slip Andersonian stress regime, implying compactional tectonics with a lateral component of tension. Large clusters with low band densities are favored for failure along the cap part of the envelope; this failure is favored in thrust Andersonian stress regime, implying compactional tectonics. This latter failure is rare since a too important burial at deformation or a small failure envelope would shift down the failure point on the elliptic envelope and favor the formation of arrays of distributed deformation bands.

the Supplementary material 3[3] for more details of the construction of the diagram, and in particular the construction of the Andersonian domain limits and possible stress-paths. We determined the stress-path and failure envelope of the diagram to be representative of the typical settings at the studied sites.

In the case of our study, the clusters formed under extensional tectonics (tensional loading represented by the blue stress-path in Fig. 15) all correspond to normal Andersonian stress regime structures. The clusters rarely exceed 800 mm in width (or the band density falls below 10%); the thinnest clusters display important band density (frequently higher than 0.5), and the thickest cluster have low band density (nearing 0.1). This result seems to agree with the hypothesis of favored localization of cataclastic deformation in extensional tectonics (Soliva et al., 2013; Ballas et al., 2014; Soliva et al., 2016). Yet, microscopic deformation of representative section analysis (degree of cataclasis - Fig. 10) indicates weighted arithmetic mean degree of cataclasis ranging from 11 to 15% and compaction ranging from 12 to 19%. These relatively low values indicate that although the extensional tectonics favors the localization of the deformation, it would not induce a maximum deformation of the grains at microscopic scale (in comparison with the strike-slip regime deformation described hereafter), therefore suggesting that the degree of cataclasis does not directly reflect the amount of shear.

In contractional tectonics (transpressive tectonic loading represented by the purple and red stress-paths in Fig. 15), we report two types of clusters: the clusters deformed in strike-slip Andersonian stress regime and the clusters deformed in thrust Andersonian stress regime. The formers are potentially larger than in normal regime and involve slightly lower band densities. The microscopic results show that the degree of cataclasis and the compaction in the strike-slip regime clusters are important, with values ranging from 19 to 33% and from 25 to 32%, respectively. The clusters formed in thrust regime, as seen at Buckskin Gulch (including no propagating fault), can be much wider than the clusters formed in normal and strike-slip regimes; they also display much lower band densities and tend to form arrays of distributed deformation bands when the density is below 0.10. The microscopy also indicates that the mean degree of cataclasis and total compaction in the cluster are low, with a values of 4% and 22%, respectively. The surprisingly higher compaction of the strike-slip regime clusters compared to the cluster formed at Buckskin Gulch in thrust regime may be explained by the fact that the high degree of cataclasis in the strike-slip regime clusters allowed a better clasts packing. The lower degree of cataclasis and higher compaction of the thrust regime clusters over the normal regime clusters is coherent with a larger strain distribution and higher compaction when failure is reached at high mean stress (Fig. 15). The clusters formed in thrust regime as seen at Blankenburg are different from the clusters at Buckskin Gulch and resemble to the clusters formed in strike-slip regime, with a mean degree of cataclasis of 18% and a compaction of 18%. This discrepancy compared to Buckskin Gulch could be explained by the fact that the deformation at Blankenburg locates above a propagating thrust fault (cf. Geological Settings), thus potentially inducing higher deviatoric stress state in the sandstone formation (Jamison and Stearns, 1982; Ballas et al., 2014). Plotting the failure of regular thrust regime deformation (i.e. Buckskin Gulch-type clusters) on the Q-P diagram (Fig. 15), we understand that the scarcity of this type of failure is expectable. Indeed, an increased burial depth at deformation (altered stress-path) or,

[3] In the thesis manuscript, the "Supplementary material 3" corresponds to section 2.3.2.

relatively, a small failure envelope (unmodified stress-path) would shift down the failure point on the elliptic part of the envelope and favor the formation of arrays of distributed deformation bands, as evidenced by Ballas et al. (2015).

Furthermore, in normal Andersonian regime, the presence of faults in a broad range of cluster thickness (from 10 to 80 cm) and for varying band densities reveals that the band density does not control the fault localization. Hence, faults could form at any stage of deformation and potentially before the cluster thickness increases beyond 80 cm (e.g. 7 meter-displacement fault in a 15-30 cm thick cluster). Besides, the presence of thin clay or clay-rich layers in the sandstone could influence the localization of the inception of a through-going slip-surface in the neighboring sandstone formations (Philit et al., in prep.).

Implication of the granular arrangement in the cluster development

Our study of the microscopic organization of the clasts as a function of increasing degree of cataclasis shows that the development of clusters is mainly controlled by the extent of particle coordination and frictional strengthening.

Because the cataclastic material of the bands is highly packed at the end of a band formation (decay of the sorting and increase of compaction with the degree of cataclasis), the particle contacts in the force chains are numerous (Arzt, 1982) (Fig. 16a-1) and consequently strong regarding the stress loading and will not further deform by cataclasis. Besides, we showed that the cataclasis partially provokes a slight increase of roughness (elongation of the clasts during the first stages of cataclasis, then slight rounding until 40% of cataclasis, agreeing with the qualitative observations of Hadizadeh, 2010). In addition to the reinforcing of the number of particle contact (e.g. Anthony and Marone, 2005), this roughening suggests an increase of friction angle potentially inhibiting shear deformation in the band (e.g. Mair et al., 2002; Cho et al., 2006; Guo and Morgan, 2006; Estrada et al., 2011; Azéma et al., 2012). Hence, after a band formed, it is hardened and will not absorb further deformation. After having long been debated (e.g. Aydin and Johnson, 1978; Mair et al., 2000; Schultz and Soliva, 2012; Nicol et al., 2013), this result corroborates the hypothesis of hardening of the deformation bands that recent experiments seem to confirm (Kaproth et al., 2010; Tran, 2016).

On the other hand, as shown by Lothe et al. (2002) at low confining pressure or by Tran (2016) in normal stress setting in tri-axial experiments, the formation of a band is accompanied by a certain amount of dilatancy at the edge of the band (Fig. 16a-2). This dilatancy is assumed very small, which probably explains why we cannot practically assess significant porosity increase at the edge of the bands in Fig. 11a. Nevertheless, this dilatancy implies less and therefore weaker particle contacts in the force chains than in the host rock (Iwashita and Oda, 2000) (Fig. 16a-n), and logically much weaker than force chain particle contacts in the bands. We think that a comparative assessment of the particle coordination numbers between the edges of the bands and the host rock would be suitable to verify this hypothesis.

Additionally, we observe quartz cementation of the cataclastic material at most of our study sites, even if some cement rims are no thicker than 10 µm (Fig. 11, synthetized in Fig. 16a-top). It has been shown that the large number of fractures generated by cataclasis enhance quartz precipita-

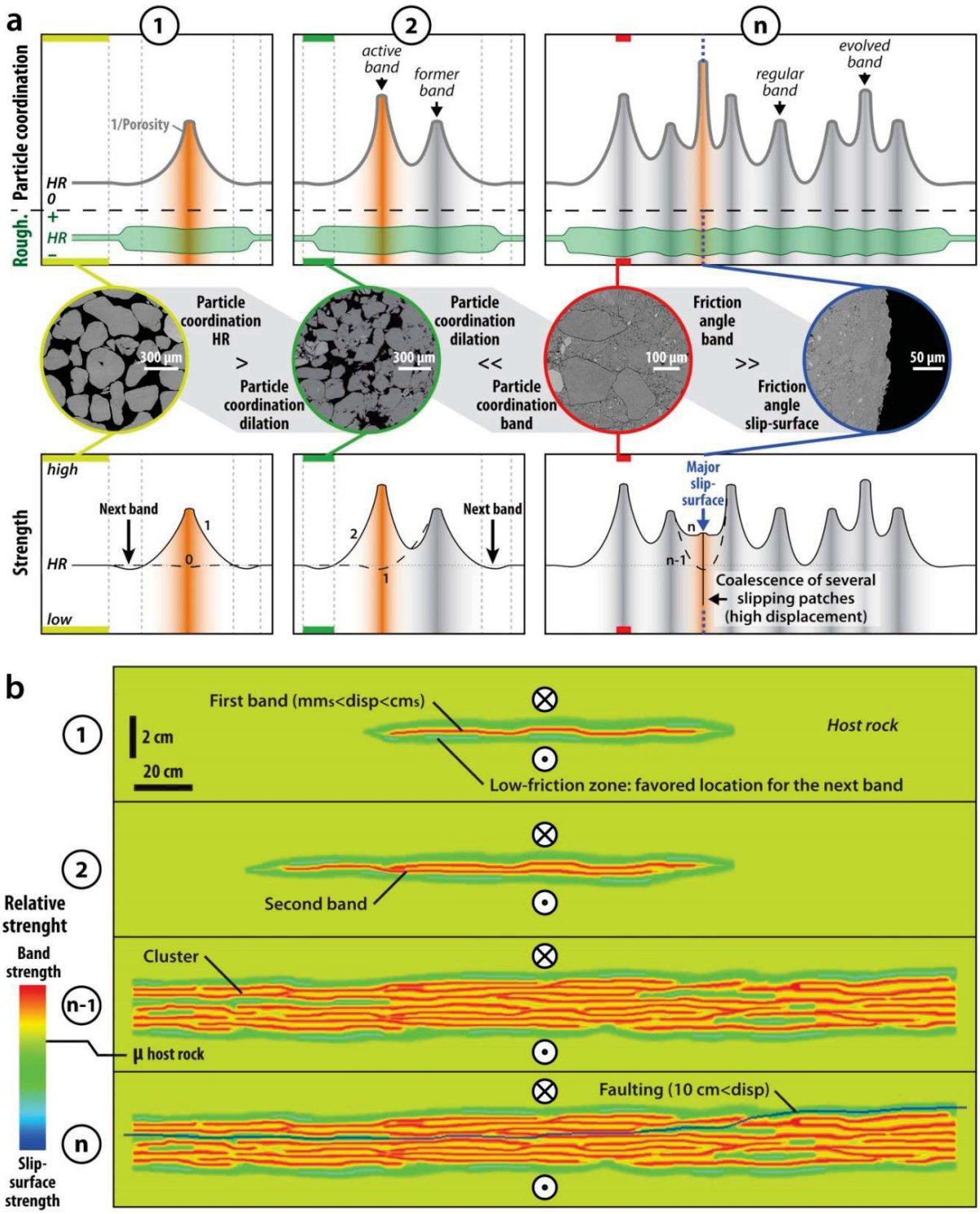

Figure 16. Synthetic representation of the evolution of the microstructural characteristics (particle coordination and roughness) involved during the cataclastic deformation of a >80% quartz sandstone for a normal Andersonian stress regime. We correlate our observations (a-top) to propose an interpretation of the evolution of the strength (a-bottom) for each step of deformation (1 through n). Low-porosity (packed), slightly angular material suggests important strength (strong particle contacts). Dilatant structures (highly porous) material implies low resistance (weak particle contacts) and would directly constrains le localization of the subsequent band. A major slip-surface can appear at any stage of development of the cluster and would locate along an interface of minimized strength and with the smoothest geometry. (b) Similar interpretation of our results relative to the strength (step 1 through n), but viewed in the out of shear plane. We remark that, in comparison to this normal regime model, the bands in the strike-slip or thrust regime could be localized farther away from the previous band as the stress loading of these Andersonian regimes display different patterns of dilatancy at the band edges.

tion on the fresh nucleation surface of the quartz clasts (e.g. Fisher and Knipe, 1998; Lander et al., 2008; Philit et al., 2015). In particular, Ngwenya et al. (2000) suggest than this cementation can be immediately contemporaneous with the deformation. Hence, if we assume that cementation was underestimated in many places since often forming very thin rims around the clasts, we suppose that it may significantly contribute to the hardening (increase of cohesion) of the bands in many geological contexts.

Consequently, the edges of the bands would be the most fragile parts of the rock, which is consistent with the proposal of Anthony and Marone (2005), and would be prone to localize the subsequent band formation. This suggests a cluster growth by successive addition of bands at the edge of the band, and so of the cluster. We observed in the deformed material of the interbands residual porosities close or equal to the host rock porosity. Hence, we infer that bands could also be formed in the cluster thickness. The observation of major slip-surfaces in the cluster thickness (meaning the end of the cluster development) confirms this hypothesis.

The greater packing for early stages of cataclasis in the case of the thrust Andersonian stress regime compared to the normal and strike-slip regimes suggests a lesser dilatancy at the vicinity of the pre-existing bands in this regime. Consistently with the results obtained by the triaxial experiments of Alikarami et al. (2015) considering the loading of particles at variable confining pressures, a higher confining stress would not favor dilation. According to the numerical modeling of Aharonov and Sparks (2002), high confining pressure rather induce a random distribution of the shear in the formation or non-localized shear. This is consistent to the conclusion of the section "Influence of the tectonic loading on cluster morphology" where we indicate that clusters are potentially thicker in contractional tectonics then in extensional regime, with a lesser band density.

According to the complementarity of these processes, we propose a model for the evolution of cataclastic deformation. We propose that the deformation would evolve by steps and that the localization of the subsequent bands would be determined by the zone of least strength at the end of the previous deformation step. Assuming a host rock with a uniform initial strength, the localization of a first band is arbitrary (certainly controlled by microscale heterogeneity). A step of deformation would comprise a slipping state during which the friction would locally drop (dynamic friction coefficient). The abrupt friction drop with increasing slip velocity in quartz materials and quartz sandstone materials has widely been shown (e.g. Dieterich, 1972; Marone et al., 1990; Beeler et al., 1996; Di Toro, 2004). We note that dilatancy is proven during this type of slip event (e.g. Marone et al., 1990). The particle coordination and friction angle in the formed band would be strongly increased. Both the particle coordination and friction angle would progressively decrease adjacent to the band until the former being locally slightly lower than the host rock particle coordination (Fig. 16a-1 and b-1). According to similar processes of deformation, the formation of a new band would subsequently localize in a neighboring part of the cluster where the strength is least (Fig. 16a-2 and b-2), and so on. Eventually, in normal regime, we hypothesize that a slip-surface could initiate in (or at the edge of) the cluster thickness, along an interface of minimized strength and with the smoothest geometry when a particularly high step of displacement occurs (Fig. 16a-n and b-n). Chambon et al. (2006) show that displacement higher than tens of centimeter permit slip-weakening (lowering of the friction angle). Therefore, if the strength of this interface is significantly lower than the host rock, the

subsequent deformation steps will be absorbed along this interface and the creation of new bands will be prevented. As mentioned in the first paragraph of this section, the slip-surface could occur at any stage of the cluster development.

Complementarily to our explanations, we remark that the initiation of slip-surfaces is dramatically enhanced if as little as a few percent of low friction material such as phyllosilicate enters the composition of the rock (e.g. Byerlee, 1978; Logan and Rauenzahn, 1987; Collettini et al., 2009). Underhill and Woodcock (1987) also note that the presence of oxide coating may lower the grain-contact friction. In agreement to this possibility, we showed that deformation bands in clean sandstones disappear in neighboring oxide-bearing fine sandstone to silt (e.g. Fig. 7b).

Cluster scale and implications for fluids

We note that, due to the quaternary sedimentary cover, we underestimate the continuity and real length of some clusters. Hence, hundred-meter long clusters are certainly more common that reported (hypothetic dashed line in Fig. 2). However, the wide outcrops of Cummingston and Goblin Valley yield valuable observations. Although the connection between the clusters is poorly quantified, the clusters frequently measure up to several hundreds of meters in length and can form km to multi-km long networks. These networks seem to locate at the vicinity of major faults (e.g Cummingston and Goblin Valley). The width of these networks show that the deformation is accommodated on tens to hundreds of meters widths. This is consistent with previous observations of localization of deformation being favored in extensional tectonics showed by Soliva et al. (2016). On the other hand, the large outcrop of Buckskin Gulch shows that the clusters are not forming network in contractional tectonics. Although the smaller site of Bédoin suffers from truncation effect where the quarry was dug, the scarceness of clusters at the quarry faces tends to confirm this observation. These results are indirectly supported by the absence or shortness of cluster (such as we describe them) in contractional tectonics at other sites. For instance, Zuluaga et al. (2015) describe in the San Rafael Swell (Utah) (deformed in contraction) clusters shorter than 20 m, the rest of the deformation being ladder deformation band structures. The same applies for the site of Valley of Fire (Nevada) (e.g. Eichhubl et al., 2004, 2010; Solum et al., 2012) where the deformation, when continuous, rather corresponds to band arrays and ladder structures. The other sites investigated in this study are too small to yield information supporting or contradicting this latter trend.

Clusters in general display two sorts of endings, described as branching or tipping, and sometimes connect in relay in the extensional tectonics out of shear plane. As proposed by Shipton and Cowie (2001, 2003), we showed that the displacement is maximum at the center of the cluster. Our measurements on a single cluster indicate a maximum displacement of the order of 1 meter for a 250 m long unfaulted cluster and for a total band thickness comprised between 5 and 10 cm. The displacement is linked to the total band thickness rather than the cluster thickness. The vertical continuity of clusters is complex to assess due to the lack of extended vertical outcrops. Clusters that are continuous along the height of the outcrop are frequently observed disappearing in underlying unclean sandstones/silts (e.g. Fossen et al., 2017 at Goblin Valley, our personal observations at Bédoin). Philit et al., (submitted) show that the partial filling of the granular material porosity with weak material such oxide-bearing oolites or phyllosilicates inhibits the formation of cluster of cataclastic bands and favors the development of a slip-surface.

We showed that the internal structure of clusters include different types of material, from the deformed interband rock to the slip-surface. It is interesting to note that the permeability of the interbands drops from two orders of magnitude compared to the host rock. Among the diversity of reported bands, apart from the extensional case of Boncavaï, all sites include between 15% and 79% of discrete bands and/or slip-surface in the cluster. We showed that these bands have permeabilities close to or lower than $1x10^{1}$ mD. Although worked out via different methods and accounting for the overestimation induced by the Tinyperm method, these values are consistent with most permeability measured on similar cataclastic deformation structures in a broader variety of porous sandstones by Antonellini and Aydin (1994), Fisher and Knipe (1998), Tueckemantel et al. (2010), Ballas et al. (2015), for instance. However, Solum et al. (2010), using bulk air permeability method on plug samples, claim lower permeabilities for the deformation bands at Buckskin Gulch, with average values of 0.25 mD and an average host rock value of 5910 mD. In comparison, we measured at the same site values of 1.5 mD in the discrete bands and 820 mD in the host rock (subtracting for the 1.8 overestimation induced by the Tinyperm measurements). This difference suggests that the type of band investigated at that site were different, and probably not concerning the clusters we investigated in the case of Solum et al. (2010). The work of Torabi et al. (2013) suggests that deformation structures corresponding to this range of permeability would have capillary pressures supporting fluid columns of a few meters to more than 80 m (considering a two-phase fluid made of oil and brine). Therefore, depending on the quantity of their connection (continuity) and provided a significantly high superposition of clean sandstones, cluster networks may represent effective baffles at reservoir scale.

CONCLUSION

We showed that the morphology of clusters essentially depends on the tectonic loading: the extensional tectonics favors the localization of normal Andersonian stress regime clusters. The generated clusters may be thin (10-30 cm) and involving high band densities (0.30-0.70) or of medium size (up to 70 cm) with lower band densities, characterized in all cases by significant degree of cataclasis and moderate compaction. The growth of the normal clusters can be stopped at any stage by the formation of a major slip-surface. The contractional tectonics favors formation of strike-slip and thrust regime clusters. The strike-slip regime clusters display varying thickness (10-100 cm), have constant medium band densities (0.20-0.55), with high microscopic deformation, both in terms of cataclasis and compaction, despite of the lack of major slip-surface. The thrust regime clusters can display a morphology similar to the strike-slip regime clusters. The can also widen extensively (>100 cm) and display low band densities (<0.10-0.40). Their microscopic structure reveals low degree cataclasis and moderate compaction.

The analysis of the granular attributes of the deformed material confronted with the literature permits to link the microscopic processes of deformation to the macroscopic morphology of the clusters. In the absence of cementation, the evolution of deformation in sandstones provokes the slight roughening and the compaction of the clasts, with the most important compaction in the bands where the sorting is the poorest. Because the combination of an important compaction and roughening implies an important particle coordination and high friction angle, the bands may be the most cohesive parts of the cluster. New bands are expected to localize along dilatant zones where the

low particle coordination induce weak particle contacts in the chain force. In extensional tectonics, at relatively small confining pressure, zones of dilatancy induced by the shear are known at the edges of the bands, explaining the band localization at the edge of former bands and therefore the high band density of these clusters. In contractional tectonics, since the confining pressure is higher, the dilatancy may be small and distributed or nonexistent, explaining the tendency of distributed and rather compactant deformation at macroscopic scale. The occurrence of a major slip-surface in normal regime can occur at any stage of deformation and implies that the subsequent deformation will localize along that low friction angle surface.

Eventually, we show that cluster networks of kilometer-scale dimension are favored in extensional tectonics (normal regime), where clusters of hundred-meter are common. On the contrary, no significant network of cluster is observed in contractional tectonics (for both strike-slip and thrust regimes); the observed clusters never reach one hundred meters in length. In any cases, the vertical dimension of the clusters seems constrained by the thickness of the sandstone formation: clusters could be formed provided that the sandstone (1) is not extensively consolidated, (2) has at least a moderate sorting, and (3) includes at least about 80% of quartz and does not bear any low friction mineral such as phyllosilicates or oxides. Given that the clusters of all sites are made of 15% and 79 % of bands/slip-surface with permeabilities close to or lower than $1 \cdot 10^{1}$ mD, we conclude that they may play a significant role of baffle in extensional deformation networks, especially if the conditions for vertical cluster continuity are matched.

AKNOWLEDGMENTS

We wish to thank the Laboratory of Geosciences Montpellier, the Gaïa Doctorate School and TOTAL E&P for their financial support in this work. We are also grateful to Doriane Delmas and Christophe Nevado for the laborious work they did by providing the numerous and quality thin sections necessary to this work. Finally, we thank our reviewers for the constructive comments on the manuscript.

REFERENCES CITED

Aharonov, E., Sparks, D., 2002. Shear profiles and localization in simulations of granular materials. Physical Review E 65, 051302. https://doi.org/10.1103/PhysRevE.65.051302

Al-Hinai, S., Fisher, Q.J., Al-Busafi, B., Guise, P., Grattoni, C.A., 2008. Laboratory measurements of the relative permeability of cataclastic fault rocks: An important consideration for production simulation modelling. Marine and Petroleum Geology 25, 473–485. https://doi.org/10.1016/j.marpetgeo.2007.07.005

Alikarami, R., Andò, E., Gkiousas-Kapnisis, M., Torabi, A., Viggiani, G., 2015. Strain localisation and grain breakage in sand under shearing at high mean stress: insights from in situ X-ray tomography. Acta Geotechnica 10, 15–30. https://doi.org/10.1007/s11440-014-0364-6

Anthony, J.L., Marone, C., 2005. Influence of particle characteristics on granular friction. Journal of Geophysical Research: Solid Earth 110, B08409. https://doi.org/10.1029/2004JB003399

Antonellini, M., Aydin, A., 1994. Effect of Faulting on Fluid Flow in Porous Sandstones: Petrophysical Properties. AAPG Bulletin 78, 355–377.

Antonellini, M.A., Aydin, A., Pollard, D.D., 1994. Microstructure of deformation bands in porous sandstones at Arches National Park, Utah. Journal of Structural Geology 16, 941–959. https://doi.org/10.1016/0191-8141(94)90077-9

Arthaud, F., Séguret, M., 1981. Les structures pyrénéennes du Languedoc et du Golfe du Lion (Sud de la France). Bulletin de la Societe Geologique de France (7) XXIII, 51–63. https://doi.org/10.2113/gssgfbull.S7-XXIII.1.51

Arzt, E., 1982. The influence of an increasing particle coordination on the densification of spherical powders. Acta Metallurgica 30, 1883–1890. https://doi.org/10.1016/0001-6160(82)90028-1

Aydin, A., 2000. Fractures, faults, and hydrocarbon entrapment, migration and flow. Marine and Petroleum Geology 17, 797–814. https://doi.org/10.1016/S0264-8172(00)00020-9

Aydin, A., 1978. Small faults formed as deformation bands in sandstone. Pure and Applied Geophysics 116, 913–930. https://doi.org/10.1007/BF00876546

Aydin, A., Johnson, A.M., 1978. Development of faults as zones of deformation bands and as slip surfaces in sandstone. Pure and Applied Geophysics 116, 931–942. https://doi.org/10.1007/BF00876547

Azéma, E., Estrada, N., Radjaï, F., 2012. Nonlinear effects of particle shape angularity in sheared granular media. Physical Review E 86, 041301. https://doi.org/10.1103/PhysRevE.86.041301

Ballas, G., Fossen, H., Soliva, R., 2015. Factors controlling permeability of cataclastic deformation bands and faults in porous sandstone reservoirs. Journal of Structural Geology 76, 1–21. https://doi.org/10.1016/j.jsg.2015.03.013

Ballas, G., Soliva, R., Benedicto, A., Sizun, J.-P., 2014. Control of tectonic settings and large-scale faults on the basin-scale distribution of deformation bands in porous sandstone (Provence, France). Marine and Petroleum Geology 55, 142–159. https://doi.org/10.1016/j.marpetgeo.2013.12.020

Ballas, G., Soliva, R., Sizun, J.-P., Benedicto, A., Cavailhes, T., Raynaud, S., 2012. The importance of the degree of cataclasis in shear bands for fluid flow in porous sandstone, Provence, France. AAPG Bulletin 96, 2167–2186. https://doi.org/10.1306/04051211097

Ballas, G., Soliva, R., Sizun, J.-P., Fossen, H., Benedicto, A., Skurtveit, E., 2013. Shear-enhanced compaction bands formed at shallow burial conditions; implications for fluid flow (Provence, France). Journal of Structural Geology 47, 3–15. https://doi.org/10.1016/j.jsg.2012.11.008

Beeler, N.M., Tullis, T.E., Blanpied, M.L., Weeks, J.D., 1996. Frictional behavior of large displacement experimental faults. Journal of Geophysical Research: Solid Earth 101, 8697–8715. https://doi.org/10.1029/96JB00411

Bense, V.F., Gleeson, T., Loveless, S.E., Bour, O., Scibek, J., 2013. Fault zone hydrogeology. Earth-Science Reviews 127, 171–192. https://doi.org/10.1016/j.earscirev.2013.09.008

Brandenburg, J.P., Alpak, F.O., Solum, J.G., Naruk, S.J., 2012. A kinematic trishear model to predict deformation bands in a fault-propagation fold, East Kaibab monocline, Utah. AAPG Bulletin 96, 109–132. https://doi.org/10.1306/05101110160

Byerlee, J., 1978. Friction of rocks. Pure and Applied Geophysics 116, 615–626. https://doi.org/10.1007/BF00876528

Caine, J.S., Evans, J.P., Forster, C.B., 1996. Fault zone architecture and permeability structure. Geology 24, 1025–1028. https://doi.org/10.1130/0091-7613(1996)024<1025:FZAAPS>2.3.CO;2

Cashman, S., Cashman, K., 2000. Cataclasis and deformation-band formation in unconsolidated marine terrace sand, Humboldt County, California. Geology 28, 111–114. https://doi.org/10.1130/0091-7613(2000)28<111:CADFIU>2.0.CO;2

Chambon, G., Schmittbuhl, J., Corfdir, A., 2006. Frictional response of a thick gouge sample: 1. Mechanical measurements and microstructures. Journal of Geophysical Research: Solid Earth 111, B09308. https://doi.org/10.1029/2003JB002731

Champion, C., Choukroune, P., Clauzon, G., 2000. La déformation post-Miocène en Provence occidentale. Geodinamica Acta 13, 67–85. https://doi.org/10.1016/S0985-3111(00)00114-5

Cho, G.-C., Dodds, J., Santamarina, J.C., 2006. Particle Shape Effects on Packing Density, Stiffness, and Strength: Natural and Crushed Sands. Journal of Geotechnical and Geoenvironmental Engineering 132, 591–602. https://doi.org/10.1061/(ASCE)1090-0241(2006)132:5(591)

Collettini, C., Niemeijer, A., Viti, C., Marone, C., 2009. Fault zone fabric and fault weakness. Nature 462, 907–910. https://doi.org/10.1038/nature08585

Cox, M.R., Budhu, M., 2008. A practical approach to grain shape quantification. Engineering Geology 96, 1–16. https://doi.org/10.1016/j.enggeo.2007.05.005

Di Toro, G., Goldsby, D.L., Tullis, T.E., 2004. Friction falls towards zero in quartz rock as slip velocity approaches seismic rates. Nature 427, 436–439. https://doi.org/10.1038/nature02249

Dieterich, J.H., 1972. Time-dependent friction in rocks. Journal of Geophysical Research 77, 3690–3697. https://doi.org/10.1029/JB077i020p03690

Doelling, H.H., 2008. Geological map of Kanab 30 x 60-minute quadrangle, Kane and Washington Counties, Utah, and Coconino and Mohave Counties, Arizona., scale 1:100000, Utah Geological Survey.

Doelling, H.H., Kuehne, P.A., Willis, G.C., Buck Ehler, J., 2015. Geologic map of the San Rafael Desert 30 x 60-minute quadrangle, Emery and Grand Counties, Utah., scale 1:62500, Utah Geological Survey.

Doelling, H.H., Willis, G.C., 2006. Geologic map of the Smoky Mountains 30x60-minute quadrangle, Kane and San Juan Counties, Utah, and Coconino County, Arizona., scale 1:100000, Utah Geological Survey.

Edwards, H.E., Becker, A.D., Howell, J.A., 1993. Compartmentalization of an aeolian sandstone by structural heterogeneities: Permo-Triassic Hopeman Sandstone, Moray Firth, Scotland. Geological Society, London, Special Publications 73, 339–365. https://doi.org/10.1144/GSL.SP.1993.073.01.20

Ehrenberg, S.N., 1989. Assessing the Relative Importance of Compaction Processes and Cementation to Reduction of Porosity in Sandstones: Discussion; Compaction and Porosity Evolution of Pliocene Sandstones, Ventura Basin, California: DISCUSSION. AAPG Bulletin 73, 1274–1276.

Eichhubl, P., Hooker, J.N., Laubach, S.E., 2010. Pure and shear-enhanced compaction bands in Aztec Sandstone. Journal of Structural Geology, Structural Diagenesis 32, 1873–1886. https://doi.org/10.1016/j.jsg.2010.02.004

Eichhubl, P., Taylor, W.L., Pollard, D.D., Aydin, A., 2004. Paleo-fluid flow and deformation in the Aztec Sandstone at the Valley of Fire, Nevada—Evidence for the coupling of hydrogeologic, diagenetic, and tectonic processes. Geological Society of America Bulletin 116, 1120–1136. https://doi.org/10.1130/B25446.1

Engelder, J.T., 1974. Cataclasis and the Generation of Fault Gouge. Geological Society of America Bulletin 85, 1515–1522. https://doi.org/10.1130/0016-7606(1974)85<1515:CATGOF>2.0.CO;2

Estrada, N., Azéma, E., Radjai, F., Taboada, A., 2011. Identification of rolling resistance as a shape parameter in sheared granular media. Physical Review E 84, 011306. https://doi.org/10.1103/PhysRevE.84.011306

Faulkner, D.R., Jackson, C.A.L., Lunn, R.J., Schlische, R.W., Shipton, Z.K., Wibberley, C.A.J., Withjack, M.O., 2010. A review of recent developments concerning the structure, mechanics and fluid flow properties of fault zones. Journal of Structural Geology, Fault Zones 32, 1557–1575. https://doi.org/10.1016/j.jsg.2010.06.009

Ferry, S., 1999. Apport des forages ANDRA de Marcoule à la connaissance de la marge crétacée rhodanienne. Etude du Gard Rhodanien, Actes des Journées Scientifiques CNRS/ANDRA. EDP Sciences, Bagnols-sur-Cèze, 63–91.

Fischer, C., Waldmann, S., von Eynatten, H., 2013. Spatial variation in quartz cement type and concentration: An example from the Heidelberg formation (Teufelsmauer outcrops), Upper Cretaceous Subhercynian Basin, Germany. Sedimentary Geology 291, 48–61. https://doi.org/10.1016/j.sedgeo.2013.03.009

Fisher, Q.J., Knipe, R.J., 2001. The permeability of faults within siliciclastic petroleum reservoirs of the North Sea and Norwegian Continental Shelf. Marine and Petroleum Geology 18, 1063–1081. https://doi.org/10.1016/S0264-8172(01)00042-3

Fisher, Q.J., Knipe, R.J., 1998. Fault sealing processes in siliciclastic sediments. Geological Society, London, Special Publications 147, 117–134. https://doi.org/10.1144/GSL.SP.1998.147.01.08

Folk, R.L., Ward, W.C., 1957. Brazos River Bar: A Study in the Significance of Grain Size Parameters. Journal of Sedimentary Research 27.

Fossen, H., Bale, A., 2007. Deformation bands and their influence on fluid flow. AAPG Bulletin 91, 1685–1700. https://doi.org/10.1306/07300706146

Fossen, H., Schultz, R.A., Shipton, Z.K., Mair, K., 2007. Deformation bands in sandstone: a review. Journal of the Geological Society 164, 755–769. https://doi.org/10.1144/0016-76492006-036

Fossen, H., Schultz, R.A., Torabi, A., 2011. Conditions and implications for compaction band formation in the Navajo Sandstone, Utah. Journal of Structural Geology 33, 1477–1490. https://doi.org/10.1016/j.jsg.2011.08.001

Fossen, H., Soliva, R., Ballas, G., Trzaskos, B., Cavalcante, C., Schultz, R.A., 2017. A review of deformation bands in reservoir sandstones: geometries, mechanisms and distribution. Geological Society, London, Special Publications 459, SP459.4. https://doi.org/10.1144/SP459.4

French, M.W., Worden, R.H., Mariani, E., Larese, R.E., Mueller, R.R., Kliewer, C.E., 2012. Microcrystalline Quartz Generation and the Preservation of Porosity In Sandstones: Evidence from the Upper Cretaceous of the Subhercynian Basin, Germany. Journal of Sedimentary Research 82, 422–434. https://doi.org/10.2110/jsr.2012.39

Gallagher Jr, J.J., Friedman, M., Handin, J., Sowers, G.M., 1974. Experimental studies relating to microfracture in sandstone. Tectonophysics 21, 203–247. https://doi.org/10.1016/0040-1951(74)90053-5

Glennie, K.W., Buller, A.T., 1983. The Permian Weissliegend of NW Europe: The partial deformation of aeolian dune sands caused by the Zechstein transgression. Sedimentary Geology 35, 43–81. https://doi.org/10.1016/0037-0738(83)90069-6

Guo, Y., Morgan, J.K., 2006. The frictional and micromechanical effects of grain comminution in fault gouge from distinct element simulations. Journal of Geophysical Research: Solid Earth 111, B12406. https://doi.org/10.1029/2005JB004049

Hadizadeh, J., Sehhati, R., Tullis, T., 2010. Porosity and particle shape changes leading to shear localization in small-displacement faults. Journal of Structural Geology, Fault Zones 32, 1712–1720. https://doi.org/10.1016/j.jsg.2010.09.010

Iwashita, K., Oda, M., 2000. Micro-deformation mechanism of shear banding process based on modified distinct element method. Powder Technology 109, 192–205. https://doi.org/10.1016/S0032-5910(99)00236-3

Jamison, W.R., Stearns, D.W., 1982. Tectonic Deformation of Wingate Sandstone, Colorado National Monument. AAPG Bulletin 66, 2584–2608.

Johansen, T.E.S., Fossen, H., 2008. Internal geometry of fault damage zones in interbedded siliciclastic sediments. Geological Society, London, Special Publications 299, 35–56. https://doi.org/10.1144/SP299.3

Kaproth, B.M., Cashman, S.M., Marone, C., 2010. Deformation band formation and strength evolution in unlithified sand: The role of grain breakage. Journal of Geophysical Research: Solid Earth 115, B12103. https://doi.org/10.1029/2010JB007406

Klimczak, C., Schultz, R.A., 2013. Fault damage zone origin of the Teufelsmauer, Subhercynian Cretaceous Basin, Germany. International Journal of Earth Sciences 102, 121–138. https://doi.org/10.1007/s00531-012-0794-z

Lanatà, P., 2014. Full-field experimental characterization of mechanical behaviour and failure in a porous rock in plane strain compression: homogeneous deformation and strain localization. Ph.D. thesis. Université de Grenoble.

Lander, R.H., Larese, R.E., Bonnell, L.M., 2008. Toward more accurate quartz cement models: The importance of euhedral versus noneuhedral growth rates. AAPG Bulletin 92, 1537–1563. https://doi.org/10.1306/07160808037

Logan, J.M., Rauenzahn, K.A., 1987. Frictional dependence of gouge mixtures of quartz and montmorillonite on velocity, composition and fabric. Tectonophysics 144, 87–108. https://doi.org/10.1016/0040-1951(87)90010-2

Lothe, A.E., Gabrielsen, R.H., Hagen, N.B., Larsen, B.T., 2002. An experimental study of the texture of deformation bands: effects on the porosity and permeability of sandstones. Petroleum Geoscience 8, 195–207. https://doi.org/10.1144/petgeo.8.3.195

Mair, K., Frye, K.M., Marone, C., 2002. Influence of grain characteristics on the friction of granular shear zones. Journal of Geophysical Research: Solid Earth 107, 2219. https://doi.org/10.1029/2001JB000516

Mair, K., Main, I., Elphick, S., 2000. Sequential growth of deformation bands in the laboratory. Journal of Structural Geology 22, 25–42. https://doi.org/10.1016/S0191-8141(99)00124-8

Marone, C., Raleigh, C.B., Scholz, C.H., 1990. Frictional behavior and constitutive modeling of simulated fault gouge. Journal of Geophysical Research: Solid Earth 95, 7007–7025. https://doi.org/10.1029/JB095iB05p07007

Mollema, P.N., Antonellini, M.A., 1996. Compaction bands: a structural analog for anti-mode I cracks in aeolian sandstone. Tectonophysics 267, 209–228. https://doi.org/10.1016/S0040-1951(96)00098-4

Ngwenya, B.T., Elphick, S.C., Main, I.G., Shimmield, G.B., 2000. Experimental constraints on the diagenetic self-sealing capacity of faults in high porosity rocks. Earth and Planetary Science Letters 183, 187–199. https://doi.org/10.1016/S0012-821X(00)00261-2

Nicol, A., Childs, C., Walsh, J.J., Schafer, K.W., 2013. A geometric model for the formation of deformation band clusters. Journal of Structural Geology 55, 21–33. https://doi.org/10.1016/j.jsg.2013.07.004

Paxton, S.T., Szabo, J.O., Ajdukiewicz, J.M., Klimentidis, R.E., 2002. Construction of an Intergranular Volume Compaction Curve for Evaluating and Predicting Compaction and Porosity Loss in Rigid-Grain Sandstone Reservoirs. AAPG Bulletin 86, 2047–2067. https://doi.org/10.1306/61EEDDFA-173E-11D7-8645000102C1865D

Philit, S., Soliva, R., Labaume, P., Gout, C., Wibberley, C., 2015. Relations between shallow cataclastic faulting and cementation in porous sandstones: First insight from a groundwater environmental context. Journal of Structural Geology 81, 89–105. https://doi.org/10.1016/j.jsg.2015.10.001

Pittman, E.D., 1981. Effect of Fault-Related Granulation on Porosity and Permeability of Quartz Sandstones, Simpson Group (Ordovician), Oklahoma. AAPG Bulletin 65, 2381–2387.

Quinn, O.F., 2005. Fault controlled fluid flow and quartz cementation in porous sandstones. Ph.D. thesis. The University of Edinburgh.

Rigby, J.K., Beus, S.S., 1987. Stratigraphy and Structure of the San Rafael Reef, Utah," A Major Monocline of the Colorado Plateau. Rocky Mountain Section of the Geological Society of America: Decade of North American Geology, Centennial Field Guide Volume 2. Geological Society of America, 269–273.

Roberts, A.M., Badley, M.E., Price, J.D., Huck, I.W., 1990. The structural history of a transtensional basin: Inner Moray Firth, NE Scotland. Journal of the Geological Society 147, 87–103. https://doi.org/10.1144/gsjgs.147.1.0087

Roure, F., Brun, J.-P., Colletta, B., Van den Driessche, J., 1992. Geometry and kinematics of extensional structures in the Alpine Foreland Basin of southeastern France. Journal of Structural Geology 14, 50.-519. https://doi.org/10.1016/0191-8141(92)90153-N

Rudnicki, J.W., 2004. Shear and compaction band formation on an elliptic yield cap. Journal of Geophysical Research: Solid Earth 109, B03402. https://doi.org/10.1029/2003JB002633

Rutter, E.H., Glover, C.T., 2012. The deformation of porous sandstones; are Byerlee friction and the critical state line equivalent? Journal of Structural Geology 44, 129–140. https://doi.org/10.1016/j.jsg.2012.08.014

Saillet, E., 2009. La localisation de la déformation dans les grès poreux : caractérisation d'un analogue de réservoirs gréseux faillés dans le Bassin du Sud-Est, Provence, France. Ph.D. thesis. Université de Nice-Sophia Antipolis, UFR Sciences.

Saillet, E., Wibberley, C.A.J., 2010. Evolution of cataclastic faulting in high-porosity sandstone, Bassin du Sud-Est, Provence, France. Journal of Structural Geology, Fault Zones 32, 1590–1608. https://doi.org/10.1016/j.jsg.2010.02.007

Savage, H.M., Brodsky, E.E., 2011. Collateral damage: Evolution with displacement of fracture distribution and secondary fault strands in fault damage zones. Journal of Geophysical Research: Solid Earth 116, B03405. https://doi.org/10.1029/2010JB007665

Scholz, C.H., 2002. The Mechanics of Earthquakes and Faulting. Cambridge University Press.

Schultz, R.A., 2011. Relationship of compaction bands in Utah to Laramide fault-related folding. Earth and Planetary Science Letters 304, 29–35. https://doi.org/10.1016/j.epsl.2011.01.001

Schultz, R.A., Fossen, H., 2002. Displacement–length scaling in three dimensions: the importance of aspect ratio and application to deformation bands. Journal of Structural Geology 24, 1389–1411. https://doi.org/10.1016/S0191-8141(01)00146-8

Schultz, R.A., Soliva, R., 2012. Propagation energies inferred from deformation bands in sandstone. International Journal of Fracture 176, 135–149. https://doi.org/10.1007/s10704-012-9730-2

Séranne, M., Benedicto, A., Labaum, P., Truffert, C., Pascal, G., 1995. Structural style and evolution of the Gulf of Lion Oligo-Miocene rifting: role of the Pyrenean orogeny. Marine and Petroleum Geology, Integrated Basin Studies 12, 809–820. https://doi.org/10.1016/0264-8172(95)98849-Z

Shipton, Z.K., Cowie, P.A., 2003. A conceptual model for the origin of fault damage zone structures in high-porosity sandstone. Journal of Structural Geology 25, 333–344. https://doi.org/10.1016/S0191-8141(02)00037-8

Shipton, Z.K., Cowie, P.A., 2001. Damage zone and slip-surface evolution over µm to km scales in high-porosity Navajo sandstone, Utah. Journal of Structural Geology 23, 1825–1844. https://doi.org/10.1016/S0191-8141(01)00035-9

Shotton, F.W., 1956. Some aspects of the new red desert in britain. Geological Journal 1, 450–465. https://doi.org/10.1002/gj.3350010505

Sibson, R.H., 1977. Fault rocks and fault mechanisms. Journal of the Geological Society 133, 191–213. https://doi.org/10.1144/gsjgs.133.3.0191

Soliva, R., Ballas, G., Fossen, H., Philit, S., 2016. Tectonic regime controls clustering of deformation bands in porous sandstone. Geology 44, 423–426. https://doi.org/10.1130/G37585.1

Soliva, R., Schultz, R.A., Ballas, G., Taboada, A., Wibberley, C., Saillet, E., Benedicto, A., 2013. A model of strain localization in porous sandstone as a function of tectonic setting, burial and material properties; new insight from Provence (southern France). Journal of Structural Geology 49, 50–63. https://doi.org/10.1016/j.jsg.2012.11.011

Solum, J.G., Brandenburg, J.P., Naruk, S.J., 2012. Characterization of deformation bands associated with normal and reverse stress states in the Navajo Sandstone, Utah: Reply. AAPG Bulletin 96, 877–890. https://doi.org/10.1306/09221111057

Solum, J.G., Brandenburg, J.P., Naruk, S.J., Kostenko, O.V., Wilkins, S.J., Schultz, R.A., 2010. Characterization of deformation bands associated with normal and reverse stress states in the Navajo Sandstone, Utah. AAPG Bulletin 94, 1453–1475. https://doi.org/10.1306/01051009137

Taylor, W.L., Pollard, D.D., 2000. Estimation of in situ permeability of deformation bands in porous sandstone, Valley of Fire, Nevada. Water Resources Research 36, 2595–2606. https://doi.org/10.1029/2000WR900120

Torabi, A., Fossen, H., Braathen, A., 2013. Insight into petrophysical properties of deformed sandstone reservoirs. AAPG Bulletin 97, 619–637. https://doi.org/10.1306/10031212040

Tran, T.P.H., 2016. Étude expérimentale de la localisation de la déformation par corrélation d'images sur un analogue de roche soumis à différentes conditions de chargement triaxiaux. phdthesis. Université Côte d'Azur.

Tueckmantel, C., Fisher, Q.J., Knipe, R.J., Lickorish, H., Khalil, S.M., 2010. Fault seal prediction of seismic-scale normal faults in porous sandstone: A case study from the eastern Gulf of Suez rift, Egypt. Marine and Petroleum Geology 27, 334–350. https://doi.org/10.1016/j.marpetgeo.2009.10.008

Underhill, J.R., 1991. Implications of Mesozoic—Recent basin development in the western Inner Moray Firth, UK. Marine and Petroleum Geology 8, 359–369. https://doi.org/10.1016/0264-8172(91)90089-J

Underhill, J.R., Woodcock, N.H., 1987. Faulting mechanisms in high-porosity sandstones; New Red Sandstone, Arran, Scotland. Geological Society, London, Special Publications 29, 91–105. https://doi.org/10.1144/GSL.SP.1987.029.01.09

Voigt, T., von Eynatten, H., Franzke, H.-J., 2004. Late Cretaceous unconformities in the Subhercynian Cretaceous Basin (Germany). Acta Geologica Polonica 54, 673–694.

Wibberley, C.A.J., Petit, J.-P., Rives, T., 2007. The mechanics of fault distribution and localization in high-porosity sands, Provence, France. Geological Society, London, Special Publications 289, 19–46. https://doi.org/10.1144/SP289.3

Wibberley, C.A.J., Yielding, G., Toro, G.D., 2008. Recent advances in the understanding of fault zone internal structure: a review. Geological Society, London, Special Publications 299, 5–33. https://doi.org/10.1144/SP299.2

Williams, R.T., Farver, J.R., Onasch, C.M., Winslow, D.F., 2015. An experimental investigation of the role of microfracture surfaces in controlling quartz precipitation rate: Applications to fault zone diagenesis. Journal of Structural Geology 74, 24–30. https://doi.org/10.1016/j.jsg.2015.02.011

Wong, T., Baud, P., 2012. The brittle-ductile transition in porous rock: A review. Journal of Structural Geology 44, 25–53. https://doi.org/10.1016/j.jsg.2012.07.010

Zhang, J., Wong, T.-F., Davis, D.M., 1990. Micromechanics of pressure-induced grain crushing in porous rocks. Journal of Geophysical Research: Solid Earth 95, 341–352. https://doi.org/10.1029/JB095iB01p00341

Zuluaga, L.F., Fossen, H., Rotevatn, A., 2014. Progressive evolution of deformation band populations during Laramide fault-propagation folding: Navajo Sandstone, San Rafael monocline, Utah, U.S.A. Journal of Structural Geology 68, 66–81. https://doi.org/10.1016/j.jsg.2014.09.008

SUPPLEMENTARY MATERIAL 2

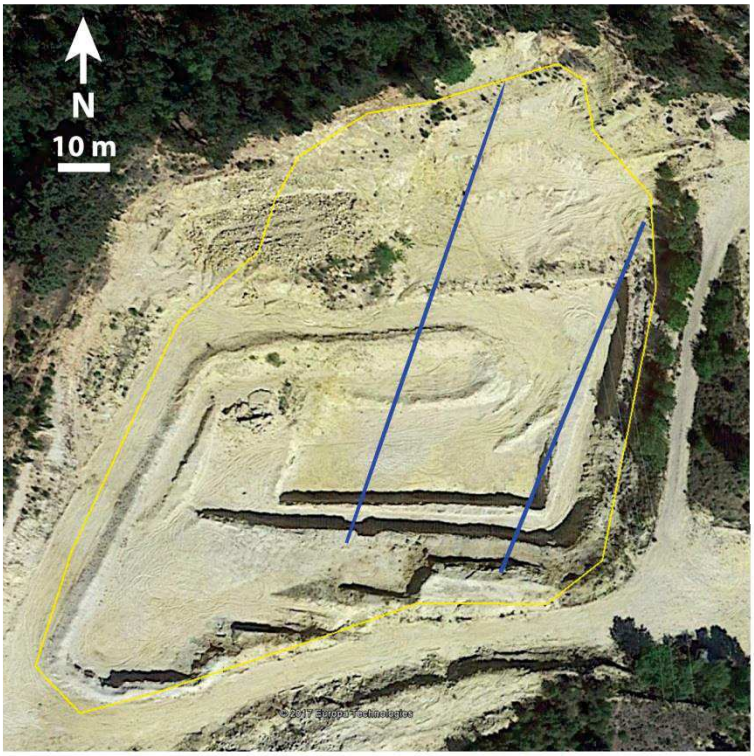

A1. Satellite view of the Boncavaï site with the mapped clusters formed in normal stress regime (blue - out of shear plane view). The thin yellow contours mark the limit of the cropping out area.

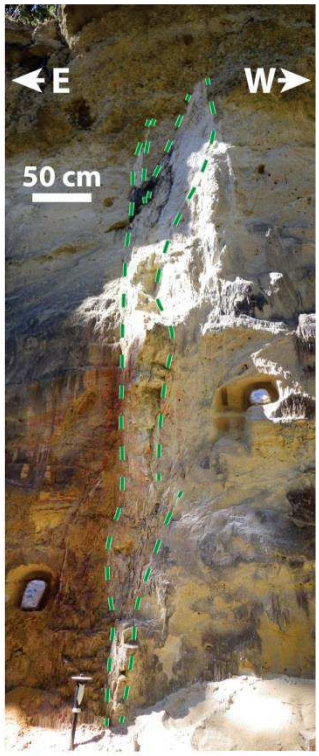

A2. Outcrop view of the site of Saint Michel. The cluster formed in strike-slip regime and is visible exclusively out of shear plane.

A3. Satellite view of the site of Bédoin with the mapped clusters formed in strike-slip stress regime (green - shear plane view). The thin yellow contours mark the limit of the cropping out area.

A4. Satellite view of the site of Blankenburg with the mapped clusters formed in thrust stress regime (red – out of shear plane view). The thin yellow contours mark the limit of the cropping out area.

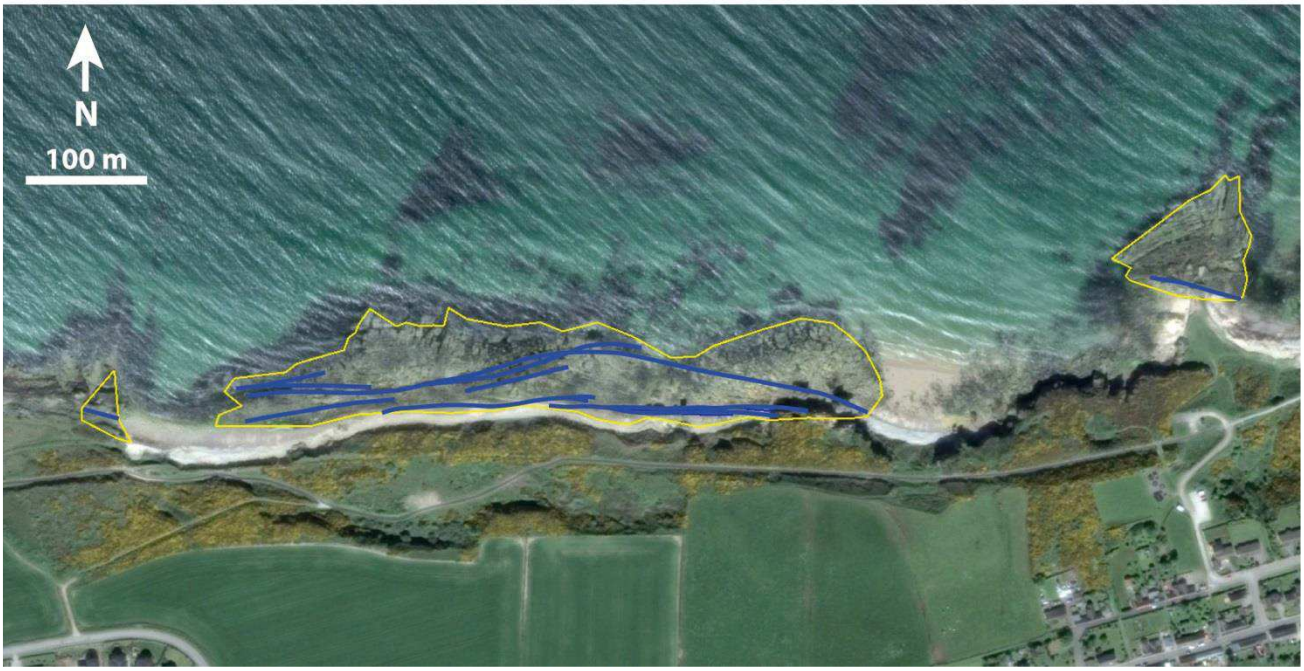

A5. Satellite view of the site of Cummingston with the mapped clusters formed in normal stress regime (blue – out of shear plane view). The thin yellow contours mark the limit of the cropping out area.

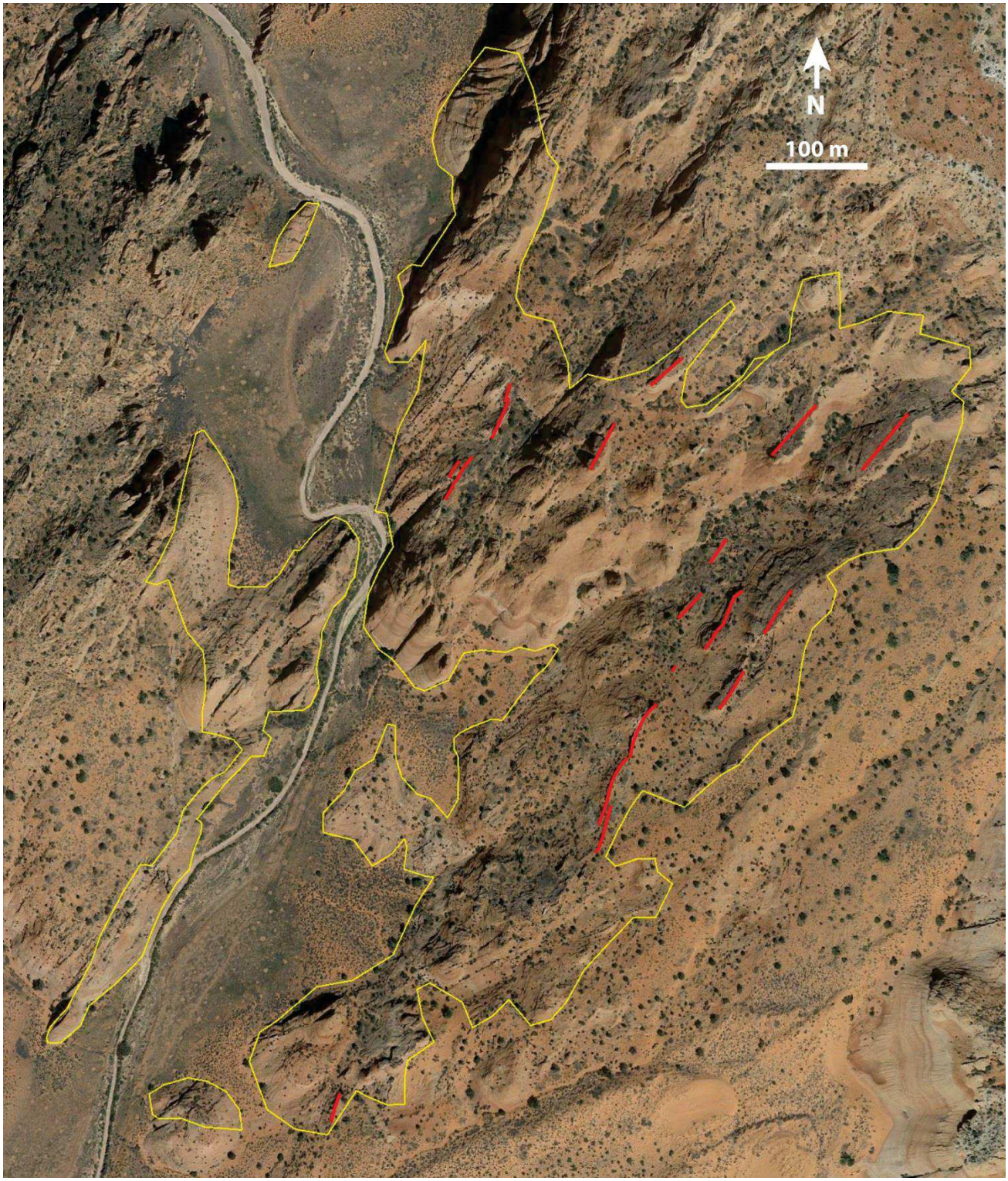

A6. Satellite view of the site of Buckskin Gulch with the mapped clusters formed in thrust stress regime (red – out of shear plane view). The thin yellow contours mark the limit of the cropping out area.

2.3.2. Analytical modeling

General hypotheses exist relating the failure position of the failure envelope and type of deformation generated in sandstone formation (e.g. Schultz and Siddharthan, 2005; Rutter and Glover, 2012; Soliva et al., 2013). However, the relation between the tectonic stress loading, the type of failure and the type of deformation generated remains unclear. As used by Soliva et al. (2013) and Ballas (2013), we developed an analytical tool to provide a semi-automated program in order to conveniently work out the different possible stress-paths until failure induced by different possible tectonic stress loadings. We will use this tool to analyze the possible stress state evolutions leading to the formation of clusters at the studied sites.

2.3.2a Model construction

We developed a VBA Excel code to automate the generation of the failure envelope of the considered host rock and the evolution of the stress-state in Q-P diagram, in which

$$\boldsymbol{Q = \sigma_1 - \sigma_3} \tag{6}$$

$$\boldsymbol{P = \frac{\sigma_1 + \sigma_2 + \sigma_3}{3} - Pf} \tag{7}$$

where σ_1, σ_2 and σ_3 are respectively the maximum, intermediate and minimum principal stresses, and Pf the isotropic fluid pressure induced by a free water column.

Failure envelope

Our program requires the lower and upper members of porosity as well as the lower and upper members of the modal grain size values of the considered host rock sandstone. These parameters are used as inputs to estimate the minimum and maximum *P** (equation (2) in section 1.3.2) for the failure envelopes of the host rock (Figure 46a). A minimum and maximum friction angles are inputted and are expressed as a minimum and maximum slope on the linear part of the envelope (simplified as the critical state line – CSL). As simplified from Schultz and Siddharthan (2005) and introduced by Ballas (2013), we use the following linear equation to model the left part of the failure envelope until *P**/2 (with *P** defined in equation (1) in section 1.3.2):

$$\boldsymbol{Q_{lin} = \frac{6 \sin \varphi}{3 - \sin \varphi} P} \tag{8}$$

where φ is the friction angle (which we take as comprised between 30 and 40°, which is a typical value in porous sandstones). The cap part of the failure envelope is described by the following ellipse equation:

$$\boldsymbol{Q_{cap}^2 = \left(\frac{6 \sin \varphi}{3 - \sin \varphi}\right)^2 P(P^* - P)} \tag{9}$$

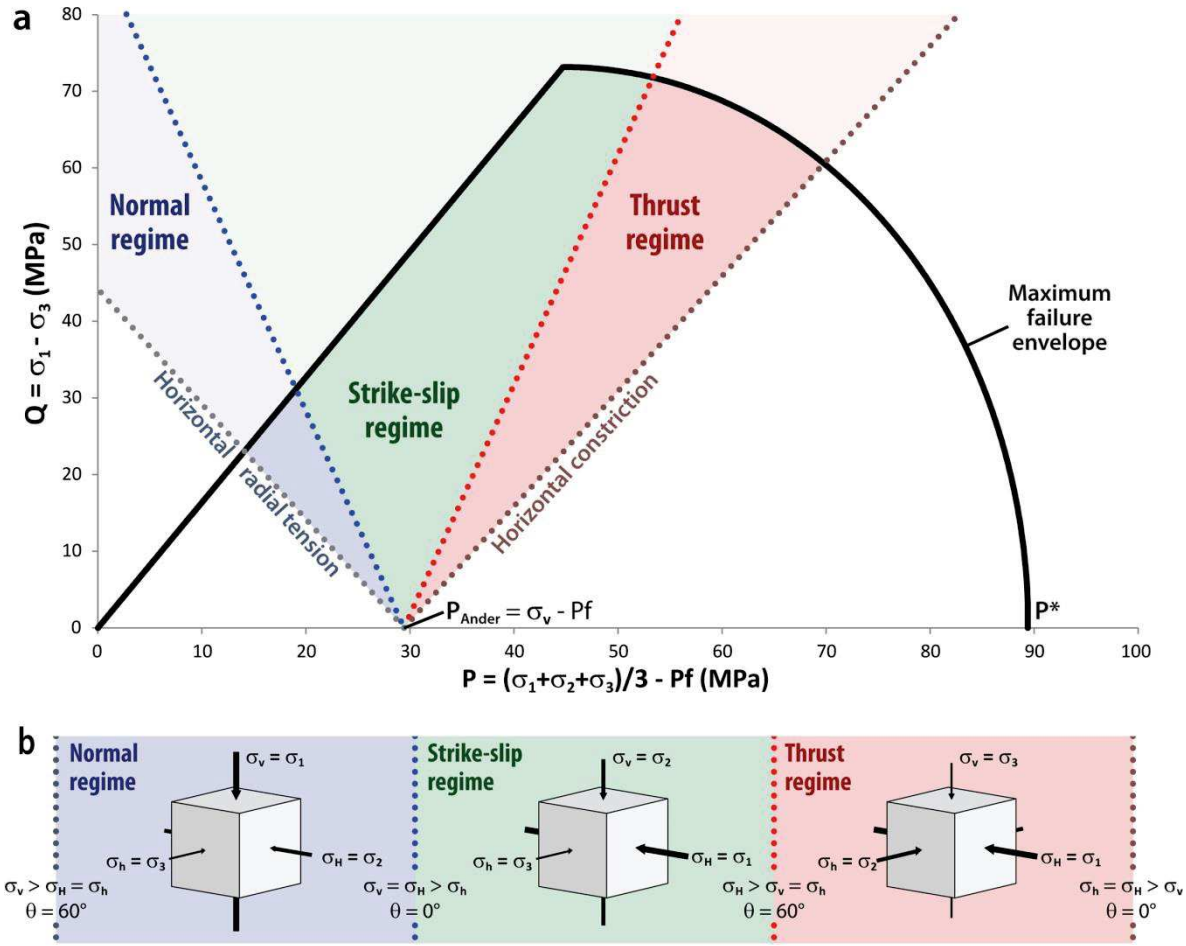

Figure 46. (a) Presentation of the setting of the failure envelopes, and Andersonian regime domains in the Q-P diagram. The size and shape of the envelope depends on several parameters (i.e. porosity, modal grain size, friction angle, burial depth, sedimentary column average density, coefficient of lateral stress and free water column). (b) Reminder of the different loading conditions defining the three Andersonian regimes as functions of the three main principal stresses, the vertical stress, and the maximum and minimum horizontal stresses. We indicate on the regime domain limits the cosine Lode angle θ corresponding to the loading stress.

Andersonian stress state domains

The relevance of reporting the Andersonian stress state domain on the Q-P diagram lies in the interest of linking the regime of deformation observed in the field to a range of possible failure locations on the failure envelope. Four lines on the Q-P diagram delimit the three Andersonian regimes (normal, strike-slip and thrust). We expose here their equation under the final form of functions $Q(P)$.

The different Andersonian stress state regimes are defined in terms of the three principal stresses σ_1, σ_2 and σ_3, and considering that two of the principal stresses axis σ_H and σ_h are comprised in the horizontal plane, and considering that the other one, σ_v, is vertical (Figure 46b):

- **Normal regime**: $\sigma_v = \sigma_1 > \sigma_H = \sigma_2 > \sigma_h = \sigma_3$
- **Strike-slip regime**: $\sigma_H = \sigma_1 > \sigma_v = \sigma_2 > \sigma_h = \sigma_3$
- **Thrust regime**: $\sigma_H = \sigma_1 > \sigma_h = \sigma_2 > \sigma_v = \sigma_3$

The conditions defining the limits between these Andersonian stress regimes are described by the following systems:

- **Maximum Normal regime limit**:

$$\boldsymbol{Limit_{NormalMax}}: \begin{cases} \boldsymbol{\sigma_1 = \sigma_v} & (10) \\ \boldsymbol{\sigma_2 = \sigma_H} & (11) \\ \boldsymbol{\sigma_3 = \sigma_h} & (12) \\ \boldsymbol{\sigma_H = \sigma_h} & (13) \end{cases}$$

- **Normal-Strike-slip regime limit:**

$$\boldsymbol{Limit_{Normal-SS}}: \begin{cases} \boldsymbol{\sigma_1 = \sigma_v} & (14) \\ \boldsymbol{\sigma_2 = \sigma_H} & (15) \\ \boldsymbol{\sigma_3 = \sigma_h} & (16) \\ \boldsymbol{\sigma_v = \sigma_H} & (17) \end{cases}$$

- **Strike-slip-Thrust regime limit:**

$$\boldsymbol{Limit_{SS-Thrust}}: \begin{cases} \boldsymbol{\sigma_1 = \sigma_H} & (18) \\ \boldsymbol{\sigma_2 = \sigma_v} & (19) \\ \boldsymbol{\sigma_3 = \sigma_h} & (20) \\ \boldsymbol{\sigma_v = \sigma_h} & (21) \end{cases}$$

- **Maximum Thrust regime limit:**

$$\boldsymbol{Limit_{ThrustMax}}: \begin{cases} \boldsymbol{\sigma_1 = \sigma_H} & (22) \\ \boldsymbol{\sigma_2 = \sigma_h} & (23) \\ \boldsymbol{\sigma_3 = \sigma_v} & (24) \\ \boldsymbol{\sigma_H = \sigma_h} & (25) \end{cases}$$

Using the equations (10) to (13) and replacing the principal stresses by the corresponding principal axis in (7), we have:

$$\boldsymbol{\sigma_h = \frac{3}{2}P - \frac{1}{2}\sigma_v + \frac{3}{2}Pf} \quad (26)$$

and using equations (10), (12) and (26) in (6), we obtain the **maximum limit of the Normal regime domain** (radial extension):

$$\boldsymbol{Q_{NormalMax} = -\frac{3}{2}P + \frac{3}{2}\sigma_v - \frac{3}{2}Pf} \quad (27)$$

Similarly, using the system of equations (14) to (17) in (7), we have:

$$\boldsymbol{\sigma_h = 3P - 2\sigma_v + 3Pf} \quad (28)$$

and using equations (14), (16) and (28) in (6), we obtain the **limit between the Normal and the Strike-slip regime domains**:

$$\boldsymbol{Q_{Normal-SS} = -3P + 3\sigma_v - 3Pf} \quad (29)$$

Using the system of equations (18) to (21) in (7), we have:

$$\boldsymbol{\sigma_H = 3P - 2\sigma_v + 3Pf} \quad (30)$$

and using equations(18), (20) and (30) in (6), we obtain the **limit between the Strike-slip and the Thrust regime domains**:

$$\boldsymbol{Q_{SS-Thrust} = 3P - 3\sigma_v + 3Pf} \quad (31)$$

Using the system of equations (22) to (25) in (7), we have:

$$\boldsymbol{\sigma_H = \frac{3}{2}P - \frac{1}{2}\sigma_v + \frac{3}{2}Pf} \quad (32)$$

and using equations (22), (24) and (32) in (6), we obtain the **maximum limit of the Thrust regime domain** (constriction):

$$\boldsymbol{Q_{ThrustMax} = \frac{3}{2}P - \frac{3}{2}\sigma_v + \frac{3}{2}Pf} \quad (33)$$

Hence, we note that the positions of the Andersonian regime domains in the Q-P diagram only depend on the fixed σ_v and the pore pressure Pf induced by a free water column.

These equations all intersect in one point P_{Ander} of the P axis, at Q = 0:

$$\boldsymbol{P_{Ander} = \sigma_v - Pf} \quad (34)$$

Finally, we remark that each of these lines correspond to a specific Lode angle θ (defined in section 3.1.1) which describes the stress loading, accounting for each principal stresses. θ varies from 60° along $Q_{NormalMax}$ to 0° along $Q_{Normal-SS}$, to 60° along $Q_{ThrustMax}$, back to 0° along $Q_{ThrustMax}$. As a reference, a stress loading at θ = 0° corresponds to triaxial tension (or constriction), and θ = 60° corresponds to triaxial compression (or radial tension). θ = 30° corresponds to pure shear.

Stress-path

To estimate the evolution of the stress loading of a sandstone from deposition until the formation of deformation bands (inelastic failure), we attempt to estimate the "*stress-path*" of the formation in the elastic domain. The *stress-path* correspond to the evolution of the stress state of a formation, depending on σ_1, σ_2 and σ_3, with $\sigma_1 \geq \sigma_2 \geq \sigma_3$. Failure occurs when the *stress-path* reaches the failure envelope.

The stress-path is built in two stages: (1) the building of the burial loading due to the vertical stress of the sedimentary column above the formation, and (2) the generation of the stress-paths induced by the different possible (horizontal) tectonic loadings. The vertical stress σ_v is obtained via the knowledge of the height of the sedimentary column Z_{sed} (from the literature) and the estimation of its average density ρ_{sed} at the time of deformation. Hence, the vertical stress is given as $\sigma_v = \rho_{sed}\, g\, Z_{sed}$, where g is the gravity at the Earth surface, taken as 9.81 m·s^{-2}. The horizontal confining pressure is considered equal to $K_0\sigma_v$, K_0 being the coefficient of Earth's pressure at rest ($K_0 = \sigma_h/\sigma_v$) in the absence of tectonic stresses in oedometric conditions. In the absence of tectonic stresses, multiple borehole analyses over the world show that K_0 inversely decreases with

increasing depth (Hoek and Brown, 1980) and suggest that K_0 depends both on the Young's modulus of the rock E, the burial depth Z, with the following relation (Sheoray, 1994):

$$\boldsymbol{K_0 = 0.25 + 7E\left(0.001 + \frac{1}{Z}\right)} \quad (35)$$

However, since the Young modulus of sands/sandstone highly varies with the state of consolidation of the rock, it would be irrelevant to calculate K_0 based on this theoretical equation. Instead, we rely on typical borehole K_0 measurement values comprised between 0.5 and 0.8 (Mitchell and Soga, 2005) from which we chose to use an intermediate value of 0.65 in our program. Taking into account the possible presence of a free water column Z_w, of density ρ_w of 1000 kg·m^{-3} responsible for an isotropic stress $Pf = \rho_w\, g\, Z_w$, we obtain the coordinates of the stress-path point $Q(P)_{bur}$ at deformation burial depth in the Q-P diagram (Figure 48):

$$\boldsymbol{Q_{bur} = (1 - K_0)\sigma_v} \quad (36)$$

$$\boldsymbol{P_{bur} = \frac{(1 + 2K_0)\sigma_v}{3} - Pf} \quad (37)$$

From the burial point and assuming that σ_v is constant, the construction of the stress-path associated with the tectonic loading includes all the possible tectonic stresses. The tectonic stresses are associated with stress differences along the horizontal principal stress axis relative to the confining pressure at rest $K_0\sigma_v$ (Figure 47). We define the stress difference along σ_H as $\Delta\sigma_H$ and the stress difference along σ_h as $\Delta\sigma_h$ with $\Delta\sigma_H \geq \Delta\sigma_h$. A positive $\Delta\sigma_H$ or $\Delta\sigma_h$ corresponds to a stress excess; a negative $\Delta\sigma_h$ or $\Delta\sigma_H$ corresponds to a stress deficit. With these components, the horizontal stresses are defined as follows:

$$\boldsymbol{\sigma_H = K_0\sigma_v + \Delta\sigma_H} \quad (38)$$

$$\boldsymbol{\sigma_h = K_0\sigma_v + \Delta\sigma_h} \quad (39)$$

This formulation affords the advantage of describing any stress loading, including all components of any potential tension or compression along the horizontal principal stress axis (Figure 48). We

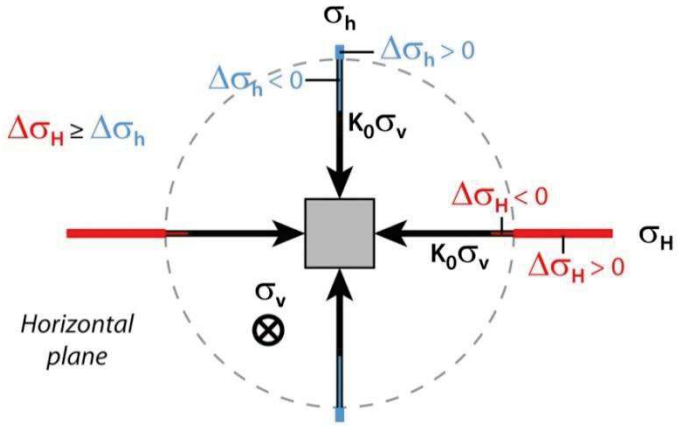

Figure 47. Setup of the horizontal stresses for the modeling of the tectonic loading.

describe here the different possible tectonic stress loadings:

- The **transtensive tectonics** corresponds to loading conditions with a major stress deficit compared to the stress excess such as $|\Delta\sigma_h| \geq |\Delta\sigma_H|$. To describe conveniently all possible stress loadings in transtensive tectonics, we define a ratio $\eta_{tens} = \frac{\Delta\sigma_H}{\Delta\sigma_h}$. η_{tens} ranges from -1 when the stress excess is as important as the stress deficit ($\Delta\sigma_H = -\Delta\sigma_h$), (**intermediate tectonics)**, to 0 when $\Delta\sigma_H = 0$ (**pure tensional tectonics**), to 1 when $\Delta\sigma_H = \Delta\sigma_h < 0$ (**radial tension**). We model 11 transtensive stress loadings corresponding to the following ratios from the pure tensional tectonics to the intermediate tectonics:

$$\boldsymbol{\eta_{tens}} = \frac{\mathbf{0}}{\mathbf{10}}; \frac{\mathbf{-1}}{\mathbf{10}}; \frac{\mathbf{-2}}{\mathbf{10}}; \frac{\mathbf{-3}}{\mathbf{10}}; \frac{\mathbf{-4}}{\mathbf{10}}; \frac{\mathbf{-5}}{\mathbf{10}}; \frac{\mathbf{-6}}{\mathbf{10}}; \frac{\mathbf{-7}}{\mathbf{10}}; \frac{\mathbf{-8}}{\mathbf{10}}; \frac{\mathbf{-9}}{\mathbf{10}}; \frac{\mathbf{-10}}{\mathbf{10}}$$

- **The transpressive tectonics** corresponds to loading conditions with a major stress excess compared to the stress deficit such as $|\Delta\sigma_H| \geq |\Delta\sigma_h|$. To describe conveniently all possible stress loadings in transpressive tectonics, we define a ratio $\eta_{comp} = \frac{\Delta\sigma_h}{\Delta\sigma_H}$. η_{comp} ranges from -1 when the stress deficit is as important as the stress excess ($\Delta\sigma_H = -\Delta\sigma_h$), (**intermediate tectonics)**, to 0 when $\Delta\sigma_h = 0$ (**pure compressional tectonics**), to 1 when $\Delta\sigma_H = \Delta\sigma_h > 0$ (**constriction**). We model 11 transpressive stress loadings corresponding to the following ratios, from the intermediate tectonics to the pure compressional tectonics:

$$\boldsymbol{\eta_{con}} = \frac{\mathbf{-10}}{\mathbf{10}}; \frac{\mathbf{-9}}{\mathbf{10}}; \frac{\mathbf{-8}}{\mathbf{10}}; \frac{\mathbf{-7}}{\mathbf{10}}; \frac{\mathbf{-6}}{\mathbf{10}}; \frac{\mathbf{-5}}{\mathbf{10}}; \frac{\mathbf{-4}}{\mathbf{10}}; \frac{\mathbf{-3}}{\mathbf{10}}; \frac{\mathbf{-2}}{\mathbf{10}}; \frac{\mathbf{-1}}{\mathbf{10}}; \frac{\mathbf{0}}{\mathbf{10}}$$

For each tectonic loading, the stress-path is obtained by solving *Q* and *P* (equations (6) and (7)) according to the conditions imposed by the Andersonian regime until the stress-path reaches a limit of Andersonian regime domain (equations (31) and (33)) or intercept the maximum failure envelope. We remark in Figure 48 that the stress-paths induced by the tectonic loadings follow linear paths with inflections when crossing the limits of the Andersonian regime domains. These inflexions correspond to switches of the principal stresses σ_1, σ_2 and σ_3 along the principal stress axis σ_v, σ_H and σ_h as $\Delta\sigma_H$ and $\Delta\sigma_h$ evolve (Figure 46b).

As an implication of this development for the stress-path analysis, we see that the same tectonic stress loading can evolve through different Andersonian regimes and consequently lead to possible failure under the three Andersonian regimes. In particular, we see from the combination of the stress-paths and regime domain geometries that deformation under transtensive tectonic loading is more likely to cause failure under normal Andersonian regime, and less frequently, under strike-slip regime if the differential stress Q is high enough. On the other hand, deformation under transpressive tectonic loading first leads to potential failure under strike-slip regime, and frequently leads to failure under thrust regime if the effective stress P is further increased.

Shortcomings

Our attempt of estimating the stress-path obviously suffers several limitations that should be submitted to improvement.

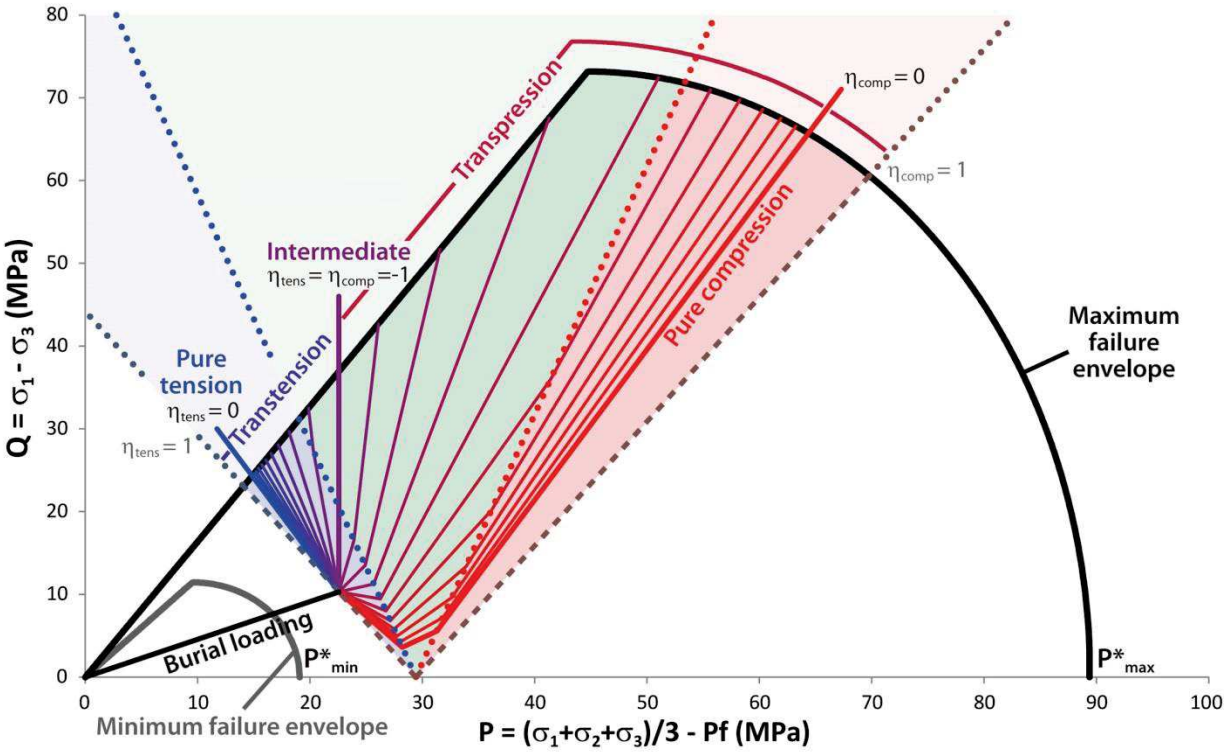

Figure 48. Building of the stress-path corresponding to several tectonic stress loadings after a fixed burial depth is attained (σ_v constant), corresponding to the burial depth at which deformation occurred. Two main types of loading are possible: (i) The transtension, encompassing radial tension (not modeled in our program), pure tension and intermediate tectonics; (ii) The transpression, encompassing the intermediate tectonics, the pure compression and the constriction (not modeled in our program). From the stress state of burial at deformation, as the horizontal stresses evolve, the different stress-paths loaded differently will possibly cross several Andersonian regime domains, from the normal regime, to the strike-slip regime, to the thrust regime.

Firstly, the estimated failure envelope of the host rock is simplified with two simple functions that correspond to a linear function simplified as the critical state line on the brittle part of the envelope (equations (8) and (9)), and an elliptic function for the cap, with an estimated maximum hydrostatic stress *P** (equation (2)) based on empirical laboratory experiments. Yet, in the detail, it is obvious that the failure envelope is continuous and depends on more parameters than the modal grain size and the porosity of the rock. Figure 49 shows examples where the linear and elliptical part of the failure envelope was smoothed to mimic a more natural shape, better fitting with triaxial test experimental results. The function used in these examples is actually divided in two parts. The part on the right is described by an ellipse equation whose center is neither necessarily aligned with the ordinate origin nor with ½ *P**. The part on the left is described by a function with a left end member described by a linear equation (not necessarily passing through the origin), and a right end member described by the ellipse equation and whose influence can be increased towards the left. A main downside of this function is that the calculation of the intercept between the stress-path and the failure envelope becomes complex. Besides, we cannot link the parameters controlling the shape of the envelope (e.g. the origin of the elliptical part, the ratio of influence of the elliptical equation on the linear part of the function) to any concrete physical constant.

Secondly, we note that even with a more natural description of the failure envelope, the representation of failure location in the Q-P diagram would remain erroneous. Indeed, it was shown that the shape of the failure envelope changes with evolving Lode angles θ (Chemenda and Mas,

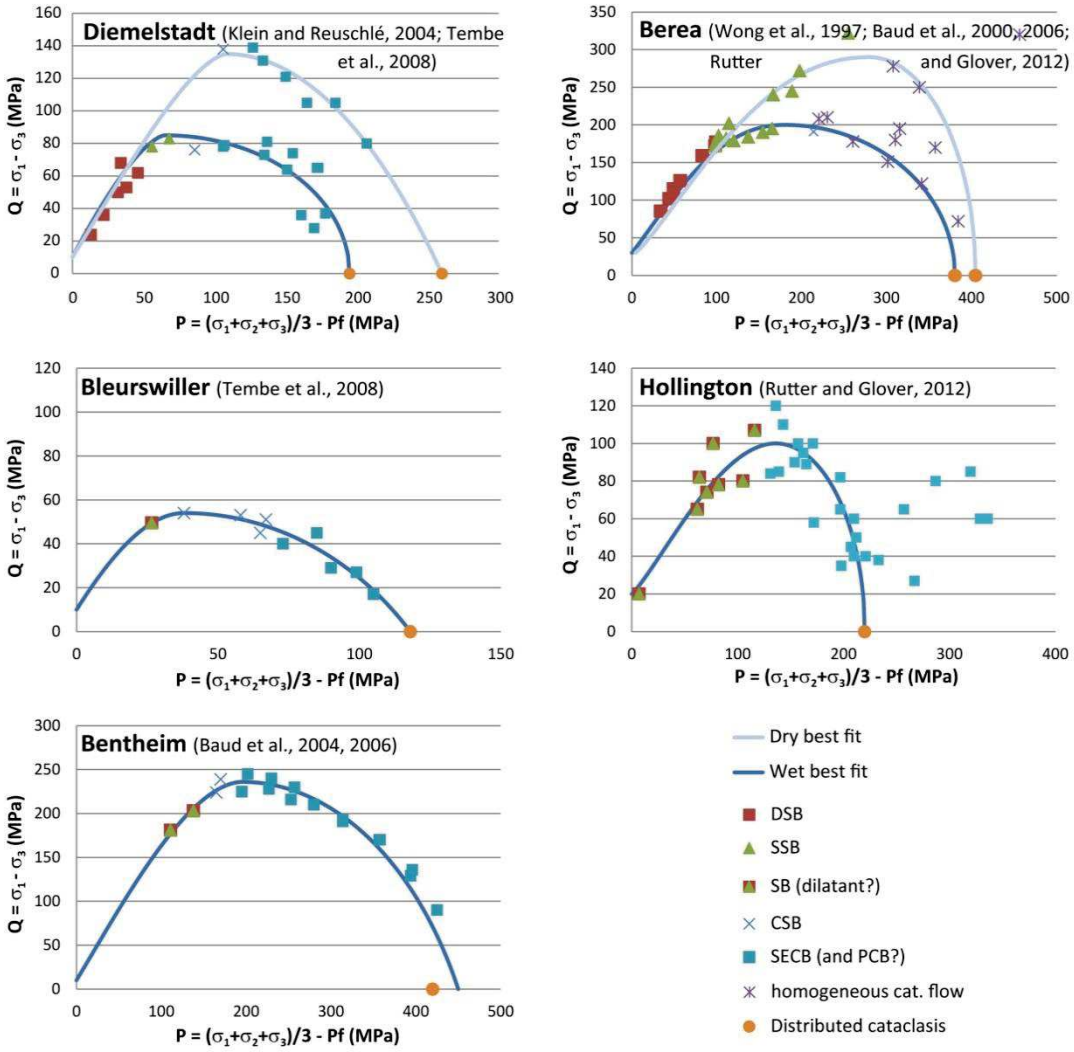

Figure 49. Examples of best fits based on a modulated linear-elliptical equation on critical stress state plots from triaxial tests. We complied the results and the description available in different works (wet tests) to create those plots. The references are indicated on the respective diagrams. The legend for the type of structures formed is common.

2016, and examples shown in . where the pore pressure in the tested samples alters θ compared to the dry tests). Hence, to enhance the correctness of the representation, the shape of the failure envelope should be plotted dynamically according to the evolution of a given stress-path along which θ varies. Another way to foresee the stress-path analysis until failure would be to represent the stress-path evolution in the space of the principal stresses $\sigma_v - \sigma_H - \sigma_h$ (Figure 50a), displaying the complex failure envelope as in Chemenda and Mas (2016) (Figure 50b), and mark the change of regime when the principal stresses σ_1, σ_2 and σ_3 switch of axis.

Thirdly, our model considers an evolution of stress-path divided in two parts, namely the burial and the tectonics loading. It is obvious that the true geological evolution of a sandstone formation undergoes in most cases synchronous burial and tectonic loading, the latter being at the origin of basin formation (e.g. rifting) or destruction (e.g. bulging).

Eventually, our development assumes that the property of the rock has a constant behavior to stress state with increasing stages of deformation, as if the cumulated inelastic deformation didn't alter the failure envelope of the host rock outside of the band. In other words, we consider that the

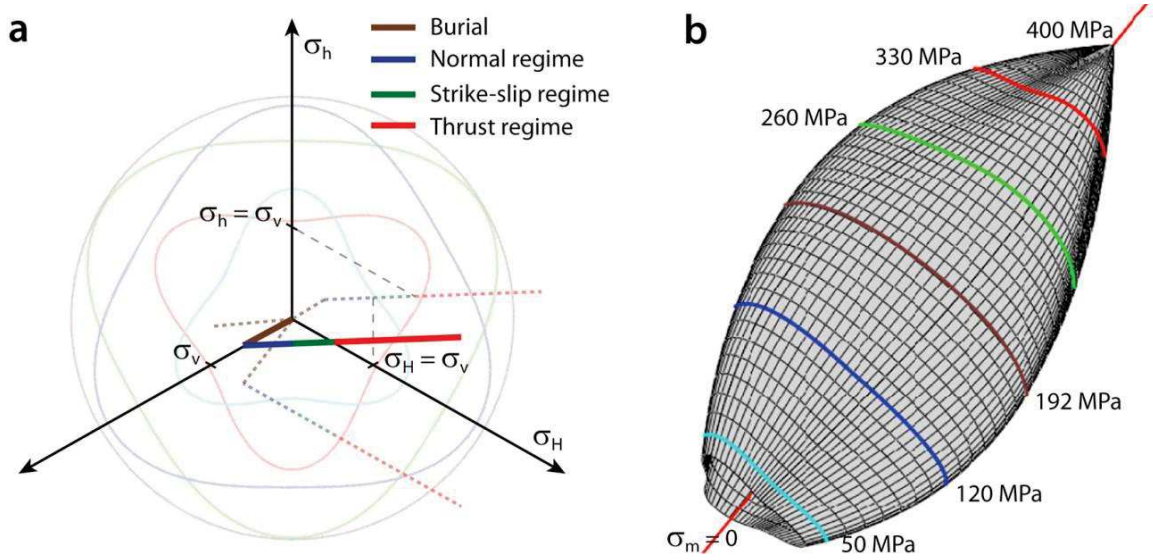

Figure 50. (a) Representation of the evolving stress-path in the $\sigma_1 - \sigma_2 - \sigma_3$ space. (b) The variyng failure envelope as a function of the Lode angle in the $\sigma_1 - \sigma_2 - \sigma_3$ space (wose colored iso-mean-stress curves are represented in transparency in (a).

sandstone formation has constant elastic behavior. This assumption seems correct if we consider that the inelastic deformation created during failure was concentrated solely in the deformation bands (hardened), locally corresponding to a material with a bigger failure envelope than the undeformed host rock. Consequently, provided that the host rock sandstone is infinite, further steps of deformation would be indefinitely accommodated by the host rock with unchanging failure envelope. However microscopic field observations and laboratory experimental analyses show that the host rock undergo a slight pervasive inelastic deformation (Lanatà, 2014). Hence, our analytical tool should be improved to account for increasing inelastic deformation in a 3D stress-state diagram, therefore proposing a yield surface as used by Mas and Chemenda (2015) described by laboratory experiments on a large population of sandstones.

2.3.2b Application of the analytical model to the study sites

In this section, we present the analytical models performed for the estimation of the stress-path at the study sites and the localization of the rupture on the possible failure envelopes. Remark that this analysis represents an exploratory part of our work and could be improved by many aspects, as pointed out in the previous section. Nevertheless, the stress-path analysis allows estimating the failure position on the failure envelope of the material, accounting for the Andersonian stress regime at deformation.

Data Input

The parameters inputted for the minimum and maximum failure envelopes are drawn from the information of modal grain size and porosity reported in the geological setting (section 2.1). In the case of sites where one single modal grain size is reported, the minimum and maximum failure envelopes account for a grain size variation of ±50 µm. In the case of sites where several modal grain size (representative of different sandstone formations) are reported, the minimum failure envelope accounts for the highest grain size (and the highest porosity), the maximum failure envelope accounts for the lowest grain size (and the lowest porosity). The average burial depth at deformation (from the literature data – cf. section 2.1) was selected in cases where the burial uncertainty was

lower than 400 m. The minimum and maximum burial depths at deformation are reported when the uncertainty spans over 400 m. Although it is possible to input a free water column in the models, we decided not to do so in absence of evidence of the water column at the time of deformation (even though some formations were certainly in aquifer at that time). This uncertainty must be considered a source of error in our models as it induces a general shift of the stress-state evolution towards the left of the Q-P diagram (cf. Figure 51). In each case, the minimum and maximum friction angles are arbitrarily set to 30 and 40 because this range is common in sandstone. The average density varies from 1800 kg·m^3 in the shallow-buried and very porous sandstone of St Michel, to 1900 kg·m^3 for the shallow-buried sandstones of Boncavaï and Bédoin, to 2200 kg·m^3 for the sandstones of Blankenburg and Cummingston, to 2500 kg·m^3 for the deeply buried sandstones of Goblin Valley and Buckskin Gulch. As mentioned previously, K_0 is set to 0.65 for all sites.

Estimation of the failure solutions

The position of failure in the Q-P diagram is constrained in the area between the maximum and minimum failure envelopes, and between the limits of the Andersonian regime domains in which the formation is recognized to have occurred (from field observations) (Figure 52). If the burial at the time of deformation is not well known, the failure is constrained between the lower limit of the regime domain for the minimum burial and the upper limit of the regime domain for the maximum burial. Besides, because specific types of bands can be associated with specific parts of the failure envelope (e.g. Figure 49), the types of band recognized in the clusters can, to some extent, constrain the area of solution for failure. We indicate for reference the approximate positions of these types of bands above the maximum failure envelope. The same positions apply for the minimum failure envelope and, virtually, for the infinite possible envelopes in between. Because the types of band reported in experimental tests are not necessarily consistent with the types of bands defined by Fossen et al., (2007 and 2017 introduced in section **Erreur ! Source du renvoi introuvable.**), we shall use these positions cautiously during the failure analysis. Solution areas for failure are represented with colored polygons. Blue polygons represent failure under normal regime, green polygons represent failure in strike-slip regime, and red polygons represent failure in thrust regime.

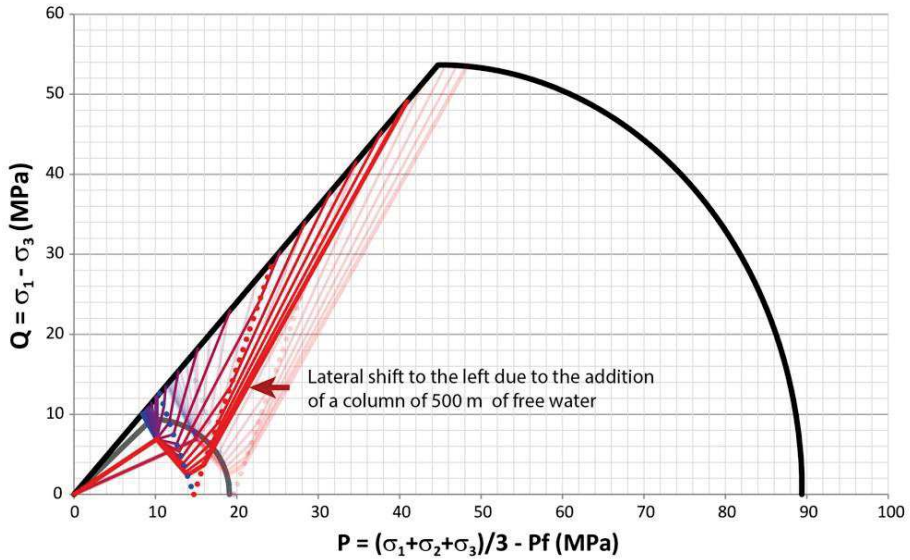

Figure 51. diagram illustrating the left-lateral shift of the general stress-state evolution induced by the addition of a column of 500 m of water.

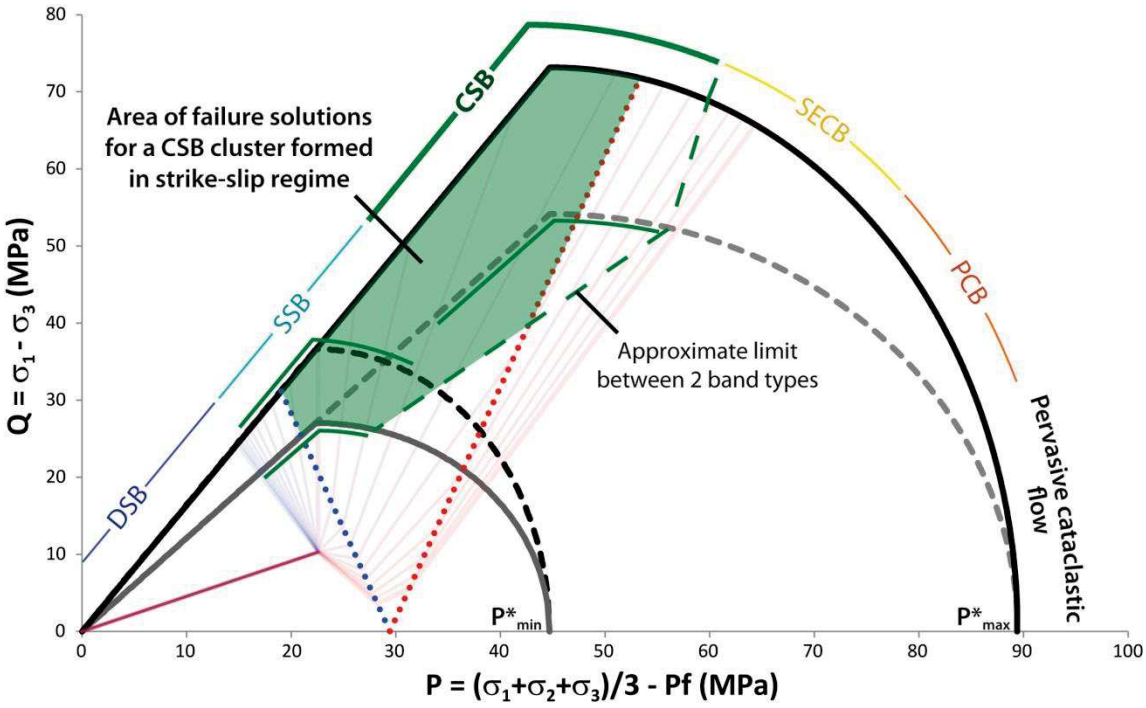

Figure 52. Synthetic illustration showing the analytical solution of a failure in the Q-P diagram. We use the example of a sandstone deformed in strike-slip regime with CSB. The general solution consists of an area (in green) delimited by specific borders (see details in the text).

Results and discussion

The analytical models performed for the estimation of the stress-path at the study sites and the localization of the failure on the possible failure envelopes are presented from Figure 53 to Figure 59 .

The site of **Boncavaï** (Figure 53) deformed in normal regime appears to fail at very low effective pressure (P ~ 3 MPa), corresponding to the extreme left to medium left of the linear part of the envelope, depending on the range of possible failure envelopes. The stress-path corresponding to such a failure is close to a pure tensional tectonic stress, which is consistent with the deformation in extensional tectonics recognized at the site. According to the approximate position of the recognized types of bands in experimental tests, these failures would correspond to the formation of Dilational Shear Bands (DSB) to Simple Shear Bands (SSB). These theoretical results do not agree with the observation of Compactional Shear Bands (CSB) in the field. This suggests either that we overestimated the size of the potential failure envelopes, or that the formation of CSB is actually possible towards the extreme left of the envelope.

The site of **St Michel** (Figure 54) deformed in strike-slip regime seems to fail at very low effective pressure (P ~ 3 MPa), corresponding to the left to summit of the envelope, depending on the failure envelope. The stress-path corresponding to such a failure is a transpressive tectonic stress, which is consistent with the deformation in contractional tectonics recognized at the site. According to the approximate position of the recognized types of bands, these failures would correspond to the formation of DSB to CSB. Because CSB compose the cluster formed at St Michel, we deduce that deformation probably occurred in a sandstone of rather small failure envelope, towards the summit of the envelope.

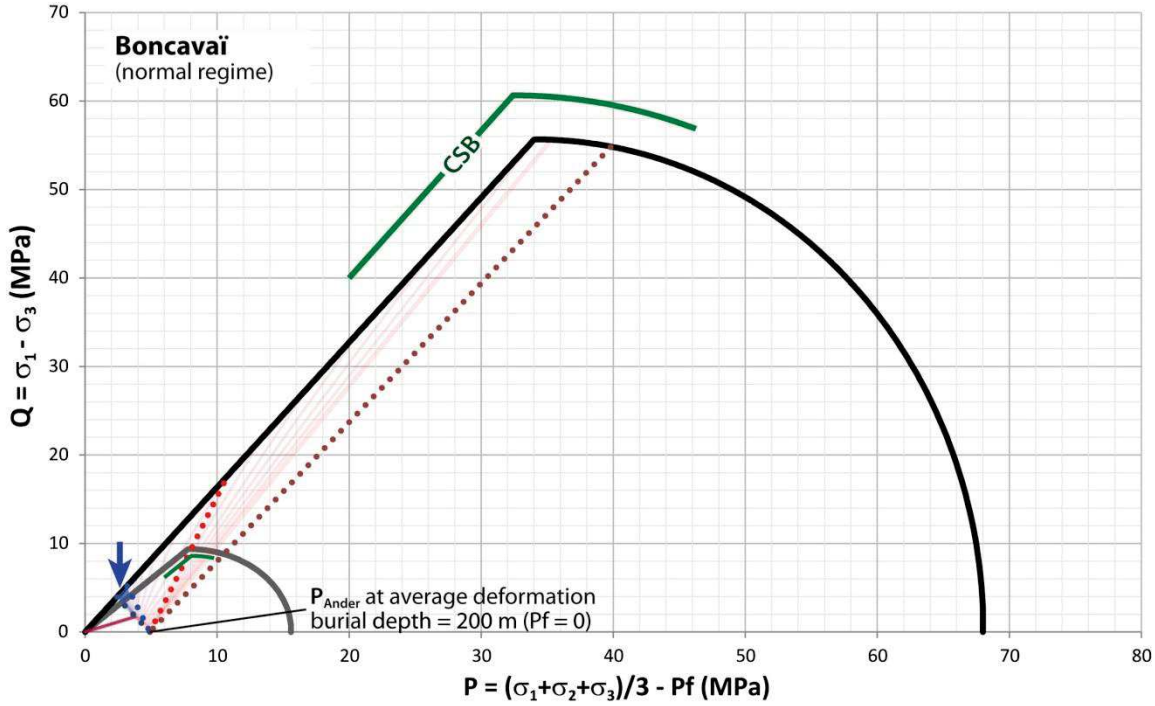

Figure 53. Q-P diagram showing the construction utilized in the analysis and resolution of the failure location on the failure envelope at the site of Boncavaï. The site is deformed in normal Andersonian regime and with a deformation localizing on the field under the form of CSB.

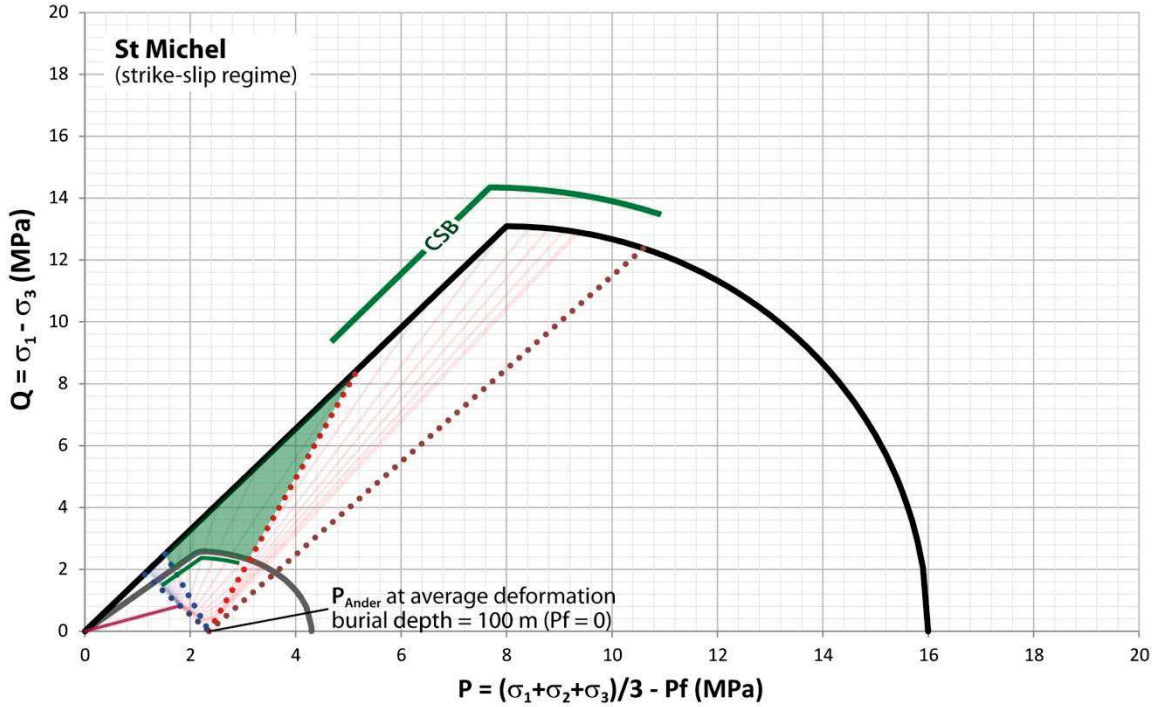

Figure 54. Q-P diagram showing the construction utilized in the analysis and resolution of the failure location on the failure envelope at the site of St Michel. The site is deformed in strike-slip Andersonian regime and with a deformation localizing on the field under the form of CSB.

The site of **Bédoin** (Figure 55) deformed in strike-slip regime displays a failure at very low effective pressure (P ~ 3 MPa), corresponding to the extreme left to summit of the envelope, on both the minimum and maximum failure envelopes. The stress-path corresponding to a transpressive tectonic stress, which is consistent with the deformation in contractional tectonics recognized at the site. According to the approximate position of the recognized types of bands in experimental tests, these failures would correspond to the formation of DSB to SSB. These theoretical results do not agree with the observation of CSB at Bédoin. Again, this suggests either that we overestimated the size of the potential failure envelopes, or that the formation of CSB is actually possible towards the extreme left of the envelope.

Because the burial depth of deformation at the site of **Blankenburg** (Figure 56) is not well constrained (i.e. between 0 and 800 m), the position of failure on the failure envelopes is inaccurate. The site underwent deformation in thrust regime and displays an effective mean stress ranging from 8 to about 30 MPa depending on the burial depth when the sandstone was deformed. Such a range of possible failure corresponds to possible failure along the middle part of the envelope, up to the summit and the left part of the cap. Because CSB are observed in the composition of the clusters at Blankenburg, and assuming that the position of the band types along the failure envelope about correct, we can constrain the failure at effective pressure lower than 30 MPa because failure at higher P would probably have generated Shear Enhanced Compaction Bands (SECB). The deformation in contractional tectonics at the site suggests a stress-path in transpressive tectonic loading. However, the wide range of possible burial depths prevents from assessing any accurate stress-path in this case.

The site of **Cummingston** (Figure 57) deformed in normal regime seems to fail at low effective pressure (P ~ 7 MPa), corresponding to the extreme left of the linear part of the envelope,

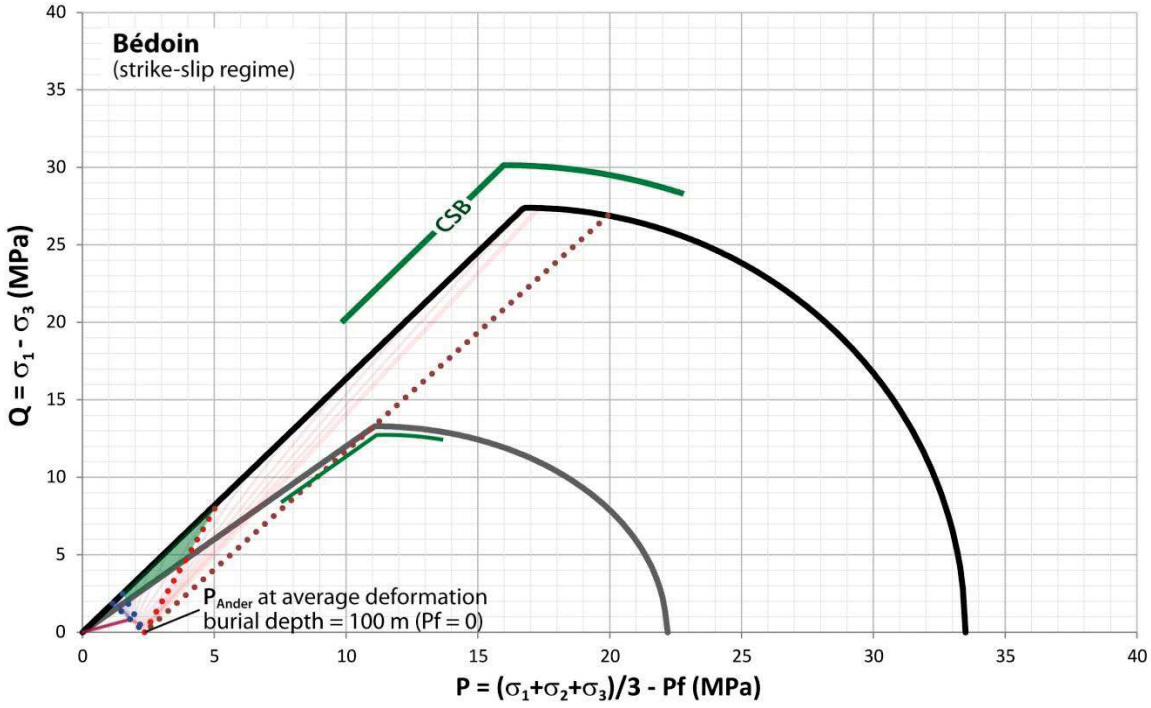

Figure 55. Q-P diagram showing the construction utilized in the analysis and resolution of the failure location on the failure envelope at the site of Bédoin. The site is deformed in strike-slip Andersonian regime and with a deformation localizing on the field under the form of CSB.

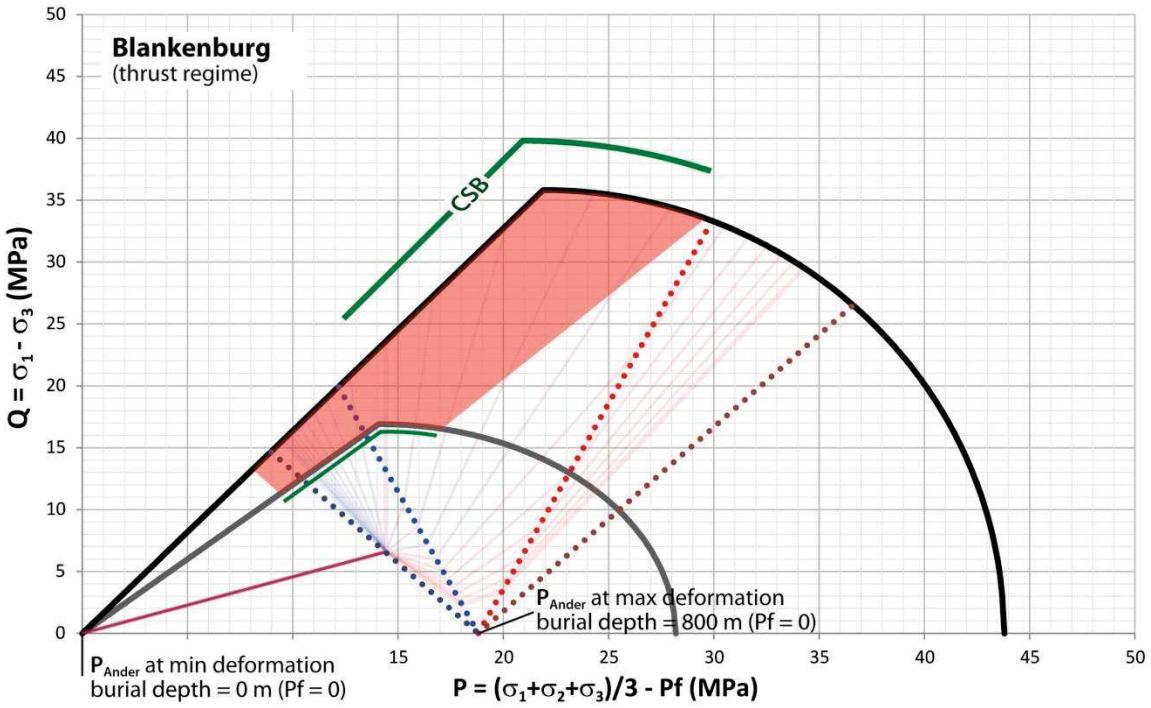

Figure 56. Q-P diagram showing the construction utilized in the analysis and resolution of the failure location on the failure envelope at the site of Blankenburg. The site is deformed in thrust Andersonian regime and with a deformation localizing on the field under the form of CSB.

on both the minimum and maximum failure envelopes. The stress-path corresponding to such a failure is close to a pure tensional tectonic stress, which is consistent with the deformation in extensional tectonics recognized at the site. According to the approximate position of the recognized types of bands, these failures would correspond to the formation of DSB to SSB. As in the case of Boncavaï, these theoretical results do not agree with the observation of CSB composing the clusters in the field. As in the cases of Boncavaï and Bédoin, this suggests either that we overestimated the size of the potential failure envelopes, or that the formation of CSB is actually possible towards the extreme left of the envelope.

The site of **Goblin Valley** (Figure 58) deformed in normal regime displays a failure at effective pressure ranging from 15 to 35 MPa according to the burial depth uncertainty. The corresponding failure locates to the left of the brittle part of the envelope on the maximum failure envelope, and up to the left part of the cap on the minimum failure envelope. The stress-path corresponding to such a failure is close to a pure tensional tectonic stress, which is consistent with the deformation in extensional tectonics recognized at the site. According to the approximate position of the recognized types of bands, these failures would correspond to the formation of DSB to CSB. Because CSB are observed in the composition of the clusters at Goblin Valley, we can constrain the failure at effective pressure lower than 35-40 MPa because failure at higher P would probably have generated SECB.

Because the burial depth of deformation at the site of **Buckskin Gulch** (Figure 59) is poorly constrained (i.e. between 1000 and 2600 m), the position of failure on the failure envelopes is very inaccurate. The site underwent deformation in thrust regime and displays effective mean pressure ranging from 40 to about 100 MPa depending on the burial depth when the sandstone was deformed. Failure at P > 100 MPa is not probable because the deformation would certainly have

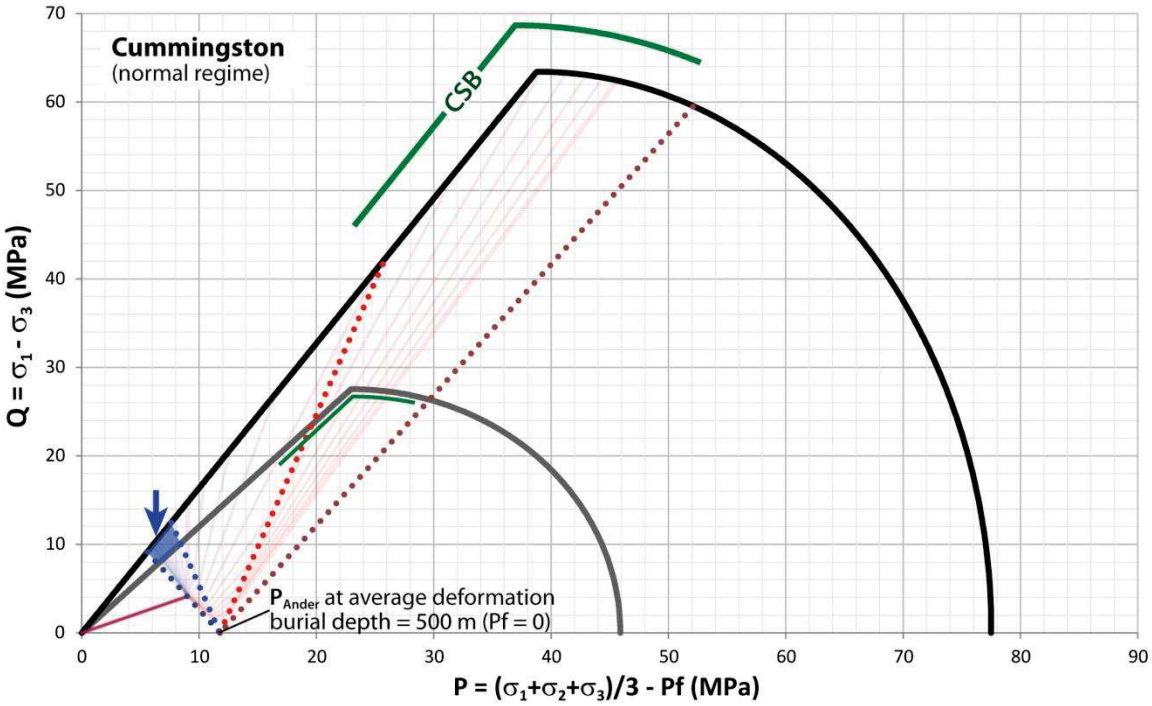

Figure 57. Q-P diagram showing the construction utilized in the analysis and resolution the failure location on the failure envelope at the site of Cummingston. The site is deformed in normal Andersonian regime and with a deformation localizing on the field under the form of CSB.

generated Pure Compaction Bands (PCB) instead of SECB such as observed in the clusters at the site. The failure location of the middle part of the cap suggest for both minimum and maximum failure envelopes a stress-path close to pure compression, which is consistent with the deformation in contractional tectonics at the site. The minimum effective pressure of about 30 MPa at failure suggests that the minimum failure envelope is bigger that estimated in the analysis.

Depending on the study site, we see that the area of solution for failure varies drastically. These variations are obviously linked to our capacity to constrain the different input parameters. In particular, the lack of constrain on the burial depth at deformation is responsible for a major surface increase in the areas of solution. We remark that, for comparable uncertainty, the area of solution for failure is larger for deformation in thrust regime than in normal regime (e.g. Blankenburg - Figure 56, Goblin Valley - Figure 58).

We can see that, for a same study site including different types of host rock sandstones of variable petrophysical parameters (i.e. modal grain size, porosity) such at Goblin Valley (Figure 58), the-stress-path evolution under similar tectonic stress loading reaches different parts of the respective failure envelopes of the different sandstones. This suggests that different neighboring sandstones fail at different times of the tectonic history and with different type of deformation structures (SECB, CSB, etc.).

Globally, we observe that, except in the case of Buckskin Gulch, all the clusters potentially formed with failure on the brittle part of the envelope, including on the very left where experimental tests predict the formation of dilatant structures, or near the summit of the envelope. The case of Buckskin Gulch indicates that clusters can be observed when failure hits the cap of the envelope near the summit. In relation with section 1.3.2, we note that the clusters on the cap part of the envelope

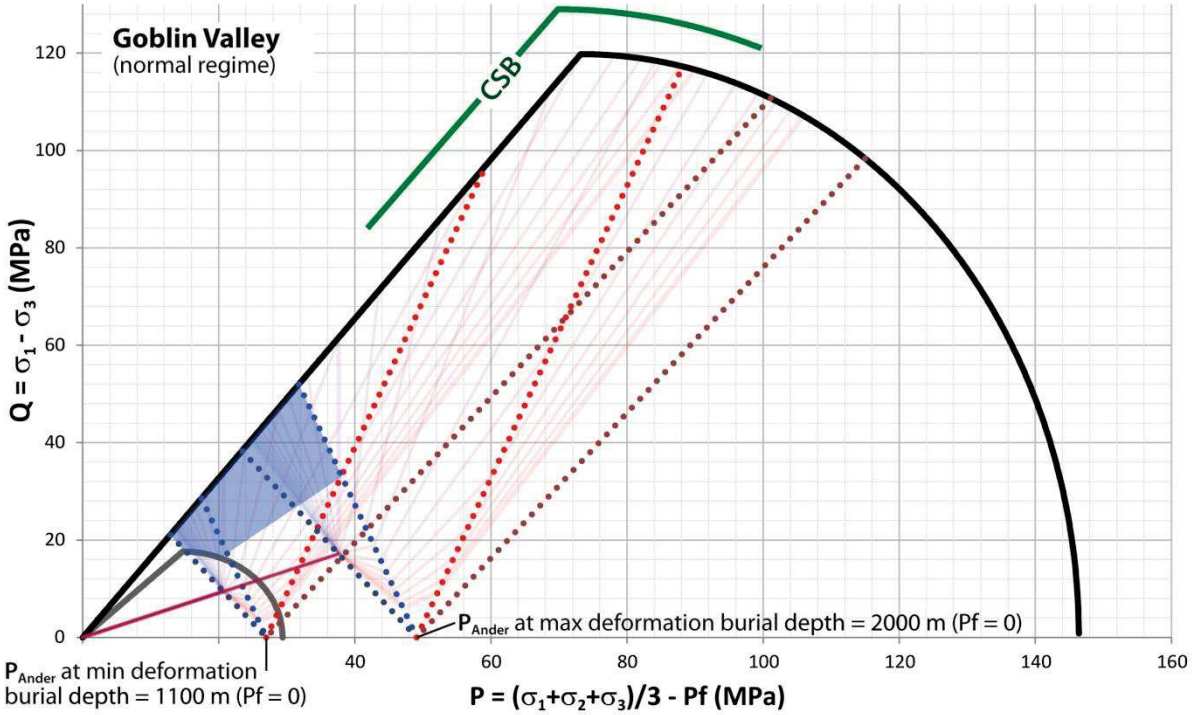

Figure 58. Q-P diagram showing the construction utilized in the analysis and resolution of the failure location on the failure envelope at the site of Goblin Valley. The site is deformed in normal Andersonian regime and with a deformation localizing on the field under the form of CSB.

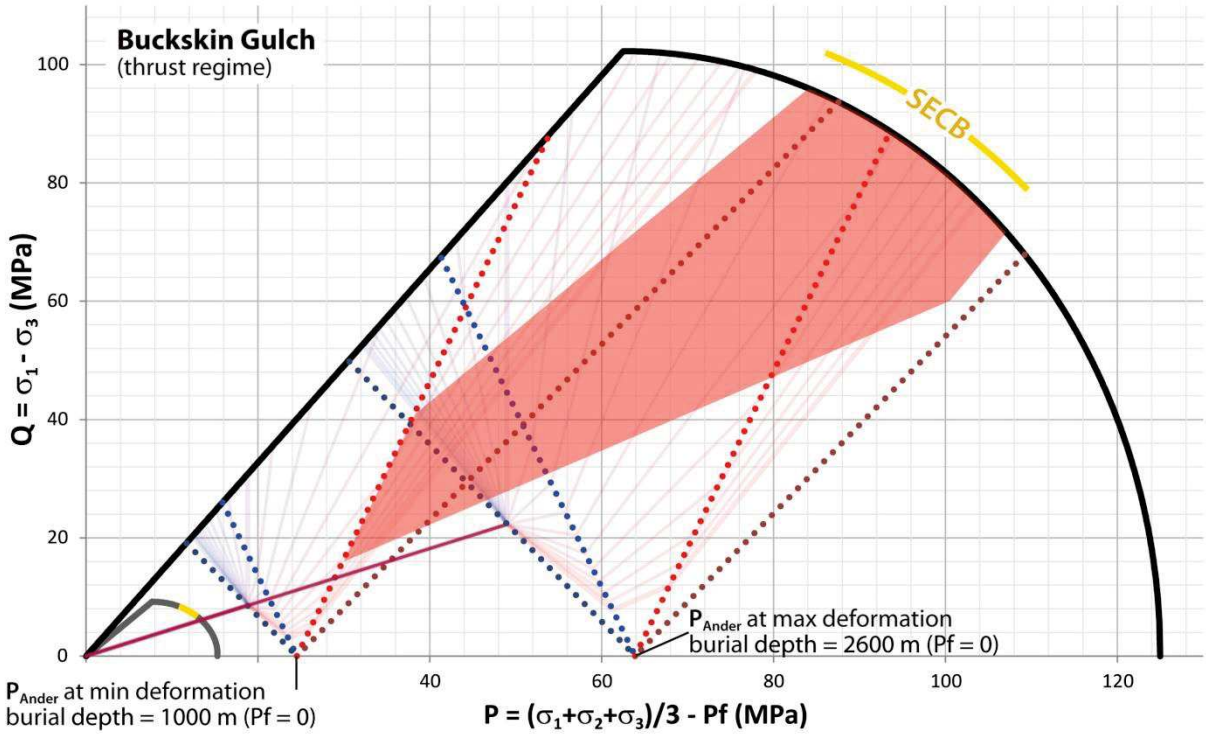

Figure 59. Q-P diagram showing the construction utilized in the analysis and resolution of the failure location on the failure envelope at the site of Buckskin Gulch. The site is deformed in thrust Andersonian regime and with a deformation localizing on the field under the form of SECB.

would be thicker, but with lower band density a lower degree of cataclasis, resembling more to arrays of distributed deformation bands. These results suggest that the localization of the deformation in sandstone under the form of clusters is possible only when failure is attained on the brittle part of the envelope or near its summit. This conclusion is consistent with the conclusion proposed by Ballas (2013) and Soliva et al. (2013). However, it also specifies that the conditions for failure on the brittle part of the envelope is not directly dependent of the tectonic loading since we show that the brittle part of the envelope can also be attained by a variety of stress-paths in transpressive tectonics (e.g. St Michel, Bédoin, Blankenburg). Depending on the burial at deformation (σ_v), the presence of a free water column (Pf) and the shape/size of the failure envelope, this failure in transpressive tectonics is generally attained under strike-slip or thrust Andersonian regime. In addition, contrary to the hypothesis made by Schultz and Siddharthan (2005) or Ballas (2013), the examples of Boncavaï, Bédoin and Cummingston reveal that compactant cataclastic deformation is also possible when failure is attained near the extreme left of the brittle part of the envelope.

2.3.3. Interband geometry assessment

In the objective of qualifying the geometry of the variably corrugated/anastomosing bands and interband volumes inscribed between the bands, we decided to measure the length and width of the interbands along the sections of the cluster. This work is similar to what was previously done by Awdal et al. (2014). In particular the study of the morphology and therefore the connectivity of the rather permeable interbands permits a refining of their potential influence of fluid flow in the cluster thickness.

We explain in this paragraph the methodology of the interband lenses. The lenses of interband will be regarded as 2D ellipses (Figure 60a and b) in the section of the cluster corresponding to the plane of shear, and in the section corresponding to the out of shear plane. In the plane of shear, the major axis of the ellipse is referred to as *a*; the minor axis is referred to as *c*. Out of the shear plane, the major axis is referred to as *b*; the minor axis is referred to as *c*. The orientation of the ellipse with respect to the local cluster orientation is also measured. In the plane of shear, the angle of the ellipse orientation relative to the cluster is referred to as α and is the angle between the major axis a of the ellipse and the local cluster direction. Out of the shear plane, the angle of the ellipse orientation relative to the cluster is referred to as β and is the angle between the major axis b of the ellipse and the local cluster direction. Note that this method does not allow intercepting the maximum dimensions *a*, *b* and *c* of the lenses of interband material, thus underestimating the size of the lenses. However, because the bias induced is the same in the plane of shear and out of shear plane, our measurement should provide a satisfying comparison between the two sections. Our measurements are performed via the ImageJ-Fidji software from photograph assembly of cluster sections. Consequently, it is noteworthy to remark that our measurements induce sampling and truncation bias. The limit of resolution of the image may prevent the record of lenses smaller than a few millimeters; the size of the picture represents a limit of sampling length.

We present through Figure 61 to Figure 65 the results of the geometrical analysis of the lenses of interband for the sites of Boncavaï, Blankenburg, Cummingston, Goblin Valley and Buckskin Gulch. The two sites of St Michel and Bédoin deformed in strike-slip regime were not analyzed

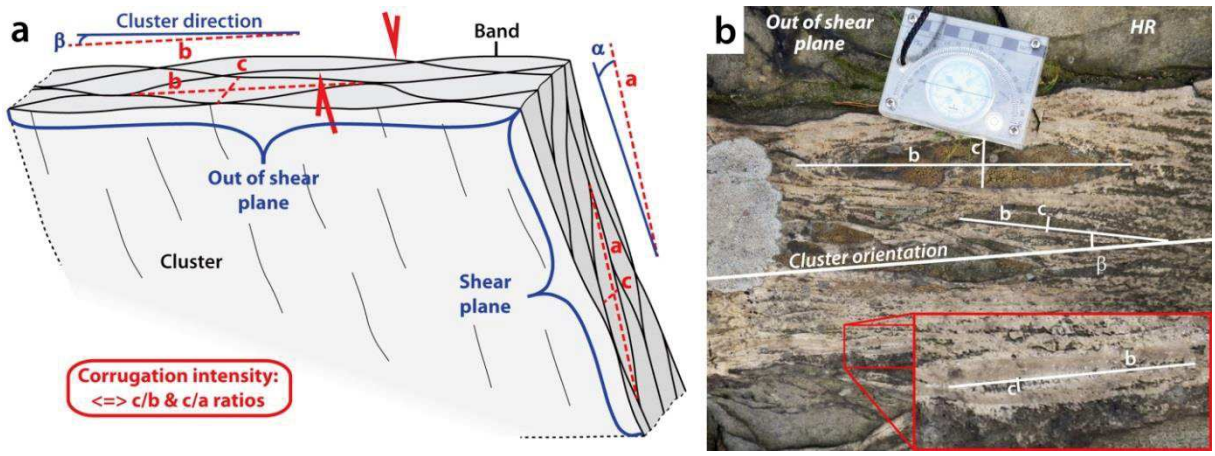

Figure 60. (a) Synthetic diagram presenting the methodology used for the measurement of the geometry on the lenses of interband material in the clusters. The section of the lenses are regarded as ellipses with a major axis a in the plane of shear and b out of the shear plane. (b) Example of cluster section photograph used for the measurements. We see that it is not necessarily possible to survey the whole cluster section area pictured due to the likely presence of lichen, for instance.

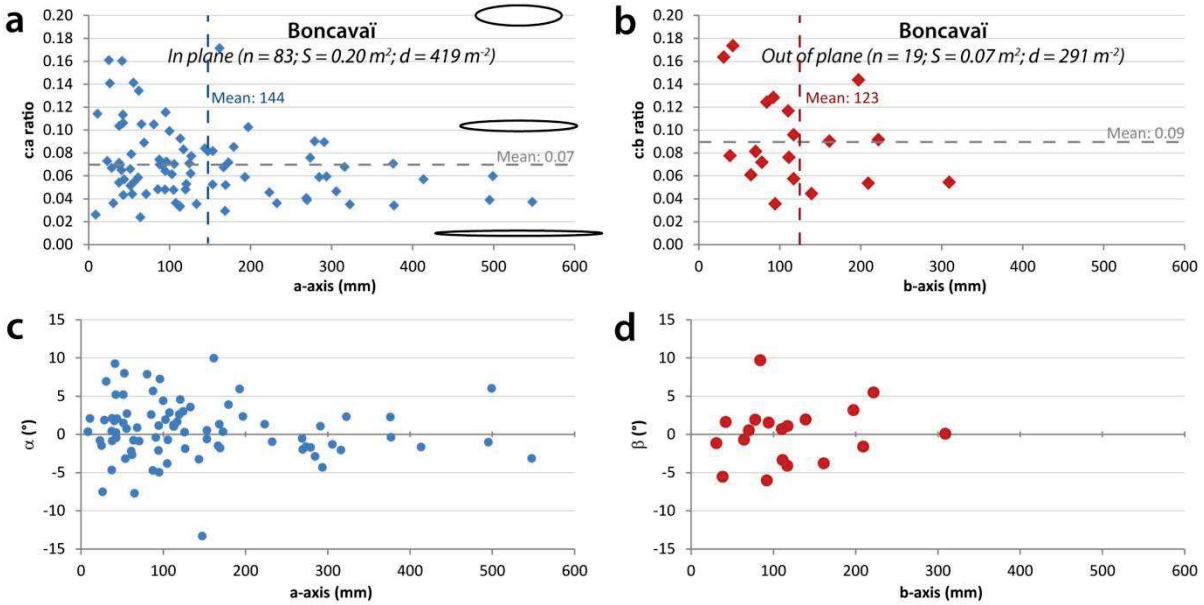

Figure 61. Shape geometry of the interband lenses at the site of Boncavaï. (a) Surface shape of the lens as a function of the maximum axis *a* in the plane of shear. (b) Surface shape of the lens as a function of the maximum axis *b* out of the shear plane. (c) Orientation of the lens in the cluster as a function of the maximum axis *a* in the plane of shear. (d) Orientation of the lens in the cluster as a function of the maximum axis *b* out of the shear plane.

because of the lack of visible continuity of the lenses along the length of the cluster, due to the presence of loose sand of lichen on the cluster section, for instance (e.g. Figure 60b). We represent the ellipse dimensions under the form of small ellipse axis over big axis (*c*/*a* and *c*/*b*) as a function of the major axis, and ellipse orientation (α and β) as a function of the big axis. The ellipses tend to be infinitely stretched out when the *c*/*a* or *c*/*b* ratios approach 0 (Figure 61a); they tend to be a circle when the ratio approaches 1. Even if we implicitly consider the smaller axis *c* of the lenses in the planes of shear and out of shear as being similar, our method of measurement does not permit plotting our data as Flinn diagrams (Flinn, 1962) because the ellipses measured in the plane of shear are different from the ellipses measures out of the shear plane.

For all sites, we observe a greater average of the major axis length in the plane of shear (67-144 mm) than out of shear (32-123 mm). This means that the lenses in the clusters are generally longer in the plane of shear than out of shear. In the plane of shear, the ratio of the minor axis c divided by the major axis a generally reaches smaller mean values than for c/b ratios out of the shear planes, implying thicker lenses out of the shear plane. Besides, we note that for both shear plane and out of shear plane, the lenses with a long major axis most probably display a long elliptical shape whereas the short lenses display a variability of shapes, from thick ellipses to narrow ellipses. Similarly, the major axis of the longest lenses describes a least angle with the alignment of the cluster whereas the smaller lenses orientation is more variable.

The density of lenses per surface area is often delicate to assess due to the lack of continuity of the lenses because of the presence of foams, lichen on the cluster section. Hence, the density number displayed in our graph are indicative and shall be considered cautiously, specifically at Boncavaï and Blankenburg. At Cummingston, Goblin Valley and Buckskin Gulch where the cluster surfaces were clearer, the measurements of density of lenses suggest, for the same surface, a higher lens density out of the shear plane than in the shear plane. At Boncavaï and Cummington, the more

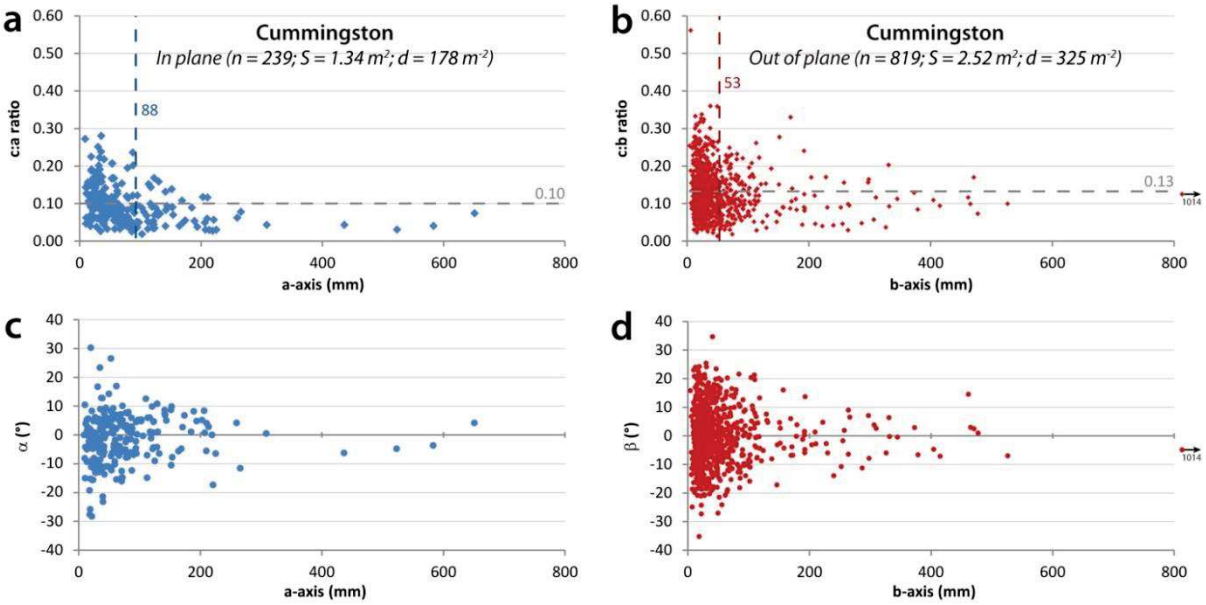

Figure 62. Shape geometry of the interband lenses at the site of Cummingston. (a) Surface shape of the lens as a function of the maximum axis *a* in the plane of shear. (b) Surface shape of the lens as a function of the maximum axis *b* out of the shear plane. (c) Orientation of the lens in the cluster as a function of the maximum axis *a* in the plane of shear. (d) Orientation of the lens in the cluster as a function of the maximum axis *b* out of the shear plane.

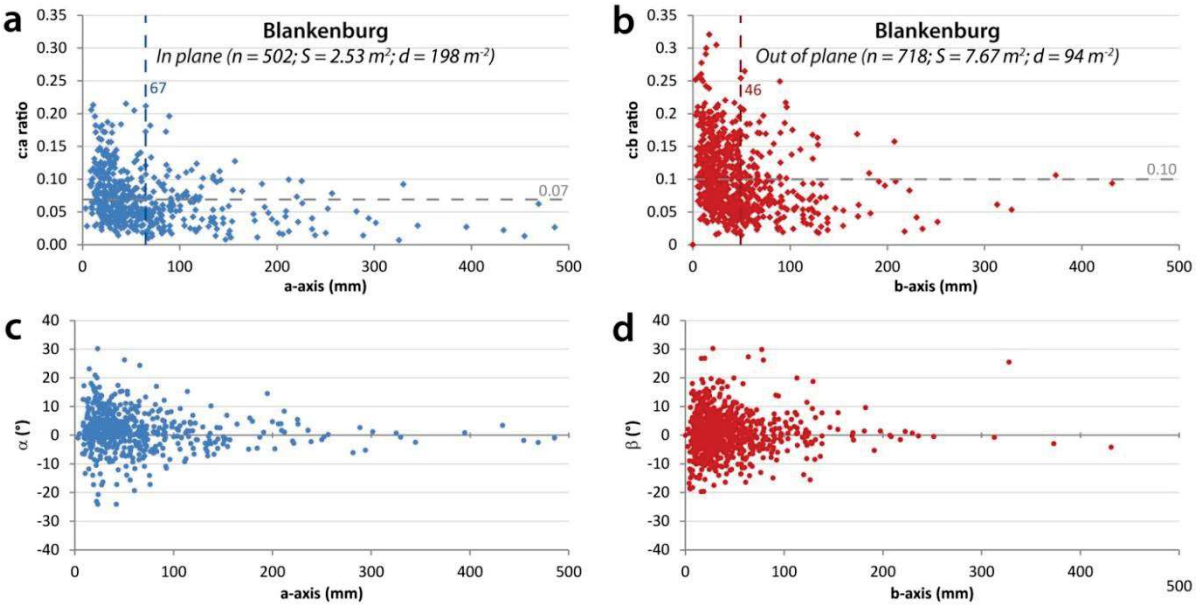

Figure 63. Shape geometry of the interband lenses at the site of Blankenburg. (a) Surface shape of the lens as a function of the maximum axis *a* in the plane of shear. (b) Surface shape of the lens as a function of the maximum axis *b* out of the shear plane. (c) Orientation of the lens in the cluster as a function of the maximum axis *a* in the plane of shear. (d) Orientation of the lens in the cluster as a function of the maximum axis *b* out of the shear plane.

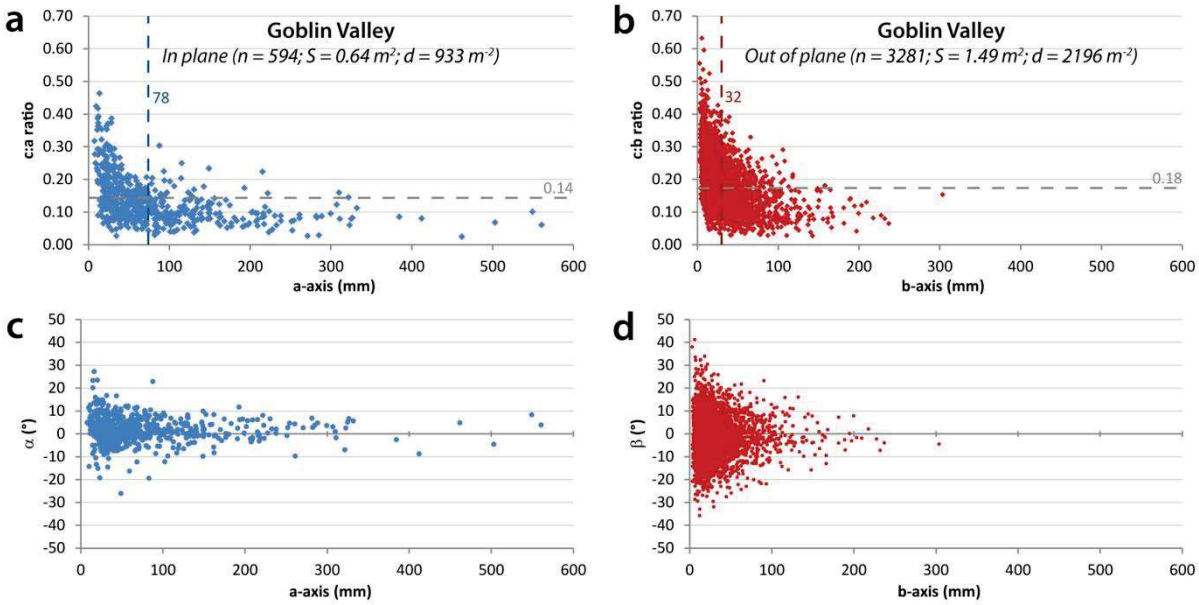

Figure 64. Shape geometry of the interband lenses at the site of Goblin Valley. (a) Surface shape of the lens as a function of the maximum axis *a* in the plane of shear. (b) Surface shape of the lens as a function of the maximum axis *b* out of the shear plane. (c) Orientation of the lens in the cluster as a function of the maximum axis *a* in the plane of shear. (d) Orientation of the lens in the cluster as a function of the maximum axis *b* out of the shear plane.

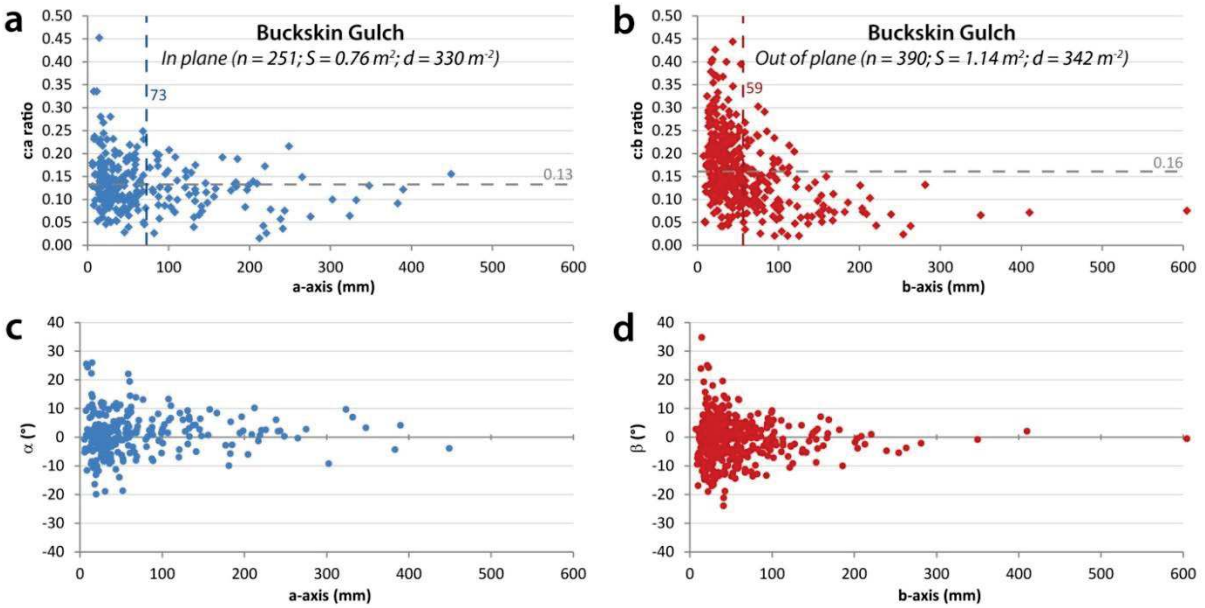

Figure 65. Shape geometry of the interband lenses at the site of Buckskin Gulch. (a) Surface shape of the lens as a function of the maximum axis *a* in the plane of shear. (b) Surface shape of the lens as a function of the maximum axis *b* out of the shear plane. (c) Orientation of the lens in the cluster as a function of the maximum axis *a* in the plane of shear. (d) Orientation of the lens in the cluster as a function of the maximum axis *b* out of the shear plane.

important lens density in the plane of shear is probably artificial, related to poorly exposed surfaces out of the shear plane.

For normal regime structures in multiple lithologies, Lindanger et al. (2007), Bastesen et al. (2009) and Awdal et al. (2014) suggest that the lenses in the plane of shear may form by the linkage of coalescing shear planes, and/or by Riedel planes linking two separate shear planes, with possible interplay of both during the evolution of the fault zone. Our ranges of c/a ratio in the shear plane fall in similar ranges than the one described in the work of the latter authors (0.04 – 0.30), hence we could hypothesize that the origin of the lenses in the studied sandstone is governed by the same process. Awdal et al. (2014) suggest that the thickest lenses would record a process of deformation by coalescence whereas thinner lenses would correspond to the synchronous growth of adjacent bands. Out of the shear plane, however, since the geometry of the lenses is different from the shear plane, is not clear if the lens shape of the interbands is due to the lateral coalescence of the bands or to the corrugated nature of bands developed one aside of the other, perpendicular to the shear direction. As discussed in section 2.3.1, the microscopic study of the cluster development suggests that the latter hypothesis is likely. On the other hand, the lens subdivision by new sets of bands during the cluster evolution evoked by Lindanger et al. (2007) is perfectly recognized in our field observations, both in the shear plane and out of shear plane (Figure 66). This lens subdivision consistently explains the presence of smaller lenses of very variable angles compared to the cluster orientation.

In summary (Figure 67), our results on the lens geometry show that the lenses of interbands are usually, longer in the plane of shear than out of the shear plan, in normal and in thrust Andersonian regime. Out of shear plane, the density of lenses is probably greater than in the plane of shear, reflecting the higher curvature of the bands. The orientations of the longest lenses are rather well aligned with the local cluster orientation. Hence, since the permeability of the interband is significantly higher than in the bands, we think that intra-cluster fluid flow is favored along the plane of shear where the connectivity is better and hampered along the out of shear plane where the connectivity is poor.

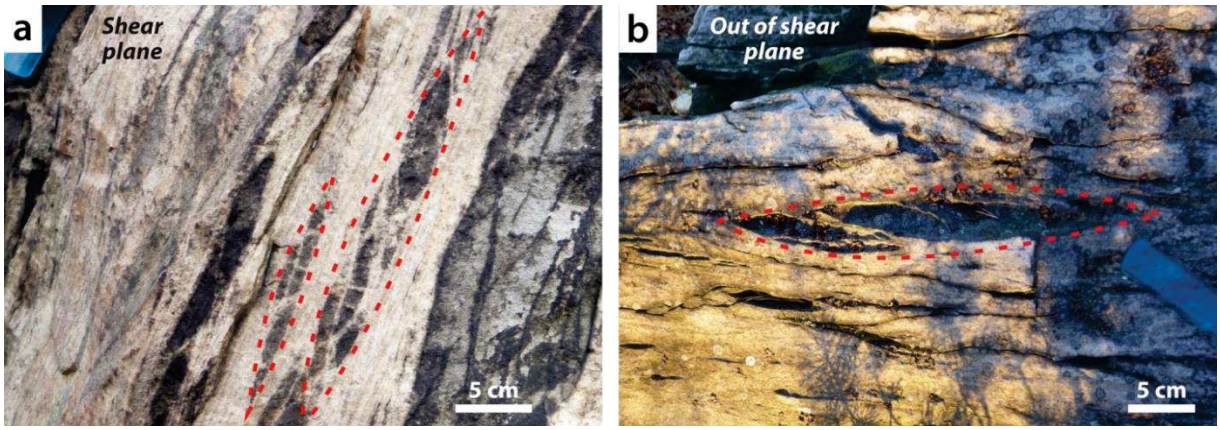

Figure 66. Photographs showing examples of subdivided lenses of interband in the shear plane (a) and out of the shear plane (b) at Blankenburg. These subdivided lenses evidence that the formation of bands can cross-cut preexisting bands during the cluster evolution and may explain why the smaller lenses have more variable orientations compared to the cluster orientation

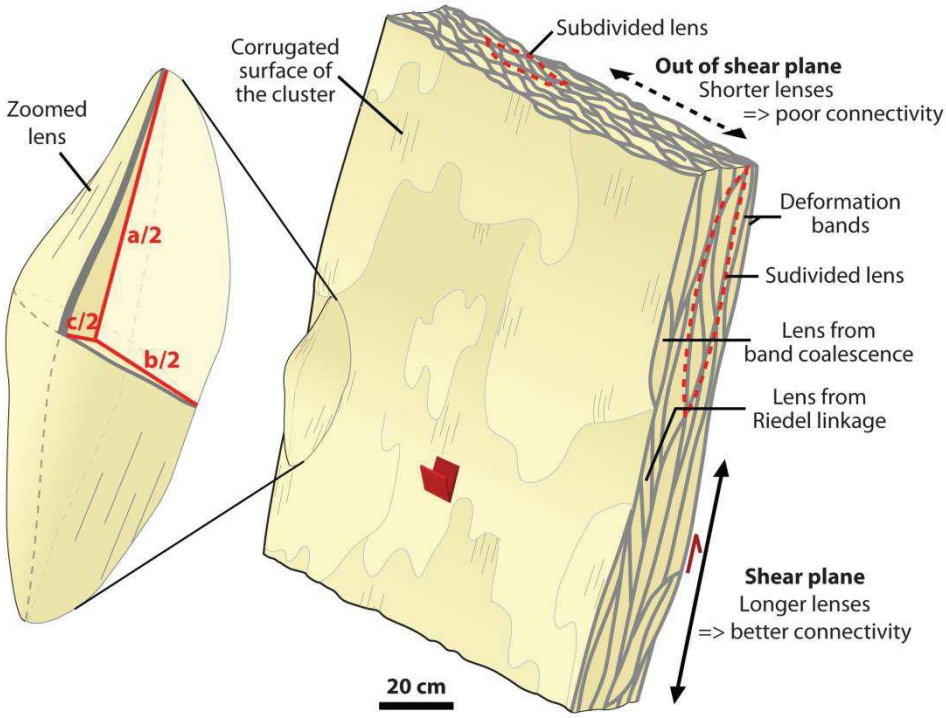

Figure 67. Synthetic diagram showing the typical lens morphology in the cluster thickness as a function of the section (in plane shear vs. out of shear plane).

2.4. Diagenetic Evolution of the cataclastic deformation structures

This section approaches the diagenetic evolution of the cataclastic deformation structures in porous quartz-rich sandstones, with a specific focus on the quartz cementation of clusters of cataclastic bands. As mentioned in section 1.1.4, the diagenetic evolution of deformation bands at burial of depths superior to 2 km are well known. However, it is unclear how cataclastic deformation structures are prone or not to diagenesis at shallower burial. Yet, the potential of cementation of these structures shall be tackled as it may involve significant alteration in the petrophysical properties and strength of the deformed material. This section intends to answer this lack of knowledge.

This section is published in the Journal of Structural Geology. The content of the section was also subjected to a poster presentation entitled "*Cataclastic faulting and cementation interplay in shallow porous sandstones: Insight from a groundwater environmental context*" at the EAGE conference (Almería, 2015).

To complement the main analysis of the influence of the cataclasis on diagenesis in this article, we add at the end of this section a supplement of information drawn from the global microscopic investigations undertaken at each of the study sites. By this means, we show that the cementation in cataclastic structures, in particular at shallow depths, is not an isolated phenomenon.

2.4.1. Relations between shallow cataclastic faulting and cementation in porous sandstone: First insight from a groundwater environmental context

Journal of Structural Geology 81 (2015) 89–105

Contents lists available at ScienceDirect

Journal of Structural Geology

journal homepage: www.elsevier.com/locate/jsg

Relations between shallow cataclastic faulting and cementation in porous sandstones: First insight from a groundwater environmental context

Sven Philit [a, *], Roger Soliva [a], Pierre Labaume [a], Claude Gout [b], Christopher Wibberley [b]

[a] Géosciences Montpellier, UMR 5243, Université de Montpellier-CNRS, Place Eugène Bataillon, 34095 Montpellier Cedex 5, France
[b] TOTAL EP, CSTJF, Av. Larribau, 64018 Pau, France

ARTICLE INFO

Article history:
Received 31 March 2015
Received in revised form
17 September 2015
Accepted 3 October 2015
Available online 21 October 2015

Keywords:
Porous sandstone
Cataclasis
Silica cementation
Shallow burial
Groundwater silcrete
Porosity

ABSTRACT

The interplay between fault zone cataclasis and cementation is important since both processes can drastically reduce the permeability of faults in porous sandstones. Yet the prediction of fault cementation in high-porosity sandstone reservoirs remains elusive. Nevertheless, this process has rarely been investigated in shallowly buried faults (<2 km; T°<80 °C) where its sealing capacity could be acquired early in the geological history of a reservoir. In this paper, the macro- and microscopic analysis of a fault zone in the porous Cenomanian quartz arenite sands of Provence (France) shows that silica diagenesis occurs in the most intensely-deformed cataclastic parts of the fault zone. This fault zone shows 19–48% of its total thickness occupied by low-porosity quartz-cemented cataclastic shear bands whose porosities range from 0 – ca. 5%. The analysis of the weathering profile around the fault zone reveals the presence of groundwater silcretes in the form of tabular, tightly silicified concretions cross-cut by the fault. Detailed transmitted light, cold-cathodoluminescence and scanning electron microscopy analyses of the silica cements (from the fault and the silcrete) reveal that all the silica cements originate from groundwater diagenetic processes. This study therefore shows that silica cementation can occur specifically in fault zones and as groundwater silcrete in the shallow context of a groundwater system, generated at the vicinity of an erosional unconformity.

1. Introduction

In geological reservoirs, fault structures are essential to understand as they can form major drains or barriers to fluid flow, depending on their internal structure (Caine et al., 1996; Aydin, 2000; Wibberley et al., 2008). Faults result from local or regional brittle deformation induced by tectonic stresses. They are generally formed of (1) a core zone composed of fault rocks and discrete slip surface(s) accommodating most of the displacement and deformation and (2) a damage zone within which the rest of the deformation occurs (Schultz and Fossen, 2008; Faulkner et al., 2010). In porous sandstones, deformation is often localized (centimeters to tens of centimeters wide at the scale of the observation window) into cataclastic shear bands (SBs), which at the larger scale are often distributed across the sandstone formation and can also occur as clusters. SBs are the main deformation elements of fault zones and are observed both far from the slip surfaces and adjacent to them, where they are generally densely clustered (Fossen et al., 2007; Fossen and Bale, 2007; Wibberley et al., 2007; Schultz and Soliva, 2012; Soliva et al., 2013). SBs are characterized by an important decrease in grain size (i.e. comminution) when grains are rearranged by rolling and splitting due to stress concentration at the grain–grain contacts (Gallagher et al., 1974; Aydin, 1978; Antonellini and Aydin, 1994). SBs are commonly characterized by strong porosity reduction, which in the most severe case can reduce the permeability by up to 6 orders of magnitude from that of the host rock, and drastically affect fluid flow in sandstone reservoirs (Antonellini et al., 1999; Fisher and Knipe, 2001; Fossen et al., 2007; Ballas et al., 2012).

It is also known that cement precipitation into fault zones can dramatically reduce their porosity and permeability (Watts, 1987; Sibson, 1994, 2000; Fisher and Knipe, 2001; Agosta et al., 2007; Eichhubl et al., 2009). In sandstones, several factors responsible for silica cementation such as burial, the role of organic complexes,

* Corresponding author.
E-mail address: sven.philit@gm.univ-montp2.fr (S. Philit).

http://dx.doi.org/10.1016/j.jsg.2015.10.001
0191-8141/

the related mechanisms of silica dissolution, transport and precipitation have been evidenced (Bjørlykke et al., 1989; Bjørlykke and Egeberg, 1993; Bjørkum, 1996; Oelkers et al., 1996; Bjørkum et al., 1998; Molenaar et al., 2007; Cavailhes et al., 2013). In particular, it has been shown that silica cementation has significant sealing impact on cataclastic structures affecting formations buried to depths >3 km (Fisher and Knipe, 1998; Labaume and Moretti, 2001). At these depths, the silica diagenesis was often depicted as a quartz pressure-solution process as a result of burial at temperatures >80 °C and tectonic stresses (Worden and Morad, 2009; Klimczak and Schultz, 2013). Recent models also show that the cementation depends significantly of the quartz grain size, abundance of coatings and clast abundance. These parameters control the nucleation, the geometry and the precipitation rate of the crystals (Walderhaug, 2000; Lander et al., 2008). On the other hand, shallow silica diagenesis (depth <2 km, T° <80 °C) in fault zones has rarely been described (e.g. Milliken et al., 2005), and the literature which documents such processes in unfaulted sandstones relates this diagenesis to pedogenetic or aquifer silcrete systems (Thiry and Milnes, 1991; Thiry, 1997; Abdel-Wahab et al., 1998). Therefore, it is important to determine if silica cementation can take place into faults in shallow porous formations and, if so, to determine the process at the origin of cementation and the impact of diagenesis on the porosity reduction in the fault.

In this paper, we study several strike-slip faults made of clusters of shear bands in porous sands at the De Cros quarry (South-East Basin, France), within which silica cements are observed. The faults are located in Cenomanian sandstones with a maximum burial of 800 m (Saillet, 2009) and are characterized by a multicolor-impregnated weathering profile and tightly silicified concretions. Firstly, we analyze the weathering profile of the host rock around the faults, providing a microscopic analysis of the host rock and tightly silicified concretions, in order to assess the environmental context of this silica diagenesis. Secondly, we undertake a field analysis of the distribution, macro- and microscopic organization of the main cataclastic structures to determine the impact of the cataclasis on cementation. From these observations, we propose a model for the fault-related cementation in a sandstone aquifer silcrete system.

2. Geological setting

The study area is located in the South-East Basin of Provence (France) (Fig. 1a), in the southern part of the De Cros quarry (northern site) near the village of Bédoin (Fig. 1b). The South-East Basin region has been affected by 3 main tectonic deformation episodes (Arthaud and Séguret, 1981; Roure et al., 1992; Séranne et al., 1995; Champion et al., 2000): (1) the N–S Pyrenean-Provencal contraction from middle Eocene to early Oligocene, (2) a NW–SE extension corresponding to the Gulf of Lion rifting from the middle Oligocene to early Miocene, and (3) the NE–SW Alpine contraction from the Miocene to Quaternary. The study site is located near the junction of 3 master faults: the sinistral-normal Nîmes fault 10 km to the West, the dextral-normal Salon-Cavaillon fault to the south, and the major Ventoux-Lure thrust, which is located a few km North as shown in Fig. 1a and c. The North-verging thrusts of the Ventoux-Lure range result both from the N–S Pyrenean contraction and the NE–SW Alpine shortening (Champion et al., 2000). The normal component of the initially-Pyrenean strike-slip faults (Nîmes and Salon-Cavaillon) was essentially due to fault reactivation during the Oligocene-Miocene extension.

The stratigraphy of the South-East Basin comprises a 1 to 4 km-thick layer of Triassic series containing an important fraction of evaporites, overlain by a 2 to 9 km-thick Jurassic and lower Cretaceous succession, mainly composed of carbonate rocks (Tempier, 1987; Pichon et al., 2010). From the Aptian, these carbonates are overlain by limestone, shales and siliciclastic formations, depending on the location in the basin. An upper Cretaceous-Paleocene hiatus due to emersion during the Durancian Uplift (Albian-Cenomanian) separates the deltaic Cenomanian deposits and lacustrine-to-palustrine Eocene deposits, which are 0–1.6 km-thick (Ford and Stahel, 1995; Rangin et al., 2010). The stratigraphic sequence cropping out in the Mont Ventoux region is described by Ford and Stahel (1995) as a thick lower-Cretaceous carbonate platform (1 km) at the South of Mont Ventoux, evolving toward the North into thinner deep marine deposits (300 m) (Fig. 1c). From the Aptian to Turonian, the series is composed of a hundred meter-thick siliciclastic level to the South and marl deposits to the North (Sornay, 1950; Ferry, 1999). The De Cros quarry is located within low-cohesion Cenomanian sands deposited in deltaic environments (Saillet and Wibberley, 2010). Notice that the Cenomanian formation at the De Cros quarry shall be qualified as *sands* in this study since their cohesion is very low. They generally comprise medium-to-fine grained porous sands (ca. 30% porosity) featuring different types of cataclastic deformation band networks formed during the Pyrenean contraction and the Oligocene extension (Wibberley et al., 2007; Saillet and Wibberley, 2010; Soliva et al., 2013; Ballas et al., 2014). These Cenomanian sands are unconformably overlain by Eocene formations visible at the outcrop at the study site.

3. Methods

3.1. Field measurements and sampling

The orientation of the cataclastic structures was measured at the outcrop so as to determine the local chronology and direction of the tectonic events (the inventory of the cataclastic structures also reveals the relative local deformation; Fig. 2a and b). The kinematics of the cataclastic structures (i.e. both faults and SBs and SB clusters) is interpreted via their mutual cross-cuttings and/or their relative dips and strikes. Following this approach, in the absence of displacement markers, structures striking between N055°E and N085°E and dipping between 55° and 80° (towards the NW or SE) are interpreted as normal cataclastic structures. Structures striking between N055°E and N085°E and dipping between 20° and 45° (towards the NW or SE) are interpreted as reverse cataclastic structures. Structures striking between N090°E and N200°E and dipping between 60° and 90° (towards either direction) are interpreted as strike-slip cataclastic structures. The kinematics of the structures is indicated on Fig. 2a whenever it was possible to observe it. This classification matches the trends proposed by Saillet (2009) in the same quarry.

In order to characterize the macroscopic interplay between the deformation and diagenesis of a fault zone, a spatial statistic study of deformation and cementation of the thickest fault zone has been undertaken. The deformation was estimated by measuring each visible cataclastic strand (ruler of millimeter-precision) along 18 transects (each corresponding to the thickness of the fault zone) with a 50 cm increment and for a total covered length of 9 m. The degree of cementation was estimated via the relative stiffness and the glassy/non glassy visual aspect of the measured material. Along a transect, this macroscopic characterization leads to a zone classification (section 4.2.4) based on the combination of the microscopic terminologies presented in sections 4.2.2 and 4.2.3.

Laboratory analysis was aimed at investigating the microstructure and diagenesis of the rock samples. The samples consist of twenty-six uncovered and polished thin sections embedded in epoxy resin. The samples were collected from several locations

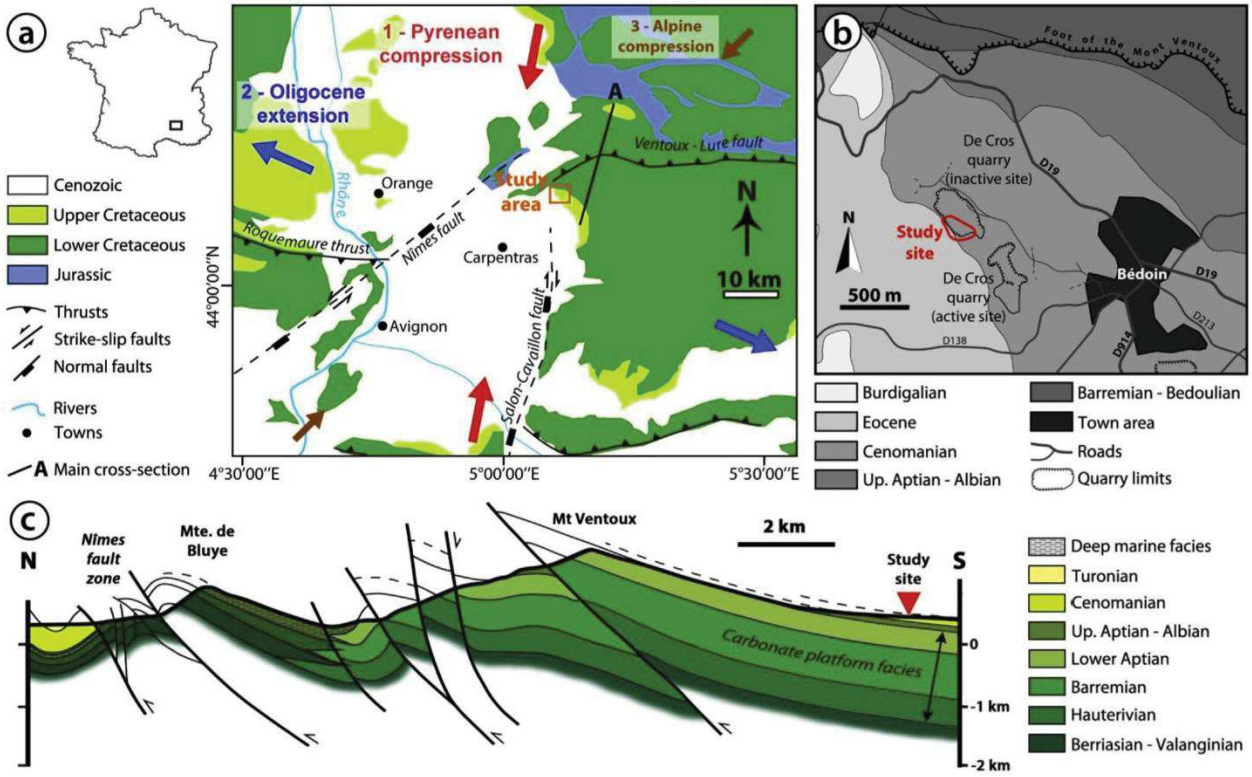

Fig. 1. (a) Location of the study area of Bédoin (Vaucluse) on a simplified structural map of Provence, modified from Soliva et al. (2013). (b) Location of the study site near Bédoin. (c) Synthetic cross-section showing the relative location of the study site (red arrow) on the Cretaceous series, modified from Ford and Stahel (1995); the location of the section is mapped as line A in (a). (For interpretation of the references to color in this figure legend, the reader is referred to the web version of this article.)

corresponding to 2 fault zones, 1 tightly cemented concretion and 1 host rock (see location of the presented figures in Fig. 2a).

3.2. XRD analysis

XRD semi-quantitative analyses were performed on powdered samples in order to recognize the mineralogical phases of the weathering profile. Measures were acquired via a PANalytical X'Pert Pro MPD Copper target X-ray tube (University of Montpellier).

3.3. Microscopy

Plane-polarized and cross-polarized transmitted light microscopies were used to obtain a first-glance observation of the microstructures and assess the mineralogy of the samples.

Cold cathodoluminescence microscopy (CL) gives a surface observation of the thin sections, allowing the distinction of the porosity and the different generations of cements compared to the detrital grains or clasts. CL was performed using a CITL Cathodoluminescence Mk5-1. Sample exposure to electronic beam triggers light emission from the sample whose color varies according to the difference in the chemical nature of the minerals (Richter et al., 2003). In the case of our study, image acquisition was performed after 3 min of exposure of the samples to the electron beam; each acquisition required 2 min of exposure to obtain a proper brightness.

Scanning Electron Microscopy (SEM) (FEI Quanta FEG 200) was used with backscattered electron and secondary electron imaging to estimate the surface porosity of the samples. The acquired high resolution photomicrographs were used to evidence the porous network and calculate the *surface porosity (%)* (i.e. porosity worked out from the 2D photomicrographs) via color post-processing and the use of an intensity threshold in the greyscale spectrum. In the case of uncemented rocks, since no clay matrix is observed, the surface porosity corresponds to the InterGranular Volume (IGV) described by Paxton et al. (2002). The IGV is the sum of the intergranular porosity, the clay matrix and the cements.

Microscope observations were undertaken for the host rock, the tightly cemented concretions (i.e. rolls and tabular concretions aligned in the bedding plane) and for the two cemented strike-slip faults studied. Apart from cases where resolution was not high enough, the cements are always clearly distinguished from the primary clasts and the porosity via CL observation: the cements are always orange-brown in the cataclastic structures, and purple to brown-orange to rose in the case of the cemented concretions. Detrital quartz grains have bluish to greenish colors, and the porosity appears dark-green to black (descriptions in sections 4.1.2, 4.1.3 and 4.2.3).

Thin sections also allowed the measurement of the degree of cataclasis, defined by the cataclastic matrix percentage within the material. The cataclastic matrix is considered as the material formed of grain clasts smaller than 1/10 of the median grain diameter D_{50} measured in the host rock (D_{50} obtained from the measurement of 600 detrital grains from the host rock). Size of the

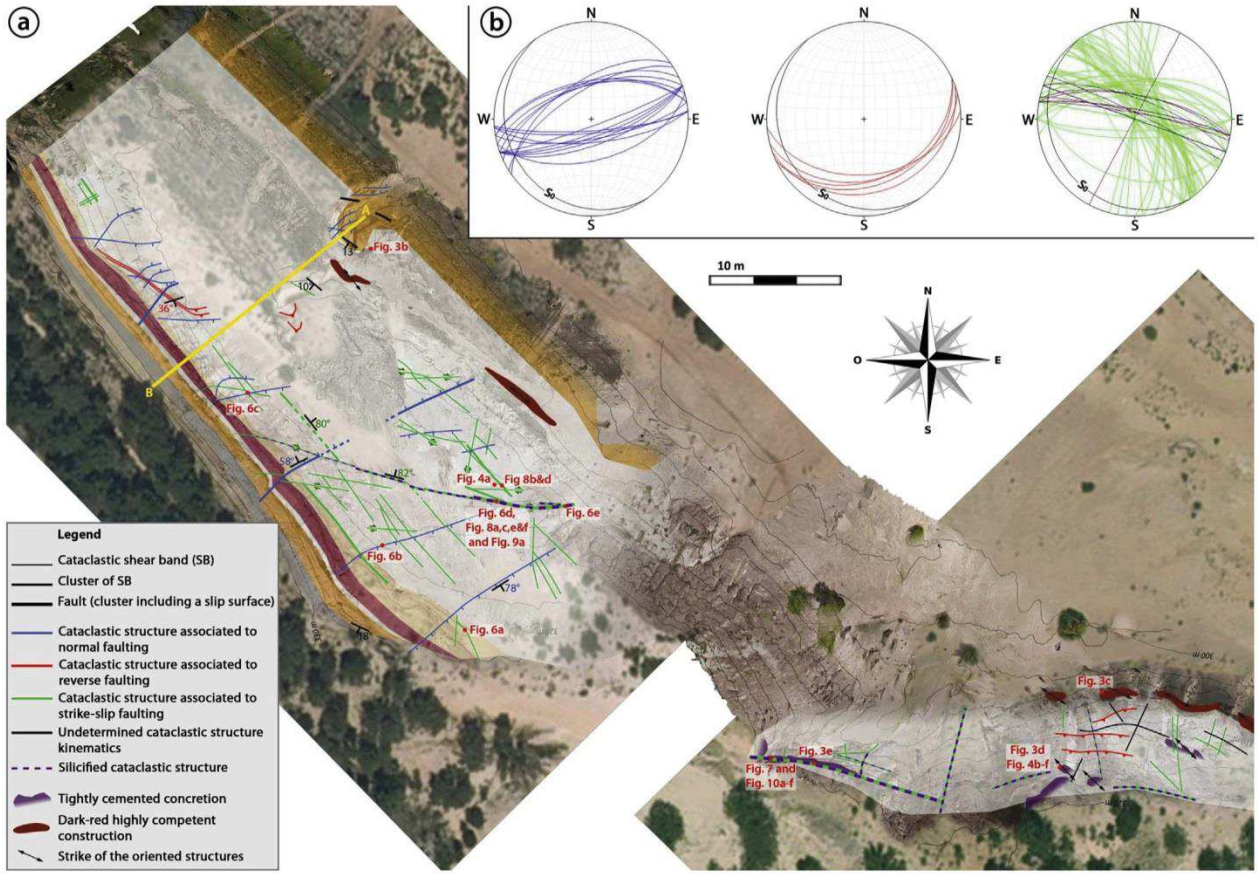

Fig. 2. (a) Georeferenced cartography of the studied site at the De Cros quarry. The document displays the weathering profile of the Cenomanian sands (light colors for pervasive weathering and strong color for localized structures) and the different cataclastic structures observed; uncolored areas are Quaternary deposits. The different terminologies used for the structures are shown in the legend. Representative strikes and dips of the different sets of tectonic structures are indicated along representative structures. (b) Stereographic projections (lower hemispheres) of the planes of the cataclastic structure measured in (a); Normal cataclastic structures are represented in blue (left hand stereogram), reverse cataclastic structures in red (central stereogram) and strike-slip cataclastic structures in green or purple when cemented (right hand stereogram). (For interpretation of the references to color in this figure legend, the reader is referred to the web version of this article.)

grains and clasts was determined by surface measurements from 2D photomicrograph analysis.

4. Field data and results

4.1. Weathering profile

4.1.1. Macroscopic analysis

The weathering profile of the Cenomanian low-cohesion sands of the De Cros quarry is characterized by an alternation of colored levels (see map in Fig. 2a and simplified log in Fig. 3a) following a N145°E 14°SW bedding alignment at the outcrop scale (100 s m). The XRD analysis shows that none of the sands of the Cenomanian interval contain detrital clays or calcite.

Fig. 3a shows that the first 2 m at the base of the outcrop are made of a yellow-orange pervasively colored level. Goethite is identified by XRD analysis in this sand interval. At the upper limit of this interval, highly-competent dark-red lenses of 5–10 mm in thickness and tens of centimeters in length are observed over a 20–30 cm-thick interval (not shown on the schematic log). White strips of silty material tend to alternate with the dark-red lenses near the top of the interval. XRD analysis revealed that this white silty material has a high kaolinite content.

Above follow 19–20 m of very low-cohesion white sands. A fair amount of kaolinite is detected. The grains do not show any traces of coating to the naked eye. This white sand interval is also marked by numerous red-orange curved features corresponding to Liesegang rings (Fig. 3b).

Dark-red highly competent constructions up to 1.5 m in height and forming clusters of pipe-shaped structures are also observed near the base of the white sand interval (Fig. 3c, dark-red in Fig. 2a). Each "pipe" measures several centimeters in diameter and is made of a competent ring; the inner part of the pipe is incohesive and often hollowed. The whole geometry and extent of such constructions is difficult to determine since they only partially crop out, but they are aligned in the same stratigraphic level. The orientation of the pipes is aligned with the bedding and strikes N126° on average, as shown in Fig. 2a. Thin-section analysis of the competent rings reveals red coatings around the detrital grains (zoom in Fig. 3c). XRD analysis shows that these coatings are made of hematite oxide; therefore these constructions can be referred to as "oxidation fronts". The presence of kaolinite in trace quantities is also shown.

The white sand interval also comprises tightly cemented concretions within the pristine rock at the southernmost part of the study site (Fig. 3d and e, purple in Fig. 2a). These concretions form slabs or oriented structures referred to as "rolls" aligned in the

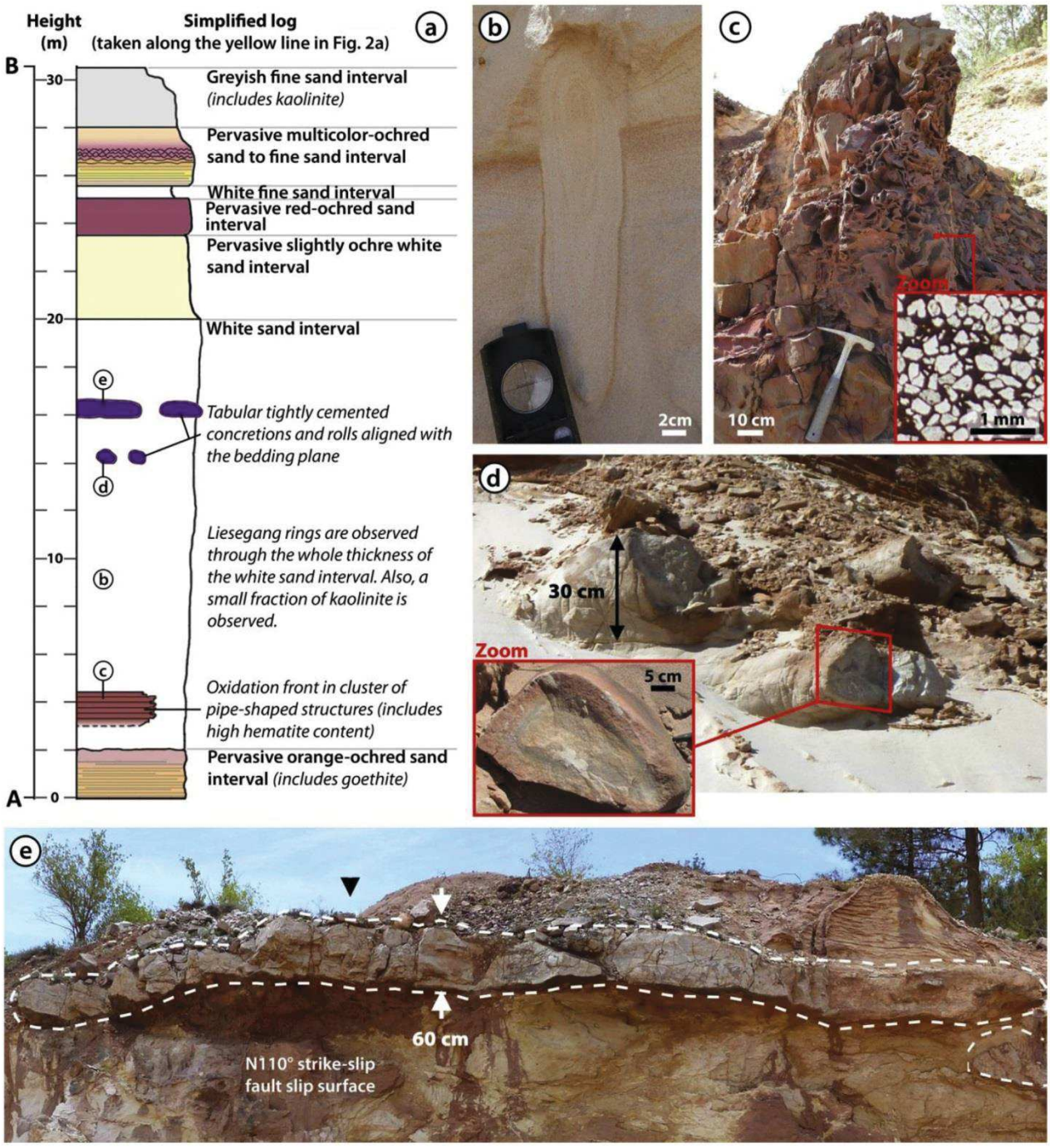

Fig. 3. (a) Synthetic log of the weathering profile at the study site (AB section in Fig. 2a). (b) Liesegang ring. (c) Dark-red highly competent constructions. The zoom shows a scanning electron micrograph (backscattered) of the competent aureoles of the cluster of pipe-shaped-structures in thin section: note the coating around the quartz detrital grains. (d) Oriented tightly cemented rolls. The zoom shows the concentric pattern of the roll underlined by the radial variation of oxide impregnation. (e) Slab of tightly cemented concretion aligned with the bedding in the white sand interval. The exposure underneath the slab is a N110° strike-slip fault slip surface.

bedding plane (measurement of the largest cemented slab observed yields a N145°E 10°SW orientation; a general azimuth and plunge of the long axis of pipes and rolls is N135°E 07°SE). The common thickness of a slab is 50 cm (similar or slightly smaller thickness is measured for the rolls); its lateral extent can reach 20 m at the outcrop. The slab geometry of the concretion shares a similar pattern to the groundwater silcretes identified by Thiry and Marechal (2001) in the Fontainebleau sandstones (see their Figs. 5c and 6b). Likewise, in cross-section, the rolls display concentric shapes highlighted by light-red impregnations (zoom in Fig. 3d) in

a comparable manner to the silcretes observed by Thiry and Marechal (2001) (see their Fig. 6c). The concretions are observed within 2–3 m-thick intervals in the white sands. In the white sand interval, and only in it, the cementation of the main cataclastic structures is also observed (more detail in Section 4.2).

The white sand interval is followed by a 11 m-thick interval encompassing several red-to-yellow pervasively colored levels of medium to fine-grained sands (8 m). At the top of this interval a greyish fining upward sand layer (3 m) is observed; the XRD analysis shows the presence of kaolinite in trace quantities.

The Cenomanian sands are overlain by Eocene formations (not represented on the log of Fig. 3a) above a poorly distinguishable unconformity (hiatus). The Eocene comprises 22–25 m-thick yellow-orange to red silty clays topped by a 1.5 m-thick limestone bed including a siliciclastic fraction as well as a few centimeter-thick nodule-shaped or lenses-shaped cherts. The limestone bed is overlain by several meter-thick beige marl intervals alternating with meter-thick siliciclastic deposits (conglomerate lenses and sands).

4.1.2. Microscopic analysis of the uncemented pristine sand

The microscopic analysis shows that the uncemented pristine sand (Fig. 4a) is characterized by more than 95% of fairly rounded quartz grains with a median diameter D_{50} of 360 μm (quartz sands). The cataclastic matrix, composed of fragments of detrital grains (also referred to as "clasts"), represents <5% of the rock. No particular grain orientation is observed. Grain point contacts generate only few intragranular fractures; no pressure-solution feature was observed. Typical IGV are between 29 and 34% (shown on the graph of surface porosity vs. the cataclastic matrix

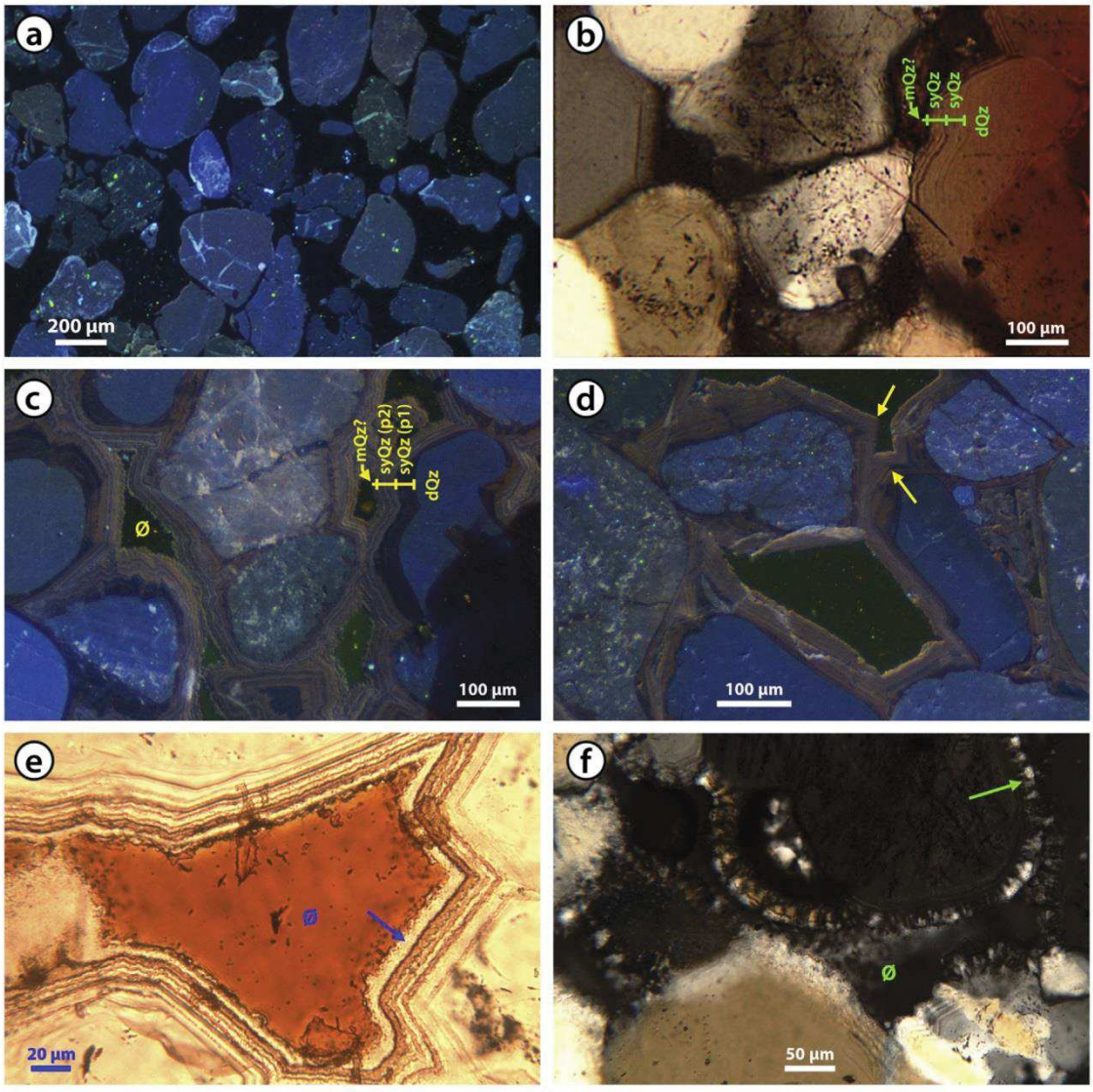

Fig. 4. (a) Host rock in CL. (b) Silica aureoles around the detrital grains in the tightly silicified concretion in cross-polarized light, and in (c) CL (same zone) showing remaining porosity (ϕ). Syntaxial quartz overgrowth cements (syQz) grown from the detrital grain (dQz) are observed . The CL imaging distinguishes the different overgrowth patterns: (p1 & p2). A thin layer of cement with a crenulated aspect coats these cements and could be microcrystalline quartz (mQz?). (d) 120° angles typical from the crystalline structure of the quartz (arrows) in CL. (e) & (f) Respectively, plane-polarized and cross-polarized microscopy showing the microcrystalline edges of the silica aureoles in the tightly silicified concretion (arrows).

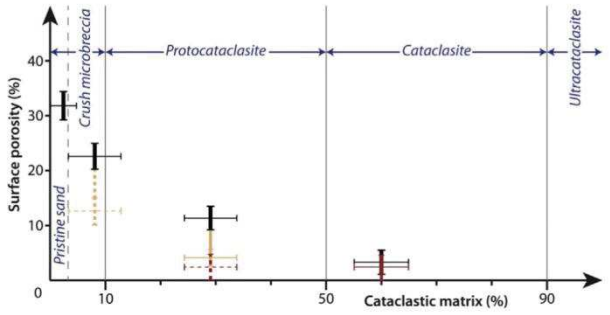

Fig. 5. Graph of the surface porosity vs. the cataclastic matrix percentage in the studied cataclastic structures (the different domains of the cataclastic matrix percentage respect the classification of cataclastic material by Sibson (1977)). The black data represent the surficial porosity of the uncemented cataclased microstructures, equivalent to the IntraGranular Volume (IGV), the yellow data represent the partially cemented microstructures and the red data represent the highly cemented microstructures. Concerning the cementation, the dashed-line data correspond to the "commonly observed occurrences"; the solid-line data correspond to the "mostly observed occurrences". For all the data, the vertical bars indicate the common range of values of surface porosity measured with the SEM; the horizontal bars indicate the range of value of cataclastic matrix measured via CL imaging. (For interpretation of the references to color in this figure legend, the reader is referred to the web version of this article.)

percentage on Fig. 5). Detrital quartz grains of the pristine sand have slightly different chemical composition, as shown by the diversity of colors imaged in CL (blue-grey to light-blue and greenish-brown colors).

4.1.3. Microscopic analysis of the tightly cemented concretions in the pristine sands

The microscopic analysis of the tightly cemented concretions (Fig. 4b–f) shows that they are characterized by fairly rounded detrital quartz grains, similar to the pristine sand described in the previous section, with cement aureoles. In cross-polarized transmitted light microscopy (Fig. 4b), we note that the cement aureoles are made of quartz (greyish first-order hue) surrounding the grains. In CL, the syntaxial overgrowth nature of the cements is evidenced by its radial organization around the detrital grains (Fig. 4c) as cements can be differentiated in CL from bluish detrital grains (dQz) thanks to their difference in color. The frequent euhedral shape of the cements at the porosity interface (Fig. 4d) confirms the quartz nature of the overgrowths. In CL, the quartz overgrowths comprise multiple μm to tens of μm-thick parallel bands. Two main overgrowth patterns are distinguished (Fig. 4c): a pattern made of 1 or 2 thick dark-purple or brown-orange band of irregular thickness (syQz(p1)) grown from the grain surface, and a pattern made of thin rose-and-purple-alternating isopach bands (syQz(p2)). A thin

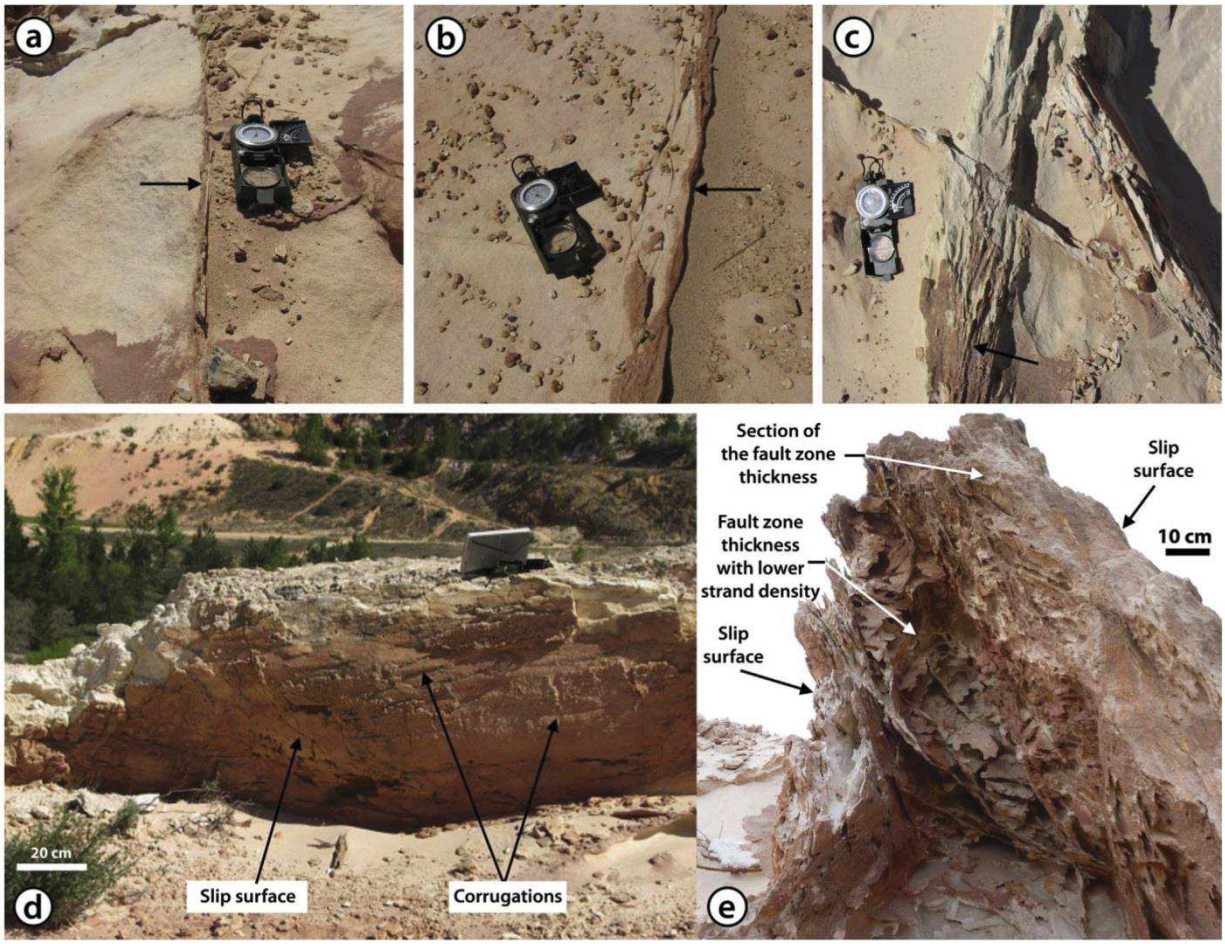

Fig. 6. Cataclastic tectonic structures observed in the study area: (a) Single-strand SB (arrow). (b) Multi-strand SB (arrow). (c) (Small) cluster of SB (arrow). (d) The corrugated slip surface of the fault. (e) View of the internal structure of a fault zone cluster in the white sand interval.

layer of cement with a crenulated appearance can be observed at the limit with porosity (mQz?) but its crystalline nature cannot be determined with certainty from this image because of the poor CL and cross-polarized light resolution. This type of cement is also shown in plane-polarized light (arrow in Fig. 4e); its morphology is comparable to microcrystalline quartz cement in French and Worden (2013) in the Fontainebleau sandstones (see their Fig. 6). Near the external part of the concretion, microcrystalline quartz cements can be observed adjacent to porosity (arrow in Fig. 4f, cross-polarized). The total thickness of the aureoles typically ranges from 10 to 100 μm. The radial sampling of a roll reveals a decreasing amount of cement around the grains on approaching the edge of the silicified concretion: within a 2 cm interval, from the inner part towards the most external part of the roll, the cement around the grain almost totally disappears. Neither the detrital grains themselves nor the cements show any pressure-solution feature. In the inner part of the concretion (with developed aureoles), CL-image analysis shows surface porosities ranging between 3 and 7%.

4.2. Cataclastic structures

4.2.1. Macroscopic classification and distribution

A summary of the distribution of the cataclastic structures at the study site is shown in Fig. 2a, and their orientations in Fig. 2b. The cataclastic structures include (1) *cataclastic shear bands* (*SBs*), (2) *clusters of SBs* and (3) *fault zones*.

Cataclastic shear bands (SBs) (Fig. 6a and b, also see Ballas et al., 2012) are made of one or several cataclastic strands for a total width ranging from 1 mm to a few centimeters in thickness. We distinguish the single-strand *SBs* (Fig. 6a) and the multi-strand *SBs* (Fig. 6b). A strand is defined by a millimeter-thickness of cataclased sand absorbing a small amount of shear and compaction within a few millimeters to centimeters displacement (displacement are determined by the presence of shifted markers in the host rock). *SBs* have a common lateral extent of 10–20 m at the outcrop.

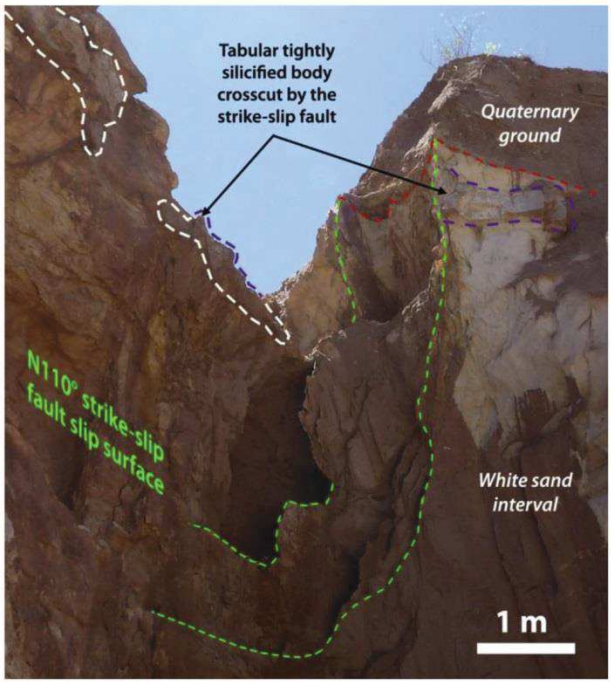

Fig. 7. Picture showing the strike-slip structures cross-cutting the tightly silicified concretions.

Clusters of SBs (or *SB clusters*) (Fig. 6c, arrow) are zones of multiple adjacent strands (densely spaced), typically comprising 15 to more than 100 strands within 5 cm to tens of centimeters thicknesses. *Clusters* typically absorb a displacement of tens of centimeters to meters. They are commonly observed with a several tens of meters extent at the outcrop.

Fault zones (Fig. 6d and e) are structured as *clusters* of shear bands adjacent to discrete slip surfaces where corrugations can be identified (Fig. 6d, also see Shipton et al., 2005 for example). *Faults zones* have thickness and strand densities similar to *clusters* (Fig. 6e) and their displacements are assumed to be similar or greater than that of *clusters* (up to several meters). They are commonly a few tens of meters in lateral extent and can lose their slip surfaces along-strike so that only the *SB cluster* remains.

Concerning the distribution of the cataclastic structures, two sets of conjugated planes are evidenced on the stereographic projections of Fig. 2b. Two sets of strike-slip planes are identified with N110°E and N140°E strikes on average. The N140°E set sinistrally cross-cuts the N110°E set and is also dextrally cross-cut by the N110°E set. A minor N005°E strike-slip set is noted and could represent a conjugate to the N140°E set. Occurrences of interaction between these sets seem to indicate that the N005°E set sinistrally cross-cuts both the N110°E and N140°E sets. Two conjugate sets of normal cataclastic structures with a N070°E strike and 65°NNW and 65°SSE dips are observed. The normal cataclastic structures cross-cut the strike-slip cataclastic structures. A minor reverse cataclastic structure set is also noted with a mean orientation of N060°E 30°SE. Interaction between the reverse cataclastic structure set and other sets is too scarce for establishing reliable relative chronological relationships. Among the structures, two fault zones are observed at the study site with a common N100-110° strike. One of these faults, located at the SE of the site (Fig. 2a) cross-cuts tightly silicified concretions of host rock (Fig. 7). The fault zones are the main silicified cataclastic structures. That is why we focus exclusively on these structures for the examination of cementation of cataclastic structures for the next part of the study.

4.2.2. Microstructure classification of the deformation in the fault zones

Four types of microstructures are distinguished depending on their degree of cataclasis, following the terminology proposed by Sibson (1977) and adopted by Scholz (1990) and Fossen (2010): (1) *pristine sand (4.1.2.)*, (2) *crush micro-breccia*, (3) *protocataclastic microstructures* and (4) *cataclastic microstructures*. The typical surficial porosity of these structures is displayed in Fig. 5.

Crush microbreccias (Fig. 8a) are zones of damaged *pristine sands*; they are generally located at the close vicinity of the strands. They are made of a majority of fairly rounded grains whose apparent diameters are similar to the *pristine sand*. The fraction of the clasts forming the matrix represents from 3 to 13% of the rock (c.f. Soliva et al., 2013; Ballas et al., 2013, 2014). Intragranular fractures originating at grain–grain contacts (Hertzian) are numerous. No consistent grain orientation is observed. IGV values of 20–25% are common.

Protocataclastic microstructures (Fig. 8b) are mainly observed in SBs and they form most of the cataclastic strand thicknesses. The *protocataclastic microstructures* are commonly made of 24–34% of cataclastic matrix (c.f. above references). The remaining detrital grains are clast-matrix supported and do not generally exhibit intragranular fractures. A general grain and clast orientation is observed (generally parallel to the strand orientation). Typical IGV values of around 9–13% are measured. We note that since clusters of SBs are mainly made of *protocataclastic microstructures*, it is sometimes microscopically impossible to distinguish the limits

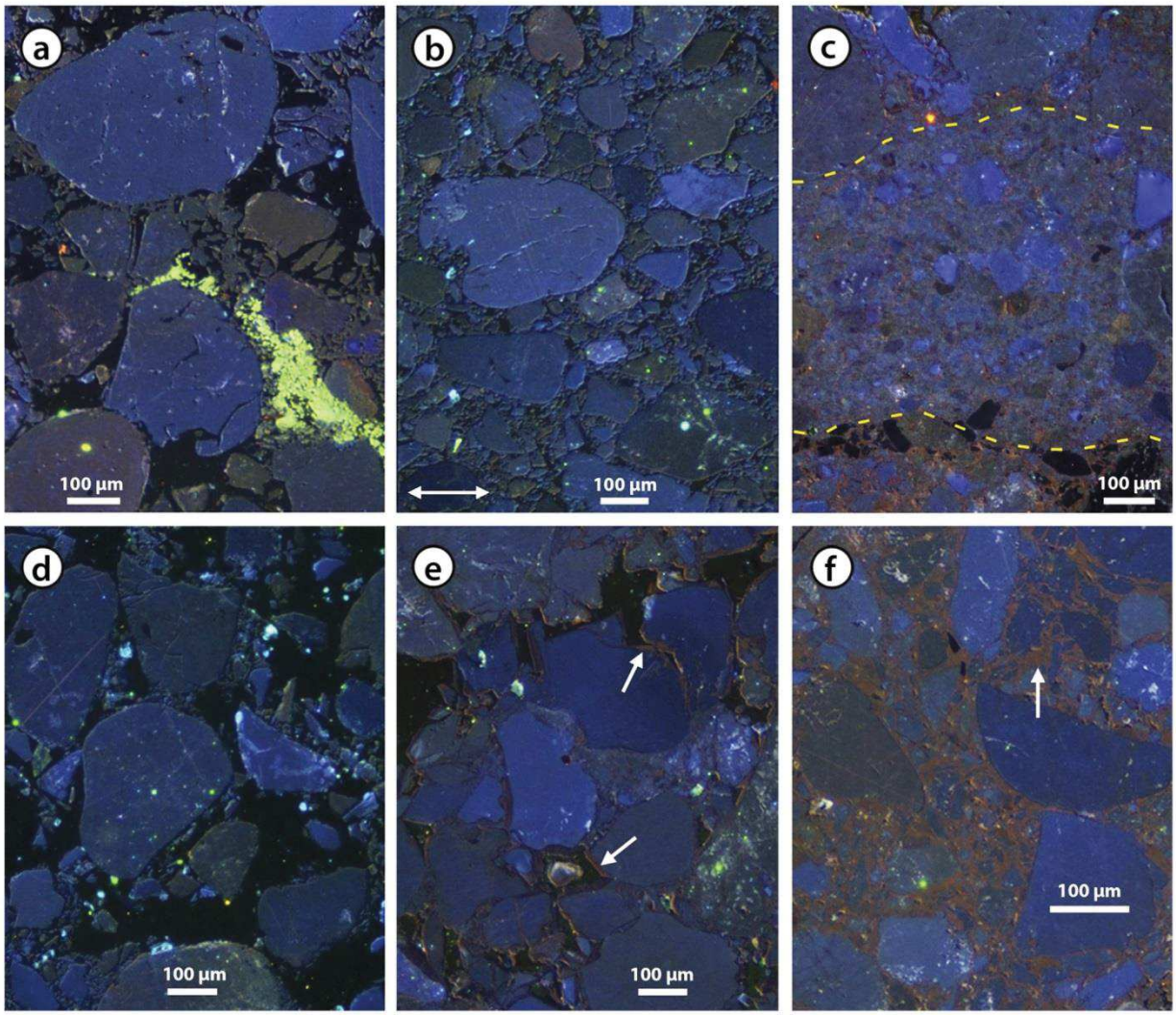

Fig. 8. (a) to (c) Classification of the different degrees of cataclasis observed in CL: (a) *Crush micro-breccia* (the bright yellow material is probably a crushed grain of feldspar among the quartz grains). (b) *Protocataclastic microstructure*. The double arrow indicates the direction of the SB strand. (c) *Cataclastic microstructure* (area defining a strand between the yellow dashed lines). Compare to the *pristine sand* in Fig. 4 a. (d) through (f) Overview of the different degrees of quartz cementation, in CL: (d) *Uncemented zone*. (e) *Partially cemented zone*, we note common 10 µm-thick cement coverings (such as those arrowed). (f) *Highly cemented zone*, the arrow is pointing to an intergranular space almost entirely filled with cement. (For interpretation of the references to color in this figure legend, the reader is referred to the web version of this article.)

between laterally-visible adjacent strands. Thus, continuous *protocataclastic microstructures* are observed in centimeter-thick zones with only little variation in clast size or proportion.

Cataclastic microstructures (Fig. 8c) are only observed in SB clusters and fault zones. They are defined by 300–600 µm-thick strands commonly composed of 55–65% of cataclastic matrix and containing no clast larger than 200 µm. Clast orientation is not clear. The SEM photomicrographs offer a limited resolution for surface porosity measurement of this type of microstructure. IGV is estimated to be lower than 5%.

4.2.3. Cement classification in the cataclastic faults

The quartz cements observed in the cataclastic fault zones display orange-brown colors in CL. They are observed as more or less developed "coverings" around the clasts. Depending on their degree of cementation, we distinguish microscopically three types of zones: (1) *uncemented zones*, (2) *partially cemented zones* and (3) *highly cemented zones*. The typical surficial porosity of these structures is displayed in Fig. 5.

Uncemented zones display quartz grains without cement covering on CL photomicrographs (e.g. uncemented *crush microbreccia* in Fig. 8d). Apart from the case of tightly silicified concretions (see Section 4.1.3), the common *pristine sand* is always observed without cement, even in places adjacent to cataclastic structures. Within fault zones, *crush microbreccias* are commonly observed without any cement, whereas *protocataclastic microstructures* are generally uncemented only in single and multistrand SBs or thin clusters.

Partially cemented zones display µm- to 30 µm-thick orange-brown cement coverings around the clasts (Fig. 8e). They are commonly observed in *crush microbreccias*, mostly observed in *protocataclastic microstructures* within major clusters constituting the fault zones and never observed in the common *pristine sand*. In *crush microbreccias*, thin incipient cement coverings are

particularly visible around some detrital grains or clasts of the matrix; they can generate interstitial surface porosities as low as 10–15%. In *protocataclastic microstructures*, surface porosities of about 5% or lower are measured. Within *cataclastic microstructures* at least a partial covering of the clasts is inferred because we perceive the orange-brown CL signature of the cements between the clasts (e.g. Fig. 8c), although the image resolution is low and does not allow the cements to be clearly distinguished from the porosity (i.e. they are not visible in CL due to the large proportion of small microclasts).

Highly cemented zones display a main or total orange-brown cementation of the material (Fig. 8f). They are commonly observed in the *protocataclastic microstructures* and are inferred in most of the *cataclastic microstructures* by their stiffness and glassy aspect, although image resolution does not allow clear optical determination. In both of these highly cemented microstructures, surface porosities are lower than 5%. These highly cemented zones are never observed in the common *pristine sand* or *crush micro-breccia* microstructures.

4.2.4. Distribution of microstructures and cements in the fault zone

In order to characterize the macroscopic interplay between the deformation and diagenesis of a fault zone, a spatial statistic study of deformation and cementation of the thickest strike-slip fault zone (sub-vertical dip) was carried out (Fig. 9). In this case, the fault zone is formed of several single SBs, multi-strand SBs and clusters (2–3), laterally limited by two fault slip surfaces (Figs. 6d,e and 9a). Combining the two terminologies introduced in the previous sections, we classified zones as: (1) *Uncemented pristine sand or crush micro-breccia* zones, (2) *Uncemented protocataclastic* zones, (3) *Partially cemented crush micro-breccia* zones, (4) *Partially cemented protocataclastic or cataclastic* zones, (5) *Highly cemented undifferentiated* zones. From the microscopic analysis (Sections 4.2.2 And 4.2.3), we infer that the zone (5) is mostly made of *protocataclastic* and *cataclastic microstructures*.

Within the 50–90 cm-thick width of the fault zone, we observe lenticular zones of both varying density of cataclastic strands (deformation intensity) and degree of cementation, forming thick zones of particularly stiff clusters of strands. These clusters are more or less segmented or branched in a comparable manner to relay zones (e.g. Peacock and Sanderson, 1991). Segmentation and branching are observed both for uncemented or partially cemented protocataclastic clusters (e.g. transects 11 to 18, yellow areas). Cementation is restricted to the clusters and seems to be constrained by their orientation as evidenced by the lens-shaped geometry of the variation of cementation intensity (e.g. transects 5 to 15, light-red areas). The segmented protocataclastic clusters present in the central part of the fault zone seem to either have slanted orientations, linking the edges of the fault zone (transects 1 to 4), or follow the orientation of the adjacent dense clusters (transects 11 to 18). The clusters located next to the edges of the fault zone are parallel to the main direction of the fault.

This segmented and overlapping distribution of structural deformation/cementation types, although quite heterogeneous in map view (Fig. 9a and b), appears actually more homogeneous and smoothly distributed when analyzed on a graph of distribution of relative proportions of structural types (Fig. 9c). The structural type distribution reveals that the percentage of *highly cemented zones*

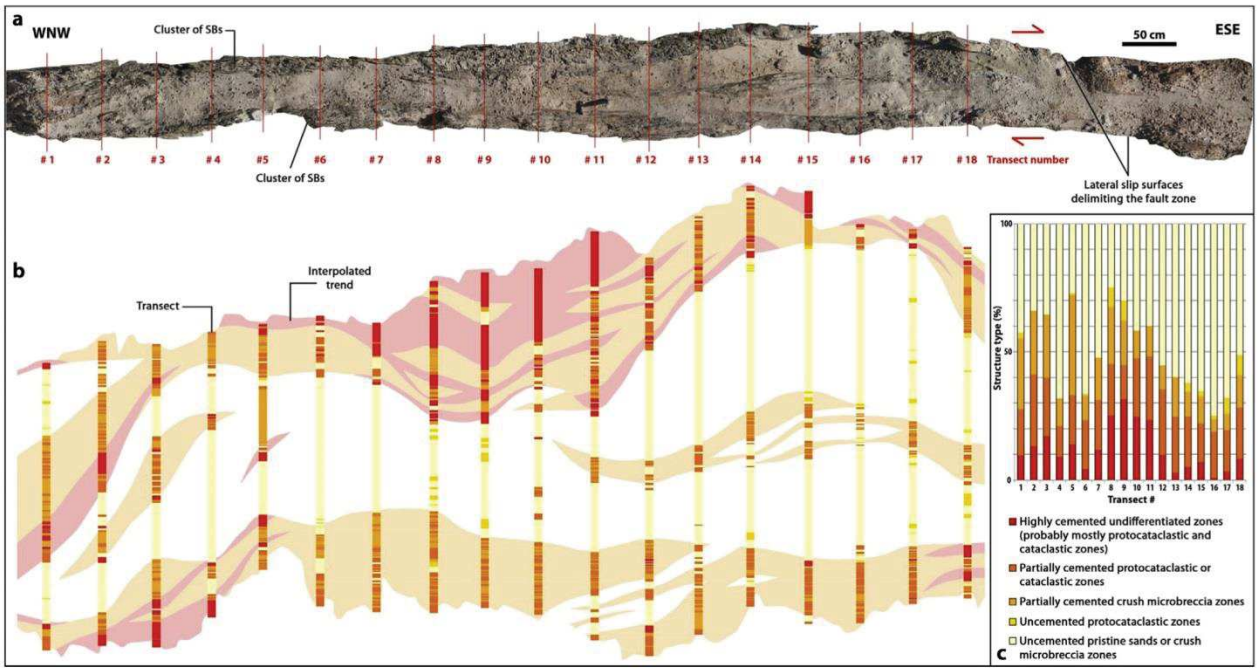

Fig. 9. (a) Map view (photographs) of the fault length and the position of the 18 transects studied for the spatial representation of the deformation and cementation. (b) Spatial representation of the deformation and cementation of the fault (represented aligned with the map view above and with a width exaggeration of 4). The scheme is built from the acquisition of the strand distribution and the cementation intensity along the transects (bright colors – see legend (c)). The trend between the transects (light colors) is interpreted by interpolating the cementation of the closer two transects and following the orientation of the structures of the fault observed in map view: red light color represents the *highly cemented* zones; orange light color represents the *partially cemented* zones. The representation reveals that the strand density (cataclastic intensity) is higher at the edges of the fault zone and sometimes at the center of this zone, forming clusters. The clusters display a segmented (in relay) pattern; the cementation is restricted to the clusters and the intensity of cementation shows a lens-shaped behavior. (c) Diagram showing the percentage distribution of the facies along the fault. (For interpretation of the references to color in this figure legend, the reader is referred to the web version of this article.)

varies progressively along the length of the fault between quite different values (min = 1%, transect #16; max = 31%, transect #9; standard deviation = 9%; mean of 12%). *Partially cemented zones*, mainly corresponding to *protocataclastic microstructures* or *crush micro-breccia*, represent on average 35% of the fault zone (min = 23%, transect #17; max = 58%, transect #5; standard deviation = 10%). *Uncemented zones* often correspond to *pristine sand* and *crush micro-breccias* preserved between the cluster lenses, they represent 52% of the fault zone thickness on average (min = 28%, transect #5; max = 77%, transect #16; standard deviation = 16%).

4.2.5. Cross-cutting of the tightly silicified concretion and cementation of the fault zone

The cataclastic microstructures of cataclastic fault zones at the contact with a tightly silicified concretion (i.e. the fault zone at the southernmost part of the quarry, Fig. 2a) have been thoroughly inspected. The fault includes some several millimeter- to centimeter-thick fragments of the tightly silicified concretion in the cataclastic material (Fig. 10a, arrow). The interface between the fragments of the concretion and the cataclastic zone (Fig. 10b) is marked by a sharp limit where the geometry of the concretion clearly shows that the assembly of the detrital grains and their overgrowths is cross-cut by the cataclasite. At some locations of the interface, small fragments from the silicified concretions are shown in the incipient stage of detachment from the host rock and inclusion into the zone of cataclastic material (Fig. 10c). Observations in cross-polarized light and CL reveal fragments on the scale of hundreds of μm-diameter of tightly silicified concretions that are cross-cut by fractures filled with cemented cataclastic material (Fig. 10d). Moreover, numerous clasts made of overgrowths such as described in the case of the tightly silicified concretions are found in the cataclastic area (Fig. 10e). These clasts are interpreted as detached from the tightly silicified concretions and incorporated into the cataclastic domain. In some places, we can observe that the orange-brown cement (coverings) seals the cataclastic material (Fig. 10f).

5. Discussion

The shallow depth of the Cenomanian sands of the De Cros quarry (max burial = 800 m after Saillet, 2009) is confirmed by host rock IGVs of 29–34%, which corresponds to depths of between 500 and 1300 m according to the Mean IGV vs. Burial depth relation established by Paxton et al. (2002). The sandstones are affected by cataclastic fault zones containing silica cements. The alteration profile is parallel to bedding, including several pervasively colored levels and a major white clean sand interval. This white clean sand interval contains at some places oriented oxidation fronts and tightly silicified concretions. Traces of kaolinite are observed within

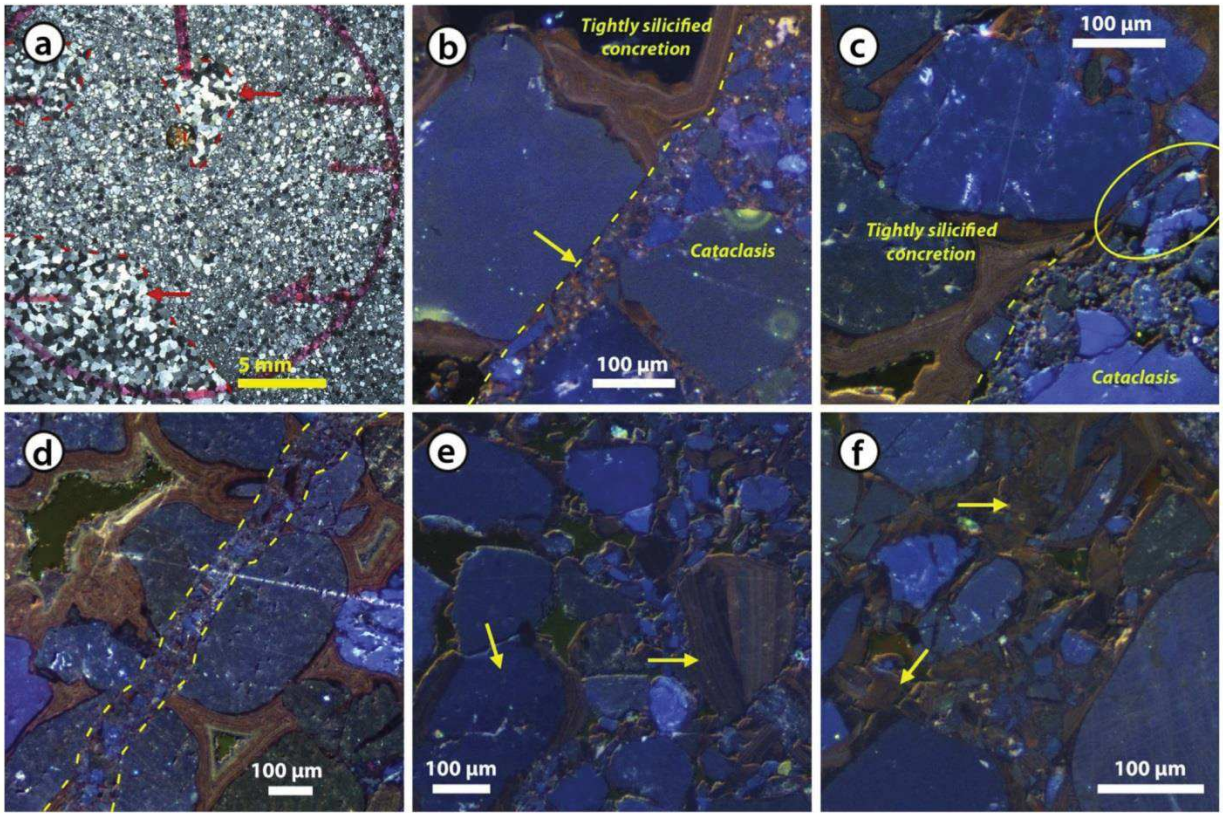

Fig. 10. Microscopy of the interaction between the cataclastic structures and the tightly silicified concretions: (a) Fragments of tightly silicified concretion in the cataclastic material (arrows), in cross-polarized light. (b) Sharp limit between the silicified concretion and the cataclasis (dashed line), in CL. (c) Piece of the silicified concretion at an incipient stage of incorporation into the cataclastic material (ellipse), in CL. (d) Tightly silicified concretion cross-cut by the thin cataclastic material (interval between the dashed lines), in CL. (e) Detrital grains interpreted as clasts of tightly silicified concretion (arrows) included in the cataclastic material, in CL. The clasts are interpreted as such because of the similarity of the multiple cement overgrowth patterns with those depicted in the tightly silicified concretions. (f) Cemented area filling the porosity and sealing the neighboring clasts (arrows), in CL.

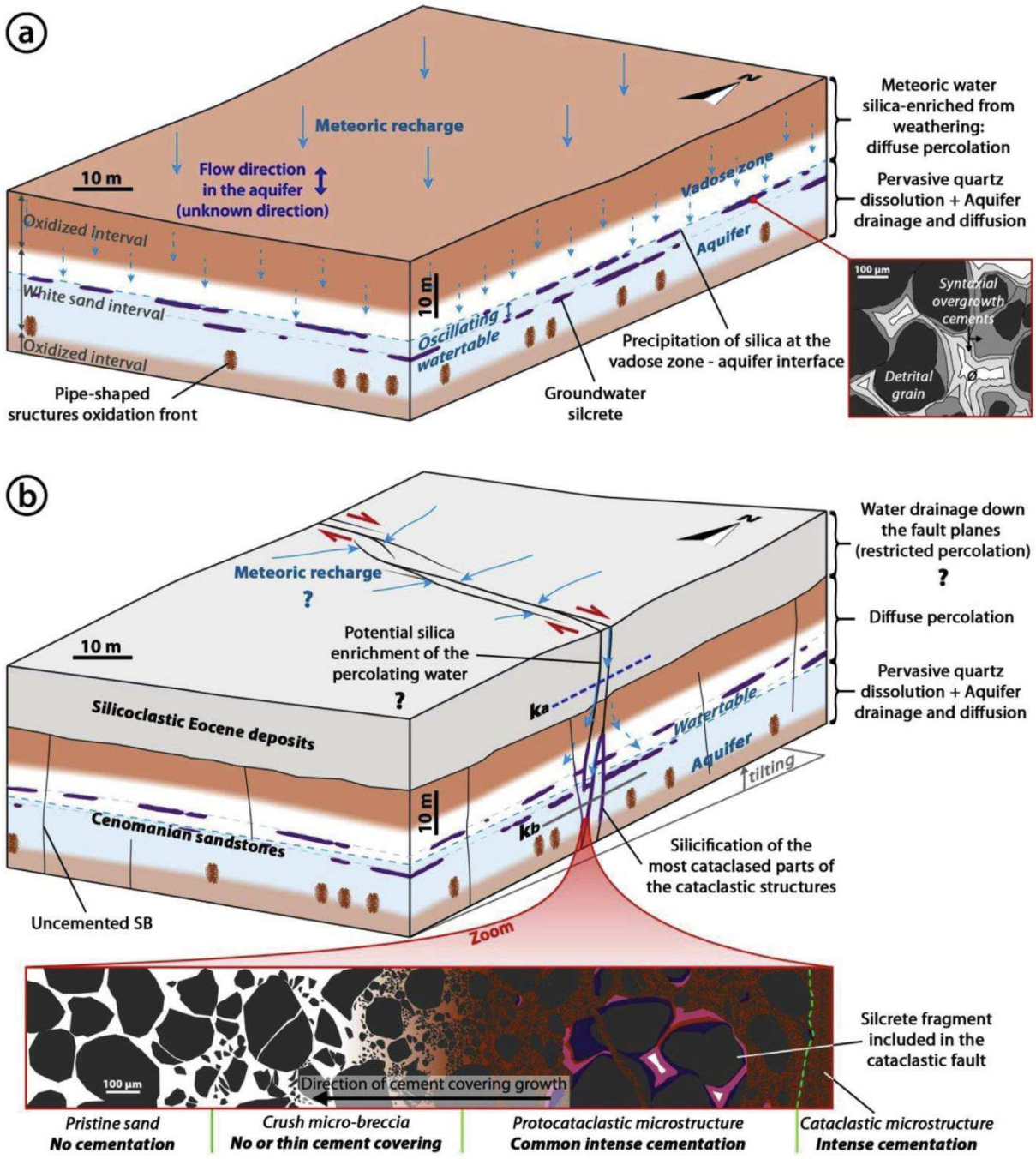
a
Meteoric recharge
10 m
Flow direction in the aquifer (unknown direction)
Oxidized interval
White sand interval
Oxidized interval
Vadose zone
Aquifer
10 m
Oscillating watertable
Pipe-shaped sructures oxidation front
Groundwater silcrete
Precipitation of silica at the vadose zone - aquifer interface
Meteoric water silica-enriched from weathering: diffuse percolation
Pervasive quartz dissolution + Aquifer drainage and diffusion
100 µm
Syntaxial overgrowth cements
Detrital grain
b
Meteoric recharge
?
10 m
Potential silica enrichment of the percolating water
?
Silicoclastic Eocene deposits
Cenomanian sandstones
Uncemented SB
Ka
Kb
Watertable
Aquifer
tilting
10 m
Silicification of the most cataclased parts of the cataclastic structures
Water drainage down the fault planes (restricted percolation)
?
Diffuse percolation
Pervasive quartz dissolution + Aquifer drainage and diffusion
Zoom
100 µm
Direction of cement covering growth
Silcrete fragment included in the cataclastic fault
Pristine sand
No cementation
Crush micro-breccia
No or thin cement covering
Protocataclastic microstructure
Common intense cementation
Cataclastic microstructure
Intense cementation
c
Permeability contrast
0
Draining faults
kb-profile (Cenomanian sandstones)
Cemented SB
Cemented cataclastic fault
Uncemented SB
ka-profile (silicoclastic Eocene deposits) ?
1 m
Length

the white sands and hematite is the main component of the oxidation fronts. The silica cementation is observed in the major strike-slip cataclastic fault zones, only in the white sand interval. Through CL microscopic observation, this cementation is characterized as colored covering of grains. Some clasts come from the tightly silicified concretions, and a phase of cementation also seals the clasts of the fault zone.

This section discusses the implications of the observations presented for determining the environment of the diagenesis, the possible sources of silica, the favored locations for the silica precipitation and the timing of the diagenesis.

5.1. Groundwater diagenetic environment

The study of the paleoenvironmental context performed through the analysis of the weathering profile yields evidence of an aquifer regime within the Cenomanian sands of the De Cros quarry during the process of silica cementation. The XRD analyses showed that the red and yellow-orange sand coatings correspond to hematite and goethite oxides, respectively. The presence of oxidation levels in the weathering profile proves that the formation was subjected to a continental environment of weathering. The regional iron oxidation (corresponding to the south and southwestern limits of the paleo Vocontian Basin in Provence) generally comes from the glauconite decay in upper Turonian sandstone formations (where deposited) exposed to continental weathering under wet tropical climate (e.g. Parron (1975) and Triat (1982) at Pont St. Esprit and in the Uzès Basin (Provence, France)). The tabular organization of these oxidation levels including a white sand interval suggests fluctuations through time in the aquifer water-table, causing the vertical remobilization and/or the leaching of the oxides in the formation. This hypothesis of a vertical leaching is also made by Thiry and Marechal (2001) for the Fontainebleau sandstones and Triat (1982) in the areas cited above. The presence of Liesegang rings corroborates the hypothesis of a groundwater system since they are typically from an aquifer environment and are the consequence of oxygen diffusion in Fe-rich waters as indicated by Balsamo et al. (2013). Hydrodynamic flows in the aquifer are inferred by the presence of NW-SE-oriented rolls and pipe-shaped oxidation fronts in the bedding plane. The oxidation fronts are interpreted as the result of the reconcentration of the oxides at the bottom of the leached interval and oriented according to the aquifer flux direction.

Both the macroscopic and microscopic geometry and texture of the tightly silicified concretions strongly resemble groundwater silcretes identified in the Fontainebleau sandstones by Thiry and Marechal (2001), French and Worden (2013) and Haddad et al. (2006). In a similar way, tightly silicified concretions are interpreted as groundwater silcretes at the De Cros quarry.

The groundwater silcretes are thought to be formed in a relatively cold diagenetic environment, such as shown by Sabouraud and Parron (1977) based on fluid inclusion analysis of cements yielding low water temperature (<40 °C). According to Thiry (1997) and Thiry and Marechal (2001), groundwater silcretes could be formed via silica precipitation at the top of the aquifer. The process of silica precipitation would result from the dismantling of silico-organic complexes contained both in the aquifer and in the percolation water in the vadose zone, where the downward percolating water meets the aquifer groundwater (i.e. watertable). There, weathering of the silico-organic complexes would lead to a local oversaturation of silica and subsequent precipitation. Fein (2000) acknowledges that silico-organic complexes can have an efficient diagenetic effect in the subsurface at relatively low temperatures in the sense that complexation increases the dissolution rate of quartz, in particular amongst other silicate minerals (also see Bennett et al., 1988). Thiry and Milnes (1991) suggest that groundwater silcretes are formed independently from the surface prevailing climate.

Concerning the source of the silica, the absence of pressure-solution features between quartz grains suggests that the silica does not originate from compaction and confirms the shallow burial of the formation. However, the presence of kaolinite in some intervals of the weathering profile put forward kaolinization processes initiating the release of silica in solution into the formation by glauconite and/or alkali-feldspars weathering. The presence of hematite and goethite is a strong argument favoring the hypothesis of a glauconite weathering for the silica release (e.g. Triat, 1982). On the other hand, the process of K-feldspar weathering by kaolinization seems to be particularly important for shallow sandstones subjected to meteoric waters (McBride, 1989; Bjørlykke, 1994; Worden and Morad, 2000; Arostegui et al., 2001). Although no glauconite is observed in the studied Cenomanian sand interval and although the percentage of feldspar is very low (a few percent), both minerals could come from an above and/or lateral external source. For instance, glauconite and feldspars are commonly observed in the Turonian deposits, existing a few km away in Provence (e.g. Triat, 1982; Ballas, 2013).

Although it would be difficult to demonstrate, another source for the silica supply could be the pervasive dissolution of the quartz in the sandstone series (Triat, 1982). In an aquifer media, silica concentration such as 10–12 ppm can be high enough to constitute a diagenetic fluid and maintain a silicification process (Thiry and Marechal, 2001). In particular, modeling by Canals and Meunier (1995) suggests that a 250,000 yr period is enough to cement approximately half of the porosity of clean sandstone at shallow conditions (20 °C temperature) and flow rates of 10 m/y.

5.2. The impact of cataclasis on cementation and diagenetic processes in the cataclastic structures

We have discussed how the silica cementation was likely related to the presence of a shallow groundwater system. In the case of the silcretes, we evoked the process hypothesized for the quartz cementation of the detrital grains. In this section, the question is "how are the cementation processes different in the case of the cementation of the cataclastic structures?" since the cements show a different macroscopic morphology (sub-vertical vs. tabular localization aligned with the bedding in the case of the silcretes) and microscopic morphology (varying degree of "covering" vs. well-developed overgrowth patterns in the case of the silcretes).

The microscopic observations clearly reveal a correlation between the intensity of cataclasis and the degree of cementation. The higher the degree of cataclasis in the sand, the more the cementation is prominent. Macroscopic observations are fully consistent with a preferential cementation of the most deformed areas since the most cataclased zones, corresponding to zones with

Fig. 11. Synthetic block-diagrams presenting the different stages and processes of silica diagenesis in the Cenomanian sands of the De Cros quarry: (a) Formation of groundwater silcretes in a shallow aquifer paleo-environment (from Turonian to middle Eocene). (b) Diagenesis of the cataclastic fault clusters in the white sand interval (middle to late Eocene Pyrenean compression). Note that the elements related to the hypothesis of a draining fault in the siliciclastic deposits are marked with a "?". K_a and k_b refer to the location of the permeability contrast profiles of the siliciclastic formation and the sandstone formation, respectively. The profiles are presented in (c). (c) Permeability contrast profiles of the potentially fractured siliciclastic Eocene deposits and the Cenomanian sandstones at the vicinity of the fault.

high strand densities, are generally more cemented, whereas zones with less cataclastic material are poorly cemented and the pristine zones are uncemented. In particular, cementation is favored next to the slip surfaces where the clusters of strands are more developed. From the spatial and statistical representation of the deformation and cementation, it is noted that at least 19% of the fault zone thickness is composed of partially cemented protocataclastic/cataclastic material to highly cemented material; a maximum of 48% is reached in some parts of the fault zone.

All these observations are coherent with the hypothesis of a favored nucleation of silica with a maximum grain-surface to grain-volume ratio, and a great amount of fresh-reactional quartz-clast surfaces (fewer small scale nucleation discontinuities) in contact with the nourishing fluid (Canals and Meunier, 1995; Fisher and Knipe, 1998; Fisher et al., 2000; Lander et al., 2008; Williams et al., 2015). Hence, we think that the two most likely factors for the cementation of the cataclastic structures are: (1) faster rates of growth on the fracture surfaces compared to detrital grain surfaces and (2) the presence of much greater surface area for cement growth. This conclusion is consistent with the previous observations of Walderhaug (2000) and Lander et al. (2008) at greater depths. The absence of quartz cementation within the cataclastic structures of the oxidized sand intervals suggests that coating of quartz grains (e.g. oxides, clays) could inhibit silica precipitation (McBride, 1989; Ehrenberg, 1993), or that the water supplying silica did not invade these areas (which are not leached zones).

Again, the sources of silica responsible for the cementation of the cataclastic structures are not constrained and could potentially match with one or several of the hypotheses considered for the silcrete concretions. Furthermore, one could hypothesize that a percentage of silica comes from the fine-grained particles of the cataclastic structures themselves.

5.3. The chronology of deformation and silicification

The organization of the different structures mapped in Fig. 2 corresponds to the tectonic events caused during the Pyrenean contraction and the Gulf of Lion extension. Dextral N110°E and sinistral N140°E conjugated sets of strike-slip SBs indicate a NW–SE oriented horizontal contraction related to the Pyrenean orogeny. The dextral N140°E and sinistral N005°E strike-slip conjugate sets probably correspond to a second NNW-SSE contractional stage. This is evidenced by both dextral and sinistral cross-cutting of the N110°E set by a second generation of N140°E and N005°E strike-slip sets, respectively. The strike-slip tectonic stages predate the normal tectonic events since they are cross-cut by normal faults. In regard to their strike orientation, the normal clusters and SBs are associated to the extensional regime of the Gulf of Lion. The few reverse-sense SBs observed are also interpreted to be related to the Pyrenean-Provencal contraction. We note that, although the tectonic structures observed could match with the tectonic events such as suggested previously, they could also be linked to a more local stress context, as for example the stress perturbations between the Nîmes fault, the Ventoux-Lure fault or the tip of the Salon-Cavaillon fault.

The two strike-slip tectonic stages cut and hence post-date a part of the weathering profile including the groundwater silcretes. Since the silcretes are parallel to the bedding plane and the oxidized and leached levels, we suggest that they formed being contemporaneous with the formation of the oxidized and leached levels (in an interval deprived of oxide coating), and prior to the first stage of Pyrenean contraction (i.e. prior to tilting). The silcrete growth, as well as the weathering profile, is therefore encompassed in a 38 Ma period ranging from Turonian to middle Eocene. Microscopically, fragments of the silcretes are observed detached in the cataclastic domains, coherent with the observation of a silcrete cross-cut and postdated by the strike-slip faults. These fragments, as well as the cataclastic material, are sealed by the orange-brown quartz cement coverings. Therefore the orange-brown cements postdate the overgrowth cements of the silcrete. Because the orange-brown cements seal the strike-slip fault zone, they are interpreted as postdating this stage of faulting. Therefore, they would be formed between middle Eocene and the end of Eocene where the latest stages of the Pyrenean compression would have tilted the Mt. Ventoux (we assume that a subsequent tilting and uplift of the Cenomanian sandstones would probably prevent the presence of an aquifer in the formation).

A burial curve of the Cenomanian sandstone at Bédoin including the tectonic and diagenetic events observed at the study site is available in the web version of this paper (supporting material).

5.4. Model for the diagenesis

Considering the statements of Sections 5.1, 5.2 and 5.3, we propose a model for the silica diagenesis in the Cenomanian sands at the De Cros quarry (Fig. 11a and b) including: (i) the formation of silcretes via silica oversaturation at the top of the aquifer; (ii) the occurrence of the N110°E, N140°E and N005°E cataclastic strike-slip structures; (iii) a second stage of cementation in the most cataclased parts of the fault zones.

As explained, groundwater silcretes would have occurred first and would have grown in a widespread area at the top of the aquifer in the Cenomanian sands during the continental exposure (Fig. 11a) until the first phase of Pyrenean shortening. Although the slight tilting of the formations triggered by the first stage of the Pyrenean orogeny could have allowed the preservation of an aquifer in the Cenomanian sands, we think that the growth of silcretes was definitely stopped because a significant thickness (e.g. ca. 40 m in total) of Eocene siliciclastic deposits (including shale units) was deposited on top, preventing meteoric percolation in the vadose zone.

Two hypotheses can be suggested for the silicification of the cataclastic structures (Fig. 11b): (1) If we assume that the occurrence of the strike-slip faults at the study site could have generated open fractures in the Eocene silty clays (e.g. Laurent et al., 2012 for an example of permeable faults in such lithologies) and in the other siliciclastic deposits overlying the sandstones, the meteoric water would have mainly been drained downward through these fractures in the low-permeability units. There, the meteoric water could have been potentially enriched in silica. When reaching the Cenomanian porous sands, the water would have precipitated silica in the cataclastic structures of the clean sand interval. This case does not require immerged structures for the cementation. (2) If we assume that the fracturing of the overlying silty clays is not possible (e.g. ductile smearing behavior), then the silica required for the silicification of the cataclastic structures would have been exclusively supplied by lateral silica sources such as pervasive dissolution of the detrital grains in the formation or glauconite and/or K-feldspar weathering in a nearby formation. The silica would have been transported in solution by aquifer drainage which could have been induced, for example, by the slight tilting and folding of the formation allowing a meteoric water recharge where the overlying formations were eroded. Structures most likely to have been cemented would have been the most cataclastic ones. Fig. 11c displays the permeability contrast profiles of both Cenomanian sandstone and the Eocene siliciclastic deposits in the vicinity of the fault, accounting for a draining behavior in the Eocene deposits.

6. Conclusion

This study reveals that silica diagenesis can occur at shallow depths (depth <2 km, T°<80 °C) in the form of (1) tabular and tightly cemented concretions recognized as groundwater silcretes and (2) tightly cemented cataclastic clusters of strike-slip fault zones. A groundwater system (continental conditions) is the favored environment for these two types of diagenesis. Provided that the sand interval is clean, groundwater-related cementation forms at the top of the aquifer in the case of the silcretes and in the most cataclastic zones of the formation. In the latter case, the diagenesis is inherent to cataclastic zones and is due to (1) the creation of fresh fracture surfaces compared to detrital grain surfaces and (2) the presence of much greater surface area for cement growth, which increased the growth rate of the cements. These fault zones could be preferential drains in the overlying non-porous layers from the surface to the aquifer, and therefore preferred zones of reflux (causing cementation) in the underlying aquifer units. Minimum silica concentrations as low as 10–12 ppm are evoked in the literature with flow rate of 10 m/y and at 20 °C temperatures to nucleate cementation. In the sand formation, we think that the sources of silica are most likely due to two processes: (1) the kaolinization of external glauconite and/or K-feldspars weathering and (2) the pervasive weathering of host rock grains (internal silica source). The first hypothesis would imply a transport from remote (up to 10 km) formations because the glauconite/feldspar-rich Turonian sandstones were never deposited on top of the Cenomanian sandstone in the southern limb of the Ventoux, since a hiatus is observed between the Cenomanian and Eocene deposits. No evidence was observed for pressure-solution processes contributing to the silica released into the solution.

In the cataclastic structures, the extent of the silicification is however limited by their geometrical extent and only tends to occur where the cataclastic material is not coated by material other than quartz. The impact of diagenesis on the porosity of cataclastic structures is significant since cemented cataclastic structures can occupy from 19 to 48% of a fault zone thickness and can represent surface porosities as low as 5% for protocataclastic microstructures, and <5% in the case of highly silicified cataclastic microstructures.

This kind of shallow silica cementation into fault zones is not restricted to the study site since it has been actually observed in others Cretaceous sandstone outcrops in Provence France (Pougnadoresse, Bastide d'Engras, Spir), but also in England (Thurstaton Hill, Valley of Eden, Milodowski et al., 2014) or Germany (Harz fault, Klimczak and Schultz, 2013). Therefore, similar cementation processes could take place at these sites. An interesting subsequent study aim would consist in looking for traces of such groundwater systems in deeper formations in order to anticipate the evolution of such cemented systems during burial.

Acknowledgments

This work was supported by the Laboratory of Geosciences Montpellier, the Institut Universitaire de France and TOTAL E&P, which are gratefully acknowledged. Special thanks are addressed to Christophe Nevado for his precious advice and the time spent on the preparation of the thin-sections. We thank M. Séranne, N. Molenaar and R. H. Lander for their constructive comments and suggestions on this manuscript. I. Basile-Doelsch is also greatly thanked for her support and advice on the geochemical properties of the quartz cements.

Appendix A. Supplementary data

Supplementary data related to this article can be found at http://dx.doi.org/10.1016/j.jsg.2015.10.001.

References

Abdel-Wahab, A., Salem, A.M.K., Mcbride, E.F., 1998. Quartz cement of meteoric origin in silcrete and nonsilcrete sandstones, Lower Carboniferous, western Sinai, Egypt. J. Afr. Earth Sci. 27, 277–290. http://dx.doi.org/10.1016/S0899-5362(98)00061-X.

Agosta, F., Prasad, M., Aydin, A., 2007. Physical properties of carbonate fault rocks, fucino basin (Central Italy): implications for fault seal in platform carbonates. Geofluids 7, 19–32. http://dx.doi.org/10.1111/j.1468-8123.2006.00158.x.

Antonellini, M., Aydin, A., 1994. Effect of faulting on fluid flow in porous sandstones: petrophysical properties. AAPG Bull. 78, 355–377.

Antonellini, M., Aydin, A., Orr, L., 1999. Outcrop-aided characterization of a faulted hydrocarbon reservoir: Arroyo Grande Oil field, California, USA. In: Haneberg, W.C., Mozley, P.S., Moore, J.C., Goodwin, L.B. (Eds.), Faults and Subsurface Fluid Flow in the Shallow Crust, Geophysical Monograph, vol. 113, pp. 7–26.

Arostegui, J., Irabien, M.J., Nieto, F., Sangüesa, J., Zuluaga, M.C., 2001. Microtextures and the origin of muscovite-kaolinite intergrowths in sandstones of the Utrillas formation, Basque Cantabrian Basin, Spain. Clays Clay Miner. 49, 529–539.

Arthaud, F., Séguret, M., 1981. Les structures pyrénéennes du Languedoc et du Golfe du Lion (Sud de la France). Bull. la Soc. Geol. Fr. 7 http://dx.doi.org/10.2113/gssgfbull.S7-XXIII.1.51. XXIII, 51–63.

Aydin, A., 1978. Small faults formed as deformation bands in sandstone. PAGEOPH 116, 913–930. http://dx.doi.org/10.1007/BF00876546.

Aydin, A., 2000. Fractures, faults, and hydrocarbon entrapment, migration and flow. Mar. Pet. Geol. 17, 797–814. http://dx.doi.org/10.1016/S0264-8172(00)00020-9.

Ballas, G., Fossen, H., Soliva, R., 2015. Factors controlling permeability of cataclastic deformation bands in porous sandstone reservoirs. J. Struct. Geol. 76, 1–21. http://dx.doi.org/10.1016/j.jsg.2015.03.013.

Ballas, G., Soliva, R., Benedicto, A., Sizun, J.-P., 2014. Control of tectonic settings and large-scale faults on the basin-scale distribution of deformation bands in porous sandstone (Provence, France). Mar. Pet. Geol. 55, 142–159. http://dx.doi.org/10.1016/j.marpetgeo.2013.12.020.

Ballas, G., 2013. Modèle structural, mécanique et pétrophysique de la localisation de la déformation dans les grès poreux (Provence, France) (Ph.D. thesis). Université Montpellier II - UFR Sciences et Techniques.

Ballas, G., Soliva, R., Sizun, J.-P., Benedicto, A., Cavailhes, T., Raynaud, S., 2012. The importance of the degree of cataclasis in shear bands for fluid flow in porous sandstone, Provence, France. AAPG Bull. 96, 2167–2186. http://dx.doi.org/10.1306/04051211097.

Ballas, G., Soliva, R., Sizun, J.-P., Fossen, H., Benedicto, A., Skurtveit, E., 2013. Shear-enhanced compaction bands formed at shallow burial conditions; implications for fluid flow (Provence, France). J. Struct. Geol. 47, 3–15. http://dx.doi.org/10.1016/j.jsg.2012.11.008.

Balsamo, F., Bezerra, F.H.R., Vieira, M.M., Storti, F., 2013. Structural control on the formation of iron-oxide concretions and liesegang bands in faulted, poorly lithified cenozoic sandstones of the Paraíba Basin, Brazil. Geol. Soc. Am. Bull. 125, 913–931. http://dx.doi.org/10.1130/B30686.1.

Bennett, P.C., Melcer, M.E., Siegel, D.I., Hassett, J.P., 1988. The dissolution of quartz in dilute aqueous solutions of organic acids at 25°C. Geochim. Cosmochim. Acta 52, 1521–1530. http://dx.doi.org/10.1016/0016-7037(88)90222-0.

Bjørkum, P.A., 1996. How important is pressure in causing dissolution of quartz in sandstones? J. Sediment. Res. 66, 147–154. http://dx.doi.org/10.1306/D42682DE-2B26-11D7-8648000102C1865D.

Bjørkum, P.A., Oelkers, E.H., Nadeau, P.H., Walderhaug, O., Murphy, W.M., 1998. Porosity prediction in quartzose sandstones as a function of time, temperature, depth, stylolite frequency, and hydrocarbon saturation. AAPG Bull. 82, 637–648.

Bjørlykke, K., 1994. Fluid-flow processes and diagenesis in sedimentary basins. Geol. Soc. Lond. Spec. Publ. 78, 127–140. http://dx.doi.org/10.1144/GSL.SP.1994.078.01.11.

Bjørlykke, K., Egeberg, P.K., 1993. Quartz cementation in sedimentary Basins. AAPG Bull. 77, 1538–1548.

Bjørlykke, K., Ramm, M., Saigal, G.C., 1989. Sandstone diagenesis and porosity modification during basin evolution. Geol. Rundsch. 78, 243–268. http://dx.doi.org/10.1007/BF01988363.

Caine, J.S., Evans, J.P., Forster, C.B., 1996. Fault zone architecture and permeability structure. Geology 24, 1025–1028. http://dx.doi.org/10.1130/0091-7613(1996)024<1025:FZAAPS>2.3.CO;2.

Canals, M., Meunier, J.D., 1995. A model for porosity reduction in quartzite reservoirs by quartz cementation. Geochim. Cosmochim. Acta 59, 699–709. http://dx.doi.org/10.1016/0016-7037(94)00355-P.

Cavailhes, T., Soliva, R., Labaume, P., Wibberley, C., Sizun, J.-P., Gout, C., Charpentier, D., Chauvet, A., Scalabrino, B., Buatier, M., 2013. Phyllosilicates formation in faults rocks: implications for dormant fault-sealing potential and fault strength in the upper crust. Geophys. Res. Lett. 40, 4272–4278. http://dx.doi.org/10.1002/grl.50829.

Champion, C., Choukroune, P., Clauzon, G., 2000. La déformation post-Miocène en Provence occidentale. Geodin. Acta 13, 67–85. http://dx.doi.org/10.1016/S0985-3111(00)00114-5.

Ehrenberg, S.N., 1993. Preservation of anomalously high porosity in deeply buried sandstones by grain-coating chlorite: examples from the Norwegian Continental shelf. AAPG Bull. 77, 1260–1286.

Eichhubl, P., Davatz, N.C., Becker, S.P., 2009. Structural and diagenetic control of fluid migration and cementation along the Moab fault, Utah. AAPG Bull. 93, 653–681.

http://dx.doi.org/10.1306/02180908080.
Faulkner, D.R., Jackson, C.A.L., Lunn, R.J., Schlische, R.W., Shipton, Z.K., Wibberley, C.A.J., Withjack, M.O., 2010. A review of recent developments concerning the structure, mechanics and fluid flow properties of fault zones. J. Struct. Geol. 32, 1557–1575. http://dx.doi.org/10.1016/j.jsg.2010.06.009.
Fein, J.B., 2000. Experimental and field constraints on the role of silica-organic complexation and silica-microbial interactions during sediment diagenesis. In: Worden, R.H., Morad, S. (Eds.), Quartz Cementation in Sandstones. International Association of Sedimentologists, Special Publication Number, vol. 29, pp. 119–127.
Ferry, S., 1999. Apport des forages ANDRA de Marcoule à la connaissance de la marge crétacée rhodanienne. In: Etude du Gard Rhodanien, Actes des Journées Scientifiques CNRS/ANDRA. EDP Sciences, Bagnols-sur-Cèze, pp. 63–91.
Fisher, Q.J., Knipe, R.J., 1998. Fault Sealing Processes in Siliciclastic Sediments. Geol. Soc. Lond. Spec. Publ. 147, 117–134. http://dx.doi.org/10.1144/GSL.SP.1998.147.01.08.
Fisher, Q.J., Knipe, R.J., 2001. The permeability of faults within siliciclastic petroleum reservoirs of the North Sea and Norwegian Continental Shelf. Mar. Pet. Geol. 18, 1063–1081. http://dx.doi.org/10.1016/S0264-8172(01)00042-3.
Fisher, Q.J., Knipe, R.J., Worden, R.H., 2000. Microstructures of deformed and non-deformed sandstones from the North Sea: implications for the origins of quartz cement in sandstones. In: Worden, R.H., Morad, S. (Eds.), Quartz Cementation in Sandstones, Special Publication Number, vol. 29. International Association of Sedimentologists, pp. 129–146.
Ford, M., Stahel, U., 1995. The geometry of a deformed carbonate slope-basin transition: the Ventoux-Lure fault zone, SE France. Tectonics 14, 1393–1410. http://dx.doi.org/10.1029/95TC02522.
Fossen, H., 2010. Deformation bands formed during soft-sediment deformation: observations from SE Utah. Mar. Pet. Geol. 27, 215–222. http://dx.doi.org/10.1016/j.marpetgeo.2009.06.005.
Fossen, H., Bale, A., 2007. Deformation bands and their influence on fluid flow. AAPG Bull. 91, 1685–1700. http://dx.doi.org/10.1306/07300706146.
Fossen, H., Schultz, R.A., Shipton, Z.K., Mair, K., 2007. Deformation bands in sandstone: a review. J. Geol. Soc. 164, 755–769. http://dx.doi.org/10.1144/0016-76492006-036.
French, M.W., Worden, R.H., 2013. Orientation of microcrystalline quartz in the Fontainebleau Formation, Paris Basin and why it preserves porosity. Sediment. Geol. 284–285, 149–158. http://dx.doi.org/10.1016/j.sedgeo.2012.12.004.
Gallagher Jr., J.J., Friedman, M., Handin, J., Sowers, G.M., 1974. Experimental studies relating to microfracture in sandstone. Tectonophysics 21, 203–247. http://dx.doi.org/10.1016/0040-1951(74)90053-5.
Haddad, S.C., Worden, R.H., Prior, D.J., Smalley, P.C., 2006. Quartz cement in the fontainebleau sandstone, Paris Basin, France: crystallography and implications for mechanisms of cement growth. J. Sediment. Res. 76, 244–256. http://dx.doi.org/10.2110/jsr.2006.024.
Klimczak, C., Schultz, R.A., 2013. Fault damage zone origin of the Teufelsmauer, Subhercynian cretaceous Basin, Germany. Int. J. Earth Sci. (Geol. Rundsch) 102, 121–138. http://dx.doi.org/10.1007/s00531-012-0794-z.
Labaume, P., Moretti, I., 2001. Diagenesis-dependence of cataclastic thrust fault zone sealing in sandstones. Example from the Bolivian Sub-Andean Zone. J. Struct. Geol. 23, 1659–1675. http://dx.doi.org/10.1016/S0191-8141(01)00024-4.
Lander, R.H., Larese, R.E., Bonnell, L.M., 2008. Toward more accurate quartz cement models: the importance of euhedral versus noneuhedral growth rates. AAPG Bull. 92, 1537–1563. http://dx.doi.org/10.1306/07160808037.
Laurent, D., Gay, A., Baudon, C., Berndt, C., Soliva, R., Planke, S., Mourgues, R., Lacaze, S., Pauget, F., Mangue, M., Lopez, M., 2012. High-resolution architecture of a polygonal fault interval inferred from geomodel applied to 3D seismic data from the Gjallar Ridge, Vøring Basin, offshore Norway. Mar. Geol. Hydrocarbon leakage through focused fluid flow systems in continental margins 332–334, 134–151. http://dx.doi.org/10.1016/j.margeo.2012.07.016.
McBride, E.F., 1989. Quartz cement in sandstones: a review. Earth Science Rev. 26, 69–112. http://dx.doi.org/10.1016/0012-8252(89)90019-6.
Milliken, K.L., Reed, M.H., Laubach, S.E., 2005. Quantifying compaction and cementation in deformation bands in porous sandstones. In: Sorkhabi, R., Tsuji, Y. (Eds.), Faults, Fluid Flow, and Petroleum Traps, AAPG Memoir, vol. 85, pp. 237–249.
Milodowski, A.E., Rushton, J.C., Hall, M., Butcher, A.S., Kearsey, T., Newell, A.J., 2014. Understanding the distribution and impact of small-scale deformation-band features on permeability and fluid flow in Permo-Triassic sandstones from the UK. In: Presented at the Small to Subseismic Scale Reservoir Deformation. The Geological Society, Burlington House, Piccadilly, London.
Molenaar, N., Cyziene, J., Sliaupa, S., 2007. Quartz cementation mechanisms and porosity variation in Baltic Cambrian sandstones. Sediment. Geol. 195, 135–159. http://dx.doi.org/10.1016/j.sedgeo.2006.07.009.
Oelkers, E.H., Bjørkum, P.A., Murphy, W.M., 1996. A petrographic and computational investigation of quartz cementation and porosity reduction in North Sea sandstones. Am. J. Sci. 296, 420–452.
Parron, C., 1975. Contribution à l'étude des paléoaltérations des grès du Crétacé supérieur du Gard (de Pont-Saint-Esprit à Uzès) - Conséquences Stratigraphiques et Paléogéographiques (Ph.D. thesis). Université de Droit, d'Economie et des Sciences d'Aix-Marseille.
Paxton, S.T., Szabo, J.O., Ajdukiewicz, J.M., Klimentides, R.E., 2002. Construction of an intergranular compaction curve for evaluating and predicting compaction and porosity loss in rigid grained sandstone reservoirs. AAPG Bull. 86, 2047–2067.
Peacock, D.C.P., Sanderson, D.J., 1991. Displacements, segment linkage and relay ramps in normal fault zones. J. Struct. Geol. 13, 721–733. http://dx.doi.org/10.1016/0191-8141(91)90033-F.
Pichon, X.L., Rangin, C., Hamon, Y., Loget, N., Lin, J.Y., Andreani, L., Flotte, N., 2010. Geodynamics of the France Southeast Basin. Bull. la Soc. Geol. Fr. 181, 477–501. http://dx.doi.org/10.2113/gssgfbull.181.6.477.
Rangin, C., Pichon, X.L., Hamon, Y., Loget, N., Crespy, A., 2010. Gravity tectonics in the SE Basin (Provence, France) imaged from seismic reflection data. Bull. la Soc. Geol. Fr. 181, 503–530. http://dx.doi.org/10.2113/gssgfbull.181.6.503.
Richter, D.K., Götte, T., Götze, J., Neuser, R.D., 2003. Progress in application of cathodoluminescence (CL) in sedimentary petrology. Mineral. Petrol. 79, 127–166. http://dx.doi.org/10.1007/s00710-003-0237-4.
Roure, F., Brun, J.-P., Colletta, B., Van den Driessche, J., 1992. Geometry and kinematics of extensional structures in the Alpine Foreland Basin of southeastern France. J. Struct. Geol. 14 http://dx.doi.org/10.1016/0191-8141(92)90153-N, 50.–519.
Sabouraud, C., Parron, C., 1977. Néoformation de cristaux de quartz par des eaux météoriques dans lesfrès albiens du Gard. Mise en évidence par l'étude des inclusions des grains. In: Compte Rendu sommaire de la Société Géologique de France, 6, pp. 322–324.
Saillet, E., 2009. La localisation de la déformation dans les grès poreux: caractérisation d'un analogue de réservoirs gréseux faillés dans le Bassin du Sud-Est, Provence, France (Ph.D. thesis). Université de Nice-Sophia Antipolis, UFR Sciences.
Saillet, E., Wibberley, C.A.J., 2010. Evolution of cataclastic faulting in high-porosity sandstone, Bassin du Sud-Est, Provence, France. J. Struct. Geol. 32, 1590–1608. http://dx.doi.org/10.1016/j.jsg.2010.02.007.
Scholz, C.A., 1990. Mechanics of Earthquake and Faulting. Cambridge University Press.
Schultz, R.A., Fossen, H., 2008. Terminology for structural discontinuities. AAPG Bull. 92, 853–867. http://dx.doi.org/10.1306/02200807065.
Schultz, R.A., Soliva, R., 2012. Propagation energies inferred from deformation bands in sandstone. Int. J. Fract. 176, 135–149. http://dx.doi.org/10.1007/s10704-012-9730-2.
Séranne, M., Benedicto, A., Labaum, P., Truffert, C., Pascal, G., 1995. Structural style and evolution of the Gulf of Lion Oligo-Miocene rifting: role of the Pyrenean orogeny. Mar. Pet. Geol. Integr. Basin Stud. 12, 809–820. http://dx.doi.org/10.1016/0264-8172(95)98849-Z.
Shipton, Z.K., Evans, J.P., Thompson, L.B., 2005. The geometry and thickness of deformation-band fault core and its influence on sealing characteristics of deformation-band fault zones. In: Sorkhabi, R., Tsuji, Y. (Eds.), Faults, Fluid Flow and Petroleum Traps, American Association of Petroleum Geologists Memoir, vol. 85, pp. 181–195. http://dx.doi.org/10.1306/1033723M853135.
Sibson, R.H., 1977. Fault rocks and fault mechanisms. J. Geol. Soc. 133, 191–213. http://dx.doi.org/10.1144/gsjgs.133.3.0191.
Sibson, R.H., 1994. An assessment of field evidence for "Byerlee" friction. PAGEOPH 142, 645–662. http://dx.doi.org/10.1007/BF00876058.
Sibson, R.H., 2000. Fluid involvement in normal faulting. J. Geodyn. 29, 469–499. http://dx.doi.org/10.1016/S0264-3707(99)00042-3.
Soliva, R., Schultz, R.A., Ballas, G., Taboada, A., Wibberley, C., Saillet, E., Benedicto, A., 2013. A model of strain localization in porous sandstone as a function of tectonic setting, burial and material properties; new insight from Provence (southern France). J. Struct. Geol. 49, 50–63. http://dx.doi.org/10.1016/j.jsg.2012.11.011.
Sornay, J., 1950. Étude stratigraphique sur le Crétacé supérieur de la Vallée du Rhône entre Valence et Avignon et des régions voisines (Ph.D. thesis). Université de Grenoble.
Tempier, C., 1987. Modèle nouveau de mise en place des structures provençales. Bull. la Soc. Geol. Fr. 8 (III), 533–540. http://dx.doi.org/10.2113/gssgfbull.III.3.533.
Thiry, M., 1997. Continental silicifications: a review. In: Paquet, H., Clauer, N. (Eds.), Soils and Sediments: Mineralogy and Geochemistry. Springer Berlin Heidelberg, pp. 191–221.
Thiry, M., Marechal, B., 2001. Development of tightly cemented sandstone lenses in uncemented sand: example of the fontainebleau sand (Oligocene) in the Paris Basin. J. Sediment. Res. 71, 473–483.
Thiry, M., Milnes, A.R., 1991. Pedogenic and groundwater silcretes at Stuart Creek Opal field, south Australia. J. Sediment. Res. 61.
Triat, J.-M., 1982. Paléoaltérations dans le Crétacé supérieur de Provence Rhodanienne. Memoir. Université Louis Pasteur de Strasbourg, Institut de Géologie.
Walderhaug, O., 2000. Modeling quartz cementation and porosity in middle jurassic Brent Group sandstones of the Kvitebjørn field, Northern North sea. AAPG Bull. 84, 1325–1339. http://dx.doi.org/10.1306/A9673E96-1738-11D7-8645000102C1865.
Watts, N.L., 1987. Theoretical aspects of cap-rock and fault seals for single- and two-phase hydrocarbon columns. Mar. Pet. Geol. 4, 274–307. http://dx.doi.org/10.1016/0264-8172(87)90008-0.
Wibberley, C.A.J., Yielding, G., Toro, G.D., 2008. Recent advances in the understanding of fault zone internal structure: a review. Geol. Soc. Lond. Spec. Publ. 299, 5–33. http://dx.doi.org/10.1144/SP299.2.
Wibberley, C.A.J., Petit, J.-P., Rives, T., 2007. The mechanics of fault distribution and localization in high-porosity sands, Provence, France. Geol. Soc. Lond. Spec. Publ. 289, 19–46. http://dx.doi.org/10.1144/SP289.3.
Williams, R.T., Farver, J.R., Onasch, C.M., Winslow, D.F., 2015. An experimental investigation of the role of microfracture surfaces in controlling quartz

precipitation rate: applications to fault zone diagenesis. J. Struct. Geol. 74, 24–30. http://dx.doi.org/10.1016/j.jsg.2015.02.011.
Worden, R., Morad, S., 2009. Quartz Cementation in Sandstones: Special Publication 29 of the IAS. John Wiley & Sons.
Worden, R., Morad, S., 2000. Quartz cementation in Oilfield sandstones. In: Worden, R.H., Morad, S. (Eds.), Quartz Cementation in Sandstones, Special Publication Number, vol. 29. International Association of Sedimentologists, pp. 01–21.

2.4.2. Supplementary study of the quartz cementation in the cataclastic deformation band clusters

The study of the quartz cementation in cataclastic deformation structures at the site of Bédoin may seem an isolated phenomenon. We provide here a qualitative description of the diagenesis by quartz cementation from our integrated microscopic study at the rest of the six sites.

Our microscopic investigation of the cataclasis led us to check up for the potential presence of cements in the cataclased material of clusters. As explained in detail in the previous section, we performed the cement examination through cold cathodoluminescence (CL) imaging of thin sections from various cluster samples of variable degree of cataclasis. The microstructural analysis of the deformed material allowed distinguishing from the potential pre-deformation cementation of the rock (revealed by the imaging of the host rocks at some sites). The pre-deformation cementation pertaining to the former grains is recognized as it does not seal the clasts (Figure 68). The syn- to post-deformation cements fill the porosity and locally connect a group of clasts together (e.g. Fig. 10 of section 2.4.1).

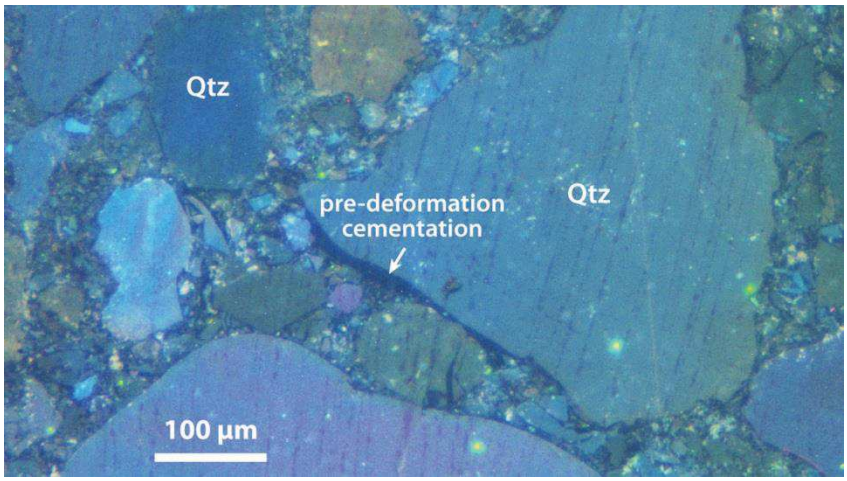

Figure 68. Example of pre-deformation quartz cement coating the edge of a broken grain. The clasts produced by the deformation are wedging themselves against the former cement rim.

We present here the qualitative state of cementation of the cataclastic material at the study sites. Although we did not perform quantitative measurements, a visual observation permits an estimation of the percentage of cement in the rock volume as low as 5% in all the studied materials.

At Boncavaï (burial at deformation comprised between 100 and 300 m; same maximum burial depth), partial cementation is observed sealing the clasts of the deformed material as thin cement rims of up to 20µm in thickness (Figure 69a). This cementation is observed in the most cataclased bands of the cluster, with a degree of cataclasis of about 20%. Previous generations of cementation (pre-deformation) are obvious and revealed by different hues respective to the different chemistry of the quartz cements. The grain contacts in the host rocks of Boncavaï do not show concave-convex geometry that would indicate that pressure-solution occurred.

At St Michel (0 m < burial at deformation < 200 m; maximum burial depth of 500 m), the cements are quite rare but thin rims of quartz cements can be observed in the deformed material either as thin rims of cement (c.a. 10 µm thick) or as rims probably grown from pre-deformation

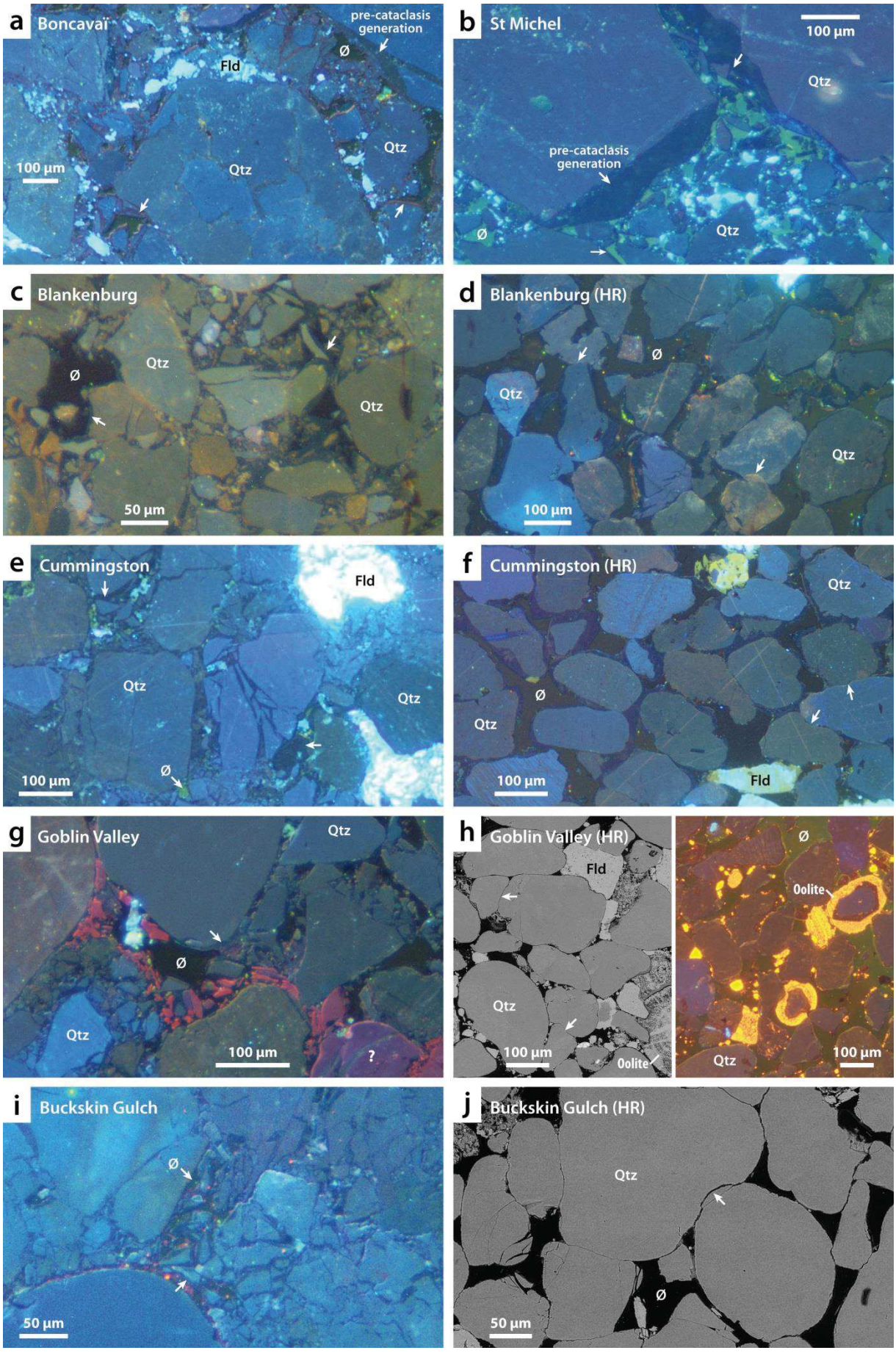
a Boncavaï
pre-cataclasis generation
Ø
Fld
Qtz
Qtz
100 µm
b St Michel
100 µm
Qtz
pre-cataclasis generation
Ø
Qtz
c Blankenburg
Ø
Qtz
Qtz
50 µm
d Blankenburg (HR)
Ø
Qtz
Qtz
100 µm
e Cummingston
Fld
Qtz
Qtz
100 µm
Ø
f Cummingston (HR)
Qtz
Ø
Qtz
100 µm
Fld
g Goblin Valley
Qtz
Ø
Qtz
100 µm
?
h Goblin Valley (HR)
Fld
Qtz
100 µm
Oolite
Ø
Oolite
Qtz
100 µm
i Buckskin Gulch
Ø
50 µm
j Buckskin Gulch (HR)
Qtz
Ø
50 µm

Figure 69. Quartz cementation of the deformed materiel in the cluster at the study sites (in CL). (a) Cataclastic band material at Boncavaï (cataclasis = 20%) impacted by cementation under the form on quartz cement rims of up to 20 µm in thickness and sealing the clasts. (b) Cataclased interband material at St Michel (cataclasis = 28%) impacted by cementation under the form of quartz cement rims of up to 10 µm in thickness and sealing the clasts. As shown by the upper arrow, syn- or post-deformation cements probably nucleated from former pre-cataclastic quartz cements. (c) Interband material at Blankenburg (cataclasis = 13%) impacted by cementation under the form of quartz cement rims of up to 20 µm in thickness and sealing the clasts. (d) Concave-convex grain contacts (arrows) in the host rock sandstone at Blankenburg (in CL). (e) Interband material at Cummingston (cataclasis = 18%) impacted by cementation under the form of quartz cement rims of up to 20 µm in thickness and sealing the clasts. (f) Slightly indented host rock quartz grains (arrows) at Cummingston (in CL). (g) Cataclastic band material at Goblin Valley (cataclasis c.a. 30%) impacted by cementation under the form on quartz cement rims of up to 10 µm in thickness and sealing the clasts. The cements in the cataclastic material of the clusters at Goblin Valley are quite rare. (h-left) At Goblin Valley, concave-convex grain contacts (arrows) are frequent where the fraction of oolites is not too important (in SEM-BSE); (h-right) they are less frequent when the fraction of oolite is important (in CL). (i) Cataclastic band material at Buckskin Gulch (cataclasis c.a. 15%) slightly cemented under the form on quartz cement rims of up to 10 µm in thickness and barely sealing the clasts. The cements in the cataclastic material of the clusters at Buckskin Gulch are quite rare. (j) Concave-convex grain contacts (arrows) in the host rock sandstone at Buckskin Gulch (in SEM-BSE).

coatings (Figure 69b). The quartz cementation is present and seals the clasts in the most cataclased parts of the interbands, corresponding to a degree of cataclasis of 28%, and in the bands (cataclasis > 28%). The contacts between the quartz grains in the host rocks do not show pressure-solution feature.

At Blankenburg (0 m < burial at deformation < 800 m; maximum burial depth of 800 m), quartz cements from 5 to 20 µm thick coat the clasts and seal them (Figure 69c). The quartz cementation is present from the most cataclased parts of the interbands, corresponding to a degree of cataclasis of 13%, and is abundant in the cataclastic material of the bands (cataclasis > 13%). Some quartz grain contacts in the host rock at Blankenburg display small concave-convex geometry suggesting that pressure-solution happened in a pervasive manner in the formation (Figure 69d).

At Cummingston (burial at deformation ca. 500 m, same maximum burial depth), quartz cements are observed as 0 - 20 µm-thick rims around the clasts (Figure 69e). These small thicknesses are sufficient to seal the clasts in most part of the deformed material from a degree of cataclasis of 18%, corresponding to the most deformed interbands, and in all the bands (cataclasis > 18%). Although the indentation is slight, some quartz grain contacts in the host rock display small concave-convex geometry suggesting that pressure-solution might have happened in a pervasive manner in the formation (Figure 69f).

At Goblin Valley (1100 m < burial at deformation < 2000 m; maximum burial depth of 2000 m), quartz cements are rare. However, cementation is frequently observed in the cluster in the most deformed types of bands (mainly the *discrete bands*) with a degree of cataclasis of about 30%. In these cases, the cementation takes the form of up to 10 µm-thick rims often sealing the clasts together (Figure 69g). At Goblin Valley, concave-convex geometry between host rock quartz grains is frequent where the population of oolite is not too important (Figure 69h-left); the contacts are less common and less pronounced in the case of high fraction of oolite (Figure 69h-right). Hence, in general, a pervasive pressure-solution is likely in the sandstones.

At Buckskin Gulch (900 m < burial at deformation < 2600 m; maximum burial depth of 2600 m), quartz cements are scarce and the 10 µm-thick cement rims (Figure 69i) are barely sufficient to effectively seal and hold the clasts together. This cementation is limited to the most cataclased bands

of the cluster attaining a degree of cataclasis of 15 to 30%. Some quartz grain contacts in the host rock display concave-convex geometry indicating that pressure-solution happened in a pervasive manner in the formation (Figure 69j).

At all sites where cementation occurs in the cataclastic material, the host rocks remain uncemented or significantly less cemented that the cataclastic material (cf. Table 1 in section 2.1).

These observations highlights that the cement diagenesis of the cataclastic material of deformation band clusters buried at shallow depths (from 0 to 800 m in the cases of Boncavaï, St Michel, Bédoin, Blankenburg and Cummingston) is frequent where the cataclasis has medium to high degrees (from 13 to 32%). On the contrary, the sites of Goblin Valley and Buckskin Gulch prove that deep burial does not guaranty an effective cementation of the deformed material, for equivalent degrees of cataclasis. Although we lack of argument to justify this, we hypothesize that the sandstone formations at Goblin Valley and Buckskin Gulch may not have been under the water table long enough to allow nourishing fluids to significantly precipitate silica into the cataclastic structures. By the same logic, we do not exclude the idea that existing cements may have been leached by the downward fluid flow of the vadose zone. The observation of frequent cementation in the most cataclased material of clusters at shallow burial is significant since it generalizes the conclusion established at the site of Bédoin, showing that the cementation of clusters is common. Consequently, the porosity and permeability reduction of clusters could be effective at early time of the cluster development via this diagenetic process. This efficiency is even more surprising when we consider that the host rock of some of the shallowest sites did not underwent pervasive pressure-solution. This process is known to release silica content into the solution (e.g. Renard et al., 1997; Gundersen et al., 2002; Molenaar et al., 2007; Gratier et al., 2009). In addition, this cementation provides an enhanced cohesion to the cataclastic material (probably responsible for the competent reliefs of the clusters at the outcrop) and surely participates to the hardening of the bands. Consequently, if cementation occurs synchronous with the band formation (i.e. “self-healing”, as proposed by Ngwenya et al., 2000) or before the formation of the subsequent band, it will be very likely to affect the processes of cluster growth by band addition, as hypothesized in section 2.3.1. We note that the self-healing is induced by thermodynamic reaction boosted by the sudden heat increase of the faulting friction with the synchronous release of high silica content into the fluid. Unless the source of silica supplying the precipitation is remote, the absence of pressure-solution in the sandstone at some of the shallow sites suggests that the self-healing cementation is probable. In the case of our investigation, given the imaging resolution, we find that it is actually very complex to characterize the microstructural relation between the cement and the clasts to such an accurate level to assess the contemporaneity of the deformation and cementation.

2.5. Summary of the field studies

In this chapter, we chose to present the results of a major part of this work, consisting of the field study of several deformed sandstones comprising clusters. We summarize here the main results and their main implications on the structuring of the deformation in sandstones.

In section 2.2, we characterized in sandstone-dominated formations (classical reservoirs for hydrocarbons, water and CO_2 sequestration) the interaction of cataclasis with other mechanical processes. Consistently with previous works, we confirmed that the process of cataclasis is possible when displacement put two porous and clean sandstones in direct contact. We also evidenced at Clashach Cove that the presence of cataclastic structures formed at a burial lower than 400m can favor the subsequent localization of deformation under the form of brecciated faults when the lithology of the formation evolved with significant diagenesis. In a first stage, the reduced permeability of the thin cluster is likely to slightly hamper the fluid flow across the structure. In a second stage, the dilatant behavior of the breccia is likely to transiently enhance along-fault fluid flow. We exposed that the juxtaposition of sandstones with phyllosilicate-bearing silt or clay layers as thin as a few tens of centimeters leads to the end of the cataclastic deformation, and consequently the end of the cluster thickening. The subsequent displacement is then accommodated by a major slip-surface, locally passing at the edge of the displaced clusters and through the smeared layer of silt or clay. Since both clay smearing and the formation of a slip-surface at the edge of the cataclastic structure display low permeabilities, the whole fault is likely to seriously baffle across-fault fluid flow, at least locally, depending on the continuity of the fault in the horizontal and vertical dimensions. The study of these two sites allows answering, at least partially, one major question of this work concerning conditions constraining the development of faults (inception of a major through-going slip surface) in clusters. The example of Clashach Cove indicates that a cluster in porous sandstone can be faulted by the initiation of a fault in an adjacent cohesive (highly cemented) formation and cluster. The example of Goblin Valley reveals that a fault can initiate and propagate from a thin ductile layer in the porous sandstone-dominated formation (e.g. silt/clay layer). These results suggest that the existence of some faulted clusters is due to the propagation of a major through-going slip-surface initiated by a lithological contrast in the sandstone-dominated formation. Nevertheless, these results do not exclude that slip-surfaces could initiate from the coalescence of small patches of sheared deformation bands into in the porous sandstone itself.

In section 2.3, we tried to characterize the dimensions and process of formation of the clusters, performing macro and microstructural analysis of the deformation. The analysis of the cluster dimensions revealed that the Andersonian stress regime under which the sandstone is deformed exerts a strong influence on the morphology of the generated clusters. The complementary analytical study shows that the Andersonian stress regime is indirectly induced by the evolution of the tectonic stress loading, with more probability of deformation under normal stress regime in extensional tectonics, and more probability of deformation under strike-slip and thrust regimes in contractional tectonics. Consistently to this analysis, the clusters formed in extensional tectonics correspond to normal regime structures in the cases of Boncavaï, Cummingston, and Goblin Valley. The clusters formed in contractional tectonics correspond to strike-slip regime structures in the cases of St Michel and Bédoin; they correspond to thrust regime structures in the cases of Blankenburg and Buckskin Gulch. Deformation in extensional tectonics (exclusively in normal regimes in our study) seems to display long clusters, with frequent lengths of

one hundred meter of more. As measured via the band density and the degree of cataclasis, these clusters are rather thin and localize the deformation. They accommodate up to 3 meters of displacement on thickness of 30 cm when they are not faulted and, precisely, often display faults (trough-going slip-surface) accommodating greater displacements. The extensional tectonics also favors dense groups of conjugate sets of clusters in the zone of deformation, where the clusters are more likely to connect to each other. The contractional tectonics seems to favor sparsely distributed clusters for both strike-slip and thrust Andersonian stress regimes. The smallness of the available area or the bias induced by truncation at the two study sites in strike-slip regime may limit our analysis of their lengths. However, these clusters tend to be of medium thickness with a medium constant band density. The clusters at Buckskin Gulch and Blankenburg indicate that thrust regime favor the formation of rather short clusters of a few tens of meters in length at the maximum. These clusters may be of medium thickness, with a medium band density (e.g. Blankenburg) and characterized by important degree of cataclasis, hence suggesting a localization of the deformation (although no clear displacement is identified). They may be thick, with a low band density (e.g. Buckskin Gulch), characterized by a low degree of cataclasis and accommodate small displacements (a few cm to tens of cm for a thickness of 20 cm). These latter thick clusters are rarely reported in the field, as the deformation in thrust regime tends to distribute in the sandstone under the form of simple deformation band arrays. We hypothesize that the difference in morphology of the two studied clusters in thrust regime is associated with different conditions of stress loading in the sense that, at one site the clusters are thought to have formed above a preexisting fault propagating from the basement whereas at the other the clusters seem to have formed isolated from fault in the sandstone formation. On the other hand, the application of the analytical tool to the studied sites suggests that the thinner clusters with the higher band density form when the stress-path hits the sandstone failure envelope towards the left of the brittle part of the envelope. The thickest clusters form towards the cap part of the envelope. In particular, in the case of the two studied clusters formed in thrust regime, the sandstone stress-path at Blankenburg is more likely to have reached the failure on the brittle part or near the summit of the envelope. In the case of Buckskin Gulch, the failure was probably attained on the cap part of the envelope. Therefore, we can also hypothesize than the morphology of the clusters depends on the position at which failure is reached on the failure envelope of the sandstone without relating to the influence of a propagating fault. This hypothesis is consistent with the way the different types of band (as observed individually) distribute along the failure envelope as reported from experimental tests.

In the same section, the microstructural analysis reveals that the clasts undergo roughening and then a slight smoothening with increasing deformation. The roughening of the clasts could induce a potential increase of the internal friction of the deformed material. The clasts are variably packed, with the densest packing observed in the bands, and lesser packing in the interband material. The high packing tends to increase the cohesion of the deformed material. For both band and interband materials, we observe that, for the same degree of cataclasis, the deformed material in the clusters formed in thrust regime displays higher compaction than deformed material formed in the other Andersonian stress regimes. In particular, some interband materials in clusters formed in normal regime have porosity close to the porosity of the host rock. These observations are very interesting as the densely packed and roughened material composing the bands suggests that they are hardened and will not further accommodate the deformation. On the other hand, the interband material of the normal regime clusters suggests potentially dilatant material with lower particle

coordination and consequently lower resistance to the stress loading. Assuming that these conclusions are correct, the cluster growth in normal regime could be explained by the successive formation of new bands at the edge of a former one, consistently explaining why the clusters formed in normal regime display higher band density. Following the same logic, the less contrasting difference in porosity in the band and interband material of the thrust regime clusters would explain why the deformation bands are more distributed, building thick clusters but of low band density. The strike-slip regime clusters would be an intermediate of the normal and thrust regime clusters. We note that the faulting of the clusters formed in extensional tectonics is expected to form quite randomly in the cluster growth, depending on parameters below our measurement capacity (e.g. favorable geometry and texture of the preexisting bands).

In section 2.4, we decided to tackle the topic of the diagenesis in the clusters. Our study of the diagenesis in the clusters at Bédoin revealed that, as evidenced by many authors for cataclastic deformation structures buried at a depth of 1 km of more, the quartz cementation of cataclastic structures is also possible at shallow depth. This process is possible due the numerous amount of fresh quartz surfaces offered by the clasts. Indeed, we showed that the most cataclastic parts of the clusters were prone to enhanced cementation, from partial to complete filling of the residual porosity. The cements sealing the quartz could be nucleated either during the deformation ("self-healing"), and/or through a slow process of precipitation from the pervasive concentration of silica in the nourishing fluid, as suggested by the presence of pressure-solution features. To reject the idea that this cementation of the cataclastic structure in aquifer environment at Bédoin would be an isolated case, we showed for the rest of our study sites that a similar type of cementation is also frequently observed. We thereby evidence that the quartz cementation sealing the clasts in the clusters is frequent at shallow depths, corresponding to burials of 0 to 800 m in this study. Quite intriguingly, the two most buried sites studied in this work (i.e. Goblin Valley and Buckskin Gulch) display the lowest cementation. This deficit in cementation compared to the other sites may be due to the lesser time of residence of the sandstone formation in an aquifer system providing the nourishing fluid necessary to the silica input and precipitation. We finally note that the cementation of the cataclastic structure implies the reduction of porosity and potentially of the permeability of the clusters. Furthermore, the cements, if abundant enough, participate to the hardening of the bands (increased cohesion) and thus certainly alter the mechanical process of growth of the cluster as discussed above.

Chapter III

3. Numerical modeling

In this chapter, we report the results from numerical modeling of formation of deformation bands and band clusters in porous sandstones. Similar modeling for the type of lithology has been conducted previously (e.g. Chemenda et al., 2012; 2014). However, this is the first time the modeling of cluster is undertaken. Our study consists of a parametric analysis aiming at defining the constitutive relations and physical parameters governing the organization of the deformation and leading to the development of clusters. We vary these parameters/functions to approach deformation structures of morphology comparable to the clusters observed in the field, and to relate the influence of these parameters to specific mechanical processes and geometries. In particular, because we observed that the cohesion increases due to both the preverential cementation of the cataclastic material (section 2.4) and the increase of the packing in the cataclastic material (section 2.3), we decided to test the influence of this parameter on the process of band accumulation leading to the formation of a cluster. On the other hand, since we observed that most of the clusters are formed in normal Andersonian regime (section 2.3), we decided to model the initiation of the deformation according to this regime.

1. Method

To model numerically the evolution of deformation of sandstones, a finite-difference, explicit code Flac3D from Itasca is used. We present hereafter the modeling setup, the constitutive model and the criteria guiding the choice of the model parameters. More details on the modeling and theoretical background can be found in (Chemenda et al., 2009, 2012).

3.1.1. Modeling setup

We simulate a single layer in 2D representing a small-cohesion porous sandstone (Figure 70) of length of 1 m and thickness of 0.25 to 0.667 m (ratios of 3:2 and 4:1 are used) and variable resolutions (150*100, 400*100 and 300*200 grid zones). The model width (in the Y-direction) is equal to 1 numerical zone. In order to simulate the initation of the inelastic deformation in normal Andersonian regime condition, the layer is subjected to a fixed horizontal extensional velocity on the X-normal model boundaries and a constant maximum normal stress in the vertical direction, which corresponds to the lithostatic stress. Roller conditions are applied to the Y-normal boundaries, which corresponds to the plane-strain deformation. The layer has elasto-plastic properties. The elastic properties are described by Hook's equations. As reported for typical sandstones (Wong et al., 1997), the Poison's coefficient ν for these materials is fixed to 0.3; the Young's modulus E is fixed to $1x10^4$ MPa. The inelastic deformation of the layer is described by the Drucker–Prager constitutive model with varying both cohesion and dilatancy factor. This model is defined by the yield condition:

$$\bar{\tau} - \alpha\sigma_m - \kappa = 0 \tag{40}$$

and the plastic potential function $\wp$

$$\wp = \bar{\tau} - \beta\sigma_m \tag{41}$$

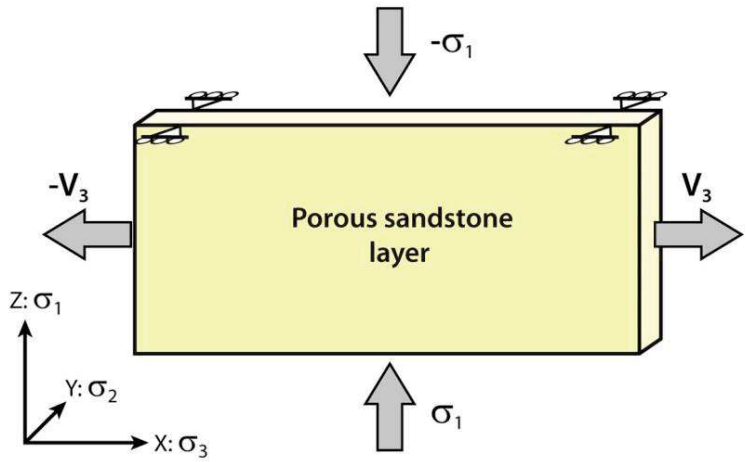

Figure 70. Modeling setup. The width of the model is constant and equals 1 m. The thickness and resolution of the model are varied.

where σ_m is the mean stress (corresponding to P), κ is the cohesion, β is the dilatancy factor and $\overline{\tau}$ is the von Mises stress, expressed as:

$$\overline{\boldsymbol{\tau}} = \sqrt{\boldsymbol{J_2}} = \frac{\mathbf{1}}{\sqrt{\mathbf{6}}}\sqrt{(\boldsymbol{\sigma_1} - \boldsymbol{\sigma_2})^2 + (\boldsymbol{\sigma_2} - \boldsymbol{\sigma_3})^2 + (\boldsymbol{\sigma_3} - \boldsymbol{\sigma_1})^2} \tag{42}$$

The Drucker–Prager model is preferred over the Mohr–Coulomb model, in particular because the latter ignores the intermediate stress σ_2 (Figure 71a), which contradicts the experimental data (e.g. Mogi, 1971; Bardet, 1990; Haimson and Chang, 2000; Colmenares and Zoback, 2002).

It should be noted that the failure/yield envelope in granular materials has a more complex shape than that for Drucker-Prager model. The recent experimental data (Nguyen et al., 2011; Ingraham et al., 2013; Ma and Haimson, 2013) and the following theoretical models (e.g., Chemenda and Mas (2016) show that the yield function depends not only of the first and the second stress tensor invariant, but also on the 3rd invariant that can be presented by the Lode-type parameter N or the Lode angle θ (e.g. Figure 71b and c), related as

$$\boldsymbol{N} = \frac{\mathbf{2}}{\sqrt{\mathbf{3}}}\,\mathbf{cos}\left(\frac{\boldsymbol{2\pi}}{\mathbf{3}} - \boldsymbol{\theta}\right) \tag{43}$$

where

$$\boldsymbol{N} = -\boldsymbol{s_2}/\overline{\boldsymbol{\tau}} \tag{44}$$

and

$$\boldsymbol{s_2} = \boldsymbol{\sigma_2} - \boldsymbol{\sigma_m} \tag{45}$$

θ = 0° ($N = -\frac{1}{\sqrt{3}}$) corresponds to the axisymmetric extension, θ = 30° (N = 0) corresponds to pure shear, and θ = 60° ($N = \frac{1}{\sqrt{3}}$) corresponds to the axisymmetric compression.

Although the Drucker-Prager model used in this study does include the Lode angle, it accounts for all the stresses and represents a reasonable compromise between the complexity of the complete description of the rock properties and the possibility of obtaining useful insights into the rock deformation.

3.1.2. Choice of the parameter values

In this section, we present the different parameters used and tested in the numerical modeling.

The α value (which influences the angle ψ formed between the direction of the maximum principal stress σ_1 and the deformation bands) is varied from 0.6 to 0.8. These values correspond to a failure on the left part of the failure envelope on the Q-P diagram (e.g., experiments of Wong et al., 1997; Baud et al., 2006; El Gonnouni, 2011; Nguyen et al., 2011) (see $\overline{\tau}$ - σ_m - $\bar{\gamma}^p$ diagram in Figure 72, where $\bar{\gamma}^p$ is the inelastic equivalent shear strain).

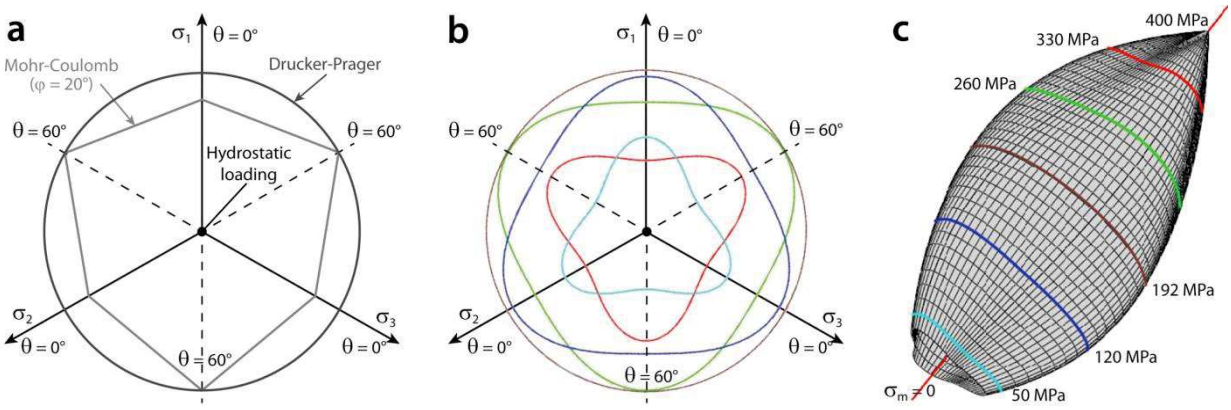

Figure 71. (a) Representation of the Mohr-Coulomb and Drucker-Prager yield/failure criteria in the deviatoric plane. (b) and (c): 3-invariant yield/failure envelope for granular materials(from Chemenda and Mas, 2016).

The relation between ψ, α, β, and N is given by the following formula:

$$\boldsymbol{cos2\psi = \frac{2(1+\nu)(\alpha+\beta+3N)-9N}{3\sqrt{4-3N^2}}} \quad (46)$$

Since we consider failure under normal Andersonian regime (corresponding to the most favorable regime for clustering), the initial vertical stress σ_{v0} = σ_1; σ_2 and σ_3 are horizontal and oriented as shown in Figure 70. Considering the high permeability of the modeled rocks (ranging from $5{\cdot}10^2$ to more than $5{\cdot}10^4$ mD (section 2.3.1)), we use Terzaghi's effective stresses to define the vertical stress as $\sigma_{v0} = (\rho_{sed} Z_{sed} - \rho_w Z_w) g$. In this equation, ρ_{sed} and Z_{sed} are the density and height of the sedimentary column at deformation, ρ_w and Z_w are the density and height of the free water column, and g is the acceleration of gravity (fixed at 9.807 m·s^{-2}). ρ_w is fixed at 1000 kg·m^3, ρ_{sed} and Z_{sed} and Z_w are varied to set a desired σ_{v0}. The values of the initial horizontal stresses σ_{X0}

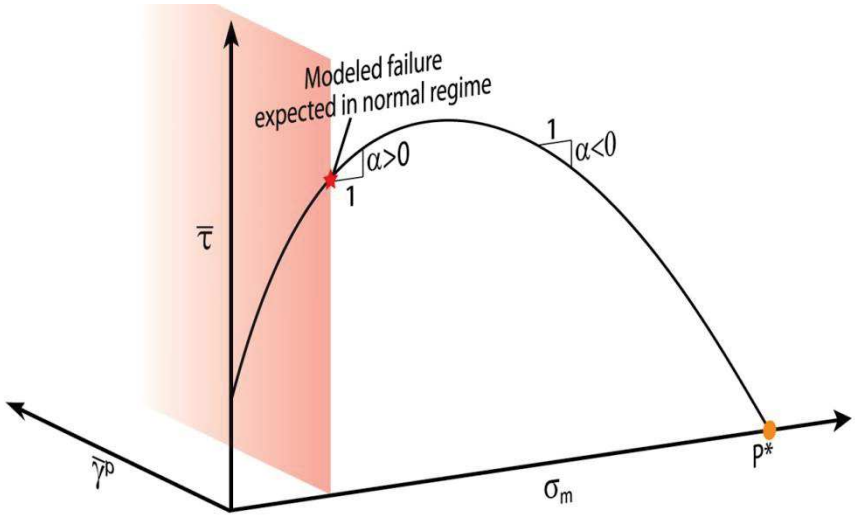

Figure 72. The point on the strength envelope corresponding to the brittle-ductile transition, where clusters form in the experimental tests of the synthetic rock analogue material GRAM1 (e.g. Tran, 2016).

and σ_{Y0} are chosen such that $\sigma_{v0} > \sigma_{X0}$ and σ_{Y0}, with $\sigma_{Y0} = \sigma_2$ and $\sigma_{X0} = \sigma_3$. Even though the constitutive model does not directly account for the influence of the deviatoric stress state (controlled by θ), σ_{X0} and σ_{Y0} were adapted to avoid failure according the Drucker-Prager constitutive model at the initiation of modeling. To satisfy this condition, we set all our tests with an initial Lode angle θ_0 = 21.8, except in one case where θ_0 = 15.6°.

Since the model simulates the evolution of the deformation at constant α and within the narrow σ_m range, the evolution of the cohesion κ with $\bar{\gamma}^p$ will completely define the hardening modulus and function $\bar{\tau}(\bar{\gamma}^p)$. Mas and Chemenda (2015) reported from their analyses of experimental data on artificial (GRAM1) and natural sandstone materials different functions $\bar{\tau}(\bar{\gamma}^p)$ for σ_m in the vicinity of brittle-ductile transition. We up-scale these GRAM1 functions by multiplying them by G_S/G_{Gr} (where G_S and G_{SGr} are the elastic shear modulus of the modeled sandstone and the GRAM1 material, respectively) to keep the normalized hardening modulus h and its evolution in the numerical models of sandstone the same as for GRAM1. Given the definition of h

$$\boldsymbol{h = \frac{1}{G}\left(\frac{\partial \kappa}{\partial \bar{\gamma}^p}\right)_{\sigma_m}} \tag{47}$$

This should insure the same conditions for the deformation localization in the model and GRAM1 experiments.

We will test five functions $\bar{\tau}(\bar{\gamma}^p)$ plotted in Figure 73a.

Function 1 ($\bar{\tau}_1$) is equal zero at $\bar{\gamma}^p$ = 0 and then rapidly grows to form a small bulge summiting at 2.69x10^6 Pa at $\bar{\gamma}^p$ = 0.01. It then decreases slightly down to 2.60·10^6 Pa at $\bar{\gamma}^p$ = 0.02 and then increases again linearly with a slope of α_{sl} =3.85x10^9.

- Function 2 ($\bar{\tau}_2$): $\bar{\tau}2(0)$ = 2.24·10^6 Pa (it then follows the same trend with slope α_{sl} as the $\bar{\tau}_1$-function).
- Function 3 ($\bar{\tau}_3$) is similar to $\bar{\tau}_1$ but with α_{sl} =1.16x10^7.
- Function 4 ($\bar{\tau}_4$) is similar to $\bar{\tau}_1$ but with $\alpha_{sl} = 0$.
- Function 5 ($\bar{\tau}_5$) is similar to $\bar{\tau}_1$ but with α_{sl} =-4.14x10^6.

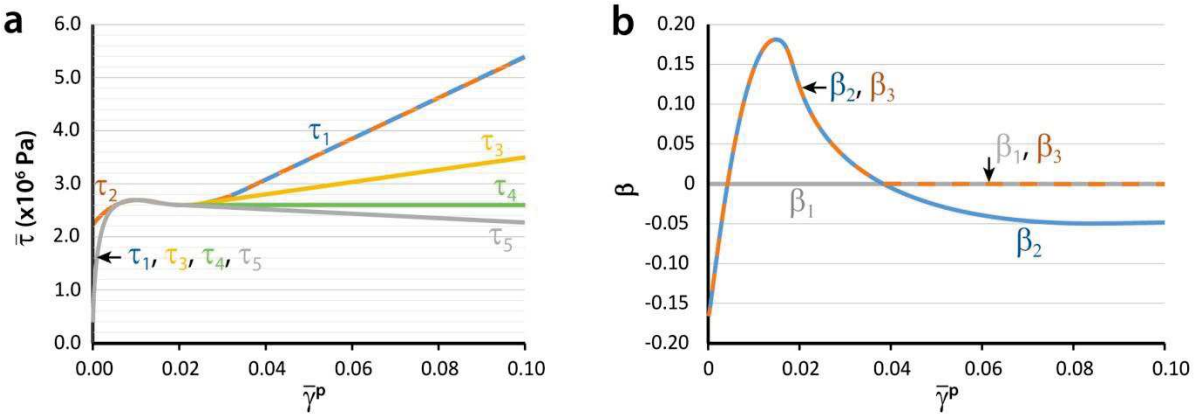

Figure 73. (a) Evolution of the cohesion $\bar{\tau}$ with the inelastic shear strain $\bar{\gamma}^p$,with $\bar{\tau}_1$ corresponding to the brittle-ductile transition obtained from triaxial experiments on granular material analog (Mas and Chemenda, 2015) at σ_m = $\sigma_{m\ brittle-ductile\ transition}$. $\bar{\tau}_4$with the stress plateau (no hardening) corresponds to a lower pressure (mean stress) and $\bar{\tau}_5$, showing strain softening, corresponds to lower pressure and to more brittle deformation regime. (b) Evolution of the dilatancy factor β with $\bar{\gamma}^p$. β_2 corresponds to σ_m = $\sigma_{m\ brittle-ductile\ transition}$ (from Mas and Chemenda, 2015) . Other functions β_i where chosen arbitrarily to test the influence of this parameter on the deformation localization.

Experimental data suggest that at the brittle-ductile transition the dilatancy factor increases and becomes positive before decreasing again to become negative (compaction) with $\bar{\gamma}^p$ (Mas and Chemenda, 2014, 2015). This compactant behavior at high inelastic strain is consistent with the field observations of SECBs where the material porosity is up to 10% (4% on average) lower than in the host rocks (Ballas et al., 2013). According to these observations, we test three functions of β with evolving $\bar{\gamma}^p$ (Figure 73b).

- Function 1 (β_1): dilatancy factor is always zero.
- Function 2 (β_2): $\beta(0)$ = -0.17 (compaction) then it rapidly increases to zero $\bar{\gamma}^p$ = 0.0045, and then becomes positive until a peak at $\bar{\gamma}^p$ = 0.0144. After this peak, the dilatancy decreases again, becoming null at $\bar{\gamma}^p$ = 0.0383, and reaches a minimum value (compactant) at $\bar{\gamma}^p$ = 0.0844. After that, the dilatancy slightly rises unitl becoming null at $\bar{\gamma}^p$ = 0.6.
- Function 3 (β_3): the initial section is the same as β_2 and then equals zero from $\bar{\gamma}^p$ = 0.0383.

3.1.3. Monitored information

During the model runs, we recorded the evolution of several parameters/properties of the rock model with increasing deformation every 5000 steps until 4 000 000 steps. The following properties were recorded:

- The accumulated inelastic shear strain $\bar{\gamma}^p$ (e.g. Figure 74b),
- The dilatancy factor β (e.g. Figure 74c),
- The cohesion κ (e.g. Figure 74d)
- The nominal stress along the X-axis, σ_X as a function of the nominal X-strain (extension) ε_X (e.g. Figure 74e),

The color scale of σ_v, $\bar{\gamma}^p$, β and κ are self-adapting to the minimum and maximum values for each property. Hence, for a given property, the same color at different modeling stages may not represent the same value.

Because we attribute a specific importance to the degree of cataclasis (which is generally regarded as a proxy of the shear, e.g. Ballas et al., 2014) and to the compaction during our field analyses (see section 2.3), we focus on the evolution of $\bar{\gamma}^p$ and β. Besides, a phase of tests before the regular modeling indicated that the deformation is well-imaged through these parameters. The analysis of the cohesion κ evolution is also fundamental to understand the state of hardening of softening of the deformation structures. We present the evolution of the deformation through these parameters in the X-Z section of the model, or as the X-Z section split horizontally in two parts, with different parameters in the upper half and the lower half.

2. Results

3.2.1. Impact of constitutive function $\bar{\tau}(\bar{\gamma}^p)$ on the modeling results

We tested the five functions $\bar{\tau}_1$, $\bar{\tau}_2$, $\bar{\tau}_3$, $\bar{\tau}_4$ and $\bar{\tau}_5$ (Figure 73a) on 3:2 model with numerical size 150*100 grid zones. The other parameters are kept constant and set as summarized in Table 2. We describe here the evolution of the deformation in terms of inelastic shear strain $\bar{\gamma}^p$, dilatancy and

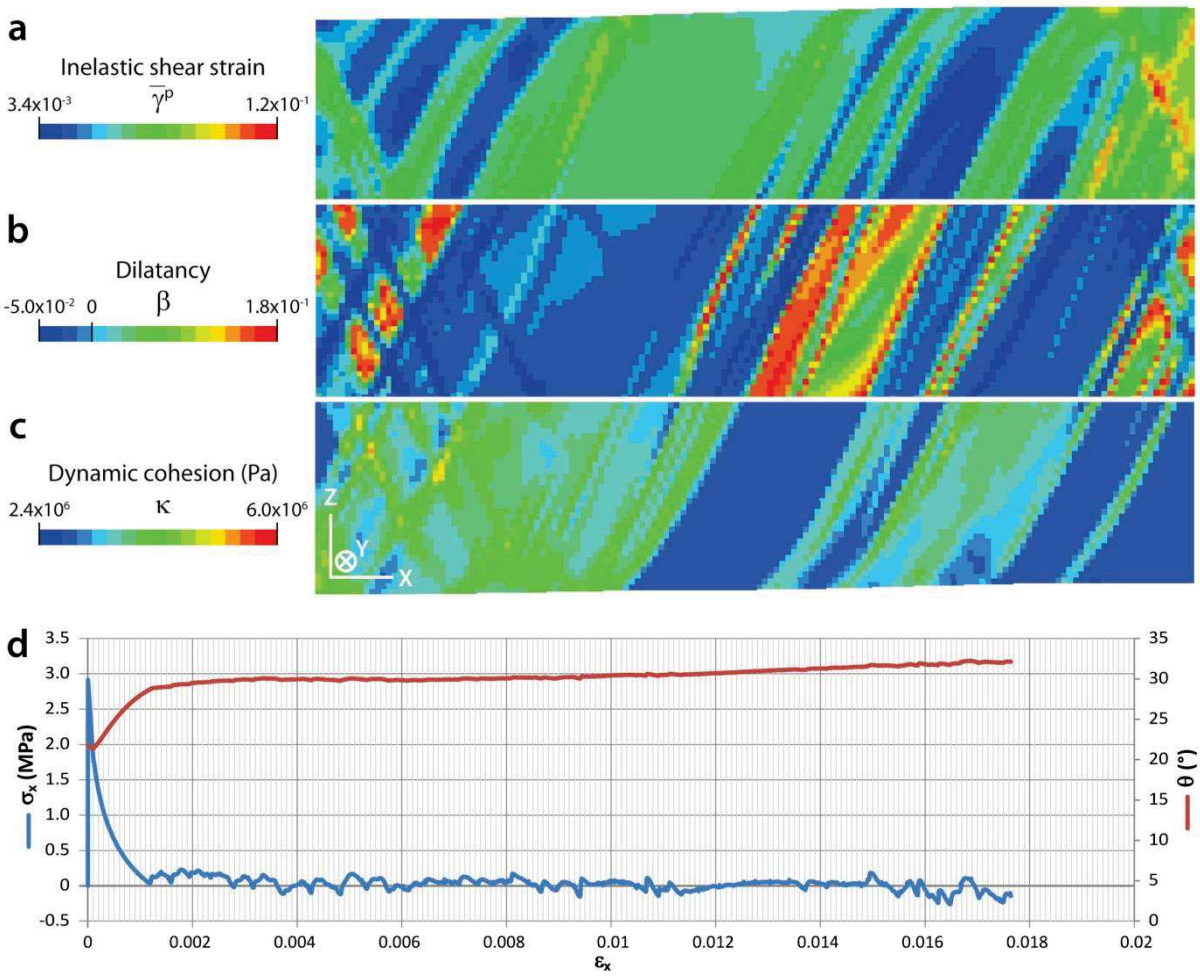

Figure 74. Illustration of the different monitored parameters during the modeling evolution (the image represents a single 3:2 model split vertically in four parts). (a) Inelastic shear strain. (b) Dilatancy. (c) Dynamic cohesion. (d) Axial stress along the X axis as a function of the axial strain. The images (a) through (e) are taken on the same model, at the same deformation stage of the modeling. In our study, we will specifically focus of the behaviors of the elastic shear strain, dilatancy and cohesion.

cohesion κ in the cases of these several scenarios, taking the evolution of σ_X with ε_X as a reference for the different phases of deformation.

Table 2. Parameter settings for the numerical modeling testing the influence of $\bar{\tau}$ $(\bar{\gamma}^p)$ function

Test #	Model Size (m)	Grid resolution	E (Pa)	ν	α	β-function	$\bar{\tau}$-function	$\bar{\tau}_0$ (MPa)	σ_{m0} (MPa)	θ_0 (°)
20	1 *0.667	150*100	$1x10^{10}$	0.3	0.7	β_2	$\bar{\tau}_1$	9.3	5.9	21.8
61	1 *0.667	150*100	$1x10^{10}$	0.3	0.7	β_2	$\bar{\tau}_2$	9.3	5.9	21.8
64	1 *0.667	100*150	$1x10^{10}$	0.3	0.7	β_2	$\bar{\tau}_3$	9.3	5.9	21.8
62	1 *0.667	150*100	$1x10^{10}$	0.3	0.7	β_2	$\bar{\tau}_4$	9.3	5.9	21.8
63	1 *0.667	150*100	$1x10^{10}$	0.3	0.7	β_2	$\bar{\tau}_5$	9.3	5.9	21.8

Case of $\bar{\tau} = \bar{\tau}_1$ (used for the description of the reference test)

In order to set a general frame on the different phases of evolution of deformation during modeling, we describe here the evolution of the $\bar{\tau}_1$-function scenario in terms of $\bar{\gamma}^p$, β and κ. This description of the deformation details the main characteristics of each distinguished *phase* as a function of the axial stress σ_X and axial strain ε_X (extension) for the reference of the evolution of the

deformation (Figure 75a). These *phases* are used as a reference for the comparison of the different tested parameters in the next sections. Obviously, the timing, the values of the observed properties and the morphology of the deformation will vary as functions of the tested parameters.

For the case $\overline{\tau} = \overline{\tau}_1$, the first phase (***phase 1*** – Figure 75b-d) of deformation corresponds to an elastic deformation which continues up to ε_X = 7.5x10^{-5} until failure.

From this stage, the inelastic straining begins (in this case, 0 < $\bar{\gamma}^p$ < 2·10^{-3}) that we refer to as ***phase 2*** (Figure 75e-g). This phase of deformation is quite homogeneous (Figure 75e-j). P*hase 2* lasts until ε_X = 1.05x10^{-3}. At the beginning of this *phase*, the deformation is slightly compactive (in this case, of β evolves from -1.5·10^{-1} to -1.0·10^{-1} - Figure 75f and i). The cohesion κ slightly increases form 1.2x10^6 to 1.8x10^6 Pa (Figure 75g and j). On the $\sigma_X(\varepsilon_X)$ plot (Figure 75a), *phase 2* corresponds to a curved and smooth reduction of the lateral stress σ_X towards small values.

From ε_X = 1.05x10^{-3} a pervasive conjugate sets of distributed incipient deformation bands is formed (***phase 3*** - Figure 75k-m). These bands are formed of a material where the dilatancy is higher than in the surrounding material (difference β of 1.0·10^{-2} in this case - Figure 75l). The cohesion within the incipient bands is about 2.0x10^6 Pa against 2.1x10^6 Pa in the least deformed material. The conjugate sets of incipient bands form an angle ψ of 40.2°. *Phase 3* ends at ε_X = 1.20x10^{-3}. On the $\sigma_X(\varepsilon_X)$ plot (Figure 75a), *phase 3* corresponds to the bottom of the smooth descending curve, where σ_X is nearing zero.

From ε_X = 1.20x10^{-3}, the deformation further localizes in one of the incipient band (***phase 4*** – Figure 75n-p) from the center of the model thickness. Within the band, $\bar{\gamma}^p$ rapidly increases. β within the bands becomes positive and firstly grows from the center of the band (Figure 75o), to a maximum value of 0.18. At the same time, κ increases to the maximum (κ = 2.7x10^6 Pa); the band is therefore hardened. κ is minimum in the least deformed material (2.0x10^6 Pa). Past this stage, the band continues growing (Figure 75q), but β at the center of the band starts decreasing with the increasing inelastic shear and becomes negative (Figure 75r), whereas the maximum of βprogressively shifts towards the edges and tips of the band. κ at the center of the band keeps increasing up to κ = 3.4x10^6 Pa (Figure 75s). We note that ψ decreases from 40.2° (from the conjugate sets of incipient bands) and stabilizes around 23° when the band is mature. The band keeps bending slightly near the top and bottom edge of the model, respective to the former 40.2° ψ angle. After a certain evolution/maturity of the deformation, the band stops growing and a new band takes birth parallel to it, a few centimeters away. The interval of band evolution from the localization of the inelastic shear strain to the inception of a new band lasts until about ε_X = 1.58x10^{-3}. On the $\sigma_X(\varepsilon_X)$ plot (Figure 75a), a phase of band formation corresponds to a slight peak of σ_X with typical amplitudes of 0.1-0.3 MPa and typical widths of 0.2-0.5x10^{-3} along the ε_X axis.

We consider the evolution of the deformation from the occurrence of a second band as the beginning of ***phase 5***. During this phase, the deformation keeps evolving under the form of bands that may develop under the form of conjugate sets, from different position in the model. In this test, conjugate sets of bands develop and distribute in the model (e.g. Figure 75t-v). From ε_X = 6.10x10^{-3}, a band localizes and starts thickening on its left edge. This lateral growth can stop temporarily to the benefit of the formation of another band at a different position in the model, and can then be resu-

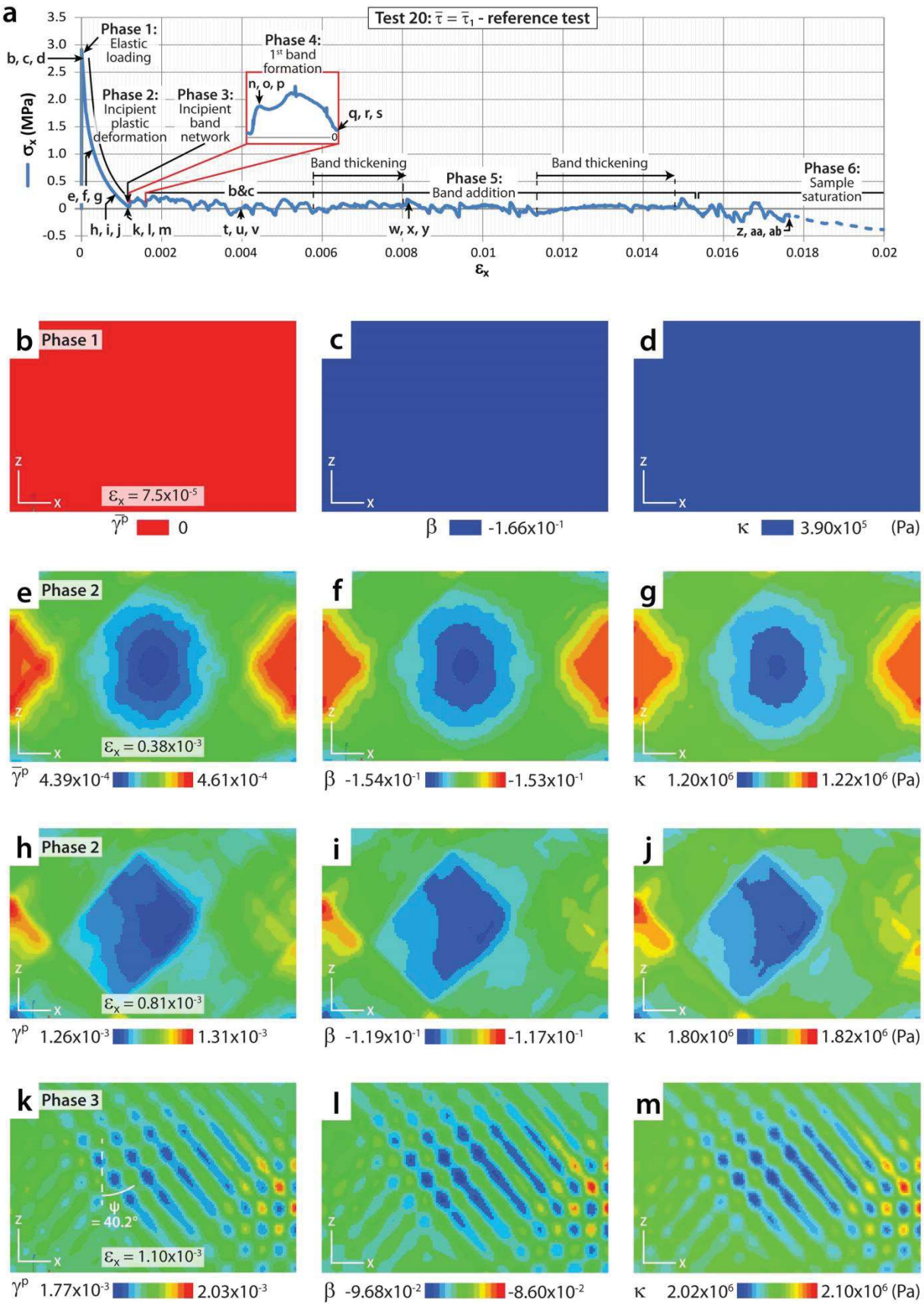
a
Test 20: $\bar{\tau} = \bar{\tau}_1$ - reference test
Phase 1: Elastic loading
Phase 2: Incipient plastic deformation
Phase 3: Incipient band network
Phase 4: 1st band formation
Phase 5: Band addition
Phase 6: Sample saturation
Band thickening
Band thickening
b, c, d
e, f, g
h, i, j
k, l, m
n, o, p
q, r, s
t, u, v
b&c
w, x, y
z, aa, ab
σ_x (MPa)
ε_x
b Phase 1
$\varepsilon_x = 7.5\times10^{-5}$
$\bar{\gamma}^p$ 0
c
β -1.66×10^{-1}
d
κ 3.90×10^{5} (Pa)
e Phase 2
$\varepsilon_x = 0.38\times10^{-3}$
$\bar{\gamma}^p$ 4.39×10^{-4} 4.61×10^{-4}
f
β -1.54×10^{-1} -1.53×10^{-1}
g
κ 1.20×10^{6} 1.22×10^{6} (Pa)
h Phase 2
$\varepsilon_x = 0.81\times10^{-3}$
$\bar{\gamma}^p$ 1.26×10^{-3} 1.31×10^{-3}
i
β -1.19×10^{-1} -1.17×10^{-1}
j
κ 1.80×10^{6} 1.82×10^{6} (Pa)
k Phase 3
$\psi = 40.2°$
$\varepsilon_x = 1.10\times10^{-3}$
$\bar{\gamma}^p$ 1.77×10^{-3} 2.03×10^{-3}
l
β -9.68×10^{-2} -8.60×10^{-2}
m
κ 2.02×10^{6} 2.10×10^{6} (Pa)

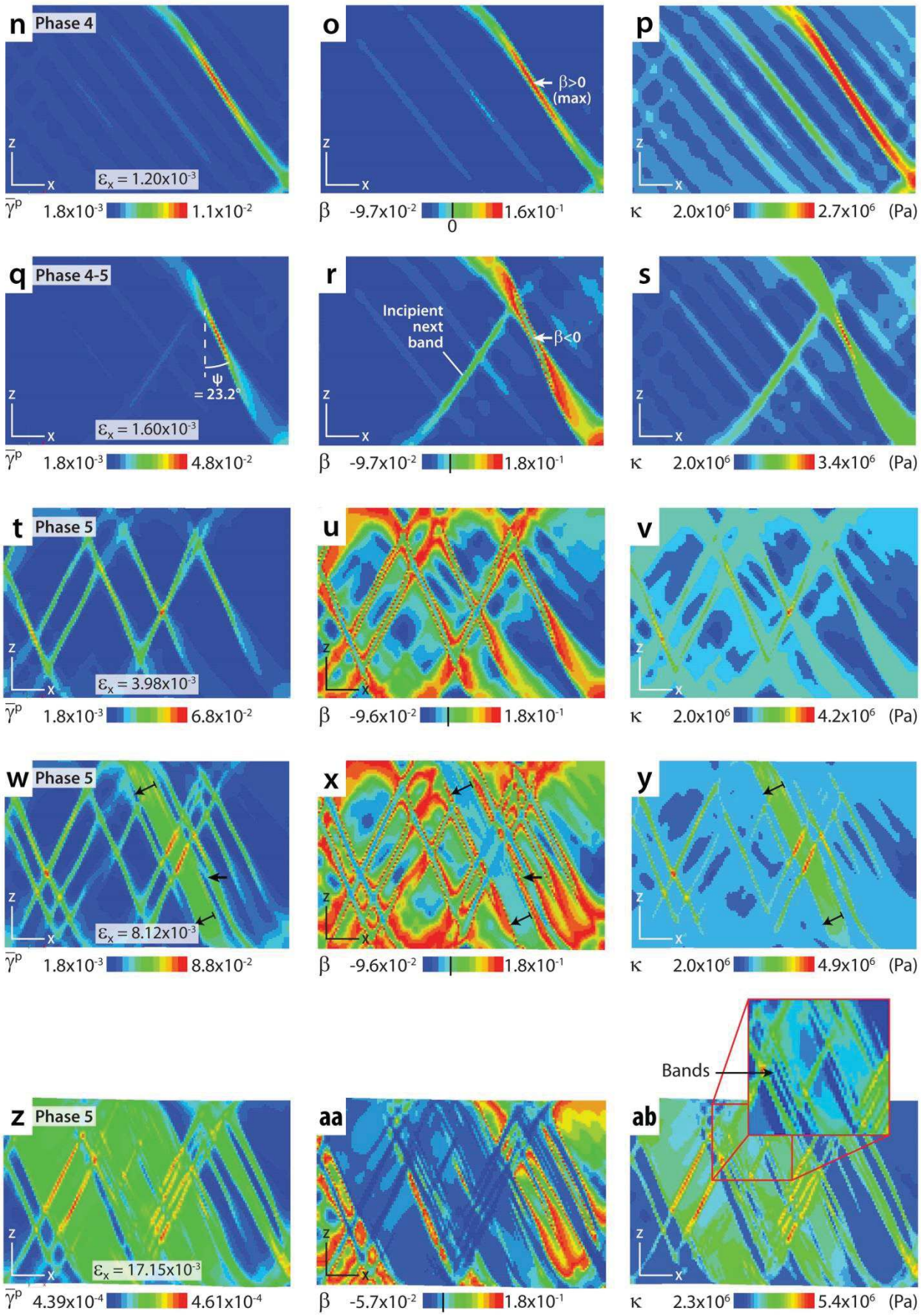
n Phase 4
$\varepsilon_x = 1.20\text{x}10^{-3}$
$\bar{\gamma}^p$ $1.8\text{x}10^{-3}$ $1.1\text{x}10^{-2}$
o
β>0 (max)
β $-9.7\text{x}10^{-2}$ 0 $1.6\text{x}10^{-1}$
p
κ $2.0\text{x}10^{6}$ $2.7\text{x}10^{6}$ (Pa)
q Phase 4-5
ψ = 23.2°
$\varepsilon_x = 1.60\text{x}10^{-3}$
$\bar{\gamma}^p$ $1.8\text{x}10^{-3}$ $4.8\text{x}10^{-2}$
r
Incipient next band
β<0
β $-9.7\text{x}10^{-2}$ $1.8\text{x}10^{-1}$
s
κ $2.0\text{x}10^{6}$ $3.4\text{x}10^{6}$ (Pa)
t Phase 5
$\varepsilon_x = 3.98\text{x}10^{-3}$
$\bar{\gamma}^p$ $1.8\text{x}10^{-3}$ $6.8\text{x}10^{-2}$
u
β $-9.6\text{x}10^{-2}$ $1.8\text{x}10^{-1}$
v
κ $2.0\text{x}10^{6}$ $4.2\text{x}10^{6}$ (Pa)
w Phase 5
$\varepsilon_x = 8.12\text{x}10^{-3}$
$\bar{\gamma}^p$ $1.8\text{x}10^{-3}$ $8.8\text{x}10^{-2}$
x
β $-9.6\text{x}10^{-2}$ $1.8\text{x}10^{-1}$
y
κ $2.0\text{x}10^{6}$ $4.9\text{x}10^{6}$ (Pa)
z Phase 5
$\varepsilon_x = 17.15\text{x}10^{-3}$
$\bar{\gamma}^p$ $4.39\text{x}10^{-4}$ $4.61\text{x}10^{-4}$
aa
β $-5.7\text{x}10^{-2}$ $1.8\text{x}10^{-1}$
ab
Bands
κ $2.3\text{x}10^{6}$ $5.4\text{x}10^{6}$ (Pa)

Figure 75. Illustration of the scenario of deformation modeled with the $\bar{\tau}_1$-function (reference test to be compared with the next tests). (a) Graph of the evolution of the axial stress σ_X and axial strain ε_X for the reference of the evolution of the Inelastic shear strain $\bar{\gamma}^p$. The different phases of deformation recognized are indicated along the σ_X curve. At the different stages of modeling, we represent the inelastic shear strain $\bar{\gamma}^p$ in (b, e, h, k, n, q, t, w and z), the dilatancy β in (c, f, l, l, o, r, u, x and aa), and the cohesion κ in (d, g, j, m, p, s, v, y and ab). (b-d): View of the model during *Phase 1* (ε_X = 0) in the X-Z model plan. (e-g): Model during *Phase 2* (ε_X = 0.38x10^{-3}). (h-j): Model near the end of *Phase 2* (ε_X = 0.81x10^{-3}). The model display $\bar{\gamma}^p$ and β isolines forming an angle ψ of 40° with the maximum vertical stress σ_v. (k-m): Model during *Phase 3* (ε_X = 1.10x10^{-3}). This phase displays pervasive conjugate sets of incipient bands. (n-p): Model during *Phase 4* (ε_X = 1.20x10^{-3}). This phase displays the localization of the first band. (q-s): Model at the end of *Phase 4* (ε_X = 1.60x10^{-3}). During the evolution of the band, we note that β is initially positive at the center of the band and becomes negative in the mature band whereas the maximum β shifts towards the edges and the tips of the band. When the band is mature, ψ is about 30°. (t-v): Model during *Phase 5*, when several bands are distributed (ε_X = 3.98x10^{-3}). (w-y): Model during *Phase 5*, when bands start to thicken (ε_X = 8.12x10^{-3}). The direction of thickening is indicated with stopped arrows. A band linkage occurs between the band at the right of the previously thickened band and the thickened band (regular arrow). We note in (y) that κ is greater in the localized deformation structures and maximum where these structures intercept each other. (z-ab): Model during *Phase 5*, when bands are thickened and clustered (ε_X = 17.15x10^{-3}). We note that, at this stage, the model becomes saturated.

med. In other words, in this case, the deformation develops in the model along one plane at a time. Note that the curve $\sigma_X(\varepsilon_X)$ is somewhat smoothened during band thickening (Figure 75a). At some point (ε_X = 8.10x10^{-3} - Figure 75w-y), a smaller band rooting in the band at the right of the thi-ckened band grows and links up with the thickened band. The thickening of the band eventually stops and other bands from the same set thicken until the end of the modeling, at ε_X = 17.15x10^{-3} - Figure 75z-ab). We note that the band thickening of one of the two sets inhibits the development of the other set such that the two conjugate sets of bands do not overlap each over significantly. During the entire *phase 5*, the central parts of the bands have constant $\bar{\gamma}^p$ values (of 4-6x10^{-2} in this test); the lowest $\bar{\gamma}^p$ are in the least deformed material (with constant values around 1.7-1.8x10^{-3}). The intersection between bands represents the highest $\bar{\gamma}^p$ (with values around 9x10^{-2} in this case). The central parts of the bands remain slightly compactant (-3x10^{-2}< β <0 in this test). The lowest β is still observed in the least deformed material with constant values (of about -0.095 in this test). The highest β is still observed at the edge and at the tip of the bands (with values of about 0.18). The least deformed material has the lowest κ (2.0-2.3x10^6 Pa in this test), the bands display κ values of about 3.5x10^6 Pa, and up to 5.0x10^6 Pa at the intersection of two deformation structures where the most important κ values are observed. On the $\sigma_X(\varepsilon_X)$ plot (Figure 75a), *phase 5* corresponds to a more or less regular oscillations of σ_X along the ε_X axis, with values of σ_X close to zero and possibly negative.

Phase 6 corresponds to the inelastic shear strain saturation of the model with bands, attained when the most part of the model is deformed (not completely attained in the case of this reference example). On the $\sigma_X(\varepsilon_X)$ plot (Figure 75a), *phase 6* seems to be associated with a slight derive of σ_X below zero with increasing ε_X. We will expose this behavior in more details later in this section.

Case of $\bar{\tau} = \bar{\tau}_2$

With function $\bar{\tau}_3$ (Figure 73a) the model evolution is as follows (Test 61 - Figure 76).

Phase 1 lasts in this test until about ε_X = 7.5x10^{-5} *Phase 2* and *phase 3* are very short as $\sigma_X(\varepsilon_X)$ drops abruptly and fall below 0 MPa down to -0.5 MPa around ε_X = 0.30x10^{-3} before recovering positive σ_X values (they are not recorded in the minimum step increment of 5000 steps used in the modeling), Fig. 35a.

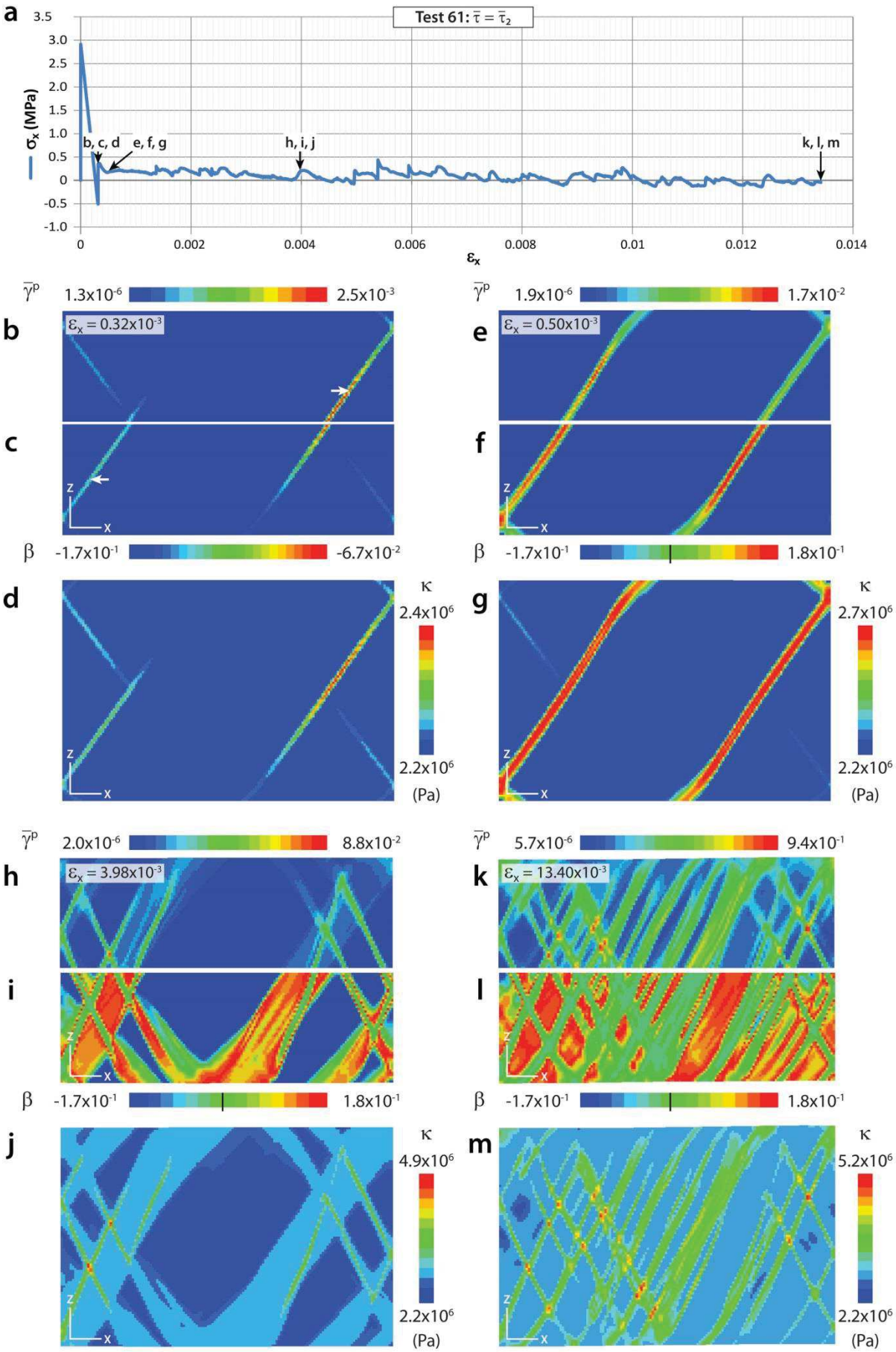
a
Test 61: $\bar{\tau} = \bar{\tau}_2$
σ_x (MPa)
ε_x
b, c, d
e, f, g
h, i, j
k, l, m
$\bar{\gamma}^p$ 1.3x10^{-6} 2.5x10^{-3}
ε_x = 0.32x10^{-3}
$\bar{\gamma}^p$ 1.9x10^{-6} 1.7x10^{-2}
ε_x = 0.50x10^{-3}
β -1.7x10^{-1} -6.7x10^{-2}
β -1.7x10^{-1} 1.8x10^{-1}
κ 2.4x10^6 2.2x10^6 (Pa)
κ 2.7x10^6 2.2x10^6 (Pa)
$\bar{\gamma}^p$ 2.0x10^{-6} 8.8x10^{-2}
ε_x = 3.98x10^{-3}
$\bar{\gamma}^p$ 5.7x10^{-6} 9.4x10^{-1}
ε_x = 13.40x10^{-3}
β -1.7x10^{-1} 1.8x10^{-1}
β -1.7x10^{-1} 1.8x10^{-1}
κ 4.9x10^6 2.2x10^6 (Pa)
κ 5.2x10^6 2.2x10^6 (Pa)

Figure 76. Illustration of the scenario of deformation modeled with the $\bar{\tau}_2$-function. (a) Graph of $\sigma_X(\varepsilon_X)$ for the reference of the evolution of the Inelastic shear strain $\bar{\gamma}^p$. The positions corresponding to the different figures exposed are indicated along the σ_X curve. At the different stages of modeling, we represent the inelastic shear strain $\bar{\gamma}^p$ in (b, e, h and k), the dilatancy β in (c, f, I and l), and the cohesion κ in (d, g, j and m). (b-d): View of the model with distributing bands at ε_X = 0.32x10^{-3}, (*phase 4*), with (b) and (c) representing the model in the X-Z plan cut in two halves. In this case, two first band occur almost simultaneously in the model, at low ε_X. (e-g): Model during the first band thickening at ε_X = 0.50x10^{-3} (*phase 4*). The bands continue to grow simultaneously, which is an exception in the model simulation we performed. (h-j): Model at ε_X = 3.98x10^{-3} (*phase 5*). At similar ε_X evolution, certain zones between the bands display more dilatancy than in the scenario using the $\bar{\tau}_1$-function. (k-m): Model at ε_X = 13.40x10^{-3} (*phase 5*). At that stage, the bands clustered without significant thickening.

Phase 4 starts from ε_X = 0.30x10^{-3}. This phase is special because two bands form and develop almost simultaneously (Figure 76b-g), which is not observed in other models. The tip propagation ofthe band is much faster (quasi instantaneous) and the following thickening of the band is much slower. This observation is coherent if we consider that the cohesion is increased instantaneously when $\bar{\gamma}^p$ starts increasing. In comparison, in the reference test (using $\bar{\tau}$ = $\bar{\tau}_1$), the (fast but) gradual increases of the cohesion allows the growth of shear at the edge of the bands. Thus, in the model using $\bar{\tau}$ = $\bar{\tau}_2$, the cohesion inhibits the thickening of the band whereas the reference test leaves a possibility for band thickening. The development of the two contemporaneous bands stops at about ε_X = 1.80x10^{-3}. The contrast of $\bar{\gamma}^p$ values is larger than the $\bar{\gamma}^p$ values in the reference test during the same phase (1.9x10^{-6}<$\bar{\gamma}^p$<1.7x10^{-2} vs. 1.8x10^{-3}<$\bar{\gamma}^p$<1.2x10^{-2}, respectively). The contrast of β values is also greater than in reference test (-1.7x10^{-1}<β<1.8x10^{-1} vs. -9.7x10^{-2}<β<1.7x10^{-1}, respectively). The ranges of κ value is similar to the values of the reference test during the same phase, with κ ranging from 2.0x10^6 Pa in the least deformed material to 2.7x10^6 Pa at the center of the band.

During *phase 5* (from about ε_X = 1.37x10^{-3}), we note via the evolutions of $\bar{\gamma}^p$ and β that the deformation keeps localizing under the form of conjugate sets of distributed bands, readily cross-cutting each other. Contrary to the scenario using $\bar{\tau}$ = $\bar{\tau}_1$, these bands do not thicken significantly (e.g. Figure 76h-j). At the same ε_X = 3.98x10^{-3}, the maximum values of $\bar{\gamma}^p$ and β in the bands have approximately the same value as in the reference test ($\bar{\gamma}^p$ c.a. 6.8-8.8x10^{-2} and β c.a. 1.8x10^{-1}). However, the model using $\bar{\tau}$ = $\bar{\tau}_2$ generates lower $\bar{\gamma}^p$ and β values (more compaction) in the least deformed material than in the reference test ($\bar{\gamma}^p$ c.a. 2.0x10^{-6} vs. 1.8x10^{-3} and β c.a. -1.7x10^{-1} vs. -9.6x10^{-2}, respectively). At the last stage of deformation recorded (ε_X = 13.40x10^{-3}), we remark that the bands are well-clustered (Figure 76k through m), but no thick localized deformation exists linked to direct band thickening. In this scenario, the bands are more frayed, have individually more variable thickness and are more interconnect than in the reference test. The range of κ value is similar to the reference test during the same phase, with κ ranging from 2.0x10^6 Pa in the least deformed material to about 5.0x10^6 Pa at band intersections.

Case of $\bar{\tau}$ = $\bar{\tau}_3$

With function $\bar{\tau}_3$ (Figure 73a) the model evolution is as follows (Figure 77).

Phase 1 lasts until about ε_X = 7.5x10^{-5}. *Phase 2* (inception of the inelastic deformation) lasts until ε_X = 1.05x10^{-3} and follows the same evolution as *phase 2* of the reference test, with similar value and amplitude of $\bar{\gamma}^p$, β and κ. *Phase 3* starts around ε_X = 1.05x10^{-3} and ends around ε_X = 1.20x10^{-3}. Again, *Phase 3* of test 64 follows the same evolution as *phase 3* of the reference test, with similar value and amplitude of $\bar{\gamma}^p$, β and κ.

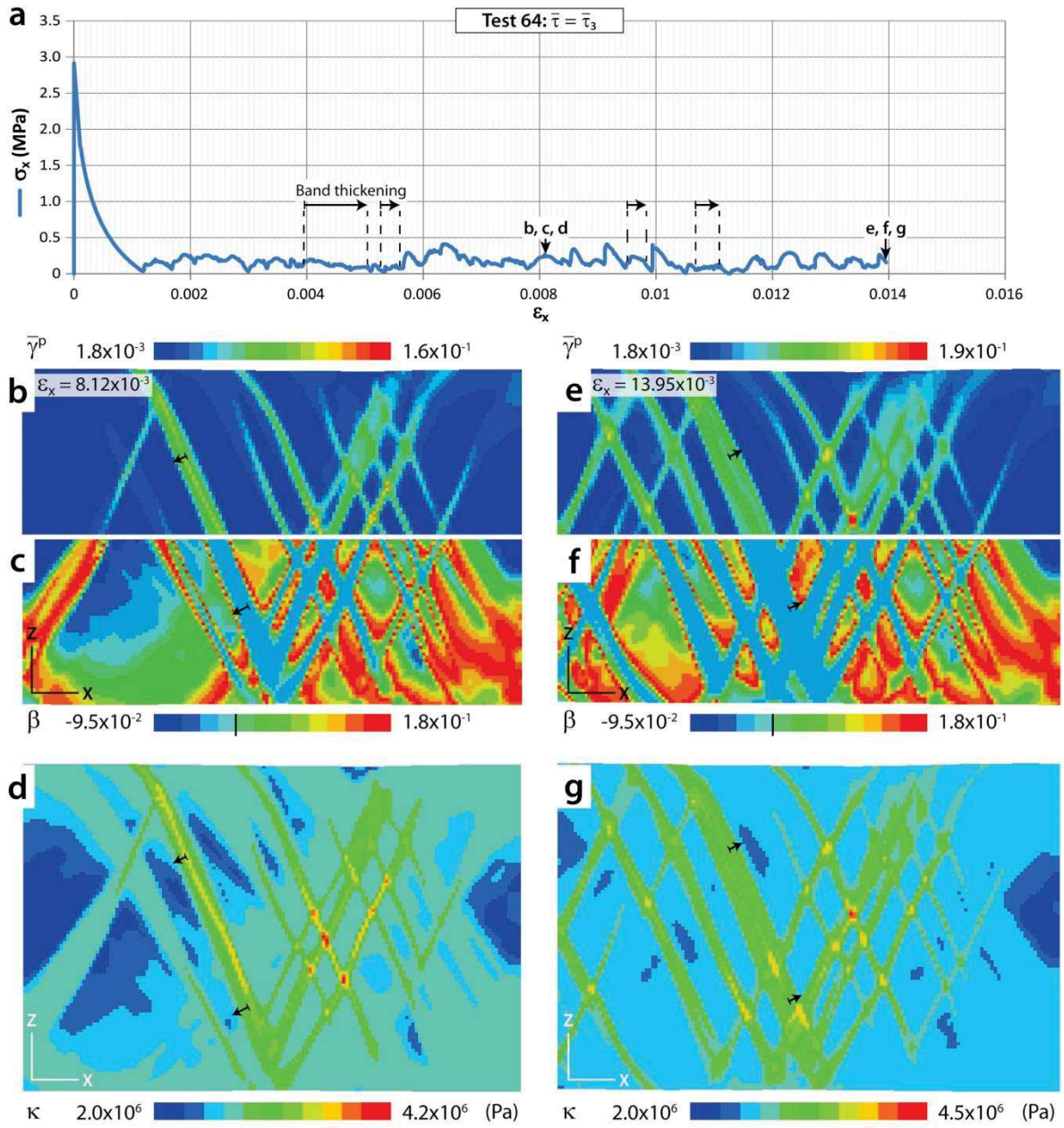

Figure 77. Illustration of the scenario of deformation modeled with the $\bar{\tau}_3$-function. (a) Graph of $\sigma_X(\varepsilon_X)$ for the reference of the evolution of the Inelastic shear strain $\bar{\gamma}^p$. The positions corresponding to the different figures exposed are indicated along the σ_X curve. At the different stages of modeling, we represent the inelastic shear strain $\bar{\gamma}^p$ in (b and e), the dilatancy β in (c and f), and the cohesion κ in (d and g). (b-d): View of the model with distributing bands at ε_X = 8.12x10^{-3}, (*phase 5*), with (b) and (c) representing the model in the X-Z plan cut in two halves. The direction of thickening, which is limited, is indicated with arrows. (e-g): Model at the end of modeling (at ε_X = 13.95x10^{-3}, *phase 5*). No real thickened structure nor band cluster appear.

The inception of the first band (*phase 4*) takes place at ε_X = 1.20x10^{-3}; the end of formation of this first band and the inception of the next one takes place at ε_X = 1.58x10^{-3}. Despite a slightly different timing, the localization of the first band of this test follows the same evolution as *phase 4* of the reference test, with similar values and evolution of $\bar{\gamma}^p$ and β. The minimum value of κ is similar to the value of the reference test during the same phase; the maximum value (at the center of the band), however, displays a slightly lower value (κ = 3.0x106 Pa vs. 3.4x106 Pa in the reference test).

During *phase 5* (from ε_X = 1.58x10^{-3}), we note via the evolutions of $\bar{\gamma}^p$, β and κ that the deformation keeps localizing under the form of conjugate sets of distributed bands, readily cross-cutting each other. Some of the bands thicken slightly, but clearly not as much as in the case $\bar{\tau} = \bar{\tau}_1$. The evolution of the deformation follows the same trend as the reference test, except that the thickening of the bands is very limited (Figure 77b through d). Only one band undergoes significant thickening; the process is divided in several stages (Figure 77a) and thickens successively from both edges. At the same ε_X = 8.12x10^{-3}, $\bar{\gamma}^p$ in this test displays similar minimum value than the reference model 1.8x10^{-3} in the least deformed material, however the maximum value (at the band intersection) is greater than in the reference test ($\bar{\gamma}^p$ = 1.6x10^{-1} vs. 8.8x10^{-2}, respectively). β displays similar ranges of values in the different deformation structures composing the model than during the *phase 5* of the reference model in the same structures. κ displays a similar minimum value than in the reference model (κ = 2.0x10^6 Pa), but has a slightly lower maximum values than in the reference test (κ = 4.2x10^6 vs. 4.9x10^6 Pa, respectively). σ_X remains positive during the whole test.

Case of $\bar{\tau}$ = $\bar{\tau}_4$

With function $\bar{\tau}_4$ (Figure 73a) the model evolution is as follows (Test 62 - Figure 78).

Phase 1 lasts until about ε_X = 7.5x10^{-5}. *Phase 2* lasts until ε_X = 1.05x10^{-3} and follows the same evolution as *phase 2* of the reference test, with similar $\bar{\gamma}^p$ and β. *Phase 3* starts at ε_X = 1.05x10^{-3} and ends around ε_X = 1.20x10^{-3}. *Phase 3* follows the same evolution as *phase 3* of the reference test, with similar values of $\bar{\gamma}^p$, β and κ.

The inception of the first band (*phase 4*) occurs at ε_X = 1.20x10^{-3}; the end of evolution of this band and the inception of the next one occur at ε_X = 1.75x10^{-3}. At the end of the evolution of the first band, $\bar{\gamma}^p$ in the least deformed material has similar minimum values as in the reference test (i.e. $\bar{\gamma}^p$ = 1.8x10^{-2}), but the maximum value at the center of the band is higher, with $\bar{\gamma}^p$ = 6.1x10^{-2} (vs. 4.8x10^{-2} in the reference test). β has the same range of values as the reference test. κ has similar minimum value as the reference test (κ = 2.0x10^6 Pa), but its maximum value is lower (i.e. 2.7x10^6 Pa vs. 3.4x10^6 Pa, respectively).

During *phase 5* (from ε_X = 1.75x10^{-3}), the deformation is only little distributed (e.g. Figure 78 b and c). At the same ε_X = 3.98x10^{-3}, $\bar{\gamma}^p$ in this test displays similar minimum value as the reference model (1.8x10^{-3}); its upper end member is higher than the one of the reference test (2.3x10^{-1} vs. 6.8x10^{-3}, respectively). β displays similar minimum and maximum values as the reference model (-9.6x10^{-2} and 1.8x10^{-1}). κ displays a similar minimum value (in the least deformed material) than in the reference model (κ = 2.0x10^6 Pa), but shows a lower maximum value than in the reference test (κ = 2.7x10^6 vs. 4.2x10^6 Pa, respectively). The maximum value of κ no more corresponds to the center of the band, but its edges. One can see that the deformation eventually localizes in a single thin band (Figure 78 e through g), where $\bar{\gamma}^p$ is maximum. As a consequence of the localization of the inelastic shear strain, the former bands progressively become invisible because the contrast of $\bar{\gamma}^p$ becomes too important. Consistently with the imposed behavior of dilatancy, we remark that the dilatancy at the center of the band localizing the deformation re-increases slightly where $\bar{\gamma}^p$ is the most important and tends toward zero. Because the deformation localizes in a single band, we record at the end of modeling a small ε_X of 6.16x10^{-3}. We note that $\sigma_X(\varepsilon_X)$ always remains positive in this scenario and slightly increases during all *phase 5*.

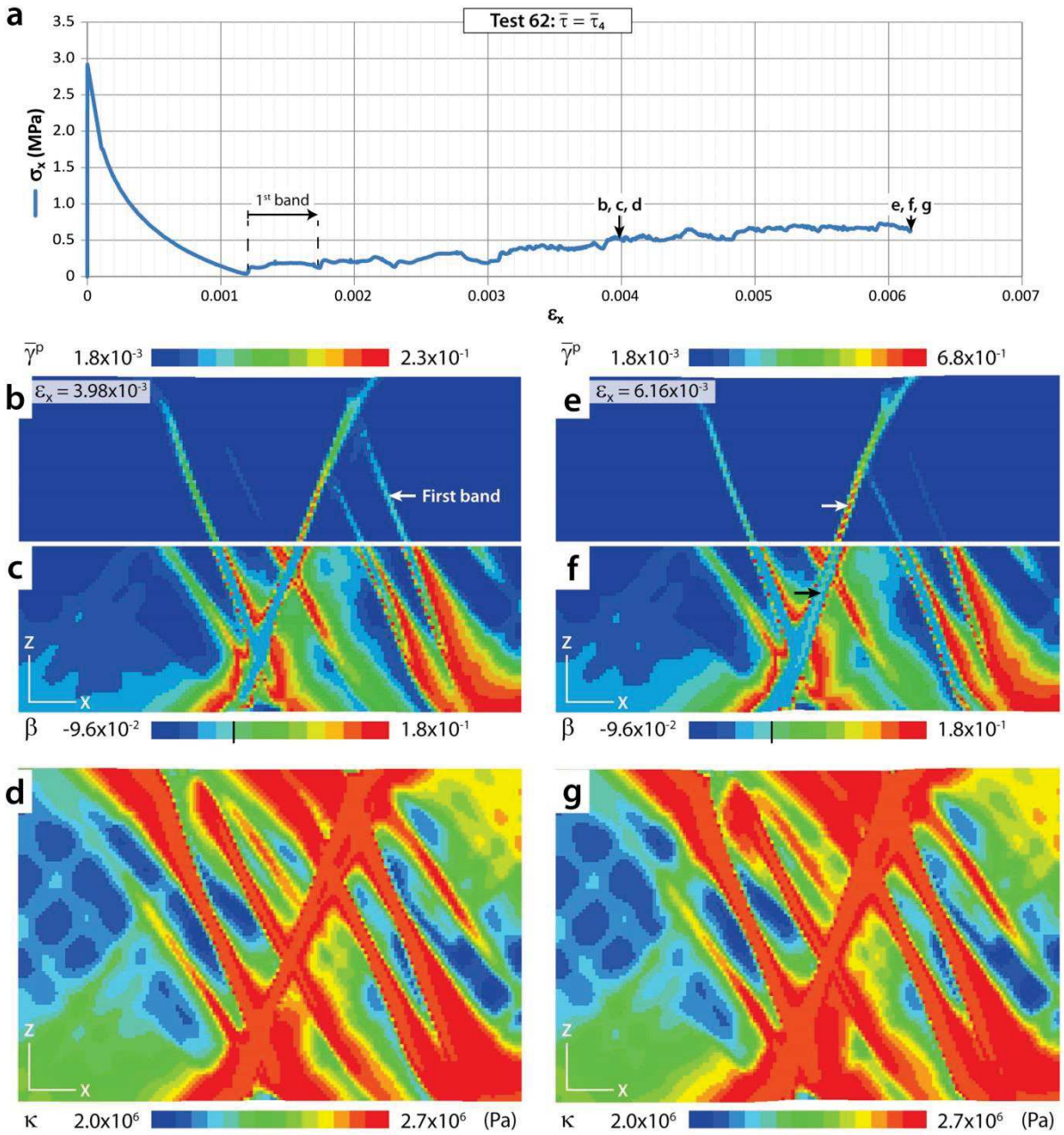

Figure 78. Illustration of the scenario of deformation modeled with the $\bar{\tau}_4$-function. (a) Graph of $\sigma_X(\varepsilon_X)$ for the reference of the evolution of the Inelastic shear strain $\bar{\gamma}^p$. The positions corresponding to the different figures exposed are indicated along the σ_X curve. At the different stages of modeling, we represent the inelastic shear strain $\bar{\gamma}^p$ in (b and e), the dilatancy β in (c and f), and the cohesion κ in (d and g). (b-d): View of the model with distributing bands at ε_X = 3.98x10^{-3}, (*phase 5*), with (b) and (c) representing the model in the X-Z plan cut in two halves. (e-g): Model at the end of modeling (at ε_X = 6.16x10^{-3}, *phase 5*). The inelastic shear strain $\bar{\gamma}^p$ almost exclusively locates in one band (arrows) so that the distribution of the deformation in the model eventually stops (no thickening and no clustering).

Case of $\bar{\tau} = \bar{\tau}_5$

With function $\bar{\tau}_5$ (Figure 73a) the model evolution is as follows (test 63 - Figure 79).

Phase 1 lasts until about ε_X = 7.5x10^{-5}. *Phase 2* lasts until ε_X = 1.05x10^{-3} and follows the same evolution as *phase 2* in the reference test, with similar values of $\bar{\gamma}^p$, β and κ. *Phase 3* starts at ε_X =

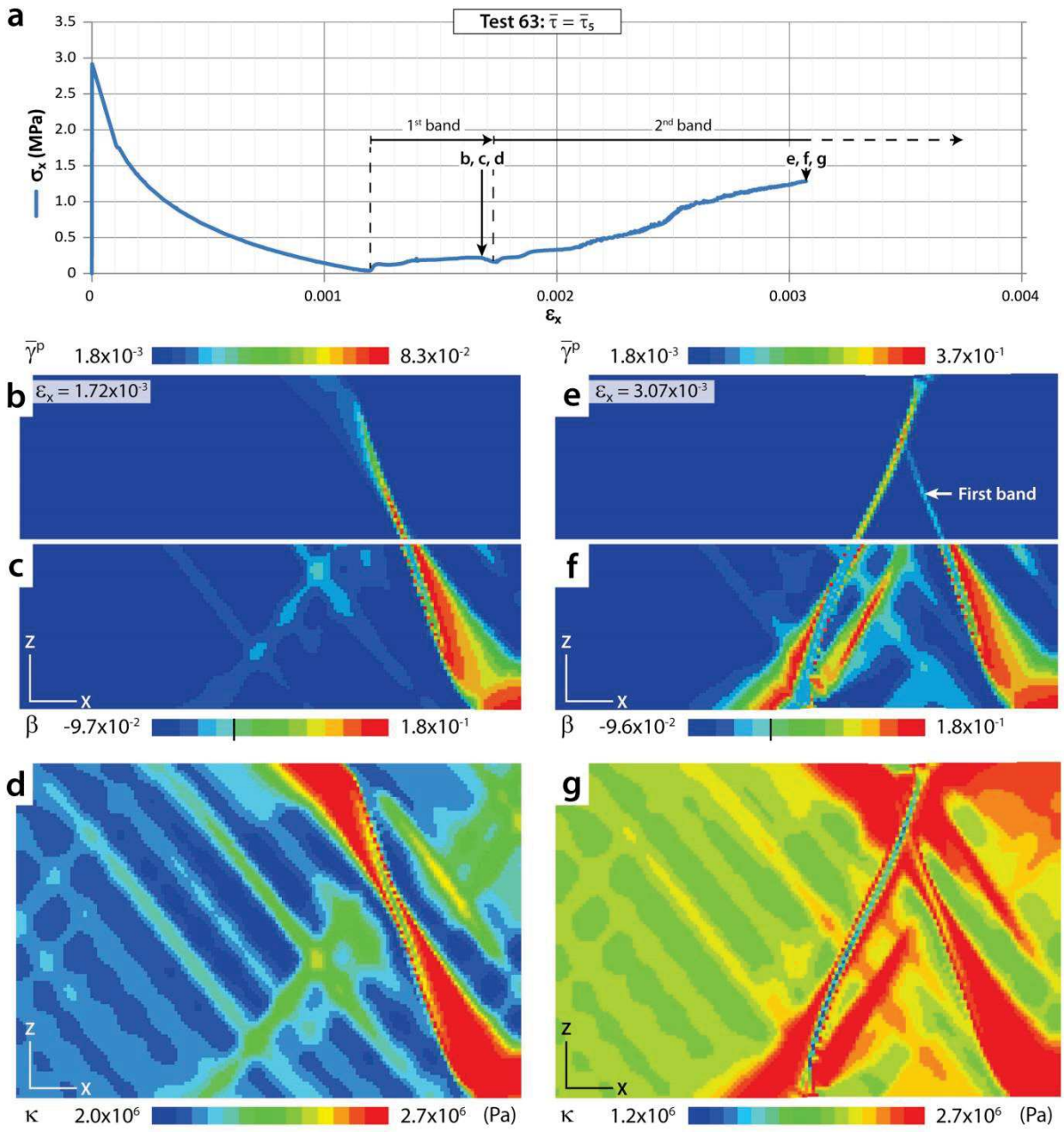

Figure 79. Illustration of the scenario of deformation modeled with the $\bar{\tau}_5$-function. (a) Graph of $\sigma_X(\varepsilon_X)$ for the reference of the evolution of the Inelastic shear strain $\bar{\gamma}^p$. The positions corresponding to the different figures exposed are indicated along the σ_X curve. At the different stages of modeling, we represent the inelastic shear strain $\bar{\gamma}^p$ in (b and e), the dilatancy β in (c and f), and the cohesion κ in (d and g). (b-d): View of the model at the end of formation of the first band at ε_X = 1.72x10^{-3}, (*phase 4*), with (b) and (c) representing the model in the X-Z plan cut in two halves. (e-g): Model at the end of modeling (at ε_X = 3.07x10^{-3}, *phase 5*). The inelastic shear strain $\bar{\gamma}^p$ almost exclusively locates in one band; the distribution of the deformation in the model is stopped (no thickening and no clustering).

1.05x10^{-3} and ends around ε_X = 1.20x10^{-3}. *Phase 3* follows the same evolution as *phase 3* of the reference test, with similar values of $\bar{\gamma}^p$, β and κ.

The inception of the first band (*phase 4*) occurs at ε_X = 1.20x10^{-3}; the end of evolution of this first band and the inception of the next one occur at ε_X = 1.72x10^{-3}, which is almost identical to the $\bar{\tau}_4$-function scenario. At the end of evolution of the first band (Figure 79b through d), $\bar{\gamma}^p$ in the least deformed material has similar minimum value as in the reference test (i.e. $\bar{\gamma}^p$ = 1.8x10^{-2}), but the

maximum value at the center of the band is higher, with $\bar{\gamma}^p$ = 8.3x10^{-2} (vs. 4.8x10^{-2} in the reference test). β displays similar minimum and maximum values as in the reference test during the same phase. κ displays a similar minimum value (in the least deformed material) as in the reference model (κ = 2.0x10^6 Pa), but shows a lower maximum value than in the reference test (κ = 2.7x10^6 vs. 3.4x10^6 Pa, respectively). As $\bar{\gamma}^p$ increases in the band, the cohesion starts increasing and attains a maximum of 2.7x10^6 Pa at the center of the band. It then decreases from the center of the band while it is still slightly increasing towards the edges and the tips (Figure 79d).

During *phase 5* (from ε_X = 1.72x10^{-3}), the deformation localizes in a second thin band (Figure 79e through e) and does not get further distributed with increasing ε_X. This second band becomes dominant and accommodates the entire shear strain as the cohesion decreases with increasing $\bar{\gamma}^p$ (softening). $\bar{\gamma}^p$ is maximum in the band and significantly higher than the maximum value attained in the reference model (up to 3.7x10^{-1} at the end of modeling vs. 9.1x10^{-2} in the reference model where the bands intersect). The minimum value of $\bar{\gamma}^p$ in the least deformed material remains similar as in the reference test during the same phase. Similarly to the $\bar{\tau}_4$-function scenario, the dilatancy at the center of the band localizing the deformation re-increases slightly where $\bar{\gamma}^p$ is the most important and tends toward zero. As $\bar{\gamma}^p$ keeps increasing almost exclusively at the center of the dominant band, the cohesion eventually becomes minimum along a very thin zone (Figure 79g). We record a maximum ε_X of 6.16x10^{-3} during this test where κ at the center of the band reaches a minimum of 1.2x10^6 Pa. We note that $\sigma_X(\varepsilon_X)$ always remains positive and increases during all *phase 5*; its slope is steeper than in the $\bar{\tau}_4$-function scenario.

Summary

This study of the impact of the evolution of the cohesions (and hence of $\bar{\tau}$) with $\bar{\gamma}^p$ on the model evolution shows that the most expressed band clusters form for $\bar{\tau} = \bar{\tau}_1$, which corresponds to the brittle-ductile transition in the GRAM1 tests, where band clusters were obtained experimentally.

Contrary to the scenario using $\bar{\tau}_1$, with $\bar{\tau}_2$, the beginning of the localization of bands will be extremely rapid when the stress loading will be applied. However, the thickening of a band and the evolution of the network of deformation bands will evolve slowly, with a fairly well distributed deformation under the form of cross-cutting conjugate sets of frayed deformation bands.

Relative to the scenario using $\bar{\tau}_1$, the scenario with $\bar{\tau}_3$, where this slope is lower (but positive), displays less band thickening and less hardening. The scenario with $\bar{\tau}_4$ (constant $\bar{\tau}$) displays deformation localized in very few bands and the deformation finally localizes in a single band with no hardening. This effect of localization is even more dramatic in the scenario with $\bar{\tau}_5$ (negative slope) because most of the deformation stops distributing after the occurrence of the second band where it indefinitely localizes due to important softening.

We think that the use of the $\bar{\tau}_1$ implying an important hardening simulates well the structures observed in the field in normal regime, both in terms of geometry and hardening (competent structures at the outcrop). Hence, we choose to select this function to test the other parameters in the next models.

3.2.2. Influence of the evolution of β with $\bar{\gamma}^p$ on the deformation banding

We test the three functions $\beta(\bar{\gamma}^p)$, β_1, β_2 and β_3, on 3:2 models of resolution 400*100 grid zones, keeping the rest of the parameters set constant as summarized in Table 3.

Table 3. Parameter settings for the numerical modeling testing the influence of $\beta(\bar{\gamma}^p)$ function.

Test #	Model Size (m)	Grid resolution	E (Pa)	ν	α	β-function	$\bar{\tau}$-function	$\bar{\tau}_0$ (MPa)	σ_{m0} (MPa)	θ_0 (°)
65	1 *0.667	150*100	$1x10^{10}$	0.3	0.7	β_1	$\bar{\tau}_1$	9.3	5.9	21.8
20	1 *0.667	150*100	$1x10^{10}$	0.3	0.7	β_2	$\bar{\tau}_1$	9.3	5.9	21.8
66	1 *0.667	100*150	$1x10^{10}$	0.3	0.7	β_3	$\bar{\tau}_1$	9.3	5.9	21.8

Case of $\beta = \beta_1$

In this case, the dilatancy facto is zero at all $\bar{\gamma}^p$ (Figure 73b). We tested this hypothesis to evaluate the influence of the dilatancy on the organization of the deformation. The model evolution is as follows (test 65 - Figure 80a.

Phase 1 lasts until about ε_X = 7.5x10^{-5}. *Phase 2* (inception of the inelastic deformation) lasts until ε_X = 1.05x10^{-3} and follows the same evolution as *phase 2* of the reference test, with similar values of $\bar{\gamma}^p$ and κ. *Phase 3* starts at ε_X = 1.05x10^{-3} and ends around ε_X = 1.20x10^{-3}. *Phase 3* follows the same evolution as *phase 3* of the reference test, with similar values of $\bar{\gamma}^p$ and κ (we remind the reader that β remains uniformly null).

Phase 4 starts from ε_X = 1.20x10^{-3} (Figure 80b, c) and never ends according the definition we proposed because the thickening of the created band is almost continuous alternatively on both edged during the whole test (Figure 80d and e). We can consider that *phase 4* ends at 3.00x10^{-3} when a distinct band localizes separated from the first thickened band. During this interval, the minimum value of $\bar{\gamma}^p$, which is constant, and the maximum value are both higher than in the reference test (2.5x10^{-3} vs. 1.8x10^{-3} and 8.0x10^{-2} vs. 4.8x10^{-2}, respectively). The minimum value of κ, which is constant, and maximum value are both higher than in the reference test (2.7x10^6 vs. 2.0x10^6 and 4.6x10^6 vs. 3.4x10^6, respectively).

During *phase 5*, the first band keeps thickening (Figure 80f and g). The thickening sometimes interrupts and a band from a minor conjugate set is formed without significant thickening. At the same ε_X = 8.12x10^{-3}, $\bar{\gamma}^p$ displays higher minimum and maximum values than in the reference model (2.5x10^{-3} vs. 1.8x10^{-3} and 9.6x10^{-2} vs. 8.8x10^{-2}, respectively). κ displays slightly higher minimum and maximum values than in the reference model (2.2x10^6 Pa vs. 2.0x10^6 Pa and 5.3x10^6 vs. 4.9x10^6 Pa, respectively). At the end of modeling (ε_X = 13.40x10^{-3}), the accumulated deformation forms a very thick band that resembles the structure formed at the end of the reference test. The narrow tabular zones aligned with the orientation of the band in $\bar{\gamma}^p$ or κ almost suggest the morphology of a deformation band cluster, such as observed in the field.

Case of $\beta = \beta_2$

The case of the β = β_2 (Figure 73b) corresponds to the reference test (test 20) previously described with $\bar{\tau}$ = $\bar{\tau}_1$.

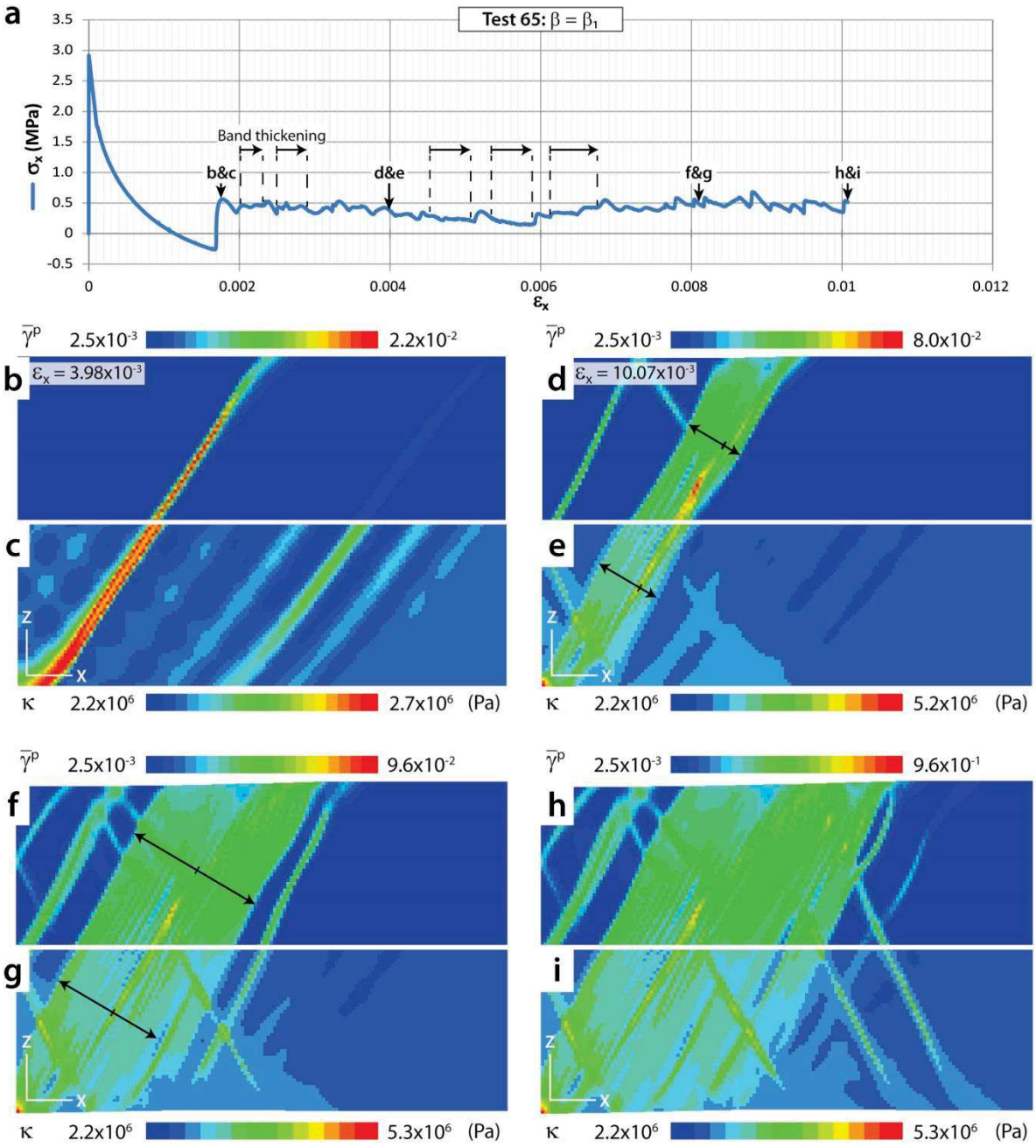

Figure 80. Illustration of the scenario of deformation modeled with the β_1-function. (a) Graph of $\sigma_X(\varepsilon_X)$ for the reference of the evolution of the Inelastic shear strain $\overline{\gamma}^p$. The positions corresponding to the different figures exposed are indicated along the σ_X curve. At the different stages of modeling, we represent the inelastic shear strain $\overline{\gamma}^p$ in (b and d), the dilatancy β in (c and e). (b-c): View of the model during the localization of the first band at ε_X = 1.75x10^{-3}, (*phase 4*) in the X-Z model plan cut in two halves. (d-e): Model during the first band thickening at ε_X = 3.98x10^{-3} (*phase 5*). The band continues to thicken alternatingly from both edges. (f-g): Model at ε_X = 8.12x10^{-3} (*phase 5*). (h-i): Model at ε_X = 10.07x10^{-3} (*phase 5*). At that stage, the bands are thickened and appear as clustered.

Case of $\beta = \beta_3$

With function β_3 (Figure 73b) the model evolution is as follows (Test 66 - Figure 81a).

Phase 1 lasts until about ε_X = 7.5x10^{-5}. *Phase 2* (inception of the inelastic deformation) lasts until ε_X = 1.05x10^{-3} and follows the same evolution as *phase 2* of the reference test, with similar va-

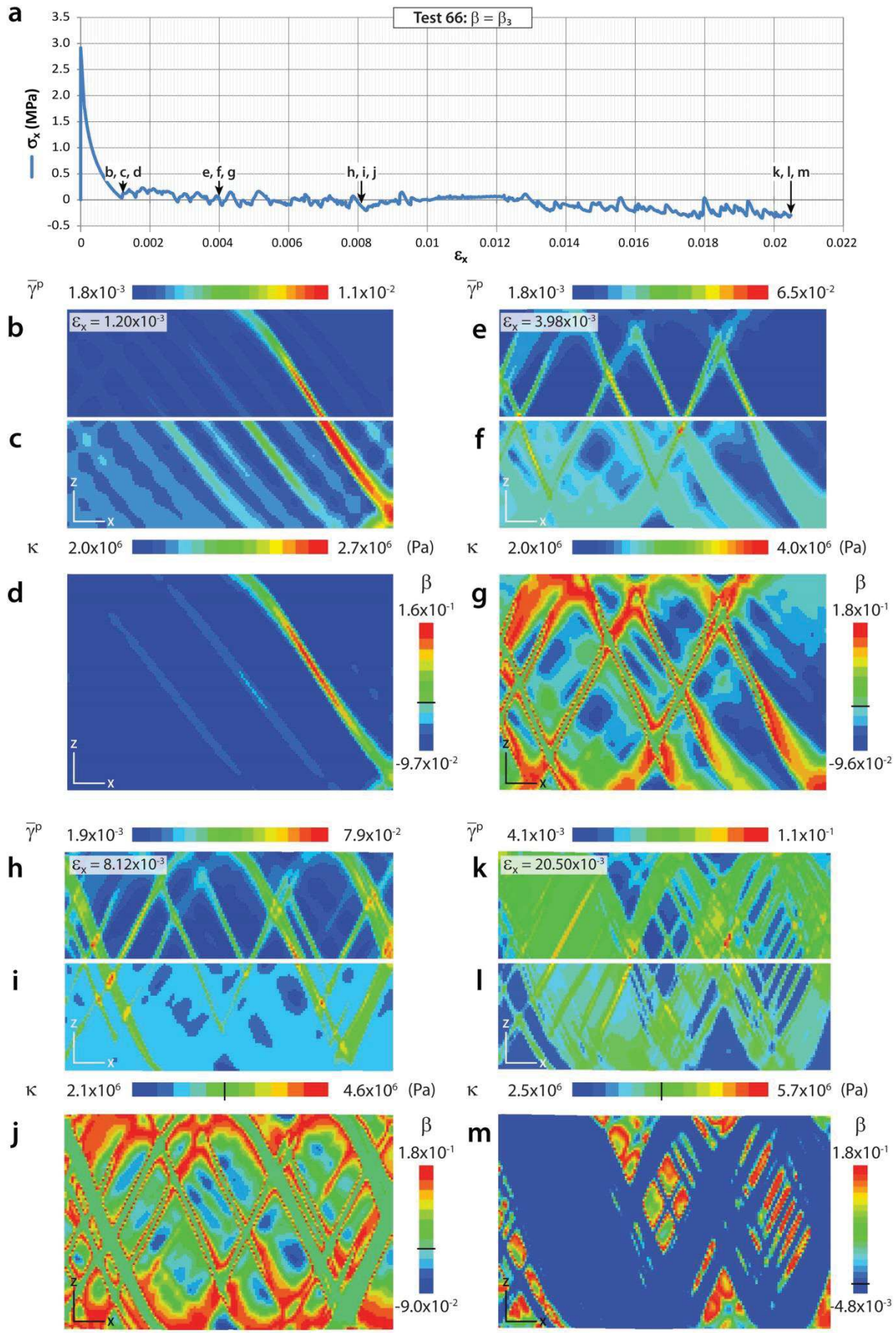
a
Test 66: β = β3
σx (MPa)
εx
b, c, d
e, f, g
h, i, j
k, l, m
γ̄p 1.8x10-3 1.1x10-2
b
εx = 1.20x10-3
c
κ 2.0x10^6 2.7x10^6 (Pa)
d
β 1.6x10-1 -9.7x10-2
γ̄p 1.8x10-3 6.5x10-2
e
εx = 3.98x10-3
f
κ 2.0x10^6 4.0x10^6 (Pa)
g
β 1.8x10-1 -9.6x10-2
γ̄p 1.9x10-3 7.9x10-2
h
εx = 8.12x10-3
i
κ 2.1x10^6 4.6x10^6 (Pa)
j
β 1.8x10-1 -9.0x10-2
γ̄p 4.1x10-3 1.1x10-1
k
εx = 20.50x10-3
l
κ 2.5x10^6 5.7x10^6 (Pa)
m
β 1.8x10-1 -4.8x10-3

Figure 81. Illustration of the scenario of deformation modeled with the β_3-function. (a) Graph of $\sigma_X(\varepsilon_X)$ for the reference of the evolution of the Inelastic shear strain $\bar{\gamma}^p$. The positions corresponding to the different figures exposed are indicated along the σ_X curve. At the different stages of modeling, we represent the inelastic shear strain $\bar{\gamma}^p$ in (b, e, h and k), the cohesion κ in (c, f, I and l), and the dilatancy β in (d, g, j and m). (b-d): View of the model at the beginning of formation of the first band at ε_X = 1.20x10^{-3}, (*phase 4*), with (b) and (c) representing the model in the X-Z plan cut in two halves. (e-g): Model at ε_X = 3.98x10^{-3} (*phase 5*). (h-j): Model at ε_X = 8.12x10^{-3} (*phase 5*). (k-m): Model at the end of modeling (at ε_X = 20.50x10^{-3}, *phase 5*).

lues of $\bar{\gamma}^p$ and κ. *Phase 3* starts at ε_X = 1.05x10^{-3} and ends around ε_X = 1.20x10^{-3}. *Phase 3* follows the same evolution as *phase 3* of the reference test, with similar values of $\bar{\gamma}^p$, κ and β.

Phase 4 occurs at ε_X = 1.20x10^{-3} (Figure 81b-d); the end of evolution of the first band and the inception of the next one occurs at ε_X = 1.58x10^{-3}. From the occurrence of the first deformation band, the $\bar{\gamma}^p$ and κ patterns are similar to those in the reference test (Figure 81e-m).

During *phase 5* (from ε_X = 1.58x10^{-3}), the evolution of β changes. β starts increasing when the deformation localizes as a band (Figure 81d) and subsequently decreases down to 0 in the center of the bands (where $\bar{\gamma}^p$ is maximum) and remains at this level with increasing deformation (Figure 81g, j and m). The maximum β is shifted towards the edges and the tips of the bands. As a consequence, the dilatancy in the most deformed zones of the never become compactive. We record at the end of modeling only a small ε_X of 29.70x10^{-3} (Figure 81k-m).

Summary

For β_1, the deformation tends not to be distributed. It evolves from the thickening of the same band, with similar ranges of $\bar{\gamma}^p$ and κ values in the band(s) as in the reference test. The result consists of a thick dominant band whose morphology could be compared to a cluster. For β_2 (reference test), the deformation is distributed, the bands thicken until becoming adjacent, eventually forming a cluster, with similar ranges of $\bar{\gamma}^p$ and κ values within the band(s). For β_3, the evolution and morphology of the deformation as well as the ranges of $\bar{\gamma}^p$ and κ values are the same as in for β_2. The only difference is observed in the band, where the minimum β is zero.

Our microstructural analysis of deformation bands in clusters revealed a compaction of the deformed material compared to the weakly-deformed host rock, confirming the previous results of Ballas et al. (2013). Therefore, we believe that β_2 is the most suitable to describe the evolution of the dilatancy with increasing deformation in the next part of the modeling analysis.

3.2.3. Influence of the internal friction coefficient

We tested the influence of the internal friction coefficient α on the deformation, by taking values of α near the initial one of 0.7. We tested α = 0.6, which represents failure on the right–hand side of the initially chosen failure envelope (**Erreur ! Source du renvoi introuvable.**), and α = 0.8, which represents failure on the left–hand side of the initially chosen failure envelope. The values of 0.6 and 0.8 of α corresponds to the expected condition of failure in normal stress regime. Tests are performed on 3:2 models of resolution 400*100 cells; the other parameters are constant as summarized in in Table 4.

Table 4. Parameter settings for the numerical modeling testing the influence of the internal friction coefficient α.

Test #	Model Size (m)	Grid resolution	E (Pa)	ν	α	β-function	$\bar{\tau}$-function	$\bar{\tau}_0$ (MPa)	σ_{m0} (MPa)	θ_0 (°)
68	1 *0.667	150*100	$1x10^{10}$	0.3	**0.6**	β_1	$\bar{\tau}_1$	9.3	5.9	21.8
20	1 *0.667	150*100	$1x10^{10}$	0.3	**0.7**	β_1	$\bar{\tau}_1$	9.3	5.9	21.8
69	1 *0.667	100*150	$1x10^{10}$	0.3	**0.8**	β_1	$\bar{\tau}_1$	9.3	5.9	21.8

Case of α = 0.6

With α = 0.6, the model evolution is as follows (Test 68 - Figure 82).

Phase 1 lasts until a step number lower than the minimum step increment of 5000 (ε_X = $6x10^{-6}$). *Phase 2* (inception of the inelastic deformation) lasts until ε_X = $2.00x10^{-3}$ and follows the same evolution as *phase 2* of the reference test, with similar evolution of $\bar{\gamma}^p$, β and κ. *Phase 3* starts at ε_X = $2.00x10^{-3}$ and stops around ε_X = $2.40x10^{-3}$. *Phase 3* follows the same evolution than *phase 3* of the reference test, with value of $\bar{\gamma}^p$ almost twice as high as the reference test. κ and β values are slightly higher than in the reference test.

The first band forms around ε_X = $2.40x10^{-3}$ (Figure 82b-d); the end of the evolution of this band and the inception of the next one takes place at ε_X = $3.10x10^{-3}$. The evolution of $\bar{\gamma}^p$, κ and β is similar as in the reference test. The band makes a higher angle with the vertical than in the reference test (c.a. 29° vs. c.a. 23°, respectively) (Figure 82b-d). At the end of *phase 4*, $\bar{\gamma}^p$ has a higher minimum value than in the reference test ($3.5x10^{-3}$ vs. $1.8x10^{-3}$, respectively); its maximum value is similar to the one of the reference test at the end of the same phase (i.e. $5.1x10^{-2}$ vs. $4.8x10^{-2}$, respectively). κ has similar minimum and maximum values as in the reference test (2.4-2.0$x10^6$ and 3.4-3.5$x10^6$, respectively). β displays a higher minimum value than in the reference test (-$2.8x10^{-2}$ vs. -$9.7x10^{-2}$, respectively); its maximum value is similar to the one of the reference test at the end of the same phase (i.e. $1.8x10^{-1}$).

During *phase 5* (from ε_X = $3.10x10^{-3}$), we observe the progressive thickening of a few bands of a dominant conjugate set (Figure 82e-g). The bands quickly connect to each other until saturation of the model (Figure 82k-m). The modeling stops at ε_X = $29.70x10^{-3}$ (Figure 82k-m). At the same ε_X = $8.12x10^{-3}$, $\bar{\gamma}^p$ in this test displays higher minimum value than the reference model ($6.8x10^{-3}$ vs. $1.8x10^{-3}$, respectively); its maximum value is lower than the one of the reference test ($6.0x10^{-2}$ vs. $8.8x10^{-2}$, respectively). β has a higher minimum value than in the reference test (-$3.9x10^{-2}$ and -$9.6x10^{-2}$); its maximum value is similar as in reference model (i.e. $1.8x10^{-1}$). κ displays a higher minimum value than in the reference model ($2.5x10^6$ Pa vs. $2.0x10^6$ Pa), its maximum value is lower than in the reference test ($2.5x10^6$ vs. $4.9x10^6$ Pa, respectively).

Case of α = 0.7

The case of the scenario with α = 0.7 (Figure 73b) corresponds to the reference test (test 20) previously described with the $\bar{\tau}$ = $\bar{\tau}$1.

Case of α = 0.8

With α = 0.8, the model evolution is as follows (Test 69 - Figure 83).

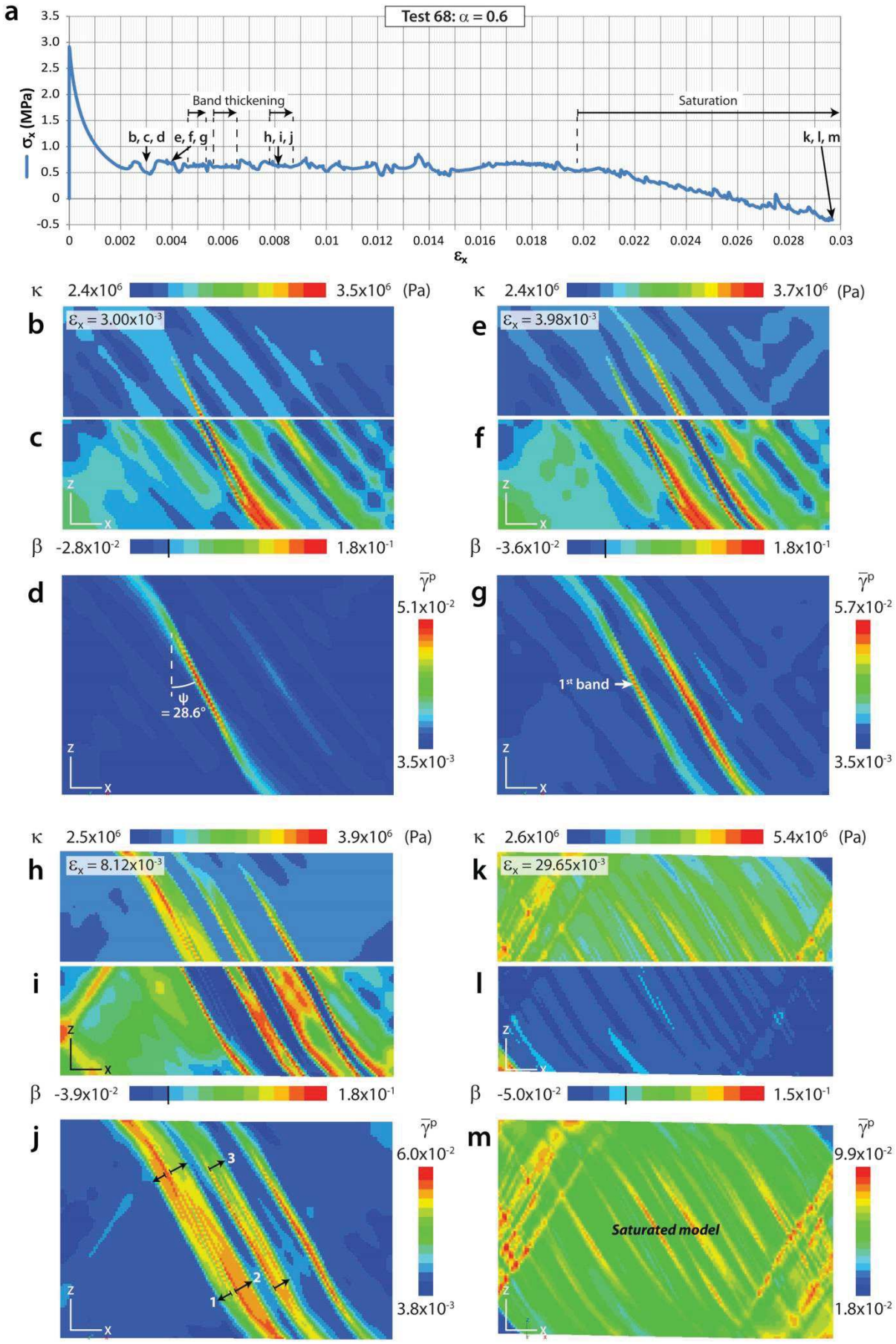
a
Test 68: α = 0.6
σx (MPa)
εx
Band thickening
Saturation
b, c, d
e, f, g
h, i, j
k, l, m
κ 2.4x10^6 3.5x10^6 (Pa)
b
εx = 3.00x10^-3
c
β -2.8x10^-2 1.8x10^-1
d
ψ = 28.6°
γ̄p 5.1x10^-2 3.5x10^-3
κ 2.4x10^6 3.7x10^6 (Pa)
e
εx = 3.98x10^-3
f
β -3.6x10^-2 1.8x10^-1
g
1st band
γ̄p 5.7x10^-2 3.5x10^-3
κ 2.5x10^6 3.9x10^6 (Pa)
h
εx = 8.12x10^-3
i
β -3.9x10^-2 1.8x10^-1
j
1
2
3
γ̄p 6.0x10^-2 3.8x10^-3
κ 2.6x10^6 5.4x10^6 (Pa)
k
εx = 29.65x10^-3
l
β -5.0x10^-2 1.5x10^-1
m
Saturated model
γ̄p 9.9x10^-2 1.8x10^-2

Figure 82. Illustration of the scenario of deformation modeled with the internal friction coefficient α fixed to 0.6. (a) Graph of $\sigma_X(\varepsilon_X)$ for the reference of the evolution of the Inelastic shear strain $\bar{\gamma}^p$. The positions corresponding to the different figures exposed are indicated along the σ_X curve. At the different stages of modeling, we represent the cohesion κ in (b, e, h and k), the dilatancy β in (c, f, I and l), and the inelastic shear strain $\bar{\gamma}^p$ in (d, g, j and m). (b-d): View of the model at the end of formation of the first band at ε_X = 3.00x10^{-3}, (*phase 4*), with (b) and (c) representing the model in the X-Z plan cut in two halves. (e-g): Model at ε_X = 3.98x10^{-3} (*phase 5*). (h-j): Model at ε_X = 8.12x10^{-3} (*phase 5*). (k-m): Model at the end of modeling (at ε_X = 29.65x10^{-3}, *phase 5*).

Phase 1 lasts until ε_X = 1.7x10^{-4}. *Phase 2* lasts until ε_X = 0.77x10^{-3} and follows the same evolution than *phase 2* of the reference test, with similar evolution of $\bar{\gamma}^p$, β and κ. *Phase 3* starts at ε_X = 0.87x10^{-3} and ends around ε_X = 0.90x10^{-3}. *Phase 3* follows the same evolution than *phase 3* of the reference test, with values of $\bar{\gamma}^p$, κ and β slightly lower than in the reference test than in the reference test.

The first band localizes around ε_X = 0.90x10^{-3} (Figure 83b-d); the end of formation of this first band corresponds to its segmentation (Figure 83e through g) and occurs at ε_X = 1.06x10^{-3}. The evolution of $\bar{\gamma}^p$, κ and β is similar than in the reference test. At the end of phase 4, $\bar{\gamma}^p$ the minimum and maximum values are slightly lower than in the reference test (1.1x10^{-3} vs. 1.8x10^{-3} and 3.3x10^{-3} vs. 4.8x10^{-2}, respectively). κ has smaller minimum and maximum values than in the reference test (1.7x10^{6} vs. 2.0x10^{6} and 2.8 x10^{6} vs. 3.4x10^{6}, respectively). β displays a smaller minimum value than in the reference test (-1.2x10^{-1} vs. -9.7x10^{-2}, respectively); its maximum value is similar to the one of the reference test at the end of the same phase (i.e 1.8x10^{-1}).

During *phase 5* (from ε_X = 1.06x10^{-3}), we observe the distribution of the deformation under the form of bands, sometimes dividing into several strands (frayed aspect – Figure 83e-m). The bands are distributed in two conjugate sets equally represented in the model. We note that the bands form on average a lower angle with the σ_v direction than the band in the reference test (c.a. 21° vs. c.a. 23°, respectively). This division into several bands frequently occurs when a band from one conjugate set abuts against a band from the other set (Figure 83h-j). We record at the end of modeling a small ε_X of 7.32x10^{-3} (Figure 83k through m). At the same ε_X = 3.98x10^{-3}, $\bar{\gamma}^p$ displays smaller minimum value than the reference model (1.2x10^{-3} vs. 1.8x10^{-3}, respectively); its maximum value is higher than the one of the reference test (7.5x10^{-2} vs. 6.8x10^{-2}, respectively). β has a smaller minimum value than in the reference test (-1.2x10^{-1} vs. -9.6x10^{-2}); its maximum value is similar as in the reference test (i.e. 1.8x10^{-1}). κ displays a smaller minimum vlaue than in the reference model (1.7x10^{6} Pa vs. 2.0x10^{6} Pa), its maximum value is higher than in the reference test (4.4x10^{6} vs. 4.2x10^{6} Pa, respectively).

Summary

The localization of the first band arrives later in the history of the extension (ε_X) with lower internal friction coefficient α. However, the formation of a band set is faster with smaller α (faster sample saturation). With low α, the deformation tends not to be distributed but localizes in a few thickening bands to form a predominant structure (only very few conjugate bands), much like a dense cluster. On the contrary, with high α, the deformation distributes under the form of conjugate band sets where the bands frequently split into several strands with geometries comparable to relays in nature. We also note that, consistently to equation (46), the angle ψ formed between the bands and the σ_v direction diminishes with increasing α. It also can be noted that, for the same ε_X, the contrast of $\bar{\gamma}^p$, β and κ values is greater for higher α.

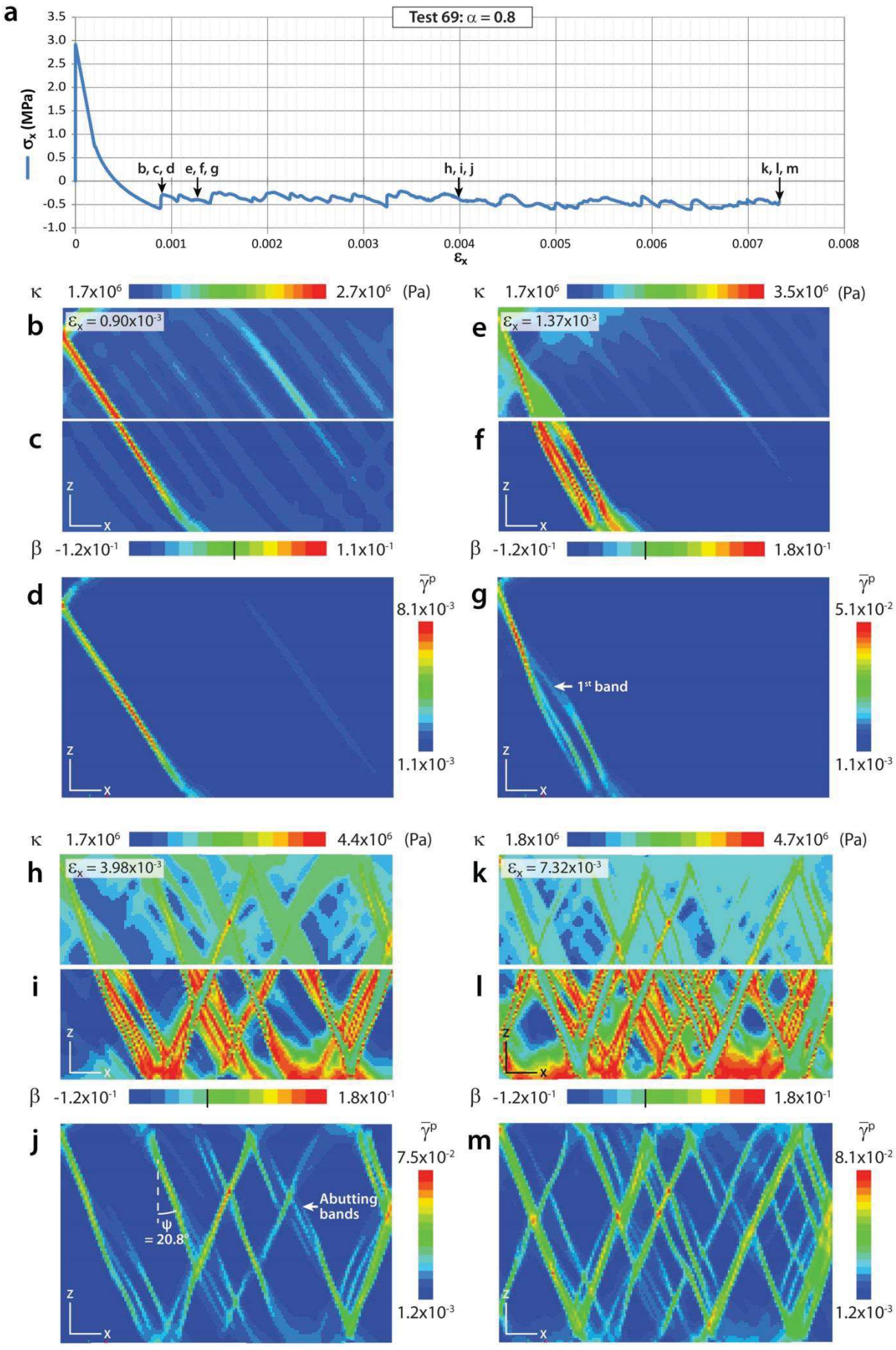
a
Test 69: α = 0.8
σx (MPa)
εx
b, c, d
e, f, g
h, i, j
k, l, m
κ 1.7x10^6 2.7x10^6 (Pa)
b
εx = 0.90x10^-3
c
β -1.2x10^-1 1.1x10^-1
κ 1.7x10^6 3.5x10^6 (Pa)
e
εx = 1.37x10^-3
f
β -1.2x10^-1 1.8x10^-1
d
γ̄p 8.1x10^-3 1.1x10^-3
g
1st band
γ̄p 5.1x10^-2 1.1x10^-3
κ 1.7x10^6 4.4x10^6 (Pa)
h
εx = 3.98x10^-3
i
β -1.2x10^-1 1.8x10^-1
κ 1.8x10^6 4.7x10^6 (Pa)
k
εx = 7.32x10^-3
l
β -1.2x10^-1 1.8x10^-1
j
ψ = 20.8°
Abutting bands
γ̄p 7.5x10^-2 1.2x10^-3
m
γ̄p 8.1x10^-2 1.2x10^-3

Figure 83. Illustration of the scenario of deformation modeled with the internal friction coefficient α fixed to 0.8. (a) Graph of $\sigma_X(\varepsilon_X)$ for the reference of the evolution of the Inelastic shear strain $\bar{\gamma}^p$. The positions corresponding to the different figures exposed are indicated along the σ_X curve. At the different stages of modeling, we represent the cohesion κ in (b, e, h and k), the dilatancy β in (c, f, I and l), and the inelastic shear strain $\bar{\gamma}^p$ in (d, g, j and m). (b-d): View of the model at the end of formation of the first band at ε_X = 0.90x10^{-3}, (*phase 4*), with (b) and (c) representing the model in the X-Z plan cut in two halves. (e-g): Model at ε_X = 1.37x10^{-3} (*phase 5*). (h-j): Model at ε_X = 3.98x10^{-3} (*phase 5*). (k-m): Model at the end of modeling (at ε_X = 7.32x10^{-3}, *phase 5*).

3.2.4. Influence of the model shape and resolution

In order to evaluate the potential influence of the size of the model on the structuring of deformation, we performed several tests equivalent to previously presented models, using similar settings but larger proportions or higher resolution (4:1, 400*100 grid zones; 3:2, 300*200 grid zones) (the settings are summarized in Table 5).

Table 5. Parameter settings for the numerical modeling testing the influence of the size and resolution of the model on the distribution of the deformation.

Test #	Model Size (m)	Grid resolution	E (Pa)	ν	α	β-function	$\bar{\tau}$-function	$\bar{\tau}_0$ (MPa)	σ_{m0} (MPa)	θ_0 (°)
20	**1 *0.667**	**150*100**	1x10^{10}	0.3	0.7	β_1	$\bar{\tau}_1$	9.3	5.9	21.8
27	**1 *0.250**	**400*100**	1x10^{10}	0.3	0.7	β_1	$\bar{\tau}_1$	9.3	5.9	21.8
61	**1 *0.667**	**100*150**	1x10^{10}	0.3	0.7	β_1	$\bar{\tau}_2$	9.3	5.9	21.8
30	**1 *0.250**	**400*100**	1x10^{10}	0.3	0.7	β_1	$\bar{\tau}_2$	9.3	5.9	21.8
66	**1 *0.667**	**150*100**	1x10^{10}	0.3	0.7	β_2	$\bar{\tau}_1$	9.3	5.9	21.8
28	**1 *0.250**	**400*100**	1x10^{10}	0.3	0.7	β_2	$\bar{\tau}_1$	9.3	5.9	21.8
21	**1 *0.667**	**100*150**	1x10^{10}	0.3	0.7	β_1	$\bar{\tau}_1$	4.6	11.0	15.6
26	**1 *0.667**	**200*300**	1x10^{10}	0.3	0.7	β_1	$\bar{\tau}_1$	4.6	11.0	15.6

Model 27 (Figure 84), 30 (Figure 85) and 28 (Figure 86) are equivalent to models 20, 61 and 66, respectively, but with a lower thickness and a higher resolution (i.e. Length = 1 m, Thickness = 0.250 m, 400*100 grid zones instead of Length = 1 m, Thickness = 0.667 m, 150*100 grid zones). In each models, we see that the formation of the first band occurs at the same extension ε_X as in their narrower equivalent. The subsequent deformation (phase 5), follows respectively to each set of parameters the same evolution of value with increasing $\bar{\gamma}^p$ as in their narrower equivalent. In all tests 27, 30 and 28 the network of deformation bands is more widespread than in their narrower equivalents. Therefore, for instance, two clusters of opposite conjugate sets are observed in the test 27 (Figure 84) instead of a single one in test 20 (Figure 75). Similarly, the distributed network already observed in the test 61 (Figure 76) is widespread in the test 30 (Figure 85). These larger models allow confirming that the presence of a set of clustered band inhibits the localization of the other conjugate set (e.g. Figure 84 and Figure 86). We also observe that, in the cases of $\bar{\tau}$ = $\bar{\tau}_1$, gaps of bands exist in the model despite the presence of the intense deformation (cluster) in another part of the model.

Model 21 (Figure 87) and model 26 (Figure 89) oppose models of similar size but with different resolutions (i.e. Length = 1 m, Thickness = 0.667 m, 150*100 grid zones vs. Length = 1 m, Thickness = 0.667 m, 300*200 grid zones). At ε_X of 3.98x10^{-3}, we observe that, in the high-resolution model, the deformation is distributed under the form of clustered and thin deformation bands which often divide into smaller strands during the first part of *phase 5* (Figure 89b-d). At the same ε_X of

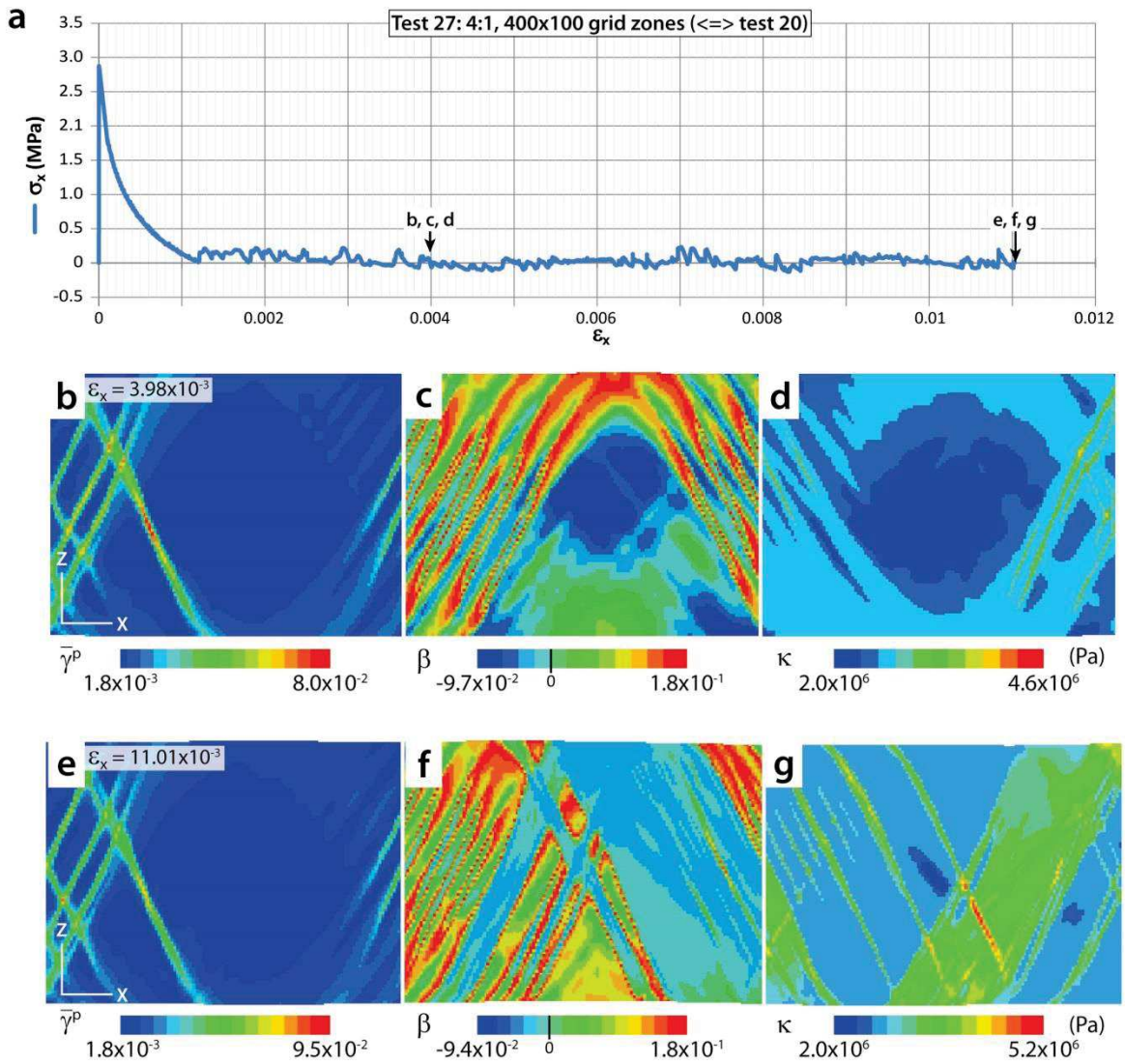

Figure 84. Illustration of the scenario of deformation modeled with a resolution of 400*100 grid zones (test 27), to be compared with the model size 300*200 (test 20 – Figure 75). (a) Graph of $\sigma_X(\varepsilon_X)$ for the reference of the evolution of the Inelastic shear strain $\bar{\gamma}^p$. The positions corresponding to the different figures exposed are indicated along the σ_X curve. At the different stages of modeling, we represent the inelastic shear strain $\bar{\gamma}^p$ in (b and e), the dilatancy β in (c and f), and the cohesion κ in (d and g). (b-d): View of the model ε_X = 3.98x10^{-3}, (*phase 5*), with (b) and (c) representing the model in the X-Z plan vertically split in three parts. (e-g): Model at the end of modeling (at ε_X = 11.01x10^{-3}, *phase 5*).

3.98x10^{-3}, the bands in the low-resolution model are distributed (Figure 87b-d). We note that the ranges of values of $\bar{\gamma}^p$, β and κ are all slightly smaller in the high-resolution model. With further extension, the deformation in the high resolution model is rather distributed in the model under the form of two conjugate sets of bands without real clustering (Figure 89e through g), while the deformation tends to form clusters in the equivalent model of smaller resolution (Figure 87e through g).

We see from these two groups of examples that the size of the model does not influence the modeling of the deformation if the resolution (number of grid zones per unit of length) remains the same. On the other hand, for a fixed size, the resolution affects the morphology of the deformation,

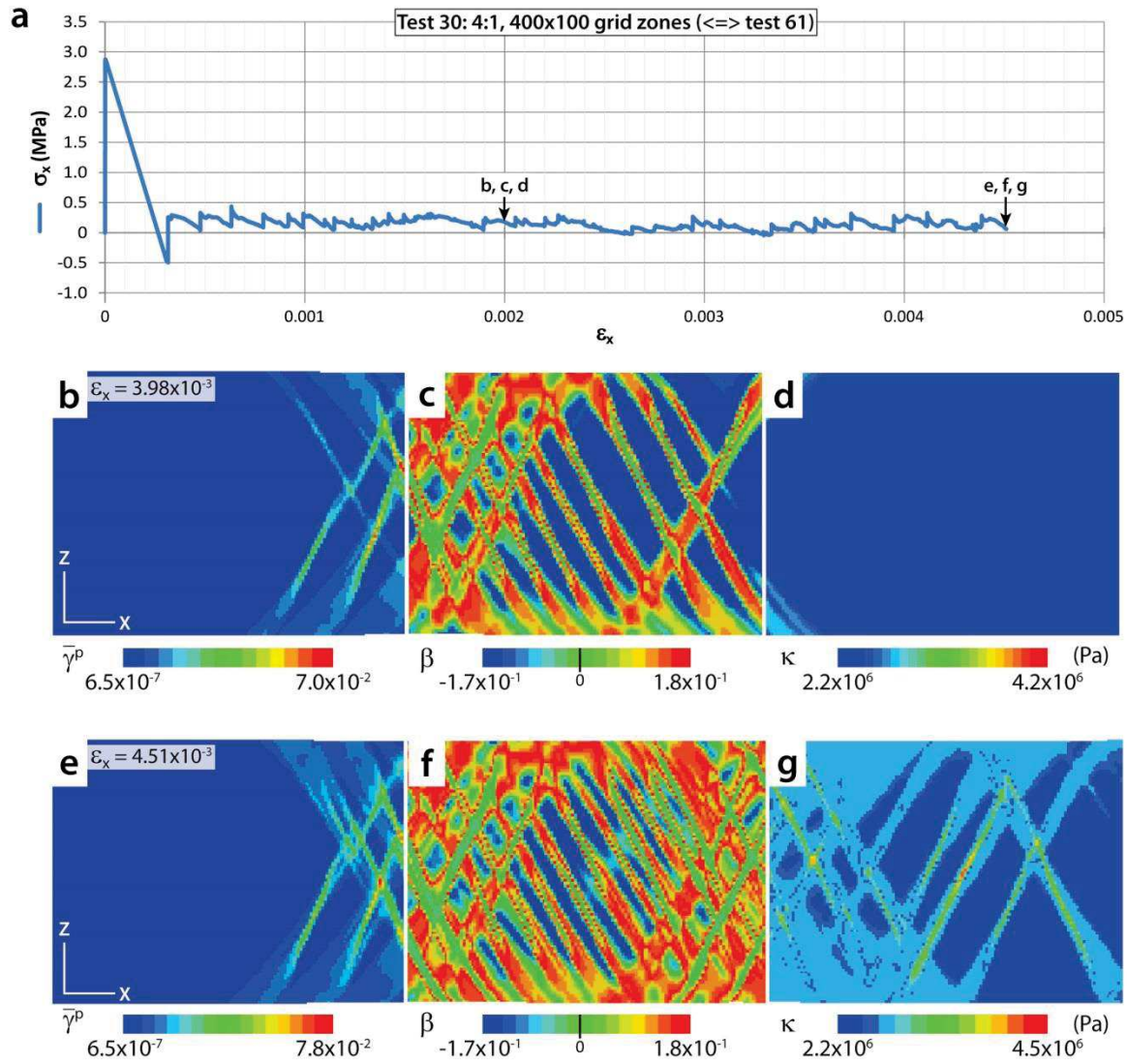

Figure 85. Illustration of the scenario of deformation modeled with a resolution of 400*100 grid zones (test 30), to be compared with the model size 300*200 (test 61 – Figure 76). (a) Graph of $\sigma_X(\varepsilon_X)$ for the reference of the evolution of the Inelastic shear strain $\bar{\gamma}^p$. The positions corresponding to the different figures exposed are indicated along the σ_X curve. At the different stages of modeling, we represent the inelastic shear strain $\bar{\gamma}^p$ in (b and e), the dilatancy β in (c and f), and the cohesion κ in (d and g). (b-d): View of the model ε_X = 3.98x10^{-3}, (*phase 5*), with (b) and (c) representing the model in the X-Z plan vertically split in three parts. (e-g): View of the model at the end of modeling (at ε_X = 4.51x10^{-3}, *phase 5*).

allowing thinner bands and more distributed (more detailed?) structures to form at higher resolution.

3.2.5. Synthesis and discussion of the parametric analysis from numerical modeling.

In this chapter, we test the influence of several functions and parameters on the organization of the failure in normal stress regime and subsequent deformation.

The analysis of the influence of the form of the $\bar{\tau}(\bar{\gamma}^p)$ constitutive function shows that a rapid growth of $\bar{\tau}$ with $\bar{\gamma}^p$ (high hardening modulus) leads to the formation of thick and clustered

deformation bands that harden during their evolution. The morphology of these structures resembles the morphology of the clusters of deformation bands observed at Goblin Valley or Cummingston for instance (Figure 89). On the contrary, the decrease of $\bar{\tau}$ with $\bar{\gamma}^p$ leads to the formation of few or one single thin band(s) concentrating most of the deformation. This type of band displays a softening behavior and resembles the morphology and behavior of a slip-surface in the field (with the limitation of the difference in displacement). The sudden increase of $\bar{\tau}$ with at the beginning of $\bar{\gamma}^p$ provokes the direct formation of thin distributed conjugate bands. The phase of incipient homogeneous inelastic shear strain seems extremely short (or nonexistent?). This behavior does not reflect the morphology of the deformation observed in the field as formed in normal stress regime. Besides, the analysis of the host rocks revealed that the grains are slightly deformed, assessing its slight pervasive inelastic deformation. Hence we see that the cohesion is a major parameter involved in the process of band accumulation leading to clustering. Clusters seem to occur if the cohesion increases significantly with the inelastic shear strain.

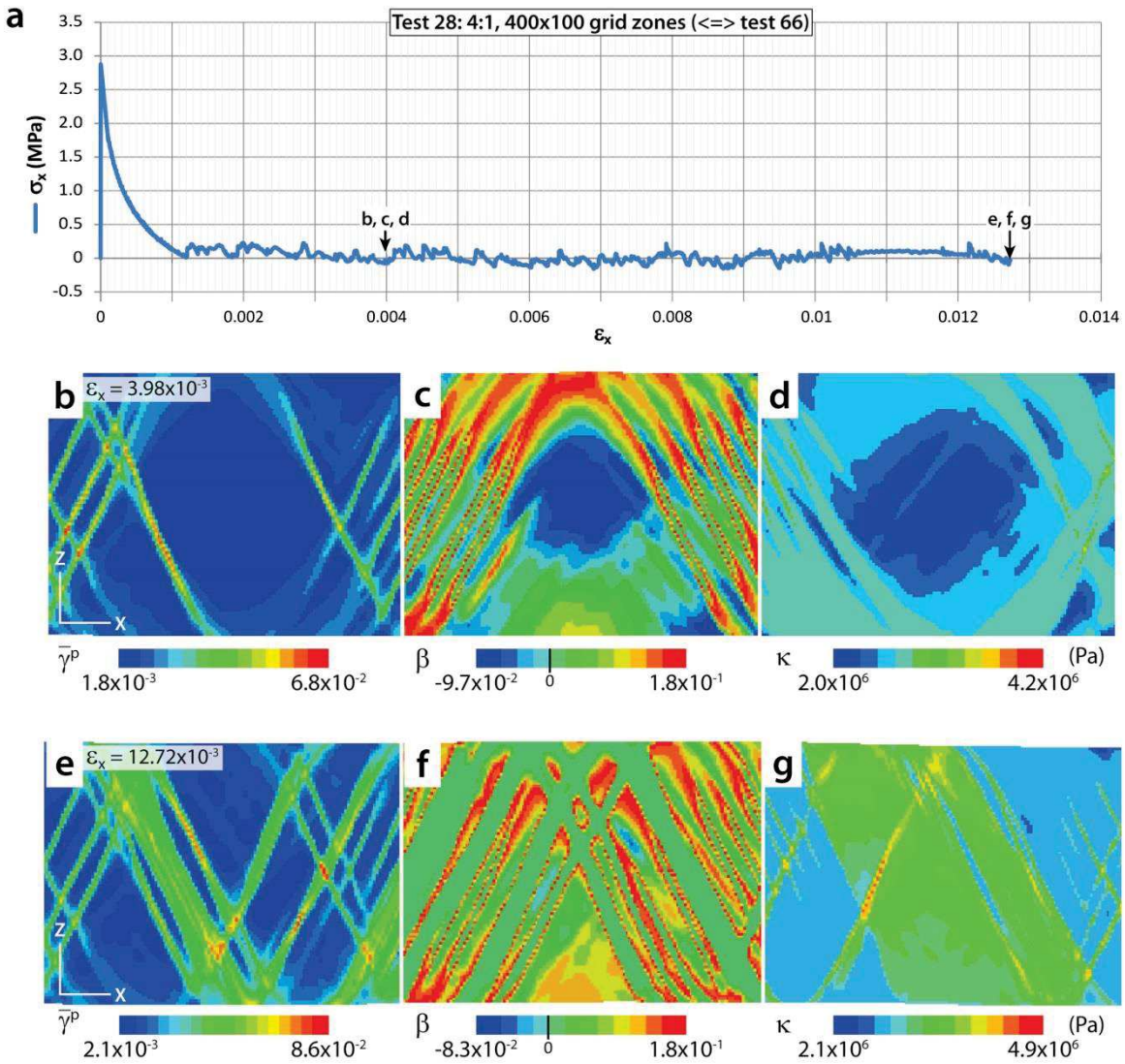

Figure 86. Illustration of the scenario of deformation modeled with a resolution of 400*100 grid zones (test 28), to be compared with the model size 300*200 (test 66 – Figure 81). (a) Graph of $\sigma_X(\varepsilon_X)$ for the reference of the evolution of the Inelastic shear strain $\bar{\gamma}^p$. The positions corresponding to the different figures exposed are indicated along the σ_X curve. At the different stages of modeling, we represent the inelastic shear strain $\bar{\gamma}^p$ in (b and e), the dilatancy β in (c and f), and the cohesion κ in (d and g). (b-d): View of the model ε_X = 3.98x10^{-3}, (*phase 5*), with (b) and (c) representing the model in the X-Z plan vertically split in three parts. (e-g): Model at the end of modeling (at ε_X = 12.72x10^{-3}, *phase 5*).

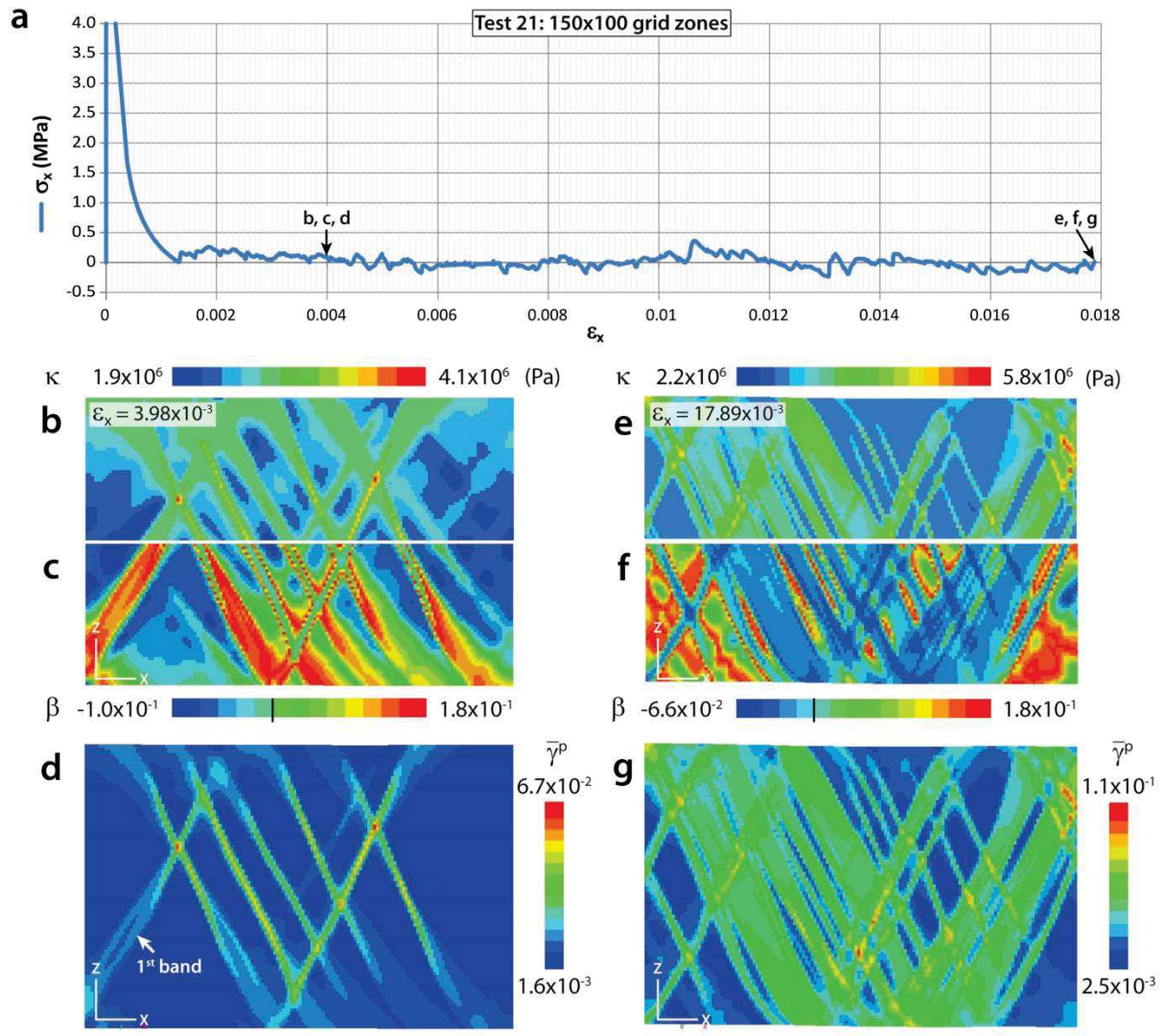

Figure 87. Illustration of the scenario of deformation modeled with a resolution of 400*100 grid zones (test 21), to be compared with the model size 300*200 (test 26 – Figure 89). (a) Graph of $\sigma_X(\varepsilon_X)$ for the reference of the evolution of the Inelastic shear strain $\bar{\gamma}^p$. The positions corresponding to the different figures exposed are indicated along the σ_X curve. At the different stages of modeling, we represent the cohesion κ in (b and e), the dilatancy β in (c and f), and the inelastic shear strain $\bar{\gamma}^p$ in (d and g). (b-d): View of the model ε_X = 3.98x10^{-3}, (*phase 5*), with (b) and (c) representing the model in the X-Z plan cut in two halves. (e-g): Model at the end of modeling (at ε_X = 17.89x10^{-3}, *phase 5*).

The analysis of the influence of the dilatancy showed that the negative evolution of the dilatancy permits the formation of compactive bands. In comparison, isochoric bands develop in models where the dilatancy is limited to zero after a certain value of $\bar{\gamma}^p$. However, this limitation does not affect the evolution of structuring of the deformation. Isochoric deformation independently of $\bar{\gamma}^p$ permits the formation of thick deformation structures resembling the clusters and inhibits the distribution of the deformation. This dilatancy behavior has no impact on the cohesion relative to the other models where dilatancy is changed. The generated structure resembles the morphology of localized clusters such as observed at Goblin Valley or Cummingston for instance. Nevertheless, in these natural examples, the deformed material (bands and interbands) are compacted. Hence, this model does not suit properly the way of formation of clusters in nature. In order to better suit the deformation observed in the field, it would be interesting to simulate the deformation using a fun-

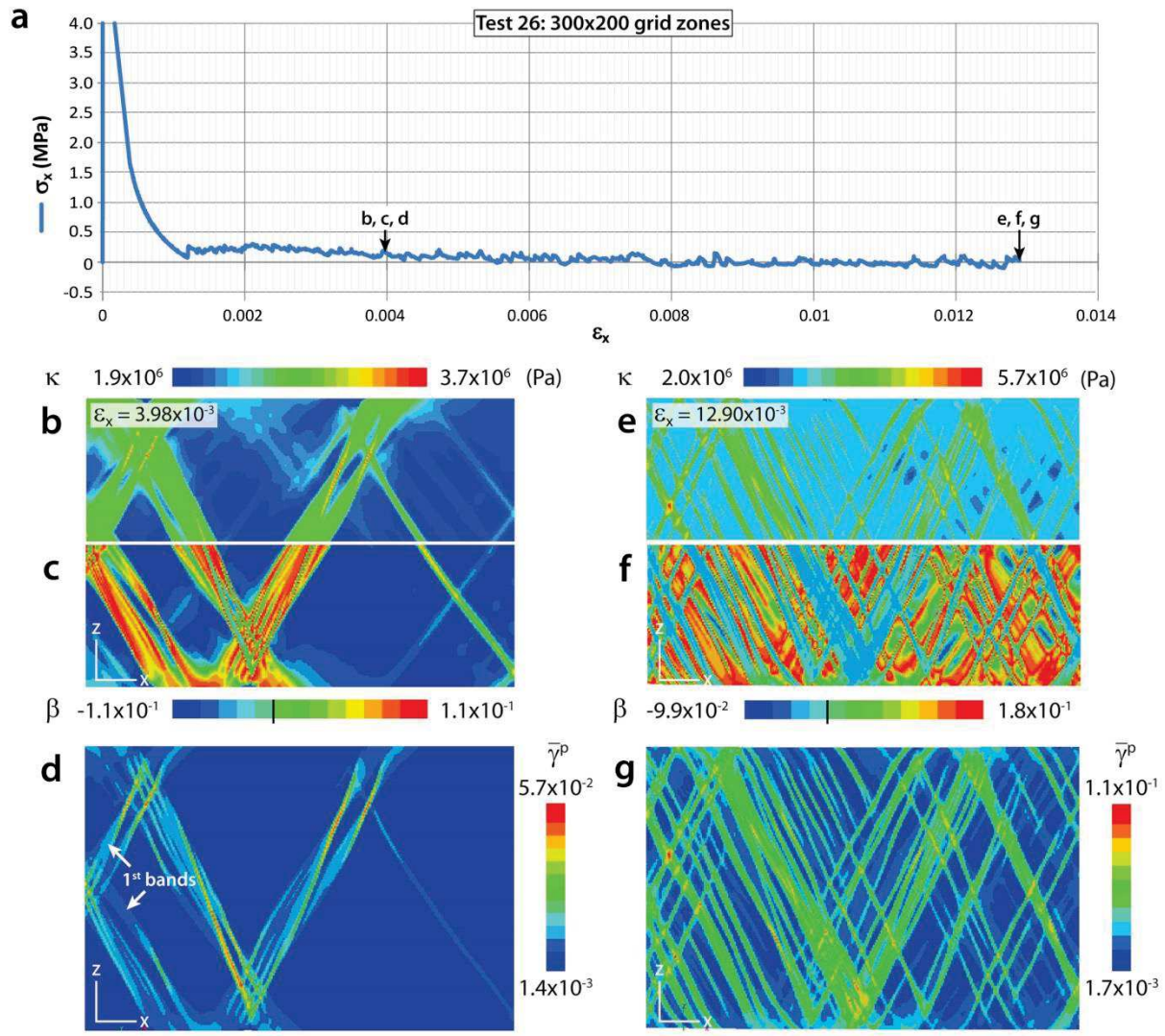

Figure 89. Illustration of the scenario of deformation modeled with a resolution of 300*200 grid zones (test 26), to be compared with the model size 150*100 (test 21 – Figure 87). (a) Graph of $\sigma_X(\varepsilon_X)$ for the reference of the evolution of the Inelastic shear strain $\overline{\gamma}^p$. The positions corresponding to the different figures exposed are indicated along the σ_X curve. At the different stages of modeling, we represent the cohesion κ in (b and e), the dilatancy β in (c and f), and the inelastic shear strain $\overline{\gamma}^p$ in (d and g). (b-d): View of the model ε_X = 3.98x10^{-3}, (*phase 5*), with (b) and (c) representing the model in the X-Z plan cut in two halves. (e-g): Model at the end of modeling (at ε_X = 12.90x10^{-3}, *phase 5*).

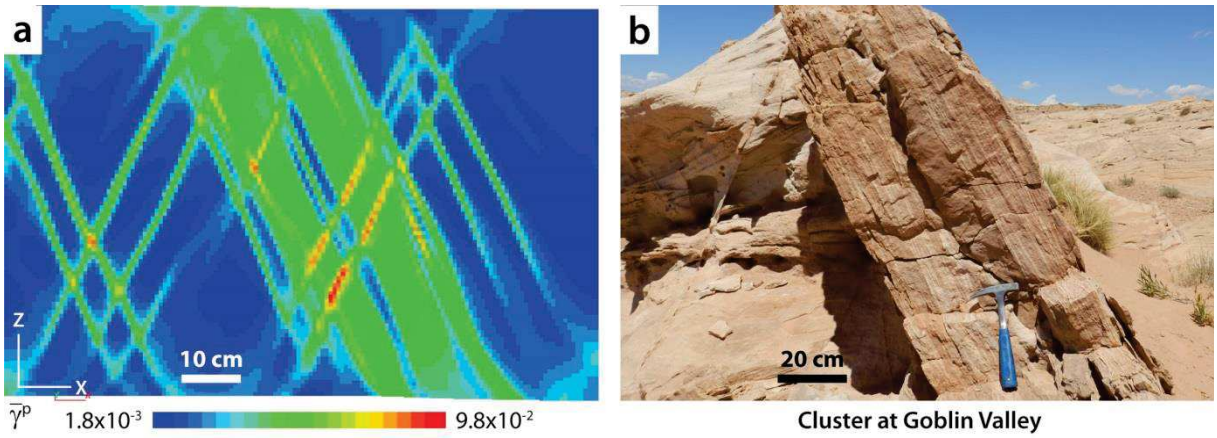

Figure 89. (a) Cluster of thickened bands in the modeling using the $\overline{\tau}_1$-function (test 20) at ε_X = 10.80x10^{-3}. (b) Cluster formed in normal Andersonian regime (extensional tectonics) at Goblin Valley.

ction of dilatancy where the dilatancy remains isochoric during the first stage of inelastic shear strain, and becomes negative after a certain value of $\bar{\gamma}^p$ (mix of the β_1 and β_2-functions).

Chapter IV

4. Concluding discussion

With regard to their potential impact on the modification of the reservoir properties and for academic purposes, the cataclastic deformation in porous sandstone has been widely studied in the literature. The cataclastic structures are intriguing because they represent deformation structures, different from conventional faults or fractures for instance, and because of the variety of morphologies that they display in the field, in terms of dimension and petrophysical properties. In addition to this, one can note that the mechanisms involved in their development are not trivial. In particular, the cataclastic deformation band clusters attract attention due to their important size and relief in the field compared to simple deformation bands. We arbitrarily distinguish the clusters from simple deformation bands or arrays of distributed deformation bands based on the threshold of the band density of 0.1 and a continuity of a minimal thickness of gathered deformation bands of 10 cm. These conventions permit the consideration of structures of significantly long and wide dimensions. The clusters can, in some cases, become faults when they comprise at least one slip-surface in the thickness of the structures.

Despite the recent advances on the subject of clusters (e.g. Lommatzsch et al., 2013; Nicol et al., 2013; Ballas, 2013; Soliva et al. 2016; Fossen et al., 2017), our field analysis was aimed at answering several poorly covered questions concerning the dimension, geometry, distribution of bands and associated mechanisms, and localization of slip-surfaces in clusters. Also, our study also had the objective of improving the understanding of the influence of the microstructural processes on the evolution of the cluster by band addition from simple band to faulting. Numerical modeling permitted the study of the influence of several physical parameters on the development of clusters.

1. Main results

We present here the main results of this thesis, organized under four attributes:

The **lithology**, regarded in terms of mineralogical composition, grain size and diagenetic state has a major influence on the mechanisms of deformation. We found in section 2.2 that a material rich in weak minerals such as phyllosilicates in the studied clay and silt layers inhibits the process of cataclasis and favors the process of smearing. This lithological contrast is also at the origin of the inception and propagation of a major through-going slip-surface (fault) in (or along) clusters of the adjacent clean sandstone. We saw that hardened materials, such as cemented sandstone, can also be at the origin of the inception and propagation of a fault in cataclastic deformation band clusters. We observed in section 2.3.1 that larger modal host rock grain size causes the formation of thicker bands, and more generally, thicker clusters. Although known long before this study, we remind the reader that the grain size and porosity of the sandstone alters the elastic resistance of the material to stress, expressed as the variation of the failure envelope of the material. We saw that oxidized sandstone inhibits the formation of clusters (and cataclastic deformation band in general).

The **degree of deformation** of porous quartz sandstones analyzed in section 2.3.1 through the degree of cataclasis and compaction was shown to be influent in several aspects. Compaction globally increases with an increasing degree of cataclasis. This increasing degree of cataclasis provokes a lowering of the sorting of the deformed material and consequently an increase of compaction of the clasts. The cataclasis also alters the roughness of the clasts: the clasts are significantly roughened at incipient deformation and are slightly smoothened at the maximum degree of cataclasis attained, remaining rougher than the host rock grains. In section 2.4, we showed that the cataclasis also favors the precipitation of quartz cements as commonly seen at several sites never buried below 800 m. This process of cementation can be very effective in the most cataclased material (i.e. the bands), reducing the porosity (and most probably the permeability) of the bands in the clusters. While the roughening of the clasts may enhance the friction in the deformed material, the packing of the clasts and the cementation increases the cohesion of the bands which are therefore hardened.

The **stress state**, accounting for both the tectonic loading and the burial, influences the mechanisms of deformation and the resulting morphology (geometry, dimension) of the generated clusters. The analysis of the stress state evolution as presented in section 2.3.2, equivalent to the study of the stress-path, reveals that the evolution of a tectonic stress loading may successively correspond to several Andersonian stress regimes. Transtension tectonics may most of the time correspond to a normal Anderonian regime, and more rarely to a strike-slip regime. Transpression tectonics mostly corresponds to strike-slip regime in the first stage of tectonic loading and corresponds to thrust regime with increased tectonic loading. We see that the mobility of the Andersonian regimes on the P axis of the Q-P diagram depends on the vertical stress (related to the burial depth of the formation at deformation). Despite uncertainties of burial at the time of deformation and of the shape of failure envelopes, we see that the Andersonian regime domains frequently have comparable positions relative to the failure envelopes of the sandstones in the case of the studied sites.

- Normal regime clusters at the studied sites all seem to hit the failure envelope on the left of the brittle part. These clusters are all formed in extensional tectonics (section 2.3.1). They commonly measure a hundred of meters in horizontal extent, and propagate vertically as long as the lithology of the sandstone is favorable to cataclasis. These clusters are often thin (10-30 cm) with high band densities (0.30-0.70), or of medium size (up to 70 cm) with lower band densities, characterized by a significant degree of cataclasis. They frequently display major through-going slip-surface(s) and form km-long networks.
- Stress-paths of clusters formed in strike-slip regime probably correspond to transpression tectonic loading. Stress-paths of clusters formed in strike-slip regime seem to hit the failure envelope on the brittle part of the envelope. As seen in section 2.3.1, these clusters are of medium size (10-100 cm), have constant medium band densities (0.20-0.55), with high degree of cataclasis and compaction. They do not display any real fault.
- Stress-paths of clusters formed in thrust regime probably correspond to near pure compressional tectonic loading. These stress-paths seem to attain the failure envelope near the summit of the envelope and on the cap. In section 2.3.1 we saw that clusters formed in thrust regime are sparse; they can resemble the strike-slip regime clusters or attain thickness wider than 1 meter, with a low band density (<0.10-0.40), a low degree of cataclasis and a moderate compaction.

The **kinematics** affects the geometry of the bands in the clusters (section 2.3.3). The interbands form lenses of deformed material whose permeability is higher than the neighboring bands. The study of these lenses reveals that, for the same thickness, the lenses are longer along the plane of shear, with varying average lengths depending on the site (67-144 mm), than out of the shear plane (32-123 mm). This indicates that the deformation bands in the clusters are rather linear in the plane of shear and corrugated out of the shear plane for both the normal regime and thrust regime clusters, independent of the stress state.

2. Discussion

In the light of the discussion of the results presented, we would like to propose hereafter a structural and mechanical model for the formation of clusters, and anticipate their potential impact on fluid migration. We illustrate the different parts of the discussion though Figure 90 to Figure 92, presenting the main conclusions of this study concerning cataclastic deformation band clusters as a function of the three Andersonian regimes studied.

We see that the type of microscopic deformation implied in porous sandstone corresponds to cataclasis, accompanied by compaction. Therefore, in the aim of constraining the conditions of formation of clusters, we first recall that the first essential setting necessary is a juxtaposition of clean porous sandstone lithologies.

4.2.1. Influence of the stress-state and lithology on the process of cluster development

We saw that the analytical approach suggests that the position of failure along the sandstone failure envelope may actually be the most determinant parameter in the morphology and band

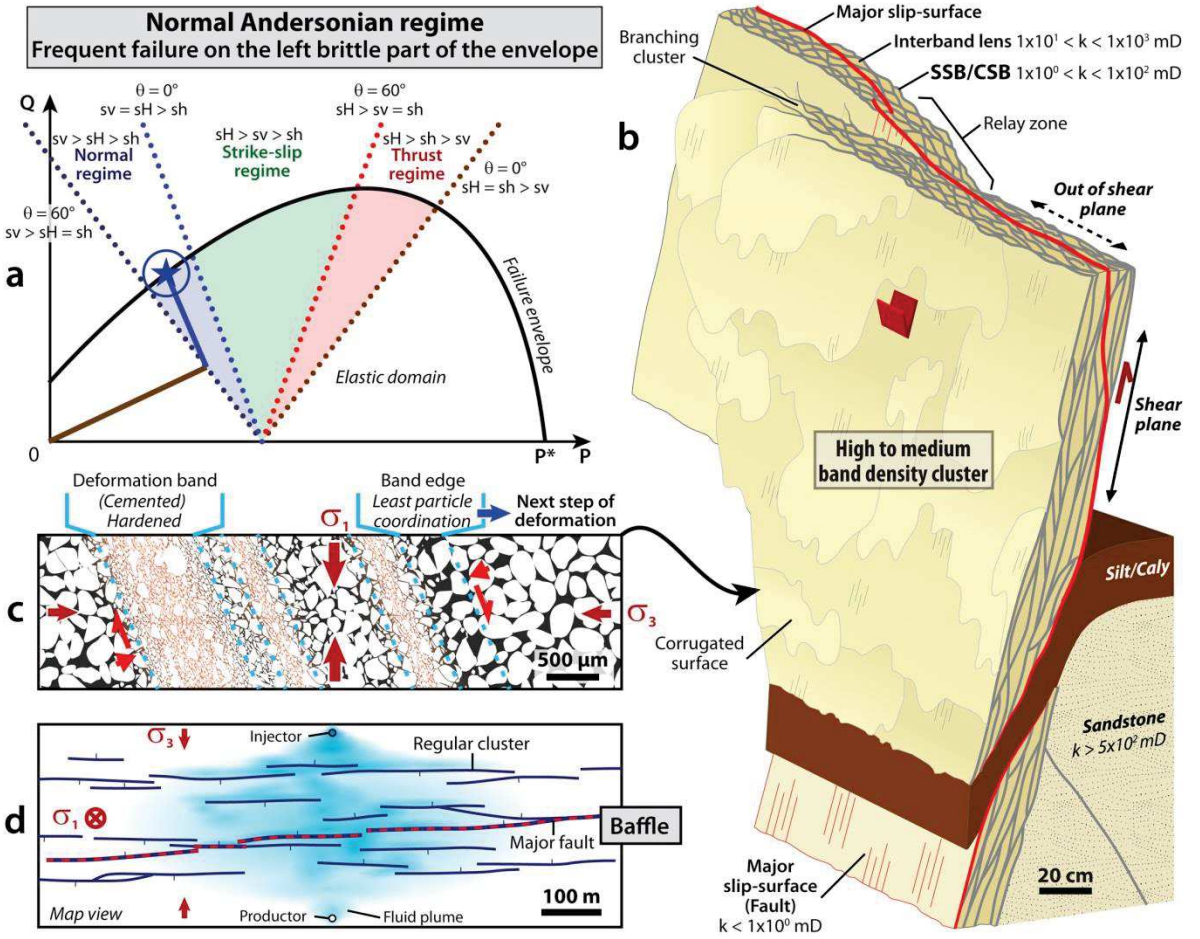

Figure 90. Synthetic representation of the typical setting and morphology of a cluster formed in normal Andersonian regime. (a) Representation of a typical stress-path evolution in extensional tectonic loading until failure (circled star). (b) Typical morphology of a cluster formed in normal regime. Note the inception of a major slip-surface at the interface between the silt/clay smear and the cluster. The slip-surface locates at the edge of the clusters near the silt/clay layer; its position varies in the thickness of the cluster as it goes away from the silt/clay layer. (c) Microscopic structuring of the deformation in the cluster. The edge of some bands may be dilatant and represent planes of weakness (low particle coordination), localizing the next step of deformation. This dilatancy would explain why the bands gathers near one to another, increasing the deformation ratio of this type of cluster. The orange-shaded area between the clasts in the bands represents the favored localization quartz cementation. (d) Structuring of the deformation at the km-scale. The dense cluster network gathered near map-scale fault forms a potential baffle for fluid flow.

density of the generated cluster, much similarly to what is described in experimental tests for the type of individual bands (compilation of Wong et al., 1997; Baud et al., 2000, 2004; Klein and Reushlé, 2004; Baud et al., 2006; Tembe et al., 2008; Rutter and Glover, 2012). Consequently, since the shape of the failure envelope depends on the lithology of the formation (as shown by the variation of P* as a function of the grain size and porosity - Zhang et al., 1990; Wong, et al., 1997), the influence of the stress state shall be considered in association with the lithology of the sandstone when anticipating the morphology of the deformation. In the case of the studied sandstones, the apparent correlation between the types of tectonic loadings and the morphology of the clusters would remain valid artificially because the position of the Andersonian regime domains in the Q-P diagram relative to the several failure envelopes is approximately the same in all cases. This constant relative position implies that each Andersonian regime domain always roughly intercept the same part of the envelope. The results of Soliva et al. (2016 – Appendix A) reinforce our observations of a

statically constant position of the Andersonian regime domains relative to the failure. Indeed, in their work, the majority of the studied structures formed in normal regime correspond to localized deformation such as thin clusters, often faulted. On the other hand, most of the deformation structures formed in thrust regime correspond to arrays of conjugate sets of bands. Nevertheless, assuming for instance two similar sandstones (same failure envelope) buried and deformed at two different depths (different vertical stresses) under similar tectonic loading (e.g. pure compressional tectonics – Figure 92a), we see that the shallowest sandstone would attain failure on the brittle part of the envelope whereas the deepest sandstone would attain failure on the cap part of the envelope. Such a situation is probably what distinguishes the medium and high band density thrust regime clusters of CSB formed at Blankenburg and the thick and low band density thrust regime clusters of SECB formed at Buckskin Gulch. According to the same logic, considering two different sandstones (different failure envelopes) buried and deformed at the same depth (same vertical stress) under the same tectonic loading (e.g. transpressive tectonics – Figure 91a and b), we see that because the failure is not attained on the same part of the failure envelope, two distinct types of clusters could be generated in the two different sandstones. Such a scenario is observed at Orange (Provence, France) where two different adjacent sandstones display different types of deformation structures coexisting (in this case arrays of SECB and SCB) while obviously deformed during the same episode of contractional tectonics (Soliva et al., 2013). In the case of two different sandstones buried and deformed at the same depth, depending of the stress-path, a similar stress loading appears likely to generate deformation under two different Andersonian stress regimes (Figure 92a).

We should remark that the loading condition (Lode angle) also influences the shape of the failure envelope of the host rock (e.g. Haimson and Chang, 2000; Chemenda and Mas, 2016 and numerical models). Consequently, because our analytical study does not account for this variation in the shape of the envelope, the general hypothesis proposed in the previous paragraph should be considered bearing in mind that slight variations are possible.

As reported in recent works (e.g. Solum et al., 2010; Soliva et al., 2013; Ballas, 2013; Soliva et al., 2016 – cf. Appendix A), we observe that the cataclastic deformation tends to get clustered in extensional tectonics whereas it distributes under the form of arrays of individual deformation bands in contractional tectonics. However, although some mechanical or geometrical explanations were proposed (e.g. Schultz and Siddharthan, 2005, Shipton and Cowie, 2001; Nicol et al., 2013), the processes responsible for such variability in the morphology of the deformation are not explained. We show in this study that the cataclasis provokes a lowering of the sorting of the deformed material, directly responsible for its increased packing, maximum in the bands. Authors like Arzt (1982) show that a higher packing correlates with higher particle coordination. We also show that the cataclasis induces an average roughening of the clasts, which implies increased friction (e.g. Mair et al., 2002; Cho et al., 2006; Guo and Morgan, 2006; Estrada et al., 2011; Azéma et al., 2012). The combination of high friction and important particle coordination in the bands indicates that they are cohesive (hardened – see Figure 90c for instance). This deduction is consistent with the experimental results of Kaproth et al. (2010) and contradicts the idea of cluster deformation where bands would readily accomodate several steps of deformation proposed by Nicol et al. (2013). Our numerical modeling, which simulates for the first time the formation of clusters, indicates for failure in normal Andersonian regime that the evolution of the cohesion with increasing inelastic shear strain has a strong impact on the organization of the deformation. The models suggest a better clustering (or at least, band thickening) when the cohesion is increased in the most deformed parts of the material

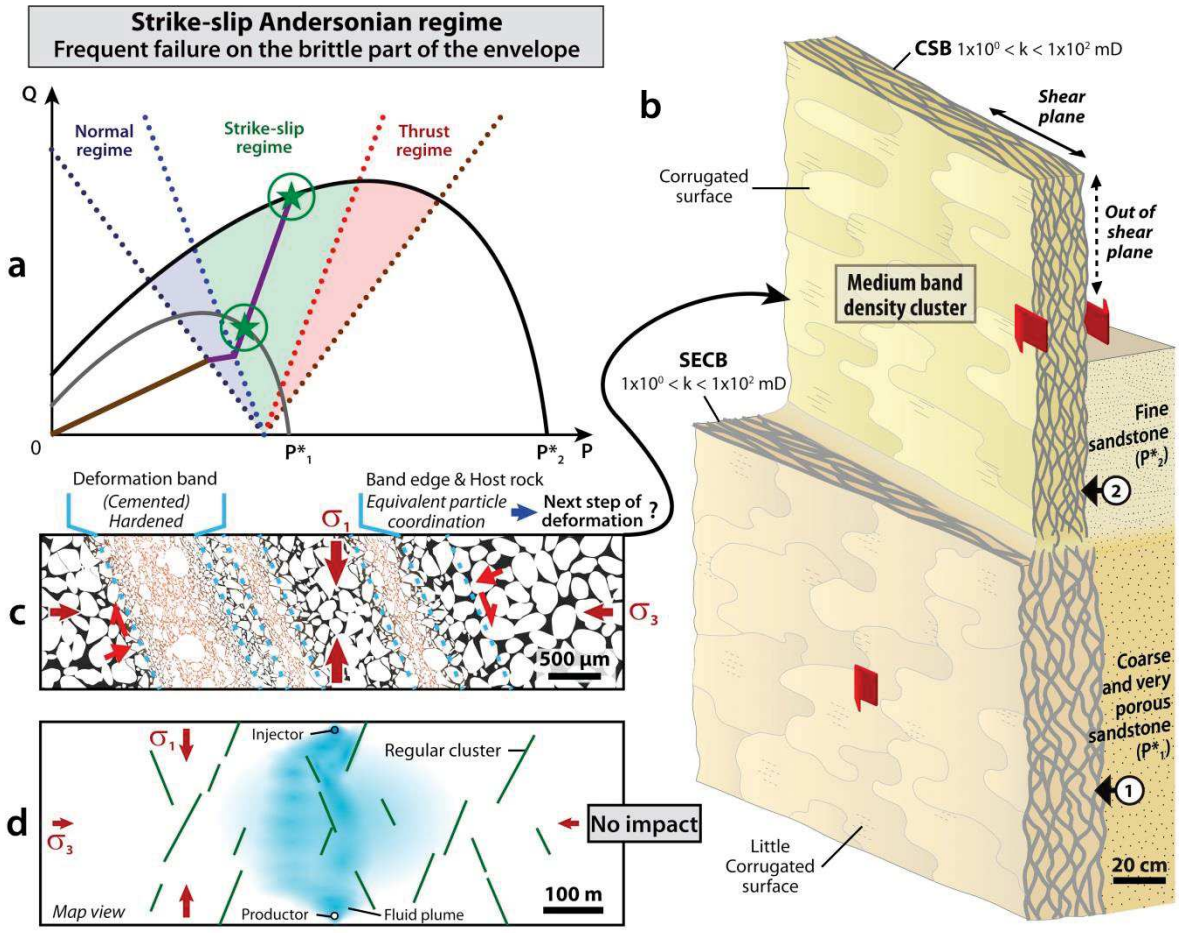

Figure 91. Synthetic representation of the typical setting and morphology of a cluster formed in strike-slip Andersonian regime. (a) Representation of a typical stress-path evolution in transpressional tectonic loading until failure (circled stars). Note that a formation including two different sandstones (having different modal grain size and porosity), display two failure envelopes that will be reached on different parts and at different times of the stress-path evolution. (b) Typical morphology of a cluster formed in strike-slip regime. Note that the deformation in the two different sandstones occurs subsequently. (c) Microscopic structuring of the deformation in the cluster. Depending on the degree of dilatancy of the edges of the bands, the deformation bands could be variably distributed in the cluster. The orange-shaded area between the clasts in the bands represents the favored localization quartz cementation. (d) Structuring of the deformation at the km-scale. The sparse distribution of the clusters will not significantly affect the fluid flow.

(band hardening). On the contrary, if the cohesion is decreased in the most deformed material (band softening), the deformation localizes in a single band that better corresponds to an incipient fault surface.

Our study shows a general correlation between the types of tectonic loading (matching with several Andersonian stress regimes during increasing loading) and the types of microscopic deformation, expressed both in terms of cataclasis and compaction. We first remind the reader that extensional tectonics commonly leads to failure in normal Andersonian regime (apparently often hitting the failure envelope on the left of the brittle part), and that contractional tectonics commonly leads to failure in strike-slip and thrust regime (often hitting the envelope on the brittle part and on the cap of the envelope, respectively). The material deformed in normal and strike-slip Andersonian regimes displays, for the same degree of cataclasis, less compaction than the material deformed in thrust regime. This suggests that the material deformed in normal and strike-slip regimes offers

lower particle coordination than in thrust regime. This lower particle coordination represents less resistant particle contact (Iwashita and Oda, 2000). Furthermore, although we do not observe direct dilatancy of the interband material in the samples of clusters formed in normal or strike-slip regimes, experimental tests on the GRAM material reveal that dilatancy actually occurs at the edge of bands being formed in samples deformed under low confining pressure (corresponding to normal stress regime conditions – Mas and Chemenda, 2015; Tran, 2016). Other numerical models simulating the elastic loading of granular material in extensional tectonics also demonstrate planes of dilatancy where the particle coordination decreases to the benefit of increased stress loading at the particle contacts of the force chains (e.g. Iwashita and Oda, 2000; Taboada et al., 2005; Estrada et al., 2008). For this reason, we hypothesize that the potentially lowest particle coordination in the interbands of the structures formed in normal (and potentially strike-slip) regime(s) would be responsible for the subsequent band localization near the edge of a former one (Figure 90c), consistently with the proposition of Anthony and Marone (2005). The band thickening towards the dilatant edge of the band is well illustrated by our numerical modeling simulating failure in normal stress regime. On the other hand, in thrust Andersonian regime the compaction of the interband material is more important than in the case of extensional tectonics. Granular models simulating contractional tectonics loading do not allow the observation of plane of dilatancy, and display balanced chains of force with a higher particle coordination (Estrada et al., 2008). This good particle coordination would prevent the localization of a new band at the vicinity of former bands. The localization of the next band would be reported further away, towards least deformed material (i.e. host rock) where the particle coordination is least (Figure 92c). We see here that the microscopic deformation mechanisms very probably explain the macroscopic morphology of deformation in sandstone. The expression of these mechanisms corresponds to the generation of potentially thin clusters localizing the deformation in normal to strike-slip Andersonian regimes, and more distributed deformation such as thick clusters of low band density to arrays of distributed bands in thrust regime.

4.2.2. Faulting

We noted that the clusters formed in normal Andersonian regime are often faulted, displaying (a) through-going slip-surface(s). Our study reveals that, in normal Andersonian regime, a means of generating the localization of the deformation consists in juxtaposing porous sandstone with a material of hardened lithology such as a cemented sandstone, or a softened lithology such as phyllosilicate-bearing materials (Figure 90b). The favored shear localization in the presence of weak minerals in the deformed structure is in agreement with other studies (Byerlee, 1978; Logan and Rauenzahn, 1987; Underhill and Woodcock, 1987; Collettini et al., 2009). This juxtaposition permits the inception and propagation of a slip-surface in or along the edge of the clusters in the adjacent porous sandstone. In that, our integrated study does not strictly support the proposal of Awdal et al. (2014), for instance, inferring slip-surfaces at the edges of the clusters. In the case of the clay/silt-sandstone juxtaposition, the fault propagation can be effective from displacements as small as 2 m. This mechanism of fault development explains why we do not observe any correlation between the thickness of a cluster (and the band density) and the presence of a fault. Even though these conditions may not represent the only means of faulting (since we do not exclude the potential faulting by coalescence of small slipped patches with more irregular geometries in the cluster thickness), we think that they are at the origin of frequent major through-going slip-surfaces. In particular, several of the faulted cluster sites comprise a layer of softer material (clay, phyllosilicate-

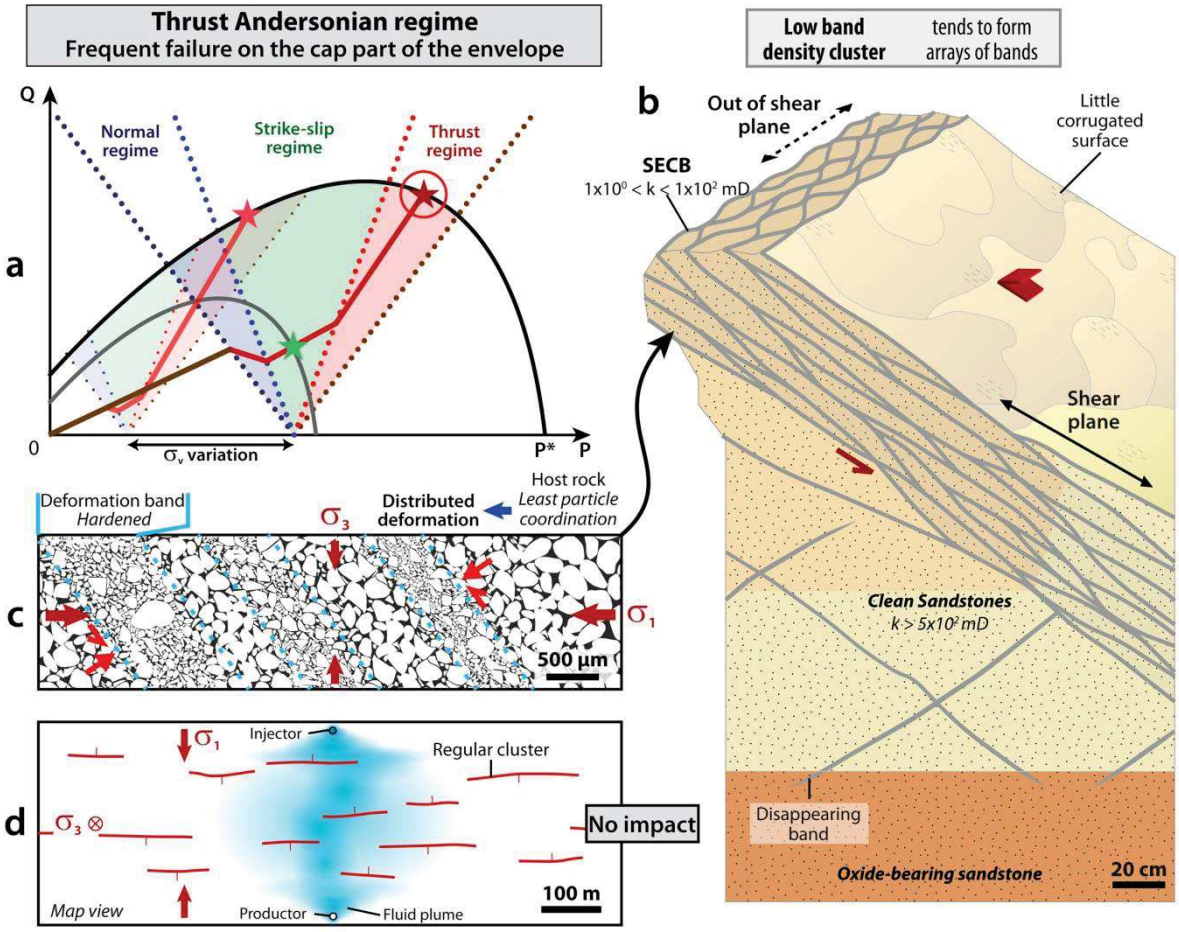

Figure 92. Synthetic representation of the typical setting and morphology of a cluster formed in thrust Andersonian regime. (a) Representation of a typical stress-path evolution in contractional tectonic loading until failure (circled star). Note that, depending on the failure envelope of the sandstone, for the same tectonic loading, the deformation could occur under different Andersonian regimes (light-green star). As well, note that a variation of the fixed vertical stress (linked to the burial) would shift the position of the regime domains along P and, for the same tectonic loading, could, provoke failure at different point of the failure envelope, therefore generating a different type of deformation (light-red star). (b) Morphology of a cluster formed in strike-slip regime such as at Buckskin Gulch. Typical thrust regime cluster is relatively thick and with a low band density. Note that the vertical transition from a clean sandstone to an unclean sandstone marks the end of the cataclastic deformation. (c) Microscopic structuring of the deformation in the cluster. Due to the high compaction of the deformed material, the bands are more distributed (and often thicker), explaining the lower band density of the clusters (or arrays of individual bands). (d) Structuring of the deformation at the km-scale. The sparse distribution of the clusters will not significantly affect the fluid flow.

bearing silts) adjacent to the studied sandstone. From these conclusions, we hypothesize that the presence of a hard lithology such as a limestone formation adjacent to porous sandstone, for example, could favor the occurrence and propagation of a slip-surface in the sandstone if deformed.

From this result, we partly answer the question of the condition and timing of the faulting during the cluster development. However, the absence of such contrasted lithologies at the sites deformed in strike-slip and thrust regimes prevents us from concluding that the strike-slip regime and thrust regime clusters are not faulted because of missing contrasted lithology or, as more commonly advocated, because the deformation is generally more distributed in these cases.

4.2.3. Diagenesis

In the previous paragraphs, we discussed the processes of evolution of the deformation in clusters only in terms of cataclasis and mechanical evolution. We would like to recall that most of the clusters observed in the context of our study display syn- or post-deformation quartz cementation in the most cataclased materials of the clusters (Figure 90c and Figure 91c), encompassing interband and most frequently, bands. In complement to the knowledge reported in the literature concerning structures formed at depths superior to 1 km (e.g. Fisher and Knipe, 1998; Milliken et al., 2005) and minimum temperatures of 40°C (Pollington et al., 2011), our integrated study reveals that the process of quartz cementation in the cataclastic material is frequent and efficient in clusters buried to a maximum depth of 800 m (provided aquifer conditions, obviously). The absence of pressure-solution features in several cases suggests a cementation by self-healing (sealing of the clast about synchronous with the deformation). To our knowledge, this is the first time a study covers this gap of information on this subject. These cements often form 10 to 20 µm rims around the clasts and are sufficiently developed to seal the clasts in most cases, where the degree of cataclasis exceeds 15-20%. As a result, the cohesion of the material is drastically increased, preventing further deformation in the material of low residual porosity and shifting the process of cluster thickening in the least cataclased and least cemented material. In addition, the cementation reduces the porosity of the cataclastic material and very probably reduces the permeability of the clusters.

4.2.4. Implications for fluid migration

Accounting for the results of the study, and taking into account the permeability of each type of structures that we report, from host rock, to interbands, to bands and to slip-surfaces, we can anticipate the potential influence of the many types of deformation on the behavior of fluid flows in sandstone reservoirs. Note that many records of cataclastic deformation structures permeability are available in the literature and complete our measurements (see section **Erreur ! Source du renvoi introuvable.** for references).

As aforementioned, clusters formed with failure on the left of the brittle part of the envelope of sandstones seem to be favored by deformation under normal Andersonian regime (Figure 90a), itself induced by the evolution of the stress-path in extensional tectonics. These clusters are long, form dense networks at the vicinity of map scale faults and include diffuse and discrete bands (mostly CSB) as well as major through-going slip-surfaces with range of permeability from $3x10^{2}$ to $5x10^{-1}$ mD. Besides, this type of cluster frequently displays important cataclasis likely to induce significant cementation further reducing the permeability. Consequently, they are likely to constitute considerable baffles for fluid flow at basin scale near a fault zone (Figure 90d).

The clusters that we described in strike-slip regime seem to form with failure on the brittle part of the failure envelope (Figure 91a) and are composed in this study of diffuse and discrete CSB of variable permeability ($4x10^{0}$ and $4x10^{1}$ mD). These deformation structures are of medium thickness with medium band density. The study sites of clusters deformed in strike-slip regime do not allow us to assess clearly the lateral extent of the clusters. At least we observed that the clusters propagate vertically as long as there is clean quartz sandstone. However, because they are sparse, they do not represent significant baffles at the reservoir scale (Figure 91d).

Based on the sole example of Buckskin Gulch, we infer that clusters or arrays of individual deformation bands form when the stress-path hits the failure envelope on the cap (more potentially attained in thrust Andersonian, induced by compressional tectonics - Figure 92a). The deformation bands entering their composition (mostly diffuse SECB) have relatively high permeability ($3x10^1$ and $3x10^2$ mD). They are thick but with low band density, they are quite short and sparse. Therefore, we estimate this type of cluster would not affect the fluid flow significantly in the reservoirs (Figure 92d).

In the case of failure near the summit or on the left part of the envelope such as inferred at Blankenburg (probably permitted by transpressional tectonic stress loading), the low permeability of the discrete bands ($0.5x10^0$ and $0.5x10^1$ mD – mostly CSB) could locally baffle the fluid flow.

3. Prospective work

Although we think that the knowledge of the deformation into sandstones, including the formation of clusters, is by now very well developed in the literature (in terms of mechanical processes, distribution, geometry and potential impact of fluid flows), we suggest in this section several axis of development so as to improve on this work.

One option to verify and enhance the accuracy of our observations would be to undertake similar macroscopic and microscopic structural analysis on more sites presenting similar settings such as the loading condition (burial and tectonic kinematics, lithology) and compare the similarities and discrepancies of the deformation structures as function of other factors potentially uninvestigated in this study. In particular, it would be interesting to know if the presence of thin silt or clay layers could initiate fault initiation during the deformation in thrust regime.

To enhance the understanding of the diagenetic evolution of clusters with increasing burial, and particularly when the formation is oil-filled, we think it would be interesting to analyze the diagenetic state of the clusters at depth. Because well-bore drilling aimed at petroleum investigation at the vicinity of seismic faults sometimes mistakenly intercept deformation structures (or faults!), the recovery of core sampling may be possible. This type of investigation was already started by authors like Tueckmantel et al. (2010) and should be continued with that goal.

Due to time constraints, we did not test all the parameters that we wish we had during the numerical modeling. Hence, we think it would be relevant to pursue more simulations testing the influence of parameters on the geometry and distribution of the deformation such as the Young's modulus of the rock or other behaviors of dilatancy. Failure in strike-slip and thrust Andersonian regimes should also be tested to understand what parameters and what behaviors influence the distribution of the bands. Besides, since it has been shown that the loading condition (represented by the Lode angle) influences the failure envelope of the sandstones, it would be fundamental to adapt the constitutive model to account for the Lode angle. Additionally, since by essence Flac3D is designed to perform numerical modeling in the 3D space, it would the very interesting to continue our test by increasing the depth dimension of the model to visualize evolution of the distribution of the deformation in this third dimension.

As evoked previously, the analytical tool designed to estimate the stress-path evolution from the Q-P diagram suffers several flaws. In order to obtain more accurate estimations of the failure

point, it would be judicious to resolve several issues. In particular, the shape of the failure envelope needs to be adapted in a more natural manner to any investigated sandstone to become free of the artificial and simplified estimated failure envelope. On the other hand, the combination of the burial and horizontal loading could improve the realism of the stress-path modeling. Additionally, it would be wise to implement a dynamic evolution of the failure envelope as a function of the evolving Lode angle, as soon as we have more knowledge of its influence on the shape of the envelope. Alternatively, the analysis of the stress-path evolution until failure could be envisioned in the principal stress space, where the representation of the varying yield surface as a function of the Lode angle could be more convenient (e.g. Chemenda and Mas, 2016). Furthermore, recent studies show that study of the stylolites and the deformation twinning in calcite may yield information on the intensity of the paleo-stresses in limestones (Burkhard, 1993; Lacombe, 2001; Amrouch et al., 2011; Beaudoin et al., 2016). This type of analysis seems complementary to our analytical method and could be used to better constrain the stress state at failure when limestone formations can be observed underlying or overlying the sandstone formations.

References

References

A

Agosta, F., Prasad, M., Aydin, A., 2007. Physical properties of carbonate fault rocks, fucino basin (Central Italy): implications for fault seal in platform carbonates. Geofluids 7, 19–32. doi:10.1111/j.1468-8123.2006.00158.x

Al-Hinai, S., Fisher, Q.J., Al-Busafi, B., Guise, P., Grattoni, C.A., 2008. Laboratory measurements of the relative permeability of cataclastic fault rocks: An important consideration for production simulation modelling. Mar. Pet. Geol. 25, 473–485. doi:10.1016/j.marpetgeo.2007.07.005

Amrouch, K., Beaudoin, N., Lacombe, O., Bellahsen, N., Daniel, J.-M., 2011. Paleostress magnitudes in folded sedimentary rocks. Geophys. Res. Lett. 38, L17301. doi:10.1029/2011GL048649

Anderson, E.M., 1905. The dynamics of faulting. Trans. Edinb. Geol. Soc. 8, 387–402. doi:10.1144/transed.8.3.387

Anthony, J.L., Marone, C., 2005. Influence of particle characteristics on granular friction. J. Geophys. Res. Solid Earth 110, B08409. doi:10.1029/2004JB003399

Antonellini, M., Aydin, A., 1995. Effect of Faulting on Fluid Flow in Porous Sandstones: Geometry and Spatial Distribution. AAPG Bull. 79, 642–670.

Antonellini, M., Aydin, A., 1994. Effect of Faulting on Fluid Flow in Porous Sandstones: Petrophysical Properties. AAPG Bull. 78, 355–377.

Antonellini, M., Aydin, A., Orr, L., 1999. Outcrop-Aided Characterization of a Faulted Hydrocarbon Reservoir: Arroyo Grande Oil Field, California, USA, in: Haneberg, W.C., Mozley, P.S., Moore, J.C., Goodwin, L.B. (Eds.), Faults and Subsurface Fluid Flow in the Shallow Crust, Geophysical Monograph. American Geophysical Union, pp. 7–26.

Antonellini, M.A., Aydin, A., Pollard, D.D., 1994. Microstructure of deformation bands in porous sandstones at Arches National Park, Utah. J. Struct. Geol. 16, 941–959. doi:10.1016/0191-8141(94)90077-9

Antonellini, M.A., Pollard, D.D., 1995. Distinct element modeling of deformation bands in sandstone. J. Struct. Geol. 17, 1165–1182. doi:10.1016/0191-8141(95)00001-T

Arthaud, F., Séguret, M., 1981. Les structures pyrénéennes du Languedoc et du Golfe du Lion (Sud de la France). Bull. Soc. Geol. Fr. (7) XXIII, 51–63. doi:10.2113/gssgfbull.S7-XXIII.1.51

Arzt, E., 1982. The influence of an increasing particle coordination on the densification of spherical powders. Acta Metall. 30, 1883–1890. doi:10.1016/0001-6160(82)90028-1

Awdal, A., Healy, D., Alsop, G.I., 2014. Geometrical analysis of deformation band lozenges and their scaling relationships to fault lenses. J. Struct. Geol. 66, 11–23. doi:10.1016/j.jsg.2014.05.006

Aydin, A., 1978. Small faults formed as deformation bands in sandstone. Pure Appl. Geophys. 116, 913–930. doi:10.1007/BF00876546

Aydin, A., Ahmadov, R., 2009. Bed-parallel compaction bands in aeolian sandstone: Their identification, characterization and implications. Tectonophysics 479, 277–284. doi:10.1016/j.tecto.2009.08.033

Aydin, A., Borja, R.I., Eichhubl, P., 2006. Geological and mathematical framework for failure modes in granular rock. J. Struct. Geol. 28, 83–98. doi:10.1016/j.jsg.2005.07.008

Aydin, A., Johnson, A.M., 1983. Analysis of faulting in porous sandstones. J. Struct. Geol. 5, 19–31. doi:10.1016/0191-8141(83)90004-4

Aydin, A., Johnson, A.M., 1978. Development of faults as zones of deformation bands and as slip surfaces in sandstone. Pure Appl. Geophys. 116, 931–942. doi:10.1007/BF00876547

Azéma, E., Estrada, N., Radjaï, F., 2012. Nonlinear effects of particle shape angularity in sheared granular media. Phys. Rev. E 86, 041301. doi:10.1103/PhysRevE.86.041301

B

Ballas, G., 2013. Modèle structural, mécanique et pétrophysique de la localisation de la déformation dans les grès poreux (Provence, France) (Ph.D. thesis). Université Montpellier II - UFR Sciences et Techniques.

Ballas, G., Fossen, H., Soliva, R., 2015. Factors controlling permeability of cataclastic deformation bands and faults in porous sandstone reservoirs. J. Struct. Geol. 76, 1–21. doi:10.1016/j.jsg.2015.03.013

Ballas, G., Soliva, R., Benedicto, A., Sizun, J.-P., 2014. Control of tectonic settings and large-scale faults on the basin-scale distribution of deformation bands in porous sandstone (Provence, France). Mar. Pet. Geol. 55, 142–159. doi:10.1016/j.marpetgeo.2013.12.020

Ballas, G., Soliva, R., Sizun, J.-P., Benedicto, A., Cavailhes, T., Raynaud, S., 2012. The importance of the degree of cataclasis in shear bands for fluid flow in porous sandstone, Provence, France. AAPG Bull. 96, 2167–2186. doi:10.1306/04051211097

Ballas, G., Soliva, R., Sizun, J.-P., Fossen, H., Benedicto, A., Skurtveit, E., 2013. Shear-enhanced compaction bands formed at shallow burial conditions; implications for fluid flow (Provence, France). J. Struct. Geol. 47, 3–15. doi:10.1016/j.jsg.2012.11.008

Balsamo, F., Bezerra, F.H.R., Vieira, M.M., Storti, F., 2013. Structural control on the formation of iron-oxide concretions and Liesegang bands in faulted, poorly lithified Cenozoic sandstones of the Paraíba Basin, Brazil. Geol. Soc. Am. Bull. 125, 913–931. doi:10.1130/B30686.1

Bardet, J.P., 1990. Lode Dependences for Isotropic Pressure-Sensitive Elastoplastic Materials. J. Appl. Mech. 57, 498–506. doi:10.1115/1.2897051

Bastesen, E., Braathen, A., Nøttveit, H., Gabrielsen, R.H., Skar, T., 2009. Extensional fault cores in micritic carbonate – Case studies from the Gulf of Corinth, Greece. J. Struct. Geol. 31, 403–420. doi:10.1016/j.jsg.2009.01.005

Baud, P., Klein, E., Wong, T., 2004. Compaction localization in porous sandstones: spatial evolution of damage and acoustic emission activity. J. Struct. Geol. 26, 603–624. doi:10.1016/j.jsg.2003.09.002

Baud, P., Meredith, P., Townend, E., 2012. Permeability evolution during triaxial compaction of an anisotropic porous sandstone. J. Geophys. Res. Solid Earth 117, B05203. doi:10.1029/2012JB009176

Baud, P., Vajdova, V., Wong, T., 2006. Shear-enhanced compaction and strain localization: Inelastic deformation and constitutive modeling of four porous sandstones. J. Geophys. Res. Solid Earth 111, B12401. doi:10.1029/2005JB004101

Baud, P., Zhu, W., Wong, T., 2000. Failure mode and weakening effect of water on sandstone. J. Geophys. Res. Solid Earth 1978–2012 105, 16371–16389. doi:10.1029/2000JB900087

Beaudoin, N., Koehn, D., Lacombe, O., Lecouty, A., Billi, A., Aharonov, E., Parlangeau, C., 2016. Fingerprinting stress: Stylolite and calcite twinning paleopiezometry revealing the complexity of progressive stress patterns during folding—The case of the Monte Nero anticline in the Apennines, Italy. Tectonics 35, 2016TC004128. doi:10.1002/2016TC004128

Berridge, N.G., Harris, A.L., May, F., Peacock, J.D., 1969. Geological Survey of Scotland, 1:63,360/1:50,000 geological map series - Elgin.

Bésuelle, P., 2001a. Evolution of strain localisation with stress in a sandstone: brittle and semi-brittle regimes. Phys. Chem. Earth Part A 26, 101–106.

Bésuelle, P., 2001b. Compacting and dilating shear bands in porous rock: Theoretical and experimental conditions. J. Geophys. Res. Solid Earth 106, 13435–13442. doi:10.1029/2001JB900011

Bésuelle, P., Desrues, J., Raynaud, S., 2000. Experimental characterisation of the localisation phenomenon inside a Vosges sandstone in a triaxial cell. Int. J. Rock Mech. Min. Sci. 37, 1223–1237. doi:10.1016/S1365-1609(00)00057-5

Bésuelle, P., Hall, S.A., 2011. Characterization of the Strain Localization in a Porous Rock in Plane Strain Condition Using a New True-Triaxial Apparatus. Springer Netherlands.

Bésuelle, P., Rudnicki, J.W., 2004. Localization: Shear Bands and Compaction Bands, in: Guéguen, Y., Boutéca, M. (Eds.), Mechanics of Fluid Saturated Rocks, International Geophysics Series. Elsevier, pp. 219–321.

Bjørkum, P.A., H.Oelkers, E., Nadeau, P.H., Walderhaug, O., Murphy, and W.M., 1998. Porosity Prediction in Quartzose Sandstones as a Function of Time, Temperature, Depth, Stylolite Frequency, and Hydrocarbon Saturation. AAPG Bull. 82, 637–648.

Blenkinsop, T.G., 1991. Cataclasis and processes of particle size reduction. Pure Appl. Geophys. 136, 59–86. doi:10.1007/BF00878888

Borst, R., Pamin, J., 1996. Some novel developments in finite element procedures for gradient-dependent plasticity. Int. J. Numer. Methods Eng. 39, 2477–2505. doi:10.1002/(SICI)1097-0207(19960730)39:14<2477::AID-NME962>3.0.CO;2-E

Brandenburg, J.P., Alpak, F.O., Solum, J.G., Naruk, S.J., 2012. A kinematic trishear model to predict deformation bands in a fault-propagation fold, East Kaibab monocline, Utah. AAPG Bull. 96, 109–132. doi:10.1306/05101110160

Brandes, C., Tanner, D.C., 2012. Three-dimensional geometry and fabric of shear deformation-bands in unconsolidated Pleistocene sediments. Tectonophysics 518–521, 84–92. doi:10.1016/j.tecto.2011.11.012

Burkhard, M., 1993. Calcite twins, their geometry, appearance and significance as stress-strain markers and indicators of tectonic regime: a review. J. Struct. Geol., The Geometry of Naturally Deformed Rocks 15, 351–368. doi:10.1016/0191-8141(93)90132-T

C

Cashman, S., Cashman, K., 2000. Cataclasis and deformation-band formation in unconsolidated marine terrace sand, Humboldt County, California. Geology 28, 111–114. doi:10.1130/0091-7613(2000)28<111:CADFIU>2.0.CO;2

Cavailhes, T., Soliva, R., Labaume, P., Wibberley, C., Sizun, J.-P., Gout, C., Charpentier, D., Chauvet, A., Scalabrino, B., Buatier, M., 2013. Phyllosilicates formation in faults rocks: Implications for dormant fault-sealing potential and fault strength in the upper crust. Geophys. Res. Lett. 40, 4272–4278. doi:10.1002/grl.50829

Champion, C., Choukroune, P., Clauzon, G., 2000. La déformation post-Miocène en Provence occidentale. Geodin. Acta 13, 67–85. doi:10.1016/S0985-3111(00)00114-5

Charalampidou, E.-M., Hall, S.A., Stanchits, S., Lewis, H., Viggiani, G., 2011. Characterization of shear and compaction bands in a porous sandstone deformed under triaxial compression. Tectonophysics, Thermo-Hydro-Chemo-Mechanical Couplings in Rock Physics and Rock Mechanics 503, 8–17. doi:10.1016/j.tecto.2010.09.032

Charalampidou, E.-M., Hall, S.A., Stanchits, S., Viggiani, G., Lewis, H., 2014. Shear-enhanced compaction band identification at the laboratory scale using acoustic and full-field methods. Int. J. Rock Mech. Min. Sci. 67, 240–252. doi:10.1016/j.ijrmms.2013.05.006

Chemenda, A.I., 2009. The formation of tabular compaction-band arrays: Theoretical and numerical analysis. J. Mech. Phys. Solids 57, 851–868. doi:10.1016/j.jmps.2009.01.007

Chemenda, A.I., 2007. The formation of shear-band/fracture networks from a constitutive instability: Theory and numerical experiment. J. Geophys. Res. Solid Earth 112, B11404. doi:10.1029/2007JB005026

Chemenda, A.I., Ballas, G., Soliva, R., 2014. Impact of a multilayer structure on initiation and evolution of strain localization in porous rocks: Field observations and numerical modeling.

Tectonophysics, Observational and Modelling perspectives on the Mechanical properties of the Lithosphere 631, 29–36. doi:10.1016/j.tecto.2014.01.021

Chemenda, A.I., Mas, D., 2016. Dependence of rock properties on the Lode angle: Experimental data, constitutive model, and bifurcation analysis. J. Mech. Phys. Solids 96, 477–496. doi:10.1016/j.jmps.2016.08.004

Chemenda, A.I., Nguyen, S.-H., Petit, J.-P., Ambre, J., 2011. Mode I cracking versus dilatancy banding: Experimental constraints on the mechanisms of extension fracturing. J. Geophys. Res. Solid Earth 116, B04401. doi:10.1029/2010JB008104

Chemenda, A.I., Wibberley, C., Saillet, E., 2012. Evolution of compactive shear deformation bands: Numerical models and geological data. Tectonophysics, Modelling in Geosciences 526–529, 56–66. doi:10.1016/j.tecto.2011.10.003

Childs, C., Walsh, J.J., Manzocchi, T., Strand, J., Nicol, A., Tomasso, M., Schöpfer, M.P.J., Aplin, A.C., 2007. Definition of a fault permeability predictor from outcrop studies of a faulted turbidite sequence, Taranaki, New Zealand. Geol. Soc. Lond. Spec. Publ. 292, 235–258. doi:10.1144/SP292.14

Cho, G.-C., Dodds, J., Santamarina, J.C., 2006. Particle Shape Effects on Packing Density, Stiffness, and Strength: Natural and Crushed Sands. J. Geotech. Geoenvironmental Eng. 132, 591–602. doi:10.1061/(ASCE)1090-0241(2006)132:5(591)

Chuhan, F.A., Kjeldstad, A., Bjørlykke, K., Høeg, K., 2002. Porosity loss in sand by grain crushing—experimental evidence and relevance to reservoir quality. Mar. Pet. Geol. 19, 39–53. doi:10.1016/S0264-8172(01)00049-6

Colmenares, L.B., Zoback, M.D., 2002. A statistical evaluation of intact rock failure criteria constrained by polyaxial test data for five different rocks. Int. J. Rock Mech. Min. Sci. 39, 695–729. doi:10.1016/S1365-1609(02)00048-5

Crawford, B.R., 1998. Experimental fault sealing: shear band permeability dependency on cataclastic fault gouge characteristics. Geol. Soc. Lond. Spec. Publ. 127, 27–47. doi:10.1144/GSL.SP.1998.127.01.04

Cuss, R.J., Rutter, E.H., Holloway, R.F., 2003. The application of critical state soil mechanics to the mechanical behaviour of porous sandstones. Int. J. Rock Mech. Min. Sci. 40, 847–862. doi:10.1016/S1365-1609(03)00053-4

D

Dautriat, J., Gland, N., Guelard, J., Dimanov, A., Raphanel, J.L., 2009. Axial and Radial Permeability Evolutions of Compressed Sandstones: End Effects and Shear-band Induced Permeability Anisotropy. Pure Appl. Geophys. 166, 1037–1061. doi:10.1007/s00024-009-0495-0

Davatzes, N.C., Aydin, A., Eichhubl, P., 2003. Overprinting faulting mechanisms during the development of multiple fault sets in sandstone, Chimney Rock fault array, Utah, USA. Tectonophysics 363, 1–18. doi:10.1016/S0040-1951(02)00647-9

Davatzes, N.C., Eichhubl, P., Aydin, A., 2005. Structural evolution of fault zones in sandstone by multiple deformation mechanisms: Moab fault, southeast Utah. GSA Bull. 117, 135–148. doi:10.1130/B25473.1

de Joussineau, G., Aydin, A., 2007. The evolution of the damage zone with fault growth in sandstone and its multiscale characteristics. J. Geophys. Res. Solid Earth 112, B12401. doi:10.1029/2006JB004711

Delfaud, J., Dubois, P., 1984. Le Bassin du Sud-Est, in: Gubler, Y. (Ed.), Dynamique des bassins sédimentaires. Livre Jubilaire. BRGM, Orléans, France.

Deng, S., Aydin, A., 2012. Distribution of compaction bands in 3D in an aeolian sandstone: The role of cross-bed orientation. Tectonophysics 574, 204–218. doi:10.1016/j.tecto.2012.08.037

Doelling, H.H., 2008. Geological map of Kanab 30 x 60-minute quadrangle, Kane and Washington Counties, Utah, and Coconino and Mohave Counties, Arizona.

Doelling, H.H., Kuehne, P.A., Willis, G.C., Buck Ehler, J., 2015. Geologic map of the San Rafael Desert 30 x 60-minute quadrangle, Emery and Grand Counties, Utah.

Doelling, H.H., Willis, G.C., 2006. Geologic map of the Smoky Mountains 30x60-minute quadrangle, Kane and San Juan Counties, Utah, and Coconino County, Arizona.

Du Bernard, X., Eichhubl, P., Aydin, A., 2002a. Dilation bands: A new form of localized failure in granular media. Geophys. Res. Lett. 29, 2176. doi:10.1029/2002GL015966

Du Bernard, X., Labaume, P., Darcel, C., Davy, P., Bour, O., 2002b. Cataclastic slip band distribution in normal fault damage zones, Nubian sandstones, Suez rift. J. Geophys. Res. Solid Earth 107, ETG 6-1. doi:10.1029/2001JB000493

E

Edwards, H.E., Becker, A.D., Howell, J.A., 1993. Compartmentalization of an aeolian sandstone by structural heterogeneities: Permo-Triassic Hopeman Sandstone, Moray Firth, Scotland. Geol. Soc. Lond. Spec. Publ. 73, 339–365. doi:10.1144/GSL.SP.1993.073.01.20

Eichhubl, P., Hooker, J.N., Laubach, S.E., 2010. Pure and shear-enhanced compaction bands in Aztec Sandstone. J. Struct. Geol., Structural Diagenesis 32, 1873–1886. doi:10.1016/j.jsg.2010.02.004

Eichhubl, P., Taylor, W.L., Pollard, D.D., Aydin, A., 2004. Paleo-fluid flow and deformation in the Aztec Sandstone at the Valley of Fire, Nevada—Evidence for the coupling of hydrogeologic, diagenetic, and tectonic processes. Geol. Soc. Am. Bull. 116, 1120–1136. doi:10.1130/B25446.1

El Bied, A., Sulem, J., Martineau, F., 2002. Microstructure of shear zones in Fontainebleau sandstone. Int. J. Rock Mech. Min. Sci. 39, 917–932. doi:10.1016/S1365-1609(02)00068-0

El Gonnouni, M., 2011. Résistance au cisaillement des sols, in: Introduction À La Mécanique Des Sols. ECOLE HASSANIA DES TRAVAUX PUBLICS - Département ponts chaussées et transports.

Ellevset, S.O., Knipe, R.J., Olsen, T.S., Fisher, Q.J., Jones, G., 1998. Fault controlled communication in the Sleipner Vest Field, Norwegian Continental Shelf; detailed, quantitative input for reservoir simulation and well planning. Geol. Soc. Lond. Spec. Publ. 147, 283–297. doi:10.1144/GSL.SP.1998.147.01.19

Engelder, J.T., 1974. Cataclasis and the Generation of Fault Gouge. Geol. Soc. Am. Bull. 85, 1515–1522. doi:10.1130/0016-7606(1974)85<1515:CATGOF>2.0.CO;2

Estrada, N., Azéma, E., Radjai, F., Taboada, A., 2011. Identification of rolling resistance as a shape parameter in sheared granular media. Phys. Rev. E 84, 011306. doi:10.1103/PhysRevE.84.011306

Estrada, N., Taboada, A., 2013. Yield surfaces and plastic potentials of cemented granular materials from discrete element simulations. Comput. Geotech. 49, 62–69. doi:10.1016/j.compgeo.2012.11.001

Estrada, N., Taboada, A., Radjaï, F., 2008. Shear strength and force transmission in granular media with rolling resistance. Phys. Rev. E 78, 021301. doi:10.1103/PhysRevE.78.021301

Exner, U., Tschegg, C., 2012. Preferential cataclastic grain size reduction of feldspar in deformation bands in poorly consolidated arkosic sands. J. Struct. Geol. 43, 63–72. doi:10.1016/j.jsg.2012.08.005

F

Farrell, N.J.C., Healy, D., Taylor, C.W., 2014. Anisotropy of permeability in faulted porous sandstones. J. Struct. Geol. 63, 50–67. doi:10.1016/j.jsg.2014.02.008

Faulkner, D.R., Jackson, C.A.L., Lunn, R.J., Schlische, R.W., Shipton, Z.K., Wibberley, C.A.J., Withjack, M.O., 2010. A review of recent developments concerning the structure, mechanics and fluid flow properties of fault zones. J. Struct. Geol., Fault Zones 32, 1557–1575. doi:10.1016/j.jsg.2010.06.009

Ferry, S., 1999. Apport des forages ANDRA de Marcoule à la connaissance de la marge crétacée rhodanienne, in: Etude du Gard Rhodanien, Actes des Journées Scientifiques CNRS/ANDRA. EDP Sciences, Bagnols-sur-Cèze, pp. 63–91.

Fischer, C., Waldmann, S., von Eynatten, H., 2013. Spatial variation in quartz cement type and concentration: An example from the Heidelberg formation (Teufelsmauer outcrops), Upper Cretaceous Subhercynian Basin, Germany. Sediment. Geol. 291, 48–61. doi:10.1016/j.sedgeo.2013.03.009

Fisher, Q.J., Casey, M., Harris, S.D., Knipe, R.J., 2003. Fluid-flow properties of faults in sandstone: The importance of temperature history. Geology 31, 965–968. doi:10.1130/G19823.1

Fisher, Q.J., Knipe, R.J., 2001. The permeability of faults within siliciclastic petroleum reservoirs of the North Sea and Norwegian Continental Shelf. Mar. Pet. Geol. 18, 1063–1081. doi:10.1016/S0264-8172(01)00042-3

Fisher, Q.J., Knipe, R.J., 1998. Fault sealing processes in siliciclastic sediments. Geol. Soc. Lond. Spec. Publ. 147, 117–134. doi:10.1144/GSL.SP.1998.147.01.08

Flinn, D., 1962. On Folding During Three-Dimensional Progressive Deformation. Q. J. Geol. Soc. 118, 385–428. doi:10.1144/gsjgs.118.1.0385

Flodin, E., Gerdes, M., Aydin, A., Wiggins, W.D., 2005. Petrophysical Properties and Sealing Capacity of Fault Rock, Aztec Sandstone, Nevada 197–217. doi:10.1306/1033724M853136

Flodin, E.A., 2003. Structural evolution, petrophysics, and large-scale permeabilty of faults in sandstone, Valley of Fire, Nevada (Ph.D. thesis). Stanford University.

Ford, M., Stahel, U., 1995. The geometry of a deformed carbonate slope-basin transition: The Ventoux-Lure fault zone, SE France. Tectonics 14, 1393–1410. doi:10.1029/95TC02522

Fortin, J., Schubnel, A., Guéguen, Y., 2005. Elastic wave velocities and permeability evolution during compaction of Bleurswiller sandstone. Int. J. Rock Mech. Min. Sci., Rock Physics and Geomechanics Rock Physics and Geomechanics 42, 873–889. doi:10.1016/j.ijrmms.2005.05.002

Fortin, J., Stanchits, S., Dresen, G., Gueguen, Y., 2009. Acoustic Emissions Monitoring during Inelastic Deformation of Porous Sandstone: Comparison of Three Modes of Deformation, in: Rock Physics and Natural Hazards, Pageoph Topical Volumes. Birkhäuser Basel, pp. 823–841. doi:10.1007/978-3-0346-0122-1_5

Fossen, H., 2016. Structural Geology. Cambridge University Press.

Fossen, H., 2010. Deformation bands formed during soft-sediment deformation: Observations from SE Utah. Mar. Pet. Geol. 27, 215–222. doi:10.1016/j.marpetgeo.2009.06.005

Fossen, H., Bale, A., 2007. Deformation bands and their influence on fluid flow. AAPG Bull. 91, 1685–1700. doi:10.1306/07300706146

Fossen, H., Hesthammer, J., 1997. Geometric analysis and scaling relations of deformation bands in porous sandstone. J. Struct. Geol. 19, 1479–1493. doi:10.1016/S0191-8141(97)00075-8

Fossen, H., Rotevatn, A., 2012. Characterization of deformation bands associated with normal and reverse stress states in the Navajo Sandstone, Utah - Discussion. AAPG Bull. 96, 608–623.

Fossen, H., Schultz, R.A., Shipton, Z.K., Mair, K., 2007. Deformation bands in sandstone: a review. J. Geol. Soc. 164, 755–769. doi:10.1144/0016-76492006-036

Fossen, H., Schultz, R.A., Torabi, A., 2011. Conditions and implications for compaction band formation in the Navajo Sandstone, Utah. J. Struct. Geol. 33, 1477–1490. doi:10.1016/j.jsg.2011.08.001

Fossen, H., Soliva, R., Ballas, G., Trzaskos, B., Cavalcante, C., Schultz, R.A., 2017. A review of deformation bands in reservoir sandstones: geometries, mechanisms and distribution. Geol. Soc. Lond. Spec. Publ. 459, SP459.4. doi:10.1144/SP459.4

Fowles, J., Burley, S., 1994. Textural and permeability characteristics of faulted, high porosity sandstones. Mar. Pet. Geol. 11, 608–623. doi:10.1016/0264-8172(94)90071-X

French, M.W., Worden, R.H., Mariani, E., Larese, R.E., Mueller, R.R., Kliewer, C.E., 2012. Microcrystalline Quartz Generation and the Preservation of Porosity In Sandstones: Evidence from

the Upper Cretaceous of the Subhercynian Basin, Germany. J. Sediment. Res. 82, 422–434. doi:10.2110/jsr.2012.39

Friedman, M., Logan, J.M., Rigert, J.A., 1974. Glass-Indurated Quartz Gouge in Sliding-Friction Experiments on Sandstone. GSA Bull. 85, 937–942. doi:10.1130/0016-7606(1974)85<937:GQGISE>2.0.CO;2

Frostick, L., Reid, I., Jarvis, J., Eardley, H., 1988. Triassic sediments of the Inner Moray Firth, Scotland: early rift deposits. J. Geol. Soc. 145, 235–248. doi:10.1144/gsjgs.145.2.0235

Fulljames, J.R., Zijerveld, L.J.J., Franssen, R.C.M.W., 1997. Fault seal processes: systematic analysis of fault seals over geological and production time scales, in: Koestler, P.M.-P. and A.G. (Ed.), Norwegian Petroleum Society Special Publications, Hydrocarbon SealsImportance for Exploration and Production. Elsevier, pp. 51–59.

G

Gallagher Jr, J.J., Friedman, M., Handin, J., Sowers, G.M., 1974. Experimental studies relating to microfracture in sandstone. Tectonophysics 21, 203–247. doi:10.1016/0040-1951(74)90053-5

Gibson, R.G., 1998. Physical character and fluid-flow properties of sandstone-derived fault zones. Geol. Soc. Lond. Spec. Publ. 127, 83–97. doi:10.1144/GSL.SP.1998.127.01.07

Gibson, R.G., 1994. Fault-Zone Seals in Siliciclastic Strata of the Columbus Basin, Offshore Trinidad. AAPG Bull. 78, 1372–1385.

Glennie, K.W., Buller, A.T., 1983. The Permian Weissliegend of NW Europe: The partial deformation of aeolian dune sands caused by the Zechstein transgression. Sediment. Geol. 35, 43–81. doi:10.1016/0037-0738(83)90069-6

Gratier, J.-P., Guiguet, R., Renard, F., Jenatton, L., Bernard, D., 2009. A pressure solution creep law for quartz from indentation experiments. J. Geophys. Res. Solid Earth 114, B03403. doi:10.1029/2008JB005652

Guéguen, Y., Fortin, J., 2005. Mécanique des roches en géologie: des processus microscopiques au comportement macroscopique. Presented at the Microstructure et Propriétés des Matériaux, ENPC.

Gundersen, E., Renard, F., Dysthe, D.K., Bjørlykke, K., Jamtveit, B., 2002. Coupling between pressure solution creep and diffusive mass transport in porous rocks. J. Geophys. Res. Solid Earth 107, 2317. doi:10.1029/2001JB000287

Guo, Y., Morgan, J.K., 2006. The frictional and micromechanical effects of grain comminution in fault gouge from distinct element simulations. J. Geophys. Res. Solid Earth 111, B12406. doi:10.1029/2005JB004049

H

Hadizadeh, J., Johnson, W.K., 2003. Estimating local strain due to comminution in experimental cataclastic textures. J. Struct. Geol. 25, 1973–1979. doi:10.1016/S0191-8141(03)00016-6

Hadizadeh, J., Sehhati, R., Tullis, T., 2010. Porosity and particle shape changes leading to shear localization in small-displacement faults. J. Struct. Geol., Fault Zones 32, 1712–1720. doi:10.1016/j.jsg.2010.09.010

Haimson, B., Chang, C., 2000. A new true triaxial cell for testing mechanical properties of rock, and its use to determine rock strength and deformability of Westerly granite. Int. J. Rock Mech. Min. Sci. 37, 285–296. doi:10.1016/S1365-1609(99)00106-9

Harris, S.D., McAllister, E., Knipe, R.J., Odling, N.E., 2003. Predicting the three-dimensional population characteristics of fault zones: a study using stochastic models. J. Struct. Geol. 25, 1281–1299. doi:10.1016/S0191-8141(02)00158-X

Hesthammer, J., Fossen, H., 2001. Structural core analysis from the Gullfaks area, northern North Sea. Mar. Pet. Geol. 18, 411–439. doi:10.1016/S0264-8172(00)00068-4

Hoek, E., Brown, E.T., 1980. UNDERGROUND EXCAVATIONS IN ROCK.

I

Ingraham, M.D., Issen, K.A., Holcomb, D.J., 2013. Response of Castlegate sandstone to true triaxial states of stress. J. Geophys. Res. Solid Earth 118, 536–552. doi:10.1002/jgrb.50084

Issen, K.A., 2002. The influence of constitutive models on localization conditions for porous rock. Eng. Fract. Mech. 69, 1891–1906. doi:10.1016/S0013-7944(02)00067-X

Issen, K.A., Rudnicki, J.W., 2000. Conditions for compaction bands in porous rock. J. Geophys. Res. Solid Earth 105, 21529–21536. doi:10.1029/2000JB900185

Iwashita, K., Oda, M., 2000. Micro-deformation mechanism of shear banding process based on modified distinct element method. Powder Technol. 109, 192–205. doi:10.1016/S0032-5910(99)00236-3

J

Jamison, W.R., Stearns, D.W., 1982. Tectonic Deformation of Wingate Sandstone, Colorado National Monument. AAPG Bull. 66, 2584–2608.

Johansen, T.E.S., Fossen, H., 2008. Internal geometry of fault damage zones in interbedded siliciclastic sediments. Geol. Soc. Lond. Spec. Publ. 299, 35–56. doi:10.1144/SP299.3

Johansen, T.E.S., Fossen, H., Kluge, R., 2005. The impact of syn-faulting porosity reduction on damage zone architecture in porous sandstone: an outcrop example from the Moab Fault, Utah. J. Struct. Geol. 27, 1469–1485. doi:10.1016/j.jsg.2005.01.014

Jourde, H., Flodin, E.A., Aydin, A., Durlofsky, L.J., Wen, X.-H., 2002. Computing permeability of fault zones in eolian sandstone from outcrop measurements. AAPG Bull. 86.

K

Kaproth, B.M., Cashman, S.M., Marone, C., 2010. Deformation band formation and strength evolution in unlithified sand: The role of grain breakage. J. Geophys. Res. Solid Earth 115, B12103. doi:10.1029/2010JB007406

Karner, S.L., Chester, J.S., Chester, F.M., Kronenberg, A.K., Jr, A.H., 2005. Laboratory deformation of granular quartz sand: Implications for the burial of clastic rocks. AAPG Bull. 89, 603–625. doi:10.1306/12200404010

Kettermann, M., Thronberens, S., Juarez, O., Lajos Urai, J., Ziegler, M., Asmus, S., Kruger, U., 2016. Mechanisms of clay smear formation in unconsolidated sediments - insights from 3-D observations of excavated normal faults. Solid Earth 7, 789–815. doi:10.5194/se-7-789-2016

Klein, E., Reuschlé, T., 2004. A pore crack model for the mechanical behaviour of porous granular rocks in the brittle deformation regime. Int. J. Rock Mech. Min. Sci. 41, 975–986. doi:10.1016/j.ijrmms.2004.03.003

Klimczak, C., Schultz, R.A., 2013. Fault damage zone origin of the Teufelsmauer, Subhercynian Cretaceous Basin, Germany. Int. J. Earth Sci. 102, 121–138. doi:10.1007/s00531-012-0794-z

Klimczak, C., Soliva, R., Schultz, R.A., Chéry, J., 2011. Sequential growth of deformation bands in a multilayer sequence. J. Geophys. Res. Solid Earth 116, B09209. doi:10.1029/2011JB008365

Kristensen, M.B., Childs, C., Olesen, N.Ø., Korstgård, J.A., 2013. The microstructure and internal architecture of shear bands in sand–clay sequences. J. Struct. Geol. 46, 129–141. doi:10.1016/j.jsg.2012.09.015

L

Labaume, P., Moretti, I., 2001. Diagenesis-dependence of cataclastic thrust fault zone sealing in sandstones. Example from the Bolivian Sub-Andean Zone. J. Struct. Geol. 23, 1659–1675. doi:10.1016/S0191-8141(01)00024-4

Lacombe, O., 2001. Paleostress magnitudes associated with development of mountain belts: Insights from tectonic analyses of calcite twins in the Taiwan Foothills. Tectonics 20, 834–849. doi:10.1029/2001TC900019

Lanatà, P., 2014. Full-field experimental characterization of mechanical behaviour and failure in a porous rock in plane strain compression: homogeneous deformation and strain localization (Ph.D. thesis). Université de Grenoble.

Lander, R.H., Larese, R.E., Bonnell, L.M., 2008. Toward more accurate quartz cement models: The importance of euhedral versus noneuhedral growth rates. AAPG Bull. 92, 1537–1563. doi:10.1306/07160808037

Leveille, G.P., Knipe, R., More, C., Ellis, D., Dudley, G., Jones, G., Fisher, Q.J., Allinson, G., 1997. Compartmentalization of Rotliegendes gas reservoirs by sealing faults, Jupiter Fields area, southern North Sea. Geol. Soc. Lond. Spec. Publ. 123, 87–104. doi:10.1144/GSL.SP.1997.123.01.06

Lewis, H., Couples, G.D., 1993. Production evidence for geological heterogeneities in the Anschutz Ranch East Field, western USA. Geol. Soc. Lond. Spec. Publ. 73, 321–338. doi:10.1144/GSL.SP.1993.073.01.19

Lindanger, M., Gabrielsen, R.H., Braathen, A., 2007. Analysis of rock lenses in extensional faults. Nor. J. Geol. 87, 361–372.

Logan, J.M., Rauenzahn, K.A., 1987. Frictional dependence of gouge mixtures of quartz and montmorillonite on velocity, composition and fabric. Tectonophysics 144, 87–108. doi:10.1016/0040-1951(87)90010-2

Lommatzsch, M., Exner, U., Gier, S., Grasemann, B., 2015. Structural and chemical controls of deformation bands on fluid flow: Interplay between cataclasis and diagenetic alteration. Aapg Bull. 99, 689–710. doi:10.1306/10081413162

Lothe, A.E., Gabrielsen, R.H., Hagen, N.B., Larsen, B.T., 2002. An experimental study of the texture of deformation bands: effects on the porosity and permeability of sandstones. Pet. Geosci. 8, 195–207. doi:10.1144/petgeo.8.3.195

M

Ma, X., Haimson, B., 2013. Failure characteristics of two porous sandstones subjected to true triaxial testing, in: Rock Characterisation, Modelling and Engineering Design Methods. CRC Press, pp. 93–98. doi:10.1201/b14917-15

Mair, K., Elphick, S., Main, I., 2002a. Influence of confining pressure on the mechanical and structural evolution of laboratory deformation bands. Geophys. Res. Lett. 29, 49–1. doi:10.1029/2001GL013964

Mair, K., Frye, K.M., Marone, C., 2002b. Influence of grain characteristics on the friction of granular shear zones. J. Geophys. Res. Solid Earth 107, 2219. doi:10.1029/2001JB000516

Marone, C., Scholz, C.H., 1989. Particle-size distribution and microstructures within simulated fault gouge. J. Struct. Geol., Friction phenomena in rock 11, 799–814. doi:10.1016/0191-8141(89)90099-0

Mas, D., Chemenda, A.I., 2015. An experimentally constrained constitutive model for geomaterials with simple friction–dilatancy relation in brittle to ductile domains. Int. J. Rock Mech. Min. Sci. 77, 257–264. doi:10.1016/j.ijrmms.2015.04.013

Mavko, G., Mukerji, T., Dvorkin, J., 2009. The Rock Physics Handbook: Tools for Seismic Analysis of Porous Media. Cambridge University Press.

Medeiros, W.E., do Nascimento, A.F., Alves da Silva, F.C., Destro, N., Demétrio, J.G.A., 2010. Evidence of hydraulic connectivity across deformation bands from field pumping tests: Two examples from Tucano Basin, NE Brazil. J. Struct. Geol., Fault Zones 32, 1783–1791. doi:10.1016/j.jsg.2009.08.019

Menéndez, B., Zhu, W., Wong, T.-F., 1996. Micromechanics of brittle faulting and cataclastic flow in Berea sandstone. J. Struct. Geol. 18, 1–16. doi:10.1016/0191-8141(95)00076-P

Mesri, G., Vardhanabhuti, B., 2009. Compression of granular materials. Can. Geotech. J. 46, 369–392. doi:10.1139/T08-123

Milliken, K.L., Reed, R.M., Laubach, S.E., 2005. Quantifying Compaction and Cementation in Deformation Bands in Porous Sandstones, in: Sorkhabi, R., Tsuji, Y. (Eds.), Faults, Fluid Flow, and Petroleum Traps, AAPG Memoir. pp. 237–249.

Mitchell, J.K., Soga, K., 2005. Fundamentals of Soil Behavior, third edition. ed. John Wiley and Sons.

Mogi, K., 1971. Effect of the triaxial stress system on the failure of dolomite and limestone. Tectonophysics 11, 111–127. doi:10.1016/0040-1951(71)90059-X

Molenaar, N., Cyziene, J., Sliaupa, S., 2007. Quartz cementation mechanisms and porosity variation in Baltic Cambrian sandstones. Sediment. Geol. 195, 135–159. doi:10.1016/j.sedgeo.2006.07.009

Mollema, P.N., Antonellini, M.A., 1996. Compaction bands: a structural analog for anti-mode I cracks in aeolian sandstone. Tectonophysics 267, 209–228. doi:10.1016/S0040-1951(96)00098-4

Morgan, J.K., 1999. Numerical simulations of granular shear zones using the distinct element method: 2. Effects of particle size distribution and interparticle friction on mechanical behavior. J. Geophys. Res. Solid Earth 104, 2721–2732. doi:10.1029/1998JB900055

Myers, R., Aydin, A., 2004. The evolution of faults formed by shearing across joint zones in sandstone. J. Struct. Geol. 26, 947–966. doi:10.1016/j.jsg.2003.07.008

N

Nguyen, S.-H., Chemenda, A.I., Ambre, J., 2011. Influence of the loading conditions on the mechanical response of granular materials as constrained from experimental tests on synthetic rock analoguematerial. Int. J. Rock Mech. Min. Sci. 48, 103–115. doi:10.1016/j.ijrmms.2010.09.010

Ngwenya, B.T., Elphick, S.C., Main, I.G., Shimmield, G.B., 2000. Experimental constraints on the diagenetic self-sealing capacity of faults in high porosity rocks. Earth Planet. Sci. Lett. 183, 187–199. doi:10.1016/S0012-821X(00)00261-2

Ngwenya, B.T., Kwon, O., Elphick, S.C., Main, I.G., 2003. Permeability evolution during progressive development of deformation bands in porous sandstones. J. Geophys. Res. Solid Earth 108, 2343. doi:10.1029/2002JB001854

Nicol, A., Childs, C., Walsh, J.J., Schafer, K.W., 2013. A geometric model for the formation of deformation band clusters. J. Struct. Geol. 55, 21–33. doi:10.1016/j.jsg.2013.07.004

O

Ogilvie, S.R., Glover, P.W.J., 2001. The petrophysical properties of deformation bands in relation to their microstructure. Earth Planet. Sci. Lett. 193, 129–142. doi:10.1016/S0012-821X(01)00492-7

Ogilvie, S.R., Orribo, J.M., Glover, P.W.J., 2001. The influence of deformation bands upon fluid flow using profile permeametry and positron emission tomography. Geophys. Res. Lett. 28, 61–64. doi:10.1029/2000GL008507

Olsson, W.A., 1999. Theoretical and experimental investigation of compaction bands in porous rock. J. Geophys. Res. Solid Earth 104, 7219–7228. doi:10.1029/1998JB900120

P

Parnell, J., Watt, G.R., Middleton, D., Kelly, J., Baron, M., 2004. Deformation Band Control on Hydrocarbon Migration. J. Sediment. Res. 74, 552–560. doi:10.1306/121703740552

Parry, W.T., Chan, M.A., Beitler, B., 2004. Chemical bleaching indicates episodes of fluid flow in deformation bands in sandstone. AAPG Bull. 88, 175–191. doi:10.1306/09090303034

Pittman, E.D., 1981. Effect of Fault-Related Granulation on Porosity and Permeability of Quartz Sandstones, Simpson Group (Ordovician), Oklahoma. AAPG Bull. 65, 2381–2387.

Poliakov, A.N.B., Herrmann, H.J., 1994. Self-organized criticality of plastic shear bands in rocks. Geophys. Res. Lett. 21, 2143–2146. doi:10.1029/94GL02005

Pollington, A.D., Kozdon, R., Valley, J.W., 2011. Evolution of quartz cementation during burial of the Cambrian Mount Simon Sandstone, Illinois Basin: In situ microanalysis of δ18O. Geology 39, 1119–1122. doi:10.1130/G32195.1

Q

Quinn, O.F., 2005. Fault controlled fluid flow and quartz cementation in porous sandstones (Ph.D. thesis). The University of Edinburgh.

R

Rawling, G.C., Goodwin, L.B., 2006. Structural record of the mechanical evolution of mixed zones in faulted poorly lithified sediments, Rio Grande rift, New Mexico, USA. J. Struct. Geol. 28, 1623–1639. doi:10.1016/j.jsg.2006.06.008

Rawling, G.C., Goodwin, L.B., 2003. Cataclasis and particulate flow in faulted, poorly lithified sediments. J. Struct. Geol. 25, 317–331.

Renard, F., Ortoleva, P., Gratier, J.P., 1997. Pressure solution in sandstones: influence of clays and dependence on temperature and stress. Tectonophysics 280, 257–266. doi:10.1016/S0040-1951(97)00039-5

Rigby, J.K., Beus, S.S., 1987. Stratigraphy and Structure of the San Rafael Reef, Utah," A Major Monocline of the Colorado Plateau, in: Rocky Mountain Section of the Geological Society of America: Decade of North American Geology, Centennial Field Guide Volume 2. Geological Society of America, pp. 269–273.

Roberts, A.M., Badley, M.E., Price, J.D., Huck, I.W., 1990. The structural history of a transtensional basin: Inner Moray Firth, NE Scotland. J. Geol. Soc. 147, 87–103. doi:10.1144/gsjgs.147.1.0087

Rogers, J.J.W., Head, W.B., 1961. Relationships Between Porosity, Median Size, and Sorting Coefficients of Synthetic Sands. J. Sediment. Res. 31.

Rotevatn, A., Torabi, A., Fossen, H., Braathen, A., 2008. Slipped deformation bands: A new type of cataclastic deformation bands in Western Sinai, Suez rift, Egypt. J. Struct. Geol. 30, 1317–1331. doi:10.1016/j.jsg.2008.06.010

Roure, F., Brun, J.-P., Colletta, B., Van den Driessche, J., 1992. Geometry and kinematics of extensional structures in the Alpine Foreland Basin of southeastern France. J. Struct. Geol. 14, 50.-519. doi:10.1016/0191-8141(92)90153-N

Rudnicki, J.W., Rice, J.R., 1975. Conditions for the localization of deformation in pressure-sensitive dilatant materials. J. Mech. Phys. Solids 23, 371–394. doi:10.1016/0022-5096(75)90001-0

Rutter, E.H., Glover, C.T., 2012. The deformation of porous sandstones; are Byerlee friction and the critical state line equivalent? J. Struct. Geol. 44, 129–140. doi:10.1016/j.jsg.2012.08.014

S

Saïag, J., Brigaud, B., Portier, É., Desaubliaux, G., Bucherie, A., Miska, S., Pagel, M., 2016. Sedimentological control on the diagenesis and reservoir quality of tidal sandstones of the Upper Cape Hay Formation (Permian, Bonaparte Basin, Australia). Mar. Pet. Geol. 77, 597–624. doi:10.1016/j.marpetgeo.2016.07.002

Saillet, E., 2009. La localisation de la déformation dans les grès poreux : caractérisation d'un analogue de réservoirs gréseux faillés dans le Bassin du Sud-Est, Provence, France (Ph.D. thesis). Université de Nice-Sophia Antipolis, UFR Sciences.

Saillet, E., Wibberley, C.A.J., 2013. Permeability and flow impact of faults and deformation bands in high-porosity sand reservoirs: Southeast Basin, France, analog. AAPG Bull. 97, 437–464. doi:10.1306/09071211191

Saillet, E., Wibberley, C.A.J., 2010. Evolution of cataclastic faulting in high-porosity sandstone, Bassin du Sud-Est, Provence, France. J. Struct. Geol., Fault Zones 32, 1590–1608. doi:10.1016/j.jsg.2010.02.007

Sammis, C., King, G., Biegel, R., 1987. The kinematics of gouge deformation. Pure Appl. Geophys. 125, 777–812. doi:10.1007/BF00878033

Sample, J.C., Woods, S., Bender, E., Loveall, M., 2006. Relationship between deformation bands and petroleum migration in an exhumed reservoir rock, Los Angeles Basin, California, USA. Geofluids 6, 105–112. doi:10.1111/j.1468-8123.2005.00131.x

Scholz, C.H., 2002. The Mechanics of Earthquakes and Faulting. Cambridge University Press.

Schueller, S., Braathen, A., Fossen, H., Tveranger, J., 2013. Spatial distribution of deformation bands in damage zones of extensional faults in porous sandstones: Statistical analysis of field data. J. Struct. Geol. 52, 148–162. doi:10.1016/j.jsg.2013.03.013

Schultz, R.A., 2011. Relationship of compaction bands in Utah to Laramide fault-related folding. Earth Planet. Sci. Lett. 304, 29–35. doi:10.1016/j.epsl.2011.01.001

Schultz, R.A., Fossen, H., 2002. Displacement–length scaling in three dimensions: the importance of aspect ratio and application to deformation bands. J. Struct. Geol. 24, 1389–1411. doi:10.1016/S0191-8141(01)00146-8

Schultz, R.A., Klimczak, C., Fossen, H., Olson, J.E., Exner, U., Reeves, D.M., Soliva, R., 2013. Statistical tests of scaling relationships for geologic structures. J. Struct. Geol. 48, 85–94. doi:10.1016/j.jsg.2012.12.005

Schultz, R.A., Okubo, C.H., Fossen, H., 2010. Porosity and grain size controls on compaction band formation in Jurassic Navajo Sandstone. Geophys. Res. Lett. 37, L22306. doi:10.1029/2010GL044909

Schultz, R.A., Siddharthan, R., 2005. A general framework for the occurrence and faulting of deformation bands in porous granular rocks. Tectonophysics 411, 1–18. doi:10.1016/j.tecto.2005.07.008

Scott, T.E., 2007. The effects of stress paths on acoustic velocities and 4D seismic imaging. Lead. Edge 26, 602–608. doi:10.1190/1.2737101

Scott, T.E., Nielsen, K.C., 1991. The effects of porosity on the brittle-ductile transition in sandstones. J. Geophys. Res. Solid Earth 96, 405–414. doi:10.1029/90JB02069

Séranne, M., Benedicto, A., Labaum, P., Truffert, C., Pascal, G., 1995. Structural style and evolution of the Gulf of Lion Oligo-Miocene rifting: role of the Pyrenean orogeny. Mar. Pet. Geol., Integrated Basin Studies 12, 809–820. doi:10.1016/0264-8172(95)98849-Z

Sheorey, P.R., 1994. A theory for In Situ stresses in isotropic and transverseley isotropic rock. Int. J. Rock Mech. Min. Sci. Geomech. Abstr. 31, 23–34. doi:10.1016/0148-9062(94)92312-4

Shipton, Z.K., Cowie, P.A., 2003. A conceptual model for the origin of fault damage zone structures in high-porosity sandstone. J. Struct. Geol. 25, 333–344. doi:10.1016/S0191-8141(02)00037-8

Shipton, Z.K., Cowie, P.A., 2001. Damage zone and slip-surface evolution over μm to km scales in high-porosity Navajo sandstone, Utah. J. Struct. Geol. 23, 1825–1844. doi:10.1016/S0191-8141(01)00035-9

Shipton, Z.K., Evans, J.P., Robeson, K.R., Forster, C.B., Snelgrove, S., 2002. Structural Heterogeneity and Permeability in Faulted Eolian Sandstone: Implications for Subsurface Modeling of Faults. AAPG Bull. 86, 863–883. doi:10.1306/61EEDBC0-173E-11D7-8645000102C1865D

Sibson, R.H., 1977. Fault rocks and fault mechanisms. J. Geol. Soc. 133, 191–213. doi:10.1144/gsjgs.133.3.0191

Sigda, J.M., Wilson, J.L., 2003. Are faults preferential flow paths through semiarid and arid vadose zones? Water Resour. Res. 39, 1225. doi:10.1029/2002WR001406

Soliva, R., Ballas, G., Fossen, H., Philit, S., 2016. Tectonic regime controls clustering of deformation bands in porous sandstone. Geology 44, 423–426. doi:10.1130/G37585.1

Soliva, R., Schultz, R.A., Ballas, G., Taboada, A., Wibberley, C., Saillet, E., Benedicto, A., 2013. A model of strain localization in porous sandstone as a function of tectonic setting, burial and material

properties; new insight from Provence (southern France). J. Struct. Geol. 49, 50–63. doi:10.1016/j.jsg.2012.11.011

Solum, J.G., Brandenburg, J.P., Naruk, S.J., Kostenko, O.V., Wilkins, S.J., Schultz, R.A., 2010a. Characterization of deformation bands associated with normal and reverse stress states in the Navajo Sandstone, Utah. AAPG Bull. 94, 1453–1475. doi:10.1306/01051009137

Solum, J.G., Davatzes, N.C., Lockner, D.A., 2010b. Fault-related clay authigenesis along the Moab Fault: Implications for calculations of fault rock composition and mechanical and hydrologic fault zone properties. J. Struct. Geol., Structural Diagenesis 32, 1899–1911. doi:10.1016/j.jsg.2010.07.009

Stanchits, S., Fortin, J., Gueguen, Y., Dresen, G., 2009. Initiation and Propagation of Compaction Bands in Dry and Wet Bentheim Sandstone, in: Vinciguerra, S., Bernabé, Y. (Eds.), Rock Physics and Natural Hazards, Pageoph Topical Volumes. Birkhäuser Basel, pp. 846–868. doi:10.1007/978-3-0346-0122-1_6

Stefanov, Y.P., Chertov, M.A., Aidagulov, G.R., Myasnikov, A.V., 2011. Dynamics of inelastic deformation of porous rocks and formation of localized compaction zones studied by numerical modeling. J. Mech. Phys. Solids 59, 2323–2340. doi:10.1016/j.jmps.2011.08.002

Sternlof, K.R., Karimi-Fard, M., Pollard, D.D., Durlofsky, L.J., 2006. Flow and transport effects of compaction bands in sandstone at scales relevant to aquifer and reservoir management. Water Resour. Res. 42, W07425. doi:10.1029/2005WR004664

Sternlof, K.R., Rudnicki, J.W., Pollard, D.D., 2005. Anticrack inclusion model for compaction bands in sandstone. J. Geophys. Res. Solid Earth 110, B11403. doi:10.1029/2005JB003764

Sulem, J., Ouffroukh, H., 2006. Shear banding in drained and undrained triaxial tests on a saturated sandstone: Porosity and permeability evolution. Int. J. Rock Mech. Min. Sci. 43, 292–310. doi:10.1016/j.ijrmms.2005.07.001

Sun, W., Andrade, J.E., Rudnicki, J.W., Eichhubl, P., 2011. Connecting microstructural attributes and permeability from 3D tomographic images of in situ shear-enhanced compaction bands using multiscale computations. Geophys. Res. Lett. 38, L10302. doi:10.1029/2011GL047683

T

Taboada, A., Chang, K.-J., Radjaï, F., Bouchette, F., 2005. Rheology, force transmission, and shear instabilities in frictional granular media from biaxial numerical tests using the contact dynamics method. J. Geophys. Res. Solid Earth 110, B09202. doi:10.1029/2003JB002955

Taylor, W.L., Pollard, D.D., 2000. Estimation of in situ permeability of deformation bands in porous sandstone, Valley of Fire, Nevada. Water Resour. Res. 36, 2595–2606. doi:10.1029/2000WR900120

Tembe, S., Baud, P., Wong, T., 2008. Stress conditions for the propagation of discrete compaction bands in porous sandstone. J. Geophys. Res. Solid Earth 1978–2012 113. doi:10.1029/2007JB005439

Tembe, S., Vajdova, V., Wong, T., Zhu, W., 2006. Initiation and propagation of strain localization in circumferentially notched samples of two porous sandstones. J. Geophys. Res. Solid Earth 111, B02409. doi:10.1029/2005JB003611

Tindall, S.E., Davis, G.H., 1999. Monocline development by oblique-slip fault-propagation folding: the East Kaibab monocline, Colorado Plateau, Utah. J. Struct. Geol. 21, 1303–1320. doi:10.1016/S0191-8141(99)00089-9

Torabi, A., Fossen, H., 2009. Spatial variation of microstructure and petrophysical properties along deformation bands in reservoir sandstones. AAPG Bull. 93, 919–938. doi:10.1306/03270908161

Torabi, A., Fossen, H., Alaei, B., 2008. Application of spatial correlation functions in permeability estimation of deformation bands in porous rocks. J. Geophys. Res. Solid Earth 113, B08208. doi:10.1029/2007JB005455

Torabi, A., Fossen, H., Braathen, A., 2013. Insight into petrophysical properties of deformed sandstone reservoirs. AAPG Bull. 97, 619–637. doi:10.1306/10031212040

Tran, T.P.H., 2016. Étude expérimentale de la localisation de la déformation par corrélation d'images sur un analogue de roche soumis à différentes conditions de chargement triaxiaux (phdthesis). Université Côte d'Azur.

Tueckmantel, C., Fisher, Q.J., Knipe, R.J., Lickorish, H., Khalil, S.M., 2010. Fault seal prediction of seismic-scale normal faults in porous sandstone: A case study from the eastern Gulf of Suez rift, Egypt. Mar. Pet. Geol. 27, 334–350. doi:10.1016/j.marpetgeo.2009.10.008

Tueckmantel, C., Fisher, Q.J., Manzocchi, T., Skachkov, S., Grattoni, C.A., 2012. Two-phase fluid flow properties of cataclastic fault rocks: Implications for CO2 storage in saline aquifers. Geology 40, 39–42. doi:10.1130/G32508.1

U

Underhill, J.R., 1991. Implications of Mesozoic—Recent basin development in the western Inner Moray Firth, UK. Mar. Pet. Geol. 8, 359–369. doi:10.1016/0264-8172(91)90089-J

Underhill, J.R., Woodcock, N.H., 1987. Faulting mechanisms in high-porosity sandstones; New Red Sandstone, Arran, Scotland. Geol. Soc. Lond. Spec. Publ. 29, 91–105. doi:10.1144/GSL.SP.1987.029.01.09

V

Voigt, T., von Eynatten, H., Franzke, H.-J., 2004. Late Cretaceous unconformities in the Subhercynian Cretaceous Basin (Germany). Acta Geol. Pol. 54, 673–694.

W

Walderhaug, O., 2000. Modeling Quartz Cementation and Porosity in Middle Jurassic Brent Group Sandstones of the Kvitebjørn Field, Northern North Sea. AAPG Bull. 84, 1325–1339. doi:10.1306/A9673E96-1738-11D7-8645000102C1865D

Walderhaug, O., 1994. Temperatures of quartz cementation in Jurassic sandstones from the Norwegian continental shelf; evidence from fluid inclusions. J. Sediment. Res. 64, 311–323. doi:10.1306/D4267D89-2B26-11D7-8648000102C1865D

Wangen, 1999. Modelling quartz cementation of quartzose sandstones. Basin Res. 11, 113–126. doi:10.1046/j.1365-2117.1999.00091.x

Wibberley, C.A.J., Petit, J.-P., Rives, T., 2007. The mechanics of fault distribution and localization in high-porosity sands, Provence, France. Geol. Soc. Lond. Spec. Publ. 289, 19–46. doi:10.1144/SP289.3

Wibberley, C.A.J., Petit, J.-P., Rives, T., 2000. Mechanics of cataclastic “deformation band” faulting in high-porosity sandstone, Provence. Comptes Rendus Académie Sci. - Ser. IIA - Earth Planet. Sci. 331, 419–425. doi:10.1016/S1251-8050(00)01423-3

Wibberley, C.A.J., Yielding, G., Toro, G.D., 2008. Recent advances in the understanding of fault zone internal structure: a review. Geol. Soc. Lond. Spec. Publ. 299, 5–33. doi:10.1144/SP299.2

Williams, R.T., Farver, J.R., Onasch, C.M., Winslow, D.F., 2015. An experimental investigation of the role of microfracture surfaces in controlling quartz precipitation rate: Applications to fault zone diagenesis. J. Struct. Geol. 74, 24–30. doi:10.1016/j.jsg.2015.02.011

Wong, T., Baud, P., 2012. The brittle-ductile transition in porous rock: A review. J. Struct. Geol. 44, 25–53. doi:10.1016/j.jsg.2012.07.010

Wong, T., David, C., Zhu, W., 1997. The transition from brittle faulting to cataclastic flow in porous sandstones: Mechanical deformation. J. Geophys. Res. Solid Earth 102, 3009–3025. doi:10.1029/96JB03281

Worden, R.H., Morad, S., 2000. Quartz cementation in oil field sandstones: a review of the key controversies, in: Worden, R.H., Morad, S. (Eds.), Quartz Cementation in Sandstones. International Association of Sedimentologists - Special Publication Number 29, pp. 1–20.

Y

Yielding, G., Freeman, B., Needham, D.T., 1997. Quantitative fault seal prediction. AAPG Bull. 81, 897–917.

Z

Zhang, J., Wong, T.-F., Davis, D.M., 1990. Micromechanics of pressure-induced grain crushing in porous rocks. J. Geophys. Res. Solid Earth 95, 341–352. doi:10.1029/JB095iB01p00341

Zhu, W., Montési, L.G.J., Wong, T., 2007. A probabilistic damage model of stress-induced permeability anisotropy during cataclastic flow. J. Geophys. Res. Solid Earth 112, B10207. doi:10.1029/2006JB004456

Zhu, W., Wong, T., 1997. The transition from brittle faulting to cataclastic flow: Permeability evolution. J. Geophys. Res. Solid Earth 102, 3027–3041. doi:10.1029/96JB03282

Zhu, W., Wong, T.-F., 1996. Permeability reduction in a dilating rock: Network modeling of damage and tortuosity. Geophys. Res. Lett. 23, 3099–3102. doi:10.1029/96GL03078

Zoback, M.L., Zoback, M.D., Adams, J., Assumpçao, M., Bell, S., Bergman, E.A., Blümling, P., Denham, D., Ding, J., Fuchs, K., Gay, N., Gregersen, S., Gupta, H.K., Gvishiani, A., Jacob, K., Klein, R., Knoll, P., Magee, M., Mercier, J.L., Müller, B.C., Paquin, C., Rajendran, K., Stephansson, O., Suarez, G., Suter, M., Udias, A., Xu, Z.H., Zhizhin, M., 1989. Global patterns of tectonic stress. Nature 341, 291–298.

Appendix

Appendix

A. Tectonic regime controls clustering of deformation bands in porous sandstone

This section presents the results of a collective work pursued over the years by R. Soliva, G. Ballas, H. Fossen and myself, focusing on the general distribution of the deformation in porous sandstone. This work, published in Geology under the title “Tectonic regime controls clustering of deformation bands in porous sandstone” gathers the data of several studies from various sites over the world as well as our own data to evaluate the degree of clustering of the deformation bands as a function of the tectonics. The article shows that the extensional tectonics favors the localization of the deformation bands under the form of clusters to faults whereas the structures formed in contractional tectonics display distributed conjugate sets of simple deformation bands.

THE GEOLOGICAL SOCIETY OF AMERICA®

Tectonic regime controls clustering of deformation bands in porous sandstone

Roger Soliva[1], Gregory Ballas[2], Haakon Fossen[3], and Sven Philit[1]
[1]Geosciences Montpellier, Université de Montpellier, Campus Triolet, CC060, Place Eugène Bataillon, 34095 Montpellier Cedex 05, France
[2]Institut Français de Recherche pour l'Exploitation de la Mer, Pointe du Diable, 29280 Plouzané, France
[3]Department of Earth Science and Museum of Natural History, University of Bergen, Allégaten 41, N-5007 Bergen, Norway

ABSTRACT

Porous sandstones tend to deform by the formation of low-permeability deformation bands that influence fluid flow in reservoir settings. The bands may be distributed or localized into clusters, and limited recent data suggest that tectonic regime may exert control on their distribution and clustering. In order to explore this suggestion, we performed a synthetic analysis based of 73 sets of bands, including 22 new sets measured for a reverse Andersonian regime that fill the important gap in data for this context. We find a surprisingly strong correlation between clustering and tectonic regime, where bands clearly are more distributed in the reverse regime compared to the normal regime. Together with the observed band distributions, capillary pressure data show evidence that efficient membrane seals are expected for extension, whereas pervasive permeability anisotropy is expected for contraction. Such a basic new rule concerning tectonic regime is very useful for assessment of reservoir properties where deformation bands are common but below seismic resolution.

INTRODUCTION

Tectonic deformation in porous sandstones generally produces cataclastic deformation bands in which grain crushing, sliding, and rolling take place (Aydin, 1978; Fossen et al., 2007). The result is typically grain-size reduction that causes porosity loss and reduction of permeability by up to six orders of magnitude (Fossen and Bale, 2007; Ballas et al., 2015). Different classes of cataclastic deformation bands have been recognized as a function of their relative amount of shear to compaction, including shear bands (SBs), compactional shear bands (CSBs), shear-enhanced compaction bands (SECBs), and pure compaction bands (PCBs) (Eichhubl et al., 2010; Soliva et al., 2013). Some of their properties, such as displacement-length scaling relationships (Schultz et al., 2008), degree of cataclasis, petrophysical properties (Ballas et al., 2014), and spatial distribution (Fortin et al., 2005; Saillet and Wibberley, 2010), seem directly linked to such differences in kinematics. Identifying the internal and external factors controlling such differences in band kinematics could be of primary importance for sandstone reservoir characterization.

Both mechanical tests and field data in porous sandstones suggest that many factors, including grain size, porosity, proximity to faults, segmentation, burial depth, and potentially fluid pressure, are thought to influence the spatial distribution of deformation bands and their relative amount of shear to compaction (e.g., Wibberley et al., 2007; Solum et al., 2010; Nicol et al., 2013; Soliva et al., 2013; Ballas et al., 2014). In this paper we inspect the role of tectonic regime on the spatial distribution of deformation bands with new data collected from 22 outcrops in contractional settings in California and Nevada (USA), France, Germany, and Taiwan. This allows for a sound synthetic analysis of band distribution in reverse regimes compared to data in normal regimes collected from the literature. We briefly discuss the origin of the observed general trend and implications for sandstone reservoirs.

GEOLOGIC SETTINGS

Band frequency data (number of bands per meter) were measured in Nevada in the fine- to medium-grained porous Jurassic Aztec Sandstone (Fossen et al., 2015). This unit was involved in the Cretaceous Sevier orogeny with the east to southeast transport of the Muddy Mountain thrust sheet. Data were collected from three principal sites: one in the Buffington window and two in the Valley of Fire State Park.

In California, data were collected from oil-filled porous sandstones of the Edna Member of the Miocene–Pliocene Pismo Basin (Antonellini et al., 1999). This basin occupies a syncline limited by the Edna thrust fault to the northeast. Layers containing deformation bands show a wide range in grain size (fine-grained sand to gravel). Measurements were made on one outcrop but are separated into three sets because of the different band distributions observed in the different layers.

In France, we measured band sets in the porous Cretaceous sandstones of the South East Basin (Ballas et al., 2014). These marine sandstones were folded and faulted during the north-south Paleocene–Eocene Pyrenean shortening, and data from ten outcrops are reported here for host rocks showing medium to coarse grain sizes.

Data from Germany were collected from the Alpine Subhercynian Basin in the medium-size porous sandstones of the lower Cretaceous Involutus and Heidelberg formations (Klimczak and Schultz, 2013). This basin is folded and mainly faulted at its southwestern border by the Harz Mountains thrust. Data reported in this paper are from four outcrops observed at different places in the basin; one outcrop is very close to the Harz thrust, and three others are relatively far from the thrust (>2 km).

Cataclastic bands from Taiwan are located on the east coast (Shihtiping), in fine- to coarse-grained volcanic-tuff sandstones. These deposits are related to the formation of the Coastal Range due to the arc-continent collision ~7 m.y. ago. A north-south–striking fold affects these deposits, and two band sets were measured in the site.

BAND SET GEOMETRY, FREQUENCY, AND CLUSTERING

Methods

Because many workers have counted the number of individual bands per meter, we proceed in the same way, using a tape ruler along outcrops, to allow for a global data synthesis. Most data sets from the Andersonian normal stress regime were acquired along scan lines oriented along the direction of maximum extension (X axis of the strain ellipsoid). For the new measurements provided for the Andersonian reverse stress regime, we counted the bands along a scan line oriented along the direction of maximum shortening (Z axis).

Band Set Geometry

Outside of fault zones, cataclastic deformation bands forming reverse band sets are generally pervasive sets of SECBs or CSBs. SECBs generally

 Data Repository item 2016137 | doi:10.1130/G37585.1

show no visible displacement in the field and crop out as conjugate sets that intersect only in some parts of the outcrops (Fig. 1A). CSBs generally crop out as regular mesh-like geometries of conjugate crosscutting bands (Fig. 1B), along which reverse-sense displacement of a few centimeters can be observed. Both types of band sets are very rare in fine sandstones, and are generally restricted to specific layers of medium to coarse porous sandstone. Within the deformed layers, the spatial distribution of the bands is extensive, generally over entire outcrop exposures (tens of meters to 100 m) with more or less evenly spaced bands (Figs. 1A and 1B). Note, however, that SBs organized as clusters can also be observed in reverse regime, but specifically located within fault zones (see Fig. 1E, Subhercynian).

Bands in the normal regime are typically CSBs and SBs clustered around normal faults, defining damage zones. Damage zones are characterized by a steep increase in band density toward a main fault surface,

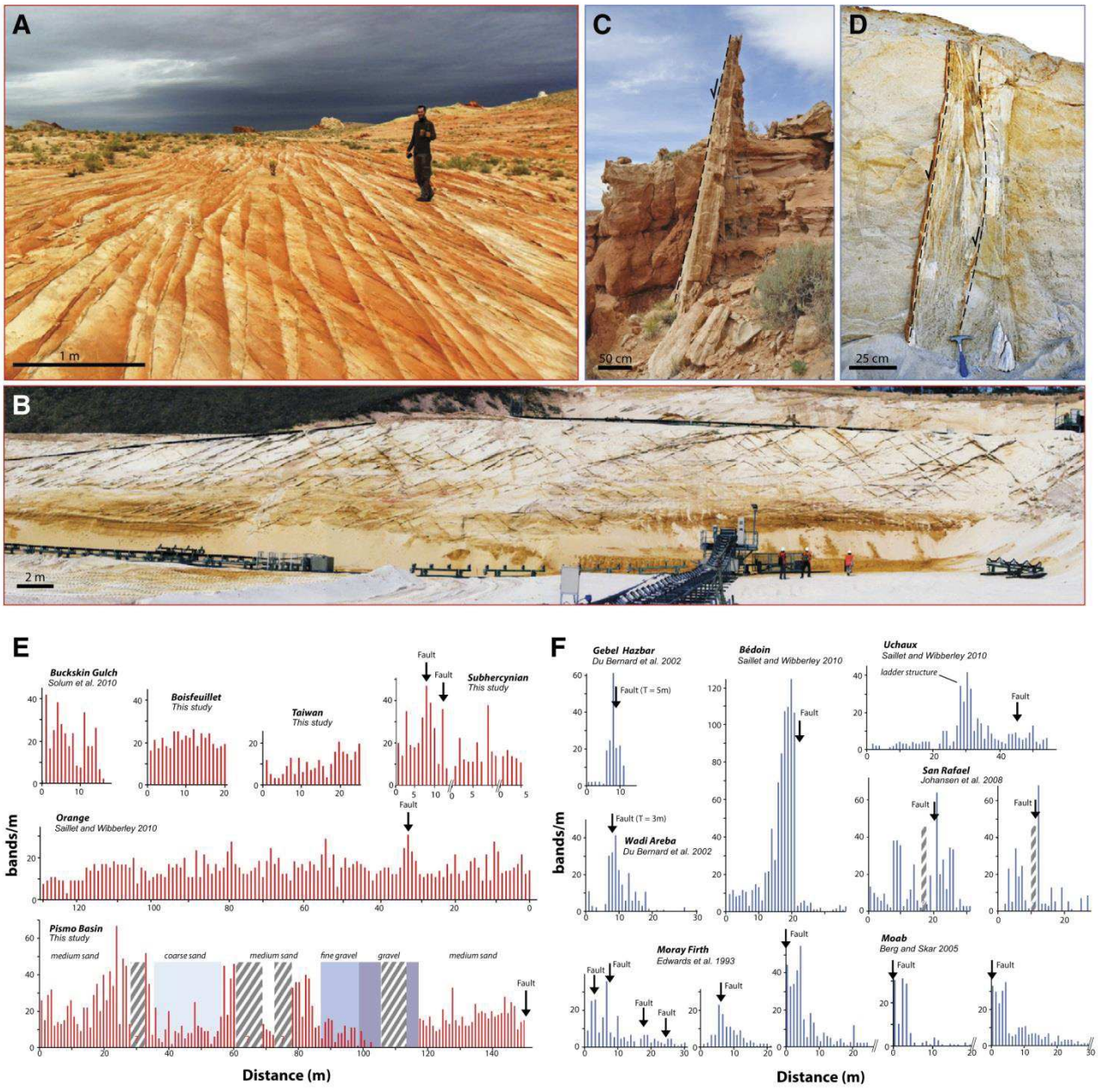

Figure 1. Examples of geometry and spatial distribution of band sets formed as reverse and normal Andersonian regimes. A: Reverse set of shear-enhanced compaction bands in Valley of Fire Sate Park (Nevada, USA) seen as limiting red oxidations. B: Reverse set of compactional shear bands in the Les Crans quarry (Provence, France). C: Normal shear band cluster adjacent to normal fault surface near Goblin Valley State Park (Utah, USA). D: Normal shear band cluster at the vicinity of two fault surfaces in the Boncavaï quarry (Provence, France). E: Histograms of number of band per meter versus distance along scan lines for various reverse band sets. F: Same type of histograms as shown in E, for normal band sets. Zones striped in gray mark intervals where the sandstone is not exposed. See Data Repository (see footnote 1) for references cited in E and F.

which is located along or within a central cluster zone (Figs. 1C and 1D). In addition, clusters can also occur as incipient fault structures far from established fault surfaces. SBs in the clusters are spaced a few millimeters or centimeters apart, and generally oriented subparallel to the fault. Bands can form parallel or conjugate sets, as branching or mutually crosscutting structures. These SBs can show centimeter- to decimeter-scale displacements and generally display more intense cataclasis than CSBs and SECBs.

Histograms of number of bands per meter are shown in Figure 1E for some of the most representative reverse band sets. These graphs show nearly homogeneous to polymodal distribution with some modes that are located at places where few faults or ladder structures are observed (see Schultz and Balasko, 2003, for definition of ladder structure). For all the reverse band sets reported in the literature (see Figure 2, and the GSA Data Repository[1] for references), the mean value of bands per meter is 12, with a standard deviation of 9.6. The spatial distribution is particularly heterogeneous in outcrops showing variations in lithology, such as in the Pismo Basin (Fig. 1E). Relatively high values of bands per meter are observed in medium-grained units (generally >10 bands/m), while lower band frequencies are observed in coarse-grained units (generally <10 bands/m), and few bands are observed in the sand matrix of gravel units. Fine sandstones, cemented sandstones, or other low-porosity rock layers are devoid of SECBs or CSBs.

The distribution of normal sense bands per meter appears Gaussian or log-normal; see Figure 1F for some of the most representative normal band sets measured. These modal distributions generally show a progressive increase in band density to a maximum value (cluster), into which bands are very closely packed (Fig. 1C). An asymmetric distribution (log-normal distribution type) generally reflects the juxtaposition of differently damaged units around a fault surface. For all the normal band sets collected from the literature (Fig. 2), the maximum number of bands per meter reaches the value of 161. Also note that zones devoid of bands are shown on the graphs presented in Figure 1F.

Data Synthesis Analysis

We synthesized all the band density data obtained from our field work and from the literature; 24, 47, and 2 band sets from the reverse, normal, and strike-slip regimes, respectively. These 73 sets represent a total of 27,074 bands recorded along scan lines from sandstones showing a wide range in porosity (18.6%–35.14%), grain size (0.24 mm in diameter to gravel sized), burial depth (0.3–2.5 km), and diagenetic context.

To precisely examine the relative spatial distribution of bands of all sets together, we calculate the cluster factor (Wibberley et al., 2007) for each set. This parameter is a standard deviation–type function describing the degree of clustering within a given band set along a scan line. The cluster factor is defined as:

$$Cf = \sqrt{\frac{\sum f_i^2}{\sum f_i} - f_{av}}, \quad (1)$$

where f_i is the number of bands encountered per meter of scan line, i represents the i^{th} meter interval along the scan line, and f_{av} is the average band frequency for the entire scan line. For all the band sets collected and measured, this factor varies between 0.47 and 8.78, where 8.78 corresponds to the highest band clustering and 0.47 is the most even band distribution.

A global data analysis shows a clear difference between reverse and normal band sets with respect to spatial distribution. Figure 2 presents all band sets measured by us and collected from the literature as a function of the cluster factor and the maximum value of bands per meter. This graph

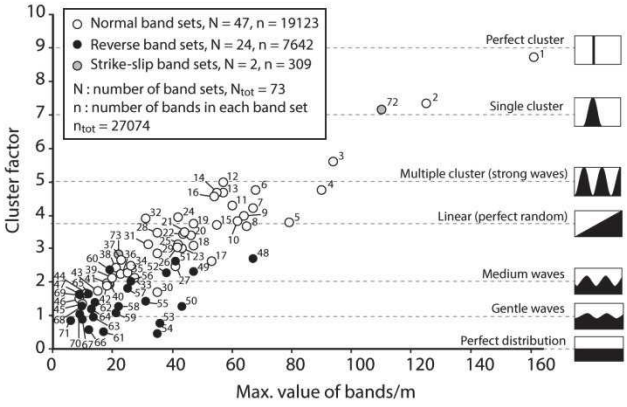

Figure 2. Data set synthesis of reverse (black circles), normal (white circles), and strike-slip (gray circles) band sets plotted as cluster factor versus maximum value of bands per meter. Schemes of synthetic data distribution are shown for different values of cluster factor. Band sets are numbered. For numbered references and number of bands per set, see the Data Repository (see footnote 1).

reveals that reverse band sets (black circles) have a low cluster factor, but also low values of maximum bands per meter as compared to normal band sets. Reverse band sets have cluster factor values between 0.4 and 2.8, with ~25% of the sets having values >2, and a maximum band per meter ranging from 6 to 67, with ~70% of the sets having values <30. In contrast, normal band sets have cluster factor values between 1.4 and 8.8, with >80% having values >2, and maximum band per meter ranging from 9 to 161, with ~70% having values >30. This synthetic data set analysis shows two different and little-overlapping graphical domains for reverse and normal band sets, revealing that sets formed in the reverse tectonic regime (contraction) are generally more spatially distributed than sets formed in the normal tectonic regime (extension). Large cluster factor values also seem possible for the strike-slip regime. Beyond the fact that the amount of strike-slip data has no significant statistical weight, this low amount of data allows questioning the extent of their occurrence in porous sandstones.

DISCUSSION

The global data set presented in Figure 2 clearly shows that reverse bands are more spatially distributed than normal bands, which are characterized by more clustered distributions. This difference in organization reveals that tectonic regime is a prominent factor for the distribution of deformation bands in porous sandstone. However, the presence of faults and even primary lithologic heterogeneities seem to be factors that can influence the distribution of bands in reverse band sets (Fig. 1E), but do not control the general trend. Spatially distributed band sets have also been observed in extensional settings, but in specific settings such as in relay zones (e.g., Davatzes and Aydin, 2003) or in cases where strong lithological contrasts impede the propagation of SBs (Schultz and Fossen, 2002).

This influence of tectonic context can be explained by the difference in stress paths occurring in sandstone under normal and reverse tectonic regimes (Soliva et al., 2013). Relatively low mean stress inherent to tectonic extension leads to a localized Byerlee-type cataclastic shear behavior, whereas high mean stress promoted by tectonic contraction leads to distributed compactional-cataclastic behavior (for the mechanical explanation, see the Data Repository; for the behavior of porous sandstones, see Wong and Baud, 2012). This analysis therefore suggests that remote tectonic stress has a stronger influence on band distribution in general than local stress, such as provided by reactivation of inherited faults, layering, or fault segmentation.

[1]GSA Data Repository item 2016137, references for Figures 1 and 2, mechanical explanation and capillary pressure method for Figure 3, is available online at www.geosociety.org/pubs/ft2016.htm, or on request from editing@geosociety.org or Documents Secretary, GSA, P.O. Box 9140, Boulder, CO 80301, USA.

Because deformation bands are well known to be subseismic structures, the exposed evidence of different strain localization together with differences in petrophysical properties between shear-dominated and compaction-dominated bands provide important conclusions for the management of sandstone reservoirs. Compilation of recent data shows that permeability is significantly lower in shear-dominated bands compared to compaction-dominated bands (Ballas et al., 2015), but rather than permeability, capillary pressure is an efficient indicator of the ability of a fault to act as a barrier to fluid flow over geologic time. A new compilation of capillary pressure and porosity (Fig. 3), measured both in reverse and normal band sets sampled in the field, clearly shows that the capillary pressure is generally higher for normal bands than for reverse bands (for method of capillarity calculation, see the Data Repository). This implies the presence of seals and stronger permeability anisotropy in porous sandstone reservoirs affected by tectonic extension, as compared to sandstones affected by contraction. Such a basic new rule of tectonic control of fluid flow and compartmentalization in sandstone reservoir is of major importance for both economic fluid exploration and production and CO_2 storage planning.

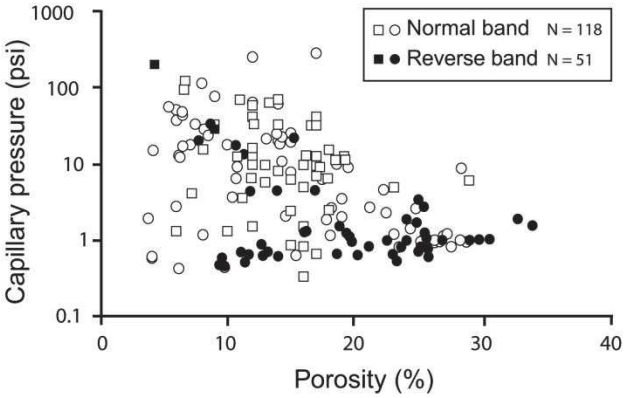

Figure 3. Compiled data for capillary pressure and porosity measured on samples from reverse and normal bands. Squares and circles are for direct and indirect measures, respectively (for method and data references, see the Data Repository [see footnote 1]).

ACKNOWLEDGMENTS

This work was funded by a post-doctoral project at the Laboratory Géosciences Montpellier (University of Montpellier) in collaboration with the University of Bergen. We thank Chia-Yu Lu from the National Taiwan University for his help in the field, editor James Spotila, Stephen Laubach, and two anonymous reviewers for their constructive comments.

REFERENCES CITED

Antonellini, M.A., Aydin, A., and Orr, L., 1999, Outcrop-aided characterization of a faulted hydrocarbon reservoir: Arroyo Grande oil field, California, USA, *in* Haneberg, W.C., et al., eds., Faults and subsurface fluid flow in the shallow crust: American Geophysical Union Geophysical Monograph 113, p. 7–26, doi:10.1029/GM113p0007.

Aydin, A., 1978, Small faults formed as deformation bands in sandstone: Pure and Applied Geophysics, v. 116, p. 913–930, doi:10.1007/BF00876546.

Ballas, G., Soliva, R., Benedicto, A., and Sizun, J.-P., 2014, Control of tectonic setting and large-scale faults on the basin-scale distribution of deformation bands in porous sandstone (Provence, France): Marine and Petroleum Geology, v. 55, p. 142–159, doi:10.1016/j.marpetgeo.2013.12.020.

Ballas, G., Fossen, H., and Soliva, R., 2015, Factors controlling permeability of cataclastic deformation bands and faults in porous sandstone reservoirs: Journal of Structural Geology, v. 76, p. 1–21, doi:10.1016/j.jsg.2015.03.013.

Davatzes, N.C., and Aydin, A., 2003, Overprinting faulting mechanisms in high porosity sandstones of SE Utah: Journal of Structural Geology, v. 25, p. 1795–1813, doi:10.1016/S0191-8141(03)00043-9.

Eichhubl, P., Hooker, J., and Laubach, S.E., 2010, Pure and shear-enhanced compaction bands in Aztec Sandstone: Journal of Structural Geology, v. 32, p. 1873–1886, doi:10.1016/j.jsg.2010.02.004.

Fortin, J., Shubnel, A., and Guégen, Y., 2005, Elastic wave velocities and permeability evolution during compaction of Bleurswiller Sandstone: International Journal of Rock Mechanics and Mining Sciences, v. 42, p. 873–889, doi:10.1016/j.ijrmms.2005.05.002.

Fossen, H., and Bale, A., 2007, Deformation bands and their influence on fluid flow: American Association of Petroleum Geologists Bulletin, v. 91, p. 1685–1700, doi:10.1306/07300706146.

Fossen, H., Schultz, R.A., Shipton, Z.K., and Mair, K., 2007, Deformation bands in sandstone: A review: Journal of the Geological Society [London], v. 164, p. 755–769, doi:10.1144/0016-76492006-036.

Fossen, H., Zuluaga, L.F., Ballas, G., Soliva, R., and Rotevatn, A., 2015, Contractional deformation of porous sandstone: Insights from the Aztec Sandstone in the footwall to the Sevier-age Muddy Mountains thrust, SE Nevada, USA: Journal of Structural Geology, v. 74, p. 172–184, doi:10.1016/j.jsg.2015.02.014.

Klimczak, C., and Schultz, R.A., 2013, Fault damage zone origin of the Teufelsmauer, Subhercynian Cretaceous Basin, Germany: International Journal of Earth Sciences, v. 102, p. 121–138, doi:10.1007/s00531-012-0794-z.

Nicol, A., Childs, C., Walsh, J.J., and Schafer, K.W., 2013, A geometric model for the formation of deformation band clusters: Journal of Structural Geology, v. 55, p. 21–33, doi:10.1016/j.jsg.2013.07.004.

Saillet, E., and Wibberley, C.A.J., 2010, Evolution of cataclastic faulting in high-porosity sandstone, Bassin du Sud-Est, Provence, France: Journal of Structural Geology, v. 32, p. 1590–1608, doi:10.1016/j.jsg.2010.02.007.

Schultz, R.A., and Balasko, C.M., 2003, Growth of deformation bands into echelon and ladder geometries: Geophysical Research Letters, v. 30, p. 2033–2036, doi:10.1029/2003GL018449.

Schultz, R.A., and Fossen, H., 2002, Displacement-length scaling in three dimensions: The importance of aspect ratio and application to deformation bands: Journal of Structural Geology, v. 24, p. 1389–1411, doi:10.1016/S0191-8141(01)00146-8.

Schultz, R.A., Soliva, R., Fossen, H., Okubo, C., and Reeves, D.M., 2008, Dependence of displacement-length scaling relations for fractures and deformation bands on the volumetric changes across them: Journal of Structural Geology, v. 30, p. 1405–1411, doi:10.1016/j.jsg.2008.08.001.

Soliva, R., Schultz, R.A., Ballas, G., Taboada, A., Wibberley, C.A.J., Saillet, E., and Benedicto, A., 2013, A model of strain localization in porous sandstone as a function of tectonic setting, burial and material properties; new insight from Provence (SE France): Journal of Structural Geology, v. 49, p. 50–63, doi:10.1016/j.jsg.2012.11.011.

Solum, J.G., Brandenburg, J.P., Naruk, S.J., Kostenko, O.V., Wilkins, S.J., and Schultz, R.A., 2010, Characterization of deformation bands associated with normal and reverse stress states in the Navajo Sandstone, Utah: American Association of Petroleum Geologists Bulletin, v. 94, p. 1453–1475, doi:10.1306/01051009137.

Wibberley, C.A.J., Petit, J.-P., and Rives, T., 2007, The mechanics of fault distribution and localization in high-porosity sands, Provence, France, *in* Lewis, H., and Couples, G.D., eds., The relationship between damage and localization: Geological Society of London Special Publication 289, p. 19–46, doi:10.1144/SP289.3.

Wong, T.-f., and Baud, P., 2012, The brittle-ductile transition in porous rock: A review: Journal of Structural Geology, v. 44, p. 25–53, doi:10.1016/j.jsg.2012.07.010.

Manuscript received 2 December 2015
Revised manuscript received 6 April 2016
Manuscript accepted 6 April 2016

Printed in USA

B. Complementary data – microstructural analysis of the shape of the clasts in the clusters

Relating to the microstructural analysis undertaken in section 2.3.1, this section aims at providing more detailed information on the measurement of the shape descriptors analyzed in the clusters with increasing degree of cataclasis. This part of the appendix is composed of 5 plates describing the evolution of the shape descriptors at the sites of Boncavaï, StMichel, Bédoin, Blankenburg and Buckskin Gulch, in the same form as the already presented in section 2.3 for Cummingston. Note that we also measured the Circularity of the same number of particles for each degree of cataclasite at each sites. However, because the evolution of the circularity with increasing degree of cataclasis being very similar to the behavior of the roundness, we chose not to present the detailed data, but only the synthetic data of the average circularity at each degree of cataclasis investigated.

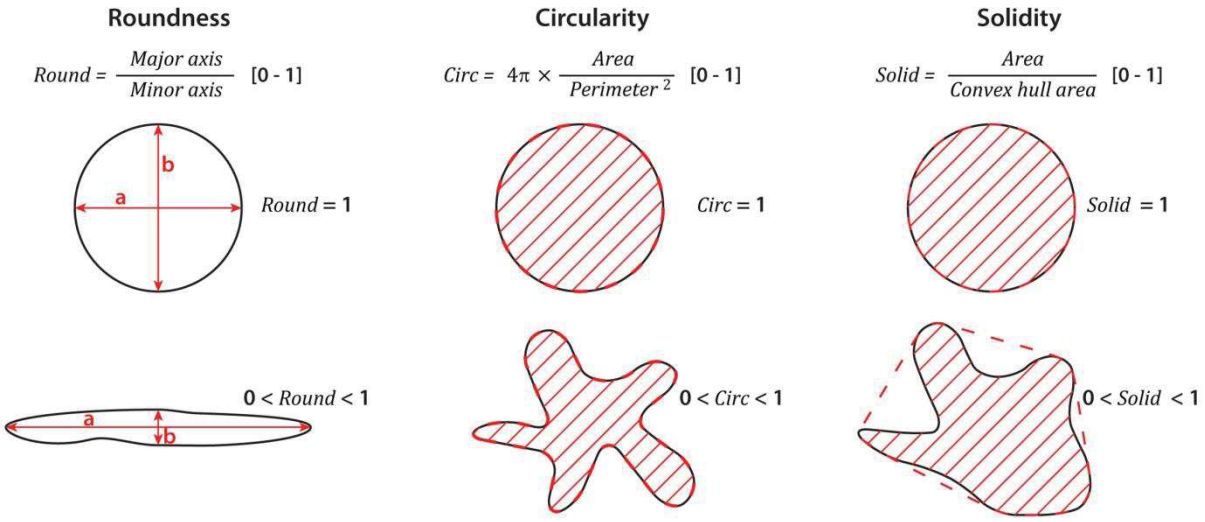

Figure B93. Figure reminding the geometrical properties measured with the shape descriptors. The roundness and circularity yield very similar evolution with increasing degree of cataclasis.

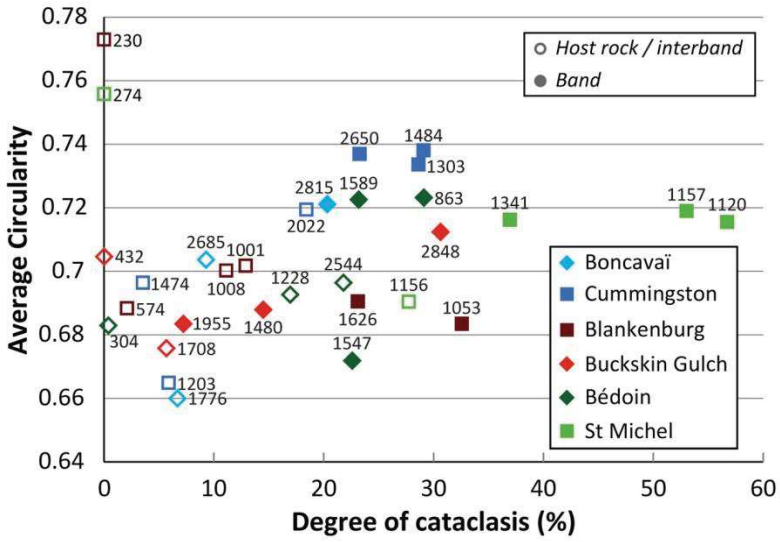

Figure B94. Synthetic data of the Circularity at different degree of cataclasis. The trend is very similar to the evolution of the average roundness with increasing degree of cataclasis. The Number of measured particles for the calculation of the average circularity (common for roundness and solidity) is indicated above the data.

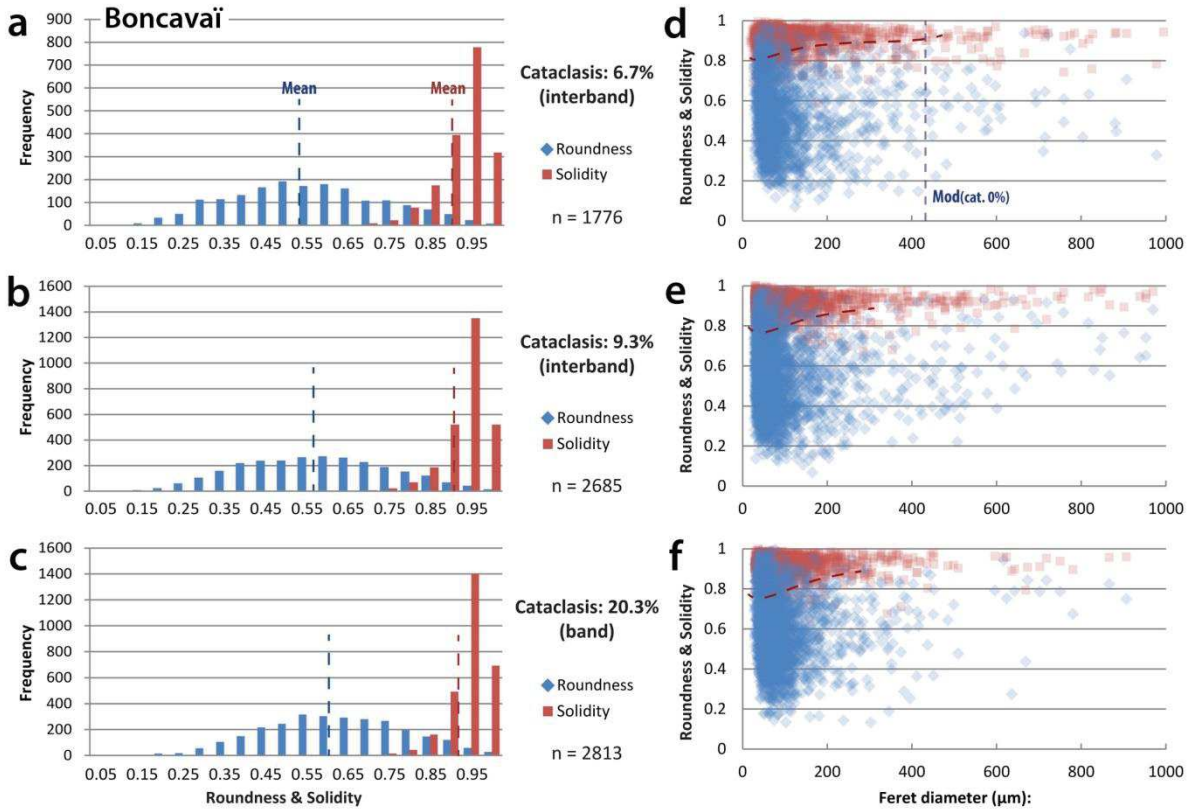

Figure B95. Evolution of particle shape with increasing degree of cataclasis at Boncavaï. (a) through (c): Distribution of the particle roundness and solidity frequencies for increasing degree of cataclasis. For the roundness shape descriptor, the value 1 describes a perfect circle; a roundness approaching from 0 describes an infinitely elongated particle. For the solidity, the value of 1 describes a particle with a totally convex hull; the presence of increasing concave parts in the particle hull lower the solidity. (d) through (f): Distribution of the particle roundness and solidity as a function of the Feret diameter. Each data point is represented with 20% opacity. The dashed red curve underlines the bottom limit of the zone where more than 4 values of solidity are overlain. In (d), the vertical dashed line (in blue) represents the modal grain size value of the host rock.

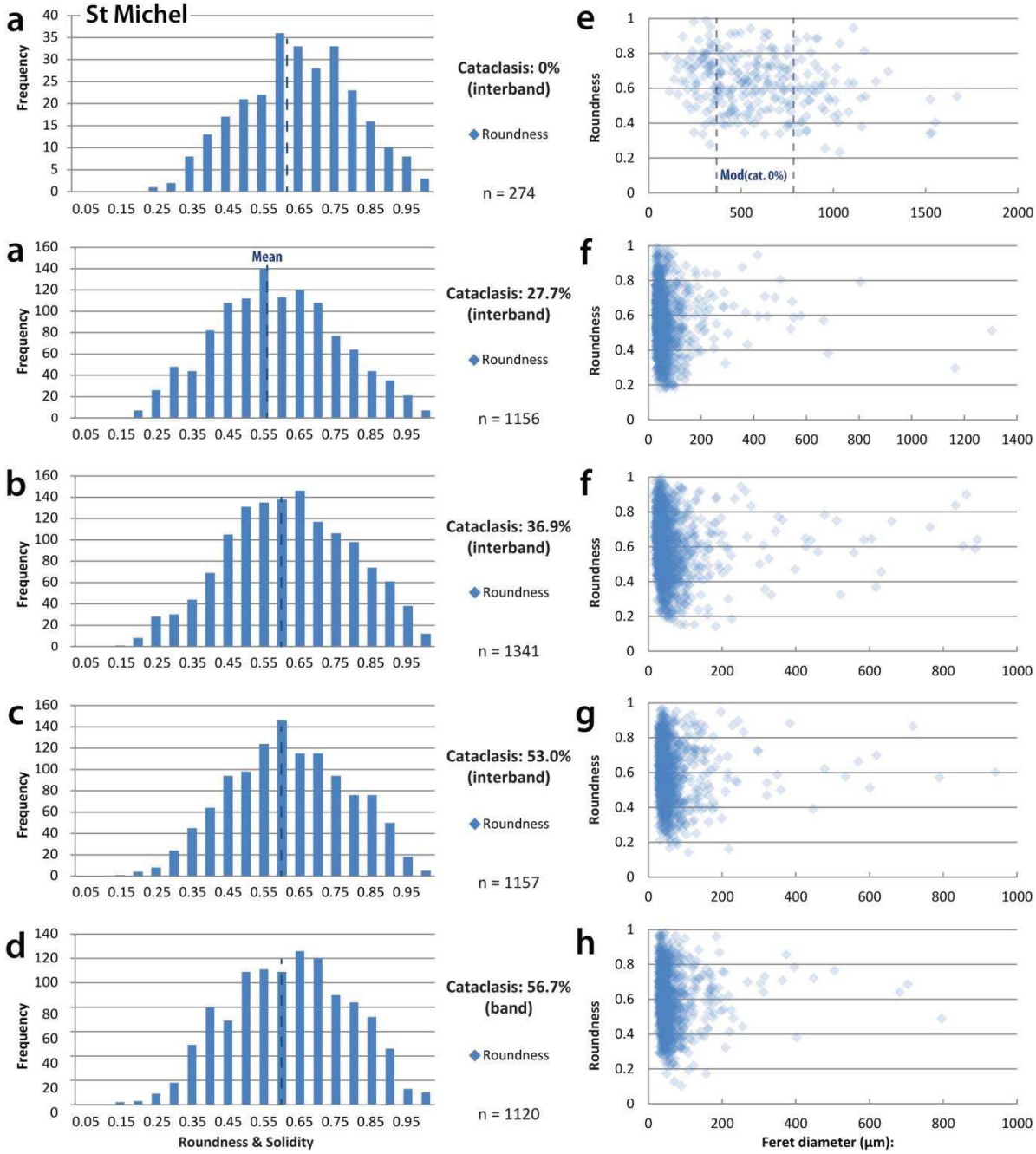

Figure B96. Evolution of particle shape with increasing degree of cataclasis at St Michel. (a) through (d): Distribution of the particle roundness frequencies for increasing degree of cataclasis. The value 1 describes a perfect circle; a roundness approaching from 0 describes an infinitely elongated particle. (e) through (h): Distribution of the particle roundness as a function of the Feret diameter. Each data point is represented with 20% opacity. The dashed red curve underlines the bottom limit of the zone where more than 4 values of solidity are overlain. In (e), the dashed vertical lines (in blue) represent the two modal host rock modal grain size encountered on the cluster sides.

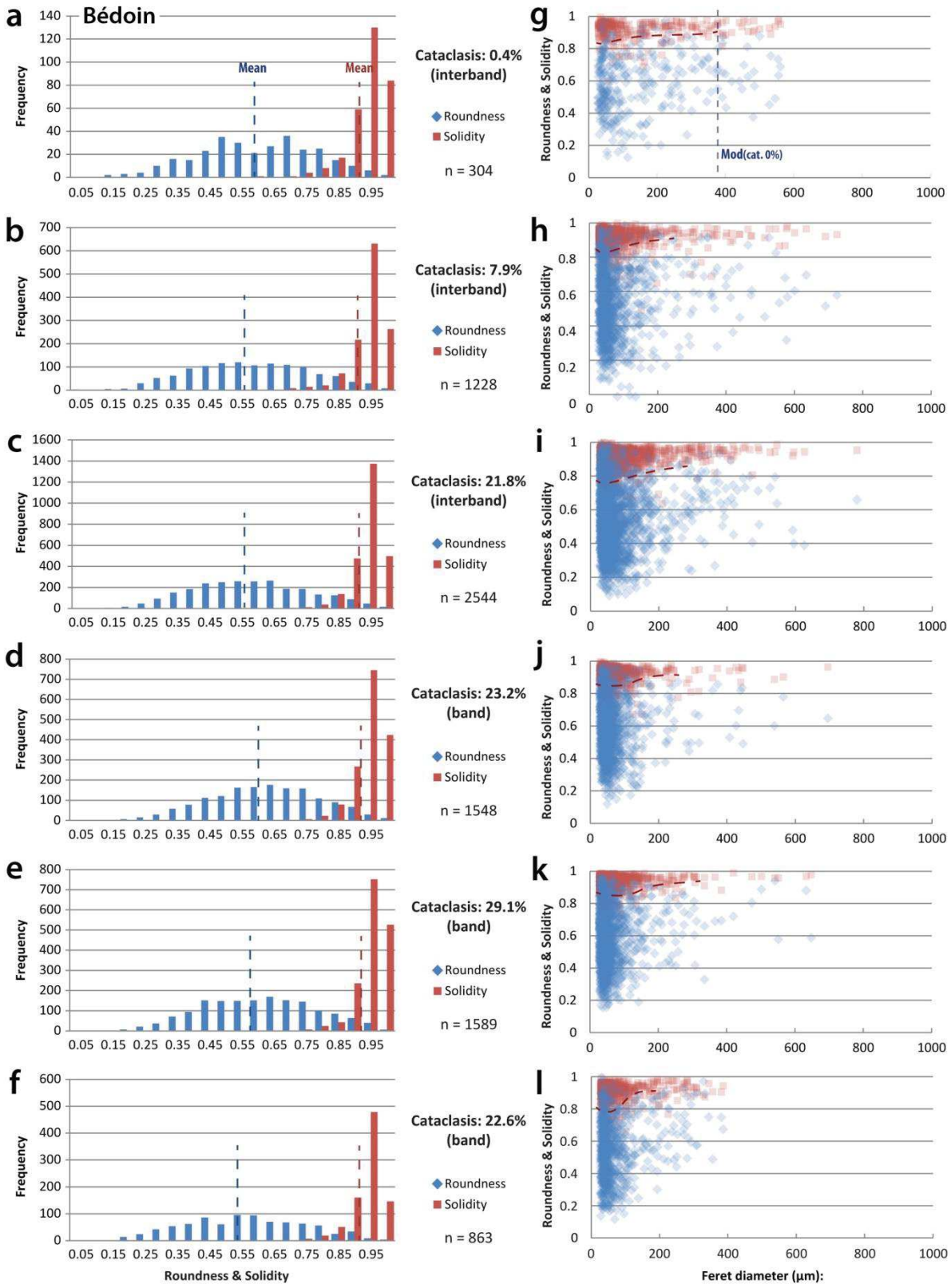

Figure B97. Evolution of particle shape with increasing degree of cataclasis at Bédoin. (a) through (f): Distribution of the particle roundness and solidity frequencies for increasing degree of cataclasis. For the roundness shape descriptor, the value 1 describes a perfect circle; a roundness approaching from 0 describes an infinitely elongated particle. For the solidity, the value of 1 describes a particle with a totally convex hull; the presence of increasing concave parts in the particle hull lower the solidity. (g) through (l): Distribution of the particle roundness and solidity as a function of the Feret diameter. Each data point is represented with 20% opacity. The dashed red curve underlines the bottom limit of the zone where more than 4 values of solidity are overlain. In (g), the vertical dashed line (in blue) represents the modal grain size value of the host rock.

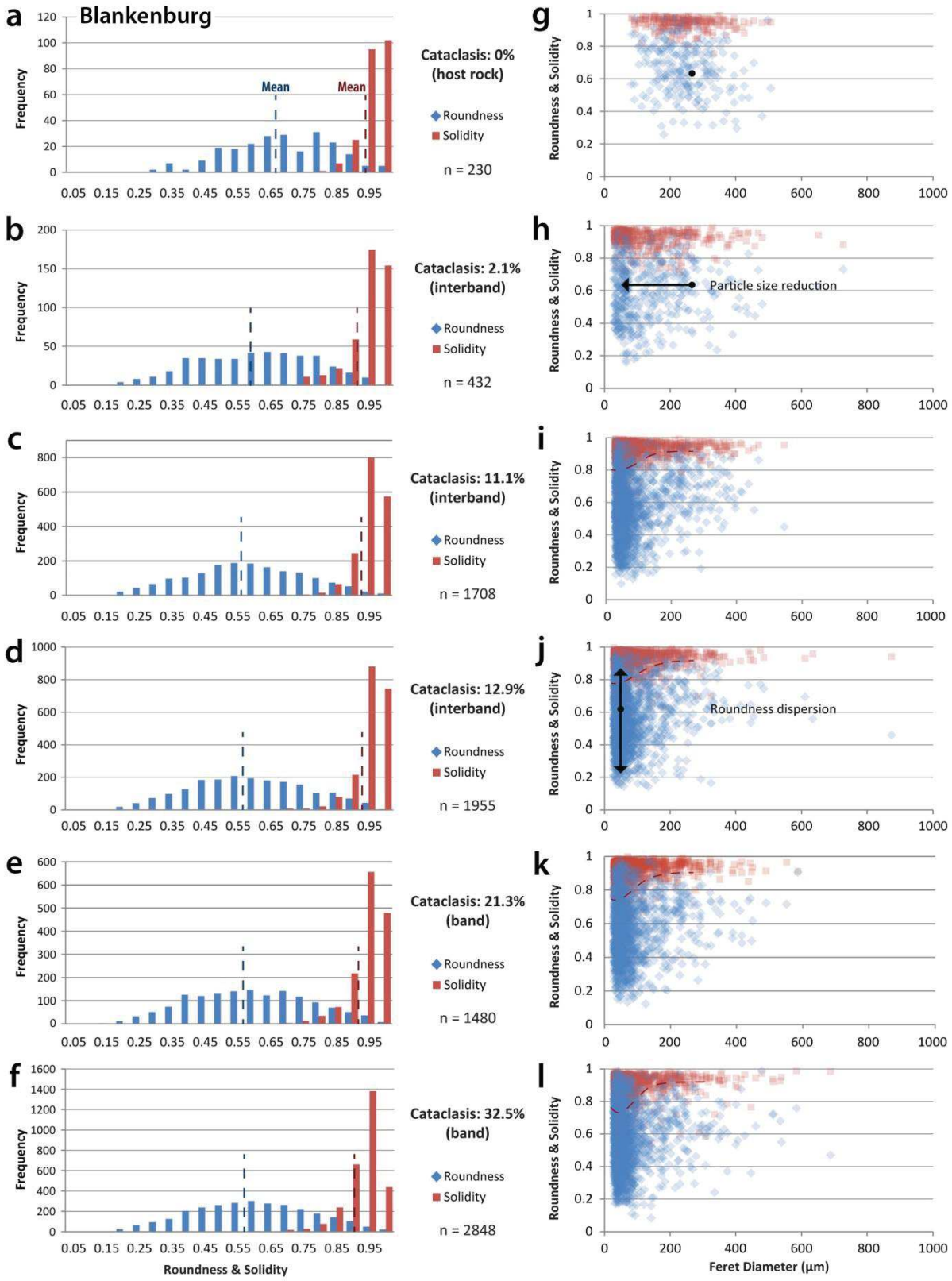

Figure B98. Evolution of particle shape with increasing degree of cataclasis at Blankenburg. (a) through (f): Distribution of the particle roundness and solidity frequencies for increasing degree of cataclasis. For the roundness shape descriptor, the value 1 describes a perfect circle; a roundness approaching from 0 describes an infinitely elongated particle. For the solidity, the value of 1 describes a particle with a totally convex hull; the presence of increasing concave parts in the particle hull lower the solidity. (g) through (l): Distribution of the particle roundness and solidity as a function of the Feret diameter. Each data point is represented with 20% opacity. The dashed red curve underlines the bottom limit of the zone where more than 4 values of solidity are overlain. In (g), the black dot represents the modal grain size value of the host rock with the associated average roundness.

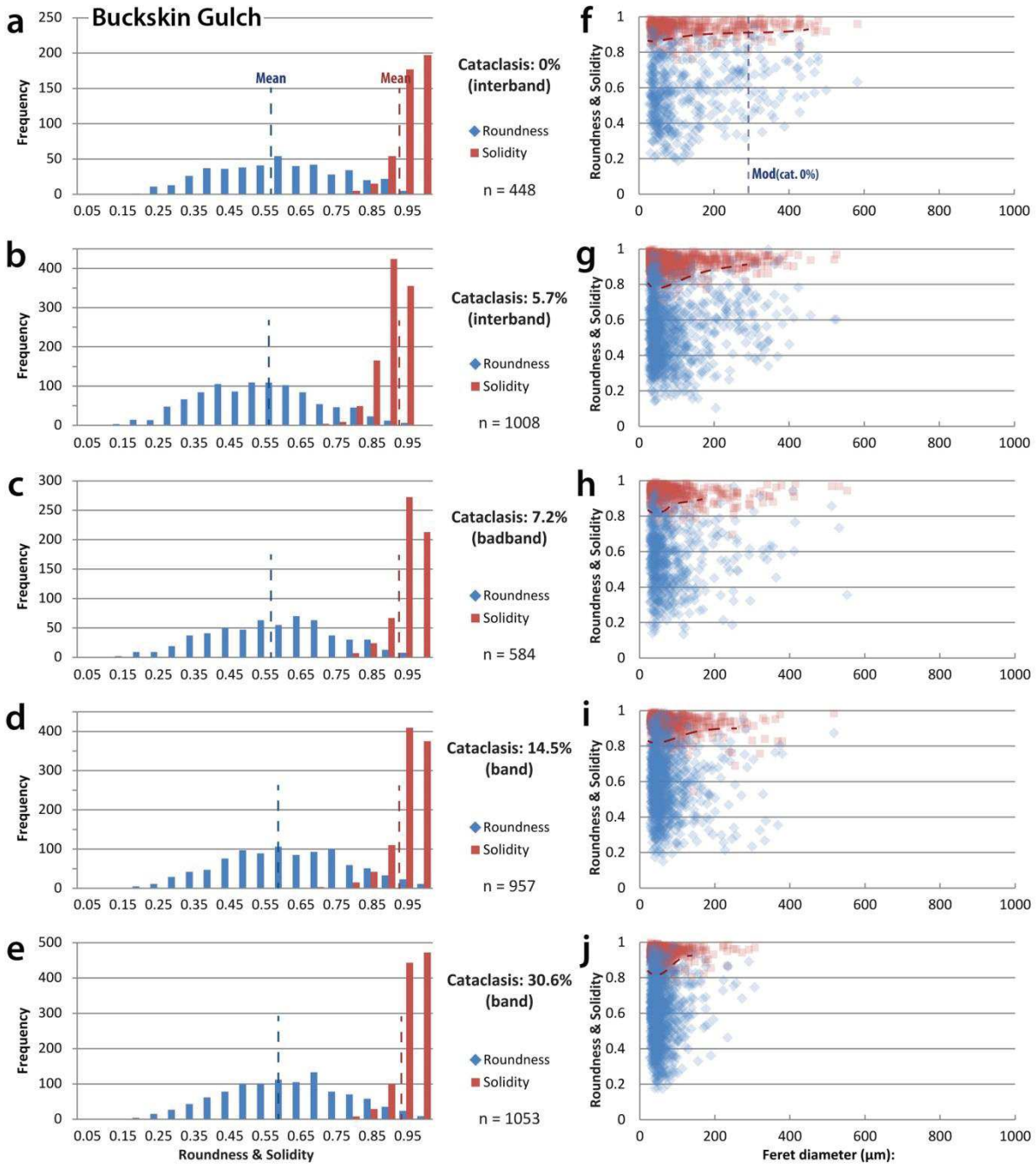

Figure B99. Evolution of particle shape with increasing degree of cataclasis at Buckskin Gulch. (a) through (e): Distribution of the particle roundness and solidity frequencies for increasing degree of cataclasis. For the roundness shape descriptor, the value 1 describes a perfect circle; a roundness approaching from 0 describes an infinitely elongated particle. For the solidity, the value of 1 describes a particle with a totally convex hull; the presence of increasing concave parts in the particle hull lower the solidity. (f) through (j): Distribution of the particle roundness and solidity as a function of the Feret diameter. Each data point is represented with 20% opacity. The dashed red curve underlines the bottom limit of the zone where more than 4 values of solidity are overlain. In (f), the vertical dashed line (in blue) represents the modal grain size value of the host rock.

Résumé étendu

Résumé étendu

Ce travail de thèse traite de la déformation dans les grès poreux et s'inscrit dans un projet de plus grande envergure entamé depuis une dizaine d'années. Ce projet comprend notamment la thèse de E. Saillet (2009), plusieurs sujets de stage de master (T. Cavailhes, 2009 ; G. Ballas, 2010) ainsi que la thèse de G. Ballas (2013).

1. Problématiques et objectifs

Les grés poreux représentent des aquifères et des réservoirs d'hydrocarbure classiques. La déformation dans les grés a pour particularité de s'exprimer sous de multiples formes largement abordées dans la littérature (Aydin et Johnson, 1978 ; Shipton et Cowie, 2001 ; Johansen et Fossen, 2008 ; Schultz et Siddharthan, 2001 ; Soliva et al., 2013). Les paramètres et les processus contrôlant ces différentes morphologies, dimensions, distributions, propriétés pétrophysiques de la déformation sont pourtant mal connus.

Dans cette thèse, nous abordons l'étude des amas « clusters » de bandes de déformation cataclastiques. Ces structures de déformation sont souvent épaisses formant des reliefs à l'affleurement. Leurs larges dimensions telles que fréquemment reportées dans la littérature suggèrent qu'ils puissent représenter des barrières potentielles pour la migration des fluides en milieu réservoir.

Nous cherchons dans ce travail à répondre aux questions suivantes :

- Quels sont les mécanismes contrôlant l'accumulation de bandes impliquées dans le développement des clusters ?
- Quels paramètres qui contrôlent dans un cluster le passage à la faille ?
- Selon quels mécanismes les clusters de bandes de déformation cataclastiques interagissent lorsque les grès sont en contact avec d'autres lithologies ?
- Quels processus diagénétiques entrent en jeu dans l'évolution précoce des clusters et quels sont leurs impacts sur l'évolution de la déformation ?

Pour répondre à ces questions, nous sélectionnons 7 sites d'études présentant différents paramètres que sont :

- Le chargement tectonique et le régime Andersonien,
- L'enfouissement au temps de la déformation,
- La lithologie (porosité, taille de grains, composition minéralogique, alternance de lithologies).

2. Présentation des sites d'étude

Les sites de Bédoin, Boncavaï et Saint Michel sont localisés dans le Bassin du Sud-Est de Provence (France). Ces sites d'étude sont localisés dans des grés quartzitiques peu lithifiés, déposés dans des

environnements deltaïques à éoliens. Leurs porosités varient de 30 à 43%. Le Bassin du Sud-Est a été affecté par 3 épisodes tectoniques principaux (Arthaud et Séguret, 1981 ; Roure et al., 1992 ; Séranne et al., 1995 ; Champion et al., 2000) :

1) La contraction Pyrénéo-Provençale N-S depuis l'Eocène moyen jusqu'à l'Oligocène inférieur,
2) Une extension NO-SE correspondant à l'ouverture du Golfe de Lion depuis l'Oligocène moyen jusqu'au Miocène inférieur,
3) La contraction alpine NE-SO du Miocène au Quaternaire.

A Boncavaï, la déformation s'est créée en extension durant l'ouverture du Golfe du Lion entre 100 et 300 m d'enfouissement (Ferry, 1997 ; Sallet, 2009 ; Ballas et al., 2013). Les clusters étudiés ont été formés en régime Andersonien normal. La plupart des bandes sont des bandes de compactions cisaillantes (CSB). Le site d'étude est localisé entre les failles normales de Montmout et Bollène liés à l'ouverture du Golfe du Lion (Saillet, 2009 ; Schultz et Soliva, 2012). A Saint Michel la déformation s'est créée durant la contraction Pyrénéo-Provençale à une profondeur comprise entre 0 et 200 m (Ferry, 1997) dans une zone où aucune faille n'est connue. Les clusters étudiés ont été formés en régime décrochant. La plupart des bandes sont des CSB. Le site de Boncavaï est sélectionné car il représente un bon exemple de localisation de la déformation en régime normal et à faible profondeur. De plus, certains rejets peuvent être identifiés, ce qui est rare dans les grès étudiés, souvent homogènes. A Bédoin, des études stratigraphiques locales et régionales permettent d'associer la déformation à la contraction Pyrénéo-Provençale et de contraindre la déformation à une profondeur de 0 à 200 m (Ferry, 1997 ; Saillet 2009). Les clusters étudiés ont été formés en régime décrochant. La majorité des bandes sont des CSB. Le site d'étude se trouve à la jonction entre trois failles majeures : la Faille de Nîmes sénestre-normale 10 km à l'ouest, la Faille de Salon-Cavaillon dextre-normale environ 10 km au sud et le chevauchement de la Faille Ventoux-Lure, localisée quelques kilomètres au nord. Les sites de Saint Michel et Bédoin sont choisis en raison du régime décrochant qu'ils exposent. Les clusters en régime décrochant sont peu décrits dans la littérature.

Le site Blankenburg se localise au nord-est des montagnes de Hartz (Allemagne), dans la partie sud-ouest du Bassin de Blankenburg. L'affleurement se situe sur une structure chevauchante sub-verticale et expose des grès quartzitiques cimentés se composant de dépôts deltaïques marins peu profonds (Voigt et al., 2004 ; French et al., 2012 ; Klimczack et Schultz, 2013). La porosité du grès avant la déformation était d'environ 30%. La partie sud-ouest du Bassin de Blankenburg a été plissée durant la contraction du socle de Hartz provoquant une déformation chevauchante du Coniacien au Campanien. Les clusters étudiés ont été formés en régime Andersonien inverse. La plupart des bandes sont des CSB. La déformation s'est formée entre 0 et 800 m d'enfouissement (Klimzack et Schultz, 2013). Ce site présente l'intérêt d'être à l'aplomb d'une faille inverse propagée à partir du socle dont on pourra comparer la potentielle influence dans la propagation de la déformation dans les grès.

Le site d'étude de Cummingston se situe sur la Moray Coast en Ecosse (UK). L'affleurement expose des grès quartzitiques éoliens légèrement cimentés. La porosité du grès avant la déformation était d'environ 30%. Le site est à proximité d'une faille majeure à une centaine de mètres au sud. Similairement aux nombreuses failles sismiques dans le Moray Firth, la déformation s'est probablement produite durant le rifting du durant tout le Jurassique à une profondeur d'environ 500 m (Underhill, 1991 ; Edwards, 1993 ; Glennie et Underhill, 1998 ; Quinn, 2005 ; Al-Hinaï et al., 2008).

Les clusters étudiés ont été formés en régime normal. La plupart des bandes sont des CSB. Comme le site de Boncavaï, le site de Cummingston offre un exemple satisfaisant de déformation en régime normal dans des grès relativement peu profonds et expose une grande surface d'affleurement (plusieurs centaines de mètres carrés). En outre, certains rejets sont identifiables.

Le site de Goblin Valley se situe dans le désert de San Rafael, dans la bordure sud du San Rafaell Swell en Utah (USA). Le site met à l'affleurement des grès de faciès éoliens et proximal très peu cimentés. Les grès peuvent contenir jusqu'à 20% de grains carbonatés. La porosité de la formation avant la déformation était d'environ 26%. La formation étudiée est majoritairement gréseuse et comprend de fins niveaux de silt et d'argile. La déformation a été formée en tectonique extensionnelle à partir l'Oligocène lié à l'extension des Basins and Ranges. Les clusters étudiés ont été formés en régime normal. La plupart des bandes sont des CSB. L'enfouissement au temps de la déformation est peu contraint et pourrait être de 1100 à 2000 m (Schultz et Fossen, 2002 ; Doelling et al., 2015). Le choix de ce site d'étude repose sur le fait qu'il offre une surface d'affleurement de plusieurs milliers de mètres carrés et présente des variations lithologiques qui nous permettront d'étudier plusieurs paramètres potentiellement influents sur la formation des clusters. Son enfouissement important lors de la formation des clusters en régime normal nous permettra de comparer les clusters formés sur ce site à ceux de Boncavaï et Cummingston.

Le site de Buckskin Gulch se situe à la frontière sud de l'Utah (USA), au sein du East Kaibab Monocline. Le site met à l'affleurement des grès éoliens très peu cimentés. La porosité des grès avant déformation était environ 34%. La zone de Buckskin Gulch a subi une déformation en contraction du Crétacé supérieur à l'Eocène pendant l'orogène Laramide. Les clusters étudiés ont été formés en régime inverse. La plupart des bandes sont des bandes de compaction cisaillante (SECB). L'enfouissement lors de la déformation est incertain et varie entre 1000 et 2600 m (Fossen et al., 2011 ; Doelling et Willis, 2006 ; Doelling, 2008). La sélection de ce site a été faite parce que la déformation à Buckskin Gulch n'est à priori pas liée à la propagation d'une faille sous-jacente. De surcroit, la zone d'étude présente un vaste affleurement (plusieurs milliers de mètres carrés).

3. Influence des variations lithologiques dans les formations à dominance gréseuses.

3.1. Objectifs et méthode

Nous avons rappelé que les grès forment des réservoirs classiques pour les hydrocarbures ou en tant qu'aquifère. Cependant, ces réservoirs étant rarement constitués exclusivement de grès poreux, il est important de comprendre l'interaction entre les différents processus de déformation induits par chaque lithologie et leur influence sur les roches de failles produites.

Dans ce chapitre, nous étudions deux sites d'étude qui présentent 3 zones de déformation cataclastique. Le premier site, Clashach Cove, correspond à une zone annexe non présentée précédemment située à proximité du site de Cummingston en Ecosse. Ce site met à l'affleurement deux grès superposés présentant deux lithologies différentes et décalées par une faille d'un rejet compris entre 20 à 50 m. La zone de faille présente la juxtaposition de plusieurs roches de failles. Ces roches de failles comprennent un fin cluster et une brèche oxydée. Le second site correspond au site

de Goblin Valley où les deux affleurements présentent des clusters faillés dans un intervalle sédimentaire incluant la présence des niveaux silteux ou argileux de quelques dizaines de centimètres d'épaisseur.

Une analyse structurale à échelle macroscopique et microscopique (microscopie optique, en cathodoluminescence froide (CL) et au microscope électronique à balayage en électrons rétrodiffusés (SEM-BSE)) nous permet d'examiner la nature des déformations, leur organisation dans l'espace et la chronologie de leur mise en place. Des tests de perméabilité sur site nous permettent d'estimer le potentiel impact des différents mécanismes de déformation sur les propriétés pétrophysiques des roches de failles formées.

3.2. Résultats

En accord avec les études précédentes, nous confirmons que le processus de cataclase se produit si les grès sont peu consolidés alors que la bréchification se produit dans des roches lithifiées et cohésives. A Clashach, nous montrons que la déformation s'est premièrement manifestée par la création d'un fin cluster de bandes de déformation cataclastiques (compactant) dans des grès peu consolidés. A cause des réductions de perméabilité fréquemment reportés dans la littérature et dans ce travail, nous déduisons que cette première étape de déformation a probablement induit un frein pour la migration des fluides au travers du cluster. Un enfouissement de 1,9 km en milieu aquifère a probablement fourni les conditions thermodynamiques pour la cimentation des grès tels qu'observés dans la partie inférieure du mur, durcissant et réduisant la perméabilité de la formation. Nous pensons que cette cimentation ainsi que la cimentation préférentielle du cluster ont permis la localisation d'une surface de glissement majeure (faille) sur l'éponte du cluster, ainsi que la formation d'une brèche entre le cluster et les grès peu lithifiés du toit. Le comportement dilatant de la bréchification est mis en évidence par l'oxydation intense de la brèche permise par la circulation de fluide le long de la faille.

A Goblin Valley, nous confirmons que le processus de cataclase est possible jusqu'à une profondeur d'au moins 1,1 km, pourvu que le grès soit peu lithifié. Nous montrons que la présence d'un fin niveau de matériel comprenant des minéraux fragiles comme des phyllosilicates suffit à provoquer un mécanisme de « smearing ». Notre étude suggère que ce smearing inhibe le processus de cataclase responsable de l'épaississement des clusters dans les grès sous- et sus-jacents lorsque les grès sont juxtaposés contre ces niveaux. Au contraire, ce smearing semble être à l'origine de l'initiation d'une surface de glissement majeure (faille) au contact du cluster décalé contre le niveau fragile, et de sa propagation dans le cluster dans les grès sous- et sus-jacents. Des rejets de quelques mètres sont suffisants pour initier le passage à la faille. Dans le cas de ce site, la faible perméabilité des argiles ou des silts combinée à la faible perméabilité des surfaces de faille dans les clusters (<1 mD) semble fournir des conditions défavorables à la migration de fluide au travers des structures faillées.

L'étude de ces deux sites nous montre donc que l'évolution de la déformation de formations à dominance gréseuse peut être à l'origine de la création et superposition de roches de failles distinctes au cours de l'évolution de la déformation. Ces évolutions de constitution du cœur de faille semblent responsables d'une forte anisotropie de perméabilité dans le temps et l'espace, influençant

la migration des fluides de manière variable. De plus ces contrastes lithologiques peuvent permettent le passage à la faille.

4. Les clusters de bandes de déformation cataclastiques dans les gés poreux - développement et implication pour la migration des fluides

4.1. Objectif et Méthode

Cette section représente une partie clé du travail de thèse puisqu'elle présente l'étude intégrative des sept sites d'étude sélectionnés pour la variété de leurs paramètres. Nous nous attachons ici à comprendre l'influence jusqu'ici mal comprise du chargement tectonique, du régime Andersonien, de l'enfouissement et de la granulométrie des grès dans les processus de formation des clusters et de la morphologie qui en résulte.

L'étude de la morphologie des clusters est permise par la mesure cartographique de la dimension latérale des clusters, une étude structurale de leur interaction, du régime Andersonien dans lequel ils ont été formés et de leur épaisseur. L'étude de l'épaisseur des clusters comprend la mesure de densité de bande en présence ; la densité de bande correspond à l'épaisseur cumulée de bande (mesuré à la règle) divisée par l'épaisseur du cluster. Des mesures de perméabilité sur le terrain permettent, en complément des données déjà disponibles dans la littérature, d'estimer l'influence des clusters sur les fluides. Une étude microscopique en CL et SEM-BSE nous permet via l'analyse d'images d'évaluer la porosité, le tri, le degré de cataclase et de compaction du matériel déformé par rapport à la roche hôte, ainsi que la forme des clasts. Une étude analytique complémentaire nous permet de faire le lien entre les types de tectoniques connus pour chaque site (contraction ou extension), le chargement tectonique correspondant et les régimes Andersoniens (normal, décrochant ou inverse). Associée à l'enveloppe de rupture des grès, cette approche analytique permet d'estimer l'évolution des contraintes jusqu'à la rupture correspondant à la formation d'un cluster.

4.2. Résultats

En accord avec les précédentes études de Soliva et al. (2013) et Ballas (2013) concernant la déformation cataclastique en générale, nous montrons que la morphologie des clusters dépend essentiellement du chargement tectonique. Une tectonique extensionnelle (chargement en tension) favorise la localisation de clusters en régime Andersonien normal. Ces clusters sont d'épaisseur fine à moyenne. Lorsqu'ils sont fins (10 - 30 cm), ces clusters montent une densité de bande élevée (0.30-0.70) ; lorsqu'ils sont d'épaisseur moyenne (jusqu'à 70 cm), ils montrent des densités de bande plus faibles. Dans tous les cas, les clusters formés en régime normal montrent des degrés de cataclase moyens (11 - 16%) et des taux de compaction moyens (12 - 18%). L'épaississement de ces clusters et leur densité de bande n'est pas corrélé avec la présence d'une surface de faille. Sur les sites où les grès sont exposés sur plusieurs centaines de mètres carrés, nous voyons que ces clusters ont fréquemment des longueurs de plusieurs centaines de mètres, peuvent se connecter sous forme de

relais, pouvant ainsi former des réseaux denses de plusieurs kilomètres de long à proximité de failles majeures.

Une tectonique en contraction (chargement transpressif pouvant se rapprocher de la compression pure) favorise la formation de clusters en régime décrochant et inverse. Les clusters formés en régime décrochant présentent des épaisseurs variables (10 - 100 cm), associées à des densités de bande également variables (0.20 - 0.55). Ces densités sont plus faibles que celles observées dans le cas des clusters fins créés en régime normal. Les clusters formés en régime décrochant montrent des degrés de cataclase élevés (18 - 33%) et des taux de compaction importants (26 - 32%). Aucune surface de glissement majeure n'est observée. Bien que la superficie des sites observés soit restreinte, les clusters formés en régime décrochant semblent plutôt épars. Les clusters formés en régime inverse présentent dans le cas de Blankenburg une morphologie ressemblante aux clusters formés en régime décrochant. Ils montrent un degré de cataclase moyen (18%) et un taux de compaction moyen (17%). Dans le cas de Buskskin Gulch, les clusters formés peuvent avoir des épaisseurs considérables (>100 cm) mais montrent un degré de cataclase faible (3%) et un taux de compaction moyen (22%). A Buckskin Gulch, où la zone d'étude expose les grès sur plusieurs centaines de mètres carrés, nous voyons que les clusters formés en régime inverse ont le plus fréquemment des longueurs maximum de quelques dizaines de mètres ; de plus, ils sont épars.

Le matériel déformé entre les bandes décrit des « lentilles » plus perméables que les bandes. Nous montrons que, dans tous les régimes tectoniques, ces lentilles sont plus allongées dans le plan de cisaillement qu'hors du plan de cisaillement, mettant en avant l'aspect ondulé des bandes telles qu'observées en section hors du plan de cisaillement.

L'analyse microstructurale nous permet d'observer que l'évolution de la déformation (associée à l'augmentation du degré de cataclase) provoque l'appauvrissement du tri de la population de clast. En conséquence, la porosité dans le matériel déformé est également réduite. En particulier, nous montrons que, pour un même degré de cataclase, la compaction du matériel déformé entre les bandes et dans les bandes des clusters formés en régime inverse est plus importante qu'en régimes normal et décrochant. De plus, nous voyons que, pour tous les régimes, la forme moyenne d'une population de clast évolue avec le degré de cataclase. Les clast deviennent rugueux/anguleux à l'initiation de la déformation (faible degré de cataclase), puis s'arrondissent légèrement avec l'augmentation du degré de cataclase sans redevenir aussi arrondis que les grains de la roche hôte. Après un certain seuil de cataclase (35%) la forme moyenne des clasts semble ne plus évoluer de manière significative. L'important taux de compaction dans les bandes et la rugosité/angulosité des clasts confirme le durcissement de ces dernières et donc l'impossibilité d'accommoder plus de déplacement. La plus faible compaction du matériel déformé dans les régimes Andersoniens normal et décrochant par rapport au matériel déformé en régime inverse suggère la présence de plans de faiblesse à proximité des bandes préexistantes (faible nombre de contact entre les particules les rendant moins résistantes à la contrainte). Ces plans de faiblesse pourraient expliquer la plus forte densité de bande dans les clusters en régime normal et décrochant. En régime inverse, la plus forte compaction garantirait l'absence de plan de faiblesse et favoriserait la distribution des bandes.

5. Diagenèse des clusters

5.1. Objectif et Méthode

Nous rappelons que l'évolution diagénétique des clusters pour des enfouissements inférieurs à 2 km est très peu décrite. En particulier, la potentielle cimentation des structures cataclastiques de ces clusters telle que reportée pour des profondeurs supérieures à 2 km est peu connue. Celle-ci pourrait pourtant induire des altérations non négligeables des propriétés pétrophysiques des clusters et influencer les processus de déformation en jeu dans la formation des clusters.

Dans ce chapitre, nous menons une étude structurale à échelle macroscopique intégrant une analyse du profil d'altération (analyses de diffraction des poudres au rayon X – XRD), et à échelle microscopique (au microscope optique en lumière naturelle, polarisée, en CL, en SEM-BSE) afin de caractériser la potentielle influence de la cataclase sur la cimentation.

Nous menons une analyse détaillée sur les clusters du site de Bédoin qui a la particularité de présenter des structures tabulaires intensément cimentées en quartz dans les grès hôtes. Nous complétons cette analyse par des observations de même type entreprises pour les six autres sites d'étude.

5.2. Résultats

Dans le cas du site de Bédoin, nous montrons que l'intense cimentation tabulaire de corps de roche hôte correspond à des silcrètes, et est liée à des variations de niveau du toit de l'aquifère. Cette cimentation développée avec une géométrie automorphe est possible à faible profondeur pour des températures inférieures à 80°C.

Les clusters présentent également des zones cimentées sous forme de bordures cimentées de 10 à 50 µm d'épaisseur autour des clasts. Nous montrons que plus le degré de cataclase est important, plus la cimentation est importante dans le matériel déformé. La cimentation est favorisée par le grand nombre de surfaces fraiches créées lors de la cataclase et sur lesquelles la nucléation du quartz est catalysée. Les ciments de quartz sont de nature similaire à certaines générations de ciment observées dans les silcrètes. Cependant, leur géométrie scellant les clasts suggère une mode de précipitation synchrone ou quasi synchrone à la déformation cataclastique, décrit comme du « self-healing » dans la littérature. Ce processus ne requiert pas de source extérieure de silice pour la précipitation des ciments et utilise la concentration de silice mise en solution lors de la déformation comme principale source de silice. Bien que la cimentation en quartz soit envisagée dans la littérature pour des températures froides (20 - 40°C selon les sources) et pour des temps longs et à de faibles concentrations de silice en solution, l'absence de figure de pression-solution dans la roche hôte suggère que ce mode de précipitation est peu probable.

Le même constat d'une cimentation efficace des parties les plus cataclastiques des clusters (les bandes, mais aussi parfois les espaces entre les bandes) sans la présence nécessaire de pression-solution dans les roches hôtes pour les sites enfouis à des profondeurs maximum de 800 m indique que la cimentation des clusters à faible profondeur est commune. Cette observation est fondamentale puisqu'elle indique que cette diagenèse provoque la réduction de porosité (et

probablement de perméabilité) des clusters. De plus, si la cimentation se fait de manière contemporaine au développement de cluster, le contraste lithologique produit pourrait favoriser le passage à la faille tel qu'introduit précédemment.

6. Modélisation numérique

6.1. Objectif et Méthode

Dans le but de mieux comprendre l'influence des processus physiques impliqués dans la formation des clusters, nous réalisons une étude paramétrique au travers de modélisations numériques simulant la rupture inélastique en régime Andersonien normal. Dans cette modélisation numérique, nous souhaitons simuler pour la première fois la formation des clusters.

La modélisation est réalisée via le logiciel Flac3D basé sur la méthode des éléments finis. Le modèle constitutif utilisé correspond à Drucker-Prager afin de prendre en compte l'influence des trois contraintes principales lors de la rupture en cisaillement inélastique. Les paramètres définissant les propriétés physiques du modèle utilisent des paramètres typiques du type de grès poreux étudiés sur le terrain. Les paramètres testés sont le coefficient de friction interne α, la contrainte de cisaillement équivalente de Von Mises $\bar{\tau}$ qui à contrainte effective et a constants exprime la cohésion κ, et le facteur de dilatance β. Trois valeurs de α sont testées (0,6 ; 0,7 ; 0,8) et correspondent à des valeurs typiques pour une rupture en régime normal. Les cinq fonctions étudiées de $\bar{\tau}$ évoluant avec la déformation cisaillante inélastique $\bar{\gamma}^p$ sont basées sur des comportements observés lors d'expériences de déformation de matériaux granulaires en presse triaxiale. Il en va de même pour une fonction principale de β évoluant avec $\bar{\gamma}^p$ à partir de laquelle nous testons deux fonctions alternatives supplémentaires. Nous étudions aussi l'influence de la taille et de la résolution du modèle.

6.2. Résultats

L'étude de l'évolution de κ avec $\bar{\gamma}^p$ montre que le processus d'épaississement localisé exprimant le mieux la formation de cluster est permise lorsque la cohésion ne cesse d'augmenter dans le matériau déformé avec l'augmentation du taux de déformation. Dans ce cas, de par la localisation et l'épaississement de bandes localisées, le modèle présente une organisation de la déformation très similaire à certains clusters observés sur le terrain. La formation de quelques bandes conjuguées est possible. Au contraire, si la cohésion vient à diminuer (même légèrement) après un certain seuil de $\bar{\gamma}^p$, la localisation tend à se localiser pour former une unique fine bande de très faible cohésion et dont la morphologie ressemble d'avantage à une surface de faille.

L'étude de l'évolution de β avec $\bar{\gamma}^p$ montre que le meilleur comportement de dilatance pour former une déformation ressemblant à un cluster correspond à un β initialement négatif qui augmente rapidement pour devenir positif lors d'une première phase d'évolution de $\bar{\gamma}^p$, puis régresse pour redevenir faiblement négative avec l'augmentation de $\bar{\gamma}^p$. Nous constatons qu'imposer β = 0 à partir d'un certain seuil de $\bar{\gamma}^p$ n'influence pas la géométrie de la déformation créée. Cette alternative ne fait qu'empêcher la compaction dans les bandes, ce qui n'est pas un modèle réaliste à la lumière des observations de terrain.

Nous voyons aussi dans le cas où nous testons une déformation à dilatance nulle que la déformation peut aussi s'épaissir à partir d'une seule bande pour former une sorte de cluster, mais dont la morphologie se rapproche moins de celle des clusters observés sur le terrain.

Nous constatons qu'une faible valeur de α (α = 0.6) a pour conséquence de générer un épaississement quasi continu à partir d'une ou deux bande dans l'espace du modèle, ne permettant pas à des bandes conjuguées de se former. La déformation semble rapidement saturer le modèle. Les modèles avec α = 0.7 correspondent aux modèles formant les structures les plus ressemblantes aux clusters précédemment discutés. Une plus haute valeur de α (α = 0.8) favorise la distribution de la déformation sous forme de fines bandes conjuguées et distribuées dans le modèle.

Finalement, nous constatons que dans la mesure où la résolution du modèle ne change pas par rapport à sa taille, l'organisation de la déformation est semblable à celle obtenue pour des modèles de taille différente. En revanche, pour une taille fixe, la résolution du modèle impacte l'évolution et l'organisation de la déformation : il semble que les bandes soient plus fines et plus distribuées sur des modèles plus résolus.

7. Discussion et conclusions

7.1. Influence de l'état de contrainte et de la lithologie sur le processus de développement des clusters

L'approche analytique de l'évolution des contraintes suggère que la position de rupture sur l'enveloppe de rupture des grès pourrait être un paramètre déterminant dans la morphologie et la densité de bande des clusters formés, à l'instar de la distribution des différents types de bande observés en test triaxiaux (compilation de Wong et al., 1997 ; Baud et al., 2000, 2004 ; Klein et Reushlé, 2004 ; Baud et al., 2006 ; Tembe et al., 2008 ; Rutter et Glover, 2012). En conséquence, puisque la forme de l'enveloppe de rupture dépend de la lithologie du grès (taille de grain et de la porosité - Zhang et al., 1990 ; Wong et al., 1997), l'influence de l'état de contrainte devrait être considérée en association avec la lithologie des grès pour anticiper la morphologie de la déformation. Dans cette hypothèse, la morphologie des formations étudiées, à part le cas de Blankenburg à l'aplomb d'une faille de socle, montre que les clusters formés en tectonique extensionnelle (favorisant un régime de contrainte Andersonien normal) sont souvent provoqués par une rupture à gauche de la partie cassante de l'enveloppe de rupture. Les clusters formés en tectonique en contraction (favorisant des régimes décrochants et inverses) sont plutôt provoqués par une rupture sur la partie cassante de l'enveloppe et vers son sommet pour les clusters formés en régime décrochant, et sur la partie ductile (proche du sommet) pour les clusters formés en régime inverse. Tel qu'indiqué par Ballas (2013) et Soliva et al. (2013), une rupture dans la partie plus à droite de la partie ductile (systématiquement atteinte en tectonique en contraction et correspondant à un régime inverse), provoque une déformation distribuée sous forme de réseaux de bandes conjuguées distribuées dans les grès.

Dans le but de mieux comprendre le processus de développement des clusters, nous avons étudié l'arrangement de la déformation à échelle microscopique. Nous avons montré que la cataclase provoque une réduction du tri du matériel déformé, directement responsable d'une

meilleure compaction, maximum dans les bandes. Des auteurs tels que Arzt (1982) montrent qu'une meilleure compaction du matériel est corrélée avec un plus grand nombre de contacts inter-particulaires. Nous avons aussi montré que la cataclase induit une augmentation de l'angulosité moyenne des clasts, ce qui implique une augmentation de la friction du matériel (ex. Mair et al., 2002 ; Cho et al., 2006 ; Guo et Morgan, 2006; Estrada et al., 2011 ; Azéma et al., 2012). La combinaison d'une friction importante et d'un grand nombre de contacts inter-particulaires dans les bandes indique que celles-ci sont cohésives (durcies). Cette déduction est cohérente avec l'hypothèse il y a longtemps formulée par Aydin et Johnson (1978) et aussi observée de manière expérimentale par Kaproth et al., (2010) d'une évolution de la déformation liée au durcissement. En revanche, le durcissement des bandes est en désaccord avec le modèle de Nicol et al. (2013) proposant des bandes susceptibles d'accommoder plusieurs phases de déformation. Nos modèles numériques simulant une rupture en régime normal montrent que la cohésion exerce une influence importante sur l'organisation de la déformation, impliquant notamment un meilleur regroupement des bandes lorsque la cohésion augmente avec le taux de déformation. Au contraire, une cohésion réduite avec le taux de déformation mène à la localisation d'une seule et fine bande ressemblant à une surface de glissement.

L'étude microscopique de la déformation dans les clusters indique aussi que l'arrangement du matériel déformé influence le processus de distribution de la déformation et, au final, la morphologie des clusters formés en fonction du chargement tectonique, et donc du régime Andersonien. Le matériel déformé en régime normal et décrochant montre, pour le même degré de cataclase, moins de compaction que dans le matériel déformé en régime inverse. Ce résultat implique que le nombre de contacts inter-particulaires est moindre dans en régime normal et inverse, représentant des contacts moins résistants à la contrainte (Iwashita et Oda, 2000). Bien que nous n'observions pas directement de dilatance entre les bandes de clusters échantillonnés, les tests expérimentaux montrent de la dilatance en bordure des bandes dans des conditions à faible pression de confinement comparable à un régime de contrainte normal (Mas and Chemenda, 2015; Tran, 2016). Dans des conditions similaires de chargement, des plans de dilatance sont aussi mis en évidence dans des modèles granulaires de déformation élastique et provoquent l'augmentation des contraintes aux contacts inter-particulaires (ex. Iwashita and Oda, 2000; Taboada et al., 2005; Estrada et al., 2008). Pour ces raisons, nous pensons que le plus faible nombre de contacts inter-particulaires dans le matériel déformé entre les bande des clusters formés en régimes normal et inverse est responsable de la localisation rapprochée des bandes telles que proposé par Anthony et Marone (2005). Dans la même logique, l'épaississement des bandes vers les bordures dilatantes est bien montré dans nos modèles numériques. La plus forte compaction du matériel déformé entre les brins en régime inverse est cohérente avec les modèles granulaires simulant, dans des conditions similaires de chargement, une déformation élastique sans plan de dilatance et avec un important nombre de contacts inter-particulaires (Estrada et al., 2008). Cet important nombre de contacts inter-particulaires semble prohiber la formation de nouvelles bandes à côté d'anciennes et suggère le report de la localisation de nouvelles bandes vers un matériel encore peu déformé (i.e. la roche hôte). L'expression de ces mécanismes explique probablement la création de clusters plutôt fins et à forte densité de bande en régime normal et décrochant, et une déformation plus distribuée en régime inverse.

7.2. Passage à la faille

Nous avons montré que, en régime normal, un moyen de créer une surface de faille consiste à juxtaposer des grès poreux à une lithologie indurée telle que des grès cimentés, ou une lithologie fragile telle que des roches riches en phyllosilicate. La localisation préférentielle du cisaillement en présence de minéraux fragiles est en accord avec de précédentes études (Byerlee, 1978; Logan and Rauenzahn, 1987; Underhill and Woodcock, 1987; Collettini et al., 2009). Cette juxtaposition permet l'initiation et la propagation d'une surface de faille à l'intérieur ou sur l'éponte des clusters dans les grès poreux adjacents. Dans le cas d'une juxtaposition de grès contre des lithologies fragiles, un rejet de 2 m est suffisant pour initier et propager une surface de faille. Ce mécanisme explique l'absence de corrélation entre l'épaisseur des clusters observés (et la densité de bande), et la présence d'une surface de glissement en leur sein. L'absence de tels contrastes lithologiques dans les grès déformés en régime décrochant et inverse empêche de conclure que les clusters formés dans ces régimes ne sont pas faillés à cause de l'absence de ces contrastes.

7.3. Diagenèse

Nous avons montré que la cimentation affecte communément les clusters enfouis à faibles profondeurs (<800 m) dans leur partie les plus déformés (les plus cataclastiques), correspondant souvent aux bandes. Cette cimentation est possible en milieu aquifère à faible température. Ces observations comblent une absence d'information sur la diagenèse des clusters pour des profondeurs inférieurs à 1 km, limite au-delà de laquelle la cimentation des structures cataclastiques est bien étudiée (ex. Fisher et Knipe, 1998 ; Milliken et al., 2005). La cimentation réduit la porosité des clusters, et probablement leur perméabilité. Le cas d'une cimentation par « self-healing » impliquerait un durcissement quasi-synchrone à la déformation et modifierait probablement le processus d'épaississement des clusters.

7.4. Implications pour la migration des fluides

Les clusters décrits en régime Andersonien normal (favorisé par une tectonique en extension) semblent se former avec une rupture sur la gauche de la partie cassante de l'enveloppe de rupture et sont composés principalement de CSB, mais aussi, potentiellement, de surface(s) de faille dont les perméabilités varient de $3x10^{2}$ to $5x10^{-1}$ mD. Ces clusters sont longs, forment des réseaux denses de plusieurs kilomètres de long à proximité de failles majeures. De plus, leur degré de cataclase étant souvent important dans les bandes, ils seront potentiellement cimentés. De fait, ils sont susceptibles de former de véritables freins ou barrières pour les fluides à proximité d'une faille majeure.

Les clusters décrits en régime décrochant (favorisés par une tectonique en contraction) semblent se former avec une rupture sur la partie cassante de l'enveloppe de rupture et sont essentiellement composé de CSB dont la perméabilité varie de $4x10^{0}$ à $4x10^{1}$ mD. Ces clusters ont des épaisseurs et des densités de bande moyennes. Parce que ces clusters sont épars, ils ne représentent pas de barrières ou de freins importants pour la migration des fluides à l'échelle du réservoir.

Basé sur le seul exemple de Buckskin Gulch, nous déduisons que les clusters ou réseaux de bandes de déformations distribuées sont générés lorsque l'état de contrainte atteint l'enveloppe de rupture du grès sur sa partie ductile (plus probablement atteinte en régime inverse induit par une tectonique en compression). Les bandes de déformation composant ce type de cluster correspondent à des SECB dont la perméabilité varie de $3x10^{1}$ à $3x10^{2}$ mD. Ces clusters sont épais avec une faible densité de bandes ; ils sont courts et épars. En conséquence, nous estimons qu'ils n'affectent pas particulièrement l'écoulement des fluides dans les réservoirs.

Résumé

La cataclase est un processus de déformation efficace en termes de réduction de porosité et de perméabilité dans les grès poreux, constituant des aquifères et réservoirs d'hydrocarbures classiques. Un enjeu majeur concernant la déformation dans les grès consiste à identifier les processus contrôlant l'évolution des structures cataclastiques et reconnaitre les paramètres influençant l'expression de la déformation à l'échelle microscopique et à l'échelle du bassin.

Dans cette étude, nous nous concentrons sur l'analyse structurale des amas (« clusters ») de bande de déformation cataclastiques afin de considérer une déformation suffisamment localisée représentant un potentiel rôle de barrière sur les fluides. Nous choisissons sept sites d'étude présentant des clusters formés en tectonique extensive et contractive, dans différent régimes Andersoniens, à différentes profondeurs d'enfouissement, et dans des grès aux lithologies variées. Nous utilisons une approche analytique afin d'estimer l'évolution de l'état de contrainte des grès jusqu'à la déformation. L'utilisation de modèles numériques permet d'analyser l'influence de certains paramètres physiques sur la structuration de la déformation.

Nous montrons que la position de l'enveloppe de rupture du grès (dépendant de sa lithologie) semble déterminer la morphologie de la déformation. D'autre part, les clusters formés en régimes Andersoniens normal, décrochant et inverse semblent respectivement couramment se former sur la même partie de l'enveloppe.

Les clusters formés en régime normal montrent des épaisseurs fines à moyennes, des densités de bande importantes et forment, avec d'autres clusters, des réseaux d'échelle kilométrique souvent localisés à proximité d'une faille majeure. Ils représentent une barrière potentielle pour les fluides. Les clusters formés en régime décrochant ont des épaisseurs et des densités de band moyennes. Parce qu'ils semblent éparses, ces clusters ne forment probablement aucun frein pour les fluides. Les clusters formés en régime inverse ont des épaisseurs et des densités de bande moyennes si la rupture est atteinte sur la partie fragile de l'enveloppe. Ils semblent potentiellement plus épais avec des densités de bands faibles voire deviennent de simples réseaux de bandes distribuées si l'enveloppe de rupture est atteinte sur sa partie ductile. Parce qu'ils sont courts et éparses, ces clusters ne représentent pas de frein pour les fluides.

Nous relions le développement des clusters et leur morphologie à l'agencement microscopique des clasts dans le matériel déformé. La faible compaction du matériel déformé des clusters créés en régimes normal et décrochant semble être à l'origine de l'étroite localisation des bandes à cause de la présence de plans de faiblesse dans le matériel déformé. Pour le même degré de déformation, la compaction plus élevée du matériel en régime inverse favoriserait la distribution des bandes.

Le passage à la faille tel qu'observé dans les clusters en régime normal est permis par la présence entre les grès de niveaux incluant des minéraux fragiles. Ces niveaux permettent l'initiation et la propagation d'une surface de glissement majeure dans les grès adjacents. L'initiation d'une faille est aussi favorisée lorsque des grès poreux sont juxtaposés contre une lithologie indurée.

Notre étude montre que la cimentation de quartz des parties les plus déformées des clusters est fréquente, même dans le cas de clusters ayant été enfouis à des profondeurs inférieures à 800 m. Cette cimentation est catalysée par l'intense degré de cataclase, semble être précipitée par « self-healing » et altère les propriétés pétrophysiques des clusters.